

MATERIALS
RESEARCH
SOCIETY
SYMPOSIUM PROCEEDINGS

VOLUME 360

Materials for Smart Systems

EDITORS

Easo P. George

Sadayuki Takahashi

Susan Trolier-McKinstry

Kenji Uchino

Marilyn Wun-Fogle



This document has been archived
for public release and sale. No
restriction is indicated.

Materials for Smart Systems

Accession For	
NTIS CRA&I	<input checked="" type="checkbox"/>
DTIC TAB	<input type="checkbox"/>
Unannounced	<input type="checkbox"/>
Justification	
By	
Distribution /	
Availability Codes	
Dist	Avail and/or Special
A-1	

19950608 145

Materials for Smart Systems

Symposium held November 28-30, 1994, Boston, Massachusetts, U.S.A.

EDITORS:

Easo P. George

Oak Ridge National Laboratory
Oak Ridge, Tennessee, U.S.A.

Sadayuki Takahashi

NEC Corporation
Kawasaki, Kanagawa, Japan

Susan Troler-McKinstry

Pennsylvania State University
University Park, Pennsylvania, U.S.A.

Kenji Uchino

Pennsylvania State University
University Park, Pennsylvania, U.S.A.

Marilyn Wun-Fogle

Naval Surface Warfare Center
Silver Spring, Maryland, U.S.A.



MATERIALS RESEARCH SOCIETY
Pittsburgh, Pennsylvania

This work was supported in part by the Army Research Office under Grant Number DAAH04-95-1-0033. The views, opinions, and/or findings contained in this report are those of the author(s) and should not be construed as an official Department of the Army position, policy, or decision, unless so designated by other documentation.

This work was supported in part by the Office of Naval Research under Grant Number N00014-95-1-0014. The United States Government has a royalty-free license throughout the world in all copyrightable material contained herein.

Single article reprints from this publication are available through
University Microfilms Inc., 300 North Zeeb Road, Ann Arbor, Michigan 48106

CODEN: MRSPDH

Copyright 1995 by Materials Research Society.
All rights reserved.

This book has been registered with Copyright Clearance Center, Inc. For further information, please contact the Copyright Clearance Center, Salem, Massachusetts.

Published by:

Materials Research Society
9800 McKnight Road
Pittsburgh, Pennsylvania 15237
Telephone (412) 367-3003
Fax (412) 367-4373

Library of Congress Cataloging in Publication Data

Materials for smart systems : symposium held November 28-30, 1994, Boston, Massachusetts, U.S.A. / editors, Easo P. George, Sadayuki Takahashi, Susan Troler-McKinstry, Kenji Uchino, Marilyn Wun-Fogle.
p. cm.—(Materials Research Society symposium proceedings, ISSN 0272-9172 ; v. 360).

Includes bibliographical references and index.

ISBN 1-55899-261-8 (alk. paper)

1. Smart materials—Congresses. 2. Detectors—Materials—Congresses.
3. Ferroelectric devices—Materials—Congresses. 4. Magnetostrictive transducers—Materials—Congresses. 5. Thin film devices—Materials—Congresses.
6. Shape memory effect—Congresses. I. George, Easo P. II. Takahashi, Sadayuki III. Troler-McKinstry, Susan IV. Uchino, Kenji V. Wun-Fogle, Marilyn
- VI. Series: Materials Research Society symposium proceedings ; v. 360.

TA418.9.S62M38 1995
620.1'1—dc20

95-1796
CIP

Manufactured in the United States of America

Contents

PREFACE	xi
ACKNOWLEDGMENTS	xiii
MATERIALS RESEARCH SOCIETY SYMPOSIUM PROCEEDINGS	xiv

PART I: FERROELECTRIC ACTUATORS

ELECTRICALLY-INDUCED STRAINS IN Sn-MODIFIED LEAD ZIRCONATE TITANATE	3
Jie-Fang Li, Xunhu Dai, Donald Forst, and Dwight Viehland	
FERROELECTRIC BEHAVIOR AND MICROSTRUCTURE OF CALCIUM- MODIFIED LEAD TITANATE CERAMICS	9
Zhiqiang Zhuang, G.A. Kulesha, H. Du, and B. Gallois	
MEASURING METHODS FOR HIGH-POWER CHARACTERISTICS OF PIEZOELECTRIC MATERIALS	15
Seiji Hirose, Sadayuki Takahashi, Kenji Uchino, Manabu Aoyagi, and Yoshiro Tomikawa	
*FERROELECTRIC DOMAIN INVERSION IN LiNbO_3 AND ITS APPLICATION TO HIGH-PRECISION PIEZOELECTRIC ACTUATORS	21
Kiyoshi Nakamura and Ken Yamada	

PART II: FERROELECTRIC COMPOSITES

*COMPOSITE PIEZOELECTRIC SENSORS AND ACTUATORS	33
R.E. Newnham, J.F. Fernandez, K.A. Markowski, J.T. Fielding, A. Dogan, and J. Wallis	
FABRICATION AND CHARACTERIZATION OF BARIUM STRONTIUM TITANATE AND NON-FERROELECTRIC OXIDE COMPOSITES	45
E. Ngo, S. Stowell, L.C. Sengupta, M.E. O'Day, and R. Lancro	

PART III: FERROELECTRIC SENSORS AND ACTUATORS

*THE DYNAMICS OF SAW STREAMING AND ITS APPLICATION TO FLUID DEVICES	53
Showko Shiokawa and Yoshikazu Matsui	
*PIEZOELECTRIC-CERAMIC CYLINDER TYPE VIBRATORY GYROSCOPE	65
T. Yoshida	
Ba/Sr DOPED ELECTROSTRICTIVE COMPOSITIONS FOR ACTUATOR DESIGN	77
Zhiqiang Zhuang, Lijun Jan, S.B. Kang, B. Gallois, Z. Yang, and H. Du	
STRESSES NEAR THE END OF AN INTERNAL ELECTRODE IN MULTILAYER ELECTROSTRICTIVE CERAMIC ACTUATORS	83
Xiao-Yan Gong	

*Invited Paper

PART IV: OPTICAL SYSTEMS

USING DX CENTERS TO WRITE ERASABLE METALLIC PATTERNS IN AlGaAs	91
Tineke Thio, R.A. Linke, G.E. Devlin, J.W. Bennett, J.D. Chadi, R.L. MacDonald, and M. Mizuta	
A DYE-DISPERSED LIQUID CRYSTAL SMART REFLECTOR	97
Ching-Chao Chang, Franklin Lonberg, and Robert B. Meyer	
FABRICATION OF THICK, SOL GEL PZT FILMS: APPLICATIONS TO MACROSCOPIC PIEZOELECTRIC DEVICES	103
D.A. Barrow, T.E. Petroff, and M. Sayer	
*ON THE USE OF ELECTROSTRICTIVE ACTUATORS IN RECOVERING THE OPTICAL PERFORMANCE OF THE HUBBLE SPACE TELESCOPE	109
James L. Fanson	
NEURAL NETWORK PROCESSING OF OPTICAL FIBER SENSOR SIGNALS FOR IMPACT LOCATION	121
Paul M. Schindler, John K. Shaw, Russell G. May, and Richard O. Claus	
DIELECTRIC, PYROELECTRIC, AND THERMAL PROPERTIES OF SOLID SOLUTIONS OF Ba(Ti,Zr)O ₃ , Ba(Ti,Hf)O ₃ , Ba(Ti,Sn)O ₃ AND (Ba,Nd)TiO ₃	127
K.K. Deb	

PART V: CHARACTERIZATION AND MODELLING

XPS STUDY OF Ni-Fe MANGANITE THERMISTOR MATERIAL	139
D.N. Braski, N.R. Osborne, and J.M. Zurbuchen	
THERMO-ELECTRIC PROPERTIES OF THIN-FILM REFRACTORY METAL THERMOCOUPLES	145
Robert G. Schinazi, Guo-Quan Lu, and Frans Spaepen	
MODELLING OF POLYDOMAIN SMART MATERIALS	151
Yongsik Yu and Alexander Roytburd	
OPTICAL NON-INVASIVE EVALUATION OF FERROELECTRIC FILMS/MEMORY CAPACITORS	157
Sarita Thakoor, A.P. Thakoor, and L. Eric Cross	

PART VI: MAGNETOSTRICTIVE MATERIALS AND APPLICATIONS

*HIGH POWER MAGNETOSTRICTIVE MATERIALS FROM CRYOGENIC TEMPERATURES TO 250 C	171
Arthur E. Clark	
STUDY OF BOUNDARY FREE Tb-Dy-Fe MAGNETOSTRICTIVE MATERIALS	183
Qiang Li, Y.L. Chang, Shixi Ouyang, and R.Z. Yuan	
TEM STUDY OF TWINNING AND MAGNETIC DOMAINS IN TERFENOL-D	189
Jennifer Dooley and M. De Graef	
THERMO-MECHANICAL PROPERTIES OF TERFENOL-D THIN FILMS	195
Quanmin Su, Y. Zheng, and Manfred Wuttig	
*AMORPHOUS MAGNETOELASTIC MATERIALS	201
H.T. Savage and Marilyn Wun-Fogle	

*Invited Paper

MAGNETOMECHANICAL PROPERTIES OF CIRCUMFERENTIALLY-FIELD- ANNEALED METGLAS® 2605SC CYLINDERS	213
J.B. Restorff, M. Wun-Fogle, A.E. Clark, and Thu-Van T. Luu	
*MATERIAL PROPERTIES AND RELATED CONSIDERATIONS FOR MAGNETOMECHANICAL SENSING DEVICES	219
Ivan J. Garshelis	
*MAGNETOSTRICTIVE METHODS OF DETECTING TORQUE FROM CASE- HARDENED STEEL SHAFTS	231
Ichiro Sasada	
HIGH PRECISION ACTUATOR WITH Tb _{0.27} Dy _{0.73} Fe _{1.95} SINGLE CRYSTAL	243
Qiang Li, Y.L. Chang, Shixi Ouyang, and X.H. Huang	
MAGNETOSTRICTIVE MOTOR DEVELOPMENT	249
Joseph P. Teter and John E. Miesner	
A NEW SUPERFLUID LEAK TIGHT LOW TEMPERATURE VALVE USING A MAGNETOSTRICTIVE ACTUATOR	253
Inseob Hahn, M. Barmatz, and A. Clark	
ULTRASONIC APPLICATIONS USING MAGNETOSTRICTIVE SMART MATERIALS	259
T. Toby Hansen and Solomon R. Ghorayeb	
DYNAMIC SHEAR CHARACTERIZATION IN A MAGNETOSTRICTIVE RARE EARTH-IRON ALLOY	265
Philippe Bouchilloux, Nicolas Lhermet, and Frank Claeysen	
A FACILITY FOR EVALUATION OF ACTUATORS BASED ON GIANT MAGNETOSTRICTIVE MATERIALS	273
H. Tiberghien and G. Engdahl	

PART VII: POSTER SESSION

LOW TEMPERATURE MAGNETIC BEHAVIOR OF Ni-Fe-Al-B SHAPE MEMORY ALLOYS: MAGNETIC SUSCEPTIBILITY AND MÖSSBAUER SPECTRA	281
V. Marquina, M. Jiménez, M.L. Marquina, R. Ridaura, S. Aburto, R. Gómez, R. Escudero, F. Morales, and D. Ríos-Jara	
COMPATIBILITY OF BaTiO ₃ AND SrTiO ₃ WITH SHAPE MEMORY ALLOY TiNi	287
Peter G. Mercado and A. Peter Jardine	
DEPOSITION PARAMETERS FOR SPUTTER-DEPOSITED THIN FILM TiNi	293
A. Peter Jardine	
DEFORMATION OF ADAPTIVE HETEROPHASE CRYSTAL	299
Alexander L. Roytburd and Julia Slutsker	
ELECTRO-MECHANICAL PROPERTIES OF PbZrO ₃ -PbTiO ₃ -Pb(Mn _{1/3} Sb _{2/3})O ₃ CERAMICS UNDER VIBRATION-LEVEL CHANGE	305
Sadayuki Takahashi, Yasuhiro Sasaki, Seiji Hirose, and Kenji Uchino	
CORRELATIONS BETWEEN THE BIPOLAR- AND UNIPOLAR-ELECTRIC FIELD INDUCED STRAIN IN Pb(Mg _{1/3} Nb _{2/3})O ₃ -PbTiO ₃ CERAMICS	311
Jae-Hwan Park, Byung-Kook Kim, and Soon Ja Park	

*Invited Paper

CARBON FIBER REINFORCED CONCRETE AS AN INTRINSICALLY SMART CONCRETE FOR DAMAGE ASSESSMENT DURING DYNAMIC LOADING	317
Pu-Woei Chen and D.D.L. Chung	
A MODIFIED TRANSMISSION LINE APPROACH TO THE ANALYSIS OF SUPERCONDUCTING MICROWAVE RESONATORS	323
Edward D. Goff and Robert J. Weber	
PRESSURE-SENSITIVE MICROVALVES MADE FROM POLYMER BRUSHES	329
E.M. Sevick and D.R.M. Williams	
LIGAND-RECEPTOR CONTACT INTERACTIONS USING SELF-ASSEMBLED BILAYER LIPID MEMBRANES	339
A. Leitmannova Ottova and H. Ti Tien	
MAGNETIC AND MAGNETOELASTIC PROPERTIES OF HIGHLY MAGNETO- STRICTIVE AMORPHOUS FILMS WITH TbFe-FeB-TbFe SANDWICH STRUCTURE	347
T. Igari, S. Ishii, M. Inoue, and T. Fujii	
MAGNETOSTRICTIVE DAMPING TO REDUCE NOISE AND VIBRATIONS	353
A. Karimi, P.H. Giauque, and J.L. Martin	
MOLECULAR SIEVE COATED SAW DEVICE FOR THE DETECTION OF CARBON DIOXIDE IN THE PRESENCE OF WATER	359
James T. Sun, Christopher B. Dartt, and Mark E. Davis	
 PART VIII: THIN FILM SHAPE MEMORY ALLOYS	
STRUCTURE AND THERMAL STABILITY IN TITANIUM-NICKEL THIN FILMS SPUTTERED AT ELEVATED-TEMPERATURE ON INORGANIC AND POLYMERIC SUBSTRATES	369
Li Hou, T.J. Pence, and David S. Grummon	
THERMO-MECHANICAL Ni ₅₀ Ti ₅₀ /Si COMPOSITE THIN FILM SWITCH	375
T. Kim, Quanmin Su, and Manfred Wuttig	
SHAPE MEMORY BEHAVIOR OF Ti-Ni THIN FILMS ANNEALED AT VARIOUS TEMPERATURES	381
A. Ishida, A. Takei, M. Sato, and S. Miyazaki	
 PART IX: THIN FILMS FOR SMART SYSTEMS	
PIEZOELECTRIC FIBER COATINGS AND MICRO-TUBES	389
G.R. Fox, D. Damjanovic, P.A. Danaï, N. Setter, H.G. Limberger, and N.H. Ky	
PULSED LASER DEPOSITION OF ZnO THIN FILMS FOR PIEZOELECTRIC APPLICATIONS	395
E.P. Donovan, J.S. Horwitz, C.A. Carosella, R.C.Y. Auyeung, D.B. Chrisey, and J.G. Smits	
AN EXPERIMENTAL EXAMINATION OF MEMS MICROACTUATOR MATERIAL ISSUES	401
T.G. Cooney, D.E. Glumac, W.P. Robbins, and L.F. Francis	
A THEORETICAL EXAMINATION OF MEMS MICROACTUATOR RESPONSES WITH AN EMPHASIS ON MATERIALS AND FABRICATION	407
D.E. Glumac, T.G. Cooney, L.F. Francis, and W.P. Robbins	

ELECTRICAL CHARACTERISTICS OF BARIUM STRONTIUM TITANATE- OXIDE COMPOSITE FILMS	413
S. Sengupta, L.C. Sengupta, S. Stowell, D.P. Vijay, and S.B. Desu	
*SMART THIN FILM TiNi/PZT HETEROSTRUCTURES	419
Peter G. Mercado and A. Peter Jardine	
PROPERTIES OF PIEZOELECTRIC PZT THIN FILMS FOR MICROACTUATOR APPLICATIONS	429
D. Damjanovic, K.G. Brooks, A. Kholkin, M. Kohli, T. Maeder, P. Muralt, and N. Setter	
EFFECTS OF THE MULTILAYER STRUCTURE ON THE RESPONSIVITY OF PYROELECTRIC THIN FILM DETECTORS	435
Zhu Jianguo, Xiao Dingquan, Qian Zhenghong, Zhang Wen, and Du Siasong	

PART X: ALLOYING EFFECTS AND TRANSFORMATIONS IN SHAPE MEMORY MATERIALS

*RECENT DEVELOPMENTS IN HIGH TEMPERATURE SHAPE MEMORY ALLOYS	443
Jeno Beyer and Jan H. Mulder	
ENGINEERING CONSIDERATIONS IN THE APPLICATION OF NiTiHf AND NiAl AS PRACTICAL HIGH-TEMPERATURE SHAPE MEMORY ALLOYS	455
Scott M. Russell and Frank Sczerzenie	
INFLUENCE OF Mn ADDITIONS ON THE THERMOELASTIC AND PSEUDO- ELASTIC BEHAVIOUR OF Cu-Al-Ni ALLOYS	461
M.A. Morris and T. Lipe	
*DEVELOPMENT OF NiAl(B2)-BASE SHAPE MEMORY ALLOYS	467
R. Kainuma, N. Ono, and K. Ishida	
THE EFFECTS OF La ON RAPIDLY SOLIDIFIED Al - 66 at.% Ni	479
Baode Sun, Yaohe Zhou, Hui Lin, and Dongliang Lin	
POROUS TiNi SYNTHESIS FROM ELEMENTAL POWDERS	483
Janet C. Hey and A. Peter Jardine	
EVOLUTION OF THE R-PHASE TRANSFORMATION TEMPERATURE OF Ti ₅₀ Ni _{50-x} Fe _x SHAPE MEMORY ALLOYS WITH IRON CONCENTRATION	489
R. Gómez, V. Marquina, R. Ridaura, M.L. Marquina, M. Jiménez, S. Aburto, R. Escudero, F. Morales, D. Ríos-Jara, and A. Canales	

PART XI: SHAPE MEMORY ALLOY APPLICATIONS

*PRESENT AND FUTURE APPLICATIONS OF SHAPE MEMORY AND SUPERELASTIC MATERIALS	497
T.W. Duerig	
THE INTERACTIVE RESPONSE OF SMA SPRINGS WHICH CONTROL THE POSITION OF DAMPERS IN PERSONAL ENVIRONMENTS™	507
Paul E. Thoma, Yefim Ivshin, and Kurt D. Schachner	
SOME DURABILITY ISSUES ASSOCIATED WITH THE USE OF SHAPE- MEMORY ALLOY 'SMART' COMPOSITES	513
Clifford M. Friend, Neil B. Morgan, and Vivienne D. Wise	

*Invited Paper

INTELLIGENT MATERIAL DESIGN USING SHAPE MEMORY ALLOY	519
Yasubumi Furuya	

SMART DAMPING TREATMENT FOR FLEXIBLE STRUCTURE	527
Q. Chen and C. Levy	

PART XII: CHEMICAL SENSORS

CHEMICAL MICROSENSORS FOR SATELLITE APPLICATIONS	535
B.H. Weiller, J.D. Barrie, K.A. Aitchison, and P.D. Chaffee	

PART XIII: LATE PAPERS ACCEPTED

THERMAL AND X-RAY DIFFRACTION STUDIES OF DOPED AND UNDOPE	
SINGLE CRYSTAL AND POLYCRYSTALLINE BaTiO ₃	543
L.G. Carreiro, J.V. Marzik, and K.K. Deb	

SHAPE MEMORY PROPERTIES OF AN IRON MODIFIED NICKEL	
ALUMINIDE ALLOY	549
J.A. Horton, C.T. Liu, and E.P. George	

AUTHOR INDEX	555
------------------------	-----

SUBJECT INDEX	557
-------------------------	-----

Preface

This volume represents a record of the proceedings of the Symposium on Materials for Smart Systems which was held in conjunction with the 1994 Materials Research Society Fall Meeting in Boston, Massachusetts. The Symposium revolved primarily around the use of ferroelectrics, magnetostrictive materials, and shape memory materials in the design of compact sensors and actuators. Productive joint sessions were also held in the areas of ferroelectric films-based transducers and chemical sensors. Ninety-six oral presentations were scheduled over the course of three days, including twelve in a joint session with the Symposium on Ferroelectric Thin Films IV, and ten with the Symposium on Chemical Perspectives of Microelectronics Materials. In addition, 35 poster presentations were scheduled during one of the lively evening poster sessions. Of the seventy-three papers in this volume, twenty-five (or roughly 35%) came from outside the U.S.

In the ferroelectric sections that follow, innovative work on new antiferroelectric-based actuators, SAW-based actuators and ferroelectric composites is presented. In addition, fundamental studies on the behavior of well-established piezoelectric compositions under severe mechanical or electrical drive conditions are discussed. Several papers highlight the incorporation of ferroelectric actuators into commercial products, including gyroscopes, actively damped automobile suspensions, and medical diagnostic equipment.

Among the magnetostrictive materials covered are the high-power magnetostrictive materials, namely the rare-earth and rare-earth-iron alloys, which exhibit large strain from cryogenic temperatures to 250°C. Papers on the rare-earth-iron alloys, especially terfenol-D, range from development of devices to characterization techniques and growth of single crystals. Other papers deal with amorphous iron-based magnetostrictive materials, magnetomechanical sensors, and magnetostrictive damping. Innovative devices, including an accelerometer requiring no pick-up coils which uses the giant magneto-impedance effect as the detection method, and a new low-temperature valve using a rare-earth alloy which is operational and superfluid helium leak-tight down to temperatures as low as 2.2 K, are also discussed.

In the shape memory sections, recent developments in thin films and high-temperature shape memory alloys are discussed. Alloy systems covered include Ni-Ti, Ni-Al, and Cu-Al-Ni. Papers covering the applications of shape memory and pseudoelastic materials indicate the growing use of these materials in commercial products, especially in the medical field. Other papers examine the issues involved in incorporating shape memory materials into composite systems along with other materials.

All papers submitted for inclusion in the proceedings were peer-reviewed in accordance with MRS procedures. We gratefully acknowledge the contributions of the individual reviewers whose assistance made the timely publication of this volume possible.

Easo P. George
Sadayuki Takahashi
Susan Trolier-McKinstry
Kenji Uchino
Marilyn Wun-Fogle

January 1995

Acknowledgments

Financial support for the Symposium on Materials for Smart Systems was provided by:

Army Research Office

Oak Ridge National Laboratory

Office of Naval Research

MATERIALS RESEARCH SOCIETY SYMPOSIUM PROCEEDINGS

- Volume 336—Amorphous Silicon Technology—1994, E.A. Schiff, A. Matsuda, M. Hack, M.J. Powell, A. Madan, 1994, ISBN: 1-55899-236-7
- Volume 337—Advanced Metallization for Devices and Circuits—Science, Technology, and Manufacturability III, S.P. Murarka, K.N. Tu, A. Katz, K. Maex, 1994, ISBN: 1-55899-237-5
- Volume 338—Materials Reliability in Microelectronics IV, P. Børgesen, W. Filter, J.E. Sanchez, Jr., K.P. Rodbell, J.C. Coburn, 1994, ISBN: 1-55899-238-3
- Volume 339—Diamond, SiC and Nitride-Wide-Bandgap Semiconductors, C.H. Carter, Jr., G. Gildenblat, S. Nakamura, R.J. Nemanich, 1994, ISBN: 1-55899-239-1
- Volume 340—Compound Semiconductor Epitaxy, C.W. Tu, L.A. Kolodziejski, V.R. McCrary, 1994, ISBN: 1-55899-240-5
- Volume 341—Epitaxial Oxide Thin Films and Heterostructures, D.K. Fork, J.M. Phillips, R. Ramesh, R.M. Wolf, 1994, ISBN: 1-55899-241-3
- Volume 342—Rapid Thermal and Integrated Processing III, J.J. Wortman, J.C. Gelpey, M.L. Green, S.R.J. Brueck, F. Roozeboom, 1994, ISBN: 1-55899-242-1
- Volume 343—Polycrystalline Thin Films—Structure, Texture, Properties and Applications, M. Parker, K. Barmak, R. Sinclair, D.A. Smith, J. Floro, 1994, ISBN: 1-55899-243-X
- Volume 344—Materials and Processes for Environmental Protection, C. Adkins, P.N. Gadgil, L.M. Quick, K.E. Voss, 1994, ISBN: 1-55899-244-8
- Volume 345—Flat Panel Display Materials, J. Batey, A. Chiang, P. Holloway, 1994, ISBN: 1-55899-245-6
- Volume 346—Better Ceramics Through Chemistry VI, C. Sanchez, M.L. Mecartney, C.J. Brinker, A. Cheetham, 1994, ISBN: 1-55899-246-4
- Volume 347—Microwave Processing of Materials IV, M.F. Iskander, R.J. Lauf, W.H. Sutton, 1994, ISBN: 1-55899-247-2
- Volume 348—Scintillator and Phosphor Materials, M.J. Weber, P. Lecoq, R.C. Ruchti, C. Woody, W.M. Yen, R.-Y. Zhu, 1994, ISBN: 1-55899-248-0
- Volume 349—Novel Forms of Carbon II, C.L. Renschler, D. Cox, J. Pouch, Y. Achiba, 1994, ISBN: 1-55899-249-9
- Volume 350—Intermetallic Matrix Composites III, J.A. Graves, R.R. Bowman, J.J. Lewandowski, 1994, ISBN: 1-55899-250-2
- Volume 351—Molecularly Designed Ultrafine/Nanostructured Materials, K.E. Gonsalves, G.-M. Chow, T.D. Xiao, R.C. Cammarata, 1994, ISBN: 1-55899-251-0
- Volume 352—Materials Issues in Art and Archaeology IV, P.B. Vandiver, J.R. Druzik, J.L. Galvan Madrid, I.C. Freestone, G.S. Wheeler, 1995, ISBN: 1-55899-252-9
- Volume 353—Scientific Basis for Nuclear Waste Management XVIII, T. Murakami, R.C. Ewing, 1995, ISBN: 1-55899-253-7
- Volume 354—Beam-Solid Interactions for Materials Synthesis and Characterization, D.E. Luzzi, T.F. Heinz, M. Iwaki, D.C. Jacobson, 1995, ISBN: 1-55899-255-3
- Volume 355—Evolution of Thin-Film and Surface Structure and Morphology, B.G. Demczyk, E.D. Williams, E. Garfunkel, B.M. Clemens, J.E. Cuomo, 1995, ISBN: 1-55899-256-1
- Volume 356—Thin Films: Stresses and Mechanical Properties V, S.P. Baker, P. Børgesen, P.H. Townsend, C.A. Ross, C.A. Volkert, 1995, ISBN: 1-55899-257-X
- Volume 357—Structure and Properties of Interfaces in Ceramics, D.A. Bonnell, U. Chowdhry, M. Rühle, 1995, ISBN: 1-55899-258-8

MATERIALS RESEARCH SOCIETY SYMPOSIUM PROCEEDINGS

- Volume 358—Microcrystalline and Nanocrystalline Semiconductors, R.W. Collins, C.C. Tsai, M. Hirose, F. Koch, L. Brus, 1995, ISBN: 1-55899-259-6
- Volume 359—Science and Technology of Fullerene Materials, P. Bernier, D.S. Bethune, L.Y. Chiang, T.W. Ebbesen, R.M. Metzger, J.W. Mintmire, 1995, ISBN: 1-55899-260-X
- Volume 360—Materials for Smart Systems, E.P. George, S. Takahashi, S. Trolrier-McKinstry, K. Uchino, M. Wun-Fogle, 1995, ISBN: 1-55899-261-8
- Volume 361—Ferroelectric Thin Films IV, S.B. Desu, B.A. Tuttle, R. Ramesh, T. Shiosaki, 1995, ISBN: 1-55899-262-6
- Volume 362—Grain-Size and Mechanical Properties—Fundamentals and Applications, N.J. Grant, R.W. Armstrong, M.A. Otooni, T.N. Baker, K. Ishizaki, 1995, ISBN: 1-55899-263-4
- Volume 363—Chemical Vapor Deposition of Refractory Metals and Ceramics III, W.Y. Lee, B.M. Gallois, M.A. Pickering, 1995, ISBN: 1-55899-264-2
- Volume 364—High-Temperature Ordered Intermetallic Alloys VI, J. Horton, I. Baker, S. Hanada, R.D. Noebe, D. Schwartz, 1995, ISBN: 1-55899-265-0
- Volume 365—Ceramic Matrix Composites—Advanced High-Temperature Structural Materials, R.A. Lowden, J.R. Hellmann, M.K. Ferber, S.G. DiPietro, K.K. Chawla, 1995, ISBN: 1-55899-266-9
- Volume 366—Dynamics in Small Confining Systems II, J.M. Drake, S.M. Troian, J. Klafter, R. Kopelman, 1995, ISBN: 1-55899-267-7
- Volume 367—Fractal Aspects of Materials, F. Family, B. Sapoval, P. Meakin, R. Wool, 1995, ISBN: 1-55899-268-5
- Volume 368—Synthesis and Properties of Advanced Catalytic Materials, E. Iglesia, P. Lednor, D. Nagaki, L. Thompson, 1995, ISBN: 1-55899-270-7
- Volume 369—Solid State Ionics IV, G-A. Nazri, J-M. Tarascon, M. Schreiber, 1995, ISBN: 1-55899-271-5
- Volume 370—Microstructure of Cement Based Systems/Bonding and Interfaces in Cementitious Materials, S. Diamond, S. Mindess, F.P. Glasser, L.W. Roberts, J.P. Skalny, L.D. Wakeley, 1995, ISBN: 1-55899-272-3
- Volume 371—Advances in Porous Materials, S. Komarneni, D.M. Smith, J.S. Beck, 1995, ISBN: 1-55899-273-1
- Volume 372—Hollow and Solid Spheres and Microspheres—Science and Technology Associated with their Fabrication and Application, M. Berg, T. Bernat, D.L. Wilcox, Sr., J.K. Cochran, Jr., D. Kellerman, 1995, ISBN: 1-55899-274-X
- Volume 373—Microstructure of Irradiated Materials, I.M. Robertson, L.E. Rehn, S.J. Zinkle, W.J. Pythian, 1995, ISBN: 1-55899-275-8
- Volume 374—Materials for Optical Limiting, R. Crane, K. Lewis, E.V. Stryland, M. Khoshnevisan, 1995, ISBN: 1-55899-276-6
- Volume 375—Applications of Synchrotron Radiation Techniques to Materials Science II, L.J. Terminello, N.D. Shinn, G.E. Ice, K.L. D'Amico, D.L. Perry, 1995, ISBN: 1-55899-277-4
- Volume 376—Neutron Scattering in Materials Science II, D.A. Neumann, T.P. Russell, B.J. Wuensch, 1995, ISBN: 1-55899-278-2

PART I

Ferroelectric Actuators

ELECTRICALLY-INDUCED STRAINS IN Sn-MODIFIED LEAD ZIRCONATE TITANATE

Jie-Fang Li, Xunhu Dai, Donald Forst, and Dwight Viehland
Department of Materials Science and Engineering and the Materials Research Laboratory,
University of Illinois, Urbana, IL 61801

ABSTRACT

Incommensurate antiferroelectric tin-modified lead zirconate titanate ceramics, $\text{PbNb}_{0.02}[(\text{Zr}_{1-x}\text{Sn}_x)_{1-y}\text{Ti}_y]_{0.98}\text{O}_3$, have been studied by Sawyer-Tower polarization and electrically-induced strain (ϵ - E) techniques. Sawyer-Tower polarization studies revealed antiferroelectric-ferroelectric (AFE-FE) P-E loops. Investigations then revealed that the electrically-induced strain associated with the AFE-FE transformation was not realized until field strengths significantly above that required for polarization saturation. It is believed that the electrically-induced strain is decoupled from the polarization due to AFE-FE switching by the modulation of the phase of a $\langle 110 \rangle$ incommensurate structure. At field strengths above saturation, the commensurate rhombohedral ferroelectric state is believed to be induced from an incommensurate orthorhombic ferroelectric, and the electrically-induced strain is then realized.

INTRODUCTION

Tin-modified lead zirconate titanate, $\text{PbNb}_{0.02}[(\text{Zr}_{1-x}\text{Sn}_x)_{1-y}\text{Ti}_y]_{0.98}\text{O}_3$ (designated as PZST $x/y/2$), exhibits phase switching under an applied electrical or mechanical field. Large shape changes are known to accompany all electrically-induced antiferroelectric-ferroelectric (AFE-FE) phase transformations, such as that for PbZrO_3 (PZ)¹⁻⁴. For most of these materials, induced transformations cannot be achieved at room temperature due to the fact that the coercive field is greater than the breakdown strength. However, an AFE-FE transformation can be electrically-induced at room temperature in PZST. Strains as large as 0.5% have been reported¹⁻⁴.

Recently, hot-stage transmission electron microscopy (TEM) and selected area electron diffraction (SAED) studies have been performed on PZST 45/y/2 for $0 < y < 9$.⁵⁻⁷ These studies revealed the existence of incommensurate $\frac{1}{x}[110]$ superlattice reflections in the previously designated antiferroelectric tetragonal state, indicating that the structure is in fact incommensurate orthorhombic antiferroelectric. Corresponding dark field images revealed the existence of (110)-polarized domain-like striations whose periodicity was equal to λ . With decreasing temperature, λ was found to become relatively temperature

independent while remaining incommensurate, indicating that the incommensurate structure becomes pinned into long-lived metastable states. At lower temperatures an incommensurate-commensurate transformation was found into either an antiferroelectric orthorhombic phase (low Ti-content) or a ferroelectric rhombohedral (high Ti-content)⁴.

The purpose of this study was to investigate the P-E behavior and ϵ -E characteristics of antiferroelectric PZST. The results will be compared to TEM investigations. It was anticipated that the combination of these studies might reveal the mechanism underlying the large electrically-induced shape changes in antiferroelectric PZST ceramics and lend insights into how high-strain slim-loop AFE-FE actuator materials might be developed.

EXPERIMENTAL PROCEDURE

A PZST composition of 45/4/2 was chosen for investigations. Ceramic samples were prepared by a hybrid coprecipitation-mixed oxide method², and were electroded with gold. Field-induced strains (ϵ -E) were measured using an inductance technique. The measurement frequencies used was 0.1 Hz. The polarization electric field behavior (P-E) was characterized using a modified computer-controlled Sawyer-Tower circuit. Measurements were made at a frequency of 0.1 Hz. The reference capacitance and resistance for each measurement was automatically determined. The linear contribution to P-E curves from leakage currents was then minimized by adjustments of the compensation capacitance and resistance.

RESULTS AND DISCUSSION

Room-temperature electrically-induced strains (ϵ -E) are shown in Figures 1(a)-(d) for maximum AC drive fields of 57, 62, 70 and 82 kV/cm, respectively. Corresponding P-E curves are shown in Figures 2(a)-(d), respectively. Only a small fraction of the total electrically-induced strains were observed in these figures below the field strength required to induce polarization saturation. Inspection of Figure 2(a) will clearly show that the FE state was induced from the AFE in the field range of 40 to 50 kV/cm, with saturation reached near 50 kV/cm. However, inspection of Figure 1(a) will clearly show that significant electrically-induced strains were not observed until field levels above that required for polarization saturation. For field strengths below 50 kV/cm, strains of $\sim 5 \times 10^{-4}$ were induced. With increased maximum AC drive, a strong increase in the electrically-induced strains was found. The magnitude of the induced strain was approximately 0.010, 0.014, 0.017 and 0.027 at field strengths of 57, 62, 70 and 82 and

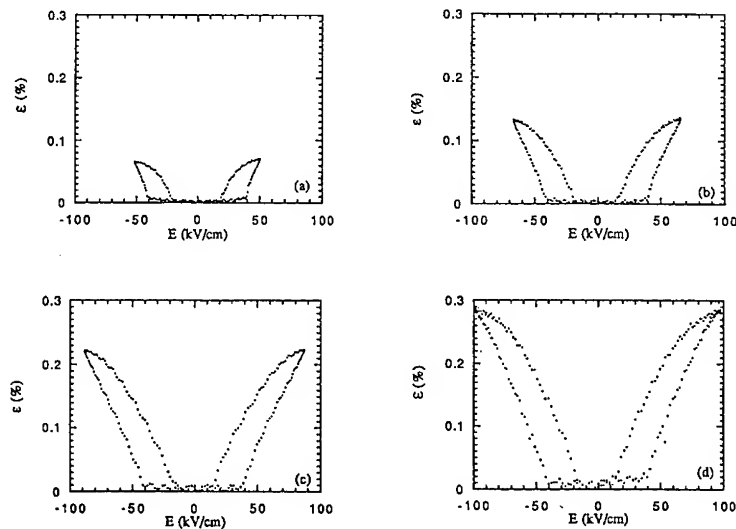


Figure 1. ϵ -E behavior for 45/4/2 at various maximum drive fields. (a) 57 kV/cm, (b) 62 kV/cm, (c) 70 kV/cm, and (d) 82 kV/cm. The measurement frequency was 0.1 Hz.

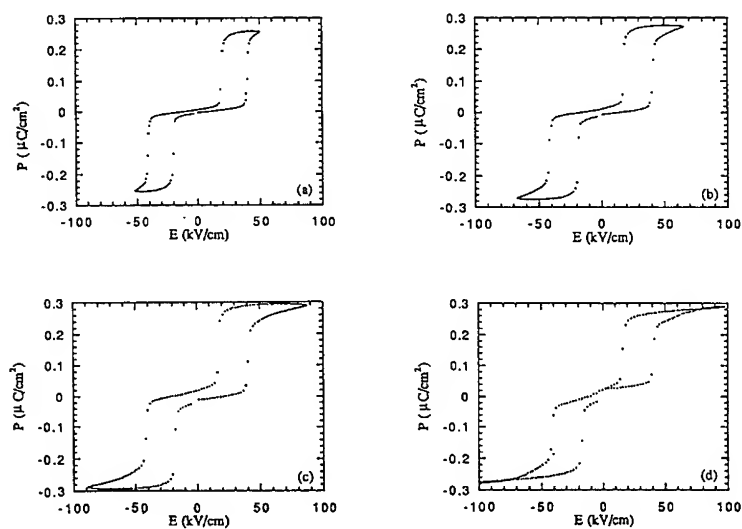


Figure 2. P-E behavior for 45/4/2 at various maximum drive fields. (a) 57 kV/cm, (b) 62 kV/cm, (c) 70 kV/cm, and (d) 82 kV/cm. The measurement frequency was 0.1 Hz.

kV/cm respectively. However, no change in the induced polarization was observed with increased field strength between 57 and 82 kV/cm. In addition, no significant changes in the temperature were observed during measurement, clearly indicating that the strains are electrical in nature and not thermal. Also, saturation effects are evident at higher field strengths in ϵ .

Comparisons of Figures 1 and 2 indicates that the AFE-FE transformation in PZST can occur without any significant change in shape of the sample, and correspondingly at higher field strengths above that required for saturation electrically-induced strains can be achieved without any additional polarization. These results seemingly indicate that the electrically-induced strain in PZST is decoupled from the polarization, i.e., that it is possible to develop polarization without strain and conversely to develop strain without polarization. These results are in complete contradiction to all previously reported mechanisms of electromechanical coupling, including: (i) electrostriction, where the strain is coupled to the square of the polarization via the electrostriction coefficient, (ii) piezoelectricity, where the strain is coupled to the electric field via the piezoelectric coefficient, and (iii) induced antiferroelectric-ferroelectric transformations where the strain is well-known to accompany the development of a remanent polarization, as previously reported by Uchino³. Uchino has reported strains of $\sim 8 \times 10^{-4}$ near polarization saturation for PZST 40/6/2. These results are distinctly different than that reported in Figures 1 and 2. We believe that this difference may be a reflection of differences in composition and electrical field strength between the two investigations.

The decoupling of the electrically-induced strain from the polarization over a relatively wide field range may be a reflection of the incommensurate polarization modulation. The magnitude of electrically-induced strains in ferroelectric and antiferroelectric materials is well-known to be dependent on the polarization switching mechanism. For example, polarization switching by the creation and subsequent motion of 90° domains results in significantly larger shape changes, than switching by 180° domains. This difference is basically a reflection of elastic strain compatibility in the domain wall regions. Large strain accommodations at twin boundaries are required for switching by 90° domains, resulting in relatively large macroscopic shape changes on polarization reversal. However, only small accommodations at the boundaries are required for switching by 180° domains, resulting in significantly smaller macroscopic shape changes. Traditionally, the polarization switching in induced AFE-FE transformations has been considered to occur by nucleation and growth of the FE phase within the AFE. Large strains accompany the formation of the ferroelectric state, as the individual dipoles are switched from an antiparallel to a parallel alignment. However, no consideration has

previously been given to polarization switching in induced AFE-FE transformations which occur through an incommensurate polarization modulation. Saturation polarization may be achieved between 40 and 50 kV/cm, however this does not prevent a long-wavelength incommensurate polarization modulation from remaining in the FE state. If the FE state maintains a long-wavelength incommensurate polarization modulation near saturation, then the elastic strains generated on transformation from the AFE state may be partly accommodated by the modulation, resulting in significantly reduced electrically-induced strains. Increase of the electric field above that required for saturation may then result in a decrease of the magnitude of the AC component and an increase in its periodicity, however no changes in the rms polarization would be observed. As a consequence, the electrically-induced strain associated with the AFE-FE transformation may not appear until field strengths significantly above saturation.

The ϵ -E data may indicate that polarization switching occurs by changes in the incommensurate polarization modulation. In consideration that the incommensurate polarization modulation is along the $\langle 110 \rangle$, the crystal symmetry of both the incommensurate ferroelectric and antiferroelectric states would seemingly be orthorhombic. Switching may then occur between incommensurate antiferroelectric orthorhombic and ferroelectric orthorhombic states. Fesenko et al.⁸ has previously reported that polarization switching occurs between antiferroelectric and ferroelectric orthorhombic states in PZ at room temperature. At higher field strengths, they reported that the rhombohedral ferroelectric state was then induced from the orthorhombic ferroelectric. Our results are suggestive of a similar electrically-induced transformational sequence in PZST, with the additional restriction that both orthorhombic states are incommensurate. Application of an electrical field in the antiferroelectric orthorhombic state may lead to changes in λ and the stabilization of the incommensurate orthorhombic ferroelectric state, however no electrically-induced strains are realized. At field strengths above saturation, the rhombohedral ferroelectric state may, then, be slowly stabilized from the incommensurate orthorhombic ferroelectric with increasing field.

The general influence of compositional heterogeneity on the paraelectric-antiferroelectric (PE-AFE) transition would seemingly be to make the transformational sequence pass through an intermediate incommensurate state. The commensurate orthorhombic antiferroelectric state is eventually reached on cooling at a temperature $\sim 200^\circ\text{C}$ below that of the dielectric maximum. Correspondingly, the electrically-induced transformational sequence would also seemingly be modified by "impurities". Again, the product state (commensurate rhombohedral ferroelectric) is eventually induced, however through a different transformational sequence than for an ideal homogeneous material.

Some of the characteristics of the electrically induced strains may be changed by the modification of the transformational sequence, however the maximum actuation strain achievable will probably not be significantly increased or decreased. The degree of strain which is recoverable from an induced AFE-FE transformation relates to changes in the unit cell dimensions, and consequently should be independent of the transformational pathway. The principle advantage of "dirty" antiferroelectric materials will probably be in how the strain is recovered (i.e., the coercive field and degree of hysteresis), and not the magnitude of the maximum induced strain achievable between the antiferroelectric orthorhombic and ferroelectric rhombohedral states.

CONCLUSIONS

Investigations have revealed that the electrically-induced strain is decoupled from the polarization for PZST 42/4/2. It is believed that the decoupling occurs due to polarization switching by modulation of the $1/x<110>$ incommensurate structure. These results are discussed in terms of a modulation of the phase of the incommensurate structure by electrical bias.

ACKNOWLEDGEMENTS

This research was supported in fully by the Office of Naval Research (ONR) under contract No. N00014-92-J-1522 and by the Naval UnderSea Warfare Center under contract No. N66604-94-C-0984.

REFERENCES

1. P. Yang, Ph. D Dissertation, University of Illinois at Urbana-Champaign, (1992).
2. W. Pan, Ph. D Dissertation, The Pennsylvania State University (1988).
3. K. Uchino, Jap. J. Applied Physics, **24**, Suppl. 24-2, 460 (1985).
4. D. Berlincourt, H. Krueger, and B. Jaffed, J. Phys. Chem. Solids **25**, 659 (1964).
5. Z. Xu, D. Viehland, P. Yang, and D.A. Payne, J. Appl. Phys. **74**, 3406 (1993).
6. D. Forst, J.F. Li, Z. Xu, and D. Viehland, Submitted.
7. Z. Xu, D. Viehland, and D.A. Payne, J. Mat. Res. (15 Feb. 1995).
8. E. Fesenko, A. Kolesova, and A. Sindeyev, Ferroelectrics **20**, 177 (1978).

FERROELECTRIC BEHAVIOR AND MICROSTRUCTURE OF CALCIUM-MODIFIED LEAD TITANATE CERAMICS

Zhiqiang Zhuang*, G.A. Kulesha,** H. Du,** and B. Gallois**

* South China University of Technology, Department of Inorganic Materials Science and Engineering, Guangzhou, China 510641

** Stevens Institute of Technology, Department of Materials Science and Engineering, Hoboken, NJ 07030,

ABSTRACT

Calcium-doped lead titanate ceramics exhibiting piezoelectric anisotropy were fabricated for applications in ultrasonic transducers, infrared detectors and surface acoustic wave devices. Transmission electron microscopy and X-ray diffraction techniques were used to characterize the development of the piezoelectric anisotropy and the dependence of the piezoelectric anisotropy on microstructure. Electron diffraction patterns indicated that most of the ferroelectric domains in samples with $[\text{Ca}_A]$ up to 30 mole% were 90° domains. The size of the ferroelectric domains was not related to piezoelectric anisotropy. Ferroelectric domains could not be detected above this concentration. Measurements of the temperature dependence of dielectric properties at different frequencies did not show any ferroelectric relaxor behavior.

INTRODUCTION

Piezoelectric lead zirconate titanate (PZT) ceramics are widely used in ultrasonic transducers,^{1,2} surface acoustic-wave devices³ and medical imaging systems.^{4,5} In applications such as non-destructive testing of metals, medical diagnostic procedures using phase-array devices and hydrophones, piezoelectric transducers which exploit the thickness vibration mode should exhibit an electromechanical coupling ratio, k_t/k_p , as large as possible to avoid coupling of transverse to thickness vibrations.⁶ Materials with high piezoelectric anisotropy are also needed for very high frequency applications.

Intensive studies of materials which exhibit piezoelectric anisotropy have been carried out in the last ten years.^{6,7} Even though some compositions with very high piezoelectric anisotropy have been developed, the effects of microstructural features on piezoelectric anisotropy have remained elusive. No mechanistic understanding has been achieved of the piezoelectric anisotropy induced by dopants in solid solutions of lead titanate (PT), lead zirconate and PZT. This research was carried out to study the effects of composition and microstructure on the piezoelectric and dielectric properties of calcium-doped lead titanate ceramics. Materials showing high piezoelectric anisotropy and a pure thickness vibration mode have been produced which are ideally suited to the fabrication of ultrasonic transducers for the measurement of the thickness of metals.

* A visiting professor at Stevens Institute of Technology

EXPERIMENTAL PROCEDURE

An oxide-mixing technique was employed to prepare the calcium-doped lead titanate (CPT) ceramic samples. The starting chemicals were reagent-grade lead oxide, titanium oxide and zirconium oxide. The weighted oxide powders were mixed with distilled water in an alumina ball-mill, dried, cold-pressed into pellets and sintered in a sealed alumina crucible. The grain size was controlled to be between 10 and 15 μm .

X-ray analysis of the sintered CPT ceramics was carried out with Cu-K α radiation in an automated x-ray diffractometer. The lattice parameter was determined from the (200) and (002) reflections. The microstructure of the ceramics was examined by transmission (TEM) and high-resolution electron microscopy (HREM) techniques.

The ceramic samples with gold or silver electrodes were poled in a DC electric field of 2-6 MV/m at 70° - 120°C. A computer-controlled LCR measurement system was used to measure the dielectric properties of poled samples. Piezoelectric properties were measured by a transmission resonance method and calculated in accordance with the IRE standard. For comparison purposes, a CAD impedance circle measurement technique was also employed to measure the piezoelectric properties.

RESULTS AND DISCUSSION

Table I shows the dependence of selected dielectric and piezoelectric properties on calcium composition. The loss tangent, $\tan\delta$, and the dielectric constant measured at room temperature, K_{RT} , increase with increasing calcium concentration whereas the crystal anisotropy, measured by the ratio c/a , decreases from a value of 1.0635 in pure lead titanate to 1.0130 at a concentration of 38 mole%. Note that the planar electromechanical coupling factor, k_p , is essentially negligible above a calcium concentration of 24 mole%. The Curie temperature, T_c ,

Table I. Effects of calcium concentration on the properties of calcium-doped lead titanate ceramics

comp.	x (mole%)	K_{RT}	$\tan\delta$ (%)	c/a	ρ (Ωm)	T_c (°C)	k_p (%)
PbTiO ₃	0	60	2	1.0635	----	490	----
CPT-1	20	190	2	1.0450	10^9	310	15
CPT-2	24	215	2	1.0390	10^9	259	0-4
CPT-3	30	262	3	1.0260	10^9	195	0
CPT-4	32	323	3	1.0210	10^9	185	0
CPT-5	34	343	3.5	1.0170	10^9	157	0
CPT-6	38	440	3.5	1.0130	10^9	102	---

decreases linearly from 490°C to 102°C as shown in Fig. 1. The temperature dependence of the dielectric constant, K , for compositions CPT-3 and CPT-4 at three different frequencies is depicted in Figs. 2(a) and 2(b). Composition CPT-3 exhibits a normal ferroelectric behavior. As the calcium concentration is increased, the nature of the cubic-to-tetragonal phase transition changes. It becomes diffuse as shown by the broad shape of the curves for composition CPT-4.

In addition, the curves at different frequencies are well separated in the high-temperature region above T_{av} , where T_{av} is average Curie temperature measured at the maximum of K . Above the Curie temperature, these features were observed to be more pronounced as the calcium concentration was increased further. This behavior is not observed for ferroelectric relaxors: the dielectric constant is not affected by frequency in the region $T > T_{av}$.⁸ It can be surmised, therefore, that the ferroelectric compositions with exhibit such diffuse phase transitions are

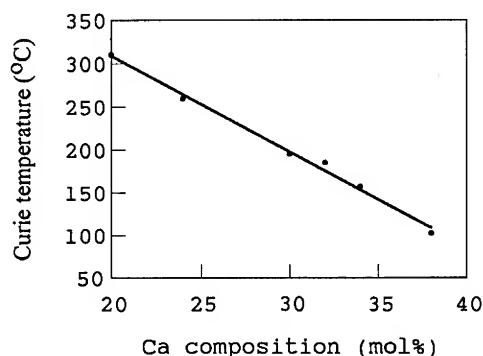


Fig. 1 Effect of calcium concentration on Curie temperature of CPT ceramics

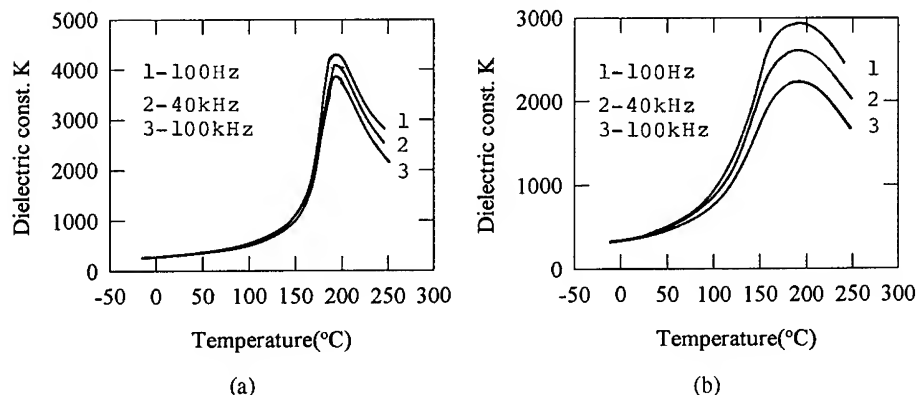


Fig. 2 Temperature dependence of dielectric constant of (a) CPT-3 and (b) CPT-4

not ferroelectric relaxors in this temperature range. More accurately, this type of ferroelectric material could be defined as a diffuse ferroelectric rather than a ferroelectric relaxor. Figs. 3(a) and 3(b) illustrate the change in ferroelectric domain structure for different calcium concentrations. It was shown that there is no direct relationship between domain size and A-side-doped calcium concentration. No ferroelectric domains were observed by TEM in samples of composition CPT-4 and above as shown in Fig. 4. HREM, TEM bright field image in CPT-4 ceramic and the corresponding electron diffraction pattern also are shown in Fig. 4. The sharp pattern coincides with the absence of ferroelectric domains in the ceramic. The material of composition CPT-4 was easily poled in a $k_p=0$ state. Fig. 5 shows the evolution of the

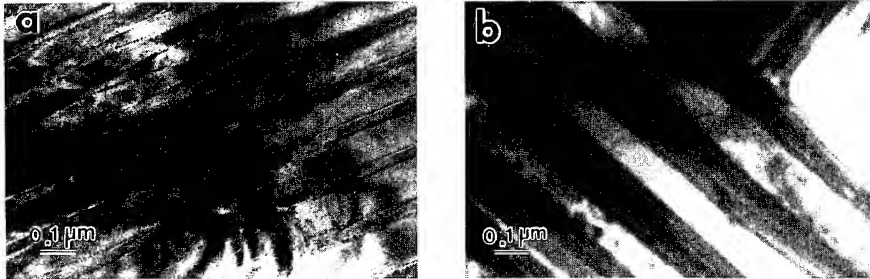


Fig. 3 Effect of calcium incorporation in A-side on the configuration of ferroelectric domains of calcium-doped lead titanate ceramics: (a) CPT-2 and (b) CPT-3

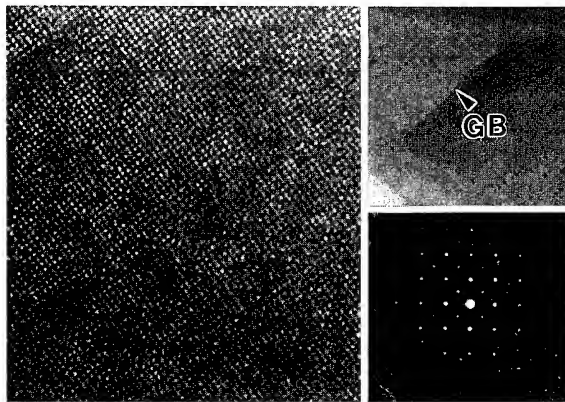


Fig. 4 HREM microscopy, TEM bright field image and corresponding electron diffraction pattern in composition CPT-4

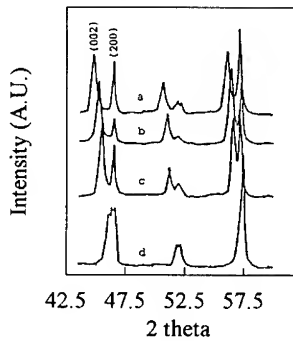


Fig. 5 Influence of Ca concentration on the X-ray diffraction patterns of Ca-doped PT ceramics with: (a) 0.24 mole, (b) 0.30 mole, (c) 0.34 mole and (d) 0.38 mole of Ca

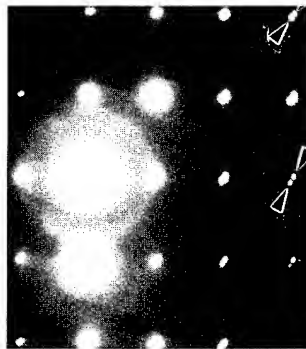


Fig. 6 TEM electron diffraction pattern of composition CPT-2 showing a superposition of two sub-patterns of 90° domains lightly tilted with respect to each other

diffraction lines as the calcium concentration is increased. The absence of detectable domains above a concentration of 30 mole% may be attributed to the quasi-cubic structure of the materials. It can be concluded that the domain size is not responsible for the piezoelectric anisotropy. Fig. 6 shows electron diffraction patterns obtained on a sample of composition CPT-2. The angular offset of the electron diffraction patterns of neighboring domains is caused by strain at the 90° domain wall. Systematic investigations showed a preponderance of 90° domain walls for composition CPT-2. The percentage of 90° domain walls and the domain wall

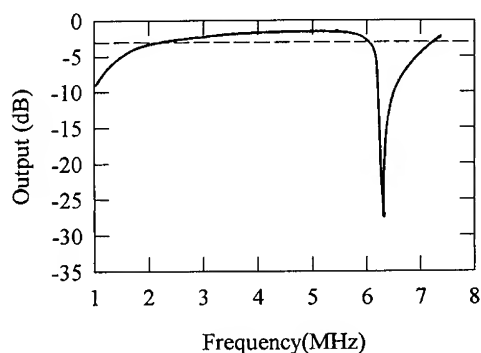
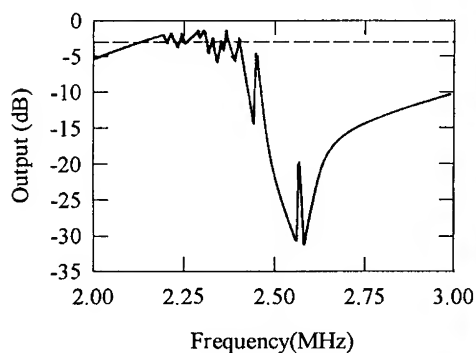
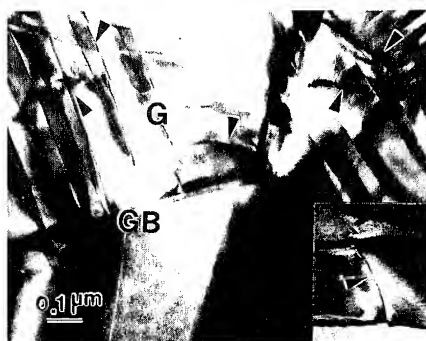


Fig. 7(a) A pure thickness resonance response of a resonator (thickness = 0.338 mm and diameter = 17 mm) of the calcium heavily doped composition CPT-3



(b)



(c)

Fig. 7(b) Thickness resonance response of a resonator (thickness = 0.765 mm and diameter = 20 mm) of the composition with $k_p=0$ and (c) microcracks in the material of the resonator observed under TEM which are believed to be responsible for the spurious response around the thickness resonance frequency

switching behavior could be controlled by varying the calcium concentration in the lead titanate solid solution up to a value of 30 mole%. The transverse and thickness electromechanical coupling factors at a calcium concentration of 20 mole% are $k_p=15\%$ and $k_t=50\%$, respectively. Because of strong transverse coupling, spurious vibrations were observed around the thickness

resonance frequency. The transverse vibration disappeared ($k_p=0$) occasionally for composition CPT-2 (24 mole% calcium). It disappeared totally at calcium concentrations larger than 30 mole%. The resonance spectrum showed then a pure thickness piezoelectric vibration mode as shown in Fig. 7(a). Fig. 7(b) shows the thickness resonance spectrum of a resonator of the composition with $k_p=0$. As illustrated in Fig. 7(c) microcracks could be observed by TEM in samples exhibiting spurious vibrations around the resonance frequency (Fig. 7(b)). These microcracks in the poled ceramics are believed to cause the spurious vibrations.

The composition with a pure thickness vibration mode was used to fabricate an ultrasonic transducer for the thickness measurement of metals.⁹ For a transducer operating in the pulse-echo mode in the frequency range of 6 MHz, the smallest detectable flaw size could be as small as 1 mm with an accuracy of ± 0.1 mm for distances between 1 mm to 2000 mm from the transducer.

CONCLUSIONS

1. Crystal anisotropy is not correlated with piezoelectric anisotropy in calcium-doped lead titanate ceramics.
2. The diffuseness of the phase transition and the 90° domain wall configuration are responsible for piezoelectric anisotropy in calcium-doped lead titanate ceramics.
3. Ferroelectric compositions with a diffuse phase transition at T_{av} are not ferroelectric relaxors but "diffuse ferroelectrics", as defined in this work.
4. Spurious vibrations observed around the thickness resonance frequency of a resonator may result from the existence of transverse vibrational coupling and the formation of microcracks in the ceramic body during DC poling for compositions with $k_p = 0$.

ACKNOWLEDGMENT

The authors thank Dr. R. Guo of the Materials Research Laboratory at Penn State University for her assistance in the measurement of dielectric properties.

REFERENCES

1. Y. Yamashita, K. Yokoyama, H. Honda and T. Takahashi, Jpn. J. Appl. Phys. 20[suppl.4], 183 (1981)
2. A.A. Shoulov, H.E. Rosar, W.A. Smith and B.M. Singer, Proc., IEEE ISAF'86, 1231 (1986)
3. Y. Ito, K. Nagatsuma, H. Takeuchi and S. Jyomura, J. Appl. Phys. 52, 4479 (1981)
4. H. Honda, Y. Yamashita and K. Uchino, Proc. of IEEE ultrasonic Symposium. 1, 845 (1986)
5. W.A. Smith, Proc., IEEE ISAF'86, 249 (1986)
6. T. Takeuchi, Am. Ceram. Soc. Bull. 69, 691 (1990)
7. Zhiqiang Zhuang, Proc. of 2nd national conference on the sensors and transducers, China, 2, 634 (1991)
8. N. Setter, PhD thesis, Pennsylvania State University, 1980
9. Z. Zhuang, unpublished results.

MEASURING METHODS FOR HIGH-POWER CHARACTERISTICS OF PIEZOELECTRIC MATERIALS

Seiji HIROSE^{***}, Sadayuki TAKAHASHI^{****}, Kenji UCHINO^{**}
Manabu AOYAGI^{*} and Yoshiro TOMIKAWA^{*}

^{*}Faculty of Engineering, Yamagata University, Yonezawa, 992 Japan

^{**}The Pennsylvania State University, MRL, University Park, PA 16802

^{***}R&D Group, NEC Corp., Miyazaki, Miyamae-ku, Kawasaki, 216 Japan

ABSTRACT Two kinds of measuring method of the high-power characteristics of piezoelectric transducers are described. One is the measurement method at the resonance frequency and another is the measurement method at the antiresonance frequency. The vibrational velocity dependences of the equivalent circuit constants and the temperature rise were measured by using each measurement method under the constant vibrational velocity control. These results are useful for designing the ultrasonic power devices such as the ultrasonic motor, and also useful for investigating the new advanced piezoelectric materials for high power use. Especially, by using the results obtained at the antiresonance frequency, a stable state driving method, named as antiresonance driving, with high-efficiency and low-temperature rise can be achieved.

§1. Introduction

In a piezoelectric ceramic transducer operating under high-power excitation at the resonance frequency, the quality factor Q of the transducer becomes lower, and therefore, heat generation at and around the maximum-stress position increases markedly. In this situation, even if the applied electric power is increased, almost only heat generation will increase, but the vibrational energy will not. Under such a high-power operation, the equivalent electric circuit constants such as the mechanical quality factor Q can be no longer measured by the ordinary admittance circle method, because the admittance circle becomes unstable.

First, in the paper, a measuring method for obtaining the high-power characteristics of the equivalent electric constants at the resonance frequency is described. During the measurement, the constant vibrational velocity control is performed for avoiding the jump phenomenon in the resonance characteristics.

Next, the measuring method at the antiresonance frequency is described. When a high-power ultrasonic devices such as an ultrasonic motor is practically used, the maximum efficiency is obtained at the antiresonance frequency, not at the resonance frequency. This phenomenon is

caused by the increase of the dielectric loss related to the vibrational velocity; that is, dielectric loss increases as a function of the vibrational velocity. Dielectric loss can be obtained by using the equivalent constants measured both at the resonance and antiresonance frequencies.

Finally, the efficiency of conversion from electric input power to mechanical output power is shown. This result has been calculated by using the experimental values of the equivalent circuit constants and the dielectric loss. A stable state driving method, named as antiresonance driving, with high-efficiency and low-temperature rise is discussed.

§2. Measurement method at the resonance frequency

As you know well, there are two resonances in the piezoelectric transducers. One is resonance and another is antiresonance. It is supposed that the piezoelectric transducer can not vibrate mechanically at the antiresonance frequency. However, even at the antiresonance frequency, transducers can vibrate mechanically up to the large vibrational level. In this paper, for making it clear that both of these resonances are the mechanical ones, the mechanical vibrations at the resonance and antiresonance frequencies are called *A*-type and *B*-type res

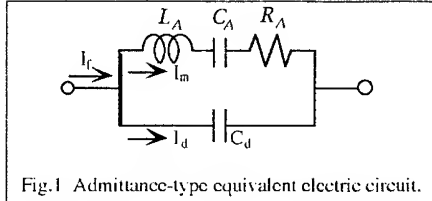


Fig.1 Admittance-type equivalent electric circuit.

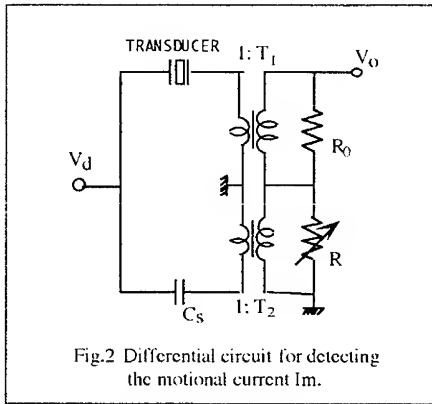


Fig.2 Differential circuit for detecting the motional current I_m .

onances. Therefore, the subscript "A" or "B" is attached to the equivalent constants.

Figure 1 shows the well-known, so-called, admittance type equivalent electric circuit. Here, L_A , C_A and R_A are the equivalent inductance, capacitance and resistance, respectively, and C_d is the damped capacitance. Currents I_f , I_m and I_d are the free current, motional current and damped current, respectively. The motional current I_m is proportional to the vibrational velocity v , and written as follows;

$$I_m = Av, \quad (1)$$

where A is the force factor.

Figure 2 shows a differential circuit for detecting the motional current. Here, C_s and R are a capacitance and a resistance, respectively, for cancelling the damped capacitance C_d .

The output voltage V_o of the differential circuit in Fig.2 is given by,

$$V_o = -(R_0/T_1)Y_m V_d - j\omega((R_0/T_1)C_d - (R/T_2)C_s)V_d, \quad (2)$$

where T_1 and T_2 are the transformation ratio of current detection transformer. When R is adjusted for the resonance curve to be symmetric, V_o becomes equal to $-(R_0/T_1)Y_m V_d$, that is, $-(R_0/T_1)I_m$. Hence, the motional current I_m can be obtained from the output voltage V_o . When V_o is controlled to be constant, the motional current I_m and therefore, the vibrational velocity v can be kept constant in the vicinity of the resonance frequency f_A .

MEASURING PROCEDURE

(1) Damped capacitance C_d : In Fig.2, R is adjusted so that the output voltage V_o under constant velocity shows a symmetric resonance curve with respect to the A-type resonance frequency on a logarithmic scale. After this adjustment, the damped capacitance is given by,

$$C_d = (T_1/T_2)(R/R_0)C_s. \quad (3)$$

(2) A-type resonance frequency f_A : When the constant vibrational velocity control (namely, constant I_m control) is employed, f_A is given by the frequency where the driving voltage V_d indicates minimum value. This frequency can be obtained by the automatic measurement system using micro-computer control¹⁾.

(3) Quality factor Q_A : Using the frequency perturbation method²⁾, the quality factor Q_A can be obtained by,

$$Q_A = \frac{2f_A}{f_2 - f_1} \sqrt{K_p(I + K_p)}, \quad (4)$$

where f_1 and f_2 are frequencies very close to the resonance frequency f_A , and are in the relation $f_1 < f_A < f_2$. In addition, K_p is the perturbation ratio, which is given by the following equation under the constant vibrational velocity control,

$$K_p = (V_d - V_{d0})/V_{d0}, \quad (5)$$

where V_{d0} is the driving voltage at the resonance frequency f_A , and V_d is that at the frequency f_1 or f_2 . These values are measured by the digital voltmeters and transferred to the micro-computer through GP-IB. In this study, the value of K_p was selected below several percent.

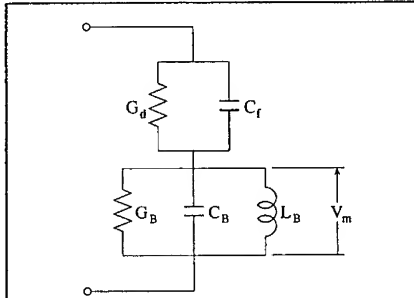


Fig.3 Impedance-type equivalent electric circuit.

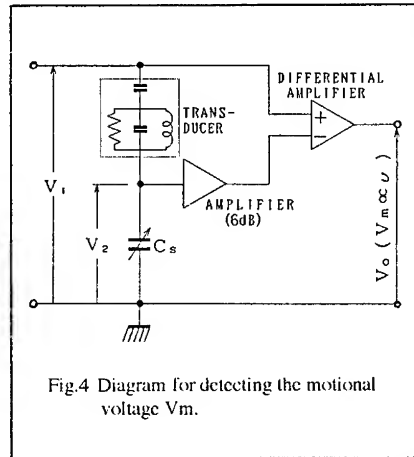


Fig.4 Diagram for detecting the motional voltage V_m .

(4)Equivalent resistance R_A : Using the motional current I_m and the driving voltage V_{d0} obtained at f_A , R_A is given by

$$R_A = |V_{d0}/I_m| (f=f_A). \quad (6)$$

(5)Equivalent inductance L_A and capacitance C_A : Since Q_A , R_A and f_A were given, equivalent inductance L_A and capacitance C_A are obtained by

$$L_A = \frac{Q_A R_A}{2\pi f_A}, \quad C_A = \frac{1}{(2\pi f_A)^2 L_A}. \quad (7)$$

§3. Measurement method at the anti-resonance frequency

Fig.3 shows the improved, advanced equivalent circuit which is called the impedance-type equivalent circuit³⁾. Here, the conductance G_B means only me-

chanical loss. G_d is the conductance resulting from the dielectric loss angle $\delta^{3)}$, and written as; $G_d = \omega C_d \tan \delta$. C_f is called the free capacitance and written by using the damped capacitance C_d and the coupling coefficient k as follows; $C_f = C_d / (1 - k^2)$.

The voltage V_m of the parallel resonance circuit indicated in Fig.3 is called the motional voltage, and written as follows;

$$V_m = j \omega_B / \omega \cdot A_B v, \quad (8)$$

where ω is the angular frequency, ω_B is the B-type resonance angular frequency, and A_B is the B-type force factor which is defined as follows;

$$A_B = A / \omega_B C_d, \quad (9)$$

where C_d is the damped capacitance and A is the A-type force factor. Therefore, V_m is proportional to the velocity v , providing $\omega \approx \omega_B$.

Figure 4 shows a diagram for detecting the motional voltage $V_m^{4)}$. Here, C_s is a capacitance for cancelling the free capacitance C_f . In detecting V_m , G_d can be neglected because it is less than one fiftieth of ωC_f . When C_s is adjusted to be equal to C_f , V_o becomes equal to V_m . Hence, the motional voltage V_m can be obtained from the output voltage V_o . When V_m is controlled to be constant, the vibrational velocity v can be kept constant in the vicinity of f_B .

MEASURING PROCEDURE

(1)Free capacitance C_f : In Fig.4, C_s is adjusted so that the current I under constant velocity shows a symmetric resonance curve with respect to the B-type resonance frequency on a logarithmic scale. After this adjustment, the free capacitance is obtained by $C_f = C_s$.

(2)B-type resonance frequency f_B : When the constant vibrational velocity control (namely, constant V_m control) is employed, f_B is given by the frequency where the terminal current I indicates minimum value. This frequency can be obtained by the automatic measurement system using micro-computer control¹⁾.

(3) Quality factor Q_B : Using the frequency perturbation method²⁾, the quality factor of B-type resonance Q_B can be obtained by

$$Q_B = \frac{2f_B}{f_2 - f_1} \cdot \frac{\sqrt{K_p(1-K_p)}}{(1-2K_p)}, \quad (10)$$

where f_1 and f_2 are frequencies very close to the B-type resonance frequency f_B , and are in the relation $f_1 < f_B < f_2$. In addition, K_p is the perturbation ratio, which is given by the following equation under the constant velocity control,

$$K_p = (I - I_0)/I_0, \quad (11)$$

where I_0 is the terminal current at the resonance frequency f_B , and I is that at the frequency f_1 or f_2 . These values are measured by the digital voltmeters and transferred to the micro-computer through GP-IB.

(4) Equivalent conductance G_B : At the frequency f_B , susceptance ($\omega C_B - 1/\omega L_B$) of the parallel resonance circuit in Fig.3 becomes 0, hence only conductance G_B remains. By using the motional voltage V_{nR} and the current I_0 obtained at f_B , G_B is given by

$$G_B = |I_0/V_{nR}| (f=f_B). \quad (12)$$

(5) Equivalent capacitance C_B and inductance L_B : Since Q_B , G_B and f_B were given, equivalent capacitance C_B and inductance L_B can be obtained by

$$C_B = \frac{Q_B G_B}{2\pi f_B}, \quad L_B = \frac{1}{(2\pi f_B)^2 C_B}. \quad (13)$$

(6) Dielectric loss factor $\tan \delta$: By using ω_A and Q_A at the A-type resonance, and ω_B , Q_B and C_B/C_f at the B-type resonance, dielectric loss factor $\tan \delta$ can be given as follows;

$$\tan \delta = C_B/C_f \cdot (1/Q_A - \omega_B/\omega_A \cdot 1/Q_B). \quad (14)$$

4. Experiments

Quality factor Q_A and Q_B , temperature rises, capacitance ratio C_B/C_f and B-type

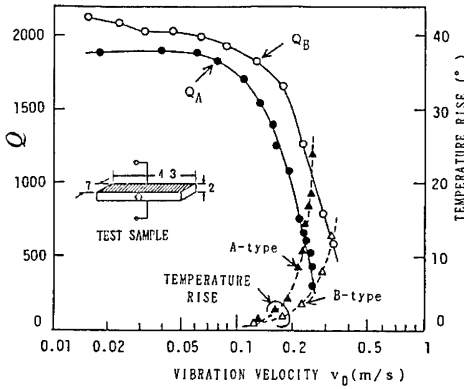


Fig.5 Vibrational velocity dependence of the quality factor and temperature rise for both A- and B-type resonances of a PZT ceramic longitudinally vibrating transducer.

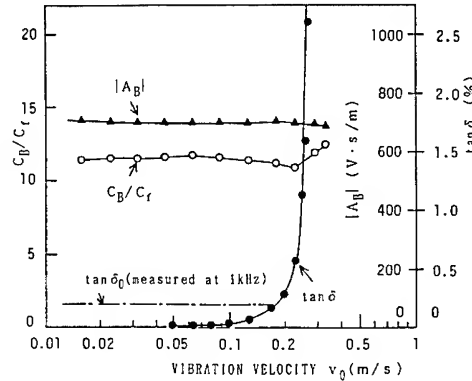


Fig.6 Vibrational velocity dependence of the capacitance ratio and force factor for B-type resonance and the dielectric loss factor $\tan \delta$.

force factor A_B have been investigated on a PZT ceramic rectangular bar. Vibrational mode considered here is the fundamental longitudinal mode. Experimental results of Q_A , Q_B and temperature rises are illustrated in Fig.5 as functions of vibrational velocity v_0 which was measured at the end of the ceramic bar using the "Fotonic Sensor". Also, temperature rise was measured at the center of the ceramic rectangular bar using a thermocouple. In

Fig.5, the configuration and the dimensions of the test sample are illustrated.

From the figure, it can be recognized that Q_B is higher than Q_A over the whole vibrational velocity range investigated here; from $v_0 \approx 0.02$ to about 0.3 (m/s), and the difference between Q_A and Q_B becomes greater with increasing vibrational velocity. Temperature rise of B -type resonance is less than that of A -type resonance because $1/Q_B$ is smaller than $1/Q_A$. These facts are caused by the presence of dielectric loss and its nonlinearity.

In Fig.6, capacitance ratio C_B/C_A , B -type force factor A_B and the dielectric loss factor $\tan\delta$ are shown. $\tan\delta$ was obtained using the experimental results of Q_A , Q_B and C_B/C_A . For comparison, $\tan\delta_0$ which is directly measured at a sufficiently low frequency (1kHz) is also shown in the figure. $\tan\delta_0$ includes an elastic loss brought by a quasi-static strain⁵⁾, therefore it is larger than $\tan\delta$ in a small vibrational velocity. C_B/C_A and A_B can be viewed as almost constant over the whole velocity range considered here. However, $\tan\delta$ has become larger markedly in the large vibrational velocity above about 0.2 (m/s).

5. Driving frequency and efficiency

Equivalent circuit shown in Fig. 3 can be converted equivalently to the one shown in Fig.7. This figure shows an equivalent electric circuit including the two resistances R_d and R_m . Here, Resistance R_d indicating dielectric loss is given by

$$R_d = \tan\delta / (\omega_A C_d), \quad (15)$$

where ω_A is the A -type resonance angular

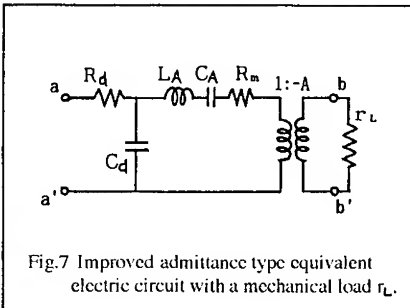


Fig.7 Improved admittance type equivalent electric circuit with a mechanical load r_L .

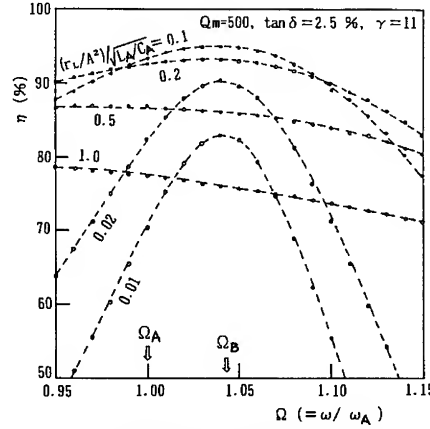


Fig.8 Frequency characteristics of the conversion efficiency η .

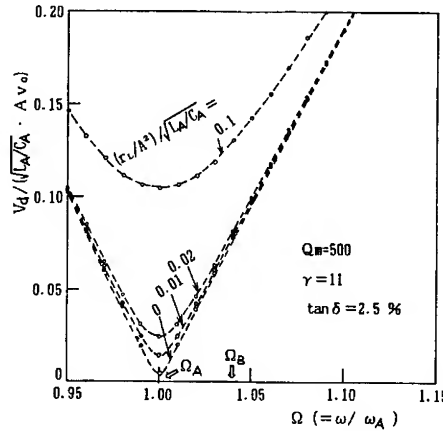


Fig.9 Driving voltage when the vibrational velocity is kept constant.

frequency. R_m is the equivalent resistance indicating mechanical vibration loss, which is given as

$$R_m = (\omega_A L_A) / Q_B, \quad (16)$$

where L_A is the A -type equivalent inductance.

A pair of the mechanical terminals indicated by b and b' in Fig.7 is placed to get mechanical power. For simulating the efficiency characteristics, mechanical load resistance r_L is connected to the mechanical terminals b and b' . Here, we as-

sume that the vibration mode of the transducer does not vary before or after connection of r_l . With the equivalent circuit shown in Fig.7, efficiency η (=mechanical output power/electric input power) can be calculated.

Figure 8 shows the calculated results of the frequency characteristics of η . Here, the horizontal axis is represented by a normalized angular frequency Ω ($=\omega/\omega_A$). In this calculation, the experimental results of $\tan\delta=2.5\%$ and $Q_B=500$ were utilized, and the parameter is the mechanical load resistance r_l normalized by the specific impedance $\sqrt{L_A C_A}$ of the equivalent circuit. When r_l is small, η represents a sharp frequency characteristics, and the apparent maximum point of η can be recognized. The value of Ω yielding maximum η is 1.045 in case of capacitance ratio γ being 11, and this value of Ω coincides with the normalized electrical antiresonance angular frequency Ω_A ($=\sqrt{1+1/\gamma}$). When r_l becomes larger, the frequency characteristics curve of η becomes less sharp.

Maximum efficiency can be calculated only by using the equivalent circuit which separately represents dielectric loss and mechanical vibration loss as shown in Fig.7. These results account for the experimental phenomena occurring in the high power operating piezoelectric devices such as an ultrasonic motor. On the other hand, in case of an ordinary equivalent circuit which incorporates dielectric loss and mechanical loss together; that is, includes only one equivalent resonant resistance, the peak point of efficiency may not appear.

Figure 9 shows the calculated results of the driving voltage when the vibrational velocity is kept constant; in other words, the driving voltage necessary to obtain the same vibrational velocity at any frequency near the resonance and antiresonance frequencies. Driving voltage at the antiresonance frequency is about several times larger than at the resonance frequency. However, this disadvantage can be overcome by the thin PZT layers such as in the multilayer actuator.

56. Conclusions

Methods of measuring the vibrational level dependence have been described for two driving frequencies; that is, resonance and antiresonance frequencies. In this paper, electrical resonance coincides with the mechanical A-type resonance, and electrical antiresonance coincides with the mechanical B-type resonance. From the experimental results, it has been shown that the quality factor Q_A of A-type resonance is always smaller than that of B-type resonance Q_B and the difference between them becomes larger with increasing vibrational velocity, and the temperature rise of B-type resonance is less than that of A-type resonance. In addition, capacitance ratio C_B/C_A and force factor A_B of B-type resonance have been shown to be almost constant over the range from $v_0 \approx 0.02$ (m/s) to about 0.3 (m/s). However, $\tan\delta$ has become larger markedly in the large vibrational velocity above about 0.2 (m/s).

By using the experimental results of the equivalent constants including the dielectric loss, efficiency of the transducers under high-power use has been calculated. From this results, maximum efficiency has been obtained at the antiresonance frequency. In addition, at this frequency, temperature rise is very small. Then, it has been concluded that the stable state driving of the high-power piezoelectric devices such as an ultrasonic motor can be achieved at the antiresonance frequency.

References

- 1) S.Hirose and H.Shimizu: Proc.1990 Spring Meeting of Acoust. Soc.Jpn. 2-2-2 [in Japanese].
- 2) S.Saito, R.Aoyagi and H.Shimizu: J.Acoust.Soc.Jpn.33-10(1977)p.540 [in Japanese].
- 3) H.Shimizu and S.Saito: J.Acoust.Soc.Jpn.(E)6-3(1985)p.225.
- 4) S.Hirose and H.Shimizu et.al.: Jpn.J.Appl.Phys.Suppl.30-1(1991)p.117.
- 5) S.Saito and H.Shimizu: Jpn.J.Appl.Phys.Suppl.24-3(1985)p.145.

FERROELECTRIC DOMAIN INVERSION IN LiNbO_3 AND ITS APPLICATION TO HIGH-PRECISION PIEZOELECTRIC ACTUATORS

KIYOSHI NAKAMURA AND KEN YAMADA

Faculty of Engineering, Tohoku University, Sendai 980, Japan

ABSTRACT

Heat treatment of bare single-domain LiNbO_3 plates near the Curie temperature induces a local polarization reversal, thereby yielding a ferroelectric inversion layer. For a sufficiently long heat treatment the inversion layer thickness becomes equal to one half of the plate thickness. Similar domain inversion is also induced by heat treatment of proton-exchanged LiTaO_3 . These domain inversion phenomena and a model for explaining the mechanism are reviewed.

The inversion layer has piezoelectric constants opposite in sign to those of the uninverted domain. Therefore, a LiNbO_3 plate with such an inversion layer can be used as a piezoelectric actuator similar to the bimorph, because bending motion or torsional motion can be piezoelectrically produced, depending on the plate orientation. The measured characteristics of these actuators are presented and demonstrated to exhibit excellent linearity and no hysteresis.

INTRODUCTION

Lithium niobate (LiNbO_3)^{1,2} is widely used in various piezoelectric devices because of its high electromechanical coupling factors. It is also important as a substrate material for optical waveguide devices. Most practical LiNbO_3 crystals are composed of a single ferroelectric domain. The Curie temperature of this crystal grown from congruent melts is as high as about 1150°C, and it is not easy to reverse the spontaneous polarization at room temperatures.

Ohnishi³ reported that heat treatment at about 1000°C of a LiNbO_3 plate etched in a mixture of HF and HNO_3 created a 1-15 μm thick domain with a reversed polarization at the +c surface. Nakamura et al.⁴⁻⁶ found that domain inversion took place when unetched bare LiNbO_3 plates underwent heat treatment at temperatures above 1070°C, and showed that the domain boundary of the resulting ferroelectric inversion layer ultimately stopped at the median plane of plate for sufficiently long heat treatment. Similar domain inversion was observed at the -c face of LiTaO_3 by proton-exchange followed by heat treatment near the Curie temperature.⁷⁻⁹ These domain inversion phenomena occur in local regions of crystals under no applied electric field.

The inverted domain with a reversed spontaneous polarization P_s has piezoelectric, pyroelectric, electro-optic, and 2nd-order nonlinear optic constants opposite in sign to those of the uninverted region. This character of inverted domains can be utilized for various devices.¹⁰ For example, the strains piezoelectrically generated in the two regions are

opposite in sign to each other. This fact enables us to obtain bending actuators¹¹ and torsional actuators¹² consisting of a single plate.

This paper reviews the domain inversion induced by heat treatment and describes applications of the resulting domains to high-precision piezoelectric actuators.

DOMAIN INVERSION INDUCED BY HEAT TREATMENT

Heat treatment of unetched bare LiNbO_3 plates at temperatures higher than about 1070°C induces local domain inversion, thereby yielding a ferroelectric inversion layer at the +surface with respect to spontaneous polarization.⁴⁻⁶ As the heat treatment temperature and time are increased, the inversion layer becomes thick. It seems that the domain boundary ultimately stops near the median plane of plate for sufficiently long heat treatment. Figure 1 shows a typical photomicrograph revealing the domain structure in the cross-section of a 140° rotated Y-cut plate about $500\text{ }\mu\text{m}$ thick. The thickness of the inversion layer also depends on the atmosphere. Although a wet atmosphere was used for the purpose of preventing outdiffusion of Li,¹³ water vapor seems to have a significant effect in promoting domain inversion.^{8,14} The domain inversion was confirmed to also take place in plates with an inclined spontaneous polarization, except X- and Y-cut plates. One would think that when a lithium niobate crystal is heat treated above the Curie temperature T_c it should become a multi-domain crystal. However, contrary to our anticipation, a domain structure similar to that shown in Fig.1 was formed even by heat treatment above T_c .¹⁴ Li outdiffusion is likely to play an important role in the domain inversion.⁶ This has been supported by the experimental fact that domain inversion has not occurred in the surface portion masked by a Ti, Pt, or Mo film.¹⁵⁻¹⁷

Lithium tantalate (LiTaO_3), which is isomorphous to lithium niobate, has a lower Curie temperature around 600°C . To examine whether the formation of inversion layers in LiTaO_3 crystals is possible or not, heat treatment of Z-cut LiTaO_3 was performed at temperatures from 570 to 590°C . However, no domain inversion was observed. The authors et al.⁷⁻⁹ surmised that inversion might be instigated by forming a Li deficient surface layer in

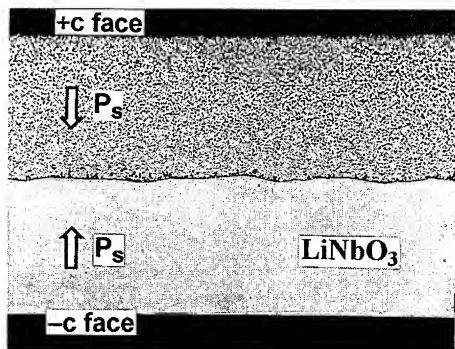


Fig.1 Etched cross-section of a 140° rotated Y-cut LiNbO_3 plate heat treated at 1140°C for 10h.

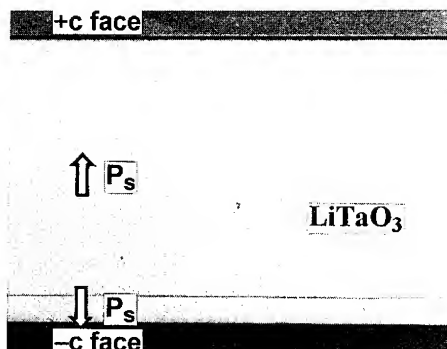


Fig.2 Etched cross-section of a Z-cut LiTaO_3 plate proton-exchanged at 220°C for 9h and heat treated at 590°C for 3h.

the proton exchange process¹⁸ and then heat-treating near the Curie temperature. In the proton exchange process Li^+ ions near the surface of LiTaO_3 are replaced by H^+ ions supplied from an acid. Figure 2 shows a photomicrograph of a cross section of a 500 μm -thick Z-cut plate proton-exchanged in a melt of benzoic acid at 220°C for 9 h, and then heat-treated for 3 h at 590°C. An inversion layer can be seen on the original $-c$ face side. This experimental result is in notable contrast with the fact that in LiNbO_3 the inversion layer is formed at the $+c$ surface.

The inversion layer thickens with increasing proton exchange time and temperature. It also thickens with increasing heat treatment time in the range less than 1 h, while remaining almost constant at longer times. When proton exchange was performed in phosphoric acid or pyrophosphoric acid instead of benzoic acid, domain inversion also took place.^{7,19} The use of appropriate masks for preventing proton exchange permits selective domain formation.^{7,19}

One model for explaining the mechanism of the domain inversion in LiTaO_3 has been proposed.^{8,20,21} This model is associated with an outward-directed space charge field built up near the surface by the excessively implanted protons, and is likely to well explain why the domain inversion takes place only at the $-c$ surface of plates heated near the Curie temperature. This model might apply to the domain inversion in LiNbO_3 with some modifications. Figure 3 shows the model for LiNbO_3 . At high temperatures over 1000°C Li^+ ions as well as Li_2O may outdiffuse and thereby negative space charges may be formed near the surface. The space charges and compensating charges on the surface may produce an inward-directed electric field near the surface. This space-charge field will cause domain inversion at the positive surface, where the field is opposite to the spontaneous polarization, if it is higher than the coercive field.

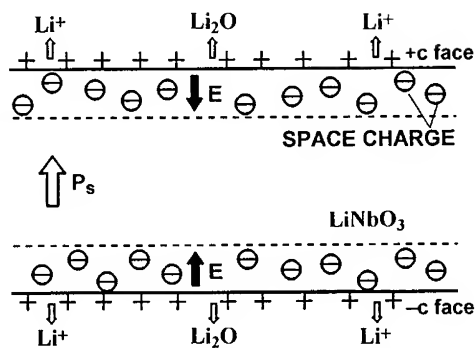


Fig.3 A model to explain the mechanism of domain inversion in LiNbO_3 .

PIEZOELECTRIC ACTUATORS

Features of LiNbO_3 as Actuator Materials

Piezoelectric ceramic actuators in wide use inherently exhibit hysteresis and creep, primarily resulting from domain reorientation. In contrast, the domain state in LiNbO_3 is unchangeable at room temperatures by application of a high electric field. Therefore lithium niobate actuators would exhibit no hysteresis and no creep. Additional advantages of LiNbO_3 single-crystal actuators over ceramic actuators are as follows: they can operate over a wide temperature range because they have a very high Curie temperature and exhibit no degradation in piezoelectricity at low temperatures; a small driving current is sufficient for operation because the electrical capacitance is small; displacement drift resulting from temperature rise during operation may be small because of their low dielectric and mechanical losses. Consequently, the LiNbO_3 actuators are most suitable for applications

requiring precise control.

One shortcoming of LiNbO_3 actuators is that the piezoelectric strain constant is considerably small as compared to that of ceramics. However, the range of displacement may not be necessarily so small because they would exhibit no definite saturation characteristics for both positive and negative high voltages.

Bending Actuators^{11,22}

In inverted domains, the crystallographic X axis is identical with that in the original crystal, while the Y and Z axes are oppositely directed to those in the original crystal. This means that in a coordinate system all the piezoelectric constants in the inverted domains are opposite in sign to the original ones. This character of the inverted domains can be utilized for various piezoelectric devices which cannot be realized using a single domain crystal. In what follows we shall consider the use of LiNbO_3 plates with an inversion layer as piezoelectric actuators, because LiNbO_3 is superior to LiTaO_3 in piezoelectricity.

Figure 4 illustrates a θ° -rotated Y -cut LiNbO_3 wafer with a ferroelectric inversion layer. If a rectangular plate with its longer side directed along the Z' axis is cut from the wafer, it serves as a bending vibrator or actuator as shown in Fig.5, because the piezoelectrically generated length-extensional strain S_3 in the inversion layer is opposite in sign to that in the other part with the original spontaneous polarization. This actuator is similar to the bimorph but consists of a single piezoelectric plate with no bonding layer.

If the heat treatment time is sufficiently long, the inversion layer thickness t_1 becomes equal to one half of the plate thickness t . This fact is favorable for fabrication of actuators. In this configuration of $t_1=t/2$, the displacement u at the free end of the plate with the other end clamped can be expressed as

$$u = \frac{3}{2} \frac{l^2}{t^2} d_{23} V \quad (1)$$

where V is the applied voltage and d_{23} is the piezoelectric strain constant associated with

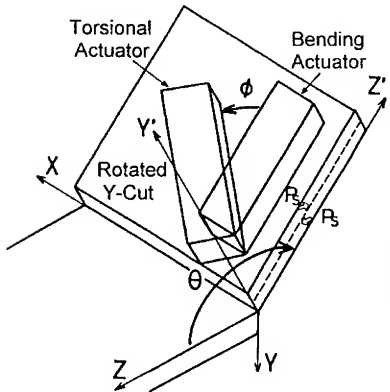


Fig.4 Cuts for actuators.

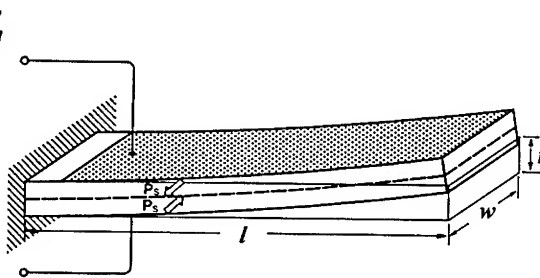


Fig.5 Bending actuator using an inversion layer.

the length-extensional strain S_3 in the rotated coordinate system. The dependence of d_{23} on the rotation angle θ was calculated using the constants in Ref.(23). The piezoelectric strain constant d_{23} has a maximum value of 30.3 pC/N at $\theta=140^\circ$. This cut is the optimal one for bending actuators and has a high coupling factor k_{23} of about 0.51. To the best of our knowledge, this is the largest transverse coupling factor.

LiNbO₃ samples used for experiments were cut from a single domain 140° rotated Y-cut wafer about 500 μm thick. Heat treatments of the unmetallized LiNbO₃ plates were performed at 1140°C for ten hours with flowing Ar gas containing water vapor. It was confirmed by an etching experiment that an inversion layer with a thickness approximately equal to half the plate thickness was formed. Finally, Al electrodes were deposited on both faces.

One end of an actuator with a thickness of 0.5 mm was clamped with a mounting assembly. When a voltage of one-cycle triangular waveform was applied to the actuator, the displacement at the other end was measured with an optical displacement measurement system. Figure 6 shows a displacement vs voltage relationship. It proves that the actuator has a hysteresis-free characteristic with excellent linearity even for such a large deformation. The displacement response of the actuator to the application of a 100V step voltage was examined. The measured response exhibited little creep as shown in Fig.7.

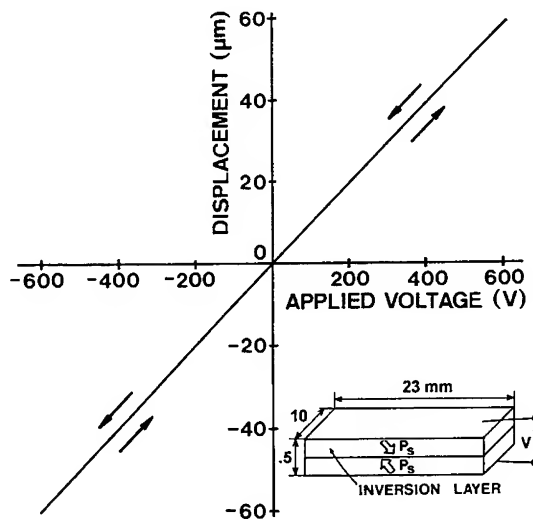


Fig.6 Displacement vs applied voltage relationship of a bending actuator.

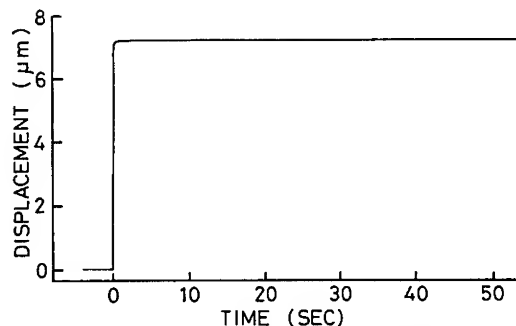


Fig.7 Displacement response of a bending actuator to a step-voltage.

Torsional Actuators¹²

If a similar torsional actuator consisting of a LiNbO₃ plate with an inversion layer can be obtained, it would be useful as a high precision light deflector or scanner. If we assume that the piezoelectric strain constant d_{25} is nonzero, the face-shear strain S_5 can be piezoelectrically generated and it is opposite in sign between the two domains. This results in torsional motion of the plate.

In a rectangular plate with its longer side directed along the Z' axis, the piezoelectric strain constant d_{25} associated with the face-shear strain S_5 is zero. However, in a rectangular plate ϕ -tilted from the Z' axis (see Fig.4), the magnitude of $|d_{23}|$ decreases and instead that of $|d_{25}|$ increases. Figure 8 shows $|d_{23}|$ and $|d_{25}|$ for 140° rotated Y-cut LiNbO₃ plates as functions of the cutting angle ϕ . When a voltage is applied across the thickness of the plate, a face-shear strain S_5 is generated in the inversion layer via d_{25} and it is opposite in sign to that in the uninverted domain layer. Thus, a torsional actuator can be obtained. However, the torsional motion is generally accompanied by bending motion. For generation of pure torsional motion the piezoelectric constant d_{23} must be zero. The optimal cut for the torsional actuator, where $|d_{25}|$ is maximum while satisfying $d_{23}=0$, was theoretically found to be $\theta=148^\circ$ and $\phi=52.2^\circ$,¹² where $d_{25}=44.6$ pC/N and $k_{25}=0.46$.

The structure of a light deflector of length l , width w , and thickness t is shown in Fig.9. We shall assume that a ferroelectric inversion layer of thickness $t/2$ is formed in the rectangular plate. When one end of the actuator is clamped, the torsion angle α at the other free end is given by^{12,25}

$$\alpha = \frac{3}{2} d_{25} \frac{l}{t^2} V. \quad (2)$$

where V is the applied voltage. The deflection angle of light is twice the torsion angle of the actuator. This device also has features similar to those of the bending actuator

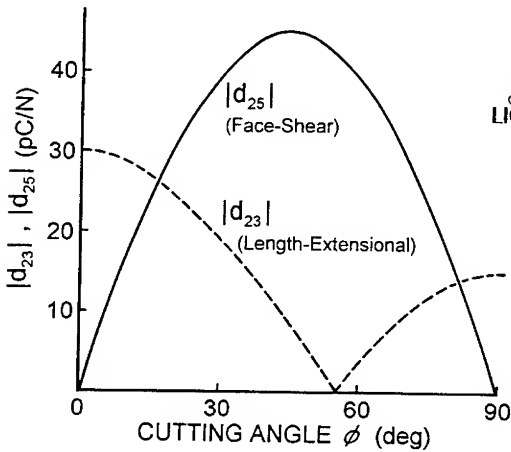


Fig.8 Piezoelectric constants, $|d_{23}|$ and $|d_{25}|$, as functions of the cutting angle ϕ for $\theta=140^\circ$.

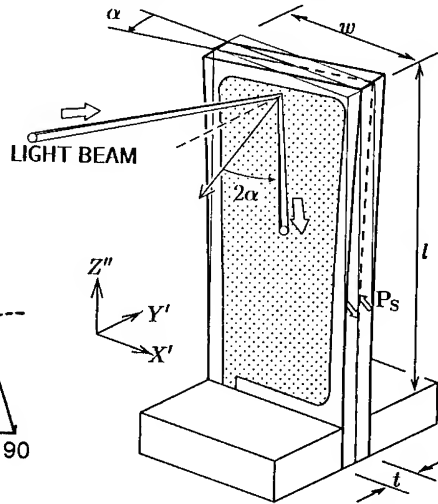


Fig.9 Torsional actuator using an inversion layer.

described above and is useful as a laser-beam scanner.

Experiments were made using rectangular plates cut from a 140° rotated Y-cut LiNbO_3 wafer at an angle ϕ of 54.5° , which also satisfy the condition $d_{23}=0$. The constants are almost the same as those of the optimal cut.

Heat treatment of a 0.1mm-thick LiNbO_3 wafer was performed at 1120°C for 90 minutes. Al electrodes were deposited on both polished major surfaces except the plate edge. The electrode also serves as a reflecting mirror for light beam deflection. When a He-Ne laser beam is incident on the mirror electrode on an actuator whose one end is clamped, the light deflection angle was measured using a position sensitive photodetector. Figure 10 shows the light beam deflection angle vs voltage relationship of a torsional actuator of $l=17$ mm, $b=5$ mm, and $t=0.1$ mm. The beam deflection angle is as large as about $\pm 12^\circ$ at an applied voltage of $\pm 1.4\text{kV}$, that is, the scanning range of light is about 24° . The linearity is excellent for such large deformation. It was also confirmed that the actuator had hysteresis-free characteristics. The measured light beam deflection angle was in good agreement with the calculated one.

In applications where a simple scanning of a light beam are required, a vibrational operation at the resonance frequencies can be used. This resonant operation enables us a large light deflection angle with a small applied ac voltage. To attain high-frequency scanning, a small-size actuator 7.5mm long and 3mm wide was fabricated. The actuator was driven at the fundamental resonance frequency. As the resonance frequency varied a little with the applied voltage, the driving frequency was always adjusted to it. Figure 11 shows the scanning angle of light beam along with the resonance frequency. This small-size light deflector operates at a high frequency and enables a fairly large deflection angle with a low applied voltage.

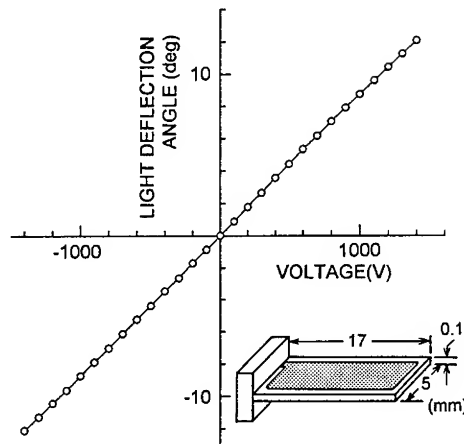


Fig.10 Light-beam deflection angle vs voltage relationship.

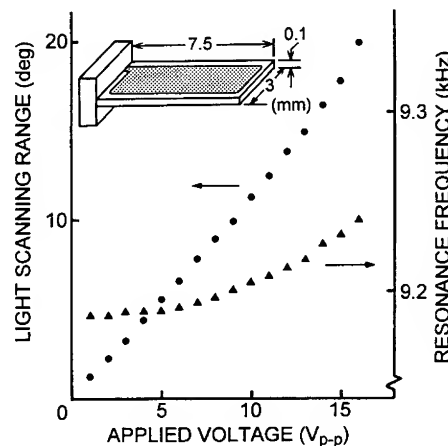


Fig.11 Scanning range of light-beam and resonant frequency for resonant operation

CONCLUSION

Ferroelectric domain inversion phenomena induced in LiNbO_3 and proton-exchanged LiTaO_3 crystals during heat treatments in the absence of applied electric fields have been reviewed. Although the mechanisms of the phenomena have not been completely understood yet, the space charge field model for the mechanism seems to be a reasonable one.

Bending actuators and torsional actuators consisting of a LiNbO_3 single crystal plate with a ferroelectric inversion layer have been described. These actuators can be obtained by using respective optimal cuts, which have been theoretically found. Some actuators fabricated using 140° rotated Y-cut LiNbO_3 wafers with an inversion layer have been demonstrated to have hysteresis-free characteristics with excellent linearity and to exhibit little creep. These characteristics of the actuators are very attractive for high-precision positioning without any feedback control.

Acknowledgments

The authors would like to thank T.Nakamura and K.Ishikawa for their contribution to fabrication of actuators. This work was in part supported by a Grant-in-Aid for Scientific Research from the Ministry of Education, Science and Culture of Japan, and the Asahi Glass Foundation.

References

1. K.Nassau, H.J.Levinstein and G.M.Loiacono, *J.Phys.Chem.Solids* **27**, 983 (1966).
2. A. Rauber, in *Current Topics in Materials Science*, edited by Kaldis (North Holland, Amsterdam, 1978) Vol.1, p.481.
3. N.Ohnishi, *Jpn.J.Appl.Phys.* **16**, 1069 (1977).
4. K.Nakamura, H.Ando and H.Shimizu, *Proc.15th EM Symp.*(1986) p.29[in Japanese].
5. K.Nakamura, H.Ando and H.Shimizu, *Proc.1986 IEEE Ultrason.Symp.* (1986) p.719.
6. K.Nakamura, H.Ando and H.Shimizu, *Appl.Phys.Lett.* **50**, 1413 (1987).
7. K.Nakamura, H.Ando, M.Hosoya and H.Shimizu, *Tech.Rep.IEICE Jpn.*, US87-37 (1987) [in Japanese].
8. K.Nakamura and H.Shimizu, *Proc.1989 IEEE Ultrason. Symp.*, p.309.
9. K.Nakamura and H.Shimizu, *Appl. Phys.Lett.* **56**, 1535 (1990).
10. K.Nakamura, *Jpn.J.Appl.Phys.* **31**, Suppl.31-1, 9 (1992).
11. K.Nakamura and H.Shimizu, *Ferroelectrics* **93**, 211 (1989).
12. K.Nakamura, T.Nakamura and K.Yamada, *Jpn.J.Appl. Phys.* **32**, 2415 (1993).
13. J.L.Jackel, V.Ramaswamy and S.P.Lyman, *Appl.Phys.Lett.* **38**, 509 (1981).
14. K.Nakamura, K.Ishikawa and T.Kawai, *Proc. 8th Meeting of Ferroelectric Materials and Their Applications* (1991) p.107[in Japanese].
15. J.Webjorn, F.Laurell and G.Arvidsson, *J.Lightwave Technol.* **7**, 1597 (1989).
16. K.Nakamura and K.Ishikawa, 1990 Tohoku-Section Joint Convension Record of Institutes of Electrical and Information Engineers Jpn.(1990) p.69[in Japanese].
17. C.Isobe, Y.Taneyama and M.Saitoh, *Proc.51st Autumn Meeting of Jpn. Society of Applied Physics* (1990) p.925 [in Japanese].

18. J.L.Jackel, C.E.Rice and J.J.Veselka: Appl.Phys.Lett. **41**, 607 (1982).
19. K.Mizuuchi, K.Yamamoto and T.Taniuchi: Appl.Phys.Lett. **58**, 2732 (1991).
20. Ailie Tourlog and K.Nakamura, Tech.Rep.IEICE Jpn., US91-49 (1991)[in Japanese].
21. K.Nakamura, M.Hosoya and A.Tourlog, J.Appl.Phys. **73**, 1390 (1993).
22. K.Nakamura, H.Ando and H.Shimizu, Jpn.J.Appl.Phys. **26**, Suppl.26-2, 198 (1987).
23. A.W.Warner, M.Onoe and G.A.Coquin, J.Acoust. Soc. Am. **42**, 1223 (1967).
24. M.Ueda, H.Sawada, A.Tanaka and N.Wakatuki, Proc.1990 IEEE Ultrason. Symp. (1990) p.1183.
25. T.Suzuki, J.Acoust.Soc.Jpn. **27**, 87 (1971)[in Japanese].

PART II

Ferroelectric Composites

COMPOSITE PIEZOELECTRIC SENSORS AND ACTUATORS

R. E. NEWNHAM, J. F. FERNANDEZ, K. A. MARKOWSKI, J. T. FIELDING, A. DOGAN
AND J. WALLIS

Materials Research Laboratory, The Pennsylvania State University, University park, PA 16802

ABSTRACT

Composite materials have found a number of structural applications, but their use in the electronics industry has been relatively limited. As the function of electroceramic composites are better understood, we can expect this picture to change. In this paper some of the piezoelectric composite sensor and actuator studies carried out in our laboratory during the past decade will be reviewed. The ideas that provide a basic understanding of functional composites have previously been discussed [1]. This paper describes recent advances in the processing and properties of composites possessing 0-3, 1-3, and 2-2 connectivity made of polymers, metals and ferroelectric ceramics. The introduction of open spaces in the previous connectivity patterns allows the development of new designs of several piezoelectric composites with connectivity patterns of 0(0)-3, 1(0)-3, 2(0)-2-2, and 2-0-2. As in most electronic systems that are developed with improved properties a push toward lower cost and smaller sizes of the piezoelectric ceramics, together with improved reliability and performance occurs. The piezocomposites with open spaces in their structures clearly demonstrate the growth of the functional ceramics into the field of the smart ceramics as the materials for the beginning of the next century.

INTRODUCTION

PZT is widely used as a transducer material because of its high piezoelectric coefficients. However, for hydrophones applications, PZT is a poor material for several reasons. The hydrostatic piezoelectric coefficient, $d_h (=d_{33} + 2d_{31})$, is very low. The piezoelectric voltage coefficients, g_{33} and g_h , are low because of the high dielectric constant of PZT (1800). The acoustic matching of PZT with water is poor because of its high density (7.9 g/cm³). Moreover, it is a brittle, non-flexible ceramic.

In the last decade, several investigators have tried to fabricate composites of PZT and polymers to overcome the above problems of PZT. The fabrication of piezoelectric composites requires careful replacement of a portion of the ceramic with a polymer. This replacement allows the reduction of the acoustic impedance of the piezoelectric ceramics for application in a system containing water or a living body. It has been shown that it is possible to improve upon the piezoelectric properties of homogeneous PZT by the composite approach. The concept that the connectivity of the individual phases controls the resulting properties has been demonstrated in a number of composites with different geometry and different connectivity of the individual phases. The hydrostatic piezoelectric properties of these composites are superior to single-phase PZT. However, some of the earlier composites suffer from disadvantages due to difficulty in preparation or reduction in hydrostatic sensitivity with increasing pressure. Thus, there still exists a need to further improve the piezoelectric properties of these composites. A primary goal is to reproducibly fabricate composite transducers with high figures of merit and minimal pressure sensitivity, under hydrostatic loading, for hydrophone applications.

COMPOSITE TRANSDUCERS

A transducer is a device that converts mechanical energy into electrical energy and vice versa. In a passive mode, operating at a low frequency, it can function as a hydrophone, detecting sound

underwater. Typical operating frequencies lie in the low kilohertz range; since the acoustic wavelengths in that range are much larger than the transducer, it must respond to an isotropic stress. Sonar transducers are quite larger. For ultrasonic imaging applications the piezoelectric composites must both transmit a strong acoustic pulse, as well as receive the weak echoes reflected from the internal structures of a living body or water systems. Typical medical ultrasonic probes are a few centimeters in size; such probes typically operate in the low megahertz frequency range. Closely allied to medical ultrasonics are other pulse-echo acoustic imaging applications in non-destructive testing. These uses span from inspecting materials for internal flaws to oil logging. The operating frequencies extend to much higher values, nearing gigahertz in some cases. Another interesting class of pulse-echo devices that requires frequencies down to the mid kilohertz range involves imaging through the air. Typical examples are autonomous vehicle guidance and manufacturing assembly. When designing a transducer for a particular application, the choice of transducer material is critical. Ideal properties would include high piezoelectric response in both transmission and receiving modes while maintaining low density and high flexibility.

Early investigators concentrated on polymer-ceramic composites for use as hydrophones [2]. Several interesting connectivity patterns [3] were developed including 3-3 structures made by the replamine process [4] and by the fugitive phase technique [5,6]. Then came the more used 1-3 composites consisting of parallel PZT fibers embedded in a polymer matrix. These structures were made by extrusion [7], by dicing [8], and more recently by injection molding [9] and lithographic lost-wax techniques [10]. The coupling between the ceramic fibers and the polymer matrix is important [11]. In optimizing hydrophone performance, the d_{hg} product was chosen as a figure of merit. The 1-3 composite increases effective values of d_h and g_h by reducing the d_{31} piezoelectric coefficient and the dielectric constant while maintaining the large d_{33} coefficient.

The usefulness of the 1-3 composite in high frequency applications for non-destructive testing and medical diagnostics was recognized later [12-14]. Biomedical transducers require resonant frequencies in the 1-10 MHz range, high electromechanical coupling coefficients, low acoustic impedance, and broad bandwidth. The 1-3 transducers manufactured by Siemens [10] have thickness resonances of 5-10 MHz, coupling coefficient $k_t=0.67$, $K=600$, $\tan \delta < 0.025$, and a mechanical Q of about 10.

Poling is sometimes difficult for the long, slender PZT fibers used in 1-3 composites. Electric breakdown often occurs before poling is complete, and the transducer is ruined. Lower poling and driving fields are obtained when the spaghetti-like PZT fibers are replaced with macaroni-like PZT tubules [15]. When electroded inside and out, the thin-walled tubes are poled and driven radially at relatively modest voltages. Radial motions are coupled to length-wise displacements through the d_{31} coefficient. Effective piezoelectric constants of about 8000 pC/N and large d_{hg} products are achieved with these composites [16]. Other variants on the basic 1-3 structure include the 1-2-3 composite with transverse load bearing fibers [17], and the 1-3-0 composite with a foamed polymer matrix [18], and the interesting woven fiber composites devised by Safari and co-workers [19].

Perhaps the simplest piezoelectric composite is the 0-3 transducer made by dispersing ceramic particles in a polymer matrix [20]. The NTK Piezo-Rubber films and cables are used as flexible hydrophones, keyboards, blood pressure cuffs, and musical instruments. They are made by hot-rolling $PbTiO_3$ /PZT ceramic powder mixtures into a chloroprene rubber matrix [21-22]. New piezoelectric mechanical dampers have been produced using composites of piezoelectric-polymer-carbon black [23]. Damping characteristics are controllable by changing the conductivity through the carbon black concentration.

It was demonstrated by Safari [24] that based on the theory of connectivity, new composites with different connectivity patterns could be fabricated with enhanced performance. Most of the work involved composites with 1-3 and 2-3 connectivity. These composites were prepared by drilling either circular or square holes in prepoled PZT blocks, in a direction perpendicular to the poled axis, and by filling the drilled holes with epoxy. On the samples optimized for hydrophone performance, the g_h and d_{hg} coefficients were about 4 and 40 times greater, respectively, for the 1-3 composites; and 25 and 150 times greater for the 2-3 composites compared to those of solid PZT. For 1-3 composites, there was practically no variation of g_h with pressure up to 8.4 MPa. In the case of 2-3 composites, there was a slight variation of g_h with pressure.

PIEZOCOMPOSITES WITH OPEN SPACES

Current research on piezoelectric sensors and actuators is moving toward miniaturization to achieve better resolution and higher power densities. High resolution and small sizes are needed in applications such as biomedical ultrasound, probes for invasive procedures, flow noise control, and non destructive testing evaluation of composites. Higher frequencies and better impedance matches are advantageous in underwater transducers and biomedical ultrasonics. The introduction of open spaces in piezocomposites meet both of these criteria. In most of the cases new careful design of piezocomposites with open spaces leads to an improvement of the properties and sometimes to development of easier, safer and lower cost applications of piezoelectric materials. Table I summarizes new trends in the design of piezocomposites with open spaces.

TABLE I
New trends in piezocomposites design with open spaces

Previous			New design		
Connectivity pattern	Type	Name	Connectivity pattern	Type	Name
0-3	PT/PZT polymer	Piezo-rubber	0(0)-3	PZT hollow spheres	BB's
1-3	PZT fiber in polymer	PZT spaghetti	1(0)-3	PZT tubules in polymer	PZT macaroni
2-2	Tape cast PZT multilayer	PZT actuator	2(0)-2-2	capped PZT	PZT moonie
2-2	cantilever	PZT bimorph	2-0-2	split bimorph	PZT zig zag

BB Transducers

BB's are hollow spherical transducers a few millimeters in diameter, about the same size as the metallic pellets used in air rifles (BB guns). PZT BB's are mass produced, by a patented forming process in which air is blown through a PZT slurry of carefully controlled viscosity [25]. The hollow spheres are 1-6 mm in diameter with wall thickness of 0.1 mm. Densities are about 1.3 g/cm³ giving the BB a low acoustic impedance close to that of water and human tissue.

When embedded in a polymer matrix to form a 0-3 composite the BB spheres are surprisingly strong, and able to withstand large hydrostatic pressure without collapse. Close-packed transducer arrays are easily assembled [26]. Investigation for electrical properties of composites is now under progress.

When electroded inside and out, and poled radially the BB becomes an omnidirectional transducer suitable for underwater or biomedical applications. For spheres with a 2.6 mm diameter and 90 nm thick walls, the resonant frequencies are 700 kHz for the breathing mode (d_{31}) and 10 MHz for the wall thickness mode (d_{33}) [26], figure 1. BB's are small enough to be used in catheters for non-invasive surgery to act as beacons, sensors, and actuators [27]. More than a million such procedures are now carried out annually.

Zig-Zags

Zig-zag actuators are split bimorphs in which two ceramic legs are driven independently to generate synchronized horizontal and vertical displacements. The legs are joined in a teepee-like configuration which imparts a rolling motion to the load. Typical motions are in the 1- 30 μ m range and look to be useful in piezomotor and conveyor belt applications due to the ability to drive a load in two directions [28]. The mechanical impedance can be optimized by changing the angle between the legs, and the actuator's working parameter controlled by changing the driving voltage and its frequency.

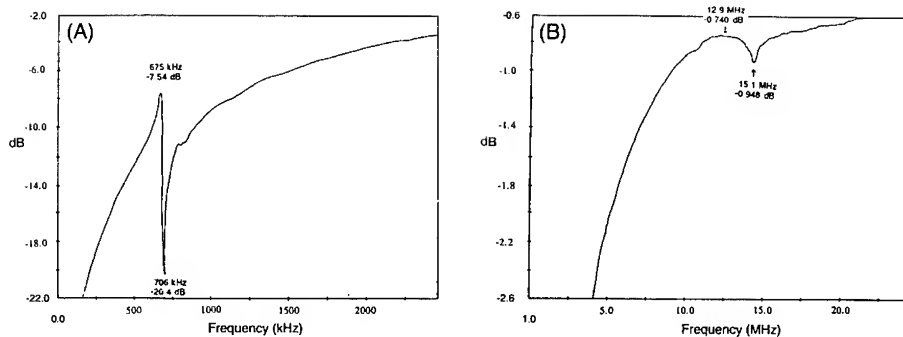


Figure 1. Admittance spectra showing (A) the fundamental or breathing mode resonance for a radially poled sphere and (B) the thickness mode resonance for a radially poled sphere having an average wall thickness of 75 μm and a diameter of 2.6 mm.

Flextensional Transducers "Moonies"

In recent years, piezoelectric and electrostrictive ceramics have been used in many actuator applications. To meet these needs a new type of composite actuator based on a flextensional transducer has been developed [29-34]. This ceramic-metal composite actuator, or "moonie", consists of either a piezoelectric ceramic disc or a multilayer stack, sandwiched between two specially designed metal end caps. The basic configuration of the moonie is shown in figure 2. The metal end caps serve as mechanical transformers for converting and amplifying the lateral motion of the ceramic into a large axial displacement normal to the end caps. Both the d_{31} ($=d_{32}$) and d_{33} coefficients of the piezoelectric ceramic contribute to the axial displacement of the composite. Figure 3 shows the enhanced displacement of the moonie actuator as a function of applied electric field compared to PZT ceramic. This design provides a sizable displacement, as well as a large generative force. In other words, it bridges the gap between the two most common types of actuators, the multilayer and the bimorph [35]. The shallow spaces under the end caps produce a substantial increase in strain by combining the d_{33} and the d_{31} contributions of the ceramic. It is attractive for hydrophone, transceiver and actuator applications, and is especially advantageous for use as a non-resonant, low frequency projector in deep water.

APPLICATIONS OF THE FLEXTENSIONAL TRANSDUCERS "MOONIES"

Three applications for this type of flextensional transducer, the moonie, have been explored [36]: they include hydrophone sensors, transceivers for fish finders, and positional actuators. Geometry and bonding effects on the resonance characteristics and displacement of the moonie transducer were investigated using finite element analysis (FEA).

Hydrophone Applications of the Moonie

Hydrophone sensitivity depends on d_h , the hydrostatic piezoelectric charge coefficient, and g_h , the hydrostatic piezoelectric voltage coefficient. The moonie transducer was introduced as a hydrophone having the highest figure of merit, $d_h \times g_h = 50,000 \times 10^{15} \text{ m}^2/\text{N}$, which is about

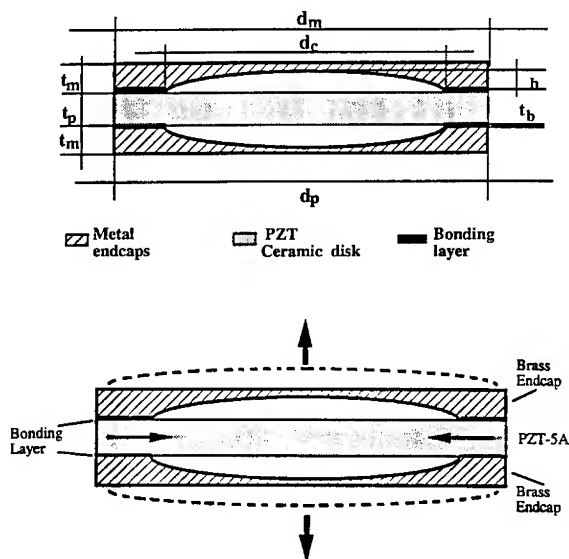


Figure 2. The geometry of the ceramic-metal composite actuator "Moonie". The arrows describe the direction of displacement when the moonie is driven under field in the same direction as the poling of the ceramic.

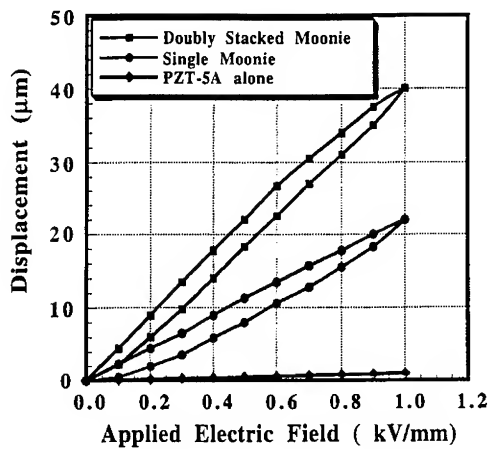


Figure 3. The displacement characteristics of the moonie actuator as a function of the applied \vec{E} field. Dimensions: $d_m=12.7$, $d_p=12.7$, $d_c=9.0$, $h=0.2$, $t_p=1.0$, $t_m=0.3$ (all in mm).

500 times larger than the PZT ceramic, as well as maintaining high capacitance and pressure tolerance. The stress distribution of the moonie hydrophone under a hydrostatic pressure was determined using FEA. FEA showed that extensional stresses along the radial and tangential directions were generated under a hydrostatic pressure, and contributed significantly to the very high figure of merit of the moonie.

In addition to this, the effect on prestresses caused by thermal treatment of the moonie were also estimated. The maximum stress concentration reached several hundred MPa. The maximum compressive stress concentration reaches about 300 MPa along the radial direction at the inner bonding edge, and 400 MPa extensive stress concentration occurs at the cavity located at the top of the cap.

The combined effect of high hydrostatic pressure (7 MPa corresponding to a 700 m water depth), and thermal processes were also estimated. Even 7 MPa hydrostatic pressure causes little deformation to the moonie hydrophone because the effect of relatively large prestress pressures exceed those of the hydrostatic environment. This is one of the reasons that the moonie hydrophone has high pressure tolerance.

Transceiver for Fishfinder: Applications of the "Moonie".

Using FEA to design the moonie fish finder made it possible to predict the flextensional resonance frequency. The effect of the following five geometrical parameters: PZT diameter, PZT thickness, cap thickness, cavity size, and bonding layer thickness on the resonant frequency were carefully investigated. Among these parameters, the resonant frequency is sensitive to the diameter, cap thickness and cavity size. The bonding layer thickness, however, has little effect on the resonant frequency. It was found that the lowest flextensional frequencies are proportional to the square root of the cap thickness and inversely proportional to the square of the diameter. These results are demonstrated in figures 4 and 5.

From the results obtained by Onitsuka [36] the moonie fish finders showed high response sensitivity but poor transmission. The high impedance of the moonie fish finder makes it difficult for practical for usage because of the impedance mismatching with water. Additional outside inductance in the circuit will help to reduce the impedance.

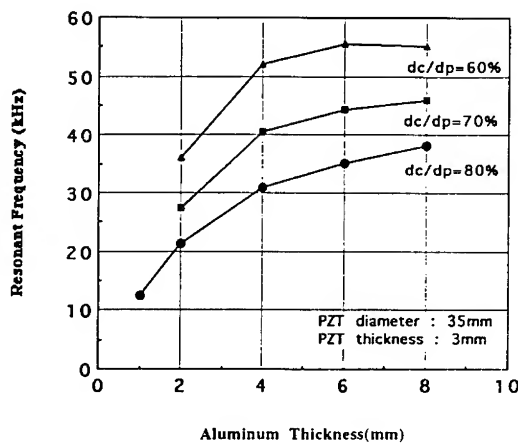


Figure 4. Calculated first resonant frequency plotted as a function of aluminum thickness and cavity size: Cavity size = $d_c/d_p \times 100\%$.

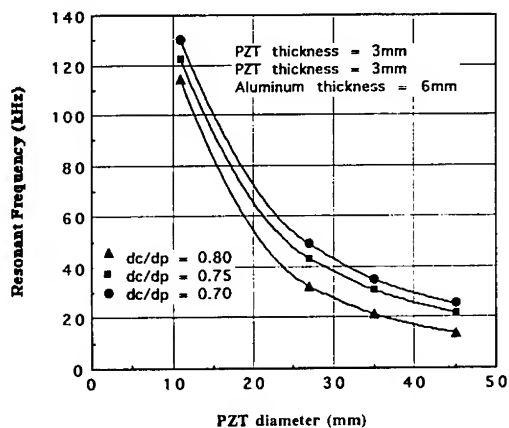


Figure 5. The first resonant frequency as a function of the PZT diameter and aluminum thickness:
Cavity size = $d_c/d_p \times 100\%$.

Actuator

Moonie actuators have very high effective d_{33} coefficients depending on the geometry. Effective d_{33} coefficients as large as 13,000 pC/N were obtained with brass caps 0.3 mm thick, but the value decreased rapidly toward the edge of the transducer. This is approximately thirty times higher than the d_{33} of a PZT-5 ceramic. The characteristics of the moonie actuator depend markedly on a combination of geometry and materials. Among the geometric parameters, cavity diameter, cavity depth, and cap thickness are the main contributors to the displacement of a moonie actuator. An applied 1 kV/mm electric field produces a displacement of 22 μm at the center of a carefully designed brass capped moonie actuator. By stacking two identical single moonies with these dimensions, the double stacked moonie actuator produced a 40 μm displacement, (figure 3).

The generative force of the moonie was measured experimentally and calculated by FEA. The calculated maximum force (300 N) at the effective working area of 3 mm² agrees with that obtained by the extrapolation of the experimental data.

For actuators, however, the stress concentration on the brass end cap just above the bonding layer reduces the effective force transfer from the PZT to the cap. It is possible to eliminate part of the stress concentration by removing the portion of the endcap just above the bonding region where the maximum stress concentration is observed. An enhancement in properties has been observed by introducing a ring shaped groove on the exterior of the end caps [36]. The higher displacement was achieved when the groove was above the bonding layer. It is found that the deeper and wider the groove, the higher the displacement. Because the stress concentration at the groove edges, this becomes a potential source of fatigue and may eventually produce failure under long term usage.

The effect of a cavity diameter on the piezoelectric coefficient of a moonie transducer with different cavity depth is shown in figure 6 and 7 [37]. The effective piezoelectric coefficient decrease with increasing the cavity diameter and cavity depth. After a certain cavity depth, the cavity does not transfer efficiently the applied stress to the ceramic.

Figure 8 shows the fatigue test of a moonie actuator with different end cap thicknesses under a high cyclic electric field (1 kV/mm, 100 Hz) [37]. Experiments were run at room temperature under no load. After cycling 107 times, a deviation in displacement of only $\pm 0.8\%$ was observed. The reason for the deviation is probably due to the effect of environmental temperature change on the bonding layer. Before and after the cycling test, the admittance spectra of the actuators were recorded with no significant changes. The resonant and anti-resonant frequencies as well as their peak amplitudes were the same as the original values found before the fatigue test.

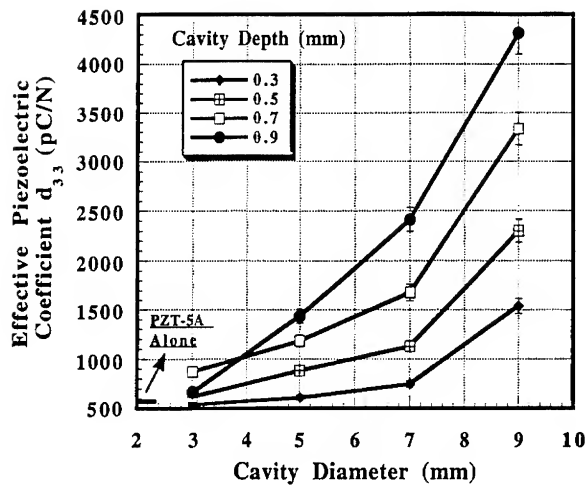


Figure 6. Effect of cavity diameter and cavity depth on the effective piezoelectric coefficient of the moonie. Dimensions: $d_m=12.7$, $d_p=12.7$, $t_p=1.0$ (all in mm).

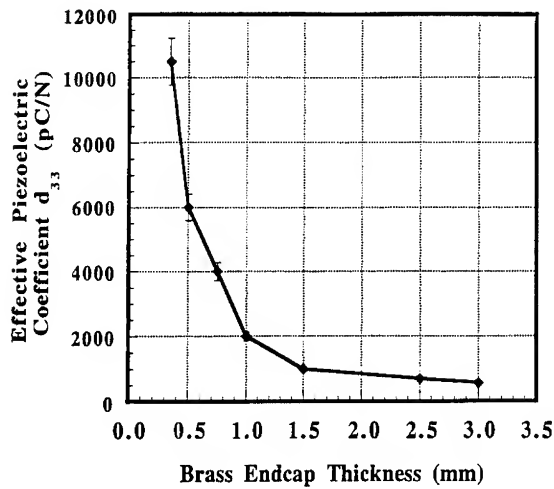


Figure 7. Effect of End cap thickness on the effective piezoelectric coefficient of the moonie. Dimensions: $d_m=12.7$, $d_p=12.7$, $d_c=9.0$, $t_p=1.0$ (all in mm).

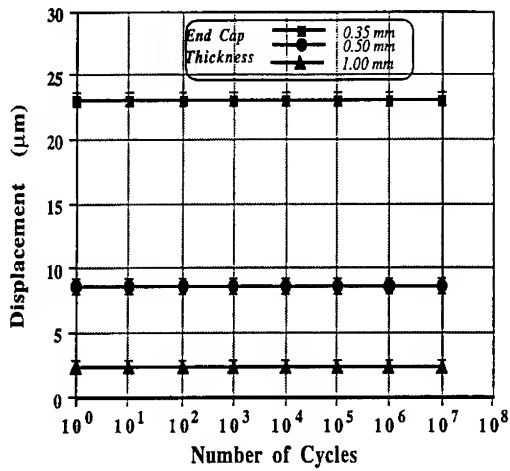


Figure 8. Fatigue characteristics of the moonie actuators.

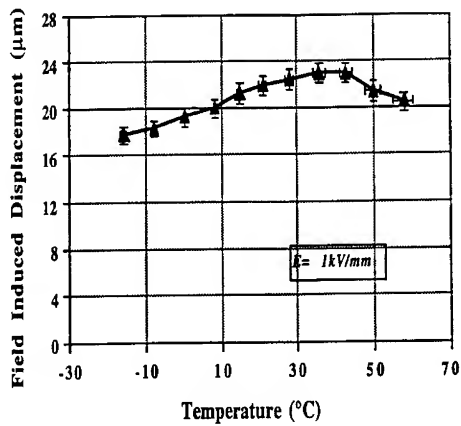


Figure 9. Temperature dependence of the multilayer moonie actuator.

The effect of the temperature on the displacement of a multilayer moonie actuator is shown in figure 9 [37]. The displacement appears to be approximately constant from 10 to 45 °C. There is only 7-8% deviation in this range. The main reason for this temperature dependence is based on the temperature dependence of the components of the multilayer actuator itself. A secondary reason is the bonding layer between the ceramic and the metal end caps. The thermal expansion mismatch between the brass end cap and the PZT ceramic causes a thermally induced flextensional displacement. This problem can be overcome by choosing an adequate thermal expansion metal for the end cap in conjunction with special epoxy compositions for bonding.

SMART MATERIALS

Smart materials [38] have the ability to perform both sensing and actuating functions. Passively smart materials respond to external change in a useful manner without assistance, whereas actively smart materials have a feedback loop which allows them to both recognize the change through an actuator circuit. Many smart materials are analogous to biological systems: piezoelectric hydrophones mentioned earlier are similar in mechanism to the “ears” by which a fish senses vibrations. Piezoelectrics with electromechanical coupling, shape memory materials that can “remember” their original shape, electrorheological fluids with adjustable viscosities, and chemical sensors which act as synthetic equivalents to the human nose are examples of smart electroceramics. “Very smart” materials, in addition to sensing and actuating, have the ability to “learn” by altering their property coefficients in response to the environment. Integration of these different technologies into compact, multifunction packages is the ultimate goal of research in the area of smart materials. There are several recently applications and materials that open the big changes to occur in this field during the coming decades.

Smarties

Smarties are a family of composite transducers which combine two or more active elements to provide the sensing and actuating functions characteristic of a smart material. There are four solid-state actuator materials currently in use throughout the world [39]: Piezoelectric PZT, electrostrictive PMN, magnetostrictive TbFe₂, and NiTi shape memory alloy. We have begun to look at ways in which these materials can be joined to take advantage of the best features of each. Preliminary results on the first of these composite actuators - NiTi strips coated with sol-gel layers of PZT have been reported [40].

Integrated sensors and actuators for active Vibration Control.

A new vibration control device based on the moonie actuator has been developed by Tressler [41], figure 10. The actuator portion of the device consist of the standard (11 mm diameter, 2 mm thick) moonie, and a small piezoelectric ceramic embedded in the upper end cap that serves as a sensor (0.1 mm thick). This prototype sensor/actuator piezocomposite is capable of detecting and suppressing in real time, small vibration displacements ($< 1 \mu\text{m}$), with low force ($< 100 \text{ gf}$). The dynamic frequency range of the device spans from 100 Hz to at least 2500 Hz. The sensor detects sinusoidal vibrations normal to the actuator surface, via a feedback loop, and send a signal of appropriate amplitude and phase shift to the actuator so that if effectively cancel is the external vibration [42]. Potential applications for this device include active optical systems, rotor suspension systems, and other low level vibration suppression devices.

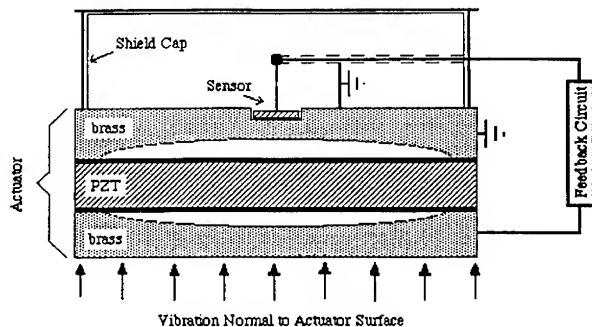


Figure 10. Integrated sensor and actuator for active vibration control.

ACKNOWLEDGEMENTS

The authors would like to express their gratitude for the support to the following agencies and organizations: Office of Naval Research Contract no. N00014-92 J 1510, National Science Foundation Grant no. DMR-9223847, and the Spanish Science Ministry (CICYT MAT-1386-E and DGICYT PR94-028)

REFERENCES

- [1] R. E. Newnham, "Composite Electroceramics," *J. Mat. Education*, 7,605-651(1985).
- [2] T. R. Gururaja, R. E. Newnham, K. A. Klicker, S. Y. Lynn, W. A. Schulze, T. R. Shrout and L. J. Bowen, "Composite Piezoelectric Transducers", in *Proceedings of the IEEE Ultrasonics Symposium*, vol. 2, 576-581(1980).
- [3] R. E. Newnham, D. P. Skinner and L.E. Cross, "Connectivity and Piezoelectric-Pyroelectric Composites", *Mat. Res. Bull.*, 13, 525-536(1978).
- [4] D. P. Skinner, R. E. Newnham and L. E. Cross, "Flexible Composite Transducers", *Mat. Res. Bull.*, 13, 599-607(1978).
- [5] T. R. Shrout, W. A. Schulze and J. V. Biggers, "Simplified Fabrication of PZT/polymer composites", *Mat. Res. Bull.* 14, 1553-59(1979).
- [6] K. Rittenmyer, T. R. Shrout, W. A. Schulze and R. E. Newnham, "Piezoelectric 3-3 Composites", *Ferroelectrics* 41,189-195, 1982.
- [7] K. A. Klicker, J. V. Biggers and R. E. Newnham, "Composites of PZT and Epoxy for Hydrostatic Transducer Applications", *J. Am. Ceram. Soc.*, 64, 5-9, 1981.
- [8] H. P. Savakus, K. A. Klicker and R. E. Newnham, "PZT Epoxy Piezoelectric Transducers: A Simplified Fabrication Procedure", *Mat. Res. Bull.*, 16, 6, 677-680(1981).
- [9] L. Bowen, Proceedings IMF (1993 Gaithersburg, MD), *Ferroelectrics* (in press).
- [10] G. Preu, A. Wolff, D. Cramers and U. Bast, "Microstructuring of Piezoelectric ceramics", *Euro-Ceramics II* 3,2005-10(1991).
- [11] C. Richard, P. Eyraud, L. Eyraud, A. Pelourson and M. Richard, "A Pressure Dependence Approach of New 1-3-1 Piezoelectric Polymer Composite for Hydrophone" *Euro-Ceramics II* 3, 2001-4(1991).
- [14] T. R. Gururaja, W. A. Schulze, L. E. Cross, R. E. Newnham, B. A. Auld and Y. J. Wang, "Piezoelectric Composite Materials for Ultrasonic Transducer Applications. Part I: Resonant Modes of Vibration of PZT Rod-Polymer Composites", *IEEE Transactions on Sonics and Ultrasonics*, vol. 32, no. 4, pp. 481-498, 1985.
- [13] T. R. Gururaja, W. A. Schulze, L. E. Cross, R. E. Newnham, B. A. Auld and Y. J. Wang, "Piezoelectric Composite Materials for Ultrasonic Transducer Applications. Part II: Evaluation of Ultrasonic Medical Applications", *IEEE Transactions on Sonics and Ultrasonics*, 32, 4, 499-513(1985).
- [14] W. Smith, "The Role of Piezocomposites in Ultrasonic Transducers", *Proceedings of the 1988 IEEE Ultrasonics Symposium* p. 755-66(1989).
- [15] Q. M. Zhang, H. Wang and L. E. Cross, "Piezoelectric Tubes and Tubular Composites for Actuator and Sensor Applications", *J. Mater. Sci.* 28,3962-68(1993).
- [16] J. Chen, Q. M. Zhang, L. E. Cross and C. M. Trotter, "Modeling and Design of 1-3 Tubular Composite for Smart Transducer Applications", *Proceedings of the Second International Conference on Intelligent Materials*, Colonia Williamsburg, Virginia, USA, pp. 316-327(1994).
- [17] M. J. Haun, R. E. Newnham and W. E. Schulze, "1-2-3 and 1-2-3-0 Piezoelectric Composites for Hydrophone Application", *Adv. Ceram. Mat.*, 1, 4, 361-365(1986).
- [18] M. J. Haun and R. E. Newnham, "An Experimental and Theoretical Study of 1-3 and 1-3-0 Piezoelectric PZT-Polymer Composites for Hydrophone Applications", *Ferroelectrics*, 68, 123-129(1986).
- [19] R. J. Card, M. P. Otoole and A. Safari, "Method of Making Piezoelectric Composites", U.S. pat # 4,726,099 1988.
- [20] J. Giniewicz, R. E. Newnham and A. Safari, "(Pb,Bi)(Ti,Fe,Mn)O₃-Polymer 0-3 Composites for Hydrophone Applications", *Ferroelectrics*, 73, 3-4, 405-418(1987).

- [21] H. Banno, "Recent Developments of Piezoelectric Ceramic Products and Composite of Synthetic Rubber and Piezoelectric Ceramic Particles", *Ferroelectrics* 50,1-4,329-338(1983).
- [22] H. Banno and K. Ogura, "Piezoelectric Properties at Polarization Reversal Process and Coercive Force of 0-3 Composite Polymers and Ceramic Powder Mixture of PZT and PbTiO_3 ", *Jap. J. Applied Physics*, 30,93,2250-52(1991).
- [23] Y. Suzuki, K. Uchino, H. Gouda, M. Sumita, R. E. Newnham and A. R. Ramachandran, "Mechanical Damper Using Piezoelectric Composites", *J. Ceram. Soc. Jap. (Int. Ed.)* 99,1096-98(1991).
- [24] A. Safari, "Perforated PZT-Polymer Composites with 3-1 and 3-2 Connectivity for Hydrophone Applications", Ph.D. Thesis, The Pennsylvania State University, University Park, PA (1983).
- [25] L.B. Torobin, "Methods of Making Hollow, Porous Microspheres", U.S. Patent #4,671,909, 1987.
- [26] R. Meyer Jr, H. Weitzing, Q. Xu, Q. Zan and R. E. Newnham, "Lead Titanate hollow Sphere Transducers", *J. Am. Ceram. Soc.* 77,6,1669-72(1994).
- [27] D. Kilkomerson, B. Gardineer and H. Hojeibane, "Quasi-Omnidirectional Transducers for Ultrasonic Electro-Beacon Guidance of Invasive Devices", *Proceedings of SPIE* 1733,154-65(1992).
- [28] M.G. Matsko, Q. C. Xu and R. E. Newnham, "Zig-Zag Piezoelectric Actuators: Geometrical Control of Displacement and Resonance", *J. of Intelligent Mat. Systems and Structures*, (in press).
- [29] R. E. Newnham, Q. C. Xu and S. Yoshikawa, Transformed stress direction-acoustic transducer, U.S. Patent # 4,999,819, March 12, 1992.
- [30] Q. C. Xu, S. Yoshikawa, J. Belsick and R. E. Newnham, "Piezoelectric Composites with High Sensitivity and High Capacitance for Use at High Pressures", *IEEE Transactions on Ultrasonics, Ferroelectrics and Frequency Control*, 38, 6, 634-639(1991).
- [31] Y. Sugawara, K. Onitsuka, S. Yoshikawa, Q. Xu, R. E. Newnham, and K. Uchino, Metal-Ceramic Composite Actuators", *J. Am. Ceram. Soc.*, 75, 4, 996-998(1992).
- [32] Q. C. Xu, A. Dogan, J. Tressler, S. Yoshikawa and R. E. Newnham, "Ceramic-Metal Composite Actuator", in *Proceedings of the IEEE Ultrasonic Symposium*, Florida, 1991.
- [33] A. Dogan, Q. C. Xu, K. Onitsuka, S. Yoshikawa, K. Uchino and R. E. Newnham, "High Displacement Ceramic-Metal Composite Actuators (Moonie)", *Ferroelectric* 156,1-6(1994).
- [34] K. Onitsuka, A. Dogan, Q.C. Xu, J. Tressler, S. Yoshikawa, and R.E. Newnham, "Design Optimization for Ceramic-Metal Composite Actuators (Moonie)", *Ferroelectric* 156,37-42(1994).
- [35] K. Uchino, "Piezoelectric and Electrostrictive Actuators", Morikita Publication, Tokyo, Japan 1986.
- [36] K. Onitsuka, "Effects of Bonding and Geometry on the Flexensional Transducer, "Moonie"", Ph.D. Thesis, The Pennsylvania State University, University Park, PA (1993).
- [37] A. Dogan, S. Yoshikawa, K. Uchino, R. E. Newnham, "The Effect of Geometry on the Characteristics of the Moonie Transducer and Reliability Issues", *IEEE-UFFC Proceedings*, Cannes France, November 1994.
- [38] R. E. Newnham and G. Ruschau, "Smart Electroceramics", *J. Am. Ceram. Soc.*, 74, 3, 463-480(1991).
- [39] R. E. Newnham (Guest Editor), "Smart, Very Smart and Intelligent Materials", *Mat. Res. Bull.*, 18,24-26(1993).
- [40] J. Chen, Q. C. Xu, M. Blaszkiewicz, R. Meyer and R. E. Newnham, "Lead Zirconate Titanate Films on Nickel-Titanium Shape Memory Alloys: SMARTIES", *J. Am. Ceram. Soc.*, 75, 10, 2891-2892(1992).
- [41] J. F. Tressler, "Smart Ceramic-Metal Composites for Active Vibration Control", M.S. Thesis, The Pennsylvania State University, University Park, PA (1993).
- [42] J. F. Tressler, Q. C. Xu, S. Yoshikawa, K. Uchino and R. E. Newnham, "Composite Flexensional Transducer for Sensing and Actuating", *Ferroelectrics* 156,67-72(1994).

FABRICATION AND CHARACTERIZATION OF BARIUM STRONTIUM TITANATE AND NON-FERROELECTRIC OXIDE COMPOSITES

E. NGO, S. STOWELL, L.C. SENGUPTA, M.E. O'DAY, AND R. LANCTO
U.S. Army Research Laboratory, Materials Directorate, AMSRL-MA-CA,
Watertown, MA 02172

ABSTRACT

Various composites of BSTO combined with other nonelectrically active oxide ceramics have been formulated. In general, the composites have adjustable electronic properties which can be tailored for use in various electronic devices. Two applications, which are of interest in regard to the composites being discussed here, are phased array antennas and capacitor-varistor monolithic devices. For the phased array antennas, these properties include reduced dielectric constants, ϵ' , where $\epsilon = \epsilon' - i\epsilon''$, and loss tangents, $\tan \delta$. The reduction of the dielectric constant and lowering of the loss tangents reduce the overall impedance mismatch and the insertion loss of the device. In addition, the overall tunability, change in the dielectric constant with applied voltage, is maintained at a sufficiently high level for all dielectric constants of interest. Another application (for one of the composite materials) is a combined capacitor-varistor device. In general, this would be used to protect against spurious voltage surges and voltage transients in electronic micro-circuits. The microstructures, including grain size and phase analysis, have been examined using SEM and X-ray diffraction.

INTRODUCTION

Phased array antennas can steer transmitted or received signals either linearly or in two dimensions without mechanically oscillating the antenna. These antennas are currently constructed using ferrite phase shifting elements. Due to the type of circuit requirements necessary to operate these antennas, they are costly, large and heavy. Therefore, the use of these antennas has been limited primarily to military applications which are strategically dependent on such capabilities. In order to make these devices available for many other commercial and military uses, the basic concept of the antenna must be improved. If ferroelectric materials could be used for the phase shifting element instead of ferrites, phased array antennas would be totally revolutionized. A ceramic Barium Strontium Titanate, $\text{Ba}_{1-x}\text{Sr}_x\text{TiO}_3$, (BSTO), phase shifter using a planar microstrip construction has been demonstrated.¹ In order to meet the required performance specifications, maximum phase shifting ability, the electronic properties must be optimized. As part of this optimization process, various composites of BSTO and non-ferroelectric oxides have been formulated.

Another application for one of these materials is a combined capacitor-varistor device. In general, this would be used as a protective device in parallel with electronic information processing circuits to protect against spurious voltage surges and voltage transients. The capacitive aspect of the device would guard against low-amplitude and high frequency transients which cause errors in signal processing or in stored signals. The varistor function of the device protects against high-amplitude voltage surges. The capacitor-varistor device has

been attempted previously by appropriately doping SrTiO₃ to form grain boundary phases or layers which exhibit the desirable characteristics.² Also discrete layers of ZnO and Pb(Fe_{1/2}Nb_{1/2})O₃-Pb(Fe_{2/3}W_{1/3})O₃ (dielectric constant of 27000 to 32000) have been fabricated.³ The problem with the former scheme has been with the high loss tangents and high threshold voltages derived from the metallic additives and the semiconducting capacitor. The problem associated with the latter scheme is with the processing of the lead based capacitor compounds and the deleterious diffusion between the ZnO varistor layers and lead-based capacitor layers.

The composites will be designated as BSTO-Oxide II, BSTO-Oxide III, BSTO-Oxide II / BSTO-Oxide III, BSTO-Oxide III Compound (A), BSTO-Oxide III Compound (B), BSTO-Oxide III Compound (C), and BSTO-Oxide IV since they all have patents pending on their formulations. All of these composites possess improved electronic properties. The comparison of the compositions and phase formation of the various BSTO-Oxide ceramic composites will be made and related to their electronic properties.

EXPERIMENTAL

The ceramics have been processed using standard solid state methods and which have been outlined in a previous publication.⁴ The electrodes were fabricated using two metallization techniques. One involved painting on two circular, aligned electrodes, one on either side of the specimens, using high purity silver paint (SPI Supplies West Chester, PA) and attaching wires using high purity silver epoxy, Magnobond 8000, made by Magnolia Plastics, Inc., Chamblee, GA. The other technique utilized the screen printing of electrodes using silver conductive ink (FERRO #3350, Electronic Materials Division, Santa Barbara, CA) and wires were attached by dipping the specimens in a bath of 2% silver, 62% tin and 36% lead solder.

The dielectric constants, ϵ' , loss, $\tan \delta$, % tunability and Curie temperatures were determined for all composites. The % tunability of a material is determined using the following equation:

$$\% \text{ tunability} = \{ \epsilon'(0) - \epsilon'(V_{app}) \} / \{ \epsilon'(0) \} \quad (1)$$

The tunability measurements were taken with an applied electric field which ranged from 0 to 3.0 V/micron (μm). The electronic properties given in the forthcoming tables were measured at a frequency of 1 KHz. Capacitance measurements for all materials were taken using an HP4284A LCR meter. Further calculations were done to correct for the effect of fringe capacitance.

RESULTS AND DISCUSSION

BSTO-Oxide III, BSTO-Oxide II / Oxide III, BSTO-Oxide III Compound Composites

SEM and X-ray Diffraction: No secondary phases (other than BSTO and the Oxide III components) were identified by X-ray diffraction for the BSTO-Oxide III and BSTO-Oxide III Compound (B) composites. Also the SEM photographs did not reveal any evidence of secondary phase formation. However, analysis of the X-ray diffraction patterns of the BSTO-Oxide II/ Oxide III, BSTO-Oxide III Compound (A) and BSTO-Oxide III Compound (C)

composites revealed the existence of secondary phases. These phases were also evident as discolorations in their respective SEM photographs.

Electronic Properties: The electronic data for the BSTO-Oxide III, BSTO-Oxide II / Oxide III and BSTO-Oxide III Compound (A)-(C) composites are shown in Table 1. As shown in the table, the dielectric constants decrease with increase in oxide content, and the tunability decreases slowly with increase in oxide content. In fact, the BSTO-Oxide III and BSTO-Oxide III Compound (B) composites exhibit high tunabilities ($>10\%$) up to 60 wt% oxide III which is not the case for the other composites reported in the table. However, at similar electric field strengths the tunability of the 60 wt% BSTO-Oxide III Compound (B) composite is nearly twice that of the 60 wt% BSTO-Oxide III composite. This may be due to the fact that the Curie temperature of the 60 wt% BSTO-Oxide III Compound (B) composite is 0°C . On the other hand, the Curie temperatures for the 60 wt% BSTO-Oxide III, BSTO-Oxide II/Oxide III and the BSTO-Oxide III Compound (A) and BSTO-Oxide III Compound (C) composites are all very low, <-50 to $<-55^{\circ}\text{C}$, (in the far *paraelectric* region). Another significant factor which affects the tunability is the size of the oxide additive. The size of Oxide II is much greater than the size of Oxide III. Therefore, composites containing Oxide II, BSTO-Oxide II / Oxide III and BSTO-Oxide III Compound (A) (which also contains Oxide II), will have much less tunability at high additive content (60 wt%) due to lack of connectivity between the BSTO in the composites. The observed tunabilities for these materials is $<2.0\%$. The differences in the tunabilities of the 60 wt% oxide content composites could also be due to the fact that the BSTO-Oxide III and BSTO-Oxide III Compound (B) compounds do not exhibit secondary phases, whereas the other composites form multiple secondary phases as discussed previously. These non-ferroelectric phases tend to inhibit tunability at high additive contents.

As shown in Fig. 1, the loss tangents of most of these composites are extremely low (< 0.01). However, the loss tangents of the BSTO-Oxide III Compound (B) composites are greater than 0.01 and greater than the loss tangents of all the other composites reported here. Again, the value of the Curie temperature for these composites may contribute to the higher losses evident in these specimens. In fact, the Curie temperature and the loss of these composites is much closer to that of undoped BSTO ($Ba=0.60$).

BSTO-Oxide IV Composites

The electronic properties and the average grain size of the BSTO-Oxide IV composites are shown in Table 2. At low doping levels (1-15 wt%), the composites have large dielectric constants, low loss tangents and reasonably high tunabilities. These properties meet the requirements for various antenna applications (especially low frequency applications). At higher levels (20-50 wt%), the addition of oxide IV content continues to increase the dielectric constant drastically especially at low frequencies, and the composites begin to conduct current and exhibit non-ohmic behavior. The threshold voltage is seen to increase with an increase in oxide IV content. The nonlinear electrical conduction in the ceramic composite is due to the addition of oxide IV (no secondary phases were observed from X-ray diffraction and SEM analysis) in which tunneling through the grain boundaries occurs.

Fig. 2 shows the current versus voltage for BSTO-Oxide IV (30 and 50 wt%) composites. It should be noted that as the oxide IV content is increased, the dielectric constant increases, and the non-linearity exponent increases. This increase in the non-linearity is also roughly related to the decrease in the grain size as indicated in Table 2.

TABLE 1. Electronic Properties of BSTO-Oxide III, BSTO-Oxide II / Oxide III, BSTO-Oxide III Compound (A), BSTO-Oxide III Compound (B), and BSTO-Oxide III Compound (C) Ceramic Composites Measured at 1 KHz. (*poor contact, **data unavailable for these specimens)

BSTO-Oxide III

<i>Oxide III Content (wt%)</i>	<i>Dielectric Constant</i>	<i>Loss Tangent</i>	<i>% Tunability</i>	<i>Electric Field (V/μm)</i>	<i>Curie Temp (C°)</i>
0.0	3299.08	0.0195	19.91	0.73	10
1.0	1276.21	0.0015	16.07	2.32	-30
5.0	1770.42	0.0014	**	**	-30
10.0	1509.19	0.0018	**	**	-35
20.0	1079.21	0.0009	15.95	2.33	-30
30.0	750.93	0.0008	9.350	1.62	-30
60.0	117.67	0.0006	11.08	2.70	<-55

BSTO-Oxide II / Oxide III

<i>Oxide II Oxide III Content (wt%)</i>	<i>Dielectric Constant</i>	<i>Loss Tangent</i>	<i>% Tunability</i>	<i>Electric Field (V/μm)</i>	<i>Curie Temp (C°)</i>
0.0	3299.1	0.0195	19.91	0.73	10
1.0	2515.3	0.0011	12.24	1.14	-15
10.0	1868.9	0.0013	11.63	1.56	-20
20.0	1016.0	0.0327*	10.89	1.33	<-55
30.0	389.06	0.0009	1.607	1.34	<-55
60.0	93.591	0.0022	0.450	0.99	<-55

BSTO-Oxide III Compound (A)

<i>Oxide III Compound (A) Content (wt%)</i>	<i>Dielectric Constant</i>	<i>Loss Tangent</i>	<i>% Tunability</i>	<i>Electric Field (V/μm)</i>	<i>Curie Temp (C°)</i>
0.0	3299.1	0.0195	19.91	0.73	10
1.0	3064.9	0.0019	18.58	1.66	-5
10.0	2209.2	0.0019	13.29	1.34	-5
20.0	1425.7	0.0014	6.910	0.91	-10
30.0	582.84	0.0030	7.347	0.51	-30
60.0	83.941	0.0176*	1.054	1.00	<-50

BSTO-Oxide III Compound (B)

<i>Oxide III Compound (B) Content (wt%)</i>	<i>Dielectric Constant</i>	<i>Loss Tangent</i>	<i>% Tunability</i>	<i>Electric Field (V/μm)</i>	<i>Curie Temp (C°)</i>
0.0	3299.1	0.0195	19.91	0.73	10
1.0	3292.5	0.0066	35.24	2.00	-10
5.0	2267.4	0.0050	29.78	2.00	0
10.0	1264.6	0.0057	19.94	2.00	-25
20.0	842.23	0.0146	19.93	2.00	-20
30.0	413.04	0.0313	22.72	2.00	-10
60.0	76.70	0.0125	17.00	2.00	0

BSTO-Oxide III Compound (C)

<i>Oxide III Compound (C) Content (wt%)</i>	<i>Dielectric Constant</i>	<i>Loss Tangent</i>	<i>% Tunability</i>	<i>Electric Field (V/μm)</i>	<i>Curie Temp (C°)</i>
0.0	3299.1	0.0195	19.91	0.73	10
1.0	2256.5	0.0014	30.96	2.00	-17
5.0	2193.2	0.0021	17.89	2.00	-15
10.0	1386.5	0.0022	18.69	2.00	-15
20.0	649.90	0.0021	15.23	2.00	-13
30.0	263.52	0.0056	11.52	2.00	-50
60.0	108.25	0.0085	3.72	2.00	<-55

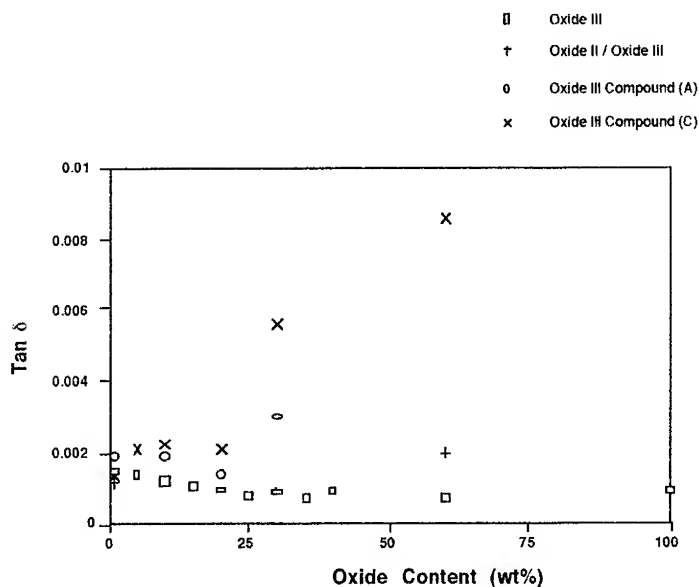


Figure 1. Loss Tangent vs. Oxide Content for BSTO-Oxide III, BSTO-Oxide II/ Oxide III and BSTO-Oxide III (A) and BSTO-Oxide III (C) Compound Composites measured at 1 KHz.

TABLE 2. Electronic Properties and Grain Size of BSTO-Oxide IV Composites Measured at 1 KHz.

Oxide IV Content wt. %	Dielectric Constant	Loss Tangent	Tunability (Percent)	Electric Field (V/ μ m)
1.0	3756	0.00236	7.334	1.0
5.0	3416	0.01276	8.957	0.8
10.0	3908	0.01320	13.11	0.7
15.0	3942	0.03708	27.97	0.6
20.0	4685	0.19113	---	---
25.0	7520	0.46976	---	---
30.0	7859	0.46927	---	---
50.0	71922	0.46891	---	---

Oxide IV Content wt. %	Threshold Voltage	Nonlinearity Exponent	Grain Size (μ m)
1.0	---	---	-----
5.0	---	---	10.24
10.0	---	---	9.774
15.0	---	---	8.610
20.0	100	6.510	8.387
25.0	25	5.390	7.514
30.0	20	10.290	6.806
50.0	5	8.349	5.909

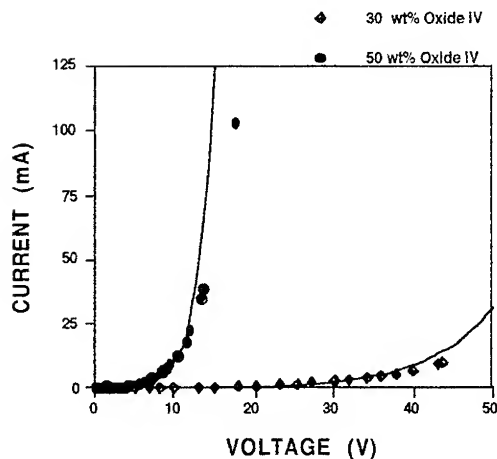


Figure 2. Current vs. Voltage for BSTO- Oxide IV (30 and 50 wt%) Composites (lines indicate a least squares fit of experimental data to an exponent lineshape).

The threshold voltage for the BSTO-Oxide IV (50 wt%) specimen is lower than reported for any bulk capacitor-varistor device (which was reported to be around 100 V)² and the capacitance is higher than that obtained for multilayered structures (nearly twice the capacitance reported)³.

CONCLUSIONS

The BSTO-Oxide III, BSTO-Oxide II / Oxide III and BSTO-Oxide III Compound (A)-(C) ceramic composites possess low loss tangents and high tunabilities. The data suggest that composites containing oxide III or an oxide III compound tend to display similar electronic behavior and can potentially facilitate the operation of ferroelectric phased array antennas at millimeter wave range frequencies. The BSTO-Oxide IV materials exhibit behavior which renders them suitable for use both (at oxide content < 15 wt%) in phased array antenna systems and (at oxide content > 15 wt%) as a capacitor-varistor protection device for microelectronic circuits. The improved properties of these composites includes very low threshold voltages (~5 V), reasonable nonlinear coefficients, moderate to low loss tangents, tunable and extremely high dielectric constants. It should be noted that the low threshold voltage accompanied by an extremely high dielectric constant was accomplished in a bulk ceramic (1mm thickness) and is less than that reported for thin film laminates³.

REFERENCES

1. R.W. Babbitt, T. E. Kosciak, and W.E. Drach, *Microwave Jour.* **35**, 63 (1992).
2. N. Yamaoka, M. Masuyama and M. Fukui, *Ceramic Bulletin* **62**, 698 (1983).
3. H.C. Ling, M.F. Yan, and W. W. Rhodes, *J. Am. Ceram. Soc.* **72**, 1274 (1989).
4. L.C. Sengupta, *J. of Int. Ferr.*, presented at ISIF 1994, Monterey, CA, 1994 (in press).

PART III

Ferroelectric Sensors and Actuators

The Dynamics of SAW Streaming and its Application to Fluid Devices

Showko Shiokawa and Yoshikazu Matsui

Department of Opto-Electronic and Mechanical Engineering,
Faculty of Engineering, Shizuoka University,
Johoku 3-5-1, Hamamatsu-shi, Shizuoka 432, Japan

ABSTRACT

Various liquid motions such as streaming and droplet formation on the surface of surface acoustic wave (SAW) propagating substrate are called SAW streaming. In this paper, the liquid dynamic motions excited by the SAW fabricated on 128° rot. Y-X LiNbO_3 at the frequency of 50 MHz with various pulse widths are demonstrated. The SAW streaming system are also tested for use as a micropump. Theoretically, SAW streaming force can be derived based on the acoustic streaming theory. The calculated SAW streaming force is found to be very large and strong enough to expel a droplet from a liquid surface.

Nonlinear behavior in a water drop vibration induced by the SAW streaming force is also experimentally investigated as a model of inverse bubble oscillation. We succeed in detecting the transformation of the water drop vibration with a single pulse frequency spectrum to $1/2$ and its harmonics.

1 INTRODUCTION

Rayleigh wave can readily radiate a longitudinal wave into a liquid when the SAW propagation surface is in contact with the liquid. In addition to the radiation, when the liquid volume is small and the acoustic power is raised above a certain threshold value, the liquid begins to move in the propagation direction of SAW and provides an observable pattern of SAW power flow. Moreover, if the substrate surface is hydrophobic, droplets are expelled from the liquid surface. We termed such liquid motion "SAW streaming"[1], because the phenomenon may involve essentially the same physics as acoustic streaming. In this paper we propose a micropump as a possible application of the SAW streaming system which can produce stable jet stream.

Theoretically, a general differential equation of second order which is used for the acoustic streaming theory[2] is developed. It is shown that the calculated force of SAW streaming due to leaky Rayleigh wave is much greater than that of acoustic streaming due to general attenuated plane traveling waves in bulk liquid.

We also experimentally investigate the nonlinear behavior in a water drop vibration excited by the SAW streaming force, as a model of inverse bubble

oscillation. When the SAW amplitude at the 50 MHz with a single pulse frequency is increased, the transformation of the droplet vibration with the single frequency spectrum to 1/2 and its harmonics are observed.

2 EXPERIMENTAL

The typical experimental set up for SAW streaming excited by an interdigital transducer (IDT) is shown in Fig. 1.

2.1 Observation of SAW streaming

A photograph of SAW streaming is shown in Fig. 2. Here, the IDT with 10 finger pairs and an aperture width of 2 mm was fabricated on 128° rot. Y-X LiNbO₃ substrate and excited continuously at the center-frequency of 50 MHz. For the purpose of visualizing the liquid streaming, the propagation surface was coated with Al to increase the optical reflectivity. In this experiment, a little detergent was mixed in the water in order to suppress the surface tension. A water droplet with volume of about 5 μ l is first put on the propagation surface by a syringe. If SAW is excited with a sufficient input power, the water begins to move in the direction of acoustic power flow. When the input power was 25 V_{p-p} , the SAW displacement without liquid loading on the surface was estimated by optical probing method to be about 5 Å. The streaming velocity was about 0.2 cm/s. In the photograph one can see clearly the two parts: a thin layer of liquid where the standing waves are observed and a thick layer with a liquid height of about 0.3 mm. In the thin-layer part, the leaky SAW radiates a longitudinal wave into the liquid and decays exponentially along the propagation path, so that in the thick layer part the leaky SAW power will sufficiently decay.

It is found experimentally that the SAW streaming velocity depends on the SAW power, frequency, volume of liquid and surface-chemical condition of the substrate. The surface-chemical condition means whether the surface is hydrophobic or hydrophilic. Since an Al-metallized surface is highly hydrophilic, streaming velocity is suppressed due to the friction between the wa-

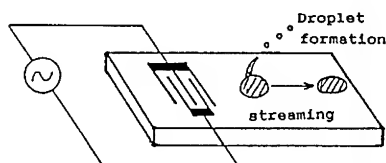


Fig. 1. Water streaming or droplet formation on the SAW propagation surface.

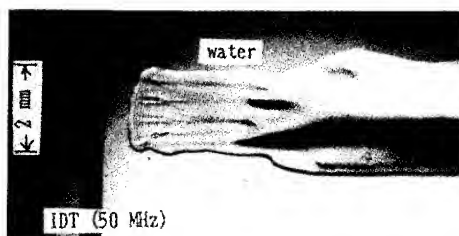


Fig. 2. Observed SAW streaming.

ter and the substrate surface. For hydrophobic surface condition, we used stearyltrichlorosilane ($\text{CH}_3(\text{CH}_2)_{17}\text{SiCl}_3$) to form a chemically bound monolayer on the surface. On the silanized surface, a stream of droplets was expelled from the liquid upward at an oblique angle.

Figure 3 shows the droplet formation time dependence after exciting the input IDT at a frequency of 50 MHz with a pulse frequency of 100 Hz and SAW input power of 2 W. Observations were made with a high speed video-camera with a microscope and the shutter speed of 1/500 sec.. The water volume put on the surface was about 6 μl . Following the pulsed input acoustic energy, a mound rose up from the liquid surface shown in Fig. 3(a), and a droplet was formed progressively as shown in Fig. 3 (b), (c), and (d). In this photograph the observed droplet diameter was 0.5 mm and ejection velocity was 1.5 m/s. The droplet size, the number of droplets per unit time and the ejection velocity were found to be dependent on the SAW power, initial volume of liquid and the driving pulse frequency. Under the pulse frequency of 1 kHz, a very fine fog can also be generated.

Figure 4 shows the water jet streams due to continuously excited SAW at 50 MHz on the silanized LiNbO_3 surface. The jet streams are continuously ejected until all water have been emptied from the surface into the air. The angle is about the value given by Rayleigh angle of $\theta_R = \sin^{-1}(V_w/V_R)$, where, V_R and V_w are the velocity of Rayleigh and liquid waves, respectively.

3 APPLICATION TO MICROPUMP

We can observe many kinetic effects using the SAW streaming. These include: transport and rotation of fluid or granular solid; visualization of SAW propagation fields; pumping or mixing fluid. We propose here a micropump as a possible application of the SAW streaming system which can produce a stable water ejection. Figure 5 shows a prototype fluid pump consists of three components: ①; 1 mm-thick plate glass for supporting SAW device, ②; 128° rot. Y-X LiNbO_3 ($7 \times 7 \times 0.5 \text{ mm}^3$) with IDT (50 MHz, 25 pairs and 1.0 mm aperture width), and ③; 0.15 mm-thick cover glass with a slit width of 0.2 mm overhanging 0.25 mm from the SAW device surface which acts effectively as a capillary wall.

Figure 6(a) shows stable locus view of pumping water when the IDT was continuously energized and the pumping height H and streaming jet angle Θ are defined in Fig. 6(b). Figure 7 represents the experimental results: (a) the streaming jet rate Q as a function of square of IDT input voltage (V_{p-p})² and (b) pumping height (H), streaming jet angle (Θ) as a function of IDT input voltage (V_{p-p}). The streaming jet rate, determined from collecting the ejected water, is proportional to square of the driving voltage.

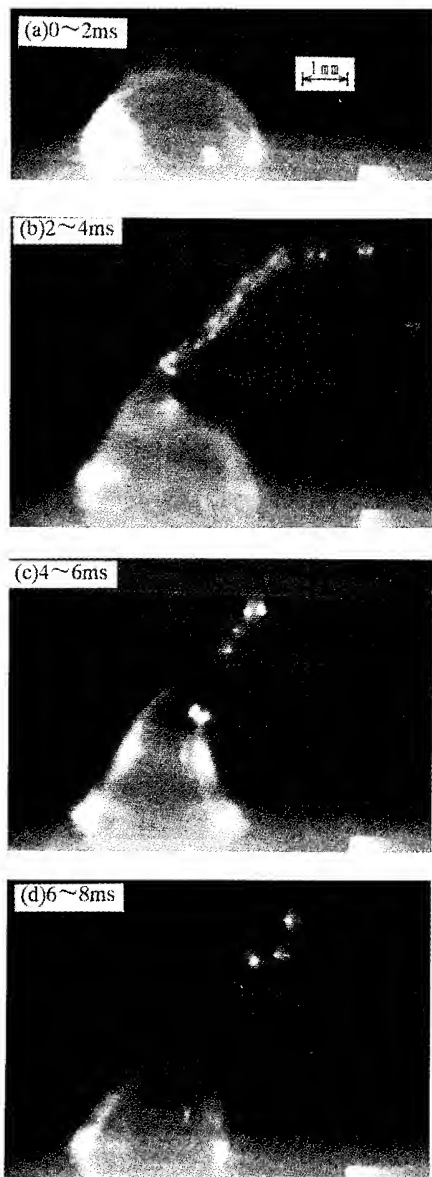


Fig. 3. Observed time elevation of droplet formation at 50 MHz SAW with a pulse frequency of 100 Hz for the initial liquid volume of $6 \mu\text{l}$.

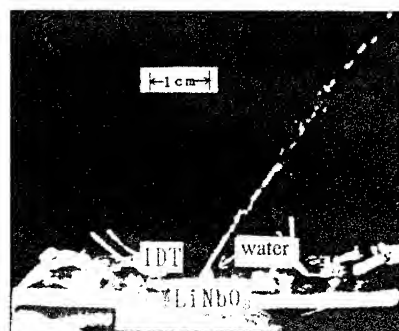


Fig. 4. Observed water jet streams ejected by continuously excited SAW.

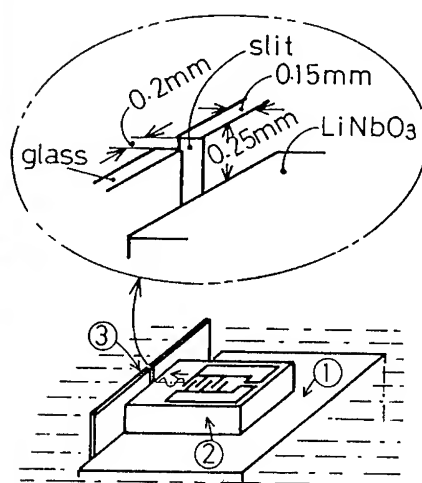


Fig. 5. Schematic construction of micropump. The enlarged section shows the slit of the glass which acts as a capillary wall.

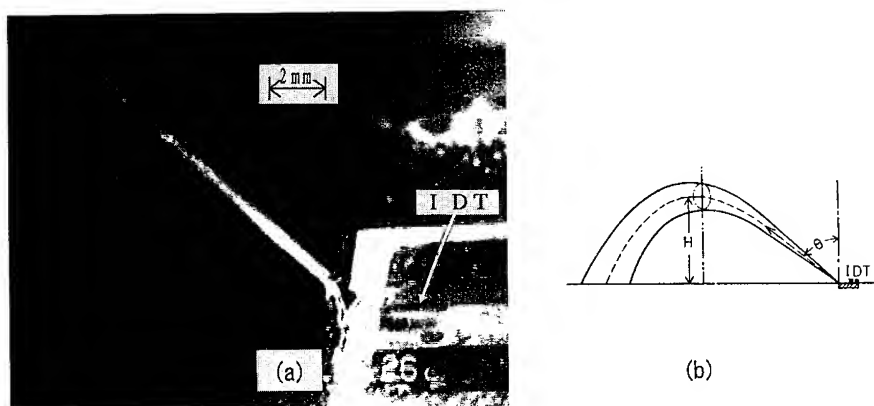


Fig. 6. (a) Observed water jet and (b) illustrated water jet.

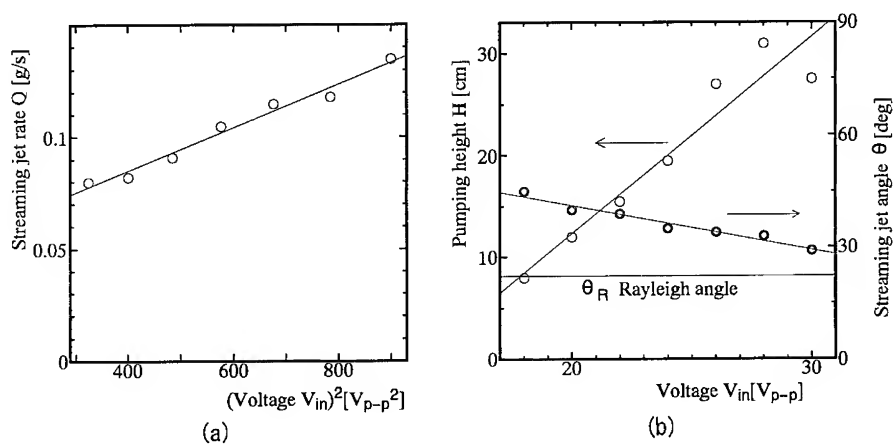


Fig. 7. (a) Streaming jet rate as a function of square of input voltage. (b) Pumping height (H) and streaming jet angle (θ) as a function of input voltage.

4 THEORY

4.1 Acoustic streaming theory

It is a well-known fact that acoustic streaming is generated by any source which radiates a high-intensity beam of sound into a liquid. Since SAW streaming is believed to be the same phenomenon as acoustic streaming, we use the acoustic streaming theory to derive the SAW streaming force[2].

The general equation of hydrodynamics for viscous fluid is as follows:

$$F = \rho \frac{D\mathbf{v}}{Dt} = \rho \frac{\partial \mathbf{v}}{\partial t} + \rho(\mathbf{v} \cdot \nabla)\mathbf{v} = -\nabla P + \eta \nabla^2 \mathbf{v} + \frac{1}{3} \eta \nabla(\nabla \cdot \mathbf{v}), \quad (1)$$

where F is the net force per unit volume due to stress, ρ is density, η is the shear viscosity coefficient and \mathbf{v} is particle velocity. Using the continuity equation:

$$\frac{\partial \rho}{\partial t} + \nabla \cdot \rho \mathbf{v} = 0, \quad (2)$$

we obtain

$$\frac{\partial(\rho \mathbf{v})}{\partial t} + \rho(\mathbf{v} \cdot \nabla)\mathbf{v} + \mathbf{v} \nabla \cdot \rho \mathbf{v} = F_0 - F_1, \quad (3)$$

where

$$F_0 = \frac{\partial(\rho \mathbf{v})}{\partial t}, \quad (4a)$$

$$-F_1 = \rho(\mathbf{v} \cdot \nabla)\mathbf{v} + \mathbf{v} \nabla \cdot \rho \mathbf{v}. \quad (4b)$$

Let us consider sound waves which vary sinusoidally in time with frequency ω . To obtain a streaming equation from eq. (4), we retain the terms up to second order and take the time average of F_0 must be zero in the steady state, the result may be written,

$$-F_1 = \langle \rho_0(\mathbf{v} \cdot \nabla)\mathbf{v} + \mathbf{v} \nabla \cdot \rho_0 \mathbf{v} \rangle \quad (5)$$

in which the symbol $\langle X \rangle$ means "time average of X ". From eq. (5) the time-independent quantity is obtained by time averaging an expression formed \mathbf{v} and its derivatives. Here, we rewrite $-F_1 = \langle -F_1 \rangle$. Hence, F_1 is, in principle, determined once the first order velocity \mathbf{v} is known. The nonlinear quantity F_1 is the exact force of acoustic streaming.

4.2 Leaky Rayleigh waves

If the SAW propagation surface is in contact with liquid, leaky SAW converted from SAW is excited. The leaky SAW propagates along the boundary and excites the longitudinal wave into the liquid with Rayleigh angle of θ_R . Figure 8 shows the

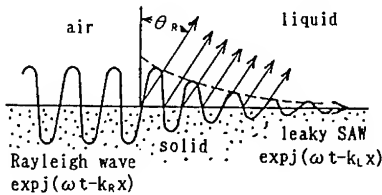


Fig. 8. Ultrasonic radiation into a water by SAW.

ultrasonic radiation mechanism. The propagation constant k_R for Rayleigh wave is real number, while k_L for leaky SAW is a complex number. In the liquid ($z > 0$), the particle displacement (u_x , u_z) can be put in the following form[3]

$$u_x = A \exp(j\omega t) \cdot \exp(-jk_L x) \cdot \exp(-\alpha k_L z), \quad (6a)$$

$$u_z = -j\alpha A \exp(j\omega t) \cdot \exp(-jk_L x) \cdot \exp(-\alpha k_L z), \quad (6b)$$

here, $\alpha^2 = 1 - (V_R/V_w)^2$.

The wave number of leaky SAW k_L can be calculated by extending the method of Campbell and Jones[4] into the liquid/solid structures assuming that the boundary conditions of both displacement and stress at $z = 0$ are continuous. The effect of viscosity is ignored in eq. (6).

4.3 Streaming force

Letting the particle displacement of eq. (6) be replaced by particle velocity using $v = du/dt$ and substituting the particle velocity into eq. (5), F_x and F_z are given by

$$F_x = -\rho_0(1 + \alpha_1^2)A^2\omega^2 k_j \exp 2(k_j x + \alpha_1 k_j z), \quad (7a)$$

$$F_z = -\rho_0(1 + \alpha_1^2)A^2\omega^2 \alpha_1 k_j \exp 2(k_j x + \alpha_1 k_j z), \quad (7b)$$

where $\alpha = j\alpha_1$, $k_L = k_r + jk_j$. F_x and F_z are x and z components of F , respectively. Since SAW streaming force F_{1s} is given by $F_{1s} = \sqrt{F_x^2 + F_z^2}$, we can derived the following form

$$F_{1s} = -\rho_0(1 + \alpha_1^2)^{3/2} A^2 \omega^2 k_j \exp 2(k_j x + \alpha_1 k_j z). \quad (8)$$

The direction of F_{1s} is the same angle as the radiation of the leaky SAW.

To compare the SAW streaming force with acoustic streaming of F_{1a} , we considered an attenuated plane wave in unbounded liquid. For this case the displacement u_x can be written in form

$$u_x = A \exp(-\alpha_w x) \cdot \exp j(\omega t - k_w x), \quad (9)$$

here, $\alpha_w = k_w \eta / (2\rho_0 V_w)$, $k_w = \omega / V_w$. Substituting this into eq. (5), acoustic streaming force is given by

Table I. Theoretical comparison of streaming force between SAW and bulk waves at 50 MHz.

Equation	Calculated value
$F_{1s} \quad \rho_0(1 + \alpha_i^2)^{3/2} k_i \omega^2 A^2$	$2.57 \times 10^6 \text{ N/m}^3 = 260 G_0 \rho_0$
$F_{1a} \quad \rho_0 \alpha_w \omega^2 A^2$	$1.4 \times 10^3 \text{ N/m}^3 = 0.14 G_0 \rho_0$

values used: $k_i = -1370 \text{ (m}^{-1}\text{)}, \alpha_i = 2.47, \alpha_w = 14.2 \text{ (m}^{-1}\text{)},$
 $A = 10 \text{ (\AA)}, G_0 = 9.8 \text{ (m/s}^2\text{)}$

$$F_{1a} = 2\rho_0 \langle (\mathbf{v} \cdot \nabla) \nabla \rangle = \rho_0 \omega^2 A^2 \alpha_w \cdot \exp(-2\alpha_w x). \quad (10)$$

The calculated values of F_{1s} and F_{1a} at $x = z = 0$ for 128°LiNbO_3 at 50 MHz are shown in Table I. We use the following values: $V_L = (3931 + j67.7) \text{ m/s}$ [3], $V_w = 1500 \text{ m/s}$, $\eta = 10 \text{ mpoise}$ and assume $A = 10 \text{ \AA}$. In this table we also represent the streaming force in another form with the gravity force G_0 of 9.8 m/s^2 . The result indicates that the SAW streaming force is much greater than that of acoustic streaming. The main reason for the large value of SAW streaming force is due to the large value of k_i in eq. (8). Here k_i is the imaginary part of the k_L and refers to the effective radiation of SAW energy into the water.

5 A WATER DROP VIBRATION INDUCED BY SAW STREAMING FORCE

Recently many attention to the acoustic bubble oscillations are paid to understanding their chaotic nonlinear vibrations. We envision that there is an inverse relationship between a bubble surrounded by water and a water drop surrounded by air as illustrated in Fig. 9. From this point of view, we start an experimental study on the nonlinear behavior in a drop vibration using the SAW streaming force. We can set up vibrations in a water drop by driving the left and right IDTs simultaneously as shown in Fig. 10, so that a drop water can be trapped at the initial location. The oscillation of the

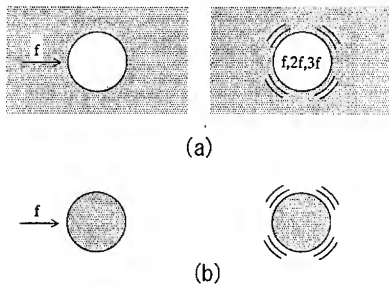


Fig. 9. Inverse relationship between a bubble and a water drop vibrations. (a): a bubble vibration and (b): a water drop vibration.

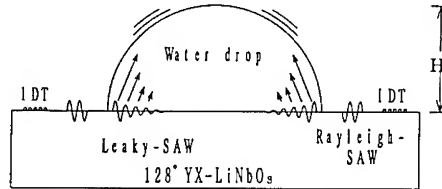


Fig. 10. A water drop vibration by driving the left and right IDTs simultaneously. H is the height of the water surface.

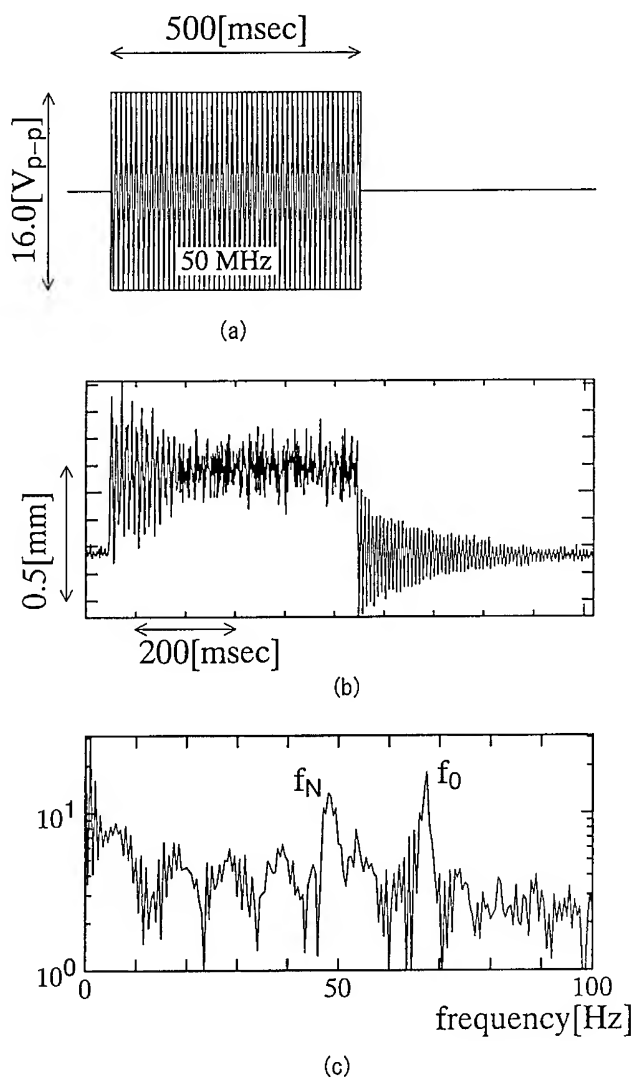


Fig. 11. Typical experimental results for 20 μ l water drop. (a) 1 Hz pulse with 16 V_{p-p} input IDT. (b) Time responses of water vibration from optical signal detecting the height of the drop surface. (c) is the frequency spectrum of the time responses (b). f_0 : vibration frequency without IDT power, f_N : vibration frequency during the period of IDT energized.

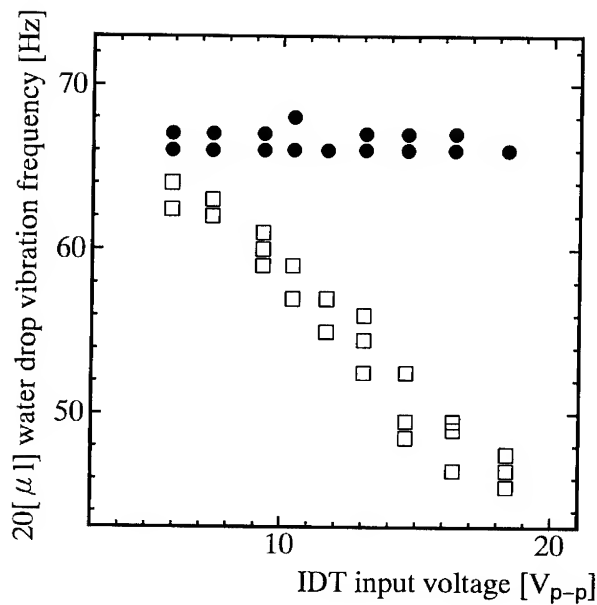


Fig. 12. The vibration frequency of f_N (□) and f_0 (●) as a function of input IDT voltage (V_{p-p}) for a water drop of $20 \mu l$.

water drop is large enough to be seen visually and measured detecting the height of the drop using optical technique. The output signals were analyzed by FFT method. A water drop vibration exhibits several interesting behaviors. Figure 11 shows typical experimental results. In Fig. 11, (a) is IDT input signals at a frequency of 50 MHz with a pulse frequency of 1 Hz, (b) shows time responses of the measured height of the drop surface when the water volume was $20 \mu l$, and (c) is the frequency spectrum of the time response (b). The frequencies of f_N and f_0 correspond to the vibration when IDT is energized and after SAW generation ceased, respectively. Figure 12 shows the vibration frequencies of f_N and f_0 as a function of input IDT voltage for water drop of $20 \mu l$. Although f_0 is not affected by the input IDT voltage, f_N depends on it strongly. When the SAW amplitude with a single pulse frequency of f_n is increased, the transformation of the water drop vibration with the single frequency spectrum to 1/2 and its harmonics are observed as shown in Fig. 13.

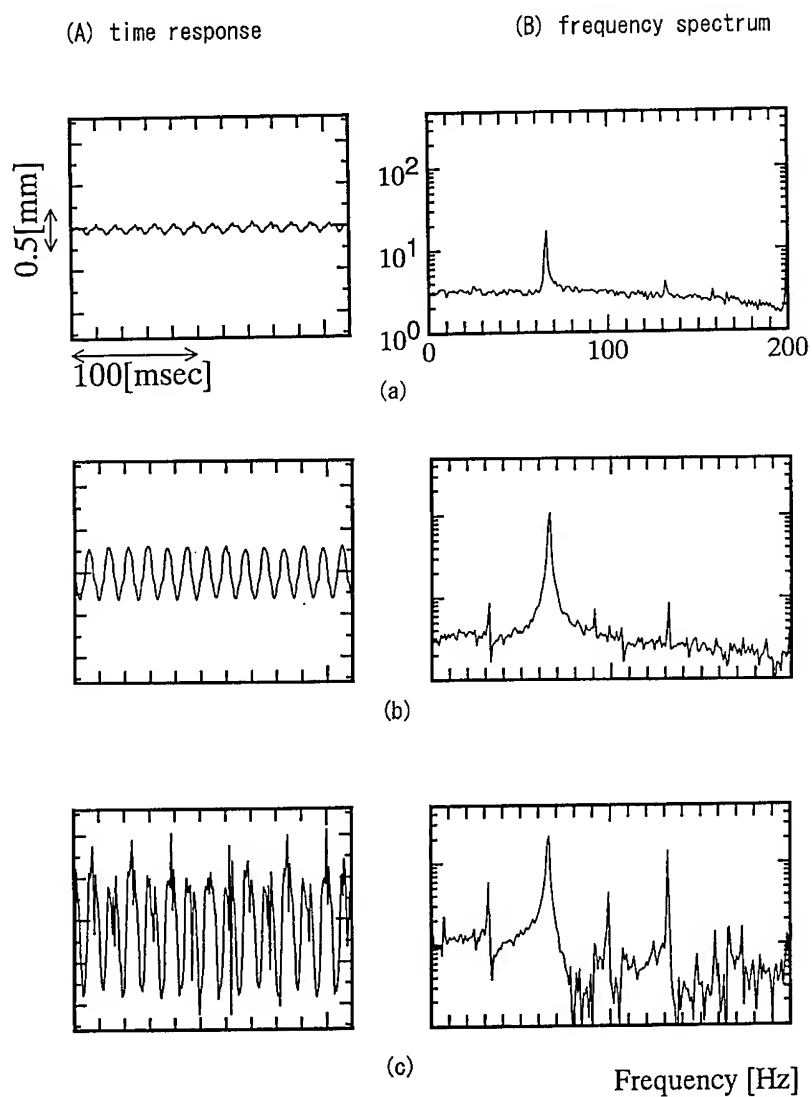


Fig. 13. Vibration of 15 μ l water drop using f_N pulse frequency of 65 Hz. The time responses (A) and the frequency spectrums (B) for variable input IDT voltage, (a) 5.9 V_{p-p} , (b) 8.3 V_{p-p} and (c) 11.6 V_{p-p} .

6 CONCLUSIONS

Liquid motions due to SAW are called SAW streaming and the dynamic behaviors have been demonstrated on 128° Y-X LiNbO₃ at 50 MHz. The liquid motion was found to depend on the chemical condition of the substrate surface. If the substrate surface is hydrophobic, small droplets are ejected from the water surface. Use of this phenomenon makes it possible to develop new fluid devices.

Theoretically, we can derive the SAW streaming force using the theory of acoustic streaming. The results showed that the SAW streaming force is very large and strong enough to expel a droplet from the liquid surface.

We applied the SAW streaming system for exciting a water drop vibration. Using the system, several interesting behaviors in the water drop vibration are observed. Further experimental and theoretical study is under way to quantify this nonlinear vibration.

References

- 1 S. Shiokawa and Y. Matsui, Jpn. J. Appl. Phys. 28, Suppl.28-1, 126(1989): 29, Suppl.29-1, 137(1990).
- 2 W. L. M. Nybovg, in Physical Acoustic, edit by W. P. Mason (Academic Press, New York, 1965, vol.2, Part B), p.265.
- 3 T. Moriizumi, M. Nakamoto and K. Kikuchi, Trans. IECE Jpn., J65A, 489(1982).
- 4 J. J. Campbel and W. R. Jones, IEEE Trans. Sonics and Ultrason., SU-17, 71(1970)

PIEZOELECTRIC-CERAMIC CYLINDER TYPE VIBRATORY GYROSCOPE

T.YOSHIDA

Product Development Laboratory, Tokin Corporation, 6-7-1 Koriyama Taihaku
Sendai Miyagi 982 Japan

ABSTRACT

A new equivalent circuit for the vibratory gyroscope and an analyzing and controlling method for the vibration mode axis of the vibrator have been studied. The vibrator of this gyroscope consists of a piezoelectric-ceramic cylinder. On its outer cylindrical surface, interdigital electrodes are formed. And these electrodes are used for poling, AC excitation as well as detection. In order to prevent some deviation of the performance of the gyroscope due to the adhesion process, these electrodes are directly printed on the cylinder surface.

By changing the electrodes pattern and making a groove on the surface of the vibrator, the vibration mode axis can be easily controlled. Optimum design suited for demanded specifications can then be obtained.

INTRODUCTION

The vibratory gyroscope is an angular velocity sensor. It is based on the physical phenomenon in which a Coriolis force develops in a right angled direction of the vibration when the vibrator is rotated.

GE type vibratory gyroscope is well known. It is constructed of a metal bar with square cross-section cemented by some piezoelectric-ceramics plates used for driving and detecting on the different surfaces of the bar.[1] Recently, a vibratory gyroscope made of a metal bar with regular triangle cross-section has been developed and used for hand-held video cameras in order to stabilize the image fluctuation caused by slight hand movement.[2] In these vibratory gyroscopes, the vibrators are constructed by cementing piezoelectric-ceramic plates onto a metal bar made of constant-elastic-modulus alloy such as Elinvar. These conventional gyroscopes are difficult to miniaturize and to reduce their cost because of their complex structure and use of adhesives.

Shimizu and Oyama showed the piezoelectric-ceramic vibratory gyroscope consisted of a square cross section piezoelectric-ceramic bar with interdigital electrodes formed on the four surfaces of the rod. [3] These electrodes were used for poling treatment, AC excitation and detection of the angular rate.

We also used piezoelectric-ceramic vibrator for the vibratory gyroscope but selected the shape of the vibrator as a cylinder because of the symmetry from the central axis of the cylinder and easiness of production.[4]

In this paper, we introduce a small-size and a simple structure vibratory gyroscope which is composed of a piezoelectric-ceramic cylinder and does not

require the gluing of conventional vibratory gyroscopes.

We introduce the equivalent circuit of the vibrator for the vibratory gyroscope taking under consideration the distribution of the driving force which is induced during strip electrodes. We also explain how the two vibration modes make a difference in both resonant frequencies.

CONSTRUCTION OF THE VIBRATORY GYROSCOPE

Construction of piezoelectric-ceramic cylinder

Figure 1 is a perspective view of the piezoelectric ceramic cylinder used for bending vibrator of the gyroscope. The six electrodes are formed at equal spaced positions on the outer surface of the cylinder. Fig.2 shows the electrodes printing apparatus and an example of the screen pattern for electrodes. When the screen moves the ceramic cylinder rotates and electrodes are printed. The first alternate electrodes are connected on both side of the cylinder as a common terminal, and the second alternate electrodes are independent and used for driving terminal and pick-up terminal. The second alternate electrodes are connected and applied DC voltages as shown in Fig.3. The inverse polarity of DC voltage are applied between the first alternate electrodes and the second alternate electrodes. The cylinder is then polarized in the directions as illustrated by solid arrows in Fig.3.

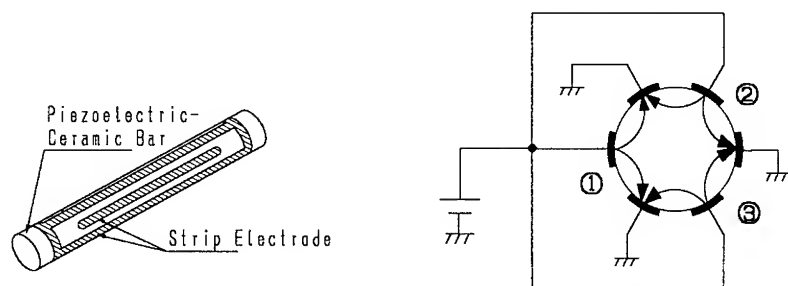


Fig.1 Piezoelectric-ceramic cylinder type bending vibrator.

Fig.3 Poling method and the direction of remanent polarization.

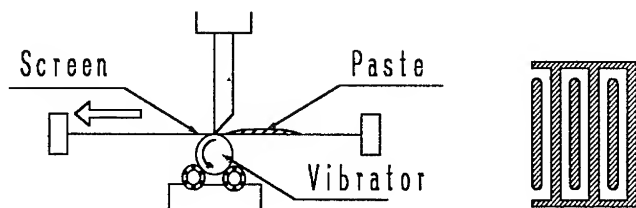


Fig.2 Electrodes printing apparatus and an example of the screen pattern.

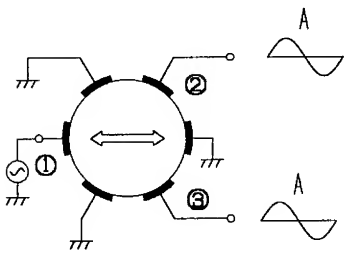


Fig. 4 The direction of the bending vibration and output wave forms.

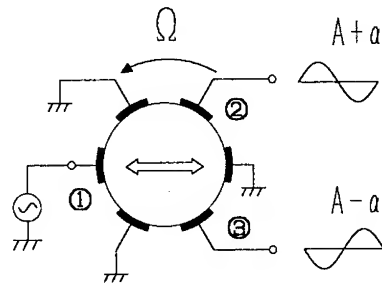


Fig. 5 The direction of the bending vibration due to Coriolis force and output wave forms.

Principle of the vibratory gyroscope

When AC voltage with the resonant frequency of the piezoelectric-ceramic cylinder's bending mode vibration is applied to the driving electrode ① as shown in Fig. 4, strain is produced between earth electrode and driving electrode ① and a bending motion occurs in the direction shown with the arrow in Fig. 4. This is due to the piezoelectric-electric transverse effect. Since the pick-up electrode ② and ③ are located at the symmetrical position against the bending mode vibration (the arrow in Fig. 4), the pick-up voltages of these two electrodes have same phase and amplitude A due to the piezoelectric effect.

When the rotational force is applied centering the ceramic cylinder's lengthwise axis while the condition in Fig. 4 is maintained, the new excitation of bending mode which is perpendicular to the vibrating direction shown as dotted arrow in Fig. 5 is occurred by the Coriolis force. The output of the pick-up electrode ② and ③ now have opposite phase and same amplitude output voltage α .

Thus, the total output voltage of the pick-up electrode ② and ③ are addition of original output and reverse phase voltage with application of Coriolis force as $A + \alpha$ and $A - \alpha$ respectively. By use of a differential amplifier connecting to the electrode ② and ③, the output voltage becomes 2α and it should be proportional to the given rotational angular velocity.

EQUIVALENT CIRCUIT AND IMPEDANCE CHARACTERISTICS

Equivalent circuit

The equivalent circuit of this vibrator can be shown the circuit with three-pair-terminal network as shown in Fig. 6.

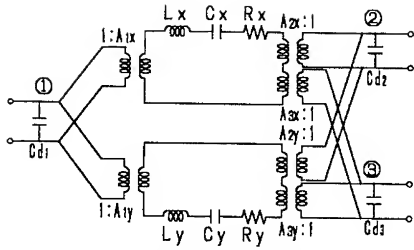


Fig. 6 Equivalent circuit of the piezoelectric vibrator with 6 electrodes.

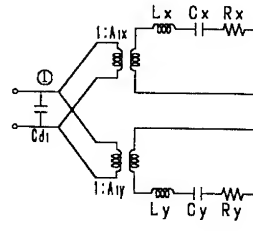


Fig. 7 Equivalent circuit of the piezoelectric vibrator when electrode ②, ③ are shorted.

In Fig. 6, the two impedance element Z_x and Z_y correspond to the vibration modes which are perpendicular to each other. The parallel capacitance of each terminal are damped capacitance. The transformation ratio A_{1x} and A_{1y} are determined by the angle δ made by the position of the driving electrode and the direction of the vibration.

To make things easier, it is assumed that terminal ② and ③ are shorted, and only terminal ① is driven. If the two perpendicular bending mode are x-mode and y mode, the equivalent circuit of Fig. 6 can be taken like Fig. 7. As shown in Fig. 8, distribution of the driving force for x-mode vibration can be shown as $\sin(\theta - \delta)$. Here, it is assumed that angle dependence of driving force for the terminal ① is constant at the range of $-\pi/3 < \theta < \pi/3$, and it is 0 at other range. Then the driving force concerning x mode can be normalized by the driving force at $\delta=0$ as follows:

$$\frac{\int_{-\pi/3}^{\pi/3} \cos(\theta - \delta) d\theta}{\int_{-\pi/3}^{\pi/3} \cos\theta d\theta} = \frac{\sqrt{3} \cos \delta}{\sqrt{3}} = \cos \delta \quad (1)$$

Similarly, the driving force concerning y-mode can be shown as the next equation.

$$\frac{\int_{-\pi/3}^{\pi/3} \sin(\theta - \delta) d\theta}{\int_{-\pi/3}^{\pi/3} \cos\theta d\theta} = \frac{-\sqrt{3} \sin \delta}{\sqrt{3}} = -\sin \delta \quad (2)$$

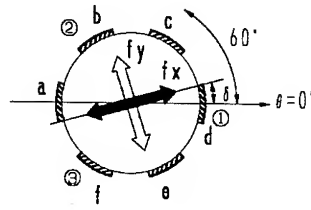


Fig. 8 Relationship between vibration axis and the electrodes.

So, thinking only of terminal ①, the A_{1x} and A_{1y} are given equation (3).

$$A_{1x} = \cos \delta \quad A_{1y} = -\sin \delta \quad (3)$$

As shown in Fig.1, when six strip electrodes are constructed on the outer surface of the piezoelectric-ceramic cylinder at even intervals, the equivalent circuit driven through ② and ③ terminal can be the same circuit as Fig.6.

Furthermore, the transformation ratio of ② and ③ terminal ($A_{2x}, A_{2y}, A_{3x}, A_{3y}$) can be obtained by changing the δ to $\delta + 120$ degrees and $\delta - 120$ degrees respectively.

$$A_{2x} = \cos(\delta + 120) \quad A_{2y} = -\sin(\delta + 120) \quad (4)$$

$$A_{3x} = \cos(\delta - 120) \quad A_{3y} = -\sin(\delta - 120) \quad (5)$$

Use of the relationship between parameters of the equivalent circuit and parameters of the vibrator, input admittance normalized by the damped capacitance is given by the next equation.

$$\frac{Y}{\omega_s C_d} = j \frac{\omega}{\omega_s} + \frac{j \cos^2 \delta}{\omega_s \gamma_s \left(1 - \frac{\omega^2}{\omega_s^2} + j \frac{\omega}{\omega_s Q_{mv}} \right)} + \frac{j \sin^2 \delta}{\omega_s \gamma_s \left(1 - \frac{\omega^2}{\omega_s^2} + j \frac{\omega}{\omega_s Q_{mv}} \right)} \quad (6)$$

Consequently, the impedance of the vibrator is given by the inverse formula (6).

Impedance characteristics comparison with the measured and calculated value

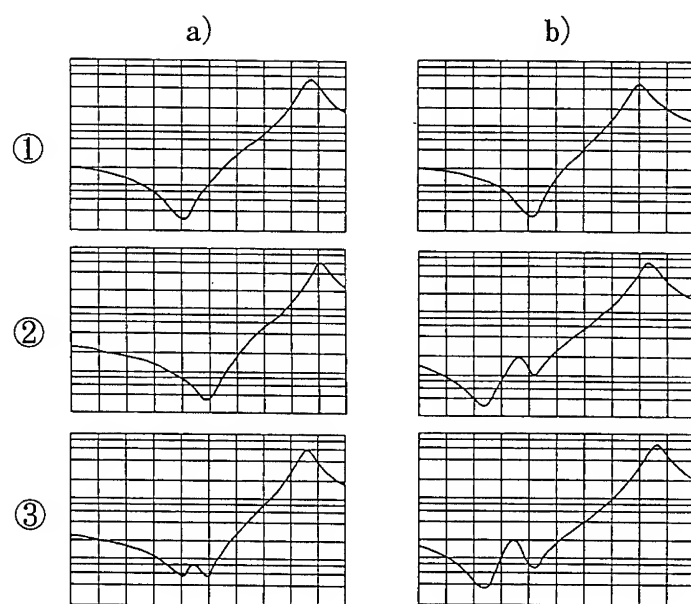
Figure 9 shows the measured impedance wave forms and calculation results of the two vibrators.

As shown in Fig.9- (a), by calculating with the value of $\Delta f_r = 30$ Hz and $\delta = 18$ degrees, the impedance wave forms corresponds to measured wave forms. In the case of Fig.9 (b), $\Delta f_r = 90$ Hz and $\delta = 5$ degrees corresponds to the measured wave forms.

In Fig.9, the position of the electrodes and directions of the vibrations are indicated. According to the angle from the vibration direction to the input electrode, it can be seen that the response of either x-mode or y-mode will expand (the impedance will be smaller). If this process is taken on the contrary, the direction of the vibration and the two resonant frequencies can be presumed.

To construct the vibratory gyroscope, it is better that the two resonant frequencies f_x and f_y should be equal. As mentioned above, because of the asymmetry of the dimensions and non uniformity of the characteristics of the material, it is difficult to coincide with these frequencies as the experimental data shown in Fig.9. Even if it becomes $f_x \neq f_y$ and the differences small, it has the possibility of constructing a vibratory gyroscope with good performance as far as the two output electrodes are located symmetrically to the direction of the pre-driven vibration.

[Measured]



[Calculated]

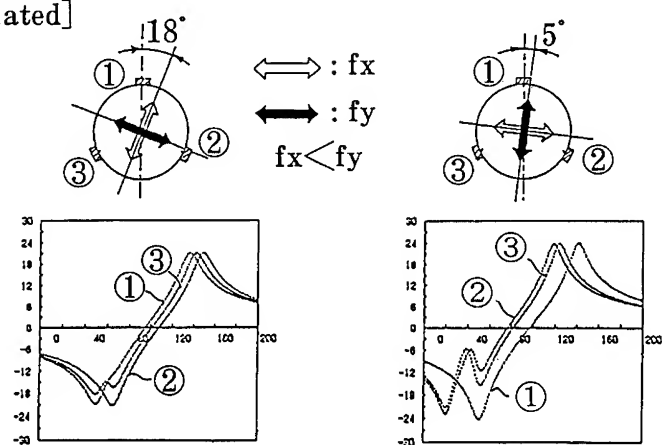


Fig.9 Comparison with measured and calculated impedance characteristics.

HOW TO CONTROL THE VIBRATION MODE AXIS

Vibrator with a groove on the outer surface

Figure 10 (a) shows the impedance characteristics of the vibrator with a groove which is made on the earth electrode opposite to the driving electrode parallel to the length direction of the cylinder.

sample	position	width	depth
a	On the earth electrode opposite to the driving electrode	100 μm	50 μm
b	On the space of the electrodes perpendicular to the driving electrode	"	"

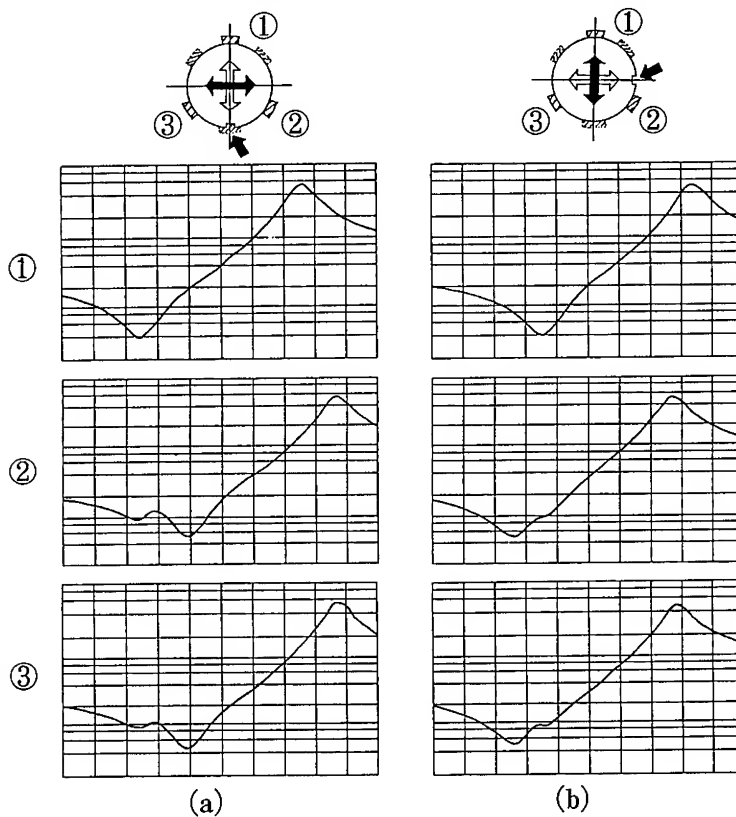


Fig.10 Measured impedance characteristics of the vibrator with a groove

In Fig.10 (a). we can observe 1) and 2).

- 1) There is no deviation in the impedance wave form of terminal ①, and the frequency that makes the impedance minimum is lower.
- 2) On the contrary, the impedance wave form of terminal ② and ③ have almost the same shape. And there is a deviation in the wave form and the frequency that makes the impedance minimum is higher.

1) and 2) show that in this vibrator, resonant frequency f_x and f_y are separated and the direction of lower resonant frequency (f_x) is toward the center of the terminal ① electrode.

Figure 10 (b) shows impedance wave forms of the vibrator with a groove which is made on the gap between electrodes perpendicular to the input electrode parallel to the length direction of the cylinder.

In Fig.10 (b), we can observe 3) and 4).

- 3) There is no deviation in the impedance wave form of terminal ① and the frequency that makes minimum impedance is higher.
- 4) On the contrary, the impedance wave form of terminal ② and terminal ③ are exactly the same. It has a deviation in the wave form and the impedance is minimum at the lower frequency.

3) and 4) show that in this vibrator, resonant frequency f_x and f_y are separated and the direction of higher resonant frequency (f_y) is toward the center of terminal ① electrode.

Through Fig.10 (a) and (b), if a groove is formed at the direction of the length of the cylinder at a particular position on the surface of it, the direction of the x mode vibration (a lower resonant frequency) will be fixed to the direction that joints the center of the groove and the cylinder.

Characteristics of the seven electrodes vibrator

Strip electrodes of this vibrator are made by screen printing as mentioned before. So the distance between initiating and terminating line of the printing is changeable.

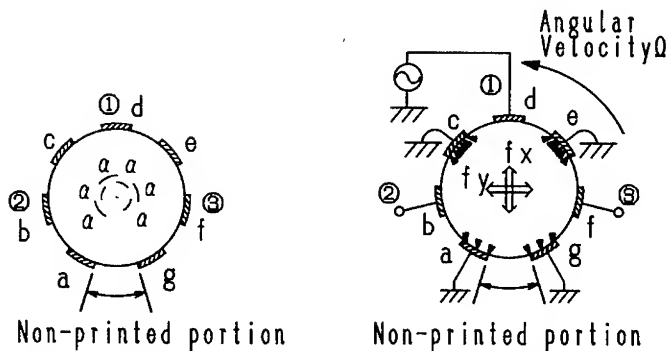


Fig.11 Electrodes distribution and directions of polarization and vibration of 7 electrode vibrator.

Figure 11 shows the cross section of the vibrator with 7 electrodes. In Fig. 11, "a" is the initiating electrode and "g" is the terminating electrode. Applying this construction, even if the distance between the electrode "a" and "g" is change, electrode "b" and "f" are located symmetrically against the line from the center of the electrode "d" to the center of the cylinder. That is to say, detecting electrode ② and ③ are located symmetrically against the direction of the driven vibration(f_x).

Table 1 shows the characteristics of the 7 electrodes vibrator with divided angle from 45, 50 and 55 degrees respectively.

Table 1 Characteristics of the 7 electrode vibrator

Divided Angle α (deg)	f_x (Hz)	f_y (Hz)	Δf_r (Hz)	Capacitance Ratio γ	Damped Capacitance (pF)	Q_m
45	23706	23463	243	57.7	133.6	806
50	23646	23465	181	52.9	133.4	862
55	23552	23469	82	46.8	143.6	830

Figure 12 shows the measured impedance characteristics of these vibrators. In Fig.12, we can see the following:

- 1) There is no deviation in the impedance wave form of terminal ① and the frequency that makes the impedance minimum is lower.
 - 2) On the contrary, the impedance wave form of terminal ② and ③ have almost the same shape. And there is a deviation in the wave form and the frequency that makes the impedance minimum is higher.
 - 3) The difference between f_x and f_y increases as the divided angle decreases.
- 1) and 2) show that in this vibrator, resonant frequency f_x and f_y are separated and the direction of lower resonant frequency (f_x) is toward the center of terminal ① electrode. The reason of 3) is that the distance between electrode "a" and "g" is larger as the divided angle is smaller, and for this piezoelectric ceramics, the elastic velocity of the polarized region is lower than that of non-polarized region.

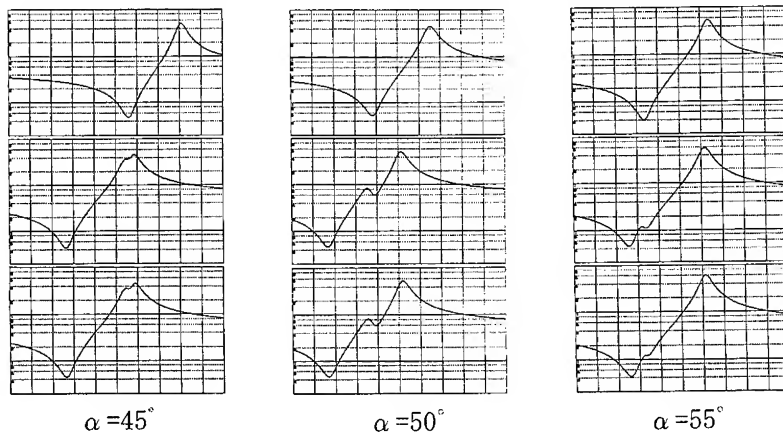


Fig.12 Impedance characteristics of the 7 electrode vibrator.

DRIVING AND DETECTING CIRCUIT

Figure 13 shows a schematic diagram of the driving and detecting circuit which consists of an oscillator to drive the resonator and a differential amplifier to detect angular rate.

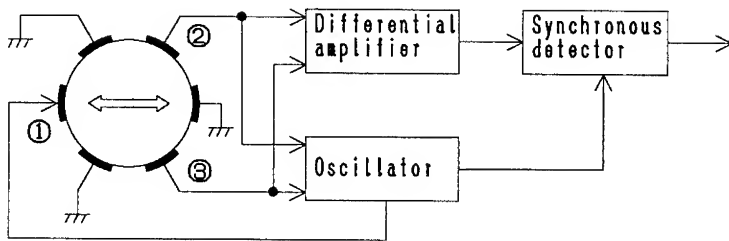


Fig.13 The driving and detecting circuit diagram

Figure 14 shows the construction of the vibratory gyroscope using the piezoelectric ceramic cylinder type vibrator.

Table 2 shows the characteristics of the vibratory gyroscope used piezoelectric ceramic cylinder bending vibrator.

Table 2 Specification of the vibratory gyroscope (CERAMIC GYRO)

Items	Unit	Characteristics
Supply voltage	V	+5
Maximum angular velocity	deg/sec	± 90
Sensitivity	mV/deg/sec	1.0
Null voltage	mV (max)	300
Frequency response	Hz (min)	100

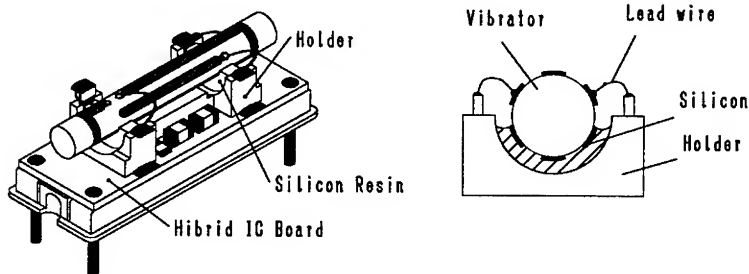


Fig.14 The construction of the vibratory gyroscope

CONCLUSION

A new structure piezoelectric-ceramic vibratory gyroscope has been developed. The vibrator of this vibratory gyroscope consists of a piezoelectric-ceramic cylinder with six and seven elongated electrodes on its outer cylindrical surface.

These electrodes are used both for poling, excitation and detection. Especially, seven electrodes vibrators do not need any frequency adjustment because they have strong anisotropy of the direction of the vibration and accurate symmetry of the detecting electrodes against the direction of pre-driven vibration then maintained.

Equivalent circuit of a piezoelectric-ceramic vibrator for a vibratory gyroscope can be derived from introducing the distribution of the driving force, difference of the direction of the vibration and the position of the driving electrode and the difference of the two resonant frequencies of the two bending vibration modes which are perpendicular to each other. By using this equivalent circuit, not only the impedance characteristics of the driving and detecting terminals but also characteristics of the gyroscope can be estimated.

Furthermore, it is possible to control the direction of the vibration by making a groove parallel to the length direction of the column or forming non-parallel electrodes. Because of its small size and simple structure, this vibratory gyroscope is now used as the shake sensor for cameras and hand-held video cameras.

ACKNOWLEDGMENTS

Finally, we would like to thank professor Kiyoshi Nakamura of the Tohoku University Engineering Department Communication Engineering Course for giving valuable advice in advancing this study.

REFERENCES

- [1] W.D.Gates:Electronics 10 (1968) p.130
- [2] T.Nakamura,K.Okano,T.Kasanami: No 150 Committee of Japan Society for the Promotion of Science, Jan. (1989) p.731 [in Japanese]
- [3]S.Oyama,H.Shimizu, I.E.I.C.E Japan US87-30(1987) p.19 [in Japanese]
- [4] H.Abe,T.Yoshida,K.Tsuruga: J.J.A.P. Vol31 (1992) p.3061

Ba/Sr DOPED ELECTROSTRICTIVE COMPOSITIONS FOR ACTUATOR DESIGN

Zhiqiang Zhuang*, Lijun Jan*, S.B. Kang**, B. Gallois**, Z. Yang** and H. Du**

* South China University of Technology, Dept. of Inorganic Materials Science and Engineering, Guangzhou, China 510641

** Stevens Institute of Technology, Dept. of Materials Science and Engineering, Hoboken, NJ 07030

ABSTRACT

Solid solutions of lead zirconate titanate (PZT) and lead magnesium niobate (PMN) doped with barium/strontium were developed for use in miniature electrostrictive actuators. The microstructural features of the materials were determined by high-resolution transmission electron microscopy (HREM) and by x-ray diffractometry. The response and the strain hysteresis were measured by applying a sinusoidal or a rectangular voltage pulse. Pulses of variable amplitude and width were applied to the elements to study the switching behavior of 90° domain walls in the materials and to elucidate the initial zero-position "walk off" mechanism. The strain hysteresis or remanent strain of PZT decreased with increasing PMN concentration. A barium-doped PZT (Ba-PZT) composition containing 4 mole% of PMN exhibited ferroelectric relaxor behavior with a field-induced strain much larger than those of lead magnesium niobate (PMN) electrostrictive materials and a small remanent strain hysteresis.

INTRODUCTION

Electrostrictive ceramics based on lead magnesium niobate (PMN) have been intensively studied because they exhibit large field-induced strains near room temperature, the temperature range at which the phase transition is diffuse.¹ Outside of this temperature range, the field-induced strain decreases and the strain hysteresis or the remanent strain increases.² The PZT-BZT (Ba-PZT) solid solution system was investigated by Ikeda.³ A barium-doped PZT composition⁴ with large electrostrictive strain was developed subsequently. In order to enhance the field-induced strain of barium-doped PZT, solid solutions modified with niobium or lanthanum have been developed in recent years. The large strain hysteresis of Ba-PZT remains, however, a major drawback in practical electrostrictor applications.

Solid solutions of Ba/Sr co-modified PMN doped PZT were investigated in this study. Compositions with giant strain and small strain hysteresis were developed. The dynamic field-induced strain behavior was studied by determining the strain response to a sinusoidal or rectangular voltage pulse and by examining microstructural features in the HREM.

EXPERIMENTAL PROCEDURE

An oxide-mixing method was used to prepare barium/strontium modified PMN doped PZT ceramics with compositions of $(\text{Pb}_{1-x}\text{Ba/Sr}_x)[\text{Zr}_{1-y-z}\text{Ti}_y(\text{Mg}_{1/3}\text{Nb}_{2/3})_z]\text{O}_3$ (Ba/Sr-PZTMN), where x varies from 0.01 to 0.50, y from 0.20 to 0.70, and z from 0 to 0.10. The starting raw materials

were reagent-grade Pb_3O_4 , ZrO_2 , TiO_2 , BaCO_3 , SrCO_3 , MgCO_3 and Nb_2O_5 . They were weighed, mixed with distilled water in an alumina ball-mill, dried and calcined at 850°C for 5 hrs. The calcined powders were made into a slurry and cast into green sheets 0.08 mm to 0.20 mm thick. After burning out of the binder, the green sheets were stacked and sintered at 1100 to 1200°C for 1 to 5 hrs in a closed alumina crucible set. The average grain size was larger than $5\mu\text{m}$ and the relative density was higher than 97%.

MEASUREMENTS

Phase identification of the calcined powders and the sintered ceramics was conducted by X-ray diffraction using $\text{Cu-K}\alpha$ radiation. TEM and High-resolution electron microscopies were used to determine the microstructural features of ferroelectric relator compositions in order to relate them to the dielectric behavior and the field-induced strain characteristics.

Silver electrodes were sintered on two major surfaces of the ceramic samples for the measurements of the dielectric property and the electromechanical coupling parameters. The temperature dependence of the dielectric properties were measured using a computer-controlled LRC impedance measurement system. The transverse and longitudinal strains were determined by a sensitive capacitance dilatometer and a differential inductance digital micrometer. The strain hysteresis was expressed in terms of $\Delta x_i/x_i$ ($i = 1$ or 2) where Δx_i is the difference of the two values of the strains measured at $E_{\text{Max}}/2$ during increasing and decreasing voltage sweeps.

The time response and the strain hysteresis of the single element were measured with a sinusoidal or a rectangular voltage pulse. Pulses of variable amplitude and width were applied to the element to study the switching behavior of 90° domain walls in the materials and to elucidate the initial zero-position "walk off" mechanism.

RESULTS AND DISCUSSION

Fig. 1(a) shows the temperature dependence of the dielectric constant, K , of a Ba-doped PZT composition which exhibits a diffuse phase transition around 130°C . The K - T curves measured at different frequencies overlap above the average Curie temperature T_{av} . The material is a high-

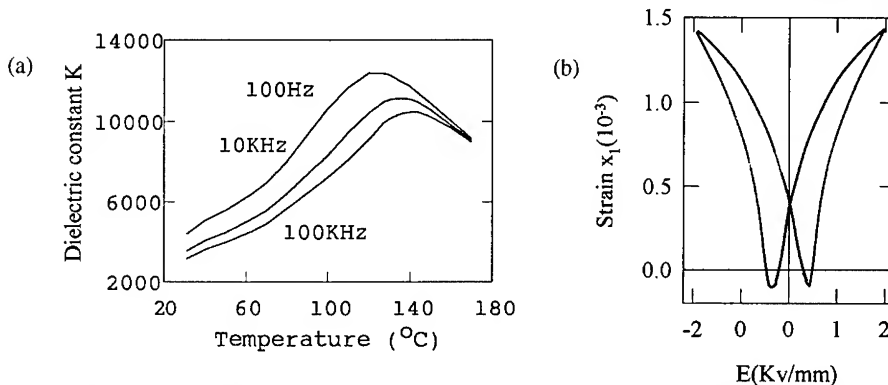


Fig. 1 Temperature dependence of dielectric constant (a) and voltage response of field-induced strain (b) of $(\text{Pb}_{0.68}\text{Ba}_{0.32})(\text{Zr}_{0.50}\text{Ti}_{0.50})\text{O}_3$ composition

temperature ferroelectric relator. The field-induced strain of this composition at room temperature exhibits a ferroelectric behavior as shown in Fig. 1(b), with a large strain hysteresis or a high remanent strain. According to the thermodynamic phenomenological theory it can be expected from Fig. 1(b) that there exists a certain piezoelectric contribution to the field-induced strain which would cause the initial-position "walk off" phenomenon.

A relaxor PMN addition was introduced to form a complex solid solution (Ba/Sr-PZTMN) in order to reduce the strain hysteresis or the remanent strain without decreasing the field-induced strain. Table I shows the dielectric properties and electro-mechanical coupling properties of PMN modified Ba/Sr-PZT compositions. The strain hysteresis of the composition doped with 1 mole% of PMN is larger than 25%. With the increase of PMN concentration the strain hysteresis decreases.

Table I Properties of PMN modified compositions (1-x)Ba-PZT-xPMN

composition	x	$T_{av}(^{\circ}\text{C})$	K_{Max}	K_{RT}	$x_1(10^{-3})$	$\Delta x_1/x_1$
500-2	0	120	12410	4410	1.49	0.30
502-1	2	115	11110	4490	1.48	0.20
504-6	4	117	11660	4880	1.94	0.13
505-2	6	112	9380	4730	1.38	0.16
506-6	8	103	8390	5000	0.93	0.22
507-2	10	98	6890	4630	0.55	0.19

The 90° domain wall switching behavior was studied while a rectangular pulse with positive and negative components (Fig. 2(a)) was applied. The positive pulse was kept constant whereas the amplitude of the negative pulse was varied step by step from -50 to -400 volts. The strain response appears in Fig. 2(b). Clearly, there is no 90° domain wall switching when the peak voltage, V_p , of the negative pulse is smaller than 100 V ($E_p = 250\text{V/mm}$). As V_p reaches around 200 V ($E_p = 500\text{V/mm}$), 90° domain walls start to switch. As V_p increases further, the switching process is observed clearly. It can be seen from Fig. 2(b) that different 90° domain walls have different switching times. The total response time is less than 1 ms.

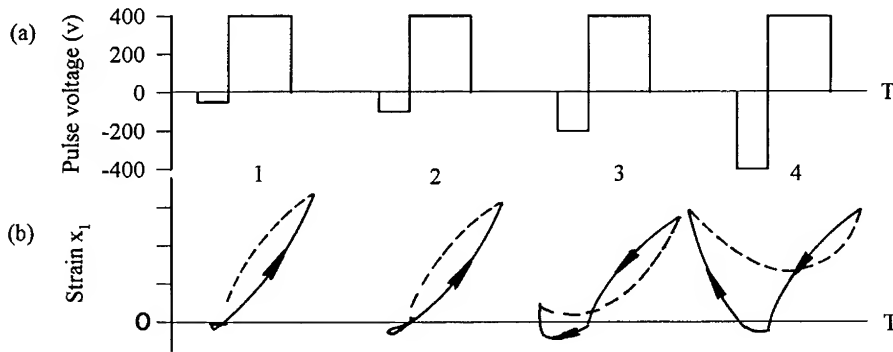


Fig. 2 Under rectangular-pulses (a) 90° domain wall switching processes can be observed (b) for composition #502-1 (refer to Table I)

Fig. 3(a) shows the influence of the $(\text{Mg}_{1/3}\text{Nb}_{2/3})$ concentration on the temperature dependence of the dielectric constant of Ba/Sr-PZTMN compositions. As the $(\text{Mg}_{1/3}\text{Nb}_{2/3})$ concentration increases the average Curie temperature (T_{av}) decreases and the K-T peak broadens. X-ray diffraction patterns (Fig. 3(b)) show the same trend as the dielectric properties (Fig. 3(a)). It seems that the incorporation of $(\text{Mg}_{1/3}\text{Nb}_{2/3})$ on the B-side is responsible for the broadening of the diffuse phase transition and of the K-T peaks.

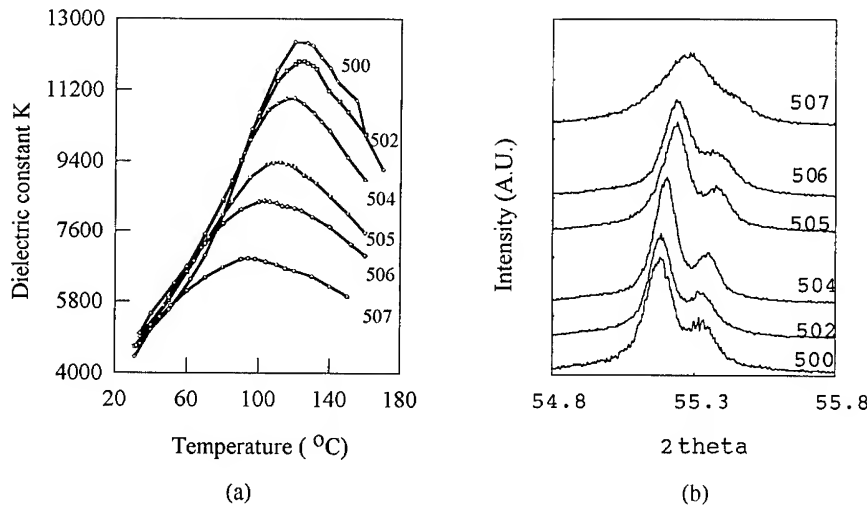


Fig. 3 Influence of $(\text{Mg}_{1/3}\text{Nb}_{2/3})$ concentration on (a) temperature dependent dielectric constants at 1kHz and (b) high-angle X-ray diffraction patterns of Ba-PZT compositions modified with the different PMN compositions shown in Table I.

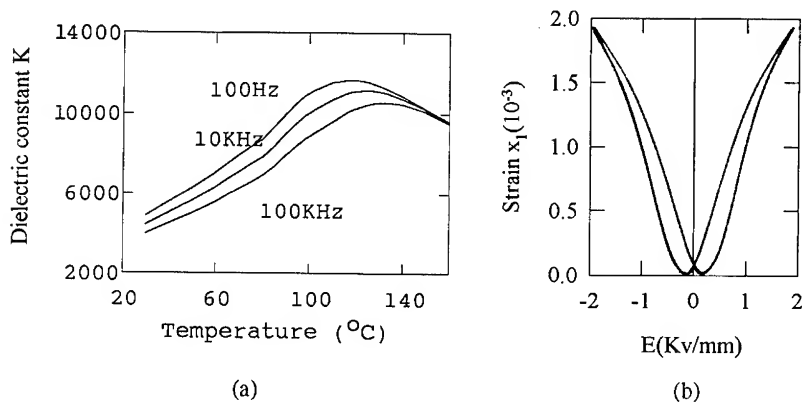


Fig. 4 Frequency dependence of dielectric constant (a) and field-induced strain (b) of 4 mole% $(\text{Mg}_{1/3}\text{Nb}_{2/3})$ doped B/S-PZT

From Table I it can be concluded that the composition doped with 4 mole% of ($Mg_{1/3}Nb_{2/3}$) exhibits the largest field-induced strain and the lowest remanent strain in the compositions listed in Table I. Fig. 4(a) shows the temperature dependence of the dielectric constant of this composition as a function of frequency. The shift of the average Curie temperature at 100 Hz and 100 kHz, a typical relaxor behavior, is 15°C.⁵ Fig. 4(b) shows the corresponding field-induced strain behavior for this composition. The change in the field-induced strain was measured to be less than 5% between 0 to 60°C.

It was found that Ba/Sr A-side co-modification could further improve the relaxor behavior and decrease strain hysteresis with a concomitant but small reduction in the value of the field-induced strain. Fig. 5 shows indeed a field-induced strain behavior with very small strain hysteresis. Normal ferroelectric domains could not be observed by TEM in these ferroelectric relaxor compositions as shown in Fig. 6. HREM micrograph, TEM bright field image and the corresponding electron diffraction pattern also was shown in the Figure. Note the sharpness of the diffraction pattern confirming the absence of ferroelectric domains.

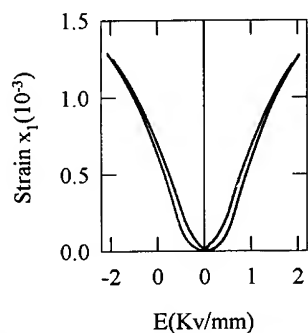
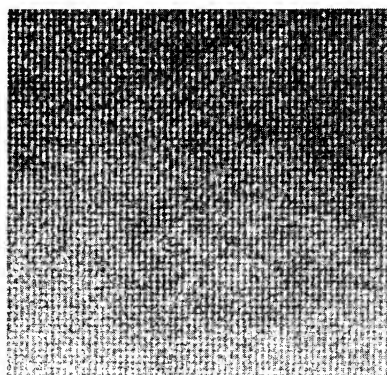
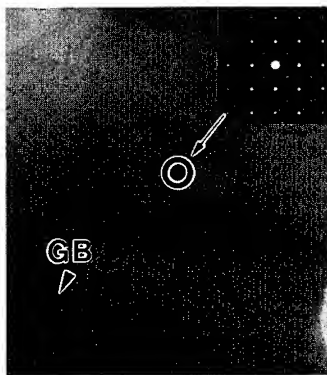


Fig. 5 Field-induced strain in composition #401, Ba/Sr co-modified PZTMN



(a)



(b)

Fig. 6 HREM micrograph of composition #401, Ba/Sr co-modified PZTMN (a) and corresponding electron diffraction pattern and bright field image (b)

CONCLUSIONS

1. The ceramic composition $(\text{Pb}_{0.68}\text{Ba}_{0.32})(\text{Zr}_{0.50}\text{Ti}_{0.50})\text{O}_3$ exhibits a high-temperature ferroelectric relaxor behavior.
2. As the PMN concentration increases, the average Curie temperatures of the PMN-modified Ba-PZT compositions decreases. The K-T peaks and phase transition broadens. X-ray diffraction patterns show similar trends.
3. The composition doped with 4 mole% of PMN exhibits a giant strain of 1.94×10^{-3} and a small strain hysteresis.
4. 90° domain wall switching can be observed by applying a rectangular voltage pulse. The peak field of the rectangular pulse needed to produce 90° domain wall switching is between 250 to 500V/mm.

REFERENCES

1. D. Damjanovic and R.E. Newnham, J. Intell. Mater. System and Struct., Vol.3, 190-208 (1992)
2. N.K. Yushin in "Choice of electrostrictive Material", presented at the 9th international symposium on the Applications of Ferroelectrics, Pennsylvania State University, PA, 1994 (unpublished)
3. T. Ikeda, J Phys. Soc. Japan 14, 168 (1959)
4. K.M. Leung, S.T Liu and J. Kyonka, Ferroelectrics 27, 41 (1980)
5. Jiehui Zheng and Zhiqiang Zhuang, J. South China University of Technology, 21(3), 63-67 (1993)

STRESSES NEAR THE END OF AN INTERNAL ELECTRODE IN MULTILAYER ELECTROSTRICTIVE CERAMIC ACTUATORS

XIAO-YAN GONG

Department of Mechanical and Environmental Engineering, University of California at Santa Barbara, Santa Barbara, CA 93106

ABSTRACT

Stresses near the end of an internal electrode in a multilayer electrostrictive ceramic actuator are studied in detail. A finite element program capable of overcoming two major difficulties is developed. The program solves both the mechanical and electrical coupling problem and the nonlinear electric field and electric displacement relationship for these materials. Results indicate that the stress difference between the coupled and the uncoupled cases can only be distinguished when a stress singularity is present. Tensile stresses are found both in front, and behind, the end of an internal electrode. The magnitude of the stresses is predetermined by the material constants.

INTRODUCTION

Recently, multilayer electrostrictive ceramic actuators,^{1,2,3} capable of generating both large displacement and force, have been proposed due to their wide applications. To achieve better performance, individual layers are made thinner, usually on the order of several tens of microns, so that a higher electric field may be obtained for a given voltage. Due to technical limitations in forming the very fine insulator lines, the capacitor-type multilayer actuator structure is adopted as shown in Figure 1. However, this structure has a defect. It contains an electrostrictively inactive area in front of the internal electrodes. This causes distortion and concentration of the electric field,⁴ thereby inducing incompatible strains which in turn produce stresses. It is suspected that the induced stresses are high enough to cause cracks which grow to fail the actuator⁵. Therefore it is necessary to predict the stress levels generated in the device precisely.

The attempt at solving the stresses caused by electrostriction was first made by Knops⁶ in 1963. At the time, it was believed that the electric displacement, D , caused by the electric field, E , in electrostrictive material was the same as that in dielectric materials, meaning, D and E were linearly related to each other, *i.e.*, $D = \epsilon E$, with ϵ the electric permittivity. Thus the electrostrictive strains would be quadratic in the electric field. Knops verified the validity of ignoring the dependence of the electric field on the dielectric deformations for small strains, and suggested that the electric field could be determined from conditions of the undeformed body. Furthermore, he derived the field equations for the uncoupled problems. Based on this framework, some further theoretical and computational stress analyses in electrostrictive materials have been done.^{1,4,7,8}

However, questions arise concerning the above assumptions. First, near the end of an internal electrode, the electric field is distorted and usually locally much higher than the applied electric field so that the D - E relationship of this kind of material, (*e.g.*, PMN-PT), is no longer linear.^{9,10,11} Second, such a highly distorted electric field causes incompatible strains which induce high stresses, meaning the electrical and mechanical coupling effects may no longer be neglected. These difficulties make it impossible for us to analytically solve the stresses caused by the electrostriction. Thus a finite element program has to be developed to understand the details of the stresses. The following sections discuss our attempts in developing the finite element program, and the results obtained.

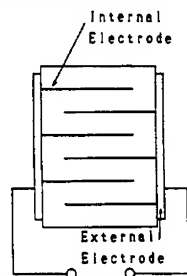


Figure 1. Structure of a capacitor type multilayer actuator

GOVERNING EQUATIONS

When a material is subjected to a field of displacement, \mathbf{u} , and electric potential, ϕ , the strain, γ , and the electric field, \mathbf{E} , can be derived from the gradients:

$$\gamma_{ij} = \frac{1}{2}(u_{i,j} + u_{j,i}), \quad E_i = -\phi_{,i} \quad (1)$$

Our attention is limited to small deformation in this work as we deal with ceramics. The stress, σ , and the electric displacement, \mathbf{D} , are defined such that, across an interface, they jump by:

$$n_i[\sigma_{ij}^+ - \sigma_{ij}^-] = t_j, \quad n_i[D_i^+ - D_i^-] = -\omega \quad (2)$$

where \mathbf{n} is the unit normal to the interface pointing from the + side; \mathbf{t} is the force and ω the charge, per unit area, externally applied on the interface.

Once these variables have been defined, The following constitutive laws can be obtained through a standard thermal dynamic approach^{4,12,13}:

$$\begin{aligned} E_i &= -2(Q_{11} - Q_{12})\sigma_{ij}D_j - 2Q_{12}\sigma_{mm}D_i + f(D)D_i/D \\ \gamma_{ij} &= \frac{1+\nu}{Y}\left(\sigma_{ij} - \frac{\nu}{1+\nu}\sigma_{mm}\delta_{ij}\right) + (Q_{11} - Q_{12})D_iD_j + Q_{12}D_nD_n\delta_{ij} \end{aligned} \quad (3)$$

Here, $D = (D_n D_n)^{1/2}$ is the magnitude of the electric displacement, ν is Poisson's ratio, Y is Young's modulus, δ_{ij} is Kronecker's delta, and Q_{11} and Q_{12} are electrostrictive coefficients. The usual summation convention is adopted. Table I lists the typical material constants for 0.9PMN:0.1PT ceramics.

The above constitutive law represents the following most important experimental observations for electrostrictive actuator type ceramics:

- The hysteresis is small enough to be neglected. There is no hysteresis in the above equations.
- When electric displacement is absent (i.e. $\mathbf{D}=0$), strain, γ , and stress, σ , obey a linear Hooke's law.
- When stress is absent (i.e. $\sigma=0$), strain, γ , is quadratic in electric displacement, \mathbf{D} .
- When stress is absent, function, f , defines the \mathbf{D} - \mathbf{E} relation.

Finally, the following postulated principle of virtual work completes our needs for governing equations:

$$\int (\sigma_{ij}\gamma_{ij} + D_i E_i) dv = \int (t_j u_j + \omega \phi) ds \quad (4)$$

where v is volume and s is the surface of the body. The equation states that when body force and space charge are taken to be negligible, the energy in the body is equal to the work applied at the interfaces.

Table I. *Representative data for a high-electrostriction ceramic*

Material	ϵ/ϵ_0	$Y(\text{GPa})$	ν	$Q_{11}(\text{M}^4\text{C}^{-2})$	$q=Q_{12}/Q_{11}$	$K_{Ic}(\text{MPa}\sqrt{\text{m}})$
0.9PMN:0.1PT	7500	112	0.26	0.025	0.38	≈ 1

($\epsilon_0 = 8.85 \times 10^{-12} \text{Fm}^{-1}$).

DIMENSIONAL ANALYSIS:

Through a dimensional analysis, we find two dimensionless parameters and two relations that are needed. These expressions are discussed below.

Saturated strain:

$$\gamma_0 = Q_{11} D_0^2 \quad (5)$$

This parameter gives the maximum magnitude of strain induced by the electrostriction only, which then leads to a characteristic stress, $\sigma_0 = Y\gamma_0$. We discover later that all stress magnitudes induced by the nonlinear electrostriction (without any other mechanical singularities, such as cracks, etc.) are on the order of this characteristic value.

Coupling parameter:

$$\alpha = \frac{Y Q_{11}^2 D_0^3}{E_0} = Y \gamma_0 \epsilon Q_{11} = \sigma_0 \epsilon Q_{11} \quad (6)$$

This parameter determines the importance of the electromechanical coupling effects. The larger the parameter, the more significant the coupling effects. From Table I we find that, for materials used to make actuators, α is on the order of 0.02.

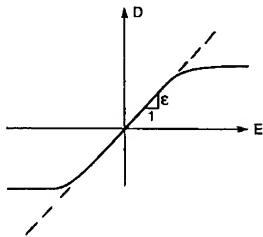
Stress induced by the electrostriction:

We find the stress induced by the electric field takes the follow form:

$$\sigma_{ij} = Y Q_{11} D_0^2 \Sigma_{ij} \left(\frac{E_{appl}}{E_0}, \alpha, q, \nu \right) = \sigma_0 \Sigma_{ij} \left(\frac{E_{appl}}{E_0}, \alpha, q, \nu \right) \quad (7)$$

Σ_{ij} refers to a function that needs to be determined. Also entering the right hand side are the D-E relation, geometric factors, etc. An immediate conclusion is then reached without doing any analysis, i.e., the stress caused by the electrostriction is proportional to the Young's modulus, Y , the electrostrictive coefficient, Q_{11} , and the saturated electric displacement, D_0 , squared.

D-E relation:



The dimensionless D-E relation is written as:

$$\frac{E_i}{E_0} = \frac{D_i}{D} f \left(\frac{D}{D_0} \right) \quad (8)$$

Figure 2. Schematic D-E relations: nonlinear but reversible (solid), linear (dash)

Figure 2 shows two one-dimensional relationships between the electric displacement and electric field.

FINITE ELEMENT APPROACH

The thickness of each individual layer is much smaller than its width or length in a multilayer actuator. We then focus our finite element studies on two dimensional problems only, *i.e.*, we adopt the plane strain assumption. In this case, the normalized constitutive law can be written as:

$$E_i = -2\alpha(1+q)\sigma_{ij}D_j + 2\alpha q\sigma_{mm}D_i + 2\alpha q^2 D_n D_n D_i + f(D)D_i / D \quad (9)$$

$$\gamma_{ij} = [(1+\nu)\sigma_{ij} - \nu\sigma_{mm}\delta_{ij}] + (1+q)D_i D_j - q(1+\nu)D_n D_n \delta_{ij}$$

All the indices here go from 1 to 2 only as we deal with the plane strain problems. The quantities are normalized in the following way:

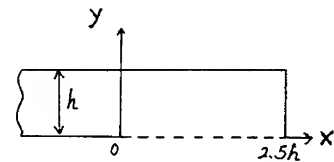
$$E_i \rightarrow E_i / E_0, \quad D_i \rightarrow D_i / D_0, \quad \sigma_{ij} \rightarrow \sigma_{ij} / \sigma_0, \quad \gamma_{ij} \rightarrow \frac{\gamma_{ij}}{\gamma_0}, \quad u_i \rightarrow u_i / h, \quad \phi = \phi / (E_0 h) \quad (10)$$

Here h is the thickness of a individual layer. For the nonlinear case, D_0 is well defined, E_0 can be obtained from $E_0 = D_0 / \epsilon$. On the contrary, when the linear **D-E** relation is used, one can define $E_0 = E_\infty$, with E_∞ the remote applied electric field, and obtains D_0 from $D_0 = \epsilon E_0$.

Equations (2), (3), (4) remain the same using the corresponding normalized quantities. Then the standard displacement approach, taking the displacements, u_1, u_2 and the electric potential, ϕ as node variables, can be adopted for the finite element analysis.¹⁴ As the coupling effect is taken into account, along with the nonlinear **D-E** relation, we must solve incrementally. We use the traditional eight node rectangular element in our finite element approach, and calculate several examples which are discussed in detail in the following section.

RESULTS AND DISCUSSIONS

The geometry and the boundary conditions we picked for the finite element analysis are shown in Figure 3. The first analysis is to see the importance of the coupling effect when **D=εE** (*i.e.*, linear case). Figure 4 shows the comparison of results. As one can tell, the coupling effect is only important near the end of the internal electrode. It is further suspected that the difference is caused by unlimited strains induced by electrostriction, leading to unlimited stresses at the end of the electrode. In other words, if the ability to produce further electric displacement is limited, which in turn limits the strains, and therefore the stresses, then the coupling effect should be negligible.



$y=h, u_2=const., \{\sigma_{yy}dx=0, \phi=0, \tau_{xy}=0.$
 $y=0, u_2=0, \tau_{xy}=0, u_1(-\infty, 0)=0.$ as electrode
 lies from $-\infty$ to 0, thus $\phi=0$, when $x \in (-\infty, 0)$,
 $\omega_n=0$, when $x \in [0, 2.5h]$
 $x=2.5h$, or $x \rightarrow -\infty, \sigma_{xx}=\tau_{xy}=\omega_x=0.$
 $x=0, y=0$ is the electrode end.

Figure 3. Geometry and boundary conditions.

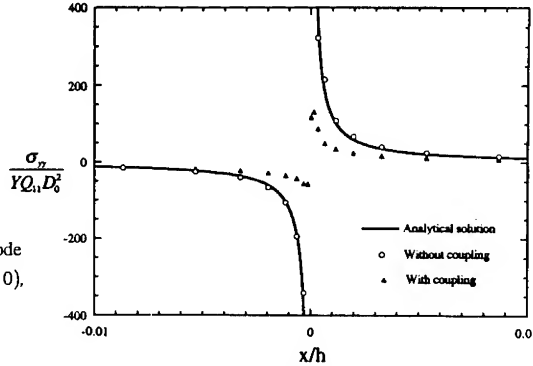


Figure 4. Stress along the X-axis. Analytical solution is uncoupled.⁴

To confirm this, we next fit the nonlinear **D-E** relation shown in Figure 2 in the explicit form:

$$E_i = \frac{D_i}{2\beta D} \ln\left(\frac{1+D}{1-D}\right) \quad (11)$$

The parameter β , which is related to the permittivity of the material, controls the slope at $D=0$.

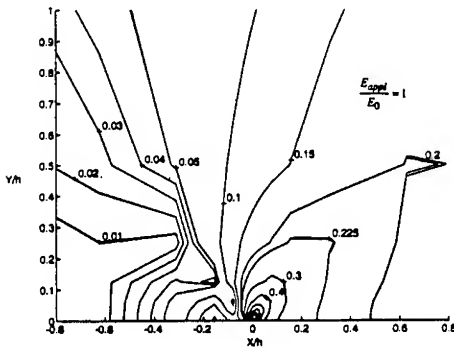


Figure 5. Maximum principal stress contours.

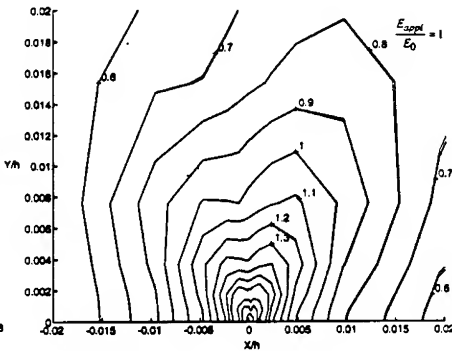


Figure 6. Maximum principal stress contours.

Figure 5 shows the maximum principal stress contours for both the coupled and uncoupled analyses, where the outer lines represent the uncoupled case, and the inner lines represent the coupled. The indistinguishable contours tell us that the coupling effect is weak for structures containing no stress singularities. Thus, ignoring the coupling effect is a good approach. Figure 6 gives us more confidence when the electrode end is amplified.

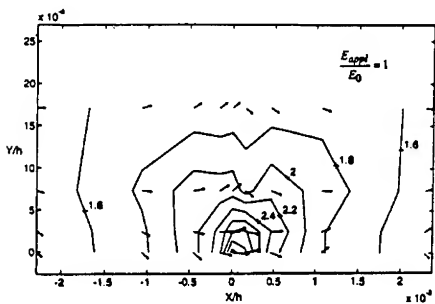


Figure 7. Maximum principal stress contours and directions.

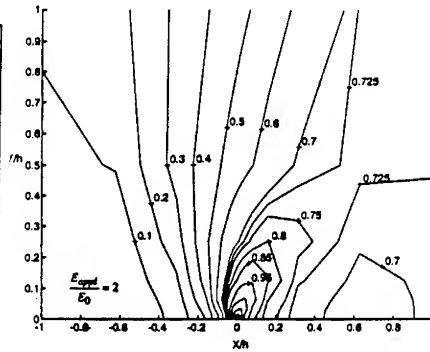


Figure 8. Maximum principal stress contours.

Another result from our finite element study is that there are tensile areas at both sides (front and back) of the internal electrode. We plot the maximum principal stress contours and directions in Figure 7. This plot suggests that the cracks should initiate from the end of an internal electrode and take directions perpendicular to the maximum principal stress. Furthermore, due to debonding of the weak electrode and ceramic interfaces, stresses in the direction normal to the electrode have been released. This suggests the existence of parallel microcracks perpendicular to electrodes at the back of the internal electrodes and declined cracks in front of them.¹⁵

Figures 8 show the stress contours for a large applied electric field. Comparing with figure 5, one can conclude that the larger the applied field, the larger the tensile stresses and their areas. On

the other hand, the larger the tensile stresses and areas, the more the interfaces debond. This result explains why a well designed multilayer actuator was observed to fail under a high applied field by interfacial debonding rather than by fracture.¹

We also study the case for $\beta=100$ in equation (11). The result is very close to that for $\beta=1$. It can be concluded that the details of the shape of the **D-E** relation play a minor role in determining the magnitude of the stress induced by the electrostriction. The dominant parameters are Young's modulus and saturated strain.

CONCLUDING REMARKS

Solving the electric field while ignoring the coupling effects is first confirmed as a reasonable assumption for structures containing no stress singularities by the finite element analysis in this paper. A tensile area at the back of the internal electrode is first found from the finite element study. This discovery explains the existence of parallel microcracks perpendicular to the electrodes.¹⁵ Moreover, as the applied field increases, the tensile area expands. This result suggests that interfacial debonding has a larger probability of occurring and failing the structure under higher electric fields, which agrees with experimental result¹. The magnitude of the stress caused by electrostriction at the internal electrode end is strongly dependent on the saturated electrostrictive strain and Young's modulus.

ACKNOWLEDGMENTS:

The author would like to thank Mr. Dominic J. Dal Bello and Dr. Christopher S. Lynch for their kind helps in writing this paper, and Professor Zhigang Suo for his encouragement. This work is supported by the Office of Naval Research through Contract No. N00014-93-1-0110.

REFERENCES:

- ¹S. R. Winzer, N. Shankar, A. P. Pitter, *J. Am. Ceram. Soc.* **72** [12] 2246-57 (1989).
- ²K. Uchino, *Ceram. Bull.* **65** [4] 647-652 (1986).
- ³H. Aburatani, S. Harada, K. Uchino, A. Furuta, Y. Fuda, *Jpn. J. Appl. Phys.* **33** [5B] 3091-3094 (1994).
- ⁴W. Yang, Z. Suo, *J. Mech. Phys. Solids* **42** [4] 649-663 (1994).
- ⁵A. Furuta, K. Uchino, *J. Am. Ceram. Soc.* **76** [6] 1615-17 (1993).
- ⁶R. J. Knops, *Q. J. Mech. Appl. Math.* **16** [3] 377-388 (1963).
- ⁷T. E. Smith, W. E. Warren, *J. Math. Phys.* **45** 45-51 (1966); **47** 109-110 (1968) (corrigenda).
- ⁸R. M. McMeeking, *J. Appl. Math. Phys.* **40** 615-627 (1989).
- ⁹S. Nomura, K. Uchino, *Ferroelectrics* **41** 117-132 (1982).
- ¹⁰R. E. Newnham, *NIST Special Publication* **804**, 39-52 (1991).
- ¹¹L. E. Cross, *Ferroelectrics* **76** 241-267 (1987).
- ¹²Z. Suo, *AD 24/AMD 123 Smart Structure and Materials*, ASME, 1-6 (1991).
- ¹³M. E. Lines, A. M. Glass, *Principles and Appl. Ferroelectrics and Related Mat.* Clarendon Press, Oxford. (1977).
- ¹⁴O. C. Zienkiewicz, *The Finite Element Method* McGraw-Hill Book Company (1977).
- ¹⁵G. A. Schneider, A. Rostek, B. Zickgraf, F. Aldinger, *Proc. 4th Int. Conf. Elec. Ceram. Appl.* 1211-1216 (1994).

PART IV

Optical Systems

USING DX CENTERS TO WRITE ERASABLE METALLIC PATTERNS IN AlGaAs.

TINEKE THIO*, R.A. LINKE*, G.E. DEVLIN*, J.W. BENNETT*, J.D. CHADI*, R.L. MACDONALD*, M. MIZUTA**,

*NEC Research Institute, 4 Independence Way, Princeton NJ 08540;

**Fundamental Research Laboratories, NEC Corp., Tsukuba, Ibaraki 305, Japan.

ABSTRACT

DX centers are semiconductor dopants which form deep states due to a large lattice relaxation. At low temperature, the DX centers exhibit persistent photoconductivity. When exposed to light in a spatial pattern, the photocarriers are confined to the illuminated regions by Coulomb interaction with the localized DX centers. The resulting spatial modulation of the free carrier density gives rise to a modulation of both the electrical conductivity and the dielectric constant. We demonstrate both effects by measurements of the conductance anisotropy and optical diffraction of samples exposed to excitation in a striped pattern. Erasure is achieved by thermal annealing. The contrast ratio of the conductivity modulation is greater than 10^5 ; in our experiment it is limited to ~ 100 by light scattering. We estimate that 100nm resolution is feasible. Optical diffraction efficiencies up to 40% have been demonstrated in a stripe-illuminated thick sample. The persistence of the written patterns at low temperature is potentially useful in high-density data storage applications and the fabrication of erasable submicron devices.

1. INTRODUCTION.

In many III-V and II-VI semiconductors, certain dopants form deep donor states called DX centers, due to a lattice relaxation around the donor site.^{1,2} The DX is a negative-U center: In the ground state it is negatively charged. Exposure to visible light converts the DX into a normal shallow donor with the release of two electrons into the conduction band, the donor impurity atom becoming positively charged. Since a structural relaxation is required to return to the DX state, this creates a barrier to recombination,³ resulting in persistent photoconductivity (PPC) at low temperature.

We demonstrate the writing of a persistent metallic pattern in an epilayer of insulating $\text{Al}_x\text{Ga}_{1-x}\text{As}$ containing DX centers ($\text{Al}_x\text{Ga}_{1-x}\text{As:DX}$), by exposing the layer to visible light of the desired pattern. The doped layer, grown on an undoped $\text{Al}_x\text{Ga}_{1-x}\text{As}$ buffer layer, is insulating when cooled in the dark. At low temperature, it is exposed to visible light in a striped pattern. The photogenerated electrons move freely in the conduction band; however, they are confined by the Coulomb interaction to the vicinity of the positively charged donor ions which are localized in the exposed regions. The resulting spatial modulation of the free carrier density is persistent, and induces a modulation of both the electrical conductivity σ and the dielectric constant ϵ . For striped excitation, the conductivity modulation is evinced by an anisotropic sample conductance,⁴ whereas the modulation of ϵ is demonstrated by optical diffraction.⁵ The written patterns are erased by thermal annealing. This effect is potentially applicable in the fabrication of submicron devices, switching applications, and in erasable high-density storage media.

2. EXPERIMENTAL DETAILS.

$\text{Al}_x\text{Ga}_{1-x}\text{As}$ samples, doped with Si or Se, were MBE-grown on a buffer layer of undoped $\text{Al}_x\text{Ga}_{1-x}\text{As}$. The Se-doped sample⁶ was $1.6\mu\text{m}$ thick and had Al content $x=61\%$. Close to room temperature the carrier density is thermally activated: $N(T)=N_\infty\exp(-E/kT)$, with $N_\infty\sim 5\times 10^{19}\text{ cm}^{-3}$. Two Si-doped samples, grown by Quantum Epitaxial Design, had $x=27\%$ with $N_\infty\sim 1\times 10^{19}\text{ cm}^{-3}$, and $x=35\%$ with $N_\infty\sim 5\times 10^{19}\text{ cm}^{-3}$; both samples were $1.0\mu\text{m}$ thick. A $390\mu\text{m}$ thick sample of $\text{Al}_x\text{Ga}_{1-x}\text{As:Te}$ ($x=33\%$) was grown by liquid phase epitaxy.

Electrical contacts were made with In-Sn solder, and remained ohmic down to $T=4\text{K}$. The samples were placed in an optical cryostat for exposure in a striped pattern. A sinusoidal intensity modulation was obtained by the interference of two collimated HeNe laser beams ($\lambda_x=632.8\text{nm}$) with intensities equal to within 1% and modulation periods $1<d<30\mu\text{m}$. A square-wave modulation ($10<d<500\mu\text{m}$) was obtained by imaging a Ronchi ruling onto the sample, with a contrast ratio ~ 20 . In both cases the contrast ratio was limited by scattering of light inside the cryostat. We measured the anisotropic sample conductance in a Van der Pauw geometry, following the method of Montgomery.⁷ Optical diffraction was measured by monitoring the intensity of a probe beam ($\lambda_p=1.5\mu\text{m}$) as a function of diffraction angle.

3. RESULTS AND DISCUSSION.

The conductivity of the AlGaAs:DX samples is similar to that reported in the

literature.^{1,6} Figure 1 shows the temperature dependence of the conductivity in a $x=35\%$ sample, on cooling in the dark (solid circles in the figure) and on heating, also in the dark, but following saturation illumination at $T=20\text{K}$ (open squares). Close to room temperature, the system is in thermal equilibrium and the conductivity is thermally activated; the activation energy is the thermal binding energy of the deep donor: $E_d\sim 54\text{meV}$ ($x=27\%$); $E_d\sim 130\text{meV}$ ($x=35\%$) and $E_d\sim 59\text{meV}$ ($x=61\%$). The PPC persists to $T\approx 50\text{--}70\text{K}$. Hall effect measurements on uniformly illuminated samples at $T=20\text{K}$ indicate⁴ that the photoconductivity and the photocarrier density both rise

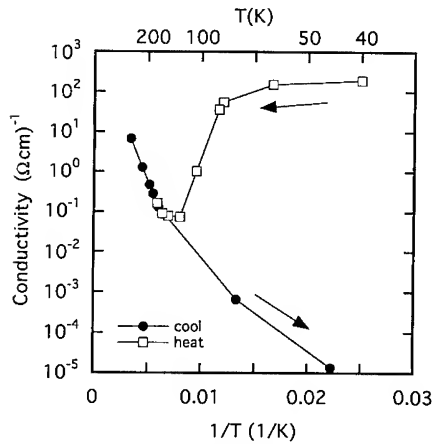


Figure 1. Temperature dependence of $\text{Al}_{0.35}\text{Ga}_{0.65}\text{As:Si}$ on cooling in the dark (solid circles) and heating in the dark after saturation illumination at $T=20\text{K}$ (open squares).

linearly with exposure time, saturating at $\sigma_{\text{sat}}=500(\Omega\text{cm})^{-1}$ and $N_{\text{sat}}\approx 4\times 10^{18}\text{ cm}^{-3}$, respectively. The $T=20\text{K}$ carrier mobility varied from $0.5\text{--}600\text{ cm}^2/\text{Vs}$.

When material containing DX centers is exposed to light in a spatially varying pattern, the photocarriers are confined to the illuminated regions, by Coulomb attraction to the positively charged DX centers from which they were excited. We

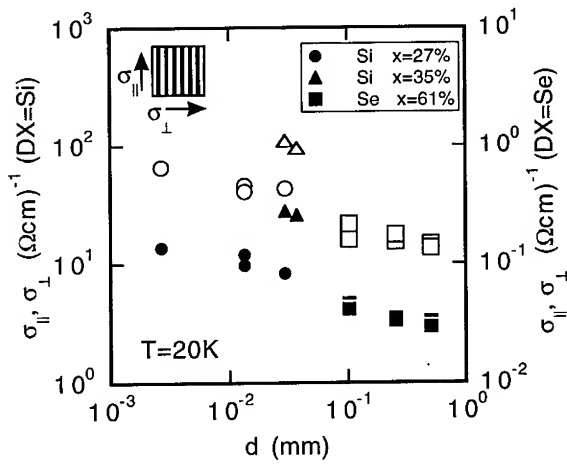


Figure 2. Effective conductivities $\sigma_{||}$ (open symbols) and σ_{\perp} (solid symbols) in striped-illuminated $\text{Al}_{0.27}\text{Ga}_{0.73}\text{As:Si}$ (\bullet, \circ), $\text{Al}_{0.35}\text{Ga}_{0.65}\text{As:Si}$ ($\blacktriangle, \triangle$), and $\text{Al}_{0.61}\text{Ga}_{0.39}\text{As:Se}$ (\blacksquare, \square ; right-hand axis); inset shows illumination pattern.

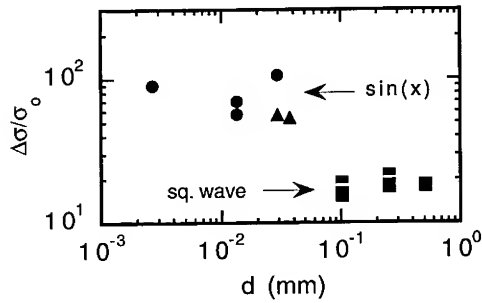


Figure 3. Conductivity contrast $\Delta\sigma/\sigma_0$ in $\text{Al}_{0.27}\text{Ga}_{0.73}\text{As:Si}$ (\bullet), $\text{Al}_{0.35}\text{Ga}_{0.65}\text{As:Si}$ (\blacktriangle), and $\text{Al}_{0.61}\text{Ga}_{0.39}\text{As:Se}$ (\blacksquare ; right-hand axis).

~ 80 for the sinusoidal excitation, independent of the grating spacing down to $d=2.7\mu$. In both cases, the contrast ratio is limited by light scattering inside the cryostat.

Using the Thomas-Fermi approximation in the $T=0$ limit, we estimate that in principle metallic features can be written in insulating $\text{Al}_x\text{Ga}_{1-x}\text{As:DX}$ films with a resolution $\sim 100\text{nm}$; this is consistent with our observation that $\Delta\sigma/\sigma_0$ is

illuminate the samples in a striped pattern (see inset of Figure 2): The light intensity $I(x,y)$ does not change in the y direction; in the x direction $I(x,y)$ varies either sinusoidally or like a square wave. Such illumination results in an anisotropy in the effective conductivity parallel ($\sigma_{||}$) and perpendicular (σ_{\perp}) to the stripes, with $\sigma_{||} > \sigma_{\perp}$. Figure 2 shows $\sigma_{||}$ and σ_{\perp} as a function of grating spacing d . The Se-doped sample was exposed with a square-wave pattern, whereas the Si-doped sample was exposed to a sinusoidal

pattern; in both cases we measure $\sigma_{||}/\sigma_{\perp} \sim 4-5$. The anisotropy is persistent in the same temperature range for which the photoconductivity itself is persistent; both are completely erased by heating the sample above $T=200\text{K}$.

From the data in Figure 2, we calculate⁴ the maximum and minimum conductivities of the modulated pattern. The conductivity contrast ratio $\Delta\sigma/\sigma_0$, plotted in Figure 3, is limited by the contrast ratio of the exciting light: ~ 20 for the square-wave and

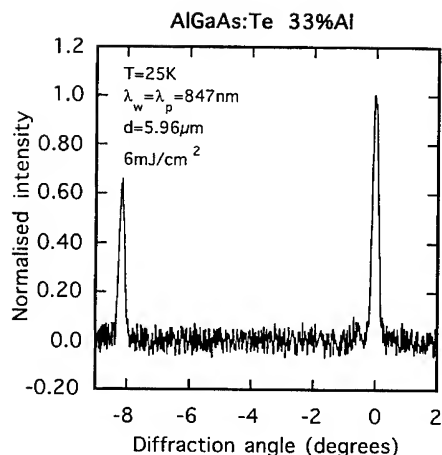


Figure 4. Optical diffraction in a $390\mu\text{m}$ thick sample of $\text{Al}_{0.33}\text{Ga}_{0.67}\text{As:Te}$. The write and read wavelength were the same, reading was done at the Bragg angle.

equal to that expected from theory assuming a modulation amplitude in the carrier density⁵ of $\Delta N = 4 \times 10^{18} \text{ cm}^{-3}$. This efficiency corresponds to an index modulation of $\Delta n = 5.4 \times 10^{-3}$, thirty times larger than that observed in conventional photorefractive materials such as BaTiO_3 .⁹ Figure 4 shows the optical diffraction of a thick ($390\mu\text{m}$) sample of AlGaAs:Te (33%Al).¹⁰ In this experiment the read wavelength was identical to the write wavelength, $\lambda = 847\text{nm}$ (but operated at much lower intensity to prevent erasure of the grating). Bragg angle matching enhanced the diffraction efficiency to $\eta = 40\%$.

In the conventional photorefractive effect, non-uniform illumination causes diffusion of the charge carriers. This results in the build-up of electric field gradients which, through the electro-optic effect, modulates the refractive index: It is therefore a non-local effect. In contrast, the excitation of a DX center is a local process. One of the most important consequences of this fact is the superposition of sequentially written gratings in AlGaAs:DX ; writing a new grating does not erase gratings which have been previously written into the material. In holographic applications, this enhances the storage capacity of DX materials with respect to that of conventional photorefractive materials by many orders of magnitude.¹¹

4. CONCLUSIONS.

We have demonstrated the writing of metallic patterns in an insulating matrix of AlGaAs:DX by exploiting the persistent photoconductivity associated with the DX centers. Materials containing DX centers have great potential for application in device fabrication at the submicron scale. Metallic features can in principle be written with a resolution $\sim 100\text{nm}$, e.g., using near-field optical techniques.¹² The

independent of grating period for $d > 2.7\mu$, and is confirmed by recent optical measurements done at $d = 130\text{nm}$.⁸ Since the written patterns persist at low temperatures, a possible application is in the fabrication of submicron devices.

The modulation of the carrier density also gives rise, through band filling and the plasma effect,⁵ to a modulation of the refractive index. A stripe-illuminated sample therefore functions as an optical grating. In the thin samples of Figures 2 and 3, a grating with 36 lines/mm showed diffraction of a probe beam ($\lambda_p = 1.5\mu\text{m}$). The first-order diffraction efficiency $\eta = 1.3 \times 10^{-4}$ is

written patterns persist after the excitation is removed, minimizing the energy dissipated in the writing process. In addition, there is potential for high-density data storage:^{4,5} data densities of order 10Gbits/cm² can in principle be obtained. Complete erasure is achieved by raising the sample temperature to overcome the barrier for free electron recapture E_b . Recapture returns the DX center to its original, negatively charged and insulating ground state. After cooling in the dark, the device can be exposed to a new pattern.

For device applications, it is important to have large values of both E_d , the binding energy of the deep DX donor, and E_b , the barrier to recombination. The former must be large in order to have a highly insulating material at low T (before exposure). E_b determines the maximum temperature at which the photoconductivity is persistent, as well as the maximum density of photocarriers N_{sat} . This is important for optimising σ_{sat} , the conductivity at full exposure, as well as the dynamic range, the difference between σ_{sat} and the dark conductivity σ_{dark} . In some samples we have measured $\sigma_{sat}/\sigma_{dark} > 10^8$ (see Figure 1). Typical recombination barriers E_b in $\text{Al}_x\text{Ga}_{1-x}\text{As:Si}$ are such that the PPC is annealed at temperatures $T < 77\text{K}$. Of particular interest in this respect are II-VI semiconductors, which may support DX centers with significantly larger E_b .^{13,14} Devices made of such materials could be operated at much higher temperatures.

REFERENCES.

- ¹P.M. Mooney, *J. Appl. Phys.* **67**, R1 (1990).
- ²D.V. Lang and R.A. Logan, *Phys. Rev. Lett.* **39**, 635 (1977).
- ³D.J. Chadi and K.J. Chang, *Phys. Rev. Lett.* **61**, 873 (1988).
- ⁴T. Thio *et al.*, *Appl. Phys. Lett.* **65**, 1802 (1994).
- ⁵R.A. Linke *et al.*, *Appl. Phys. Lett.* **65**, 16 (1994).
- ⁶M. Mizuta and K. Mori, *Phys. Rev. B* **37**, 1043 (1988).
- ⁷H.C. Montgomery, *J. Appl. Phys.* **42**, 2971 (1971).
- ⁸R.A. Linke *et al.*, unpublished.
- ⁹J. Hong *et al.*, *Optics Lett.* **15**, 334 (1990).
- ¹⁰R.L. MacDonald *et al.*, accepted for publication in *Optics Lett.* (1995).
- ¹¹D. Psaltis *et al.*, *Appl. Opt.* **27**, 1752 (1988).
- ¹²E. Betzig *et al.*, *Appl. Phys. Lett.* **61**, 142 (1992).
- ¹³K. Khachatryan *et al.*, *Phys. Rev. B* **40**, 6304 (1989);
J.W. Bennett *et al.*, unpublished.
- ¹⁴N.G. Semaltianos *et al.*, *Phys. Rev. B* **47**, 12540 (1993).

A DYE-DISPERSED LIQUID CRYSTAL SMART REFLECTOR

CHING-CHAO CHANG, FRANKLIN LONBERG AND ROBERT B. MEYER

The Martin Fisher School of Physics, Brandeis University, Waltham, MA 02254-9110, U.S.A.

ABSTRACT

We report a liquid crystal smart reflector, consisting of a cholesteric liquid crystal doped with dye. Light entering the liquid crystal is absorbed by the dye, generating heat which raises the average temperature of the liquid crystal. This in turn changes the pitch length of the cholesteric liquid crystal, causing an increase in its reflectivity, and thus reducing the amount of light absorbed by the dye molecules. A negative feedback stabilized condition is reached, in which the reflectivity is proportional to the incident light intensity. This effect is demonstrated both theoretically and experimentally.

INTRODUCTION

Recently a liquid crystal smart reflector was demonstrated [1]. In that case a cholesteric liquid crystal (CLC) with a temperature sensitive helix pitch, backed by a light absorbing dye layer, was used. This device was based on two basic properties of cholesteric liquid crystals [2].

The first property is its selective total reflection of light in a band of wavelengths centered on the pitch length P of the helix, a phenomenon similar to the Bragg reflection of x-rays by a periodic crystal structure. Consider light approximately normally incident on a thin layer of CLC in which the axis of the helicoidal structure is oriented normally to the plane of the layer. One circular polarization of light in the reflection band, which matches the sense of rotation of the helix, will be totally reflected as a circularly polarized beam of the same sense, while the opposite circularly polarized component of the incident beam will be transmitted by the CLC. The spectral width $\Delta\lambda$ of the total reflection band is given approximately by the equation [3]:

$$\Delta\lambda = P\Delta n. \quad (1)$$

Δn is the birefringence of the CLC, the difference between the indices of refraction parallel and perpendicular to the local nematic director.

The second property of the CLC is the strong temperature dependence of the pitch length of its helicoidal structure near the phase transition from the cholesteric phase to the smectic A phase. As temperature T is lowered toward the transition temperature T_{AC} , the pitch length diverges toward infinity, with a power law dependence, $P \propto (T - T_{AC})^{-0.67}$ [4].

This device works in the following way. At ambient temperature, the liquid crystal is in the smectic A phase, and incident light passes through it to the absorbing dye layer, where the light is converted to heat. This raises the temperature of the liquid crystal, converting it to the cholesteric phase, and the pitch of the helicoidal structure of the CLC is initially in the infrared. With further heating, the pitch grows shorter, until the reflection band of the CLC begins to reflect part of the incident light. The resulting reduction of optical power reaching the absorbing layer constitutes a negative feedback mechanism, controlling the temperature of the CLC and allowing just enough light to reach the absorbing layer to maintain the device

at its correct operating temperature. This negative feedback stabilizes the reflector for a given light intensity. Any increase in light intensity results in a compensating increase in temperature and reflectivity, and conversely, any decrease in incident light intensity results in a corresponding decrease in temperature and reflectivity.

In this paper a different kind of absorptive mechanism is used. Dichroic dye was dissolved in the CLC directly, so light is absorbed by the dye molecules distributed everywhere in the liquid crystal. Once the light enters the cholesteric layer, some light will be reflected, some will be absorbed because of the dye molecules, and the rest of it will be transmitted. The light absorbed in the sample is converted to heat and raises the average temperature of the mixture and the glass substrates. Again, just as in the previous case, the negative feedback mechanism will stabilize the system. The advantage of this system is that the heat transfer is expected to be more efficient because the liquid crystal absorbs the incident light, rather than a separate backing layer. On the other hand, the maximum reflectivity will be lower due to the absorption in the reflecting layer.

EXPERIMENT

The liquid crystal used in this experiment belongs to the cyanobiphenal group [5]. Details can be found in [1]. The dichroic dye, which has an elongated structure similar to liquid crystal molecules, has been studied and used in liquid crystal applications for many years. Because of the similar shapes, all the molecules are compatible with each other, and the dye molecules are expected to follow the alignment of liquid crystal molecules, a relationship known as the guest-host effect. Dichroic dye D37 (2.7%, EM Chemicals) is put in the liquid crystal material as the absorptive component.

The liquid crystal mixture was sandwiched between two glass substrates separated by a $12\mu\text{m}$ Mylar spacer. Both substrates were treated before using in order to get homogeneous alignment. This can make the helical axis normal to the substrates and higher reflectivity can be achieved. This device was then placed in a temperature controlled oven to set the ambient temperature.

An argon ion laser with linear polarizer and quarter wave plate was used to produce an intensified circularly polarized light, as a heat source and a probe for reflectivity measurement. A power meter based on a silicon photodiode was used to monitor the reflected light intensity from the device at near normal incidence.

Results of our experiments are shown in Fig. 1. At the lowest power, the reflection coefficient is essentially similar to that of the CLC with no heating or feedback effect. As power is raised, the reflection coefficient on the low temperature side of the curves increases, which indicates the negative feedback that stabilizes the system. On the high temperature side, the reflection coefficient at high power drops suddenly below its low power level, indicating the positive feedback that makes the device unstable in this region. The reflectivity is generally low because light is always absorbed by the dye molecules. Besides that, there are many disclinations distributed throughout the CLC layer which scatter light. Notice that the maximum reflectivity at high power is a little bit larger than that at the lowest power. The reason might be that at high power, the heat can shorten the pitch length slowly enough to avoid creating disclination lines; at the lowest power, the pitch length is shortened by adjusting the ambient temperature, thus causing more defects. It may also be that at high power, the optical \mathbf{E} field has a significant aligning effect.

The reflectivity as a function of incident power at fixed ambient temperature is shown

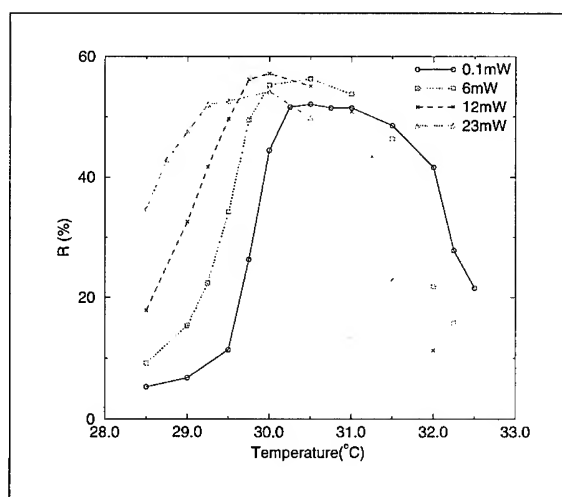


Figure 1: Reflectivity of our device as a function of ambient temperature for four incident laser powers.

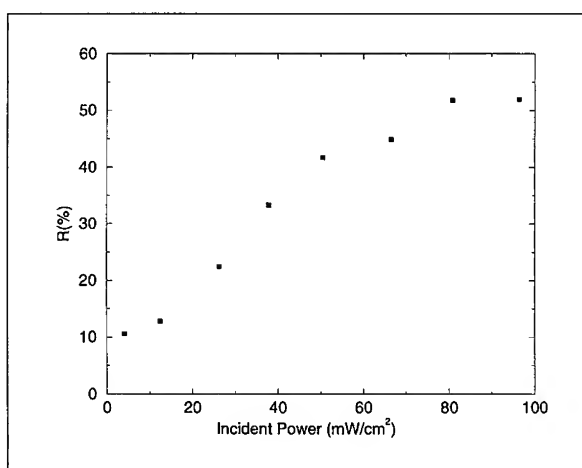


Figure 2: Reflectivity of our device as a function of laser power at a fixed ambient temperature.

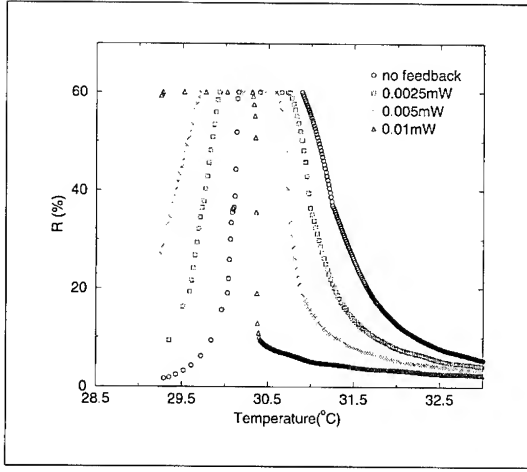


Figure 3: Calculated reflectivity R of the model as a function of ambient temperature.

in Fig.2. Here it is clear that the reflectivity of the device can increase with the increasing incident power, and then reach its maximum. The slope of this reflectivity change depends on the concentration of dye and $|\frac{\Delta P}{\Delta T}|$.

MODEL CALCULATION

The exact solution to the wave equation for the propagation of light along the helical axis of a CLC was presented by Mauguin, Oseen and de Vries [6][7][3]. Nityananda and Kini [8] applied this theory and used continuity at the boundary to get the reflectivity when a CLC was sandwiched between two isotropic media. Hajdo and Eringen [9] proposed a multilayer model to explain the effect of a pitch gradient in the CLC on the reflectivity.

We used a multilayer model and calculation described in [8] to determine the optical properties of the CLC. Because of the guest-host effect, we can treat this mixture as an “absorptive cholesteric liquid crystal”, which is circular dichroic in this case. The first intuitive modification is that the indices of refraction n_{\parallel} and n_{\perp} become complex where the imaginary parts of n_{\parallel} and n_{\perp} represent the absorption parallel and perpendicular to the direction of the dye molecule, which is also the direction of the director.

The two glass substrates were put into consideration in the calculation because the heat absorbed in the cholesteric liquid crystal is transferred to the glass substrates, which means that the heat raised the average temperatures of both the liquid crystal and the glass substrates. Here the heat conduction equation in equilibrium

$$\frac{d^2 T_i}{dx_i^2} + \frac{Q_i}{KA\Delta x} = 0 \quad (2)$$

is used in each liquid crystal layer with the same thickness Δx , where A is the area of the sample, K the thermal conductivity of the material, and T_i and Q_i the temperature and the

heat source at each layer, respectively. For each layer, the heat source is calculated from the optical propagation equation. The cut-off reflectivity was set at 60% to allow for the effect of the defects. The reflectivity of the cholesteric liquid crystal for laser of wavelength $0.515\mu\text{m}$ as a function of ambient temperature is shown in Fig. 3. The no-feedback curve corresponds to the case where the absorption is ignored. Here the theoretical curves agree with the experiment qualitatively. The feedback mechanism becomes active and the reflectivity increases with increasing optical power. At high power, the curves shift in the low temperature direction due to optical heating.

SUMMARY

We have demonstrated a dye-doped liquid crystal reflector, where the reflectivity is a function of ambient temperature and the incident optical power. Because dichroic dye is dissolved in the cholesteric liquid crystal directly, the geometry of the device is simpler than the previously reported device and the response time should be smaller. The power needed to drive this device to its maximum reflectivity is of the order of 10 mW/cm^2 . This number can be changed by adjusting the concentrations of chiral dopants and dichroic dye, depending on the specific applications.

We thank EM Chemicals for providing us with chiral dopant materials. Prof. Seth Fraden at Brandeis provided constant help and advice. This research was supported by the ARO program in smart materials, through grant #DAAL03-92-G-0387.

REFERENCES

1. C.-C. Chang, F. Lonberg, and R.B. Meyer, Proceedings of the Second International Conference on Intelligent Materials, edited by C.A. Rogers, G.G. Wallace (Technomic Publishing Co., Lancaster, PA, 1994) pp. 304-311.
2. For general reference, see, e.g., S. Chandrasekhar, Liquid Crystals, 2nd ed. (Cambridge University Press, Cambridge, 1992).
3. H. de Vries, Acta Cryst. **4**, 219 (1951).
4. R.S. Pindak, C.C. Huang, and J.T. Ho, Phys. Rev. Lett. **32**, 43 (1974).
5. G.W. Gray and A. Mosley, J.C.S. Chem. Comm. 147 (1976).
6. M.C. Mauguin, Bull. Soc. Franc. Miner. Cryst. **34**, 71 (1911).
7. C.W. Oseen, Trans. Faraday Soc. **29**, 883 (1933).
8. R. Nityanada and U.D. Kini, Proceedings of the International Liquid Crystals Conference, Bangalore, Pramana Supplement I, p. 311 (1973).
9. L.E. Hajdo and A.C. Eringen, J. Opt. Soc. Am. **69**, 1017 (1979).

FABRICATION OF THICK, SOL GEL PZT FILMS: APPLICATIONS TO MACROSCOPIC PIEZOELECTRIC DEVICES

D.A. BARROW¹, T.E. PETROFF² and M. SAYER¹

1. Department of Physics, Queen's University, Kingston, Ontario.

2. Department of Chemistry, Queen's University, Kingston, Ontario.

ABSTRACT

Lead zirconate titanate (PZT) films of up to 60 μm in thickness have been fabricated on a wide variety of substrates using a new sol gel process. The dielectric properties ($\epsilon = 900$), ferroelectric ($E_c = 16 \text{ kV/cm}$ and $P_r = 35 \mu\text{C/cm}^2$) and piezoelectric properties are comparable to bulk values. The characteristic Curie point of these films is at 420 °C. Piezoelectric actuators have been developed by depositing thick PZT films on both planar and coaxial substrates. Stainless steel cantilevers and optical fibres coated with a PZT film exhibit flexure mode resonant vibrations observable with the naked eye. A low frequency in-line fibre optic modulator has been developed using a PZT coated optical fibre. The high frequency resonance of a 60 μm film on an aluminum substrate has been observed.

INTRODUCTION

In recent years, there has been an increased interest in ferroelectric PZT films for piezoelectric device applications. To date, most of the development has centred around silicon micromachined structures. Combining micromachined silicon with ferroelectric films has produced novel microdevices that include membrane sensors¹, accelerometers² and micromotors³. Generally, these devices are based on geometries ranging from μm^2 to 100 μm^2 and film thicknesses of < 1 μm . However, the application of devices based on piezoelectric films is not limited to the realm of microdevices. Many potential applications exist which require film thicknesses of 1 to 30 μm and geometries of μm^2 to cm^2 . Some examples of these macroscopic devices include ultrasonic high frequency transducers which are required for detailed imaging of the eye⁴, fibre optic modulators⁵, where a PZT film coated on the fibre is used to modulate light and for self controlled vibrational damping systems⁶. The film thicknesses and device geometries required for these devices are difficult to achieve using conventional sol gel methods.

Recently, a new sol gel technique has been developed for fabricating thick PZT films on a wide variety of substrates. With this new process, it is now possible to fabricate sol gel films of up to 60 μm in thickness on a wide range of substrates. In this paper, the dielectric, ferroelectric, and piezoelectric properties of these thick PZT films are presented and the development of actuators based on these thick coatings is described.

EXPERIMENTAL

The (52/48) PZT films are fabricated using a new sol gel technique developed at Queen's university. The films were fired at 400 °C between each layer and a final anneal of 650 °C for 30 minutes was used to crystallize the material. An SEM cross section of a 13 μm film on

Pt coated silicon is given in figure 1. Capacitors for studying the dielectric and ferroelectric properties were made by coating a 18 μm film on a Pt-Ti-SiO₂-Si substrate and evaporating a top aluminum electrode. The dielectric data was measured using an HP impedance bridge. The ferroelectric hysteresis loop of the film was observed using a standard oscilloscope and the piezoelectric data was measured from 3 samples:

- 1) A 60 μm film deposited on a 3 mm thick aluminum disk
- 2) A 50 μm unsupported membrane
- 3) A 9 μm film deposited on stainless steel cantilever

All samples were coated with an aluminum top electrode and the devices were poled at 100 kV/cm at 170 °C. Samples 2 was used to determine the d_{33} coefficient, sample 3 was used to calculate d_{31} and sample 1 was used to demonstrate high frequency resonance.

Electrical Measurements

The electrical properties of the PZT films and bulk ceramic PZT are listed in Table 1.

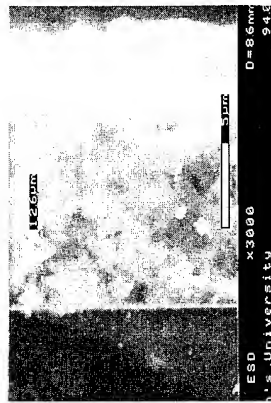


Figure 1. SEM cross section of 18 μm PZT film on Pt-Si

Table 1: Electrical Properties of a 18 μm PZT film on Pt-Ti-SiO₂-Si

PZT	ϵ	Curie Temp (°C)	E_c (kV/cm)	P_r ($\mu\text{C}/\text{cm}^2$)	d_{33} (N/C)	d_{31} (N/C)
Film	900	420	20	35	250	-80
Bulk	700-2000	300-400	18	40	300	-88

The Dielectric Constant

The temperature dependence of an 18 μm PZT film on platinum coated silicon is plotted as a function of frequency in figure 2. At room temperature the capacitance corresponds to a dielectric constant of 900 and this value increases as a function of temperature. A sharp peak indicative of the Curie temperature is observed at 420 °C.

Ferroelectric Properties

The hysteresis loop of an 18 μm film on Pt-Si is shown in figure 3. The remnant polarization ($P_r = 35 \mu\text{C}/\text{cm}^2$) and coercive field ($E_c = 20 \text{ kV}/\text{cm}$), listed in table 1, are comparable to the bulk values.

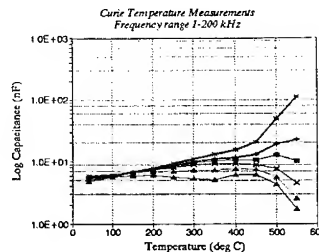


Figure 2. Temperature dependence of the capacitance (or dielectric constant)

Piezoelectric Properties

The piezoelectric strain coefficients of thick PZT films were determined from vibrational analysis of thick film device structures. The relevant equations for determining the piezoelectric properties of a thin film are determined in the following manner.

d₃₃ Evaluation. The d₃₃ coefficient is determined using the converse piezoelectric effect by measuring the displacement produced by an applied electric field using an interferometer. The coefficient was determined from the vibration of a 50 micron film mounted as an unsupported membrane.

$$\delta z = d_{33} \times V \quad (1)$$

The frequency of vibration was set at a high enough value so that the flexure modes of this device were clamped.

d₃₁ evaluation. The d₃₁ coefficient for a piezoelectric film can be evaluated by analyzing the motion of a piezoelectric cantilever. For this work the cantilever was made by coating a 3 x 0.5 cm stainless steel strip with a 10 μm PZT film. The d₃₁ coefficient was determined from the equation ⁷:

$$\delta z = Z(k, R) \times d_{31} \times V \times \frac{L^2}{t_f} \quad (2)$$

Z(k, R) is a response function which depends on k and R, L is the length of the cantilever and t_f is the film thickness.

4 Device Fabrication

High Frequency Ultrasonic Transducers

There is interest in high frequency ultrasonic transducers in the frequency range of 50-200 MHz for medical imaging of detailed structures like the eye. Higher resolution is achieved at high frequencies at the expense of attenuation of the signal. The PZT thickness required is determined from the equation ⁸:

$$f_{res} = \frac{c}{2 \times t_{pz}} \quad (3)$$

where c is the speed of sound in PZT and f is the frequency. The frequency range 50-200 MHz corresponds to PZT thicknesses of 5-50 μm. It is difficult to achieve these thickness by lapping bulk ceramics and until now it has been difficult to fabricate films of these thicknesses. Thin film transducers are fabricated by spin coating multiple layers of PZT, heating each layer at 400 °C followed by a subsequent anneal at 650 °C. The impedance of a 60 μm PZT deposited on



Figure 3. Hysteresis Loop Of 18 μm PZT film on Pt-Si (Grid Scale: X - 12 V/div, Y - .1 V/div)

aluminum metal by spin coating multiple layers is shown in figure 4. The sharp peak in the dissipation and the drop in the capacitance characteristic of a piezoelectric resonance is observed at 40 MHz.

In-Line Fibre Optic Modulator

Phase modulators are necessary components in fibre optic sensors that are based on interferometry. The interferometers detect phase shifts between the reference arm and the sensor arm. An optical modulator can be incorporated into this arrangement to maintain operation in the region of maximum sensitivity⁵. The current technique involves wrapping an optical fibre around a bulk PZT cylinder, fig 5 so that the fibre expands when the cylinder is actuated. Changes in length of the fibre will change the relative phase of light waves in each arm of the interferometer.

A simpler, more compact system would be to coat a piezoelectric material onto the fibre. A voltage applied across the film will produce both radial and axial strain in the fibre. The axial strain will change the length of the fibre and the radial strain will change the index of refraction⁹. Both these effects will produce phase modulation. Several authors have reported the application of PVDF⁹ and zinc oxide¹⁰ coatings to optical fibres as mechanisms for modulation. However, PVDF has a relatively low piezoelectric constant which can not induce adequate strains into the fibre and zinc oxide, a more suitable material, can only be deposited by physical sputtering. Sol gel on the other hand is a simple process which does not require expensive equipment and PZT has the highest reported piezoelectric coefficients.

A modulator was developed by coating a 25 μm PZT film on the centre section of an aluminum coated fibre, figure 6. A coating in the middle of the fibre, facilitated its integration into a Mach Zender interferometer for testing. Low frequency modulation as high as 1.2 radians was observed when a 10 volt a.c signal was applied.

CONCLUSIONS

A novel sol gel process has made it possible to fabricate thick PZT films on a variety of substrates. Films ranging from 5 μm to 60 μm have been fabricated thus far by spin and dip coating multiple layers. The electrical properties are comparable with ceramic PZT. Actuator devices based on both d_{33} and d_{31} operation have been developed using both planar and coaxial geometries. This new technological development opens the door to many new applications which are difficult to achieve using conventional sol gel.

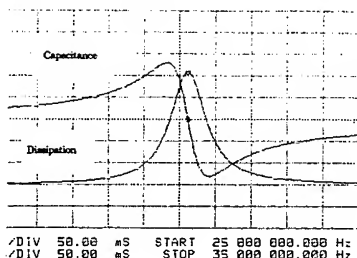


Figure 4. High frequency resonance of 60 μm PZT film on Al metal

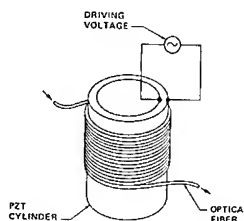


Figure 5. Optical Modulator by wrapping optical fibre around PZT ring

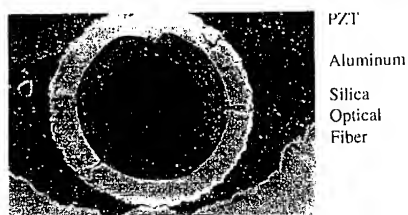


Figure 6. 25 μm PZT film coated onto an Al coated optical fibre.

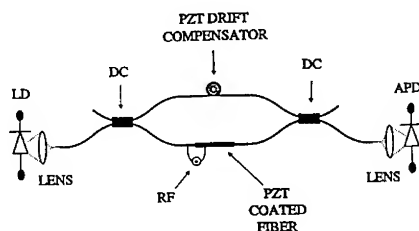


Figure 7. PZT coated fibre integrated into a Mach Zender interferometer.

ACKNOWLEDGEMENTS

The authors would like to thank Dr. C.K. Jen and O. Lisboa of the Industrial Materials Research Institute arm of NRC, Dr. E. Prasad of B.M. Hi-Tech, Dr. R.P. Tandon of Indian Industrial Research Institute, S. Sherritt of RMC, D. Schindel, Queen's University and Dr. C.V.R. Chivakula of Northern Telecom for their help with measurements and fruitful discussions. This research was funded by the Ontario Centre for Materials Research.

REFERENCES

1. D.L. Polla. (1992) Ferroelectric Microsensors and Microactuators, in Proc. 8th IEEE Int. Symp. Appl. Ferroelect., IEEE, Piscataway.
2. K.R. Udayakumayer, J. Chen, K.G. Brooks, L.E. Cross, A.M. Flynn, and D.J. Erlich, (1991), Piezoelectric Thin Film Ultrasonic Micromotors, Mat. Res. Soc. Symp. Proc.. **243**, 49-54.
3. H. van Lintel, F. van der Pohl and S. Boustra, (1988), Sensors and Actuators, **15**, 153.
4. C.J. Pavlin, K. Harasiewicz, M.D. Sherar and S. Foster, (1991) Clinical use of Ultrasound Biomicroscopy', Opthamology, **98**, 3, 287.
5. A. Dandridge, (1991) Fibre Optic Sensors Based on the Mach-Zender and Michelson Interferometers, in Fibre Optic Sensors, Ed. E Udd, John Wiley & Sons.
6. J.W. Laangelaan, (1992), Active Damping of Spacecraft Structures using a Piezoelectric Thin Film, 4th year Eng. Phys. Thesis, Queen's University.
7. M.R. Steel, F. Harrison, and P.G. Harper, (1978), The Piezoelectric Bimorph: An Experimental and Theoretical Study of its Quasistatic Response, J. Appl. Phys. **11**, 979-989.

8. B. Jaffe, W.R. Cooke, and H. Jaffe, (1971) *Piezoelectric Ceramics*, Academic Press, New York.
9. E.F. Carome and K.P. Koo, (1980), PVF_2 Phase Shifters and Modulators for Fibre Optic Sensor Systems, *Proc. IEEE Ultrason. Symp.*, 710-712.
10. D.S. Czaplak, J.F. Weller, L. Goldberg, F.S. Hickernell, H.D. Knuth and S.R. Young, (1987) AO Phase Modulator for Single Mode Fibres using Cylindrical Zinc Oxide Transducers, *Proc. IEEE Ultrason. Symp.*, 491.

ON THE USE OF ELECTROSTRICTIVE ACTUATORS IN RECOVERING THE OPTICAL PERFORMANCE OF THE HUBBLE SPACE TELESCOPE

JAMES L. FANSON

Jet Propulsion Laboratory, California Institute of Technology, 4800 Oak Grove
Drive, Pasadena, CA 91109

ABSTRACT

This paper describes the development of a space qualified active mirror—the Articulating Fold Mirror—which forms part of the scheme for recovering the optical performance of the Hubble Space Telescope. Three Articulating Fold Mirrors are incorporated into the optical train of the Jet Propulsion Laboratory's Wide Field and Planetary Camera-2, which was installed into Hubble by astronauts in December, 1993. Each Articulating Fold Mirror utilizes six electrostrictive ceramic multilayer actuators to precisely position a mirror in tip and tilt in order to correct the spherical aberration of the Hubble Space Telescope's primary mirror. Flight qualification aspects of the electrostrictive actuators are described. Pre- and post-repair images from the Wide Field and Planetary Camera, showing the effect of the optical correction, are presented.

INTRODUCTION

Occasionally we encounter design situations where compact, precision actuation mechanisms are needed. This occurred recently during the development of the Wide Field and Planetary Camera-2 (WFPC2) for the Hubble Space Telescope (HST). The Wide Field and Planetary Camera was developed by the Jet Propulsion Laboratory (JPL) as the primary science instrument aboard the Hubble Space Telescope; nearly all of the images from HST are obtained using this camera (see Figure 1). The first generation Wide Field and Planetary Camera (WFPC1) was launched with Hubble in April of 1990. Shortly thereafter, images from WFPC1 revealed a serious defect in the HST optics—the celebrated *spherical aberration* of the telescope's primary mirror.

It was soon widely recognized that the spherical aberration flaw in the HST primary mirror could, in principle, be corrected by making a minor alteration to the optical design of the Wide Field and Planetary Camera-2, a flight spare camera (essentially a copy of WFPC1) that was nearing completion at JPL. NASA directed JPL to make the necessary changes to WFPC2, and to accelerate the development schedule such that the new camera would be completed in time to be installed into HST during the first servicing mission, planned for late 1993.

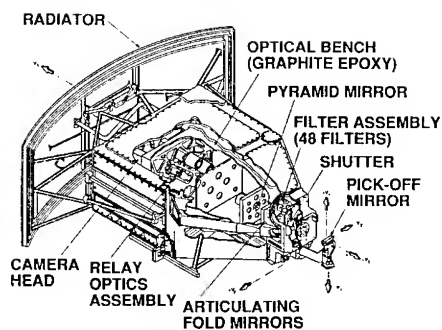


Figure 1. The Wide Field and Planetary Camera-2. About the size of a baby grand piano, this instrument was installed into Hubble by astronauts in December, 1993, and is designed to correct the spherical aberration of the telescope's primary mirror.

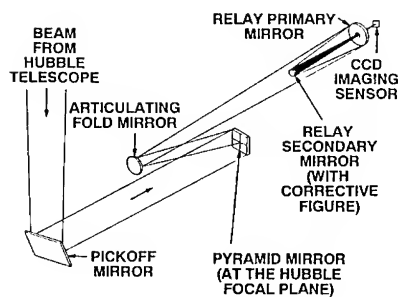


Figure 2. Optical Train. The pyramid mirror splits the incoming beam into four optical trains, each of which contains a fold mirror and a corrector mirror (about the size of a dime) where the spherical aberration is "canceled."

Three steps needed to be successfully accomplished in order to correct the spherical aberration of HST: First, the amount of aberration in the primary mirror (its optical prescription) needed to be accurately and unambiguously quantified—not a trivial feat given that the telescope was in orbit 600 km above the earth. The interested reader is referred to Vaughan [1] for an entertaining account of how the optical diagnosis was made. Second, corrector mirrors needed to be manufactured with a surface shape that precisely matched the shape of the error on the HST primary mirror, but having the opposite sign. This turned out to be within the manufacturing state of the art for at least one optics house in the United States—Tinsley Laboratories, Inc. Third, the telescope exit pupil (the image of the HST primary mirror) needed to be precisely centered on the corrector mirrors to within 0.5% of the diameter of the pupil. If the pupil image were not centered to this accuracy, comatic aberration would result, rendering the optical correction ineffective. This turned out to be the most troublesome step. Alignment of the HST pupil with the four corrector mirrors in WFPC2 requires optical alignment accuracy and stability approximately ten times more stringent than for WFPC1—well beyond the original design specifications for the instrument.

After much analysis and some testing, it was determined that in order to guarantee that all four optical trains (necessary to form a complete image) in WFPC2 would be in proper alignment, three of these trains would need to have their hard-mounted fold mirrors replaced with articulating mirrors that could be adjusted in tip and tilt angle in response to commands from the ground (one optical train is aligned using the pickoff mirror mechanism). The amount of adjustment required to achieve proper alignment would be determined from analysis of star images returned from WFPC2 following installation into HST. The optical layout of WFPC2, showing the location of the fold and corrector mirrors is shown as Figure 2.

The Articulating Fold Mirrors (AFMs) are thus the result of a need to ensure proper optical alignment between WFPC2's corrector mirrors and the Hubble Space Telescope, so as to ensure that the spherical aberration of the telescope is effectively "canceled" in the new camera. The AFMs were required to retrofit into the same locations vacated by the hard-mounted fold mirrors. Figure 3 illustrates the challenge: the AFMs needed to mount into existing apertures in an Invar bulkhead of the optical bench—a volume too small for conventional actuators or mechanisms. Clearly, a very compact design was needed. Figure 4 shows a nearly completed Articulated Fold Mirror assembly (the mirror has not yet been coated).

The remainder of this paper presents the performance requirements for the AFM subsystem, outlines key features of the design and operation of the AFM, and discusses the spaceflight qualification testing of the electrostrictive actuators. Finally, images from the repaired Hubble Space Telescope are presented to illustrate the improvement in performance achieved by correcting the spherical aberration of the telescope.

FUNCTIONAL REQUIREMENTS

Misalignment between the Hubble Space Telescope (HST) exit pupil and the corrector mirror in the Wide Field and Planetary Camera (WFPC2) is called "pupil shear," and is expressed as a percentage of the diameter of the pupil. Failure to center the pupil image on the corrector mirror results in over-correction on one side of the pupil and under-correction on the other side—a situation that produces coma in the point spread function of the image, as illustrated in Figure 5. The point spread function is the image formed at the focal plane of a point-like object (a star).

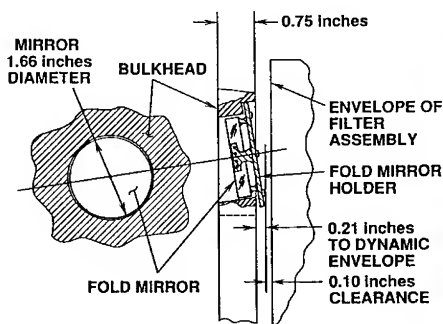


Figure 3. Fold Mirror Mounting Interface. This figure shows the hard-mounted fold mirror installed in the optical bench bulkhead. The Articulating Fold Mirrors were required to fit into the same volume.

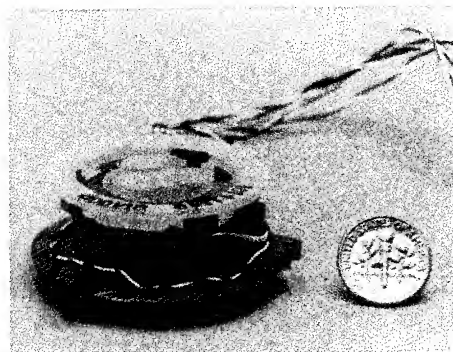


Figure 4. Articulating Fold Mirror (AFM). The AFM is less than 0.9 inches thick from front-to-back, including the mirror (shown here prior to a reflective coating being applied to the glass).

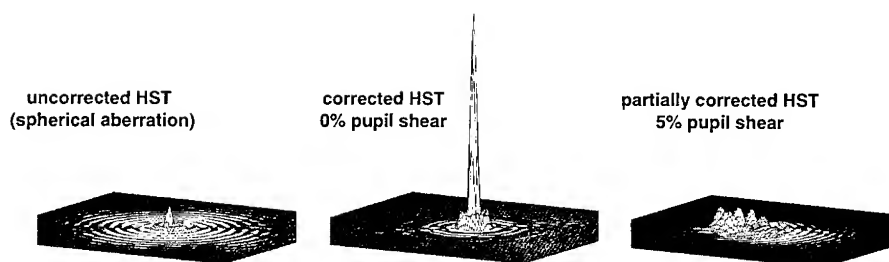


Figure 5. The Effect of Pupil Shear on Optical Performance. Various point spread functions are plotted to illustrate the effect of pupil shear on image quality. Notice that 5% pupil shear is actually worse than the original spherical aberration. The AFM was designed to correct as much as $\pm 6\%$ pupil shear.

Correcting HST requires pupil shear to be less than 0.44%, which corresponds to 51 microns of lateral misalignment at the corrector mirror, in each of the four optical trains of WFPC2 [2]. To gain a feel for this level of stability, 0.006 degrees of tilt misalignment of the fold mirror produces 0.5% pupil shear.

Reliance on mechanisms to achieve performance was considered a risk. Therefore, the WFPC2 optical alignment strategy called for a precise ground alignment of the instrument that would remain as passively stable as possible. The passive stability requirement had the added practical benefit of making it possible to continuously verify the alignment of the instrument throughout its many system level tests—an important confidence building measure. This strategy meant, however, that the Articulating Fold Mirror (AFM) must return to a fiducial “ground aligned” position every time power is removed. Returning to a ground aligned position also offered a “fail safe” contingency in the event of a power or commanding failure to the AFM subsystem.

The functional requirements for the AFM subsystem are listed in Table I. Operational alignment stability is broken into short term (3000 sec), and long term stability. Short term stability is driven by a requirement that the image remain stable on the focal plane detector to ± 0.1 pixel during an exposure; long term stability is based on the error budget associated with pupil shear correction.

The AFM, like all other components in WFPC2, was required to be clean with respect to outgassing of condensable volatile contamination. This is because WFPC2 achieves far-ultraviolet (120 nm) imaging using charge coupled devices (CCDs) that are cooled to -85°C while the remainder of the instrument is maintained near $+10^{\circ}\text{C}$. The CCDs are thus cold traps for any contamination in the instrument. A few monolayers of organic contamination on any of the optical surfaces or on the CCDs will absorb far-ultraviolet photons, compromising the performance of the camera.

Table I. Articulating Fold Mirror Functional Requirements

<i>Optical:</i>	Scratch/Dig	20-5 per MIL-O-13830
	Surface (f/12.9 channel)	flat
	Surface (f/28.3 channel)	convex; radius = 231.2 inch ± 1 inch
	Surface Deviation (at 633 nm)	$\leq \lambda/100$ rms
	Surface Roughness	≤ 3 nm rms
	Reflectance at 122 nm	$\geq 78\%$
	Reflectance at 254 nm	$\geq 86\%$
<i>Mechanical:</i>	tip/tilt range	± 206 arcseconds (± 1 mrad)
	short term (3000 sec) stability	± 0.86 arcseconds
	long term stability	± 13.6 arcseconds
	ground-to-orbit passive stability	± 10 arcseconds
	repeatability	± 2 arcseconds
	failsafe	return to home position ± 2 arcseconds
<i>Thermal:</i>	operating temperature range	+10C to +14C
	survival temperature range	-15C to +40C
	heat dissipation	"none" (no distortion of optical bench)
<i>Contamination:</i>	outgassing rate	≤ 1 ngram/cm ² per hour as detected by a quartz crystal microbalance at -70C with the AFM at +20C

DESIGN APPROACH

Simply put, the challenge was to develop a compact Articulating Fold Mirror (AFM) that would meet the performance requirements in Table I, survive the launch environment, and be ready for integration into the WFPC2 optical bench within 10 months. It was not immediately obvious that a solution to this need could be found. We concluded rather quickly that conventional actuation approaches, such as stepper motors and gears, were not feasible due to the lack of available packaging volume; solid state actuation appeared to hold the greatest promise.

The Prime Mover

Three alternative solid state prime movers were evaluated—magnetostrictive alloy, piezoelectric ceramic, and electrostrictive ceramic. Magnetostrictors and piezoelectrics were rejected because of their hysteresis and tendency to drift, which would have required the additional complexity of proximity feedback sensors in the assembly in order to meet the stability and repeatability requirements. The remnant polarization behavior of these materials would also have meant that the return-to-ground-aligned ("failsafe") requirement could not be met. Electrostrictive ceramic materials were known to have low hysteresis and remnant offset at room temperature, but there behavior over the AFM operating temperature range was not known. We therefore began by testing available lead-magnesium-niobate (PMN) actuators over the temperature range of interest—and encountered a few surprises!

Figure 6 shows a PMN actuator manufactured by Litton/Itek Optical Systems of the type that was tested (and later used for the flight AFMs). Figure 7 shows the data from these early tests. Our first discovery was that the PMN material produced more strain per volt as the temperature was reduced, by an amount of about 3% per degree-C over the temperature range of interest. Our second discovery was that the material exhibits a growing amount hysteresis as the temperature is lowered. Both of these phenomena are undesirable from the standpoint of meeting the alignment stability and repeatability requirements.

But, we made a third discovery which ultimately enabled us to proceed with confidence in the AFM design. Both the temperature dependent gain change and the hysteresis are the result of an electric field induced piezoelectric phase that develops in the bulk material at temperatures below the Curie temperature (room temperature for the PMN formulation used in the Itek actuators). Since the piezoelectric phase is field-induced, it breaks up when the field is returned to zero, with the result that the material returns to a fiducial strain. This means that the length of the actuators (and the position of the AFM) can be "reset" to a known position simply by returning the voltages to zero.

The AFM is therefore capable of precision (stable and repeatable) open loop performance provided that the temperature of the actuators is controlled, and changes in actuator voltage are implemented by first reducing the voltage to zero (to reset the actuators) and then increasing the voltage monotonically to the new value. We control the temperature of the actuators by maintaining the temperature of the entire optical bench to within $\pm 1^\circ\text{C}$, and make all AFM position adjustments by first "resetting" the actuators.

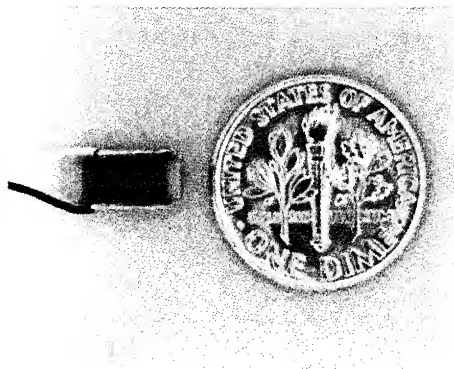


Figure 6. Electrostrictive Ceramic (PMN) Actuator. This type of actuator was tested over the AFM operational temperature range to produce the data shown in Figure 7, and was eventually used in the flight AFMs.

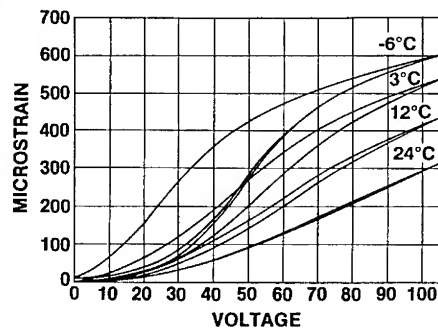


Figure 7. PMN Actuator Performance. The PMN actuator strain vs. voltage was measured as a function of temperature. Voltages were ramped up from zero to maximum, and then returned to zero in three 1-second period cycles.

Articulating Fold Mirror Design

Figure 8 shows an exploded view of the Articulating Fold Mirror assembly. Each device utilizes six of the actuators depicted in Figure 6, arranged in three sets of two, bonded end-to-end. Since electrostrictive ceramic is unpoled and can therefore only expand in response to applied electric field, plus and minus tip and tilt of the mirror is achieved by placing the mirror in a bezel that is in turn supported on a kind of three-legged stool, the lengths of whose legs are adjustable by variously applied voltages. For more detail on the design and fabrication of the AFM, the interested reader is referred to Fanson and Ealey [3] and Fanson and Trauger [4].

The tilting of the mirror is accomplished as follows: A PMN actuator is energized electrically, causing the length of the actuator to increase. The actuator reacts against the cover, pushing the surrounding six sided hollow "canister" (at the tip of the arrow labeled "tilt mechanism") forward. As the canister moves forward, it pushes the attached pin flexure forward, which in turn pushes the bezel forward at its point of attachment. The remaining two pin flexures resist the forward push, resulting in an overturning moment on the bezel. The bezel tilts accordingly (the pin flexures bend in the process) carrying the mirror with it.

Each of the PMN actuators consists of 39 active wafers of 178 microns thickness. To ensure that microcracking would not weaken the actuator structurally, we selected a maximum operating strain of 300 microstrain, corresponding to approximately 2.1 microns of stretch per actuator. This amount of stretching is equal to the length human hair grows in about 10 minutes. Four microns of total stretch per leg is then converted to approximately 250 arcseconds of tilt by the mechanism previously described.

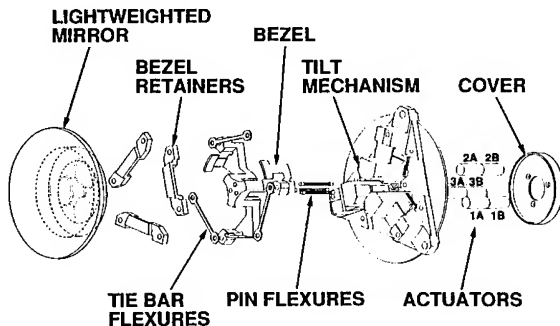


Figure 8. Articulating Fold Mirror (AFM). The AFM utilizes six PMN actuators, each individually controllable. The total stroke of each actuator is approximately 2 microns, giving each two-actuator "leg" an adjustable length up to approximately 4 microns.

FLIGHT QUALIFICATION OF THE ELECTROSTRICTIVE ACTUATORS

Electrostrictive actuators had never been used in a space application prior to the Articulating Fold Mirror (AFM) development. No data were available regarding the radiation tolerance of the material. Little data existed regarding structural strength at other than room temperature. And as previously mentioned, strain performance at reduced temperature was not well known, and the actuators had never been operated in a vacuum.

Mechanical strength and radiation tolerance were two significant factors that needed to be investigated in order to gain confidence that on-orbit performance would be as expected. The following summarizes test results in these two areas.

Actuator Mechanical Strength

Normally, mechanism designs provide for a compressive preload on ceramic components to prevent tension from being applied to the brittle material. This was impractical with the AFM because of the lack of packaging volume. Consequently, the electrostrictive ceramic actuators in the AFM are subject to tensile stress, primarily due to launch vibration. The manufacturer of the actuators, Litton/Itek Optical Systems, typically utilizes its actuators in deformable mirrors where tension capability is also required. They have established an allowable stress for these actuators of 6.9 MPa. We elected to derate this value to 3.4 MPa for the AFM application.

A test program was undertaken at JPL with the goal of establishing actuator strength statistics over a broad temperature range. The first part of this investigation performed tensile tests on a number of actuators that were adhesively bonded to Invar pull tabs by the same process that was followed for the AFM flight actuators. Itek had determined that actuation strain in excess of 500 microstrain weakens the tensile strength of the actuator. The AFM allowable strain was therefore set at the derated value of 300 microstrain prior to launch, and 450 microstrain post-launch. The actuators tested at JPL were previously cycled at Itek to 300 microstrain.

Figure 9 plots the ultimate strength for 15 actuators tested to failure over a temperature range of -40C to +100C. Most of the actuators were not tested to destruction, but were rather taken to various stress levels over a range of temperatures to establish minimum strength values for design. If only actual failures are considered, the mean failure stress is 23.9 MPa with a standard deviation of 5.2 MPa. If all failures and nonfailures are considered, the mean demonstrated stress is 21.6 MPa with a standard deviation of 3.7 MPa. If only actual failures at 20C are considered, the mean failure stress at 20C is 20.8 MPa with a standard deviation of 4.2 MPa. If all values at 20C are considered, the mean demonstrated stress at 20C is 20.8 MPa with a standard deviation of 3.6 MPa. The most conservative of four different mean-less-three standard deviation measures of

strength is 8.2 MPa, and this is therefore the value we used for actuator strength over a temperature range from -40C to +100C.

A single actuator was tested at 20C and 18.2 MPa for 21.75 hours, followed by failure at 23.0 MPa. This indicates that there was no extreme sensitivity to long duration loading, but such loading in brittle materials is very sensitive to initial imperfections, and the single test sample may not have been representative.

Failure in the actuators took place both in the parent ceramic material and at the interface of the ceramic and the platinum electrodes. No failures were observed at the bond between the actuator and the Invar end caps.

Proton Radiation Effects

The effect of radiation exposure on strain performance of the actuators was tested by Itek personnel, using the Harvard University cyclotron. An engineering model AFM was mounted to an optical tooling plate adjacent to a fixed reference mirror. Both mirrors were viewed by a Zygo Mark III interferometer, which could measure the tilt positions of both mirrors relative to each other to a resolution of 1 arcsecond. The AFM was commanded into position by energizing one set of actuators. The applied voltage was maintained constant during the radiation exposure, and the position of the mirror relative to the fixed reference mirror was monitored throughout the test for changes. The assembly was first subjected to 8.7 krad of energetic protons at a rate of approximately 5.8 krad/hour. After this test, the AFM was returned to its home position and articulated through a standard set of motions for comparison with pretest values.

After the first exposure, the AFM was returned to its actuated orientation and the assembly was subjected to an additional exposure of 87 krad at a rate of approximately 14.5 krad/hour. The functional test was repeated after the second test. No shift in position of the AFM was observed during either test to the resolution of the measurement, indicating that the electrostrictive actuation strain is not affected by proton radiation exposure to these levels. The functional tests performed after the exposures indicated no change in functional performance.

ON-ORBIT EXPERIENCE

The flight Articulating Fold Mirrors (AFMs) were delivered on budget and on schedule for integration into the Wide Field and Planetary Camera-2 (WFPC2) in June, 1992. Figure 10 shows a flight-ready AFM, complete with wire bundle and electrical connector.

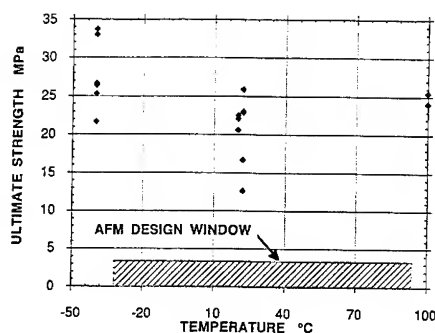


Figure 9. Actuator Tensile Test Data.

This figure plots the ultimate strength of PMN actuators tested to destruction. The test program produced a conservative estimate of actuator strength of 8.2 MPa.



Figure 10. Completed AFM
Three AFMs were successfully integrated into WFPC2 in June, 1992.

Optical Alignment

Shortly after WFPC2 was installed into the Hubble Space Telescope (HST) by astronauts in early December, 1993, the three AFMs were commanded to the positions believed to represent the best alignment based on pre-launch tests of the camera using an optical simulator of the HST. The first images returned from WFPC2 showed that the camera was very nearly in proper focus and pupil alignment—the camera had in fact been aligned on the ground with great skill, and the passive alignment had remained nearly intact. Visual inspection of star images produced a set of updated AFM positions which were uplinked to HST on December 28th. The AFM positions were further refined after through-focus measurements of the residual wavefront error were performed in February, 1994. Table II lists the AFM actuator voltages uplinked to HST on March 6th, and represent the current positions of the AFMs. As can be seen, the maximum correction being affected is 1.1% pupil shear, approximately one sixth the total range of the AFM. After nearly one year in orbit, the WFPC2 and AFMs continue to perform nominally.

Table II. AFM Voltages Uplinked to HST on March 6, 1994.

Optical Train	Actuator Voltages			Pupil Shear
	1A&B	2A&B	3A&B	
PC1	18.8	0.0	16.5	0.39%
WFC3	27.0	0.0	32.4	1.13%
WFC4	0.0	9.7	0.14	0.14%

Imaging Results

Figure 11 compares three images of the same star field taken by a ground based telescope (with resolution limited by the earth's atmosphere), by WFPC1 before the correction of the spherical aberration, and by WFPC2 after spherical aberration had been corrected. Hubble's improved spatial resolution over ground based telescopes is clearly evident in these images. More interesting is the comparison of the two HST images taken before and after the optical fix. The aberrated image clearly shows the large skirt of light surrounding the central core of the star image caused by the spherical aberration. The image taken after the correction shows a normal diffraction pattern, and since the light is now properly focused, much fainter stars are visible.

Similarly, Figure 12 shows before and after images of the core of M100, a spiral galaxy in the Virgo cluster. Both contrast and limiting magnitude are greatly improved, restoring Hubble to its originally specified performance.

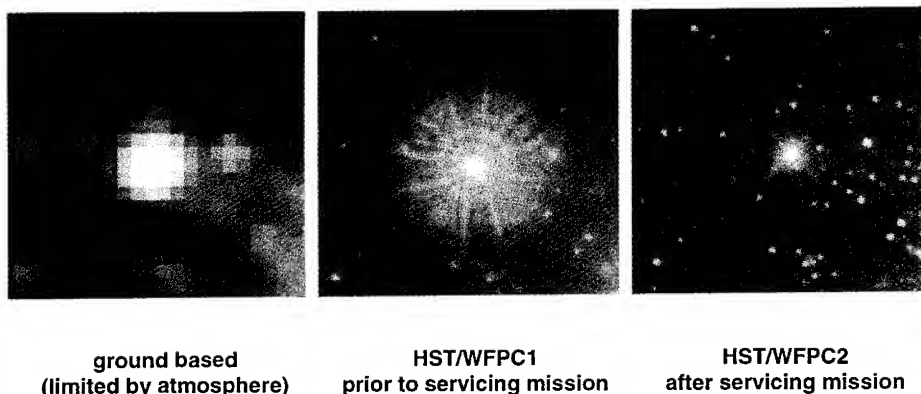
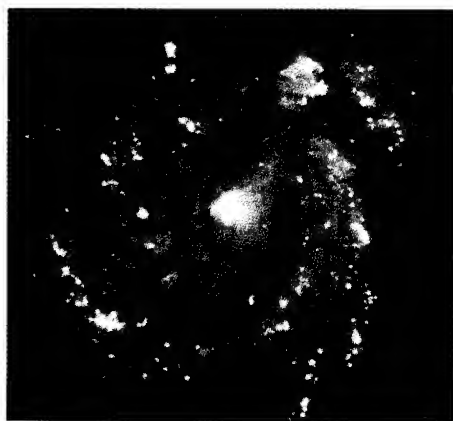


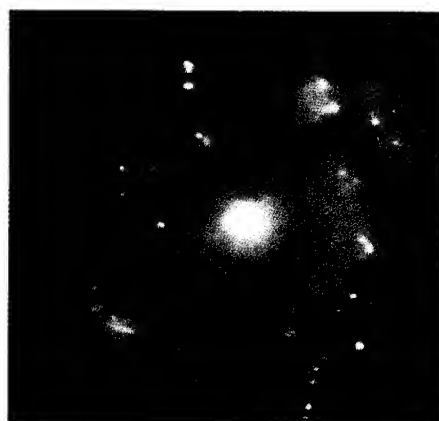
Figure 11. Imaging Comparison. These three images are of the same portion of a star cluster located in the 30 Doradus Nebula, a giant star-forming region within the Large Magellanic Cloud. The image at left is the best available ground-based image taken under optimum atmospheric conditions. The center image is from WFPC1, taken prior to the HST servicing mission. The image at right is from WFPC2 after the spherical aberration had been corrected. Note that many more stars are visible in this image because the light is being properly focused to a sharp, bright core.

ACKNOWLEDGMENTS

The author wishes to express his appreciation to the many individuals at JPL and Litton/Itek Optical Systems who contributed to the successful development of the Articulating Fold Mirror for WFPC2. In particular, Mr. Mark Ealey of Itek worked tirelessly to successfully complete the AFM on schedule and on budget, Mr.



HST/WFPC2
after servicing mission



HST/WFPC1
prior to servicing mission

Figure 12. M100 Galaxy Comparison. These two images are of the core of the spiral galaxy M100 in the Virgo cluster. Correction of the spherical aberration improves image contrast on extended objects such as the gas and dust lanes in the spiral arms, and permits fainter features to be seen. Studies of Cepheid variable stars (previously undetectable at the distance of the Virgo cluster) will determine the Hubble constant, and thus reveal the true size and age of the universe.

Bob Bamford of JPL lead the design and structural analysis of the AFM, and Dr. Gary Blackwood of JPL performed the early characterization of the PMN actuators at reduced temperature. The work described in this paper was carried out by the Jet Propulsion Laboratory, California Institute of Technology, under contract to NASA.

REFERENCES

1. A. H. Vaughan, J. British Interplanetary Soc. **44**, 487 (1991).
2. J. P. McGuire and R. P. Korechoff, in Quality and Reliability for Optical Systems, SPIE **1993**, San Diego, 1993.
3. J. L. Fanson and M. A. Ealey, in Active and Adaptive Optical Components and Systems II, SPIE **1920**, Albuquerque, 1993.
4. J. L. Fanson and J. T. Trauger, in Optical Alignment, SPIE **1996**, San Diego, 1993.

NEURAL NETWORK PROCESSING OF OPTICAL FIBER SENSOR SIGNALS FOR IMPACT LOCATION

PAUL M. SCHINDLER*, JOHN K. SHAW**, RUSSELL G. MAY*,
AND RICHARD O. CLAUS*

*Fiber and Electro-Optics Research Center, Department of Electrical Engineering, Virginia Tech,
Blacksburg, VA 24061-0111

**Department of Mathematics, Virginia Tech, Blacksburg, VA 24061-0123

ABSTRACT

A system to detect and locate impacts by foreign bodies on a surface was developed and tested. Fiber optic extrinsic Fabry-Perot interferometer (EFPI) strain sensors were attached to or embedded in the surface, so that stress waves emanating from an impact could be detected. By employing an artificial neural network to process the sensor outputs, the impact location could be inferred to centimeter range accuracy directly from the arrival time data. In particular, the network could be trained to determine impact location regardless of material anisotropy. Results demonstrate that a back-propagation network identifies impact location for an anisotropic graphite/bismaleimide plate with the same accuracy as that for an isotropic aluminum plate.

OVERVIEW

An investigation was initiated in the use of neural networks to determine impact location by processing the output of a network of fiber optic strain sensors distributed on a surface. This approach extends the results of Gunther, et al¹ and Sirkis, et al⁴, who showed that impact location by triangulation could be used by comparing the arrival times at several sensors of the acoustic signal generated by the impact. For this study, a commercially available neural network simulator running on a personal computer was used to train a network using a back-propagation algorithm^a. The ability of the network to determine impact location by differential arrival times of acoustic signals was assessed by comparing network outputs with actual experimental results using impacts on a panel instrumented with optical fiber sensors.

THE EFPI FIBER OPTIC SENSOR

Optical fiber strain gages have been implemented using the conventional Extrinsic Fabry-Perot Interferometric (EFPI) sensor system as shown in Figure 1². Here, a 1300 nm single mode silica fiber transmits light from a laser diode to the EFPI sensor element. At the opposite end of the input fiber, the laser light signal is partially reflected and partially transmitted, exiting the fiber (hence, an "extrinsic" sensor design) and traversing the air gap separating the ends of the input fiber and an output fiber used solely as a reflector. This signal and the signal reflected from the facing fiber endface interfere and propagate back through the input fiber. They travel through a fiber coupler to a photodiode detector. The observed intensity at the detector is given by²

$$I_{\text{det}} = A^2 \left(1 + \frac{2 \tan}{a + 2s \tan[\sin^{-1}(NA)]} \cos\left(\frac{4\pi s}{\lambda}\right) + \left\{ \frac{\tan}{a + 2s \tan[\sin^{-1}(NA)]} \right\}^2 \right), \quad (1)$$

^a NeuralWorks Professional II plus™ v5.02, NeuralWare, Pittsburgh, PA 15276.

where A is the amplitude of the first reflection, t is the transmission coefficient of the air-glass interface (≈ 0.98), a is the fiber core radius, s is the length of the air gap, λ is the wavelength of operation in free space, and NA is the numerical aperture of the single-mode fiber, given by $NA = (n_1^2 - n_2^2)^{1/2}$, where n_1 and n_2 are the refractive indices of the core and the cladding, respectively.

For our application, the EFPI sensors were configured in two possible ways, either as shown in Figure 1b, with the reflector fiber “free floating” for use in surface-mounting applications, or as shown in Figure 1c, with the reflector fiber bonded to the hollow core tube as with the input/output fiber, used for applications where the sensor is embedded. The latter configuration was used to keep the composite resin from wicking into the air gap region. With surface mounts, the reflector fiber is bonded to the surface of the specimen to increase the gage length of the sensor, or the distance between the two bond points; this increases the strain sensitivity of the sensor, since strain is given as $\epsilon = \Delta l / l$.

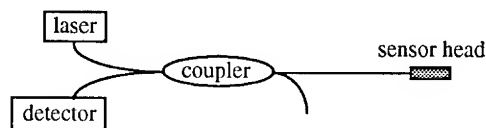


Figure 1a: EFPI support system

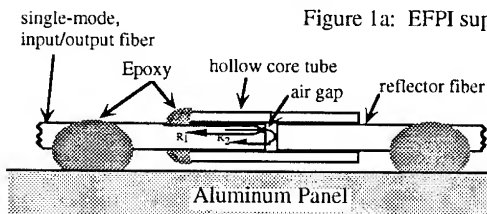


Figure 1b: EFPI sensor, surface mounted

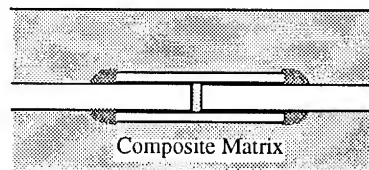


Figure 1c: EFPI sensor, embedded

DEVELOPMENT OF IMPACT DETECTION AND LOCATION SYSTEM USING ADAPTIVE NEURAL NETWORKS

The method we used to detect surface impacts involved analyzing the propagation of acoustic surface waves produced by the impact. Namely, the time-of-flight differences of these waves were examined between several sensor points on the impacted surface. One method of calculating the location of an impact using these time differences is triangulation. Instead, we utilized an adaptive neural network to analyze these time differences and calculate the location of the impact. One inherent advantage in using neural networks is that their performance is independent of a particular system's complexities; the physics of boundary conditions, velocity of surface acoustic waves, sensor contact and mounting, etc. are transparent to the neural network. The success of the neural network is more dependent on the consistency of signal patterns. However, to successfully locate impacts, the neural network must first be trained, to learn a system's particular response.

Overview of neural networks

Neural networks are structured much in the same way the human brain is structured. Unlike a conventional computer which consists of one central processing unit performing a rigid set of instructions on given inputs, a neural network consists of many smaller processing elements (PEs), or neurons, which are all interconnected. The connections between the PEs are made

stronger or weaker as the network is trained, thus affecting the output. Training involves giving the network a series of typical inputs along with the known desired outputs. After processing the inputs once, the neural network calculates the RMS error between the actual output and the desired output. Adjustments are then fed back to the connection weights so as to minimize this error on the next training run; the same input set is then repeatedly used until the weights for each connection have been sufficiently modified to minimize global error. This type of network is called a back propagation network, since information concerning the error flows opposite to the flow of processing information. After the RMS error has been sufficiently minimized through repeated training, the network can be tested. The only difference between training and testing is that the connection weights are not adjusted after each input is processed during testing.

Impact detection and location

To ensure the feasibility of impact location by neural networks, a set of hypothetical impact locations were generated. The impact locations were randomly generated and uniformly distributed across the hypothetical surface. From these, the time-of-flight differences were calculated for each equation by

$$\Delta t_{12} = \frac{\sqrt{(x_1 - x_0)^2 + (y_1 - y_0)^2} - \sqrt{(x_2 - x_0)^2 + (y_2 - y_0)^2}}{v}, \quad (2)$$

where (x_0, y_0) are the Cartesian coordinates of the impact, (x_1, y_1) and (x_2, y_2) are those of the first and second sensor, respectively, and v is the velocity of the surface wave in the material. Here, the assumption was made that the material impacted is acoustically isotropic. Since one of the advantages behind using neural networks is that they scale the input before processing, the value used for v in equation (2) was simply 1. The dimensional values used corresponded to what was to be measured during the actual tests, that is, a 100 cm x 50 cm sheet of aluminum.

These results were then fed into a back propagation neural network, using the Δt 's as input, and the impact coordinates as output. The best results after presenting 1,000 simulated impacts through 50,000 iterations were an average error of 0.462 cm in the x-direction, and 0.220 cm in the y-direction. The difference between the average errors is probably due to the x-dimension being twice that of the y-dimension. From this we concluded that the neural network should work well in detecting actual impacts.

IMPACT TEST RESULTS

Two sets of experiments were performed, first on a 100 cm x 50 cm x 3 mm aluminum panel, then on a 38 cm x 44 cm x 4 mm graphite/bismaleimide composite panel with 12 plies. In the aluminum panel case, EFPI sensors were surface mounted in each of the four corners of the plate. The composite panel was fabricated with a sensor embedded in each corner. One sensor failed to survive the composite panel fabrication process and had to be replaced with a surface mounted EFPI sensor. Overviews of each test are given below, along with the results for each one.

Aluminum panel tests

Three sets of impact data were acquired, the first consisting of 37 impact points, and the second and third consisting of 35 impact points. All data were read using cursor placements on a digital sampling oscilloscope, which was triggered on the first acoustic event detected by any sensor. Impact location could be performed using two different measurement schemes, depending on

where the cursor was placed. In one, the time reference could be taken as the first threshold of an event above the noise floor of the oscilloscope trace; alternatively, the peak sensor output for a given trace could be used. The best results were obtained using the first threshold event, due to sensor quiescent point instability that caused ambiguous output; in some cases, the maximum strain on the sensor did not register as the peak output on the oscilloscope, due to a turn-around point in the sinusoidal sensor output. The first and third sets were acquired using the first-threshold cursor method, and the second using the peak sensor output cursor method.

The values that were read off the oscilloscope were the time differences between sensor 1 and sensors 2,3, and 4 (yielding Δt_{12} , Δt_{13} , and Δt_{14}). The other three time differences, Δt_{23} , Δt_{24} , and Δt_{34} were simply calculated from the other three ($\Delta t_{23} = \Delta t_{13} - \Delta t_{12}$, etc.). These six time differences were the inputs into the back propagation neural network. Although these additional three calculated time differences might seem to be redundant, it was found that the accuracy of the neural network improved when this redundancy was introduced, i.e. when the number of inputs increased from three to six. It was empirically determined that the neural network trained faster when these redundancies were included. The outputs were the x and y coordinates of the impact, also presented to the network during training.

The back propagation neural network that was used consisted of one input layer, with six processing elements (PEs), one hidden layer with three PEs, and one output layer with two PEs. This architecture was developed using³

$$H \approx \frac{T}{5(I + O)} , \quad (5)$$

an empirically derived equation which calculates H, the approximate number of PEs in one hidden layer, from the number of training cases (T), the number of PEs in the input layer (I), and the number of PEs in the output layer (O). It should be noted that using three PEs in the hidden layer for the aluminum panel test gave better results than if the equation was used; this demonstrates that equation (5) is only a guideline, and not an absolute measure of how many hidden layer PEs should be used. Also, a "Save Best" utility on the neural network software package was implemented, which trained the network for one full training set, and then tested the network. The root-mean-square (RMS) error was calculated for each test and compared to the result obtained in the previous test; if there was a reduction in the RMS error, the network weights were saved, and the training/testing process was repeated. The entire process stopped when there was no improvement after 500 successive tests.

The initial approach to training a neural network was to separate a few points from each data set, to be used to test the effectiveness of a trained network. For the first set, thirty points were used to train the neural network, and seven were used to test it after training. Five points were used to test the second and third sets, still using thirty to train. It was later discovered, mostly from trial and error, that a network's success in locating an impact was very much dependent on which points were removed from the data set to be used for testing. This is most likely due to outlying points (points with a high amount of error) within the data set being used to test the network. Therefore, we adopted a method for finding an average impact location error for a given neural network, by training and testing with many different combinations of points. The method used was as follows: (1) The data set was "shuffled" by row, i.e. the order of impact point location was randomized, (2) the last seven (five) points were taken as the testing set, the remaining thirty as the training set, (3) a neural network was trained and tested using these sets, (4) the above three steps were repeated nine more times, resulting in ten impact location neural networks, each with a different impact location error. The average location error for the x and y directions was calculated from the ten sets, along with the standard deviation. This averaging scheme was incorporated to give a better

overall picture of the generic ability of the neural network architecture. The results are summarized for all three tests in Table I.

Table I: Statistical data for averages, in centimeters - aluminum panel

	Test 1, average	Test 1, st. dev.	Test 2, average	Test 2, st. dev.	Test 3, average	Test 3, st. dev.
x	6.2879	0.7385	6.1716	2.8018	5.2314	2.1944
y	5.1961	1.6673	3.8862	1.6100	3.4300	0.9458

As can be seen from this table, the best results were obtained from the third test; this was probably from a higher precision in data measurement, due to experience gained in performing the first two tests. The relatively high error over all three data tests can be attributed to the low number of points (30) used to train the network, since it was empirically determined that using a low number of training samples hinders the performance of back propagation networks.

Composite Panel Tests

A graphite/bismaleimide composite coupon measuring 38 cm x 44 cm x 4 mm was fabricated; the panel consisted of twelve plies, all with the carbon fibers running along the longer dimension. This lay up was chosen to produce a panel with a high degree of anisotropy with respect to the acoustic velocity. The EFPI sensors were embedded close to the surface, between the third and fourth plies, oriented along the diagonals of panel. After processing the panel through the hot press and testing the sensors, one sensor (#4) was found to have failed, and a surface-mounted EFPI sensor took its place.

Only one test was performed on the panel, but many more impact points were taken than in the case of the aluminum panel. The entire set comprised 132 impacts, with 120 being used for training, and twelve for testing. The same method of randomizing the data set that was performed for the aluminum panel was done with this data set. A similar summary is given in Table II.

Table II: Composite panel statistical data for averages, in centimeters

	Average	st. dev.
x	2.1619	0.6211
y	3.1973	0.9744

The results for the composite panel were much better than the aluminum panel tests. The principal reason is believed to be the increased number of impacts used to train the neural network.

An attempt was made to improve the aforementioned results, by eliminating the edge impacts (impacts near the edge of the panel). By inspecting the time differences, we discovered that the values for edge impacts were inconsistent, which presumably created an ill posed data set to the neural network. This inconsistency is illustrated below in Figure 2, where the x and y axes represent the x and y coordinates of the panel, and the z axis represents the time difference between sensor #1 and sensor #4. Theoretically, the mesh plot should be a flat plane, tilted with its highest corner over sensor #1, and its lowest corner over sensor #4. Here, the surface behaves mostly in this fashion, except for the boundary points. This is why the impact location performance was expected to improve when these edge points were removed from the training set. However, after eliminating these boundary points, there was a significant increase in impact location error. This increase in error is most likely attributed to the reduction in the overall number of impact points used to train the network, which was the same problem encountered with the aluminum panel tests.

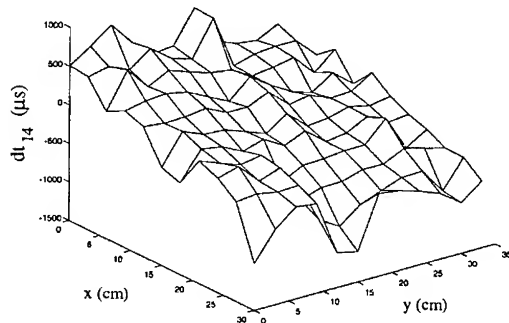


Figure 2: Three dimensional mesh plot of Δt_{14} (sensor #1 at (0,0), sensor #2 at (0,30), sensor #4 at (30,35))

CONCLUSION

We successfully implemented a back propagation neural network to perform impact location on both isotropic and anisotropic materials, by post-processing data from extrinsic Fabry-Perot interferometer (EFPI) sensors functioning as acoustic sensors. Although the magnitude of the error for impact tests performed on the aluminum panel was twice that for the composite panel, the aluminum panel was roughly twice the size of the composite panel; hence, we can conclude that the accuracy was generally the same for both set of tests. The limiting factor in minimizing the impact location error was found to be the inadequate number of impact data points presented to the neural network; the larger the typical data set, the better the neural network will train to the system. Additional human error could also be eliminated by automating data collection. Further studies should be conducted, exploring other factors of impact location, for example, non-planar geometries, boundary affects, different sensor configurations, etc.

ACKNOWLEDGMENTS

The authors gratefully acknowledge Dr. Robert Rogowski and the NASA Langley Research Center for partial sponsorship of this project, under grant NAG-1-1292.

REFERENCES

1. Gunther, M.F., A. Wang, B.R. Fogg, S.E. Starr, K.A. Murphy, and R.O. Claus: "Fiber optic impact detection and location system embedded in a composite material," SPIE, Boston, September 1992.
2. Murphy, K., Gunther, M., Vengsarkar, A., and Claus, R.: "Quadrature phase-shifted, extrinsic Fabry-Perot optical fiber sensors," *Optics Letters*, Vol. 16, No. 4, February 1991.
3. NeuralWare: "Using NeuralWorks," NeuralWorks Professional II/PLUS software package (NeuralWare Inc., Pittsburgh, PA 15276, 1993), p. 20.
4. Sirkis, J.S., K. Shaw, T.A. Berkoff, A.D. Kersey, E.J. Friebele, and R.T. Jones: "Development of an Impact Detection Technique Using Optical Fiber Sensors and Neural Networks," SPIE #2191, pp. 158-165.

DIELECTRIC, PYROELECTRIC, AND THERMAL PROPERTIES OF SOLID SOLUTIONS OF Ba (Ti, Zr)O₃, Ba (Ti, Hf) O₃, Ba (Ti, Sn) O₃ and (Ba, Nd)TiO₃

K. K. DEB

U.S. Army Research Laboratory, Infrared/Optics Technology Office, Fort Belvoir, VA 22060

ABSTRACT

Modified BaTiO₃ ceramics are candidate materials for infrared sensors in night vision equipment. Measurements of dielectric constants, dielectric losses, pyroelectric coefficient, and heat capacities as functions of temperature and frequency are performed. Crystallographic and grain size data are also presented. It is shown that additions of these impurities to BaTiO₃ alters the temperature of phase transformations and, with it, dielectric and pyroelectric properties. The results of these measurements were compared with those of PZT and PbTiO₃ ceramics, which are currently the favored materials for uncooled detector arrays, as well as PbTiO₃ and PZT thin films. It is concluded that these oxide ceramics offer the combination of preparative ease of property modification and show good performance at low impurity concentrations.

INTRODUCTION

The use of pyroelectric materials for infrared (IR) detection and thermal imaging is now well-established technology. There is a continuing growth of interest in the development of newer pyroelectric materials with a high figure of merit for focal plane array applications. To have a high figure of merit, pyroelectric materials must have a Curie temperature close to the operating temperature [1]. While barium titanate (BaTiO₃), lead titanate (PbTiO₃), or lead zirconate titanate (PZT) are the most commonly used pyroelectric materials, there are other promising pyroelectric materials with the perovskite structure.

Barium titanate ceramics are interesting in that they possess the perovskite structure and their physical properties are readily modified by the inclusion of selected dopants into either of the cation sublattices [2]. It is known, for example, that a partial substitution of zirconium or hafnium ions for the titanium ions [3] significantly influences the dielectric and structural characteristics of BaTiO₃. These additions are found to increase the temperature of the orthorhombic-to-tetragonal transition (O-T), while lowering the Curie temperature (T-C).

For the purpose of clarifying which compositions of BaTiO₃ are of interest from the point of view of their applications as IR detectors, we investigated samples of solid solutions of Ba (Ti, Zr) O₃, Ba (Ti, Hf) O₃, Ba (Ti, Sn) O₃ and (Ba, Nd) TiO₃. These materials were prepared in the National Institute of Standards and Technology, Gaithersburg, MD, and provided to us under an R&D contract. This paper describes the physical properties of these BaTiO₃ compositions, with the goal of assessing their potential applications for night vision devices. Published data for undoped BaTiO₃ [4] examined under the same conditions as the present materials are included for comparison.

EXPERIMENTAL PROCEDURE

1. Materials

The materials were prepared following the procedures described in reference [4] and sintered at 1350°C in air for 4–6 hr. The result is a dense cylinder that is cut into thin circular sections that are polished down to a 1-μm finish. The compositions and surface quality were determined by SEM/

EDX analysis. The average grain size of each of the ceramic specimens was determined with the SEM at 5000 \times magnification. After the final calcining, each of these powders was examined with the powder x-ray diffraction to determine phase purity and unit-cell parameter for each composition. A least-squares fit of each set of diffraction data was used to determine unit cell parameters.

2. Property measurements

Circular sample disks were gold electroded before either poling or electrical measurements. Before poling, each specimen was heated for 20 min above the high-temperature ferroelectric transition of the dielectric permeability. Efficient poling was then achieved by a slow cooling of the sample down to -30°C in a clean dielectric oil with an applied dc electric field of 10–12 kV/cm. The dielectric measurements were performed as a function of frequencies, f , using a QuadTec 1689 M LCR meter. The pyroelectric coefficient was determined by using the Byer and Roundy technique. The temperature range for both measurements was -20 to 160°C with a heating rate of $3^{\circ}\text{C}/\text{min}$. The ramp linearity for the pyroelectric measurement was 0.1°C for ramps of $3^{\circ}\text{C}/\text{min}$.

The temperature variation of specific heat (C_p) was determined on a differential scanning calorimeter following the procedures described in reference [4].

RESULTS AND DISCUSSION

1. X-ray diffraction and scanning electron microscopy/EDX analysis

A. Least squares analysis (XRD)

Typical x-ray diffraction patterns taken on a sintered BaTiO_3 ceramic are shown in figure 1. Powder x-ray diffraction results indicate that each sample is a single perovskite. The values of the unit cell parameters ranged from 4.0023 to 4.0527 Å. The crystal structure of pure BaTiO_3 was studied by x-ray diffraction [5]. Its unit cell parameter is lower than for the present ceramics, by as much as 0.9%. The theoretical density of each sample, which is calculated with the pseudo-cubic cell dimensions, is listed along with other characteristic parameters in table 1.

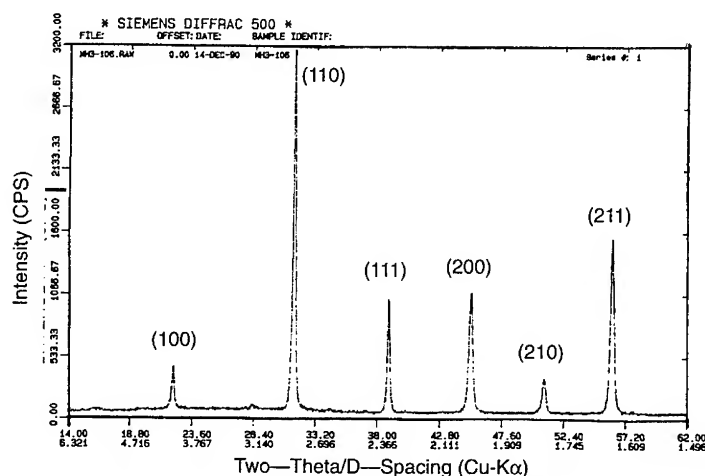


Figure 1. X-ray diffraction patterns for $\text{BaTiO}_3 + 5.7\% \text{BaSnO}_3$.

Table 1. Density, grain size, and specific heat for doped barium titanate ceramics.

Composition	Theoretical ^a ρ (gm/cm ³)	Actual ^b ρ (gm/cm ³)	Average grain size (μ m)	Specific heat (J/gm·°C)
BaTiO ₃ ceramic	ND	5.71	4-5	0.442
BaTiO ₃ + 3.5% BaZrO ₃	6.045	5.888	6-8	0.3201
BaTiO ₃ + 12.6% BaZrO ₃	6.063	5.875	5-7	0.5748
BaTiO ₃ + 13.6% BaZrO ₃	6.065	5.901	ND	0.5218
BaTiO ₃ + 16.5% BaZrO ₃	6.071	5.828	5-7	0.4858
BaTiO ₃ + 19.2% BaZrO ₃	6.072	5.802	3-4	0.4286
BaTiO ₃ + 19.5% BaZrO ₃ ^c	6.077	5.785	4-6	0.4245
BaTiO ₃ + 21.5% BaZrO ₃	6.080	5.762	3-5	0.4614
BaTiO ₃ + 27.8% BaZrO ₃ ^c	6.098	5.767	5-8	0.3498
BaTiO ₃ + 3.8% BaHfO ₃ ^c	6.124	5.885	ND	0.2901
BaTiO ₃ + 11.5% BaHfO ₃ ^c	6.302	5.922	ND	0.3084
BaTiO ₃ + 13.0% BaHfO ₃ ^c	6.331	6.007	ND	0.4144
BaTiO ₃ + 1.2% BaSnO ₃	6.053	5.859	5-7	ND
BaTiO ₃ + 5.7% BaSnO ₃	6.107	5.875	4-6	ND
BaTiO ₃ + 11.2% BaSnO ₃ ^c	6.173	5.729	2-4	ND
BaTiO ₃ + 13.0% BaSnO ₃	6.194	5.891	8-10	ND
BaTiO ₃ + 13.8% BaSnO ₃	6.185	5.882	3-4	ND
BaTiO ₃ + 4.4% Nd ₂ Ti ₂ O ₃	6.051	5.857	4-6	0.6771
BaTiO ₃ + 4.8% Nd ₂ Ti ₂ O ₃	6.053	5.829	3-5	0.4829

^aDetermined from x-ray diffraction analysis

^bDetermined by use of Archimedes principle

^cIndicates solid-state process route

ND: Not determined

B. SEM/ EDX results

Figure 2 shows SEM micrographs of the fracture surface for two typical compositions studied here. The present materials show uniform grains of about 4-6 μ m in diameter. EDX results show that there is no detectable variation in the elemental composition at the micrometer level. EDX-determined compositions are all within 3 wt.% of their intended stoichiometry. For the purpose of this examination, a material with nominal composition Ba(Ti_{0.87}, Zr_{0.13}) O₃ was selected for a reference material.

2. Dielectric properties

Typical variations of dielectric constant (ϵ_r) with temperature and frequency are shown in figure 3 ((a) and (b), respectively). A summary of the dielectric data is presented in table 2. The figure indicates that the dielectric properties of undoped BaTiO₃ are strongly influenced by the presence of Zr ions in the lattice of BaTiO₃. Very similar results are also observed for the substitution of hafnium or tin ions for the Ti ions and the substitution of neodymium ions for the Ba ions. The results in table 2 conclude that a partial substitution of these impurity ions in BaTiO₃ results in a state where the high-temperature ferroelectric transition maximum of the dielectric permeability is displaced in the direction of low temperatures. The peak value of the dielectric constant near the ferroelectric transition temperature is increased with doping concentration with respect to the corresponding peak value for pure BaTiO₃ ceramics. The bulk of these results agree with those reported earlier by either Jaffe et al [3], or by Herbert [6].

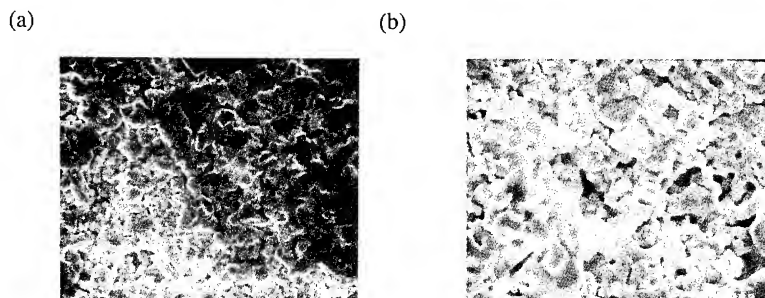


Figure 2. SEM microstructure of (a) $\text{BaTiO}_3 + 3.5\% \text{BaZrO}_3$ and (b) $\text{BaTiO}_3 + 5.7\% \text{BaSnO}_3$.

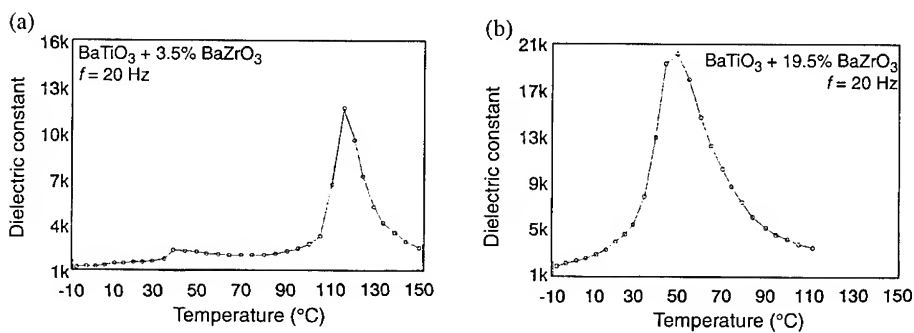


Figure 3. Dielectric constant versus temperature for BaTiO_3 compositions: (a) $\text{BaTiO}_3 + 3.5\% \text{BaZrO}_3$ and (b) $\text{BaTiO}_3 + 19.5\% \text{BaZrO}_3$.

Table 2. Dielectric properties of unpoled barium titanate ceramics.

Sample	Frequency (kHz)	Transition temperature (°C)	Peak ϵ_r $\times 10^3$	Tan δ at transition peak temperature $\times 10^{-3}$	$\Delta\epsilon_r^*$ $\times 10^3$
BaTiO_3	0.02	128.4 (23.7)	6.07 (2.45)	58.6 (49.4)	0.65 (0.27)
	1.00	128.5 (23.8)	5.68 (2.31)	36.2 (28.4)	
	100.00	128.3 (23.8)	5.42 (2.18)	10.0 (16.6)	
BaTiO_3 + 3.5% Zr	0.02	113.4 (43.6)	11.11 (2.61)	63.3 (37.4)	2.06 (0.28)
	1.00	113.5 (43.8)	9.78 (2.43)	46.7 (14.9)	
	100.00	113.6 (43.9)	9.05 (2.33)	22.6 (18.1)	
BaTiO_3 + 12.6% Zr	0.02	73.5	14.36	62.1	2.27
	1.00	73.7	12.89	30.0	
	100.00	73.8	12.09	23.5	
BaTiO_3 + 16.5% Zr	0.02	56.0	10.35	44.2	1.25
	1.00	56.2	9.64	24.3	
	100.00	56.3	9.10	23.0	

Table 2. Dielectric properties of unpoled barium titanate ceramics (cont'd).

Sample	Frequency (kHz)	Transition temperature (°C)	Peak ϵ_r $\times 10^3$	Tan δ at transition peak temperature $\times 10^{-3}$	$\Delta\epsilon_r^*$ $\times 10^3$
BaTiO ₃ + 19.2% Zr	0.02	33.6	31.76	30.0	3.35
	1.00	33.8	29.72	20.5	
	100.00	33.9	28.41	118.0	
BaTiO ₃ + 19.5% Zr	0.02	49.4	20.16	25.3	1.56
	1.00	49.8	19.29	12.9	
	100.00	49.9	18.60	12.0	
BaTiO ₃ + 21.5% Zr	0.02	21.2	11.09	30.2	1.01
	1.00	21.4	10.47	16.6	
	100.00	21.5	10.08	40.8	
BaTiO ₃ + 27.8% Zr	0.02	-21.5	20.60	25.8	2.64
	1.00	-20.7	19.61	23.3	
	100.00	-16.7	17.96	50.1	
BaTiO ₃ + 3.8% Hf	0.02	108.3 (43.5)	8.90 (2.69)	123.6 (34.1)	1.75 (0.28)
	1.00	108.4 (43.7)	7.55 (2.53)	30.0 (17.4)	
	100.00	108.4 (43.8)	7.15 (2.41)	20.6 (21.5)	
BaTiO ₃ + 11.5% Hf	0.02	83.3	10.29	178.0	2.32
	1.00	83.5	8.58	284.0	
	100.00	83.6	7.97	251.0	
BaTiO ₃ + 13.0% Hf	0.02	68.4	10.99	82.0	1.89
	1.00	68.5	9.79	246.5	
	100.00	68.5	9.10	32.8	
BaTiO ₃ + 5.7% Sn	0.02	84.3 (-5.8)	2.09 (1.41)	647 (1050)	1.32 (1.07)
	1.00	84.8 (-5.6)	1.00 (0.42)	298 (376)	
	100.00	84.9 (-5.9)	0.77 (0.34)	229 (127)	
BaTiO ₃ + 11.25% Sn	0.02	43.6	11.12	149.4	2.97
	1.00	43.8	9.12	50.5	
	100.00	3.9	8.15	37.8	
BaTiO ₃ + 13.0% Sn	0.02	18.9	7.36	82.1	1.44
	1.00	19.5	6.46	40.0	
	100.00	19.7	5.92	24.4	
BaTiO ₃ + 13.8% Sn	0.02	23.9	15.77	36.7	1.51
	1.00	24.1	14.84	16.0	
	100.00	24.2	14.26	61.8	
BaTiO ₃ + 2.4% Nd	0.02	33.6	14.62	30.5	1.14
	1.00	33.8	13.89	11.8	
	100.00	33.8	13.48	12.7	

* $\Delta\epsilon_r = \epsilon_r(20 \text{ Hz}) - \epsilon_r(100 \text{ kHz})$

Note:

The peak ϵ_r of BaTiO₃ + 2.2% Nd was very high ($\sim 44 \times 10^3$), giving a dielectric peak temperature of 33.9°C.

The values in the parentheses represent the corresponding values due to O-T transition in BaTiO₃.

The effect of isovalent substitutions on the ferroelectric transition temperature of ceramic BaTiO_3 is shown in figure 4. All curves were adjusted to the measured transition temperature for pure BaTiO_3 of 128.5°C . It is seen that the partial substitution of Zr and Hf or Sn ions monotonically lowers the ferroelectric transition temperature of BaTiO_3 towards the low temperatures. The rates of displacement for Zr or Hf ions were the same for our samples. However, the rates of displacement for Sn-doped BaTiO_3 compositions prove to be somewhat higher than the rates observed for either Hf- or Zr-doped BaTiO_3 compositions. It is seen from figure 4 that the most rapid displacement of the ferroelectric transition of BaTiO_3 occurs by the substitution of Nd ions for Ba ions. It may be noted that the measured shifts in Curie temperature as a function of doping (as listed in table 2) do not fully agree with the data reported earlier [6]. This suggests that the present preparation techniques did not possibly provide complete solid solution in all the BaTiO_3 compositions studied in this paper. The large value of $\Delta\epsilon_r$ observed in some of the highly doped samples, as seen in table 2, could be due to the compositional inhomogeneity in these solid solutions ceramics.

3. Pyroelectric properties

Typical variations of the pyroelectric coefficient (P_i) and spontaneous polarization (P_s) as a function of temperature are shown in figure 5 ((a) and (b), respectively). It can be seen that BaTiO_3 containing small amounts of Zr or Hf or Sn ions shows a strong peak at the O-T transition and a relatively weak peak at the T-C transition. At higher doping concentration, however, only one broad transition is normally seen (see fig. 5(b)). The values of P_i at the T-C transition are seen to be 1.12 and $0.8 \mu\text{C}/\text{cm}^2 \cdot ^\circ\text{C}$, respectively. These values agree with previous research on single crystal as well as polycrystal BaTiO_3 ceramics [7]. The peak values of P_i at the ferroelectric transition temperature are listed in table 3, which also lists ϵ_r and the values of F_v (figure-of merit for responsivity). The F_v values are calculated by dividing the pyroelectric peak value by the dielectric peak value. It is seen from tables 2 and 3 that the pyroelectric peak temperature at T-C normally differs from the temperature of the dielectric peak maximum in the samples of BaTiO_3 ceramics containing higher impurity concentration. It is seen that a temperature difference of 29°C is observed for BaTiO_3 containing 5.7% of Sn ions. In the 0.8 PZN-0.1PT-0.1BT composition, a temperature difference of 26°C was observed [8]. In the PLZT system, as well, a temperature difference of 100°C has been reported [9] between the dielectric and pyroelectric peak positions. The fact that the pyroelectric coefficient peak and the dielectric constant peak occur at different temperatures confirms some sort

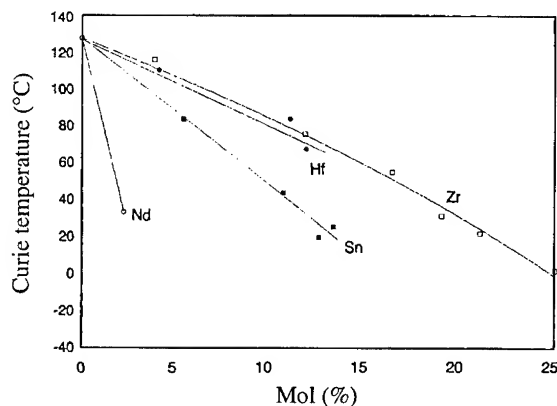


Figure 4. Effect of several isovalent substitutions on the ferroelectric transition temperature of BaTiO_3 ceramic.

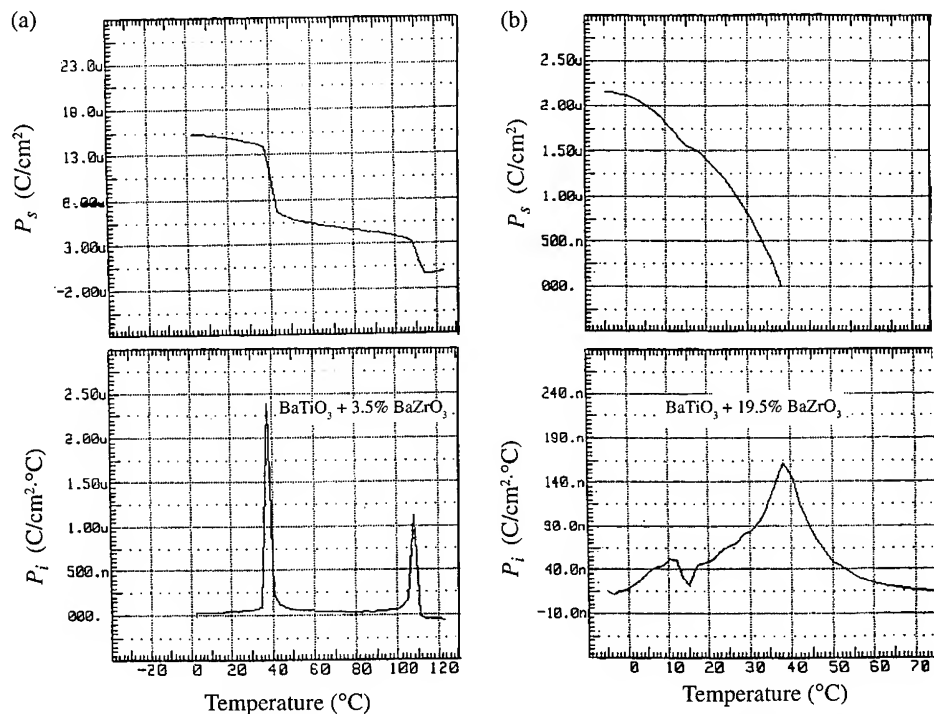


Figure 5. Temperature variation of the pyroelectric coefficient (P_i) and spontaneous polarization (P_s) of modified BaTiO_3 ceramics: (a) $\text{BaTiO}_3 + 3.5\% \text{BaZrO}_3$ and (b) $\text{BaTiO}_3 + 19.5\% \text{BaZrO}_3$.

Table 3. Pyroelectric characteristics of BaTiO_3 ceramics.

Sample	T_c (from pyro) (°C)	Peak pyroelectric coefficient ($\mu\text{C}/\text{cm}^2\cdot^\circ\text{C}$)	Peak $\epsilon_r(1 \text{ kHz})$ $\times 10^3$	F_v $\times 10^{-10}$ ($\text{C}/\text{cm}^2\cdot^\circ\text{C}$)
BaTiO_3	126.2 (T-C)	0.30	5.68	0.5 (T-C)
	21.0 (O-T)	1.12	2.35	1.19 (O-T)
$\text{BaTiO}_3 + 3.5\% \text{Zr}$	108.0 (T-C)	1.12	9.38	1.2 (T-C)
	39.2 (O-T)	2.42	2.65	9.13 (O-T)
$\text{BaTiO}_3 + 12.6\% \text{Zr}$	71.9 (T-C)	0.45	12.89	0.35 (T-C)
	51.5 (O-T)	0.78	—	—
	16.0 (R-O)	3.0	—	—
$\text{BaTiO}_3 + 13.6\% \text{Zr}$	Not measured			

Table 3. Pyroelectric characteristics of BaTiO₃ ceramics (cont'd).

Sample	T_c (from pyro) (°C)	Peak pyroelectric coefficient ($\mu\text{C}/\text{cm}^2\cdot^\circ\text{C}$)	Peak ϵ_r (1 kHz) $\times 10^3$	F_v $\times 10^{-10}$ ($\text{C}/\text{cm}^2\cdot^\circ\text{C}$)
BaTiO ₃ + 16.5% Zr	40.5 (T-C) 24.7 (O-T)	0.24 0.30	9.64 —	0.25 (T-C) —
BaTiO ₃ + 19.2% Zr	24.9	0.165	29.72	0.5
BaTiO ₃ + 19.5% Zr	38.0	0.8	19.29	0.40
BaTiO ₃ + 21.5% Zr	20.5	0.30	10.47	0.29
BaTiO ₃ + 27.8% Zr	-23.5	0.16	19.61	0.08
BaTiO ₃ + 3.8% Hf	108.4 (T-C) 43.4 (O-T)	0.33 2.75	7.55 2.553	0.4 (T-C) 10.86 (O-T)
BaTiO ₃ + 11.5% Hf	68.0 (T-C) 18.0 (O-T)	0.235 0.56	8.58 —	0.27 (T-C) —
BaTiO ₃ + 13.0% Hf	52.5	0.135	9.79	0.137
BaTiO ₃ + 5.7% Sn	55 8 (O-T)	0.120 0.48	1.0 —	1.2 4.8 (O-T)
BaTiO ₃ + 11.2% Sn	24 (T-C) 10.5 (R-O or O-T)	0.28 0.28	9.12 —	0.31 (T-C) —
BaTiO ₃ + 13.0% Sn	5.0	0.375	6.46	0.58
BaTiO ₃ + 13.8% Sn	21.2	0.490	14.84	0.33
BaTiO ₃ + 2.2% Nd		Not measured		
BaTiO ₃ + 2.4% Nd	26.0 1.0 (R-O)	0.33 0.44	13.89 —	0.24 —

T-C: Tetragonal to cubic

O-T: Orthorhombic to tetragonal

R-O: Rhombohedral to orthorhombic

of compositional inhomogeneity as suggested from dielectric measurements. As a result, some of the data in table 3 is descriptive only of these specific samples but not characteristic of the highly doped BaTiO₃ ceramics in general. It can be seen from table 3 that the F_v values are reasonably high at both T-C and O-T transitions when BaTiO₃ is doped with a small amount of Zr and Hf or Sn ions. However, at higher impurity doping, the F_v values are relatively low, and there is not a great deal of difference between the F_v values of these materials.

Table 4 summarizes the results of some of the compositions studied regarding their suitability as IR detector materials. Although these compositions compare favorably with the PLZT or BST, the F_v value is well below that of Ca-doped PbTiO₃, as well as PbTiO₃ or PZT thin films [11,12]. In general, the O-T transition gives the largest value of F_v , making it more responsive for bolometric applications than the T-C transition [10].

Table 4. Figure of merit of selected perovskites.

Material	F_v (T-C) $\times 10^{-10}$	F_v (O-T) $\times 10^{-10}$
BaTiO ₃ + 3.5% Zr	1.2	9.13
BaTiO ₃ + 3.8% Hf	0.5	10.86
BaTiO ₃ + 5.7% Sn	1.2	4.8
*PbTiO ₃ + 30% Ca	4.04	—
*PLZT(8/40/60)	2.04	—
†BST(66/34)	2.0	—
‡PbTiO ₃ thin film	3.2	—
**PZT thin film	8.47	—

*Reference 4

†K. K. Deb, unpublished results

‡Reference 11

**Reference 12

CONCLUSIONS

It is concluded that BaTiO₃ ceramic containing small amounts of either BaZrO₃ or BaHfO₃ is a candidate material for pyroelectric CCD arrays. The performance characteristics of these materials at the respective O-T and T-C temperatures are comparable with or better than PLZT and BST ceramics. However, highly doped BaTiO₃ ceramics are generally diffuse, and their F_v values are well below that of either PLZT or BST ceramics.

ACKNOWLEDGEMENT

The author wishes to thank B. Clark, L. Green, J. Slattery, and E. Doran of ARL at Fort Belvoir, and K. Bennett and S. Blomquist of ARL at Adelphi for technical help. I also extend special thanks to K. Bennett for technical review and suggestions.

REFERENCES

1. R. W. Whatmore, Rep. Prog. Phys. **44**, 1335 (1986).
2. L. A. Xue, Y. Chen and R. J. Brooks, Mater. Sci. Eng. **B1**, 193 (1988).
3. B. Jaffe, W.R. Cook, and H. Jaffe, *Piezoelectric Ceramics* (Academic Press, New York, 94 (1971).
4. K. K. Deb, M. D. Hill, and J. F. Kelly, J. Mater. Res. **7**, 3296 (1992).
5. H. F. Kay and P. Vousden, Phil Mag [7] **40**, 1019 (1949).
6. J. M. Herbert, Ceramic Dielectric and Capacitors, Gordon and Breach, **284** (1985).
7. S. B. Lang, L. H. Rice, and S. A. Shaw, J. Appl. Phys. **40**, 4335 (1969).
8. K. K. Deb, J. Electron. Mater. **20**, 653 (1991).
9. S. T. Liu and D. Long, Proc IEEE **66**, 14 (1976).
10. R. A. Hanel, J. Opt. Soc. Am., **51**, 220 (1961).
11. K. K. Deb, K. W. Bennett, and P. S. Brody, to be published in J. Vac. Science and Technology (1994).
12. K. K. Deb, K. W. Bennett, P. S. Brody, and B. M. Melnick, to be published in J. of Integrated Ferroelectrics (1994).

PART V

Characterization and Modelling

XPS STUDY OF Ni-Fe MANGANITE THERMISTOR MATERIAL

D. N. BRASKI*, N. R. OSBORNE†, AND J. M. ZURBUCHEN‡

*Oak Ridge National Laboratory, Oak Ridge, TN 37831

†University of Dayton Research Institute, Dayton, OH 45469

‡Yellow Springs Instruments, Inc., Yellow Springs, OH 45387

ABSTRACT

The resistivity of the as-fabricated thermistor material, nickel-iron-manganite, changes during initial aging in the temperature range of 150-300°C before becoming stable. X-ray photoelectron spectroscopy (XPS) was used to determine if any valency change or chemical shift of the cations or oxygen occurred during aging. The goal of the study was to identify any ionic changes that might affect thermistor stability. The only observed changes in $2p_{3/2}$ peaks due to aging were those related to Ni ions; the same peaks for Mn, Fe, and the O-1s peak were unchanged. The changes in the Ni $2p_{3/2}$ peak may possibly be related to: (a) the migration of Ni^{2+} ions from octahedral to tetrahedral sites, (b) subtle changes in the energy states of Ni^{2+} which promoted a more stable ionic structure, or (c) the presence of Ni^{3+} ions, some of which revert to Ni^{2+} .

INTRODUCTION

Nickel-iron-magnetite, $Ni_{1-x}(MnFe)_{2+x}O_4$, is a semiconducting oxide exhibiting a negative temperature coefficient of resistance (NTC) that is widely used in a number of applications to sense temperature. Theoretically, this thermistor material should have an inverse spinel structure (cubic) with the A^{2+} ions and half the B^{3+} ions on octahedral sites, and the other half of the B^{3+} on tetrahedral sites, or $B(AB)O_4$.¹ In actuality, the cation valency distribution which controls the electrical properties of the material is not well understood. Previous investigators have used x-ray photoelectron spectroscopy (XPS),²⁻⁵ magnetic or electrical measurements,⁶⁻⁸ and other techniques to study the cation valencies in similar oxides. Unfortunately, the conclusions drawn from the different studies have often been in disagreement.

In this study, the effect of thermal aging on the ionic structure of the thermistor material was analyzed using XPS. Any changes in structure that developed after fabrication during the initial aging at 150-300°C was of specific interest because of the relatively large resistivity changes previously observed. Standard 100 k Ω thermistors were analyzed before and after aging with particular attention paid to binding energy measurements of the cations at the $2p$ levels. The goal of the study was to identify any ionic changes that might affect the stability of the thermistor's resistivity.

EXPERIMENTAL

Small, 2.3 mm diam. x 0.43 mm thick thermistor disks were taken from the YSI production stock of 100 k Ω devices for analysis. The disks were fabricated by blending powders of NiO, Mn_2O_3 , and Fe_2O_3 , adding binder, ball-milling, pressing into disks, and finally firing in air at 1300°C. The composition contained about 20 wt.% Ni, with the balance about evenly distributed between Mn and Fe. The disks were analyzed in the as-fabricated as well as the thermally-aged conditions. Aging was conducted in an electrical-resistance furnace, in air, at 300°C for 3 and 9 days. The furnace temperature was controlled within $\pm 1^\circ\text{C}$.

The thermistor disks were analyzed in a PHI Electronics 5600 x-ray photoelectron spectrometer, using monochromated $Al_{K\alpha}$ x-rays at 15 kV and 400 watts with a 0.4 mm diam. aperture. A low-energy electron flood gun was employed to minimize specimen charging. Samples of the starting NiO, Mn_2O_3 , and Fe_2O_3 powders, used to fabricate the thermistors, were analyzed under identical operating conditions and used as standards. Examination of these oxide powders by

x-ray diffraction verified their respective identities and showed there were no extraneous oxides or other second phases present. Pure metal standards of Ni (99.998%), Mn (99.99%), and Fe (99.999%) from Geller Microanalytical Laboratory, Peabody, MA (Standard UHV-EL) were also analyzed under the same operating conditions. Argon sputtering at 4 kV was used to remove normal surface contamination. In analyzing the XPS spectra, binding energies were referenced to 285.0 eV for the C 1s peak of hydrocarbon contamination due to air exposure (adventitious carbon). Curve-fitting of the spectra was conducted using Gaussian/Lorentzian line shapes after removal of the background.

RESULTS

Results of the XPS analyses are summarized in Fig. 1. The $2p_{3/2}$ peaks for the pure metal standards of Mn, Fe, and Ni (Fig. 1a) and starting oxide powders (Fig. 1b) are shown at the bottom of each figure. The same peaks for each respective ion in the spinel are shown for the as-fabricated thermistor material (Fig. 1c), and after aging at 300°C for three (Fig. 1d) and nine days (Fig. 1e). Binding energies (BE) for Mn, Fe, and Ni for each material and condition are listed in Table 1 under the column labeled $2p_{3/2}$. The full width half maximum (FWHM) for each peak is also listed, along with data for the satellite structure and the $2p_{3/2}$ - $2p_{1/2}$ separation. The O-1s BE of 529.6 eV, for the spinel, did not change for any of the conditions and is not listed.

The $2p_{3/2}$ peak for Mn metal had a BE of 638.6 eV and a $2p_{3/2}$ - $2p_{1/2}$ separation of 11.1 eV (Table 1) which compares favorably with the values of 639.0 and 11.05 eV, respectively, listed in the handbook.¹ The same Mn peak in the Mn_2O_3 powder had a BE of 641.6 eV with a shake-up satellite of 645.7 eV and a $2p_{3/2}$ - $2p_{1/2}$ separation of 11.6 eV. The Mn peaks in the as-fabricated spinel were virtually identical to those in the Mn_2O_3 powder and thermal aging for 3 or 9 days did not affect the peaks (Fig. 1 and Table 1).

A $2p_{3/2}$ BE of 706.38 eV and a $2p_{3/2}$ - $2p_{1/2}$ separation of 13.2 eV was measured for Fe metal (Table 1) which, again, compared well with handbook values of 707.0 and 13.10 eV.⁹ The same two parameters for the Fe_2O_3 powder were 710.1 and 13.7 eV (Table 1) while handbook values were 710.9 and 13.6 eV.¹ As in the case for Mn, the $2p_{3/2}$ peak shape and BE's for Fe were the same for the starting oxide, the as-fabricated disks, and the thermally aged material (Fig. 1 and Table 1). The two shake-up satellite peaks in the left portion of the broadened $2p_{3/2}$ peak of the oxide were also found in the spinel.

The $2p_{3/2}$ peak for Ni metal had a slightly lower BE of 852.0 eV (Table 1) compared to the 852.7 eV handbook value.⁹ However, the experimental value for the $2p_{3/2}$ - $2p_{1/2}$ separation of 17.2 eV agreed closely with that in the handbook, 17.27 eV.⁹ A weak, broad peak due to plasmon losses was observed at 857.8 eV. The $2p_{3/2}$ Ni peak in the starting NiO powder has a complex structure as shown in Fig. 1. Its measured BE of 852.8 eV is 1 eV lower than the 853.8 eV handbook value,⁹ but the $2p_{3/2}$ - $2p_{1/2}$ separation of 17.3 eV agrees well with the handbook value of 17.49 eV. As shown in the handbook⁹ and by others,^{5,10-12} the $2p_{3/2}$ peak exhibits multiplet splitting and a number of shake-up satellites. Although the BE of this peak remained the same in the as-fabricated and thermally-aged materials, the satellite structure was remarkably different, as shown in Fig. 1, and in more detail in Fig. 2. The $2p_{3/2}$ Ni peak in NiO exhibited three shake-up satellites while that for the as-fabricated spinel had only two. The first satellite in the as-fabricated spinel (855.2 eV) was relatively large and decreased substantially after 3 days of thermal aging at 300°C, as shown in Fig. 2. Further aging at the same temperature for 9 days had no effect on the peak shape.

DISCUSSION

Nickel was the only cation in the 100 k Ω thermistor material that exhibited changes in its $2p_{3/2}$ peak after thermal aging. The intensity of the first satellite relative to the $2p_{3/2}$ was lowered by nearly a factor of 2 after the initial aging treatment of 3 days at 300°C, and then remained constant

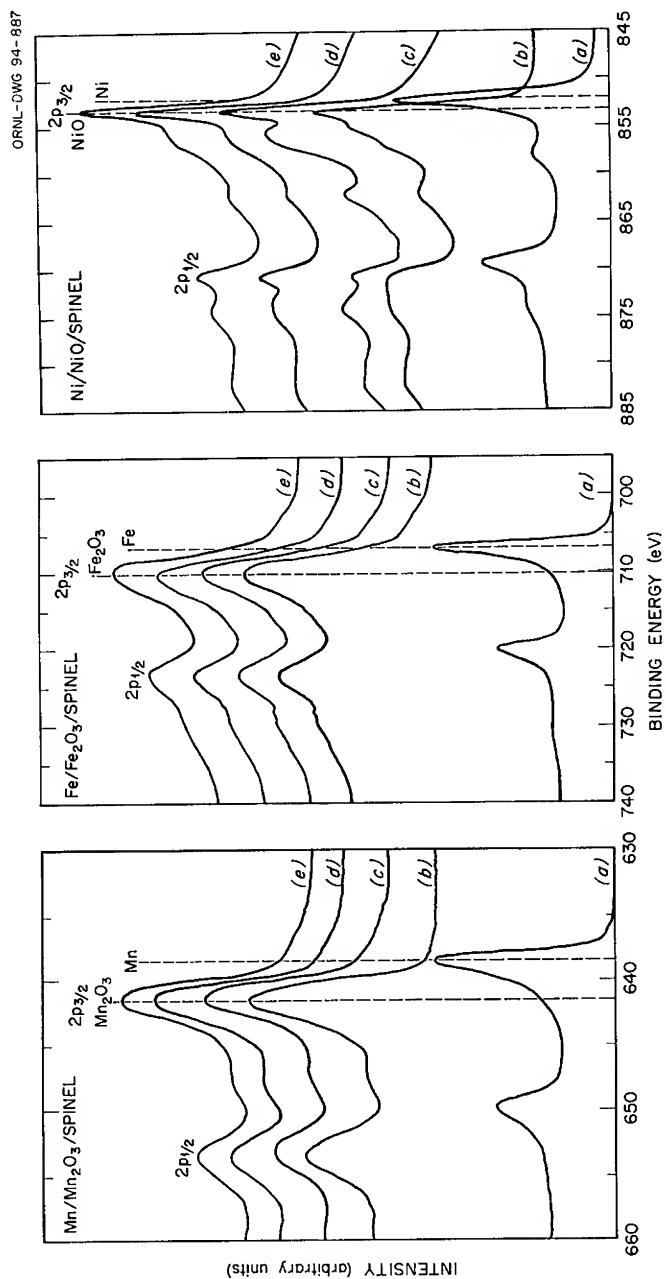


Fig. 1 Mn-, Fe-, and Ni- $2p_{3/2}$ and $2p_{1/2}$ XPS peaks in (a) metal, (b) oxide, (c) as-fabricated thermistor spinel, (d) spinel after 3 d at 300°C, and (e) spinel after 9 d at 300°C.

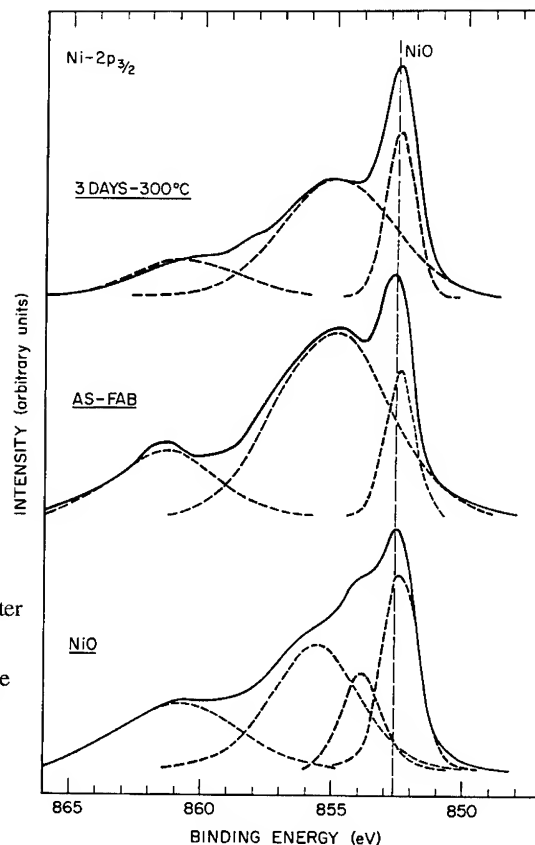


Fig. 2 Ni-2p_{3/2} satellite structure for NiO compared to that in as-fabricated spinel and spinel after aging for 3 days at 300°C. Dashed lines are Gaussian/Lorentzian line shapes that were curve-fit to experimental data.

TABLE 1 - XPS DATA										
ELEMENT	CONDITION	2p3/2 (eV)	FWHM (eV)	Satellite1 (eV)	FWHM (eV)	Satellite2 (eV)	FWHM (eV)	Satellite3 (eV)	FWHM (eV)	2p3/2-2p1/2 (eV)
Mn	Metal	638.6	1.3							11.1
Mn Oxide	Powder	641.6	3.1	645.7	5.8					11.6
SPINEL (Mn)	As-Fabricated	641.4	3.6	646.4	4.4					11.4
SPINEL (Mn)	3 days @ 300C	641.3	3.5	646.3	6.0					11.8
SPINEL (Mn)	9 days @ 300C	641.3	3.6	646.3	4.1					11.5
Fe	Metal	706.4	1.4							13.2
Fe Oxide	Powder	710.1	3.5	713.1	4.8	718.0	5.0			13.7
SPINEL (Fe)	As-Fabricated	709.9	4.0	713.3	4.8	717.4	4.4			13.5
SPINEL (Fe)	3 days @ 300C	710.2	4.6	713.8	4.9	717.9	5.1			13.2
SPINEL (Fe)	9 days @ 300C	709.9	4.4	713.1	5.4	717.8	6.1			13.3
Ni	Metal	852.0	1.6			857.8	5.6			17.2
NiO	Powder	852.8	1.5	854.3	2.2	856.5	3.4	861.1	5.2	17.3
SPINEL (Ni)	As-Fabricated	852.8	1.3	855.2	5.0			861.6	4.3	17.3
SPINEL (Ni)	3 days @ 300C	852.8	1.4	855.2	5.1			860.9	4.8	17.2
SPINEL (Ni)	9 days @ 300C	852.9	1.4	855.4	5.4			861.3	3.9	17.2

upon further aging. At the same time, the Mn and Fe 2p peaks as well as the O 1s peak showed no evidence of chemical shifts or even changes in peak shape. It is possible that the changes in the Ni 2p_{3/2} /satellite structure were due to Ni³⁺ as reported by Hashemi and Brinkman² for a similar thermistor material which contained Cu instead of Fe. The apparent Ni³⁺ binding energy was ≈2.1 eV higher than that for Ni²⁺ which agreed with the 2.2 eV measured by Ng and Hercules⁵ for Ni in Ni-oxides. The relatively intense satellite peak observed in the present work is located somewhat further away (≈2.5 eV) but still might be interpreted as Ni³⁺. If Ni³⁺ was present after fabrication, then a portion of it would have to revert back to Ni²⁺ upon aging to account for the reduction of intensity shown in Fig. 2. However, it is difficult to prove that Ni³⁺ is present and that there is not just a complex satellite structure similar to the one found in NiO (Fig. 2). Moreover, the presence of the Ni³⁺ ion in nickel iron manganite would be considered somewhat unusual because most investigators^{4,7,13-15} list only Ni²⁺ in their cation distributions in nickel manganite.

The observed changes in the Ni 2p_{3/2} peaks could be due to changes in the shake-up satellite structure itself. Vernon et al.¹⁶ point out that intense satellites are often observed in Ni compounds and that the structure can often be convoluted into more than one peak. Therefore, a subtle change in the energy states of the Ni ions in the as-fabricated spinel due to thermal aging could have promoted a different, but more stable ionic and 2p_{3/2}-satellite structure configuration.

Other possible explanations for changes in Ni 2p level peaks include the effect of defects in the microstructure. Beard et al.¹⁷ have shown that order of magnitude increases in dislocation density in ammonium perchlorate caused increases in the FWHM of an XPS peak. However, very few, if any, dislocations were found in the thermistor material using transmission electron microscopy.¹⁸

Finally, there exists the possibility that incomplete inversion of the Ni occurred during fabrication with Ni²⁺ ions left in both tetrahedral (A-sites) and octahedral (B-sites).¹⁹ With suitable energy, Ni²⁺ ions migrate from B to A sites.¹⁹ Macklen⁸ determined the onset of this migration in NiMn₂O₄ to be 352°C. This mechanism might have also been active in the Ni-Fe-manganite at 300°C but how it relates to resistivity is still unclear. The Ni-Fe manganite ionic structure and the possibility of Ni²⁺ migration will be investigated further in the near future using neutron diffraction.

CONCLUSIONS

1. The only changes in the cation 2p_{3/2} peaks of the thermistor material that could be related to thermal aging at 300°C were those associated with the Ni ions. The 2p_{3/2} peaks for Mn, Fe, and the O-1s were unchanged.
2. Possible explanations for the changes in the Ni 2p_{3/2} peaks include:
 - (a) the migration of Ni²⁺ ions from octahedral to tetrahedral sites,
 - (b) subtle changes in the energy states of the Ni²⁺ ions which promoted a more stable ionic and 2p_{3/2} satellite structure, or
 - (c) the presence of Ni³⁺ ions, some of which revert to Ni²⁺ upon aging.

ACKNOWLEDGMENTS

The authors thank Dr. John Grant, University of Dayton Research Institute, for helpful discussions and Yellow Springs Instruments, Inc., for supplying the thermistor material.

The research was sponsored by U.S. DOE, Ass't Sec. for Energy Efficiency & Renewable Energy, as part of the High Temp. Matls. Lab User Prog., under contract DE-AC05-84OR21400 managed by Martin Marietta Energy Systems, Inc.

REFERENCES

1. W. D. Kingery, Introduction to Ceramics, John Wiley & Sons, Inc., N.Y. (1963) p115.
2. T. Hashemi and A. W. Brinkman, J. Mater. Res. Vol.7, No. 5 1278 (1992).
3. J. S. Foord, R. B. Jackman and G. C. Allen, Phil Mag. A Vol. 49, No. 5 657 (1984).
4. V. A. M. Brabers, F. M. van Setten and P. S. A. Knapen, J. of Solid State Chem. 49, 93 (1983).
5. K. T. Ng and D. M. Hercules, J. of Phys. Chem., Vol. 80, No. 19, 2094 (1976).
6. P. K. Baltzer and J. G. White, J. Appl. Phys., Vol.29, No. 3, 445 (1958).
7. G. T. Bhandage and H. V. Keer, J. Phys. C: Solid State Phys., Vol. 9, 1325 (1976).
8. E. D. Macklen, J. Phys. Chem. Solids, Vol. 47, No. 11, 1073 (1986).
9. J. F. Moulder, W. F. Stickle, P. E. Sobol, and K. D. Bomben, Handbook of X-ray Photoelectron Spectroscopy, Ed. J. Chastain (Perkin-Elmer, 1992).
10. N. S. McIntyre and M. G. Cook, Anal. Chem., Vol. 47, No. 13, 2208 (1975).
11. W. T. Evans and M. Schlesinger, J. Electrochem. Soc., Vol 141, No. 1, 78 (1994).
12. D. Briggs and M. P. Seah, Practical Surface Analysis. 2nd Edition, Vol. 1 - Auger and X-ray Photoelectron Spectroscopy, (John Wiley & Sons, N.Y., 1990) p.505.
13. A. P. B. Sinha, N. N. Sanjana and A. B. Biswas, Acta Cryst. 10, 439 (1957).
14. P. K. Blatzer and J. G. White, J. appl. Phys. 29, 445 (1958).
15. E. G. Larson, R. J. Arnott, D. G. Wickham, J. Phys. Chem Solids 23, 1771 (1962)
16. G. A. Vernon, G. Stucky and T. A. Carlson, Inorg. Chem. 15, No. 2, 278 (1976).
17. B. C. Beard, H. W. Sandusky, B. C. Glancy and W. L. Elban, Surface and Interface Anal. Vol. 20, 140 (1993).
18. K. L. More, Oak Ridge National Laboratory, private communication.
19. V. A. M. Brabers and J. C. J. M. Terhell, Phys. Stat. Sol. (a) 69, 325 (1962).

THERMO-ELECTRIC PROPERTIES OF THIN-FILM REFRACTORY METAL THERMOCOUPLES

ROBERT G. SCHINAZI*, GUO-QUAN LU*, AND FRANS SPAEPEN**

*Virginia Polytechnic Institute and State University, Blacksburg, VA 24061

**Harvard University, Cambridge, MA 02138

ABSTRACT

Thin-film thermocouples are well suited for "smart" processes where the mass of traditional two-lead thermocouples inhibits their wide utilization. However, current thin-film thermocouples lack the robustness desired for abrasive environments. To address this issue, thin-film refractory metal thermocouples consisting of combinations of molybdenum, tantalum, tungsten, vanadium, or nickel were produced by ion-beam sputtering on an alumina substrate. To speed up the process of sampling a large number of material combinations, the thermocouples were made small, about 200 nm thick, 2.5 mm wide, and 12 mm long. An apparatus was fabricated to measure the thermo-electric responses of these short-length thermocouples. Materials design and heat-transfer issues relating to the applications and testing of these thermocouples are discussed.

INTRODUCTION

"Smart" processing of materials, currently an active area of research and development^{1,2,3}, requires various sensors to monitor the actual production conditions, such as pressure and temperature. Thermocouples are widely used for temperature-sensing because of their simplicity, accuracy, and low cost. However, traditional two-lead thermocouples are too bulky⁴ for many "smart" processing systems, and existing thin-film thermocouples⁵ are not designed for use in rough environmental conditions. An example that requires more rugged thin-film thermocouples is measuring temperatures on machining tools to prolong their lifetimes by controlling cutting rate with temperature feedback. Here, the rough conditions caused by the use of coolant, shear abrasion of the removed chips, and sharp temperature gradient⁶ demand more robust thin-film thermocouples. For such applications the material selection is restricted to those materials having high melting temperatures, high resistance to corrosion, and high hardness. While one could consider using carbides or ceramics we chose to investigate the refractory metals because they are relatively easier to make. The purpose of this study was to test short length thin film refractory metal thermocouples.

EXPERIMENT

Preparation of Thin-Film Thermocouples

An ion-beam sputtering machine was used to deposit thin-film thermocouples. Target materials used were molybdenum, tantalum, tungsten, vanadium, and nickel. Thermocouples with all the possible combinations of these materials were deposited on a polished alumina substrate that measured roughly 12 x 50 x 0.4 mm. To minimize the number of deposition runs, thermocouples were made small, such that all combinations being investigated could be produced in a single run in the three-inch diameter deposition area of the ion-beam sputtering machine. The

various thermocouples were produced by depositing overlapping strips of metal by basic masking techniques. Gold tabs were deposited on the ends of the metal strips to facilitate electrical connections since these refractory metals readily form native oxides. Once all thermocouples and gold tabs were deposited, the substrate was cut with a three axis dicing saw to separate the individual thermocouples.

Apparatus for Testing Short Thin Film Thermocouples

An apparatus was designed to test these Short Thin-Film ThermoCouples (STFTCs). The thermocouples used in this paper were substantially smaller than those typically used for calibration purposes (Figure 1), and were laid out in a linear fashion as opposed to the traditional "U" pattern^{7,8,9}.

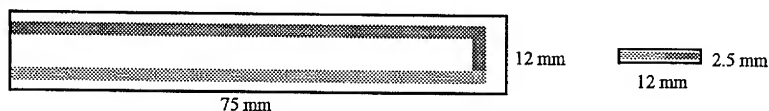


Figure 1. Traditional calibration thin film thermocouple *left* vs. short thin film thermocouple *right*.

In contrast to traditional testing where the thermocouple junction is placed in a furnace and the other end is held constant, both ends of the STFTC were held constant while the center was heated (see Figure 2). This configuration is different from the traditional one which has a long distance to moderate the thermal gradient; our design had a very small cross sectional area to minimize the thermal transfer from the junction to the ends.

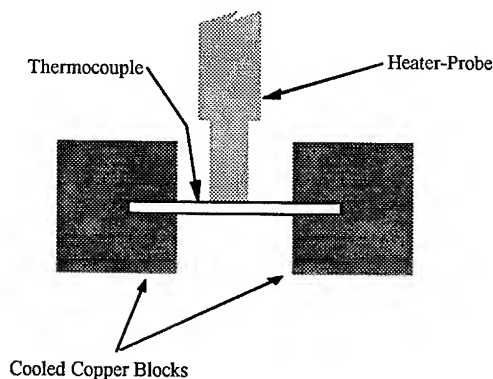


Figure 2. Schematic representation of the testing apparatus used for short gauge length thermocouples.

In the apparatus, the heater-probe is affixed to an optical-slide via 1/8" diameter stand-off dowels. The slide/heater assembly was counter balanced with lead weight through a cable pulley system. The slide/heater assembly was intentionally left a few grams out of balance so that gravity could be used to hold the probe on the specimen's surface. The heater's motion in the vertical

direction is free to allow for thermal expansion, while it is constrained in the horizontal plane to ensure proper alignment with the thermocouple junction.

The copper blocks are far more complex than depicted. Each block was machined into a modified C-channel such that the bottom flange is larger than the top flange (Figure 3a). The channel is machined so as to leave a raised area which serves as a contact point with the thermocouple (Figure 3b, c). The thick gray line in Figure 3a represents Kapton® tape used to electrically insulate the two blocks from each other. The copper blocks have matching guide holes, (Figure 3b), that in conjunction with alumina dowels serve for assembly and alignment.

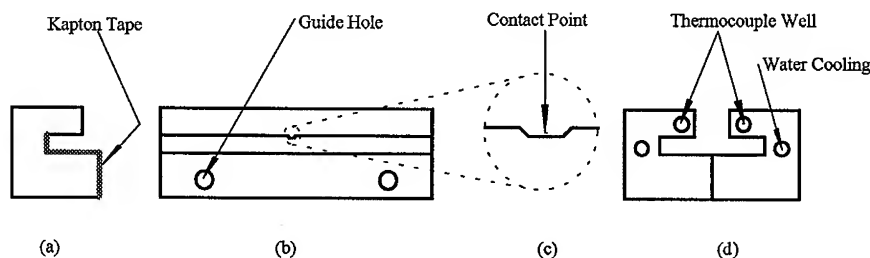


Figure 3. Illustrations of the copper block. (a) side view showing insulated area; (b) side view looking into the channel showing guide holes and contact point; (c) enlargement of the contact point; and (d) both blocks assembled showing thermocouple wells and water cooling holes.

Each copper block had a thermocouple well for a regular two wire sheathed thermocouple, and a through hole for water cooling; the thermocouple well is located in the top flange, (Figure 3d), and extends up to the contact point; the thermocouples in the copper blocks allow the temperature of the ends of the STFTC to be monitored during testing. The water cooling holes were connected to a water chiller to maintain a constant temperature on the end tabs of the STFTC. To overcome the effects of oxide growth, the actual testing was performed in an argon-filled bell jar.

Sample Mounting Procedure

The thin film thermocouples were mounted on the copper blocks using a special vertical stage. The stage was made from two mating 2.5° wedges and a threaded rod (Figure 4a). The stage is raised by tightening the threaded rod. The threaded rod was intentionally left long enough to extend beyond the copper blocks to facilitate sample mounting. Note that the stage had a slot machined on the top surface so that the thermocouple junction and surrounding materials were not in physical contact with the stage (Figure 4b).

To mount a STFTC in the copper blocks, the sample is placed on the stage and the threaded rod was tightened until electrical contact was made between the STFTC and the copper blocks. The advantage of this design is that the contact point can be readily lapped by placing polishing compound on an alumina substrate placed on the stage. Lapping is necessary to ensure that the contact point and the stage are exactly parallel so contact can be made on both sides of the

thermocouple simultaneously. Because the apparatus can be dressed easily, electrical contact between the STFTC and the copper blocks can be made with surprisingly little vertical pressure. It is desirable to minimize the clamp pressure to allow lateral movement to relieve thermal strain during testing.

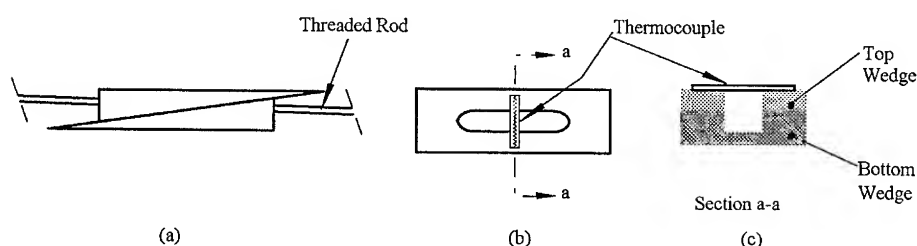


Figure 4. Illustration of the vertical stage. (a) side view of stage showing wedges and threaded rod; (b) top view showing slot and a STFTC mounted; and, (c) sectional view showing air gap below thermocouple junction.

Testing Procedure

Testing was performed under constant power conditions which simply means that the power supplied to the heater was held at a constant level. Initially attempts were made to ramp the temperature of the heater-probe at a constant rate. Unfortunately, the switching of the heater power created voltage spikes that introduced error to the thermocouple signals. Constant-power testing eliminated those spikes. If the same power is introduced during each run, with all things being equal, the apparatus will heat up the same way.

While power was supplied to the heating elements, three types of measurements were collected: (1) the voltage or EMF from the STFTC; (2) the probe temperature; and (3) the copper blocks' temperature. It is assumed that the temperature of the STFTC junction will follow the probe temperature in a predictable way. Therefore, under constant power conditions, the temperature of the junction can be estimated using a look-up table produced from a calibrated thin-film thermocouple. Hence, the EMF values are collected as a function of probe temperature. The temperature of the copper block is collected to perform cold junction compensation for variations in the copper blocks' temperature during testing. Testing was performed for all the thermocouples between 25°C and 600°C.

RESULTS AND DISCUSSION

Figure 5 shows the EMF of a Mo-Ta thin-film thermocouple along with that of a Mo-Ta foil thermocouple as a function of probe temperature. While the temperature of STFTC was expected to lag behind the probe, the actual lag was much greater than expected. Since the EMF's of the foil and thin-film thermocouples should be nearly equal, the junction temperature can readily be obtained. Plotted in Figure 6 is the percent lag in temperature read by the STFTC as a function of probe temperature. It shows that above 150°C, the lag remains relatively constant at ~60%. While the magnitude of this lag is large, the uniformity is encouraging and suggests that the apparatus is behaving predictably. The initial region of the plot, below 200°C corresponds to the

working range of the silicon based heat sink compound that was initially used to decrease the probe-junction temperature lag.

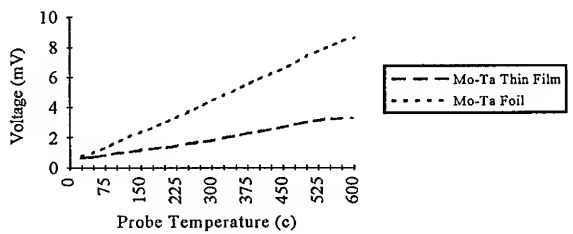


Figure 5. Mo-Ta thin-film and foil thermocouple voltage vs. probe temperature

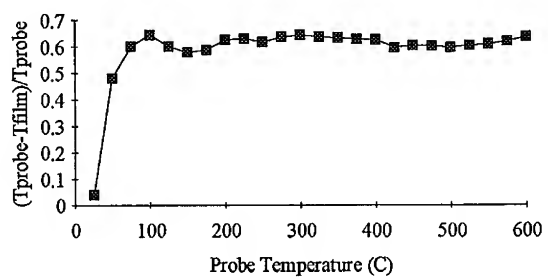


Figure 6. Percent thermal lag vs. probe temperature.

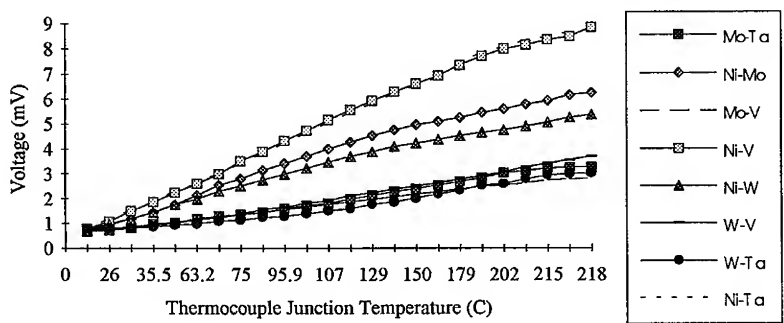


Figure 7. Voltage (mV) vs. temperature for various short thin-film thermocouples.

Even with the large probe-junction temperature lag, the apparatus was able to provide some useful information. Figure 7 is a compilation of EMF vs. temperature plots for all the STFTCs tested in this study. From this data, it is clear that the Ni-Ta and Ni-V STFTCs had the highest thermo-electric coefficients.

After conducting this initial study, it is believed that having a resistive heating element in such close proximity to the thin film device is an undesirable design. Future work will be directed toward modifying the current apparatus to allow the heater-probe to be replaced with a non-contact heat source such as a laser or microwave. The next apparatus will likely employ non-conductive coatings, selectively applied over the thermocouple junction, that are highly absorbent in the wavelength of the energy source used for heating. The use of such coating is necessary since metals are notoriously reflective in wavelengths that are commercially available. In the proposed configuration, the junction temperature will be measured either by optical pyrometry, or with a second calibrated thin film thermocouple deposited in proximity close to the unknown thermocouple.

CONCLUSIONS

We conducted an initial investigation in the feasibility of using refractory metal thin-film thermocouples as process sensors in extremely abrasive environments such as metal cutting. Thin-film thermocouples were produced from vanadium, tungsten, molybdenum, nickel and tantalum. In addition an apparatus has been constructed for the testing of short length thin film thermocouples. Preliminary thermo-electric properties of refractory metal thin-film thermocouples have been collected. The Ni-Ta and Ni-V thin-film thermocouples had the highest thermo-electric coefficients in this study.

ACKNOWLEDGMENTS

We are grateful to Mark, John and Manny Souza, Joe Bell, Keith Wright, Randy Waldron and Jeff Snider for their valuable technical assistance. We also express our sincere gratitude to Dr. Kenneth Kreider for his patient guidance and helpful advice.

REFERENCES

1. M.A. Alfromowitz, *Journal of Lightwave Technology*, **6** (10), 1591-1594 (1988); K.Y. Lam, *SPIE* **986**, 135-139 (1988).
2. P.J. Werbos, *The Roots of Back Propagation, From Order Derivatives to Neural Networks and Political Forecasting*, (John Wiley & Sons, New York, NY, 1993).
3. D. White, and D. Sofge, (Eds.), *Handbook of Intelligent Control: Neural, Adaptive and Fuzzy Approaches*, (Van Nostrand Reinhold Co., New York, NY, 1992).
4. D.A. Stephenson, *Sensors and Signal Processing for Manufacturing* American Society of Mechanical Engineers, Production Engineering Division, **55**, 81-95 (1992).
5. E. Charles, R. Lorival, A. Boyer and P. Malbrunot, *Sens. and Actuators*, **6**, 135-142 (1984).
6. A.O.O. Tay and K.H. Lee, *Journal for Materials Processing Technology*, **29**, 47-62 (1992).
7. K.G. Kreider, *J. Vac. Sci. Technol. A*, **4**(3), 606-607 (1986); **4** (6), 2618-2623 (1986); S. Semancik, **3** (6), 2582-2587 (1985); *Sensors and Actuators A*, **34**, 95-99 (1992).
8. T.C. Kuo, J. Flattery, P.K. Ghosh, and P.G. Kornreich, *J. Vac. Sci. Technol. A*, **6** (3), 1150-1152 (1988).
9. M. Yust and K.G. Kreider, *Thin Solid Films*, **176**, 73-78 (1989).

MODELLING OF POLYDOMAIN SMART MATERIALS

YONGSIK YU AND ALEXANDER ROYTBURD

University of Maryland, Department of Materials and Nuclear Engineering, College Park, MD
20742-2115

ABSTRACT

Polydomain materials with periodic (modulated) domain structures are of potential practical importance since they can possess unique and desirable mechanical and physical properties. A twin related domain formation can be a result of constrained structural, ferroelectric or ferromagnetic transformations. The thermodynamic theory on the deformation of layer composites containing a polydomain (polytwin) ferroelectric component is analyzed. The deformation of the layer composite under different directional electric fields and constraints is calculated.

INTRODUCTION

Often in the phase transformation of solids, a single crystal or a grain of parent phase is transformed into regular systems of structural domains as a result of the reduction in crystal symmetry. They are related to each other as twins.¹⁻³ If transformations proceed in a mechanically restricted area such as layer composites consisting of "active" and neutral "inactive" phases with perfect interfacial cohesion between the phases, the twins serve as elastic domains. The elastic domains form the equilibrium structure with hierarchical arrangement of mixture of all possible domains.⁴ A controlled evolution of modulated polydomain structures under external, mechanical and electric, fields is the microstructural base of "smartness".

The linear and nonlinear electric and electromechanical responses of ferroelectric, such as BaTiO₃, PbTiO₃, (Pb_{1-x}Zr_x)TiO₃ [PZT], ceramics and thin film to an external electric field have been presented by several authors.⁵⁻⁹ The domain interface movement under mechanical stress and electric or magnetic fields enables an additional mode of deformation.

In previous paper we showed the effect of a bias electric field on the mechanical deformation beyond the saturated domain under the electric field.¹⁰ The electric field creates a stable polarization and makes the mechanical deformation much more difficult. In this work we describes the deformation of layer composites due to the evolution of equilibrium domain structure under the electric field at different constraint condition.

EQUILIBRIUM DOMAIN STRUCTURES OF POLYDOMAIN MATERIAL

According to the symmetry relation between the parent cubic and the product tetragonal phase as a result of phase transformation, e.g., BaTiO₃, three different orientational variants (or domains) of the tetragonal phase can be formed in the active layer. Three domains are characterized by the self-strain (or spontaneous strain) as shown in Figure 1:

$$\hat{\epsilon}_1 = \epsilon_o \begin{pmatrix} \kappa & 0 & 0 \\ 0 & -1 & 0 \\ 0 & 0 & -1 \end{pmatrix} \quad \hat{\epsilon}_2 = \epsilon_o \begin{pmatrix} -1 & 0 & 0 \\ 0 & \kappa & 0 \\ 0 & 0 & -1 \end{pmatrix} \quad \hat{\epsilon}_3 = \epsilon_o \begin{pmatrix} -1 & 0 & 0 \\ 0 & -1 & 0 \\ 0 & 0 & \kappa \end{pmatrix} \quad (1)$$

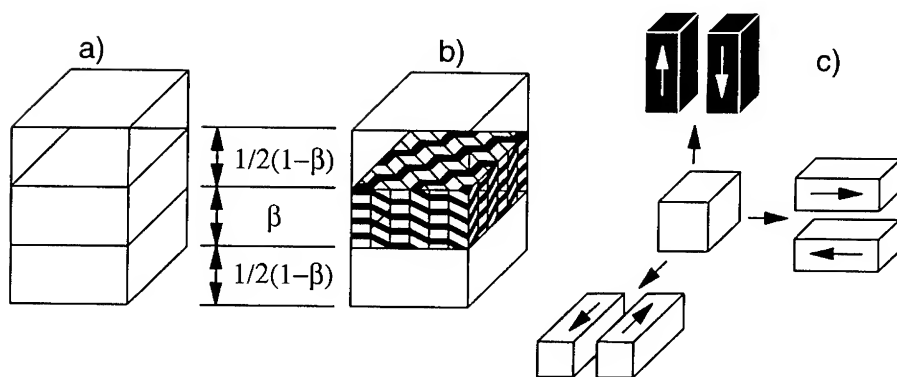


Figure 1. Elementary unit of a layer composite before (a) and after (b) the transformation (c) 90° and 180° domains in the ferroelectric phase.

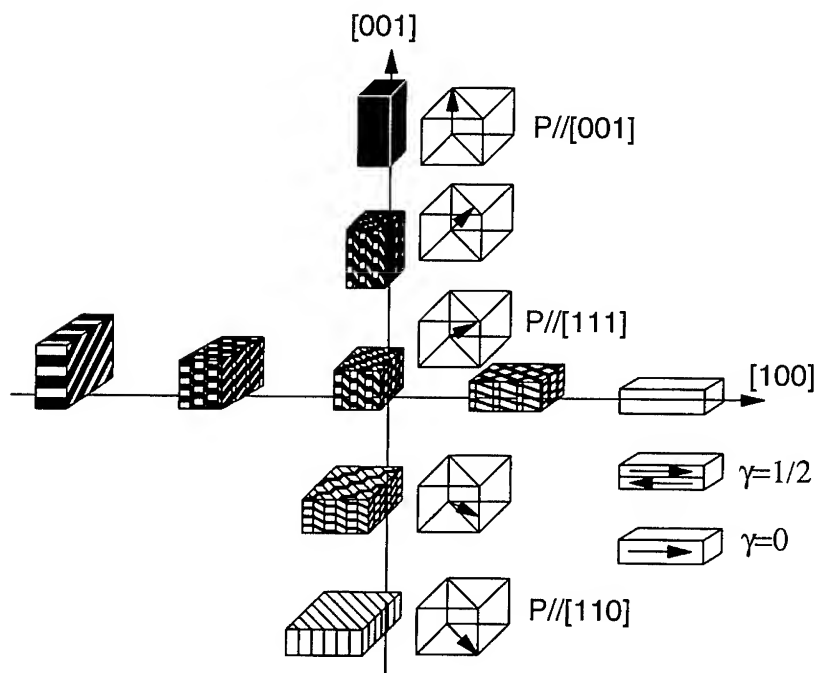


Figure 2. Polarization and "striction" of polydomain phase under electric field.

where $\epsilon_0 = (a_0 - a)/a_0$, and $\kappa = (c - a_0)/(a_0 - a)$ is the parameter of transformation tetragonality, a_0 is a lattice parameter of the cubic phase, and a and c are lattice parameters of the tetragonal phase.

The minimum of the elastic energy corresponds to equilibrium domain structure consisting of all three types of domains with self strain and the polarization as follows:

$$\hat{\epsilon} = \alpha_1 \hat{\epsilon}_1 + \alpha_2 \hat{\epsilon}_2 + \alpha_3 \hat{\epsilon}_3, \quad \vec{P} = (\alpha_1 \vec{x} + \alpha_2 \vec{y} + \alpha_3 \vec{z}) (1 - 2\gamma) P_s \quad (2)$$

The components of $\hat{\epsilon}$ are $\epsilon_{xx} = \epsilon_0(\kappa+1)(\alpha_1 - \alpha_1^0)$, $\epsilon_{yy} = \epsilon_0(\kappa+1)(\alpha_1^0 + \alpha_3^0 - \alpha_1 - \alpha_3)$, $\epsilon_{zz} = \epsilon_0(\kappa+1)(\alpha_3 - \alpha_1^0)$ where $\alpha_1^0 = 1/(\kappa+1)$, $\alpha_3^0 = (\kappa-1)/(\kappa+1)$, α_i , $i=1,2,3$, is a volume fraction of each domain, γ is a volume fraction of polarization along electric field (E), and P_s is saturated polarization of each domain. γ is the same in all domains due to compatibility of electric field across domain boundaries as shown in Figure 2. So the direction of polarization (P) as well as total self strain is determined only by domain composition.

EQUILIBRIUM DOMAIN STRUCTURES UNDER EXTERNAL ELECTRIC FIELD

The enthalpy of the layer composite under the external electric field (E) is

$$h(\alpha, E) = \beta(1-\beta) e(\alpha_i) + \beta h_E(\alpha_i, \gamma) \quad (3)$$

The elastic energy is obtained as a result of constraint as shown in Fig. 1 with a simple approximation that the elastic moduli of both phases are the same and the phases are isotropic as follow:

$$e = \beta(1-\beta) e(\alpha_i) = \beta(1-\beta) G/(1+\nu) (\epsilon_{xx}^2 + \epsilon_{yy}^2 + 2\nu \epsilon_{xx} \epsilon_{yy}) \quad (4)$$

where $G = E/2(1-\nu)$ is effective modulus, E is Young's modulus, ν is Poisson's ratio of the layer, β is a fraction of the active phase in a layer composite.

The enthalpy contribution due to the electric field along the polar axis, $h_E(\alpha, \gamma)$, is as follows:

$$h_E = \frac{1}{2} \epsilon_E P_s^2 \alpha_3^2 (1-2\gamma)^2 - \vec{P} \cdot E (1-2\gamma) \text{ for } E < E_{cr}, \quad h_E = \frac{1}{2} \epsilon_E P_s^2 \alpha_3^2 - \vec{P} \cdot E \text{ for } E > E_{cr} \quad (5)$$

where $\epsilon_E = 1/\epsilon_0 \epsilon_r$, ϵ_0 is permittivity of free space, ϵ_r is relative permittivity (or dielectric constant), and E_{cr} is the electric field which disappears 180° domain.

In the case when the electric field is less than the critical field, $E < E_{cr}$, the minimization of $h_E(\alpha, \gamma)$ with respect to γ gives:

$$\begin{aligned} \gamma &= \frac{1}{2} (1 - \alpha_3^{-1} \bar{E}), & h_E(\alpha_i, \gamma) &= -\frac{1}{2} P_s^2 \bar{E}^2 & \text{along } E//[001] \\ \gamma &= \frac{1}{2} (1 - \alpha_1^2 \alpha_3^{-2} \bar{E}), & h_E(\alpha_i, \gamma) &= -\frac{1}{2} \alpha_1^2 \alpha_3^{-2} P_s^2 \bar{E}^2 & \text{along } E//[100] \\ \gamma &= \frac{1}{2} [1 - (1 - \alpha_3) \alpha_3^{-2} \bar{E}], & h_E(\alpha_i, \gamma) &= -\frac{1}{2} (1 - \alpha_3)^2 \alpha_3^{-2} P_s^2 \bar{E}^2 & \text{along } E//[110] \\ \gamma &= \frac{1}{2} (1 - \alpha_3^{-2} \bar{E}), & h_E(\alpha_i, \gamma) &= -\frac{1}{2} \alpha_3^{-2} P_s^2 \bar{E}^2 & \text{along } E//[111] \end{aligned} \quad (6)$$

If $E > E_{cr}$, the equilibrium domain fraction as well as the deformation under the electric field are determined by minimizing the enthalpy with respect to α_i in Equation (3) and substituting into Equation (2):

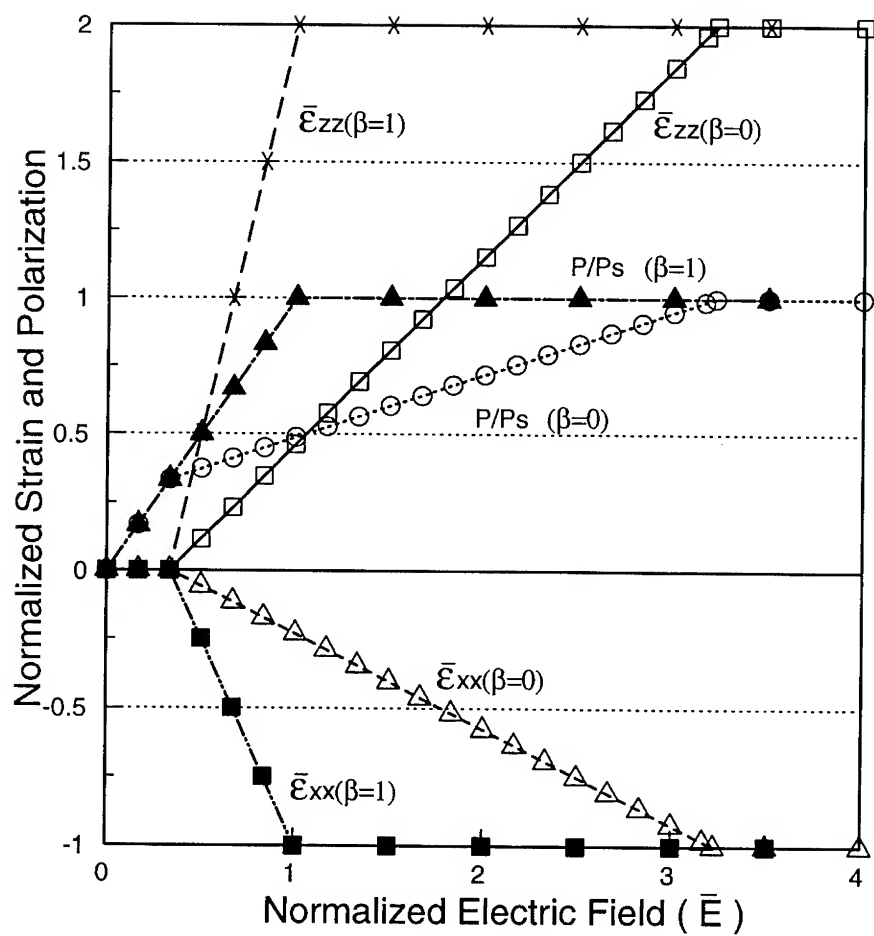


Figure 3. The polarization and the deformation under $E//[001]$ at different constrained condition ($\beta=0$ or 1 with $\phi=0.3$).

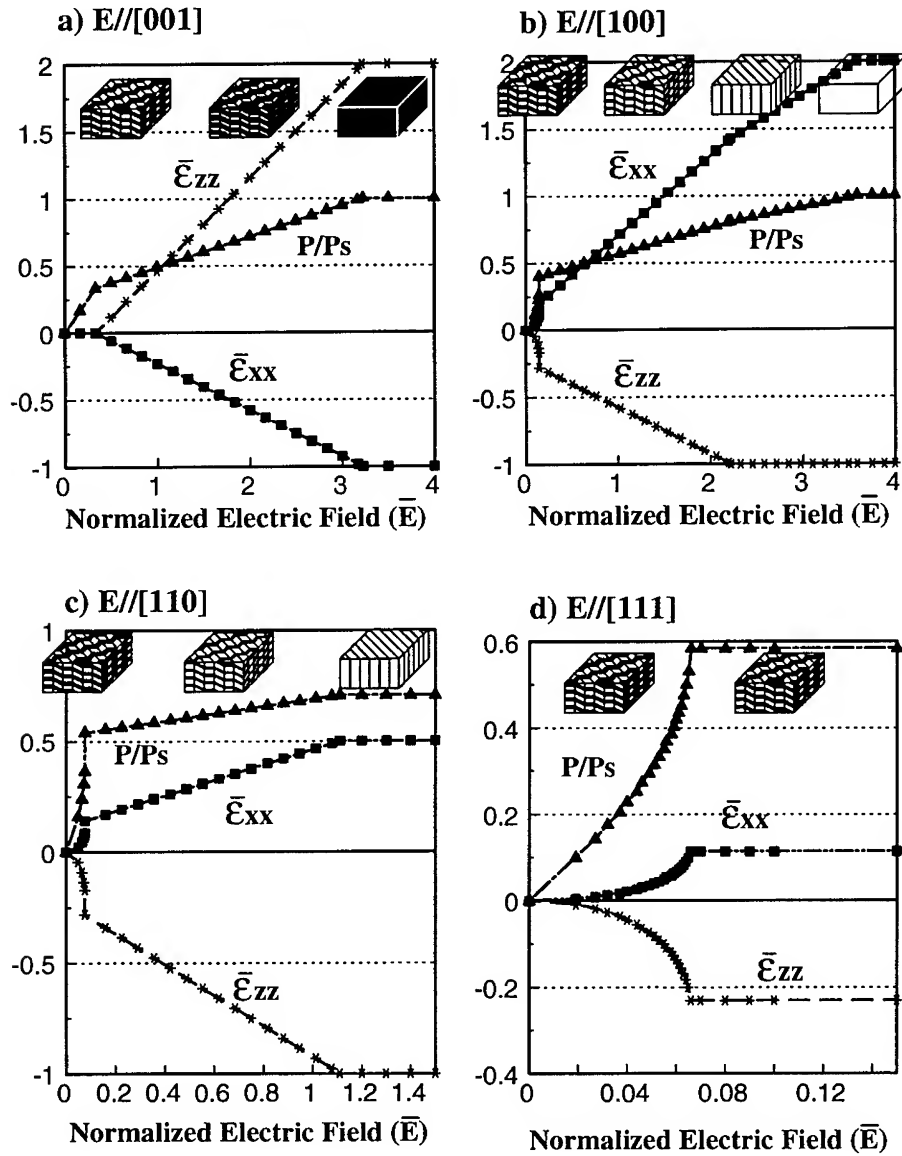


Figure 4. The dependence of the polarization and the deformation under different electric fields at same constraint condition ($\varphi=0.3$ and $\beta=0$).

$$\begin{aligned}
\alpha_3 &= [(1-\beta)\alpha_3^0 + \varphi \bar{E}]/(1-\beta + \varphi), & \bar{\epsilon}_{zz} &= (\kappa+1)[- \varphi \alpha_3^0 + \bar{E}]/(1-\beta + \varphi) & \text{along } E//[001] \\
\alpha_3 &= [(1-\beta)\alpha_3^0 - \frac{1}{2}\varphi \bar{E}]/(1-\beta + \varphi), & \bar{\epsilon}_{zz} &= (\kappa+1)[- \varphi \alpha_3^0 - \frac{1}{2}\varphi \bar{E}]/(1-\beta + \varphi) & \text{along } E//[100] \\
\alpha_3 &= [(1-\beta)\alpha_3^0 - \varphi \bar{E}]/(1-\beta + \varphi), & \bar{\epsilon}_{zz} &= (\kappa+1)[- \varphi \alpha_3^0 - \varphi \bar{E}]/(1-\beta + \varphi) & \text{along } E//[110] \\
\alpha_3 &= [(1-\beta)\alpha_3^0]/(1-\beta + \varphi), & \bar{\epsilon}_{zz} &= (\kappa+1)[- \varphi \alpha_3^0]/(1-\beta + \varphi) & \text{along } E//[111]
\end{aligned} \tag{7}$$

where $\bar{\epsilon}_{zz} = [\epsilon_{zz}(E) - \epsilon_{zz}(E=0)]/\epsilon_o$, $\varphi = \xi_E P_s^2/[G\epsilon_o^2(1+\kappa)^2]$, $\bar{E} = E/(\xi_E P_s)$

$\bar{\epsilon}_{zz}$ and \bar{E} are a normalized strain and electric field where $\bar{\epsilon}_{zz}(E=0)$ corresponds to a reference state. φ is the ratio between the electric and the mechanical energy which is of the order of 0.1~1 for BaTiO₃, PbTiO₃, and PZT.

The polarization and the deformation under the electric field are essentially different in the dependence on the constrain condition as shown in Figure 3 and the absence or presence of depolarization charges creating additional resistance to the polarization.

According to Equation (7), domain structures depend on the direction of polarization as shown in Figure 4: 1) In $E//[001]$, the enthalpy contribution due to the electric field less than saturated polarization of domain 3 is not dependent on the size of domain 3. Further polarization proceeds against the mechanical resistance in broadening domain 3 without passing through the polytwin. 2) In $E//[100]$, $E//[110]$ and $E//[111]$, the enthalpy contribution of electric field at $E < E_{cr}$ are valid due to the increase the domain fraction with polarization vector close to the applied direction. 3) In $E//[100]$, as the electric field increase, the domain structure goes through four different states. 4) In $E//[111]$, the polarization is obtained for very small electric field and the domain structure is slightly changed.

The calculation shows that considerable strains can be obtained in polydomain composites under relatively small electric fields.

ACKNOWLEDGEMENT

This work was supported by the Office of Naval Research under Contract No. N00014-93-1-0506.

REFERENCES

1. A.L. Roytburd, *Phase Transitions*, **45**, 1 (1993).
2. A.L. Roytburd, in *Solid State Physics* vol. 33, edited H. Ehrenreich, F. Seitz, and D. Turnbull (Academic Press, New York, 1978), pp. 317-390.
3. A.L. Roytburd, in *Shape Memory Materials and Phenomena - Fundamental Aspects and Applications*, Mat. Res. Soc. Symp. Proc. **246**, 91 (1992).
4. A.L. Roytburd and Yongsik Yu, *Ferroelectrics*, **144**, 137 (1993).
5. G. Arlt, N.A. Pertsev, *Ferroelectrics*, **132**, 27 (1992); *J. Appl. Phys.* **70**, 2283 (1991).
6. S. Li, W. Cao, R.E. Newnham, L.E. Cross, *Ferroelectrics* **139**, 25 (1993); V. Sundar, R.E. Newnham, *ibid.*, **135**, 431 (1992).
7. W. Cao, L.E. Cross, *Phys. Rev. B*, **44**, 5 (1991); S. Li, W. Cao, L.E. Cross, *J. Appl. Phys.* **69**, 7219 (1991).
8. B.S. Kwak, A. Erbil, B.J. Wilkens, et al., *Phys. Rev. Lett.* **68**, 3733 (1992).
9. Y. Ohba and M. Daimon et al., *Jpn. J. Appl. Phys.* **33**, 5305 (1994); *ibid.*, **32**, 4095 (1993); *ibid.*, **31**, 3090 (1992).
10. A.L. Roytburd and Yongsik Yu, in *Twinning in Advanced Materials*, edited by M.H. Yoo and M. Wuttig (The Mineral, Metals & Materials Society, 1994) pp. 217-230.

OPTICAL NON-INVASIVE EVALUATION OF FERROELECTRIC FILMS/ MEMORY CAPACITORS

SARITA THAKOOR*, A. P. THAKOOR* AND L. ERIC CROSS**

*Jet Propulsion Laboratory, California Institute of Technology, Pasadena, CA 91109

**Pennsylvania State University, Materials Research Laboratory, University Park, PA

ABSTRACT

NON-INVASIVE photoresponse (photocurrent/voltage, reflectance and transmittance) from ferroelectric thin films and memory capacitors, with its strong dependence not only on the remanent polarization, but also on the film microstructure, crystal orientation, and nature of the interfaces (state of formation/degradation, etc.) offers an excellent "tool" for probing the ferroelectric capacitors at virtually any stage of fabrication, including on-line quality control. In fact, simultaneous measurement of spectral photoresponse and spectral reflectance, as a distinctive signature of the device probed, is an ideal, high speed, non-invasive means of evaluation for such thin films at high spatial resolution (~ 100 nm) using beam scanning. This paper discusses three aspects of such evaluation. First, the spectral transmittance of the film as a direct function of the microstructure, second, the use of band-gap illumination (365 nm) to condition a fatigued capacitor; and third, the optical E field interaction with the ferroelectric capacitor, yielding a high speed photoresponse which is related to the remanent polarization and the operational history (status of internal fields) of the ferroelectric capacitor. Combined, these different kinds of photoresponses provide a good signature of the device quality.

INTRODUCTION

Non-volatile ferroelectric memories are now in the advanced stages of development where issues such as high-yield manufacturability and long-term reliability are receiving increasing attention today. The leading implementation scheme¹⁻⁴ selected for the VLSI ferro-memories is based on remanent polarization within a ferroelectric capacitor, where the high speed switching of the polarization state provides a memory readout.

The performance characteristics (such as **fatigue**: loss of polarizability with read-write cycling, and **memory retention** issues-(a) aging: logarithmic decay of remanent polarization with storage time (b) imprint: the tendency of polarization to gradually return to a previously written state leading to a bit error) of ferroelectric memory capacitors are governed by parameters such as:

- (a) stability of the electrode/ferroelectric interfaces,
- (b) orientation/epitaxy/crystallization status of the ferroelectric film,
- (c) microstructure of the film: compactness, void density, surface smoothness, grain size, etc. and
- (d) operational history.

Although all such device parameters listed above are typically attempted to be well-controlled during the fabrication of the memories, there is no suitable "tool" to conveniently and non-destructively "probe" the memory cells (during or after fabrication), with high spatial resolution and at high speed, for their polarization behavior which in effect dictates their ultimate

performance with respect to fatigue, lifetime, imprint, etc. These problems are suspected to be originating due to the following causes:

- (a) charged mobile defects (such as oxygen vacancies),
- (b) existence of a-axis inclusions/90° domain walls,
- (c) charge injection from the electrodes into traps in the ferroelectric material, and
- (d) polarization of slow moving dipoles.
- (e) phase transformation from ferroelectric to non-ferroelectric phase

Particularly fatigue is suspected to occur because of the screening of the applied voltage/pinning of domains by the accumulated space charge/defects/traps. In the recent past^{1,2,5}, significant strides have been made to address the issue of fatigue with the advent^{5,6} of new fatigue free, bismuth strontium tantalate thin films and oxide/perovskite electrodes that provide a more stable chemical/structural template for the growth of the ferroelectric thin film. Long term retention problems such as imprint, however, continue to be a major reliability impediment.

NON-INVASIVE photoresponse (photocurrent/voltage, reflectance and transmittance) from ferroelectric thin films and memory capacitors⁷⁻¹⁵, with its strong dependence not only on the remanent polarization, but also on the film microstructure, crystal orientation and nature of the interfaces (state of formation/ degradation, etc.) offers¹⁶ just such an ideal "tool" for probing the ferroelectric capacitors at virtually any stage of fabrication, including on-line quality control. In fact¹⁶, simultaneous measurement of spectral photoresponse and spectral reflectance, as a distinct signature of the device probed, is an ideal, high speed, non-invasive means of evaluation at high spatial resolution (~100 nm) using beam scanning. This paper discusses three aspects of such evaluation of ferroelectric lead zirconate titanate (PZT) thin films. First, the spectral transmittance of the film as a direct function of the microstructure, second, the use of band gap illumination (365 nm) to condition a fatigued capacitor; and third, the optical E field interaction with the ferroelectric capacitor using pulsed lasers at 532 nm, yielding a high speed photoresponse which is directly related to the remanent polarization and the operational history (status of the internal fields) of the ferroelectric capacitor. This high speed photoresponse promises to be a unique non-invasive measure of the internal fields in the ferroelectric device as an evolving function of operation history, storage time and environmental history. Combined, these different kinds of photoresponses provide a good signature of the device quality.

EXPERIMENTAL DETAILS

PZT Sputter Deposition

The PZT films were deposited by multi-target dc-reactive sputtering of lead, zirconium and titanium sequentially on a substrate rotating about the central axis of the chamber. The details of the chamber and sputtering process are discussed elsewhere¹⁷. A variety of substrates, including borosilicate glass, quartz, indium tin oxide (ITO) coated glass, sapphire, and passivated silicon were used for the deposition. No intentional substrate heating was used. The temperature of the substrate during deposition was monitored using a thermocouple and was observed to stay below 60°C. The sputtering was carried out in a reactive gas mixture of high purity (99.999%) argon (inert gas) and oxygen (reactive gas). The flow rates of Ar and O₂ were independently controlled by their respective flowmeters. The deposition routine typically consisted of setting up the argon ambient and presputtering the targets to clean the surface. Next, oxygen was added and the ambient stabilized. The target powers were set and the targets conditioned. Following this, the shutter was removed and deposition initiated on the rotating

substrates. Typical deposition conditions in our chamber for obtaining PZT films at the morphotropic phase boundary are presented elsewhere¹⁷.

As deposited, the films were amorphous. The composite film so obtained was baked in an open air furnace at 525°C for one half hour after attaining steady temperature to yield the Zr rich rhombohedral phase. The surface topography of these films was studied using a Cambridge S250 Scanning Electron Microscope. The transmission response of these films in the spectral range of 200 nm to 800 nm was observed using a Carey Model 5A Spectrophotometer.

Sol-Gel Deposition

The sol-gel lead zirconate titanate (PZT) thin films with a nominal composition of (Zr:52, Ti:48) were deposited by a modified Sayer's Technique^{18,19} on oxidized silicon substrates covered with an evaporated Ti/Pt ($\sim 1000 \text{ \AA}/1000 \text{ \AA}$) base electrode. The lead zirconate titanate (PZT) film contained $\sim 18\%$ excess lead and were $\sim 2000 \text{ \AA}$ thick. Crystallization of the as deposited PZT was accomplished by annealing the films at 550°C for 10 minutes in oxygen ambient. To complete a standard sandwich capacitor test structure⁸, semitransparent thin films of platinum ($\sim 150 \text{ \AA}$ thick) were sputter-deposited as the top electrode. The top electrodes were patterned by conventional lift-off techniques as dots of 125 μm and 250 μm diameter. Optical transmission through the semitransparent top electrode films ($\lambda = 300$ to 800 nm) was about 30%.

365 nm Illumination Set-up

Photonic probing at 365 nm was done using a short arc mercury lamp as the near UV/visible (300 nm to 600 nm) illumination source with the strongest line at 365 nm isolated using a filter. The choice of this light source to obtain maximum photoresponse was motivated by the bandgap value of PZT $\sim 3.5 \text{ eV}$ ¹¹. A custom built liquid light guide was utilized to deliver a 5 mm divergent beam with an intensity of $\sim 0.1 \text{ watt/cm}^2$ onto the sample. A shutter controlled by a solenoid valve allowed a pulse illumination with a minimum pulse length of about 1 sec. The effect of this illumination on fatigued and unfatigued capacitors was observed. The details of the set-up utilized have been presented elsewhere^{12,20}. The hysteresis loops were all recorded at a 500 Hz frequency.

High Speed Photoresponse Set-up

The high speed photoresponse measurements were done using an energetic laser pulse. The doubled output at 532 nm from a Nd-YAG pulsed laser utilizing accousto-optic switching was used for this experiment. The advantages of utilizing an accousto-optically switched laser over the electro-optically switched laser^{7,9,10}, in obtaining a low noise response signal free from electromagnetic pickup of the high voltages ($\sim \text{KV}$) used for electro-optic switching, have been illustrated elsewhere¹⁵. The incident photon energy was lower than the PZT bandgap (3.5 eV)¹¹, and was therefore weakly ($< 1\%$) absorbed by the PZT. The laser pulse, has a full width at half maximum (FWHM) of $\sim 10 \text{ ns}$ and delivers power in the range of $2 \text{ mW}/\mu\text{m}^2$ - $20 \text{ mW}/\mu\text{m}^2$ per pulse at 532 nm at a repeat frequency of 20 KHz. For the measurement of the photocurrent,

the top and bottom electrodes of the ferro-capacitor were connected across the $50\ \Omega$ internal impedance of an oscilloscope, which recorded the zero bias photoresponse from the capacitor on illumination with the laser pulse. The capacitor was poled positively by using a +4 V pulse for 1 msec or negatively by a -4 V pulse for the same duration.

RESULTS AND DISCUSSION

Surface Topography & Optical Transmission Correlation

The angle of incidence of the sputter deposit was a very critical parameter in determining the morphology and physical characteristics of the films. Fig. 1a shows the Scanning Electron Microscope (SEM) picture of the surface of a film deposited in an unrestricted manner, allowing all angles of deposition. This film (type A film) was rough, opaque, and of ceramic quality. Fig. 1b shows the surface micrograph of a film obtained using identical deposition parameters, except a collimator around each gun, restricting the deposition to a near-perpendicular incidence. Transparent electro-optic quality films (type B film) were obtained as a result of this restriction in the incidence angle of deposition. As expected, devices made from films of type B exhibited higher yield, unlike the type A films which suffered from frequent shorts.

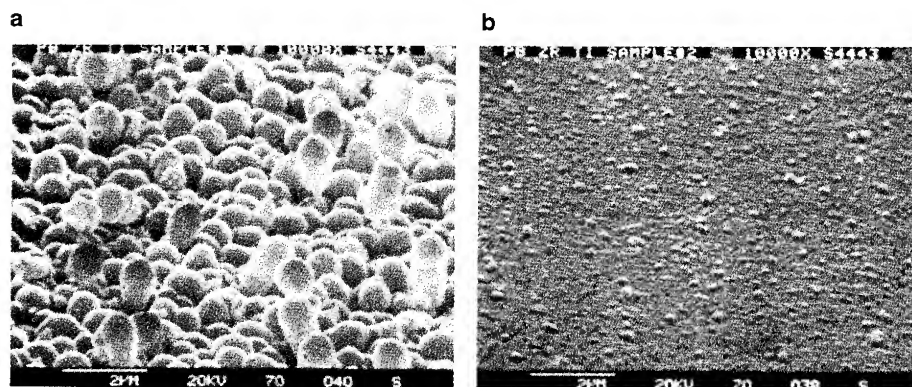


Figure 1: SEM photographs of (a) sputtered PZT film with surface roughness $\sim 1\ \mu\text{m}$ (Type A film) (b) PZT sputtered at near perpendicular incidence angle of deposit, lowering surface roughness to $\sim 0.2\ \mu\text{m}$ (Type B film).

Figs. 2(a) and 2(b) are the transmission spectra for PZT with surface topographies corresponding to Figs. 1(a) and 1(b) respectively. Therefore, as is well-known, the transmission spectra serve as a simple screening tool for films with high surface roughness and high optical scattering from the films with good optical transmission quality.

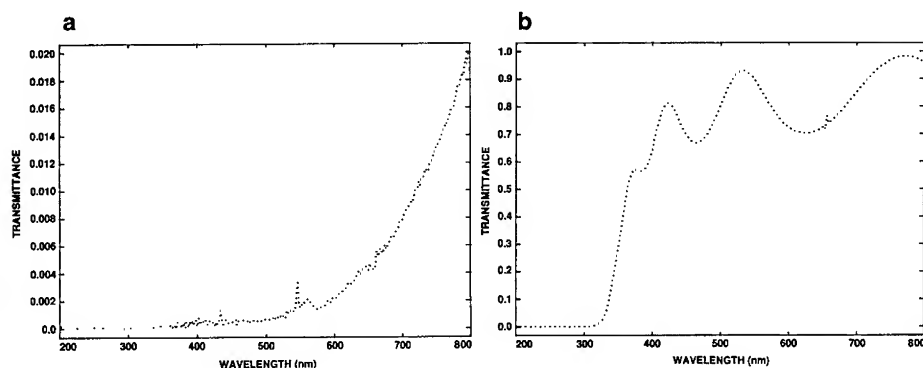


Figure 2: Comparison of Transmission Spectra of multimagnetron DC Sputtered PZT (a) Type A and (b) Type B films respectively

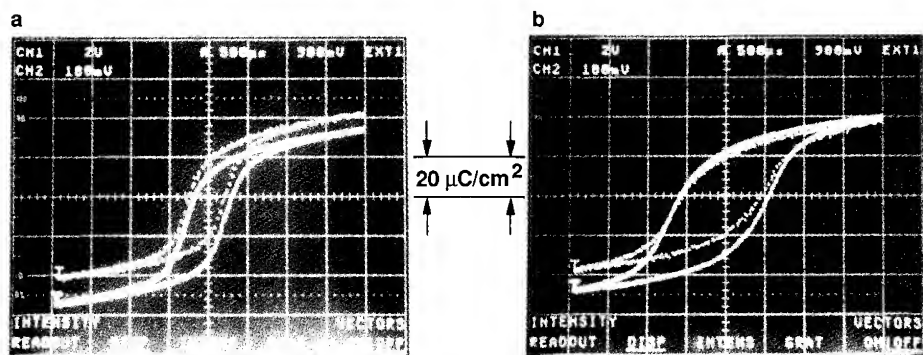


Figure 3: Comparison of (a) unfatigued and (b) fatigued state, 10^8 cycles, hysteresis loops without (dotted line) and with 365 nm illumination (full line)

Effect of 365 nm Illumination on Ferroelectric Memory Device:

Figure 3(a) shows the effect of band-gap light (365 nm) illumination on a fresh unfatigued ferroelectric memory capacitor. The dotted hysteresis loop is the one with no illumination and the solid line exhibits the hysteresis loop with illumination on (10 sec pulse of 365 nm). It clearly shows that the 365 nm illumination causes the hysteresis loop to shift along the Y-axis and also there is a marked blooming of the hysteresis loop. Earlier ⁸⁻¹² we have reported on the generation of a photovoltage/photocurrent due to such illumination for the duration of the light pulse. The figure 3(b) shows a similar comparison of the "with" and

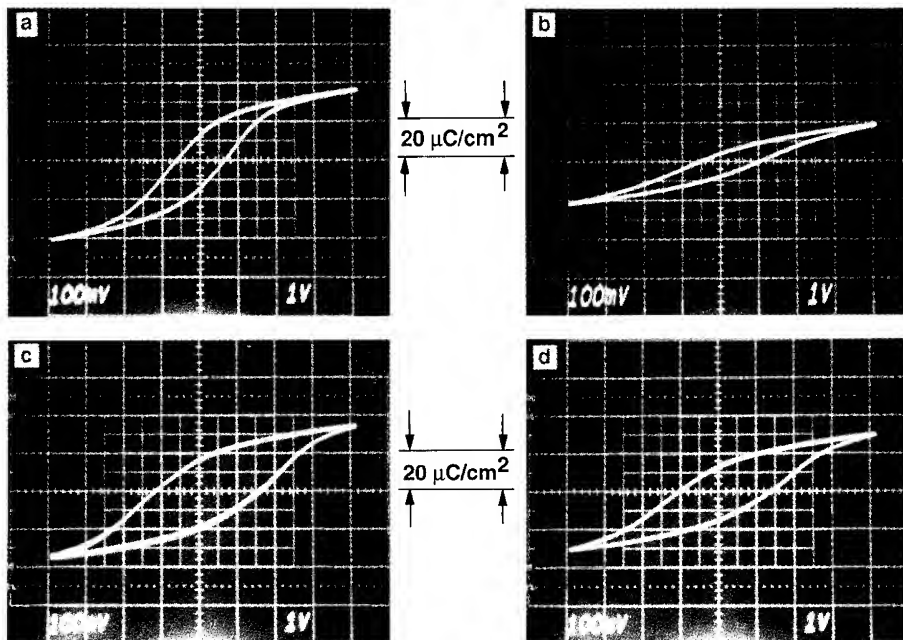


Figure 4: Comparison of hysteresis loops at 500 Hz, (a) unfatigued state (b) fatigued to 10^{10} cycles (c) fatigued state: first loop after illumination turn - off, (d) fatigued state: steady state loop - five hours after illumination turn off.

"without" illumination states of the hysteresis loop for this memory capacitor fatigued to $\sim 10^8$ cycles. However, in both these cases when the illumination was removed, the hysteresis loops reverted back to their original unilluminated status. This suggests that the unfatigued capacitors and mildly fatigued capacitors primarily show only a reversible photoinduced change. Also it is noteworthy that this mildly fatigued capacitor has changed its characteristics with respect to the fresh capacitor, only as a slight increase in its coercive voltage, however, its remanent polarization remains virtually unchanged. Figure 4 illustrates the effect of the 365 nm illumination on the ferroelectric capacitor fatigued to 10^{10} cycles. Figure 4(a) is the loop for the fresh unfatigued capacitor, Fig. 4(b) is the capacitor fatigued to 10^{10} cycles, Fig. 4(c) is the loop just after turn-off of illumination and figure 4(d) is the loop in the steady state 5 hours after turn-off of illumination. The illumination could thus be used as a quick indicator/estimator of the status of the fatigue.

Cycling has two effects: increase in coercive voltage, V_c , and reduction in remanent polarization, P_R . The increase in V_c appears to be due to the irreversible degradation in the ferroelectric film (possibly a phase transformation from ferroelectric to non-ferroelectric phase either within the film or at the ferroelectric/electrode interface). V. K. Chivikula²¹ has also suggested the formation of a non-ferroelectric surface layer based on their dispersion data. The decrease in P_R on the other hand is due to local screening of the applied voltage. This could arise from presence of charged defects and /or traps that could pin the domains. As is observed,

the reduction in P_R is clearly recoverable (by 365nm illumination). The temporal nature of the enhancement of the hysteresis loop in terms of remanent polarization suggests the existence of traps with different time constants. Illumination induced charge pairs could either recombine with the free space charge and/or cause emptying of the filled traps. On one hand, the net result is to give rise to the observed^{8,11} steady photocurrent for the duration of the illumination. On the other hand, this also leads to removal of the local screening fields due to the space charge and/or unpinning of domains pinned by the traps and hence, a recovery of the fatigued state by regaining the loss of polarization. Such a loss of polarization and its recovery (by 365 nm illumination) therefore appears to be predominantly electronic (trap mediated) in nature. Similar observation of recovery from fatigue by UV illumination has been made by Warren et al²² and Lee et al²³. However, in order to avoid confusion from the temporary photoeffects, the photoinduced recovery must be verified beyond just one switching cycle (or a single hysteresis loop). A temporary compensation/cancellation of the screening field by photoinduced charges would clearly not qualify as a photo-triggered recovery.

It is interesting to note that the bandgap illumination either has no effect on the coercive voltage, or in the fatigued cases, causes a slight increase in the coercive voltage suggesting that the re-distribution of the charges could lead to a net increase of the resistive layer. This further re-affirms the contention that this initial mode of fatigue (increase in V_C) is material degradation and is not easily recovered by illumination.

High Speed Photoresponse Results

A bipolar high speed photoresponse is obtained from freshly made capacitors and capacitors with bipolar cycling history for positive and negatively poled states respectively.

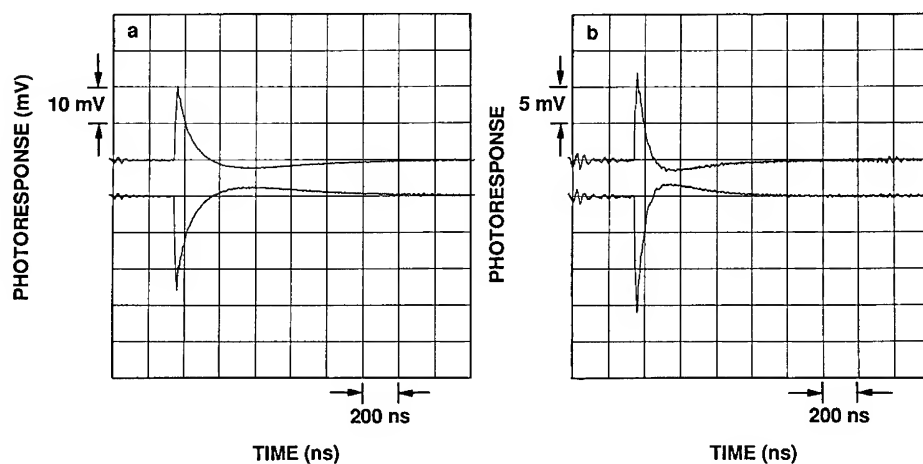


Figure 5: Comparison of High Speed Photoresponse (a) unfatigued state and (b) fatigued state.

Table 1. High speed photoresponse, ratio of area under the peak, and comparison with corresponding ratios of remanent polarization as obtained from conventional hysteresis loops, for unfatigued and fatigued capacitors respectively.

Polarity of Applied Voltage	$P_{R, unfatigued} / P_{R, fatigued}$ Determined By hysteresis loop	$A_{R, unfatigued} / A_{R, fatigued}$ Determined By Photoresponse
positive	2.57	2.57
negative	2.62	2.65

Figure 5 shows a comparison of the high speed photoresponse from the unfatigued and fatigued states of the memory capacitor (Pt/PZT/Pt). The capacitance of the unfatigued state was 2.4 nF and the capacitance of the fatigued state was 1.3 nF. This data was compared with the corresponding hysteresis loop data for the unfatigued and fatigued states of the memory, respectively. As shown in table 1, the ratio of the unfatigued remanent polarization ($P_{R, unfatigued}$) to the fatigued remanent polarization ($P_{R, fatigued}$) as determined from the hysteresis loops is identical to the ratio of the corresponding area under the peaks of the photoresponse signal for unfatigued ($A_{R, unfatigued}$) and fatigued ($A_{R, fatigued}$) case. This clearly shows that the area under the photoresponse signal is proportional to the remanent polarization of the memory capacitor. Also, the area under the photoresponse signal is interpreted^{6,8-10} as being proportional to ΔP , the net shift in the dipole moment due to the incidence of energetic laser pulse onto the capacitor. The area under the photoresponse peak therefore provides an excellent non-invasive, quantitative measure of remanent polarization. Further, we observe that the speed of the photoresponse is directly dictated by the device capacitance and hence, the photoresponse is expected to become faster with reducing ferroelectric pixel size, allowing very high speed non-invasive measure of the memory state for the high density memories. The illumination pulse is non-invasive. The change ΔP is followed by an equivalent $-\Delta P$ so that there is no net change in the remanent polarization, P_R , as verified by cross checking using the conventional pulse switching measurement (DRO). Also, it was verified that the remanent polarization did not change for over 10^8 laser pulse readout cycles.

Measurement of the photoresponse as a function of frequency shows that the amplitude of the response saturates for frequencies lower than 10 KHz suggesting that this transient response attains its maximum value at $\sim 100 \mu\text{sec}$. The rising edge of the response may contain higher speed ($\leq 10 \text{ ns}$) contributions from the photovoltaic effect and/or photoresponse due to deep traps occurring at the incident wavelength of 532 nm. If isolated, identification of such deep traps and the ability to probe their evolution as a function of the process parameters /operation cycles/environmental stress cycling can be another useful aspect of this technique to provide feedback on the materials/device quality control.

The mechanism^{6,8} by which the shift ΔP occurs could be pyroelectric (thermally triggered, associated with temperature change within the PZT), piezoelectric (due to propagation through PZT of an acoustic deformation wave, initiated by a sudden thermal expansion of the platinum top electrode), or optical rectification (due to interaction of the E-field associated with the incident photons and the internal fields within the ferroelectric).

Furthermore, the photoresponse has a dependence on the history of the memory capacitor. Fig. 6 illustrates how the high speed photoeffect sensitively reflects the polarization history of the ferroelectric capacitor. A history has been induced in an accelerated manner by applying a unidirectional voltage for extended duration of 10 sec. The figure shows that the conventional pulse polarization destructive read-out (DRO) merely exhibits a slight asymmetry

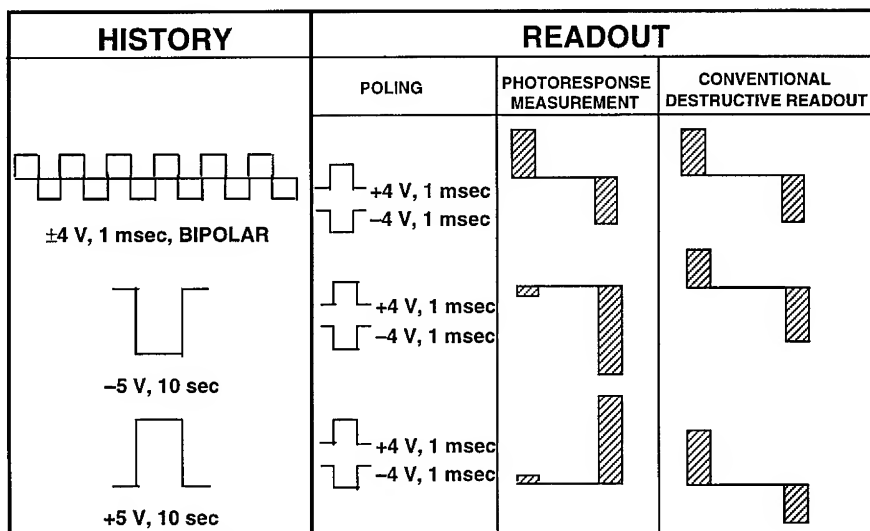


Figure 6: Photoresponse probing of "history" of the ferroelectric capacitors and comparison of photoresponse peak amplitude data with corresponding conventional destructive readout data of remanent polarization.

as a reflection of the history. In contrast, the high speed photoresponse shows an overall change from bipolar to unipolar response and therefore, is used directly for detecting the operational/environmental history of the ferroelectric memory **non-invasively**. This result may be of significant fundamental importance because it demonstrates that the photoresponse signal in addition to its dependence on remanent polarization is also dependent on the status of the evolving internal fields within the ferroelectric (i.e., is the optical rectification effect). Such measure of the internal screening fields within the ferroelectric is not available as sensitively and non-invasively by conventional electrical techniques.

CONCLUSIONS:

UV Illumination (365 nm) can be used to condition/recover the loss of polarization in fatigued ferroelectric memories and such photoresponse can also serve as a quick indicator/estimator of the status of fatigue in a ferroelectric capacitor.

The high speed photoeffect provides an excellent non-invasive, quantitative measure of remanent polarization and reflects sensitively the polarization history of the ferroelectric capacitor suggesting a unique measure of the internal fields within the ferroelectric. If the subtle reflections of the complex fatigue and retention characteristics of a device on its high speed photoresponse could be properly harnessed, it holds the potential for an effective quality control and reliability screening tool.

ACKNOWLEDGEMENTS

Useful discussions with Dr. Steve Bernacki on film deposition and Dr. Wayne Kinney and Dr. Dan Gealy on ferroelectric memories are gratefully acknowledged. Expert help from Dr. Hamid Hemmati and Mr John Michael Morookian on the high speed photoresponse measurement set-up are gratefully acknowledged. The work described in this paper was performed by the Jet Propulsion Laboratory, California Institute of Technology, and was sponsored in parts by the National Aeronautics and Space Administration's Office of Space Access and Technology and the JPL Director's Research and Development Fund.

REFERENCES

1. W. Kinney, *Integrated Ferroelectrics*, **4**(2), 131, (1994).
2. W. Kinney and F. D. Gealy, *IEEE International Solid State Circuits Conference*, p. 266, (1994).
3. J. T. Evans and R. Womack, *An Experimental 512 bit Non-volatile Memory with Ferroelectric Storage Cell*, *IEEE Journal of Solid-State Circuits*, **23**, 1171-1176 (1988).
4. D. Bondurant and F. Gnandinger, *Ferroelectric Non-volatile RAMs*, *IEEE Spectrum*, **18**, 30-33 (1989).
5. J. F. Scott and C. A. Paz De Araujo, *Ferroelectric Memories*, *Science*, **246**, 1400-1405 (1989). *Proceedings of the International Symposium on Integrated Ferroelectrics 1993 and 1994 - Integrated Ferroelectrics Volume 4 & 5. Ferroelectric Thin Films II (Vol. 243) and III (Vol. 310)*, Published by Materials Research Society.
6. M. Huffman, C. A. Paz De Araujo, L. D. McMillan, M. C. Scott and C. Echer, *Paper # I2-10.3, Proceedings MRS Symposium on Ferroelectric Thin Films IV, Vol 361, (Fall 1994)*.
7. S. Thakoor, *Appl. Phys. Lett.* **60**, 3319, 1992.
8. S. Thakoor, A. P. Thakoor and S. E. Bernacki, *Proc. Third International Symposium on Integrated Ferroelectrics*, Pg. 262, April 3-5, 1991, Colorado Springs, Colorado.
9. S. Thakoor, *Appl. Phys. Lett.* **63**, 3233, 1993.
10. S. Thakoor, *Ferroelectrics*, **134**, 355, 1992.
11. S. Thakoor and J. Maserjian, "Photoresponse Probe of the Space Charge Distribution in Ferroelectric PZT Thin Film Memory Capacitors" *J. Vac. Sci. & Tech A*, **12**, 295, Mar/April (1994). C. E. Land, *J. Am. Ceram. Soc.*, **72**, 2059 (1989).
12. S. Thakoor, *Journal of Appl. Physics*, **75** (10), 5409, May 15 (1994). S. Thakoor, U.S. Patent # 5372859, December 13, 1994.
13. S. Thakoor, E. Olson and R. H. Nixon, "Optically Addressable Ferroelectric Memory and its Applications" *Integrated Ferroelectrics*, **4**, 257 (1994).
14. S. Thakoor and A. P. Thakoor, "Optically Addressed Ferroelectric Memory with Non-Destructive Read Out", *Applied Optics* (in press, 1995).
15. S. Thakoor, J. M. Morookian, H. Hemmati and A. P. Thakoor, *International Symposium of Applied Ferroelectrics held August 7-10, 1994 at Penn State Scanticon, State College, Pennsylvania* (unpublished).
16. S. Thakoor, *New Technology Report # NPO - 19393/8994*. S. Thakoor, *NASA TechBriefs*, Vol. 17, p. 54 May (1993).
17. S. Thakoor, U. S. Patent # 5196101, March 23, 1993.
18. G. Yi, Z. Wu and M. Sayer, *J. Appl. Phys.* **64**, 2717 (1988).

19. S. E. Bernstein et al., Proc. MRS Fall Meeting: Symposium on Ferroelectric Thin Films II, Vol 243, p 343, Published by Materials Research Society, Pittsburgh, Pennsylvania, Boston, Dec 2-4 (1991).
20. M. Lakata and S. Thakoor, "Automated Ferroelectric Capacitor Testing System", NASA Tech Briefs, **18**, 30 (1994)15.
21. V. K. Chivikula, Proceedings MRS Symposium on Ferroelectric Thin Films IV, Vol 361, (Fall 1994).
22. W. L. Warren, D. Dimos, B. A. Tuttle, R. D. Nasby, and G. E. Pike, Proceedings MRS Symposium on Ferroelectric Thin Films IV, Vol 361, (Fall 1994).
23. J. Lee, S. Esayan, A. Safari and R. Ramesh, Appl. Phys. Lett. **64** 3646 (1994).

PART VI

Magnetostrictive Materials and Applications

HIGH POWER MAGNETOSTRICTIVE MATERIALS FROM CRYOGENIC TEMPERATURES TO 250 C

ARTHUR E. CLARK
Clark Associates
Adelphi, MD 20783-1225, USA

ABSTRACT

The rare earths, both in elemental form and in compounds, are widely known as possessing many extraordinary magnetic properties. In this paper, we focus on the huge magnetically induced displacements (magnetostrictions) based upon the element terbium. A proper balance of magnetic anisotropy and magnetostriction, plus a proper choice of crystal axes lead to materials which can switch large quantities of energy between the internal (magnetic) and external (mechanical) states with the application of small triggering magnetic fields. Power densities 2000 times those of conventional magnetostrictive materials and 10-20 times those of typical piezoceramics are available. These materials are particularly valuable for smart systems where large energy transduction is needed such as active structure stiffening and active vibration control.

INTRODUCTION

One of the most important ways electrical energy can be converted into mechanical energy is via magnetostrictive materials. These materials do not need high electrical fields and are, in general, rugged, impervious to adverse environmental conditions, and have a record of high reliability. Failure mechanisms are few. Although efficiencies are somewhat lower in magnetostrictive actuators than in electromechanical actuators, magnetostrictive actuators do not suffer from electrical breakdown and malfunctions due to high voltage arcing. One of the long-standing shortcomings of magnetostrictive materials has been their characteristically low saturation strains ($\sim 5 \times 10^{-5}$). Clearly very large strains are needed to deliver the large displacements often required for smart system components. In this paper, we review the magnetostrictive properties of three classes of high power magnetostrictive materials: (1) the hexagonal $\text{Tb}_x\text{Dy}_{1-x}$ alloy system ($0 \leq x \leq 1$), (2) the body centered cubic (bcc) TbZn compound, and (3) the face centered (Laves Phase) cubic RFe_2 compounds ($\text{R} = \text{Tb}, \text{Dy}, \text{and Sm}$). The first two classes possess high magnetostrictions at cryogenic temperatures and at temperatures up to ~ 150 K. For the $\text{Tb}_x\text{Dy}_{1-x}$ system and the TbZn compound, ordering temperatures are ~ 200 K. Saturation magnetostrictions (λ_s 's) exceed 0.5% at 77 K.^{1,2} The $\text{Tb}_x\text{Dy}_{1-x}$ system is ductile and is very useful for compressive loads up to ~ 25 MPa. The magnetization process is rotational and the hysteresis is small. On the other hand, the intermetallic TbZn compound is machinable, does not flow under stress, and is useful up to much higher compressive loads (> 60 MPa). Because of a higher magnetic anisotropy, however, the hysteresis is larger. The cubic Laves phase RFe_2 compounds are unique. The combination of the highly magnetostrictive rare earths with strongly magnetic iron yields highly magnetostrictive materials with extraordinarily high ordering temperatures (~ 700 K). These compounds are not ductile and are particularly important at room temperature and above. At

these temperatures, the magnetostrictions are approximately 1/4 to 1/2 of the cryogenic materials. Saturation magnetostriction values (λ_s) are 0.1% to 0.3% over the -80 C to 250 C temperature range.³

Some magnetic and magnetostrictive properties of Tb, Dy, and compounds containing these elements are listed in Table I. Note that the densities of the Tb atoms in the cubic structures are about 2/3 of that in elemental Tb. Thus we expect that the intrinsic magnetostrictions (at absolute zero) of the compounds to be approximately 2/3 of that in the element. Even though the structures are all different the maximum magnetostrictions (λ_{γ^2} for Tb, λ_{100} for TbZn, and λ_{111} for TbFe₂) extrapolated to absolute zero are roughly proportional to the Tb atom densities.

Table I. Magnetic and Magnetostrictive Properties of Tb and Dy containing materials.

	T _C (K)	$\mu_0 M_{s,T \rightarrow 0}$ (Tesla)	$\lambda_{T \rightarrow 0}$ (10 ⁻³)	Tb atom density (atoms/nm ³)	Easy Axes	Reference
Tb	230	3.3	$\lambda_{\gamma^2} = 9.6$	31.3	[10·0] (b-axis)	4
Dy	179	3.6	$\lambda_{\gamma^2} = 9.4$	--	[11·0] (a-axis)	5
TbZn	204	2.2	$3\lambda_{100}/2 = 6.0^*$	21.9	[100],[110]	6
DyZn	140	2.3	$3\lambda_{100}/2 = 6.5$	--	[100]	6
TbFe ₂	710	1.4	$3\lambda_{111}/2 = 6.6$	20.2	[111]	3
DyFe ₂	635	1.6	$3\lambda_{111}/2 = 6.4^*$	--	[100]	3

* Extrapolated from higher temperatures.

In addition to the saturation magnetostriction (λ_s), two other magnetic properties are important for magnetomechanical transduction. They are: (1) the saturation magnetization (M_s) or magnetic moment per volume, and (2) the magnetic anisotropy energy (K). Since all the electrical energy which is transduced into mechanical energy must appear as magnetic energy within the material ($E_m = M_s \cdot H$), the magnetization should be high. Without a large magnetization the magnetic field strength (H) becomes unacceptably high. Both the cryogenic materials and the rare earth-iron compounds discussed in this paper have high magnetizations. See Table I. The magnetic anisotropy (K) is a measure of the difficulty of magnetization rotation. For large magnetic anisotropies, the magnetization process proceeds by domain wall motion, whereas for small magnetic anisotropies, the magnetization process proceeds primarily by reversible magnetization rotation. The less hysteretic magnetization rotation process is generally more preferable. Thus, in addition to the need for a large saturation magnetostriction, λ_s , it is desirable to maximize the magnetostriction to anisotropy ratio, λ_s/K .³ Methods which have been successful to improve this ratio, while maintaining both M_s and λ_s large, are discussed in the following sections for both the Tb_xDy_{1-x} alloy and the RFe₂ compounds.

Tb_xDy_{1-x} ALLOYS

The largest magnetostrictions known ($\lambda_s \sim 10^{-2}$) are the basal plane strains in the hexagonal rare earth metals Tb and Dy.^{4,5} Easy magnetization rotation and minimum hysteresis require a large basal plane magnetostriction to basal plane anisotropy ratio ($\lambda\gamma^2/K_6^6$). Fortunately, the rare earth elements Tb and Dy possess basal plane anisotropies (K_6^6 's) of the opposite sign. For Tb, the basal plane magnetic anisotropy $K_6^6 > 0$; for Dy, the anisotropy $K_6^6 < 0$. The easy axes shown in Table I reflect the signs of K_6^6 .

To determine the optimum Tb_xDy_{1-x} alloy for a given temperature, the value of x is chosen to minimize K_6^6 . The magnetostriction ($\lambda\gamma^2$) and anisotropy (K_6^6) were experimentally determined for Tb_xDy_{1-x} for x from 0 to 1.⁷ The magnetostrictions are shown in Fig. 1. Note that the values of $\lambda\gamma^2$ are large and almost independent of x at the lowest temperatures. From magnetostriction measurements as a function of magnetic field, the basal plane anisotropy constants K_6^6 for each temperature were calculated. See Fig. 2. From these measurements, the maximum values of $\lambda\gamma^2/K_6^6$ for each temperature can be determined. For $T \sim 60$ K, $x = .67$; ~ 100 K, $x = .5$; ~ 120 K, $x = .33$; ~ 135 K, $x = .17$.

An example of the huge magnetostrictions which are achieved by applying a magnetic field to Tb_xDy_{1-x} rods at 77 K is shown in Fig. 3. This figure illustrates the magnetostrictions found for Tb_{0.6}Dy_{0.4} under moderate loading conditions of 4.4 MPa and 12.4 MPa.

Here $K_6^6 \equiv 0$ and the desired full magnetostrain ($\lambda\gamma^2$) of $\sim 6.5 \times 10^{-3}$ is achieved with a low applied magnetic field. Thus a 10 cm rod of Tb_{0.6}Dy_{0.4} will expand ~ 0.65 mm at this temperature. Since K_6^6 is small, the magnetization process is essentially rotational, with saturation occurring at relatively low magnetic fields. The power capabilities of Tb_xDy_{1-x} magnetostrictive

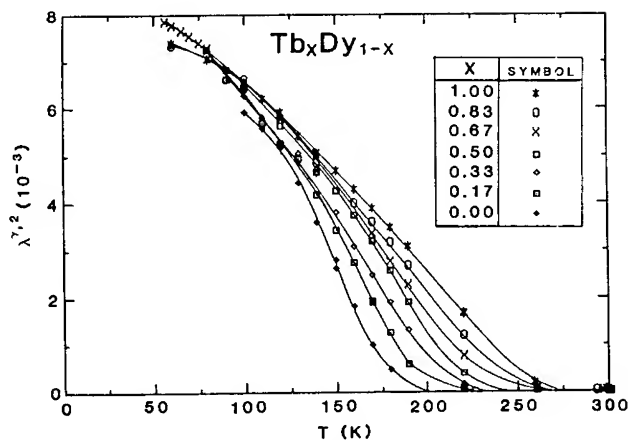


Fig. 1. $\lambda\gamma^2$ vs Temperature for Tb_xDy_{1-x}.

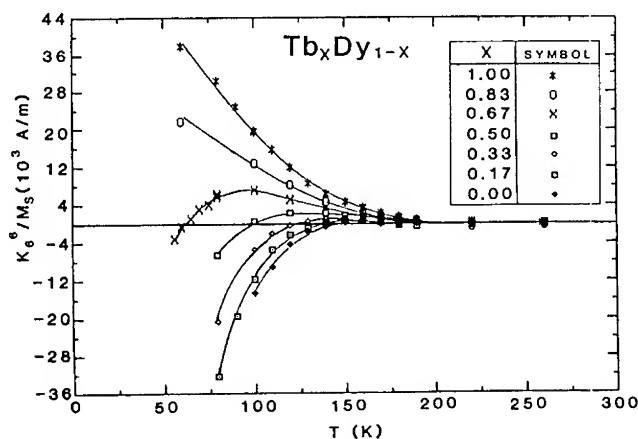


Fig. 2. K_6^6 vs Temperature for Tb_xDy_{1-x}.

devices can be estimated from Figures 1 and 2. For example, the Hooke's law blocked mechanical force is given by $F_b = -Y\lambda\gamma^2$ and the maximum elastic energy which can be stored is $E = (1/2)Y(\lambda\gamma^2)^2$, where Y (≈ 50 GPa) is the Young's modulus under blocked magnetic conditions (constant magnetic induction).¹

TbZn

Many of the RZn compounds crystallize into the cubic CsCl structure and thus the magnetostriction in these compounds to lowest order can be specified by two constants, λ_{100} and λ_{111} . In TbZn and DyZn, $\lambda_{100} \gg \lambda_{111}$.⁶ Therefore, like the Tb_xDy_{1-x} alloy system, sample orientation is

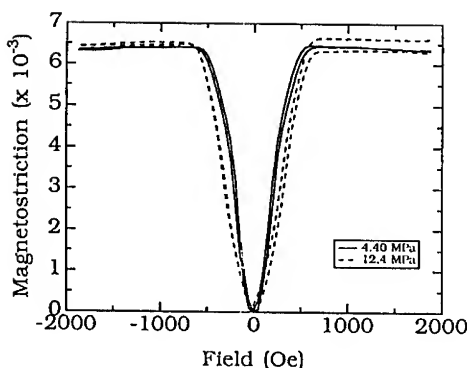


Fig. 3. Magnetostriction of a-axis rod of Tb_6Dy_4 at 77 K.

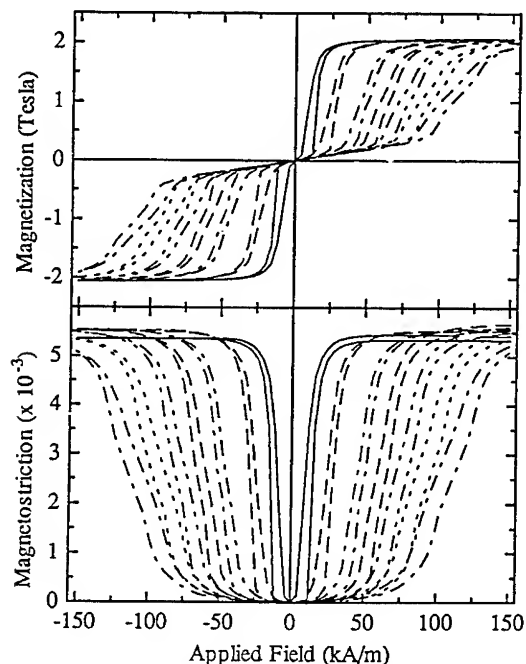


Fig. 4 Magnetization and magnetostriction of single crystal TbZn along the easy [100] axis at 77 K for compressive stresses of 5.3 MPa (—), 13.3 MPa (---), 24.6 MPa (-.-.), 31.1 MPa (---), 37.5 MPa (-----), 44.0 MPa (....), and 50.5 MPa (-----).

important for optimum performance. TbZn has $\langle 100 \rangle$ axes magnetically easy above 67 K and $\langle 110 \rangle$ axes easy below 67 K.⁸ At 77 K, single crystal samples of TbZn aligned along a [100] direction can magnetize easily via 90° domain wall motion, achieving very large saturation strains, $(3/2)\lambda_{100}$'s, in low applied magnetic fields.² See Fig. 4. Magnetostrictions at 77 K reach 5.5×10^{-3} , nearly equal to those of basal plane crystal Tb_6Dy_4 . However, unlike the Tb_xDy_{1-x} alloys, they can reach these large displacements even under high compressive loads. They are not ductile and do not deform. On the other hand, TbZn possesses a rather large intrinsic magnetocrystalline anisotropy at 77 K. The presence of a strong magnetocrystalline anisotropy can be seen in the magnetization (M) vs H and the magnetostriction (λ) vs H curves of Fig. 4. As a magnetic field is applied, three distinct

magnetic regions are observed: (1) a low field region consisting of a stress controlled magnetic moment rotation away from a perpendicular easy direction, (2) a region of high permeability and high magnetostriction where the magnetic moments rotate from a direction near the perpendicular easy axes to the easy [100] axis along the magnetic field direction, and finally (3) magnetic saturation. Compounds tailored for temperatures above the easy axis transition temperature of TbZn (67K) can be synthesized by substituting Gd for Tb in TbZn.⁹ Because of the higher Curie temperature of GdZn, the easy axis transition temperature increases, resulting in a lower magnetic anisotropy at these higher temperatures. Using

similar reasoning, one can optimize the compounds for temperatures below the TbZn easy axis transition temperature of 67 K by the substitution of Dy for Tb. Since DyZn has <100> easy axes at all temperatures, the easy axis transition temperature in the Tb_xDy_{1-x}Zn compounds move to lower temperatures. For these cubic compounds, the Hooke's law blocked mechanical force is given by $F_b = (3/2)Y\lambda_{100}$ and the maximum elastic energy which can be stored is $E = (9/8)Y(\lambda_{100})^2$, where Y is the Young's modulus for TbZn under blocked magnetic conditions ($Y \approx 50$ GPa).²

In this system the conversion of magnetic energy into mechanical work is almost perfect. Fig. 5 is a plot of the work done with the application of a magnetic field to single crystal TbZn along a crystallographic [100] direction. Measurements were taken at 77 K. The 45° solid line indicates unity transformation of magnetic energy into work. The open circles are the experimental results taken at various stress (σ) levels. Utilizing optimum values of magnetic d.c. bias, the same amount of work can be done with only small applied magnetic fields. These values are shown by the triangle data points. Thus a transfer between internally stored energy and external work is achieved with the application of only a moderate magnetic field.

SINGLE CRYSTAL AND POLYCRYSTAL RARE EARTH-IRON COMPOUNDS

Above temperatures of ~150 K, the magnetostrictions of the rare earth elements fall rapidly. Higher values of magnetostriction for room temperature devices must be achieved through rare earth compounds having high Curie temperatures ($T_C > 200$ C). Many materials, including rare earth-(3d) transition metal compounds, oxides and amorphous metals have been investigated. In

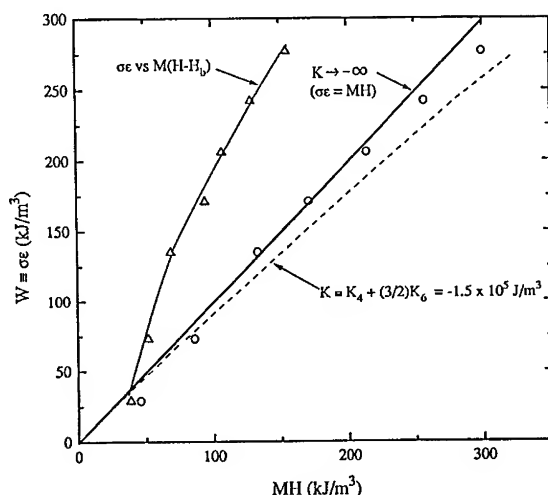


Fig. 5. Magnetic energy (MH) converted to work ($\sigma\epsilon$) during the magnetization process. The solid line represents lossless conversion.

Table II, the Curie temperatures T_C of some rare earth-Fe₂ and rare earth-Fe₃ compounds are listed, along with their room temperature magnetostrictions taken on polycrystal samples ($\lambda_{||} - \lambda_{\perp} = (3/2)\lambda_s$). These values are compared to the room temperature magnetostrictions of Ni, Fe, and Co. Large strains are found in the cubic TbFe₂ ($\lambda_s > 0$) and SmFe₂ ($\lambda_s < 0$) compounds. Strains in single crystals are even larger. Fig. 6 shows the temperature dependence of the single crystal magnetostriction ($\lambda_{||} - \lambda_{\perp} = (3/2)\lambda_{111}$) of TbFe₂ attained by 90° rotation of the magnetization.¹⁰ At room temperature $\lambda_{||} - \lambda_{\perp} = (3/2)\lambda_{111} \cong 3600 \times 10^{-6}$. This room temperature magnetostriction value for TbFe₂ is $\cong 60\%$ of the saturation strains of Tb_xDy_{1-x} and TbZn at 77 K.

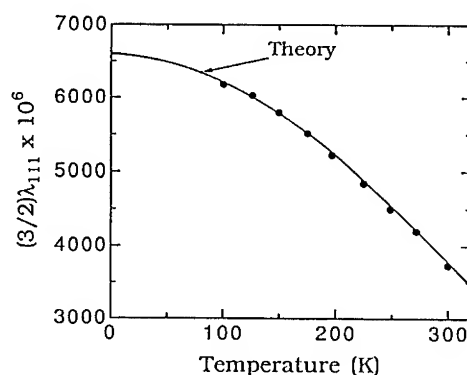


Fig. 6. Single Crystal Magnetostriction, $\lambda_{||} - \lambda_{\perp} = (3/2)\lambda_{111}$, of TbFe₂ for temperatures between 100 K and 300 K.

Table II. Magnetostriction and Curie Temperatures of Ni, Fe, Co, and some rare earth-iron compounds.*

Material	$(3/2)\lambda_s \times 10^6$	$T_C(^{\circ}\text{C})$
Ni	-50	360
Fe	-14	770
Co	-93	1130
SmFe ₂	-2340	415
GdFe ₂	59	525
TbFe ₂	2360	431
DyFe ₂	650	362
HoFe ₂	120	332
ErFe ₂	-449	320
TmFe ₂	-185	287
SmFe ₃	-317	377
TbFe ₃	1040	379
DyFe ₃	528	333
HoFe ₃	86	300
ErFe ₃	-104	280
TmFe ₃	-65	264

*From a compilation by A. E. Clark in Ferromagnetic Materials, Vol. I, Chapter 7 and K. H. J. Buschow, Vol. I, Chapter 4, ed. E. P. Wohlfarth, North Holland Press, 1980. For the rare earth compounds $(3/2)\lambda_s$ denotes $\lambda_{||} - \lambda_{\perp}$ at 25 kOe.

The magnetostrictions of all cubic materials, such as the highly magnetostrictive RZn and RFe₂ compounds, consist of contributions made by two constants, λ_{100} and λ_{111} , where λ_{100} represents the strain along the [100] direction as the sample becomes magnetized along this direction from a completely demagnetized state, and λ_{111} represents the strain along the [111] direction from the corresponding magnetization along the [111] direction. In contrast to the RZn compounds, where $\lambda_{100} \gg \lambda_{111}$,⁶ the large magnetostriction in the RFe₂ compounds are accounted for almost entirely by a strong λ_{111} ($\lambda_{111} \gg \lambda_{100}$).¹¹ Hence to achieve the highest magnetostrictions in these materials, crystallite orientations in which λ_{111} dominates is desirable.

Table III lists the saturation single crystal magnetostriction constant $(3/2)\lambda_{111}$ at room temperature and 0 K for the rare earth-Fe₂ Laves phase compounds. While the magnetostrictions are very large in many of these compounds, a large cubic magnetic anisotropy frequently inhibits easy magnetization rotation, particularly at low temperatures. In TbFe₂ and SmFe₂, having large magnetic anisotropies, the magnetization process proceeds primarily by non-reversible and hysteretic domain wall motion. To attain the more desirable domain rotation magnetization process, an alloy of the highly magnetostrictive TbFe₂ and DyFe₂ compounds was synthesized to maximize λ_{111}/K .³ TbFe₂ and DyFe₂ both possess large positive λ_{111} values, but possess opposite signs of magnetic anisotropy, K, and thus different easy directions of magnetizations. See Table I. For TbFe₂, K < 0; DyFe₂, K > 0. Similar to the cryogenic Tb_xDy_{1-x} alloy, to achieve a large magnetostriction/anisotropy (λ/K) ratio, we arrive at the alloy Tb_xDy_{1-x}Fe₂ (Terfenol-D). Like the magnetostriction and magnetic anisotropy of Tb_xDy_{1-x}, λ and the anisotropy constant K are both temperature dependent. At room temperature anisotropy compensation ($K \approx 0$) occurs with $x = 0.27$ in Tb_xDy_{1-x}Fe₂. Other multicomponent compensating alloys with two or more rare earths have been synthesized using the elements Sm, Ho, Er and Tm. HoFe₂ has a "+" magnetostriction, SmFe₂, ErFe₂ and TmFe₂ have "-" magnetostrictions; K's for DyFe₂ and HoFe₂ are "+", and K's for SmFe₂, TbFe₂, ErFe₂ and TmFe₂ are "-".³ Of these compounds, Terfenol-D possesses the largest magnetostriction and magnetization at room temperature.

Table III. Single Crystal Magnetostrictions of Rare-earth-Fe₂ Compounds*

Rare Earth	$(3/2)\lambda_{111} \times 10^6$	
	room temperature	0° K
Sm	-3150	-4800
Tb	3690	6600
Dy	1890	6300
Ho	288	2400
Er	-450	-2200
Tm	-315	-5550

* $(3/2)\lambda_{111}$ denotes the magnetostriction measured by rotating the magnetization from perpendicular to parallel to a crystalline [111] direction. See A. E. Clark in Ferromagnetic Materials, Vol. I, ed. E. P. Wohlfarth, North Holland Press, 1980.

In Terfenol-D, the temperature at which the absolute value of the anisotropy minimizes (T_m) is determined by the Tb/Dy ratio. At temperatures higher than T_m , the highly magnetostrictive $\langle 111 \rangle$ axes are easy; at temperatures below T_m , the low magnetostrictive $\langle 100 \rangle$ axes are easy. Since $\lambda_{111} \gg \lambda_{100}$, this behavior leads to interesting magnetostrictive and thermal effects. For example, at a fixed magnetic field, the magnetostriction always exhibits a maximum near the anisotropy minimization temperature, T_m . At temperatures less than T_m , the low magnetostrictive constant, λ_{100} , rather than λ_{111} , is sensed; at temperatures greater than T_m , the natural slow decrease of the λ_{111} magnetostriction with temperature occurs. In Fig. 7 we display the temperature dependence of $(3/2)\lambda_{111}$ vs temperature at fields of 3 kOe to 10 kOe for $\text{Tb}_{0.3}\text{Dy}_{0.7}\text{Fe}_2$. Magnetostrictions at higher temperatures are discussed in a latter part of this section.

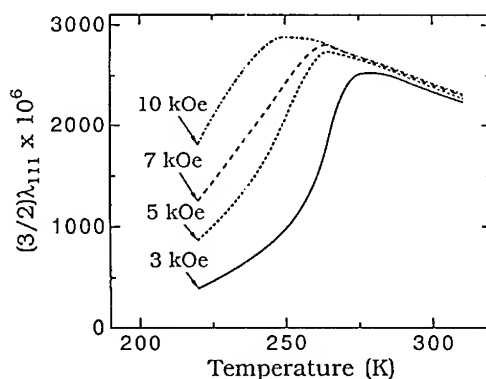


Fig. 7. Single Crystal Magnetostriction, $\lambda_{111} - \lambda_{11}$ = $(3/2)\lambda_{111}$, vs temperature of $\text{Tb}_{0.3}\text{Dy}_{0.7}\text{Fe}_2$ for magnetic fields of 3 kOe, 5 kOe, 7 kOe, and 10 kOe.

Fig. 8 shows the decrease in T_m that corresponds to the increase in the Tb/Dy ratio for $\text{Tb}_x\text{Dy}_{1-x}\text{Fe}_2$. For example, for a magnetostrictive device operating at a temperature of -100 C, the optimum value of $x \approx 0.36$. For temperatures near T_m , the magnetization rotation process takes place with relatively low hysteresis. For temperatures significantly higher than T_m , a "jumping" (more hysteretic) process occurs as the magnetization jumps from one easy $[111]$ axis to another. Huge changes in length accompany these jumps. When these jumps occur, a large amount of internally stored magnetic energy (magnetocrystalline anisotropy energy) is abruptly converted to elastic energy and appears as work done against the externally applied stress. This transformation between internal energy and work is similar to that discussed earlier for TbZn. See Fig. 9. At temperatures below T_m the magnetostriction rapidly decreases in value with temperature, becoming of minimal utility. Further

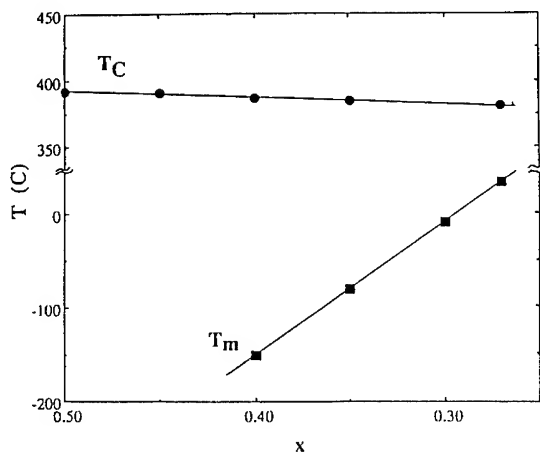


Fig. 8. Anisotropy Minimization Temperature (■) and Curie Temperature (●) of Terfenol-D having a slight addition of Tb-Fe eutectic, $\text{Tb}_x\text{Dy}_{1-x}\text{Fe}_{1.9}$.

magnetization and magnetostriction details can be found in Ref. 12.

$Tb_xDy_{1-x}Fe_2$ grows preferentially along a crystallographic [112] direction in twinned dendritic sheets.¹³ Crystal morphology is depicted in Fig. 10. Large [112] actuator rods of this morphology have been successfully prepared by both free standing zone (crucibleless) methods and by specialized casting processes. While the saturation magnetostriction is largest, $(3/2)\lambda_{111}$, for [111] axial rods; for [112] rods, its saturation value is $(5/4)\lambda_{111}$.¹⁴ Typically, values of 1500×10^{-6} or $\sim 75\%$ of the $(5/4)\lambda_{111}$ value are realized in commercially available materials. Magnetostriction vs field curves are illustrated in Fig. 11 for commercially available alloys of $Tb_xDy_{1-x}Fe_2$ using (a) a free stand rf zone method of preparation, and (b) a modified bridgman preparation method. An extensive set of performance curves of large diameter (5 - 6 cm) Bridgman grown rods for high power transducer applications is given in Ref. 15. A description of magnetostriction 'jumps' in twinned crystals of Terfenol-D is given in Ref. 16.

Temperature dependences of the magnetostrictions for $Tb_{0.3}Dy_{0.7}Fe_{1.9}$ are summarized in Fig. 12 for $\sigma = 7.6$ MPa and 18.9 MPa and for various fields strengths from 250 Oe to 2000 Oe. Note that the onset of the magnetostrictive state ($\langle 111 \rangle$ easy) occurs as expected near -10 C in $Tb_xDy_{1-x}Fe_{1.9}$ with $x = 0.3$. (The peak in the temperature dependence of the magnetostriction can be adjusted by varying x . See Fig. 8.) An important characteristic of twinned single crystal

Terfenol-D is the large change in length at low applied fields. Magnetostrictions $\sim 800 \times 10^{-6}$ exist at 250 Oe for $\sigma = 7.6$ MPa, and $\sim 600 \times 10^{-6}$ at 500 Oe with $\sigma = 18.9$ MPa.

In the region above room temperature, the magnetostrictions of the Terfenol compounds slowly decrease to zero as the temperature is raised toward the Curie temperature. Fig. 13 illustrates the magnetostrictions of $TbFe_2$ and $Tb_{0.27}Dy_{0.73}Fe_2$ resulting from a 90 degree rotation of

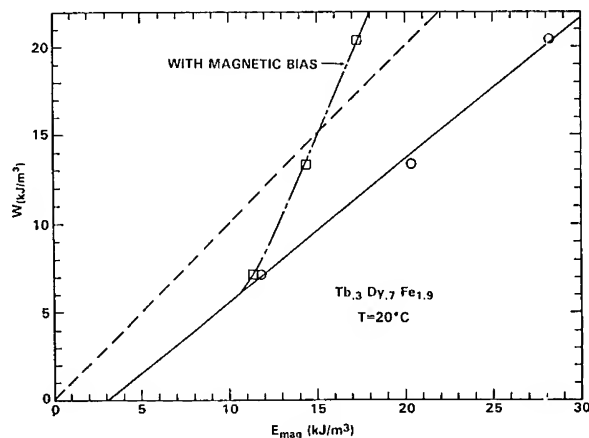


Fig. 9. Magnetic Energy (MH) converted to work ($e\sigma$) during the magnetization process. The dashed line represents lossless conversion.

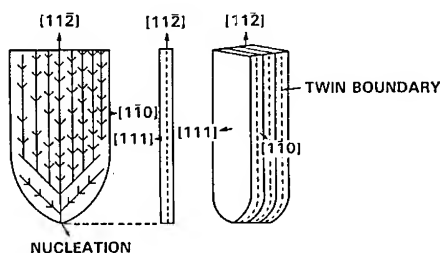


Fig. 10. Twinned Dendritic Structure of Terfenol-D.

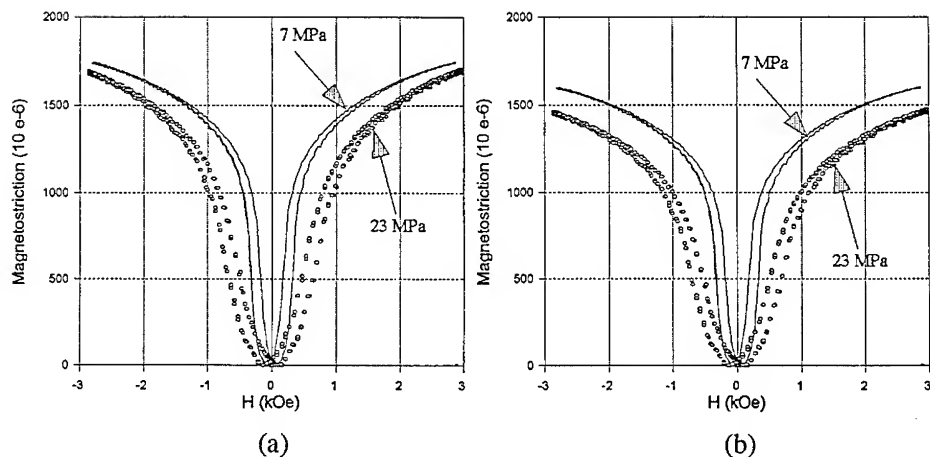


Fig. 11. Magnetostriction vs field for compressive stresses of 7 MPa (—) and 23 MPa (O) for commercially available Terfenol-D prepared by: (a) a free stand rf zone method and (b) a modified bridgman method. Data supplied by ETREMA Products, Inc., Division of Edge Technologies, Inc. Ames, IA.

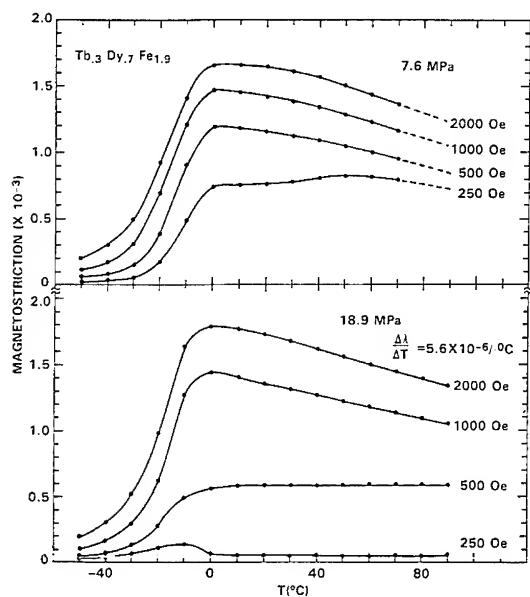


Fig. 12. Magnetostriction of $\text{Tb}_3\text{Dy}_7\text{Fe}_{19}$ vs Temperature for compressive stresses of 7.6 and 18.9 MPa.

the magnetization in a field of 9 kOe.¹⁷ Because of the magneto-crystalline anisotropy, the magnetostriction is not saturated at the lower temperatures, particularly in TbFe_2 . The theoretical curves are shown by the dotted lines. Substantial magnetostrictions ($> 10^{-3}$) persist as high as 150 °C in $\text{Tb}_{27}\text{Dy}_{73}\text{Fe}_2$ and 250 °C in TbFe_2 . Thus unlike many transduction materials, high power magnetostrictive actuators can be designed for continuous performance at high temperatures. At these high temperatures, the magnetic anisotropy is small and saturation is attained at low applied fields.

A large number of magneto-mechanical transducers and actuators utilizing Terfenol-D have been designed and manufactured. See, for example,

Butler,¹⁸ Kvarnsjo,¹⁹ and Claeysen²⁰ for design parameters. The high energy density of these actuators, plus their ruggedness and relative absence of failure mechanisms makes them attractive for many smart system applications, such as active structures and vibration isolators. Structures with infinite stiffness, as well as structures which are extremely soft, can be fabricated using highly magnetostrictive materials. Additionally,

because of large ΔE Effects, feedback controlled variable frequency resonators with large frequency spans can be designed. For $Tb_{0.3}Dy_{0.7}Fe_2$, $\Delta f/f > 57\%$.³ Structures using composite magnetostrictive/piezoelectric materials have been shown to produce unconventional non-reciprocal performance, such as large front to back displacements under a.c. drives.²¹ The high displacements possible with magnetostrictive actuators yield broad bands and large dynamic ranges. Because of the large λ_s and the large blocking forces ($F_b = -Y\lambda_s$), structures designed to be infinitely rigid can withstand strong impulses, and structures designed to be soft can isolate vibrations at low frequencies.

ACKNOWLEDGMENT

The author wishes to thank the many members and the former members of the Magnetic Materials Group at the Naval Surface Warfare Center, Silver Spring, MD, in particular, R. Abbundi, W. Gillmor, H. T. Savage, J. B. Restorff, M. L. Spano, J. P. Teter, and M. Wun-Fogle, for their research on magnetostrictive materials and magnetoelastic effects.

REFERENCES

1. A. E. Clark, M. Wun-Fogle, J. B. Restorff, and J. F. Lindberg, IEEE Trans. on Magn. **28**, 3156 (1992).
2. A. E. Clark, J. B. Restorff, M. Wun-Fogle, and J. F. Lindberg, Proc. International Conference on Magnetism, Warsaw, Poland, Aug. 1994.
3. A. E. Clark, in Ferromagnetic Materials, edited by E. P. Wohlfarth, (North Holland Publishing Co. 1980) p. 531.

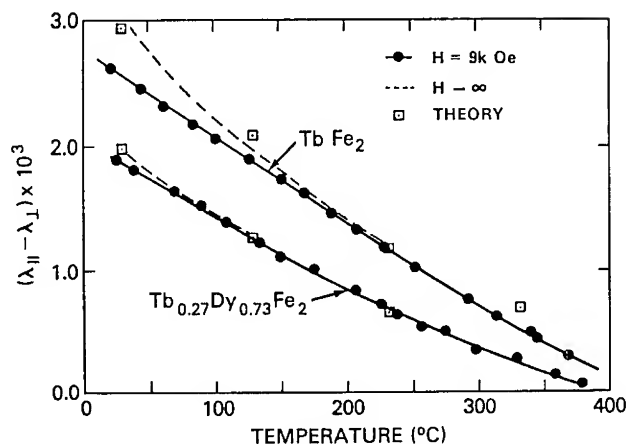


Fig. 13. Magnetostriction of $TbFe_2$ and $Tb_{0.27}Dy_{0.73}Fe_2$ from 20 C to 380 C.

4. J. J. Rhyne and S. Legvold, Phys. Rev. 138, A507 (1965).
5. A. E. Clark, B. F. DeSavage, and R. M. Bozorth, Phys. Rev. 138, A216 (1965).
6. P. Morin, J. Rouchy, and E. du Tremolet de Lacheisserie, Phys. Rev. B16, 3182 (1977).
7. M. B. Spano, A. E. Clark, and M. Wun-Fogle, IEEE Trans. on Magnetics, 25, 3794 (1989).
8. P. Morin and J. Pierre, Solid State Communications 13, 537 (1973).
9. A. E. Clark, J. P. Teter, W. Wun-Fogle, J. B. Restorff, and J. F. Lindberg, Intermag Conference, San Antonio TX, April 1995.
10. A. E. Clark, R. Abbundi, H. T. Savage, and O. D. McMasters, Physica 86-88B, 73 (1977).
11. R. Abbundi and A. E. Clark, IEEE Trans. MAG-13, 1519 (1977).
12. A. E. Clark, J. P. Teter, and M. Wun-Fogle, J. Appl. Phys. 69, 5771 (1991).
13. A. E. Clark, J. D. Verhoven, O. D. McMasters, and E. D. Gibson, IEEE Trans. on Magnetics MAG-22, 973 (1986).
14. J. P. Teter, A. E. Clark, and O. D. McMasters, J. Appl. Phys. 61, 3787 (1986).
15. M. B. Moffett, A. E. Clark, M. Wun-Fogle, J. Lindberg, J. P. Teter, and E. A. McLaughlin, J. Acoust. Soc. Am. 89, 1448 (1991).
16. A. E. Clark, J. P. Teter, and O. D. McMasters, J. Appl. Phys. 63, 3910 (1988).
17. A. E. Clark and D. N. Crowder, IEEE Trans. on Magnetics MAG-21, 1945 (1985).
18. J. H. Butler, "Applications for the Design of Etrema Terfenol-D Magnetostrictive Transducers," Edge Technologies, Inc., 306 South 16 St., Ames, IA (1988).
19. L. Kvarnsjo, "Principles and Tools for Design of Magnetomechanical Devices Based on Giant Magnetostrictive Materials," Royal Institute of Technology, Dept. of Plant Engineering, S-100 44, Stockholm, Sweden.
20. F. Claeysen and D. Boucher, "Design of Lanthanide Magnetostrictive Sonar Projectors," Proc. Defense Technologies Conf., page 1059, Paris, France (1991).
21. J. H. Butler, S. C. Butler, and A. E. Clark, J. Acoust. Soc. Am. 88, 7 (1990).

STUDY OF BOUNDARY FREE Tb-Dy-Fe MAGNETOSTRICTIVE MATERIALS*

QIANG LI, Y.L.CHANG, SHIXI OUYANG AND R.Z.YUAN
Wuhan University of Technology. Advanced Materials Research Institute,
Wuhan, Hubei 430070, China.

ABSTRACT

As a promising candidate of advanced smart materials Tb-Dy-Fe system has been studied for many years. It is well known that the boundaries (which exist in polycrystal and grain oriented crystals of magnetostrictive materials) heavily hinder the motion of domain walls. Therefore to eliminating those boundaries will improve their magnetostrictive behaviors to a large extent. A single crystal growth method (which is called: growth with magnetic levitation cold crucible in CZ technique) has been successfully developed in our lab. since a few years ago. Now bulk cubic Laves phase $RFe_2 Tb_xDy_{1-x}Fe_{1.95-2.0}$ single crystals with boundary free structure can be prepared. Studies have been focused on comparing the performances of polycrystal, grains oriented crystal with a single crystal of the same composition. Some results indicate that λ_g and d_{33} performed by the single crystal are much higher than the two former materials under the same conditions.

INTRODUCTION

It was in the early seventies people came to realize that the Laves phase RFe_2 rare earth-transition intermetallic compounds possessed extraordinary magnetostrictive performances at room temperature^[1]. New progresses have been achieved in preparation and applications of Tb-Dy-Fe pseudo binary magnetostrictive materials since then. Now large amount of high performances device-quality Tb-Dy-Fe alloys, which are manufactured by advanced Bridgman and Free-Standing-Zone-Melt techniques^[2], could be available for both research and commercial purposes. The representative one is called Terfenol-D, which produced by Edge Technologies Inc. at first, has been used successfully in the fields of ultrasonic transducers, mechanical actuators and for many other corresponding military and civil purposes. Prepared by oriented solidification techniques, microstructure of Terfenol-D was usually influenced by the rapid crystallized rate. It was well known that the easy axis of $Tb_xDy_{1-x}Fe_2$ compounds is along the $\langle 111 \rangle$ direction. But the oriented $Tb_xDy_{1-x}Fe_2$ alloys are kinetically favored to crystallize along the direction of $\langle 112 \rangle$ instead of $\langle 111 \rangle$ with the dendrite twinned sheets structure. Boundaries and second phases exist in its microstructure will act as sites for domain wall motion, and prohibit the magnetostrictive performances, especially for its low field magnetostriction^[3]. Therefore, it is recognized as the most significant advance work to eliminate the boundaries and second phases which exist in the microstructure of Terfenol-D, and prepare the applicable Tb-Dy-Fe boundary free single crystals. Recently a method, which is called growth with magnetic

*Supported by the National Key Lab. of Crystal Materials, Shandong University, China.

levitation cold crucible in CZ technique, has been developed to manufacture bulk boundary free Tb-Dy-Fe single crystals⁽⁴⁾. The relations between the microstructure and growth conditions will be discussed in this paper.

EXPERIMENTAL

Samples of composition $Tb_xDy_{1-x}Fe_{1.95-2.0}$, with x from 0.27 to 0.32, were prepared by the magnetic levitation cold crucible in CZ technique. Investigations were focused on the relations between their crystallized structure and growth conditions. Favorable growth parameters were also explored. Large bulk boundary free Tb-Dy-Fe single crystals (see Figure 1) have been prepared and its microstructure has been investigated by X-ray diffraction and backscattering techniques.

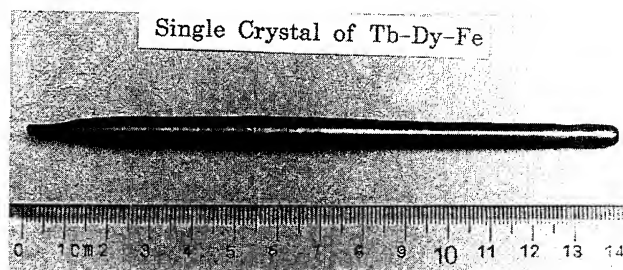


Figure 1. CZ Tb-Dy-Fe single crystal.

RESULTS AND DISCUSSION

RFe_2 Laves Phase

Tb-Dy-Fe pseudobinary phase diagram^[5] (see Figure 2) shows that RFe_2 Laves phase (LP) could only be achieved over an extremely narrow region. In addition the $Tb_xDy_{1-x}Fe_2$ pseudobinary compound was reported to melt peritectically. During the crystallization process, the solidification front will grow easily from the melt alloy by dendrite or cellular crystals to form a twinned sheets structure. The second phase such as R (rare earth rich phase) will appear between the sheets. Hence to optimize the kinetic conditions of crystallized front and grow with flat front instead of dendrite or cellular front is a promising method to eliminate the defects formed in the microstructure of $Tb_xDy_{1-x}Fe_2$ alloys. It has been found that the twinned sheets structure could appear in the alloys when their crystallized rate were too fast (see Figure 3), even though their compositions were just inside the Laves phase region. This phenomenon could be explained as the moving rate of solid and liquid interface was too fast such that a dendrite growth front formed during the crystallized procedure. The situation is quiet similar to what happens in the procedure of

oriented solidification. Therefore the slower growth rate is helpful for the elimination of the twinned sheets structure. The advantage of the CZ technique is that directions and growth

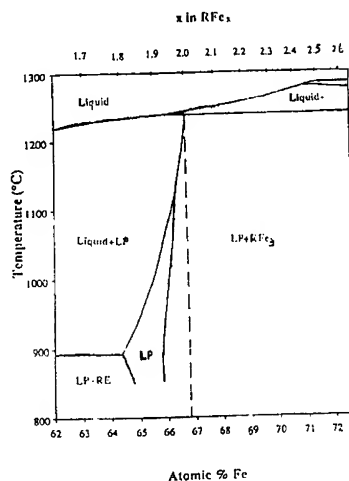


Figure 2. Tb-Dy-Fe pseudobinary phase diagram

rate of crystallization could be controlled effectively. That makes it possible to eliminate the defects formed during the crystallization procedure. Seed crystal selection is also very important for CZ technique. If you were planning to get a boundary free Tb-Dy-Fe single crystal, you have to find a perfect (at least nearly perfect) seed crystal with the correct composition. Orienting and selecting the crystallized direction is also a very important work to manufacture a high quality Tb-Dy-Fe single crystal. To decrease pulling rate, to increase the rotation rate, to slow down the moving rate of solid-liquid interface and to reduce the temperature gradient at the growth front will give the rare earth atoms enough time for them to diffuse from the melt alloy to the solid phase. Under above improved conditions, the composition of melt alloy could be expected to be kept more homogeneous, and the boundary free Tb-Dy-Fe single crystal (see Figure 4) could be expected to be obtained with the magnetic levitation cold crucible in CZ technique. It has been estimated that the favorable parameters for RFe_2 Laves phase Tb-Dy-Fe single crystal growth in CZ technique are

Composition	$Tb_xDy_{1-x}Fe_{1.95-2.0}$, $0.27 < x < 0.32$
Pulling rate	$0.1-5 \mu m/s$
Rotation rate	20-60 rpm

Twinned sheets structure also could be observed when the pulling rate is over $10 \mu m/s$ in CZ growth procedure.

Phase Structure and Crystallization Structure

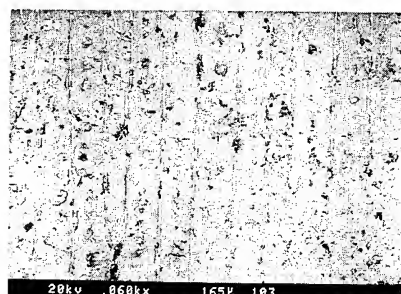


Figure 3. Twinned sheets structure
backscattering photo 60 \times .

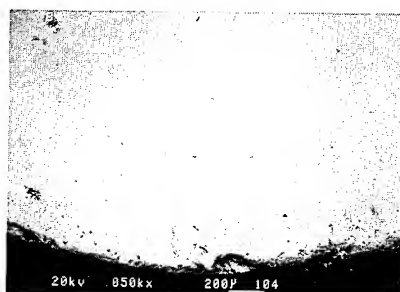


Figure 4. Boundary free single crystal
backscattering photo 50 \times .

Powder X-ray diffraction analysis (see Figure 5) shows that the CZ Tb-Dy-Fe single crystal possesses a single (pure) Laves phase structure. No rare earth metal rich phase(R)

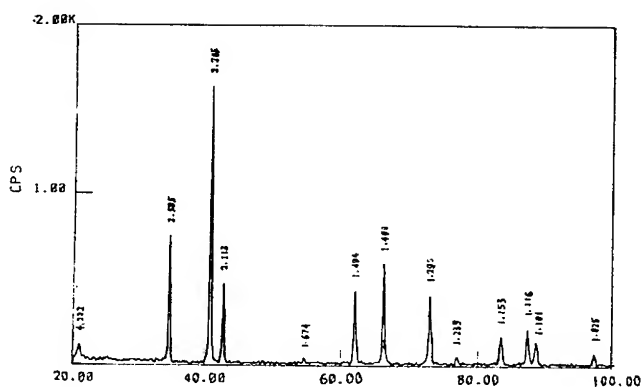


Figure 5. Powder X-ray diffraction analysis

and Wiedmanstatten precipitate (WSP) were found in its microstructure. This result is the same as the analysis result by backscattering techniques(see Figure 4). Chemical analysis indicates that Iron atomic percentage (Fe atm%) content in CZ RFe_2 Laves phase is a little lower than its theoretical prediction. Ordinarily the excessive rare earth metals could form ductile R phase exists in the boundaries or between the twinned sheets in the polycrystal or oriented crystal Tb-Dy-Fe materials. This ductile phase is beneficial to reduce the brittleness of pure cubic RFe_2 Laves phase. The same situation does not happen in the structure of CZ Tb-Dy-Fe single crystal. Further studies indicated the crystallographic

structure of CZ Tb-Dy-Fe pure phase is not the same as the formal RFe_2 Laves phase structure. A superlattice phenomenon, which may cause a lower symmetry, was found for the first time by X-ray crystallographic analysis in the CZ Tb-Dy-Fe single crystal. But the detailed information has not yet been obtained through the experiments until now. Further researches will be carried on the detail crystallographic structure of the superlattice, and the relationship between structure and performances of the single crystal in the future work.

Magnetostrictive Performances

The pure Laves phase have been obtained by eliminating boundaries in CZ Tb-Dy-Fe single crystal. Hence its domain walls will move more easily than in polycrystal or oriented crystals. That makes the CZ single crystal have better magnetostrictive behavior than the polycrystal or oriented crystal with the same composition, especially for its lower field magnetostriction. For instance $\langle 112 \rangle$ direction $Tb_{0.3}Dy_{0.7}Fe_{1.95}$ boundary free single crystal exhibits the performance shown in Figure 6.

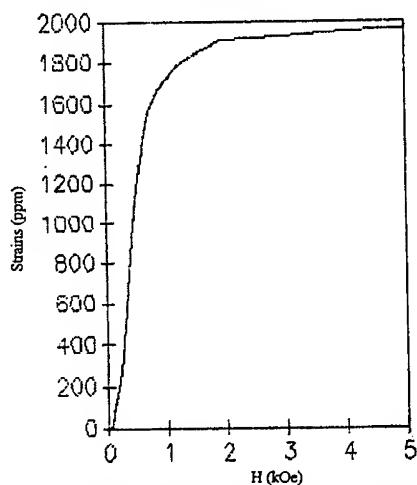


Figure 6. Magnetostriction of Tb-Dy-Fe single crystal

$$\begin{aligned} \lambda &= 1700 \text{ ppm} & (10 \text{ MPa}, 1 \text{ kOe}) \\ d_{33} &= 4.0 \text{ ppm} & (10 \text{ MPa}, 1 \text{ kOe}) \end{aligned}$$

The saturation magnetostrictive coefficient λ_s exceeds 2000 ppm under compressed condition (10 MPa). In order to prepare the higher magnetostriction Tb-Dy-Fe single crystal with $\langle 111 \rangle$ crystallized direction, various techniques and alloy compositions have been examined for a long period. Unfortunately satisfactory results, that is growth $\langle 111 \rangle$ direction Tb-Dy-Fe single crystal directly from melting alloy, has not been obtained even though our experiments, through the most slowly pulling rate has been employed. Therefore, our continual research will be concentrated on the crystallized mechanism of

Tb-Dy-Fe alloys.

SUMMARY

Boundary free Tb-Dy-Fe single crystals, with various compositions and high magnetostriction, have been prepared successfully by magnetic levitation cold crucible in CZ technique. Investigations on their microstructures indicate that there may be a new superlattice structure among their crystallization structures. The performance of CZ Tb-Dy-Fe has been improved to a large extent by eliminating defects.

REFERENCE

1. A.E.Clark, Ferromagnetic Materials, Vol.1, Edited by E.P.Wohlfarth, (North-Holland Publishing Company, 1980), P.533-584
2. J.D.Verhoeven, E.D.Gibson, O.D.McMasters and H.H.Baker, Metal.Trans.A, 18A, 223, (1987)
3. A.E.Clark, J.D.Vehoeven, O.D.McMasters and E.D.Gibson, IEEE Trans.Magn., Mag-22, No.5, 973, (1986)
4. Qiang Li, Y.L.Chang, R.Z.Yuan, X.H.Huang and D.J.Jin, J.Crystal growth, 128, 1092-1094, (1993)
5. P.Westwood, J.S.Abell and K.C.Pitman, J. Appl. Phys., 69(9), 4998,(1990)

TEM STUDY OF TWINNING AND MAGNETIC DOMAINS IN TERFENOL-D

JENNIFER DOOLEY AND M. DE GRAEF

Department of Materials Science and Engineering, Carnegie Mellon University, Pittsburgh, PA 15213

ABSTRACT

This paper reports the results of detailed TEM observations on $[\bar{2}11]$ oriented single crystal samples of Terfenol-D. Domain structures are interpreted in terms of recent micromagnetic models developed by James and Kinderlehrer. Lorentz transmission electron microscopy was performed on a JOEL 120CX equipped with a low field objective lens. We also report for the first time *energy-filtered magnetic domain images*, recorded using a Gatan Imaging Filter on a JOEL 4000EX high resolution TEM. This observational mode allows for enhanced resolution and improved image contrast.

INTRODUCTION

Terfenol-D, an alloy of terbium, dysprosium and iron, has the largest known room-temperature magnetostriction coefficient. It is used in low frequency, high power sonar devices, micro-positioning and anti-vibration devices. Terfenol-D ($\text{Tb}_{0.3}\text{Dy}_{0.7}\text{Fe}_2$) has a high temperature crystal structure of the cubic MgCu_2 Laves phase type, with lattice parameter $a = 0.732 \text{ nm}$ [1] and space group $\text{Fd}\bar{3}\text{m}$. There are 24 atoms per unit cell: Tb and Dy share the 8a sites and Fe occupies the 16d sites. At room temperature, the cubic unit cell is rhombohedrally distorted along the magnetically soft $\langle 111 \rangle$ directions. The distortion is extremely small: e.g., the cubic $[100]$ direction tilts by 1.13 mrad towards a new orientation. Terfenol-D single crystals grow along the $[\bar{2}11]$ direction, which will be taken as reference direction throughout this paper.

The spontaneous magnetic moment as a function of temperature has been measured for $\text{Tb}_{0.27}\text{Dy}_{0.73}\text{Fe}_2$ by Clark et al. [2]. Domain structure studies have been performed by a bitter colloid-scanning electron microscopy (SEM) technique [3], differential interference contrast (DIC) [4] and by x-ray topography [5]. Conventional transmission electron microscopy (CTEM) and Lorentz microscopy have also been used [6, 7]. Magnetic domain configurations can be interpreted in terms of magnetization directions parallel to $\langle 111 \rangle$ with 71° or 109° domain walls, in addition to 180° domain walls. The wall energy as a function of temperature has been calculated by Clark et al. [5].

James and Kinderlehrer [8] have proposed a mathematical model for the magnetostriction in Terfenol-D and have worked out fine-scale magnetic domain configurations in the vicinity of growth twins. If the four magnetic orientation variants derived from the cubic phase are denoted 1, 2, 3, and 4, then a rotational growth twin on the (111) plane gives rise to an additional 4 variants, denoted 1', 2', 3', and 4' (see Table 1 for the indices of the 8 magnetization directions with respect to the *cubic* reference frame; the angle θ is

Table 1: Magnetization directions for Terfenol-D, according to [8]

#	direction	θ	#	direction	θ
1	$[1\bar{1}1]$	90.0°	1'	$[1\bar{1}1]$	90.0°
2	$[\bar{1}11]$	19.5°	2'	$[\bar{5}\bar{1}\bar{1}]$	160.5°
3	$[1\bar{1}\bar{1}]$	118.1°	3'	$[\bar{1}5\bar{1}]$	61.9°
4	$[11\bar{1}]$	118.1°	4'	$[\bar{1}\bar{1}5]$	61.9°

the angle between the magnetization direction and the growth direction $[\bar{2}11]$). James and Kinderlehrer worked out all possible combinations for lamellar domain sequences on both sides of the growth twins, and found that several combinations (e.g., $\frac{12}{172}$ in their notation) are not exactly compatible across the growth twin. Whereas all of the domain configurations proposed in their paper agree favorably with experimental observations by DIC methods [4], observations of the differences between the compatible and exactly compatible configurations have thus far not been reported. The present work was undertaken in an attempt to characterize fine-scale magnetic domain configurations across (111) growth twins. This paper presents TEM observations of domain walls in $[\bar{2}11]$ -oriented Terfenol-D single crystals.

EXPERIMENTAL PROCEDURE

The Terfenol-D rods of stoichiometry $\text{Tb}_3\text{Dy}_7\text{Fe}_{1.95}$ used for the experiments were supplied by Etrema Products Inc. The material was prepared by the free-standing float-zone (FSZ) method [9, 10], which has been shown to be the most successful technique available to date [11]. Twinned $[\bar{2}11]$ rods with a small percentage of a rare earth-rich phase are obtained under these conditions.

Thin cross-section disks were cut from $[\bar{2}11]$ rods and mechanically polished to a thickness of 200 μm . The thin disks were dimpled on both sides and ion milled (5 kV Ar^+ ions) to perforation. Transmission electron microscopy (TEM) observations were carried out on a JEOL 120CX operated at 120 kV, with a side entry, low-field objective pole-piece. Since the low field strength in the objective lens reduces the useful magnification range, an alternative method was sought for magnetic domain observations with higher spatial resolution. A JEOL 4000EX top-entry microscope, dedicated for high resolution observations, was recently equipped with an *imaging energy filter* [12] or *GIF*; this filter consists of a magnetic sector which acts as a "prism" for electrons and produces an Electron Energy Loss Spectrum (EELS). A mechanical slit is used to select a narrow energy range from this spectrum and a set of quadrupole and sextupole lenses then reconstruct the image corresponding to the electrons with energy losses in this range. The image is observed on a TV-rate camera or recorded on a 1024 \times 1024 CCD camera.

The *GIF* has an internal magnification of 18.75X. The combination of a JEOL 4000EX and a *GIF* is extremely well suited for applications in Lorentz microscopy. When the microscope is operated in LOW MAG mode (magnifications from 200X to 3000X) the upper pole pieces of the objective lens are not excited, thus providing a field free region for the specimen; the normal field strength in the upper pole piece region is about 2 Tesla, much higher than the saturation field for Terfenol-D. The lower pole piece is weakly excited and provides enough field strength to focus the electrons into an image. Normally, the LOW MAG range on a dedicated high resolution TEM is rarely used, but in this case the subsequent magnification by a factor of 18.75 in the *GIF* provides a direct way to produce Lorentz micrographs with a total magnification of up to 56kX at the CCD camera. This camera has dimensions of 25.4 \times 25.4 mm², hence the recorded images at maximum magnification measure 450 nm along a side. All images are gain-normalized and reduced to an intensity scale with 256 grey levels to allow digital output on a printer or graphics display (the original data contains $2^{14} = 16384$ intensity levels). In LOW MAG mode, the intermediate lens stigmator coils are used to correct image astigmatism (instead of the objective stigmator coils).

EXPERIMENTAL RESULTS

TEM Observations

A $[\bar{2}11]$ oriented thin foil was mounted in both a JEOL 120CX microscope and in the field-free region of a JEOL 4000EX microscope, equipped with a *GIF*. Figure 1a shows a $[\bar{1}10]$ twinned electron diffraction pattern; the indexed pattern in b) is a kinematical

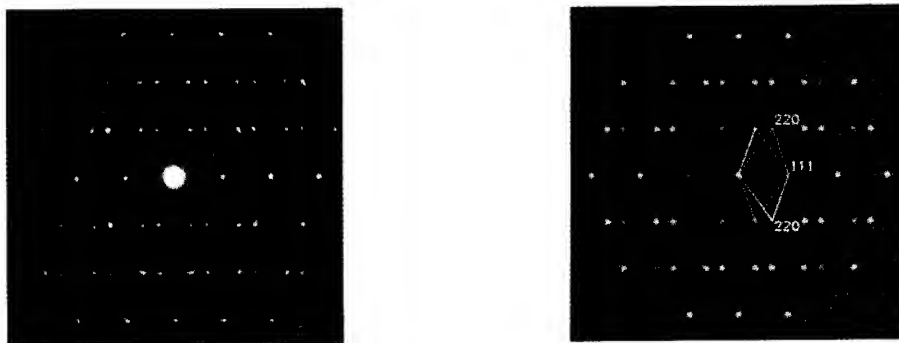


Figure 1: a) $[110]$ zone axis pattern of a growth twin in Terfenol-D, taken in a low field objective lens in a JEOL 120CX microscope; b) computed kinematical diffraction pattern.

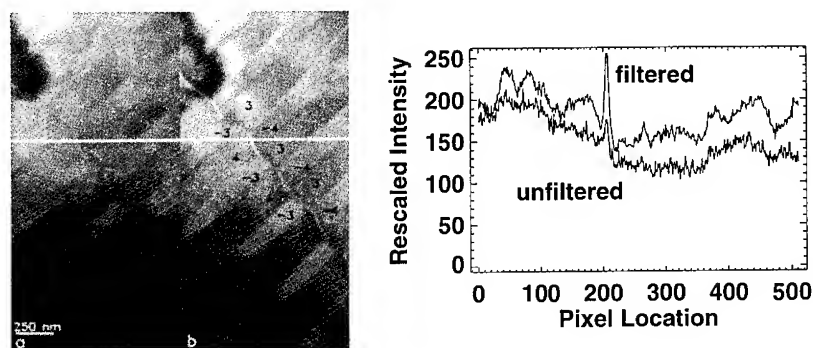


Figure 2: a) unfiltered and b) filtered (zero-loss) images of two sets of magnetic domain walls, separated by a wavy line with average orientation along the (111) plane. c) shows the intensity profiles corresponding to the white lines in a) and b): zero-loss imaging leads to enhanced contrast and reduced noise content.

simulation of the twin pattern. The twin plane is (111) , i.e., a growth twin, consistent with earlier reports [4].

Two types of magnetic domain contrast can be observed using Lorentz microscopy: *Fresnel* contrast outlines the domain walls with a parallel magnetization component with bright or dark lines upon defocusing the objective lens and is caused by deflection of high energy electrons by the internal magnetic field of the sample. *Foucault*-type contrast can arise because the lattice orientation change upon crossing a domain wall in Terfenol-D is of the order of a few milliradians, similar to the magnitude of Bragg angles for diffraction of 400 keV electrons. This will give rise to substantial contrast differences between the magnetic domains. Since the objective lens of the JEOL 4000EX is switched off for magnetic domain observations, the back focal plane no longer coincides with the location of the diffraction aperture; therefore, the standard procedure for Foucault imaging (shifting the diffraction aperture such that only one of a set of closely spaced reflections contributes to the image) is not possible. Instead, one can use the small shifts of bend contours crossing magnetic walls to obtain diffraction contrast between the domains.

Figure 2a shows an unfiltered Foucault image of two sets of domain sequences, for a crystal orientation a few degrees from $[211]$ towards the $[100]$ zone axis. The diagonal zig-

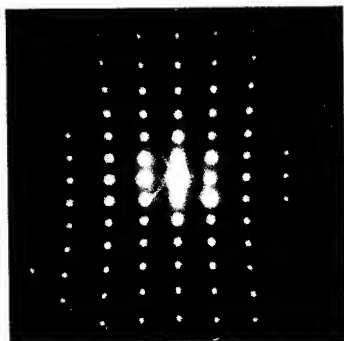


Figure 3: Electron diffraction pattern of the $[211]$ zone axis orientation of Terfenol-D, obtained using the method described in the text.

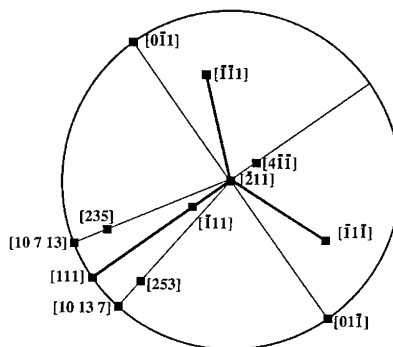


Figure 4: Stereographic projection of the relevant directions in the $[211]$ orientation; the solid lines indicate the magnetization vectors, the thin lines correspond to the normals to the segments of the zig-zag line in Figure 3.

zag line delineates a boundary between the two sets of domains and has the trace of the (111) plane as average orientation. The image on the right (Figure 2b) is a zero-loss image of the same region and was obtained with a 10 eV imaging slit width. Only electrons which have suffered an energy loss smaller than 5 eV contributed to this image. The acquisition times were 0.48 s for the image in a) and 0.96 s for the energy filtered image. The image quality is substantially improved by removing most of the inelastically scattered electrons; the horizontal white line across both a) and b) corresponds to the intensity trace shown in c).

Since the objective lens is turned off for magnetic domain observations, diffraction patterns cannot be obtained by simply switching the lenses to diffraction mode. Instead, one can use the lens control routines offered by the *GIF* control program to modify the current through the third intermediate lens of the 4000EX. One obtains a diffraction pattern, such as the one shown in Figure 3, which suffers from pin-cushion lens aberrations (typical for low magnification observations). Although no quantitative information can be obtained from this pattern because of the aberrations, the observation mode just described can be used to determine the orientation of features in the image since there is no rotation of the diffraction pattern relative to the image.

The stereographic projection in Figure 4 shows the relevant planes and directions. The normals to the traces of the zig-zag boundary are of the type $[10713]$ and $[10137]$. The domain walls perpendicular to the (111) trace are of the type $[0\bar{1}1]$. From James and Kinderlehrer's work [8] we know that the only pair of magnetization directions with this type of domain wall is the 3-4 combination. The symbols in the domains in Figure 2b indicate the type of magnetization vector (-4 stands for the direction $[\bar{1}11]$). The zig-zag boundary consists of 180° domain walls; therefore, the magnetization direction must lie in the domain wall plane. The indices of the boundary planes are $[235]$ for the $[10713]$ trace and $[253]$ for the $[10137]$ trace. The direction common to the boundary planes is $[4\bar{1}\bar{1}]$ which is at 15.8° from the foil normal towards the $[\bar{1}00]$ zone axis. These values are consistent with the electron diffraction data.

Energy filtered observations also enhance contrast in the Fresnel imaging mode. Figure 5 shows 4 images of a region close to the one shown in Figure 2 : a) is an in-focus, energy filtered micrograph, showing the absence of domain contrast (the sample was oriented such that no Foucault-type contrast was observed). In b) and c) the underfocus and overfocus images are shown, both energy-filtered with a slit width of 10eV. The overfocus filtered image in c) can be compared with the unfiltered version in d); all imaging condi-

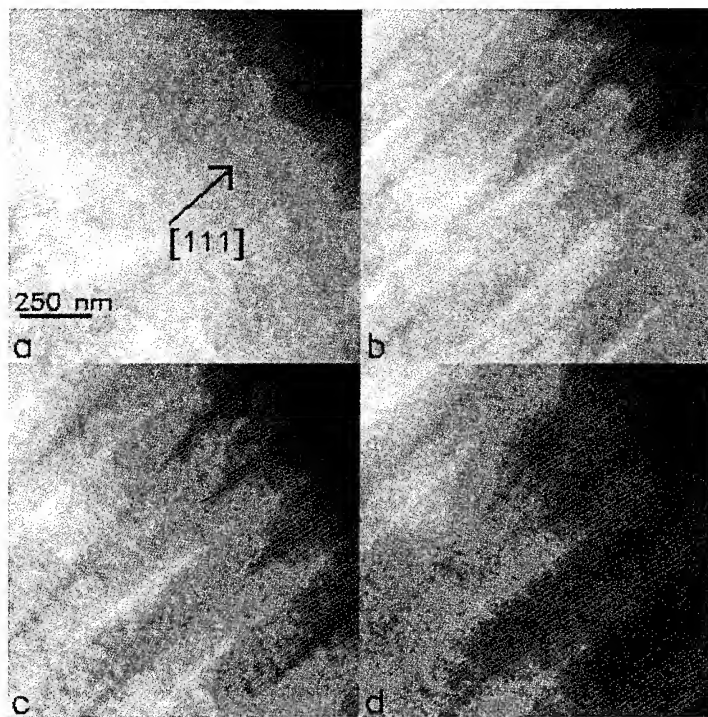


Figure 5: a) zero-loss in-focus, b) zero-loss underfocus and c) zero-loss overfocus Fresnel images of a region close to the one shown in Figure 3. d) shows the unfiltered over-focus image. The marker in a) corresponds to 250 nm.

tions are identical for c) and d), only the filtering slit was removed before acquisition of image d). Figure 6 shows a lower magnification overview of various domains with Fresnel contrast; the domain types could be determined by comparison of the domain wall traces with the crystallographic directions indicated in the figure. Note the jumps in the location of a bend contour on the lower right hand side of the figure when the contour crosses a domain wall.

CONCLUSIONS

We presented for the first time *energy-filtered* magnetic domain images obtained on a 400 kV TEM equipped with a *GIF*; this technique, which yields digital images, is promising for the study of fine-scale magnetic domain configurations and will be used to verify the theoretical micro-magnetic magnetostriction models by James and Kinderlehrer [8].

ACKNOWLEDGEMENTS

The authors would like to thank Prof. Mike McHenry and Prof. David Kinderlehrer for stimulating discussions and Mr. Tom Nuhfer for first suggesting the combined use of a JEOL 4000EX and the Gatan Imaging Filter for Lorentz type microscopy and for assistance with the TEM specimen preparation and observations.

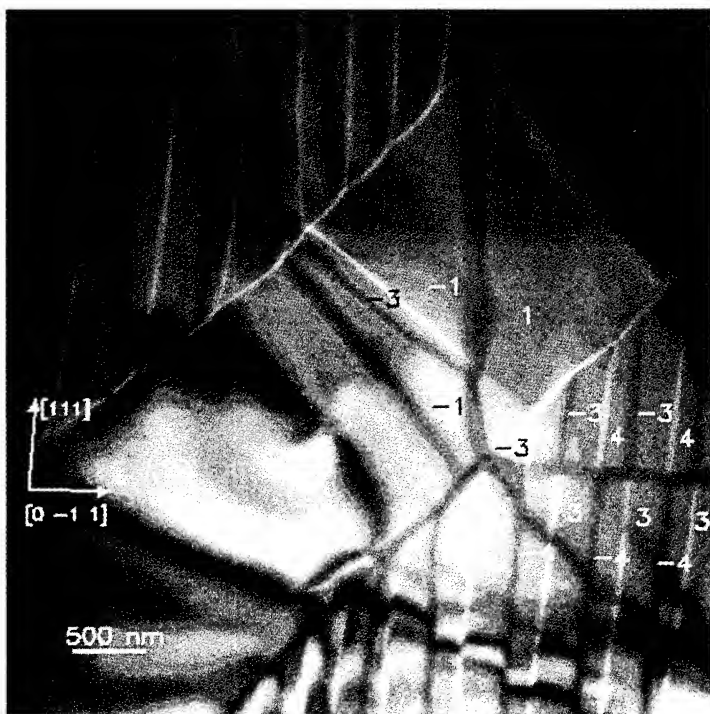


Figure 6: Overview of an area with various domain orientations (scale bar corresponds to 500 nm), close to the $[211]$ zone axis orientation (energy filtered underfocus image).

References

- [1] M. Al-Jiboory and D.G. Lord, *IEEE Trans. Magn.*, **26**, 2583 (1990)
- [2] A.E. Clark, R. Abbundi and W.R. Gillmor, *IEEE Trans. Magn.*, **14**, 542 (1978)
- [3] A.L. Janio, A. Branwood, R. Dudley and A.R. Piercy, *J. Phys. D: Appl. Phys.*, **20**, 24 (1987)
- [4] D.G. Lord, V. Elliot, A.E. Clark, H.T. Savage, J.P. Teter and O.D. McMasters, *IEEE Trans. Magn.*, **24**, 1716 (1988)
- [5] G.F. Clark, B.K. Tanner and H.T. Savage, *Phil. Mag. B*, **46** 331 (1982)
- [6] Y.J. Bi, J.S. Abell and A.M.H. Hwang, *J. Magn. Magn. Mat.*, **99**, 159 (1991)
- [7] A.G.I. Jenner, D.G. Lord and C.A. Faunce, *IEEE Trans. Magn.*, **24**, 1865 (1988)
- [8] R.D. James and D. Kinderlehrer, *Phil. Mag. B*, **68**, 237 (1993)
- [9] O.D. McMasters, J.D. Verhoeven and E.D. Gibson, *J. Magn. Magn. Mat.*, **54-57**, 849 (1986)
- [10] J.D. Verhoeven, E.D. Gibson, O.D. McMasters and H.H. Baker, *Metall. Trans. A*, **18**, 223 (1987)
- [11] D.C. Jiles, *J. Phys. D: Appl. Phys.*, **29**, 1 (1994)
- [12] O.L. Krivanek, A.J. Gubbens and N. Dellby, *Microsc. Microanal. Microstruct.*, **2**, 315 (1991)

THERMO-MECHANICAL PROPERTIES OF TERFENOL-D THIN FILMS

QUANMIN SU, Y. ZHENG AND MANFRED WUTTIG

Department of Materials and Nuclear Engineering

University of Maryland

College Park, MD 20742-2115, USA

ABSTRACT

The thermo-mechanical properties of Terfenol-D thin films deposited on Si substrates were studied by static and dynamic measurements of film/substrate composite cantilevers. The Curie transition, ΔE effect and mechanical damping of the film were measured simultaneously. The stress in the film was controlled by annealing below the recrystallization temperature and determined to vary from -500 MPa, compression, in as deposited films to +480 MPa, tension, in annealed films. The Curie temperature shifts from 80°C to 140°C as the tension increases while the structure of the film remains amorphous. The stress change induced by annealing also drastically effects the film's damping characteristics. The ΔE effect of the amorphous material, about 20%, was used to estimate the magnetostriction, $\lambda_s \approx 4 \cdot 10^{-3}$.

INTRODUCTION

The giant magnetostriction of Terfenol-D is attracting increasing attention to this material for its use in thin film form applying it for micro-actuation^{1,2,3,4}. Crystalline Terfenol films exhibit magnetostriction hysteresis loops and their application is difficult due to large remanence and coercivity². In contrast, amorphous Terfenol-D films show a sharp increase of the magnetostriction at low fields and no hysteresis during cycling of the magnetic field. Technologically, these characteristics of amorphous film are advantageous. Recent experiments revealed that stress in the film plays a crucial role in determining the increment of magnetostriction in small fields as well as the coercivity of the film⁵. A tensile stress in the film was reported to enhance the giant magnetostriction effect below fields of 0.05 T while compression substantially reduces striction in the same range of magnetic fields. In reference 5 the stress was varied by changing the substrate material from Si to CuBe potentially complicating the problem because different interfaces are involved. Our studies indicate that the stress in sputtered Terfenol-D film can be adjusted from highly compressive to tensile by suitable sputter processing and subsequent annealing in a temperature region far below the recrystallization temperature where the film stays amorphous. It may therefore be interesting to monitor the evolution of the physical properties of the same specimen at different stresses obtained by annealing. Furthermore, to the authors' knowledge, the ΔE effect and damping of Terfenol-D films have not yet been reported. Both parameters are vital for sensor and actuator applications⁶. Hence, below, the results of dynamic mechanical measurements will be reported which yield modulus, damping, an estimate of the magnetostriction and the relative magnetization simultaneously.

EXPERIMENT

Film Deposition

A commercially available Kurt J. Lesker Super Sputtering System III was used to deposit films. The system is equipped with 2-inch RF & DC magnetron sputtering sources. The base vacuum ranges between $6 \cdot 10^{-8}$ and $2 \cdot 10^{-7}$ and films are routinely deposited under 10 mTorr Ar pressure with no intentional substrate heating. The substrates used were Si/SiO₂ with 200 nm SiO₂ serving as a diffusion barrier. The deposition rate was 0.2 nm/sec for all Terfenol-D films. The deposition source voltage is adjusted to between 250V and 280 V and the current varies accordingly in the range between 150 mA to 250 mA. At such conditions no additional effort is needed to maintain the target alloy composition. Rutherford backscattering (RBS) measurements indicate the same compositions in the film as compared to the alloy target used to deposit them. Terfenol-D so deposited at room temperature is amorphous.

Magneto Mechanical Measurement System

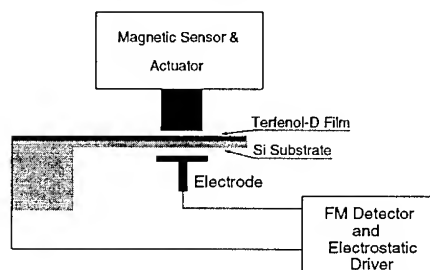


Fig. 1: Schematic of the magneto-mechanical measurement system.

Dynamic Magneto-Mechanical Characterization

A special design for magneto-mechanical characterization making use of the high mechanical Q of the film/substrate composite and based on previous designs⁷ is shown in fig. 1. The sample and electrode comprise the capacitor of a frequency modulation detector. The same electrode is also used to excite vibrations of the film/substrate composite cantilever electrostatically. The upper part is a magnetic driving and sensing device. The system provides parameters such as the damping (internal friction) and modulus defect of the film/substrate composite which can be deconvoluted into intrinsic properties of the films⁸. It is able to excite the composite vibration both electrostatically and magnetically. In the case of magnetic excitation the cantilever deflection is proportional to the interaction force between the cantilever and the field generated by a solenoid magnet above the film. Due to the inhomogeneity of the magnetic field as well as the undefined domain structure in the film, it is impossible to extract absolute quantitative values of the magnetization from the measurements. The data is therefore normalized to the deflection at the lowest temperature and specified as the relative magnetization. In the following figures this relative magnetization is used.

The static stress in the film/substrate composite was determined using a cantilever deflection method. Standard deconvolution procedures were used to obtain the stress in the film itself.

The domain structure in the deposited Terfenol-D films was recorded by a Digital Nanoscope III atomic force microscope operating in the frequency measurement mode.

Thermo-Mechanical Properties of Terfenol-D Film

The results of a combination of dynamical measurements on a Terfenol-D film grown on a Si/SiO₂ substrate are shown in Fig. 2. All three parameters shown were measured simultaneously on the same specimen in a single thermal cycle. In Fig. 2 the Curie temperature is indicated by a sharp drop of the normalized magnetization. For all amorphous films it ranges from 80°C to 140°C and depends systematically on the film thickness and heat treatment.

The elastic modulus of the film displays a sharp decrease at the Curie transition, as evident from Fig. 2b. This change, measured in zero (the earth's) magnetic field, at the Curie transition is believed to be the result of the magnetostrictive property of amorphous films. The saturation magnetostriction can be

$$\frac{\Delta E}{E} = \frac{2}{5} \cdot \frac{\lambda_s \cdot E_s}{\sigma_i} \quad (1)$$

evaluated from the experimentally measured modulus defect through eq. (1) where the quantities E_s and σ_i represent Young's modulus in the saturated ferromagnetic states and the internal stress of the film, respectively

⁹. Taking the measured stress $\sigma_i=500$ MPa, $E_s=55$ GPa and the measured modulus defect of 20% one obtains $\lambda_s \approx 4 \cdot 10^{-3}$. This result over estimates the magnetostrictive coefficient by a factor of two compared to magnetic measurements⁵. However, eq. (1) was derived for randomly oriented domains in bulk materials. The domain structure of the Terfenol film, imaged by atomic force microscopy with LiftTM Phase Mode, indicates strong anisotropy and hence deviations from eq. 2 must be expected.

The damping measurements shown in Fig. 2c parallel the modulus defect at the Curie temperature and indicate an enhanced mechanical energy loss in the ferromagnetic state caused by magneto-mechanical hysteresis. It is worth noting that the magnitude of the magnetic damping is as high as in typical high damping materials¹⁰.

Curves 1 through 5 of Fig. 3 represent the relative magnetization as a function of increasing annealing temperature. X-ray diffraction indicates that the film appears to be amorphous after the annealing treatments corresponding to curves 1 through 4. Recrystallization occurs during the annealing treatment corresponding to curve 5. The static film stresses at room temperature, determined as mentioned above, are marked in Fig. 3 as well. Before recrystallization the Curie temperature shifts to higher temperatures as the stress evolves from compressive to tensile (curves

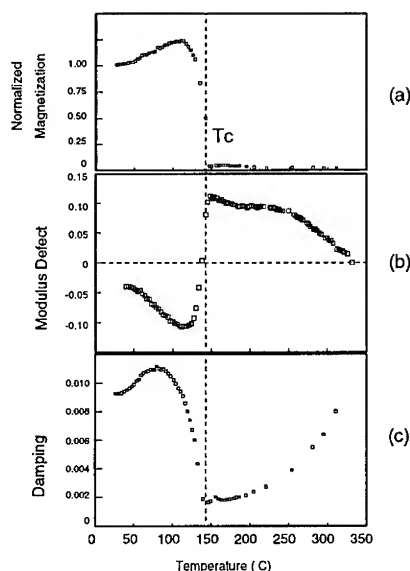


Fig. 2: Intrinsic film parameters of a 1.5 μm Terfenol-D film deposited on a 80 μm Si/SiO₂ substrate.

- a. Remanent magnetization,
- b. Modulus defect,
- c. Damping capacity.

1 through 3). It stabilizes upon annealing between 400°C and 650°C (curves 3 and 4). Recrystallization substantially changes the features of the measured curves (Fig. 3, curve 5).

While the Curie temperature shifts only slightly during anneals between 400°C and 650°C, the magnitude of the damping is drastically reduced in this region of annealing temperature as displayed in Fig. 4. Taking into account that the structure still appears to be amorphous, it is assumed that the sharp change of damping characteristic between curves 1 and 3 in Fig. 4 is caused by the variation of the stress towards high tension.

SUMMARY

The ΔE effect, damping capacity as well as the Curie transition temperature of amorphous Terfenol-D films in different states of stress were measured. The magnetostriction, λ_s , estimated from ΔE effect of the film is larger than reported previously but of the same order of magnitude. The damping, relevant to the mobility and density of magnetic domains, is of the order of 10^{-2} and may be controlled by domain orientation. The Curie temperature shifts to higher temperature with increasing annealing temperature as does the tensile stress in the films.

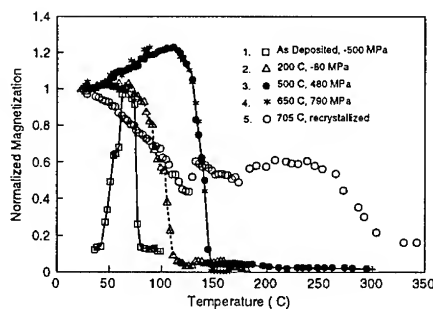


Fig. 3: Magnetic properties of Terfenol-D film after different anneals.

a. As deposited,
b-d. Annealed at 200°C, 500°C and 750°C respectively.

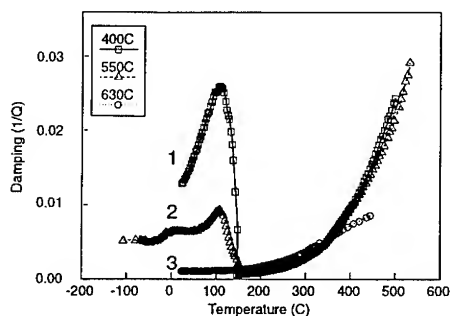


Fig. 4: Damping of Terfenol-D films heat treated at different temperatures shown in the insert. The thicknesses of the film and substrate are 1 μm and 40 μm respectively.

ACKNOWLEDGEMENTS

This study was supported by the Office of Naval Research, contract No. N00014-93-10506 and the National Science Foundation, Grant No. DMR-93-21185, it also benefitted from support by the Army Research Office, contract No. DAAL03-92-G-0121.

REFERENCES

1. D. W. Forester, C. Vittoria, J. Schellinh and P. Lubitz, *J. Appl. Phys.* **49**, 1966 (1978)
2. G. Flik, M. Schnell, F. Schatz and M. Hirsher, in *Proceedings of 4th International Conference on New Actuators*, Bremen, 1994, p. 232
3. Y. Hayashi, T. Honda, K. I. Arai, K. Ishyama and M. Yamaguchi in *Proceedings of Intermag. Conference*, Stockholm '93, in press
4. new terfenol reference
5. F. Schatz, M. Hirscher, M. Schnell, G. Flik and H. Kronmüller, *J. Appl. Phys.* **76**(9) (1994)
6. G. Stemme, *J. Micromech. Microeng.*, **1**, 113 (1992)
7. F. Vollkommer, H.G. Bohn, K.-H. Robrock and W. Schilling, 28th Ann. Proc. Reliability Phys. 1990, p. 51
8. B.S. Berry in *Diffusion Phenomenon in Thin Films and Microelectronic Materials*, D.Gupta and P.S Ho, eds., C. Noyes, Park Ridge, NJ, p. 73 (1988)
9. R.M. Bozorth, *Ferromagnetism*, Norstrand, NY, 1951, p. 690
10. Quanmin Su, S. Z. Hua and M. Wuttig, Martensitic Transformation in $\text{Ni}_{50}\text{Ti}_{50}$ Films, *Proceeding of International Conference on Martensitic Transformations*, Tokyo, 1993

AMORPHOUS MAGNETOELASTIC MATERIALS

H. T. SAVAGE* AND MARILYN WUN-FOGLE**

*BCS Inc., 1003g Sunnyvale Lane, Madison, WI 53713

**NSWC, Carderock, Code 684, Silver Spring, MD 20903-5000

ABSTRACT

The outstanding feature of amorphous magnetoelastic alloys is the controllability of the magnetic anisotropy energy, Curie point, magnetostriction and magnetic moment. This control of material characteristics, achieved by magnetic and stress annealing plus changes in composition, is impossible in crystalline materials. The control allows the design of tactile and magnetic field sensors with special features and very high sensitivity. The materials discussed are prepared by rapid solidification through melt spinning in ribbon and wire geometries and magnetron sputtering onto substrates. As an example of the advantages of sputtered material, an accelerometer on silicon micro-cantilevers is shown. It has no coils. The basic magnetoelastic theory that governs tactile sensors is shown. Low-noise magnetic field sensors with novel twist anisotropies and Barkhausen instabilities in wires are discussed.

INTRODUCTION

The outstanding characteristic of amorphous materials for device exploitation is the control of the magnetic anisotropy energy K . Using magnetic annealing, direction of the easy axis and uniformity can be controlled.¹ By altering alloy composition magnitudes can be controlled.¹ We will show later that a good figure of merit for magnetoelastic devices is $(3\lambda_s)^2 E_0 / 2K$, where E_0 is Young's modulus and λ_s is the magnetostriction constant.² In Fe based materials the magnetostriction cannot be made much larger than that of Ni (3×10^{-5}). Control of Young's modulus is limited. The salient feature is that the magnitude of K , via magnetic annealing, can be made a 1000 times smaller than transition metal anisotropies at room temperature. Magnetic annealing, annealing above the Curie point and below the crystallization temperature in the presence of a magnetic field, greatly relieves the random internal stress. The direction of the easy axis (direction in which the magnetic anisotropy energy is a minimum) is in the direction of the annealing field. This degree of control is not possible in crystalline materials.

The small value of K implies that a small applied magnetic field H will rotate the magnetic moment, thus making changes in length possible with very small field changes. Conversely microscopic changes in length rotate the magnetic moment appreciably, making high figure of merit strain gages possible. Control of the easy axis direction implies that the magnetic field can be applied in a convenient direction.

Another feature is the possibility of achieving near-zero magnetostriction by altering composition. This is normally done by adding Co to iron-based alloys. In this way magnetically softer materials are prepared. The addition of Co increases cost greatly and reduces the room temperature magnetic moment. The anisotropy is not as uniform as in Fe based materials, possibly because of the two-ion (Fe-Co) anisotropy. However Barkhausen noise is reduced so that low-noise fluxgate magnetometers are possible. It is also possible to anneal twist anisotropies into the materials for device facilitation. Large Co additions³ lead to negative magnetostriction materials. While strain gage figures-of-merit are not as high, tensile stress sensors built with these materials have a large dynamic range. Increasing the tensile stress pulls the moment perpendicular to the stress axis. If the applied ac and dc fields used for measuring the permeability are along the stress axis, the dc field can counteract the stress. This results in a very wide dynamic range device.³

The materials are made amorphous by many different methods of rapid cooling at rates of about 10^6 deg/sec. The three discussed here are: (1) rapid cooling on a wheel to form ribbons, (2) rapid cooling into water in a spinning wheel to form wires, and (3) magnetron sputtering. The materials display essentially the same intensive magnetic characteristics. The cylindrical geometry of the wire changes the macroscopic magnetic behavior considerably. Stresses induced by substrates can change the behavior of the sputtered material. These stresses can be reduced by matching the thermal coefficient of expansion of the substrate with that of the sputtered material.

Prototype Strain Gage To illustrate the useful properties of the amorphous magnetostrictive materials we discuss a prototype strain gage experiment. To begin we first describe magnetostriction and the experiment that verified the high value of the figure-of-merit. The simple magnetostrictive effect is shown in Fig 1. For positive magnetostriction the sample elongates as the magnetic moment vector \mathbf{M}_s rotates from

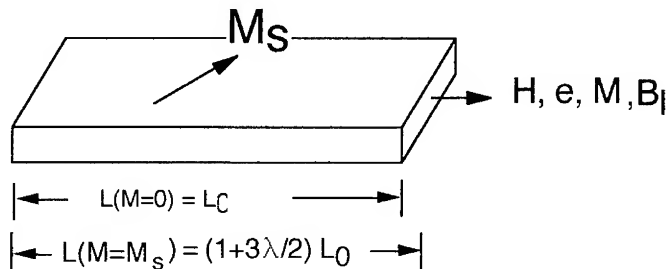


Fig. 1. A ribbon of amorphous ferromagnetic material. Only one magnetic domain is shown here. As the magnetic moment vector \mathbf{M}_s rotates, the sample elongates and becomes narrower. The maximum possible value of strain e is $3\lambda_s/2$ where λ_s is the magnetostriction constant. H is the applied magnetic field, e the longitudinal strain and M the longitudinal component of \mathbf{M}_s .

perpendicular to parallel to the longitudinal axis. The moment is rotated by increasing the value of the longitudinal magnetic field H . Conversely, changing the length of the sample rotates M_s . The rotation of M_s changes the value of the longitudinal component of M_s , M .

In a previous article² it was shown that "Hooke's Law" for the amorphous magnetostrictive materials is $e = T/E_0 + (3\lambda_s/2)(M/M_s)^2$, where E_0 is Young's modulus at infinite field, e is the strain and T the longitudinal stress.² When the sample is stressed there is an additional strain, $(3\lambda_s)^2(M/M_s)^2$, that tends to reduce the stress and hence the value of Young's modulus E . This is the origin of the ΔE effect, the change in Young's modulus E with magnetic field. The field dependence comes in through the $(M/M_s)^2$ term. A large ΔE effect implies a large magnetomechanical coupling factor k , the figure of merit that determines how efficiently the material transfers energy between the magnetic and elastic systems. E can be changed in value by a factor of ten with a field about three times the earth's field in the best ribbon materials.⁵ The maximum value of the coupling factor, with defects ignored, is $(3\lambda_s)^2 E_0 / 2K$. This is also a measure of the ΔE effect.²

The change in Young's modulus with field leads to period doubling bifurcations.^{4,5} This allows acoustic parametric amplification, i.e., a sound wave scattering off a device can be mechanically amplified via the magnetic field. Because the ΔE effect is large, a small ac magnetic exciting field will reach threshold conditions for parametric amplification.

In magnetostrictive materials the value of the permeability μ depends⁶ on the longitudinal strain e , i.e.,

$$\mu = \partial B_1 / \partial H = \mu_0 + M_s^2 / (2K + [3\lambda_s E_0] e).$$

B_1 is the longitudinal component of the flux density vector B and μ_0 is the permeability of free space. This equation illustrates the strain dependence of the magnetic permeability μ . The magnetic model we have used is the simple rotational model evaluated at low magnetic fields with $\mu/\mu_0 \gg 1$. The complete theory is given in Ref. 5.

To calculate the figure-of-merit FM we compare the use of the magnetostrictive material in a strain gage configuration with the use of resistance strain gages. In a simple resistance strain gage $FM = 1/R \partial R / \partial e$ because we measure R as a function of strain. In the magnetostrictive strain gage we measure the permeability μ so that $FM = 1/\mu \partial \mu / \partial e = 3\lambda_s E_0 / 2K$. There is nothing unusual about the values of λ_s and E_0 in the materials presented here. By simple magnetic annealing we are able to achieve values of K less than 50 J/m³. This is a factor of 10^3 less than crystalline iron, which was considered to have a low value of anisotropy in the past. Thus we obtain a value for FM of about 2×10^5 . This is to be compared with values of 250 for semiconductor strain gages.

The experiment⁶ to confirm the above theory was effected by attaching a ribbon of material to a beam that was bent with a constant radius of curvature. Instead of using glue, a highly viscous liquid was used for the attachment. Glue introduces

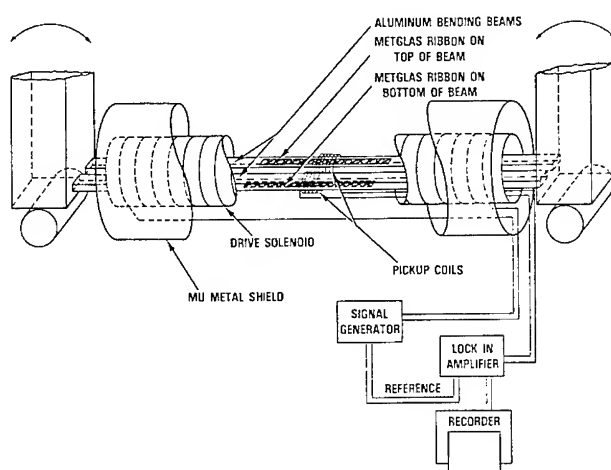


Fig. 2. Diagram of the experimental bending beam apparatus used to measure the strain gage figure-of-merit for amorphous ribbons with high magnetoelastic coupling factors. The pickup coils are connected in opposition. The amorphous ribbons are bonded with a high viscosity fluid to the top of one beam and the bottom of the other beam.

excessive inhomogeneous strains when hardening. The permeability of the material was measured as the beam was bent by means of a coil around the beam. The experiment used a double structure where one ribbon went into tension and the other ribbon went into compression when the beam bent. The measured value of FM was 4×10^5 , double the predicted value.

The temperature dependence of the figure-of-merit was found to be quite small. Strains of less than 10^{-9} at a frequency of 0.05 Hz were measured with no temperature control or compensation. There are theoretical reasons for expecting the small temperature dependence. As cryogenic temperatures are approached the temperature dependence should become much smaller with values of FM remaining about the same. The amorphous material itself retains its properties at as low a temperature as desired. Other tactile devices will have similar figures of merit.

MAGNETIC ANNEALING AND CHARACTERIZATION

Introduction The rapid cooling required to prevent crystallization

results in random internal stresses in the material. If the temperature at which crystallization starts is high enough, holding the temperature for a few minutes just below this temperature will relieve these stresses. Any crystallization impairs performance since even a tiny crystallite acts as a pinning point for magnetic domains. (Domain walls are about $1\text{ }\mu\text{m}$ in the soft Fe based materials, so that a crystallite must be significantly smaller to avoid pinning.) Unfortunately, some embrittlement always accompanies the stress relief.

Magnetic Annealing The prescription is to raise the temperature to just below crystallization. In the original work on $\text{Fe}_{81}\text{Si}_{3.5}\text{B}_{13.5}\text{C}_2$ this temperature was about $390\text{ }^\circ\text{C}$, slightly above the Curie point. After 10 minutes of stress relief, as the temperature is lowered through the Curie point, magnetic exchange forces become effective if an applied field is present. The applied field must be slightly in excess of the demagnetizing field. The starting material is amorphous, i.e., a nonunique, nonequilibrium structure. An infinite number of configurations are available. To minimize the magnetic energy a structure with an easy axis in the direction of the annealing field is selected from the infinite number of structures available. The easy axis is the direction the magnetic anisotropy energy is a minimum. The direction of the exciting field or bias field is normally placed along the hard axis, orthogonal to the annealing field. Thus we are able to establish a convenient direction for the magnetic field exciting or biasing a magnetic device.

Another important feature is the possibility of annealing under longitudinal stress and torsion. This permanently influences the atomic configuration of the material. An example is a unique fluxgate magnetometer^{3,7} that uses torsional stress annealing to yield a helical magnetic anisotropy. This device can exploit current excitation because of the helical magnetic anisotropy. An exciting coil is unnecessary.

Characterization The best way to characterize a sample with respect to easy axis direction, uniformity of easy axis direction and influence of defects is to use magnetic domain observation. Domains seen with an electron microscope are shown in ref. 1. For good performance domains should be stripelike. When local deviations in internal stresses are present, the magnetostriction causes deviations in the direction of the magnetic moment.

This is shown in Fig.3 where the preferred pattern is seen on one side of the sample and considerably more inhomogeneous moment distribution on the other. The sputtered material⁸ was removed from the substrate and subsequently magnetically annealed. Annealing failed to eliminate the damage caused by the removal process on the inhomogeneous side. The orthogonal stripes as seen on one side of the sample are the desired configuration. They are in the direction of the annealing field. Deviations degrade device performance. Samples are normally cut from a large sheet. Care must be taken by grinding the edges to remove worked material. The stripe spacing is also important. If the surface is not uniform, walls can be straight but pinned. Domain spacing will then be much closer. Equilibrium spacing can be calculated and has been realized in samples with very good surfaces. It should be noted that in applications for transformers, a wide spacing is not

desirable because it leads to anomalous eddy current losses. For

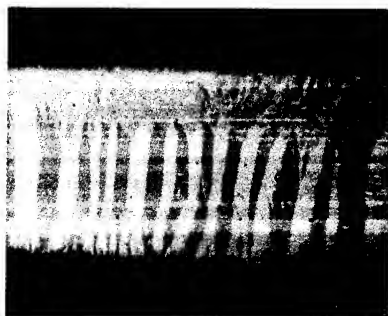


Fig.3. Domains in magnetron-sputtered material. The material has been removed from the substrate and field annealed. The stripe-like part of the pattern is the desired pattern. In the other part defects have dispersed the magnetic moment. This is the reason that the coupling factor is not as large as in high quality melt-spun material.

this case defects are sometimes introduced on the surface to obtain closer domain wall spacing. The anomalous losses are normally not a problem with magnetoelastic devices because magnetization proceeds by moment rotation, not domain wall translation.

Wires have proven to be much more difficult to characterize because domains are difficult to observe in the cylindrical geometry. Some observations have been made.⁹ However, coupling factor measurements can show sample perfection.⁹ In general anisotropy fields (the field at which the magnetoelastic coupling factor peaks) should be low. Coupling factor curves are shown in Fig.4 for samples annealed at 723K and 748K. The samples are 100 mm long and have been annealed in a transverse field of 7.8 kOe. It is clear that better stress relief improves the coupling factor, the figure of merit that indicates how efficiently energy is transferred between the magnetic and elastic systems. The falloff above the anisotropy field should be rapid as shown in Fig. 4. Defects broaden and decrease the peak of the coupling factor vs field plot. A theory that describes the effects of defects on the coupling factor is given in Ref. 4.

AMORPHOUS WIRES

Introduction Wires are made by injecting the molten alloy into a rotating water filled wheel. The maximum diameter is about .125 mm. The diameter is not uniform, but "pearled". It can be drawn down to .01 mm. The drawing causes a highly worked condition that may be difficult to remove by annealing. The as-cast material is

very tough and ductile. The strength to weight ratio is so high that it has been considered for use as tow cables. The material is elastically linear up to its breaking point because of the lack of dislocation motion. The ruggedness of this geometry compared with the ribbon geometry can make it more desirable for some applications. It must be remembered that annealing makes the material considerably more brittle. Wires of the same composition as ribbon material show the same characteristics with respect to saturation moment and magnetostriction. However B-H loops are quite different, showing that the magnetization process is quite different. This is due to the cylindrical geometry.

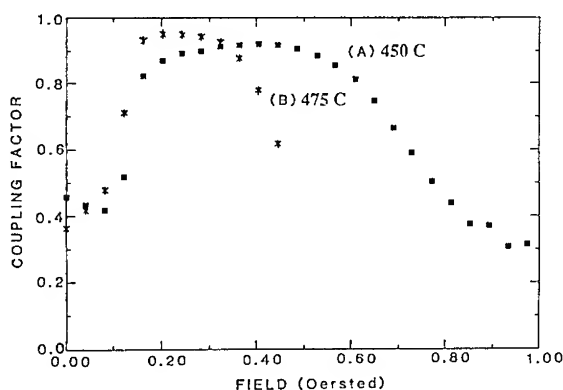


Fig. 4. Coupling factor vs field in amorphous wires.⁸ The wires are annealed at two different temperatures. The lower temperature does not give complete stress relief. Therefore the maximum coupling factor is lower and values are more widely distributed.

The magnetization of the wire with zero applied stress and field can be pictured as consisting of two parts, a core and a sheath.¹⁰ The moment in the core is always longitudinal as required by the wire geometry. The moment distribution in the sheath depends on annealing and external variables. Magnetization is a nonlocal process because of the nonuniform moment distribution. During the rapid solidification process the sheath cools before the inner core. As a result the sheath is compressed by the core. Unannealed wires with positive magnetostriction material then exhibit a chevron pattern with the moment sometimes normal to the surface.¹¹

Transversely Annealed Wires Amorphous wire with composition $\text{Fe}_{77.5}\text{Si}_{7.5}\text{B}_{15}$ and 0.125 mm diameter was kindly provided by Unitika, Inc to various researchers. These wires have magnetostriction constants of $30 - 40 \times 10^{-6}$. The high maximum coupling factor shown in Fig. 4 indicates the achievement of very good stress relief and an extremely small transverse anisotropy in magnetically-annealed amorphous wire. Annealing can change the domain structure

to a probable bamboo pattern⁹, i.e., the domains may have a circular magnetization because the field induced transverse anisotropy is so small.

In the experiments to measure the quasi-dc magnetization, a pickup coil about 10 mm long and placed at the center of the sample is used. If the voltage along the length of the wire is simultaneously measured, the circular component of the moment is known. This is nonzero even in annealed wires indicating that residual torsional stress remains after annealing.¹²

Barkhausen Jumps Unannealed amorphous wires can show conventional giant Barkhausen jumps that result in a simple rectangular hysteresis loop.¹⁰ There is a range of domain wall depinning fields so that if the depinning field for central magnetization is high enough, magnetization reversal takes place by domains becoming depinned at the ends of the wire. Magnetization in giant Barkhausen jumps proceeds by walls propagating from the ends of the wire toward the middle.¹⁰ The propagation is continuous, i.e., once the wall starts to move it continues, without an increase in field, until the magnetization is reversed. This leads to the rectangular hysteresis loop characteristic of giant Barkhausen effect. We choose to call this a first order process because once the process starts, it goes to completion without an increase in field. There is a large singularity in the susceptibility because it is an instability process.

A different kind of Barkhausen effect in Fe-B-Si amorphous wires has been observed under a variety of conditions.¹³ In one experiment the wires were subjected to a static twist and a static longitudinal stress during magnetization.¹³ The longitudinal strain was unimpeded. It is still giant Barkhausen in nature because the central magnetization is still impeded by domain wall pinning, but magnetization takes place by another process. This new process is different from first-order giant Barkhausen because it follows the field, i.e., the value of the magnetization does not jump. Once magnetization starts, it does not go to apparent saturation if the field is not increased. This is an instability process, but it is a second order giant Barkhausen jump. The singularity in the susceptibility is smaller because there is only a small jump in the magnetization to apparent saturation. Also the critical exponent was found to be about 1/2, typical of a second-order process.¹³ The magnetization starts linearly at low fields, then displays a quadratic field dependence as it proceeds to apparent saturation. This is not full saturation. At apparent saturation the magnetization in the sheath is at an angle roughly 45 deg to the longitudinal axis. This angle depends on the values of the twist, field and longitudinal stress.

In addition to the instability in the magnetization process, the anomalous losses caused by domain wall motion are extremely high.¹³ In the transverse-field-annealed wire the anomalous losses are so large that there is a significant difference between the area of the quasi-dc hysteresis loop and ones taken at less than 10 Hz.

In summary Barkhausen jumps are unstable routes to magnetization caused by domain wall pinning. The unstable structure can proceed to equilibrium in a hierarchy of processes, depending on details of domain wall structure and pinning.

PROTOTYPE ACCELEROMETER USING SPUTTERED MATERIAL

Introduction Sputtering has been successfully done by many different experimenters. Our material was magnetron-sputtered onto an Al substrate and subsequently removed with KOH. It was then annealed conventionally.⁸ The composition of the film is essentially that of the target. A domain pattern is shown in Fig. 3 and is discussed in the characterization section. The sputtered material, in spite of imperfections, showed a coupling factor of .71. This was considered proof enough that sputtered materials would exhibit properties close to those prepared by spinning techniques. Sputtering has advantages over casting techniques. An example is illustrated below.

Prototype Accelerometer A small, conventional cantilever can be machined on a silicon chip. Then a simple multilayer combination of conductors, insulators and active material are sputtered onto the chip. There has been significant success reported here.¹⁴ Normally a magnetic device uses coils for detection. However, coils do not scale well to small sizes. They are not necessary here. A current excitation is used that detects the change in permeability by the change in the impedance of the magnetostrictive material. It is not a magneto-resistance effect. The temperature dependence of the figure-of-merit will be considerably smaller at room temperature than for semiconductor strain gages. At cryogenic temperatures the dependence will be extremely small. What could result is a miniature, cheap, extremely sensitive accelerometer or displacement device.

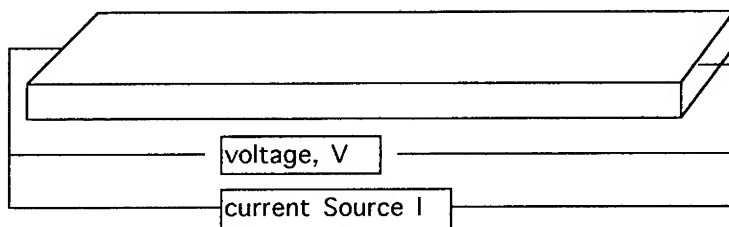


Fig. 5. Measurement of the impedance of an amorphous ribbon. The ribbon has width W and thickness $2a$. The thickness dimension is x .

We first show the measurement of the self-impedance of a ribbon (Fig. 5). If an ac current $I \sin(\Omega t)$ is imposed on a sample with constant amplitude I , the impedance z of the ribbon is V/I , where V is the voltage drop. Since the ribbon is ferromagnetic, the reactive component of V , V_r (90 deg out of phase with I), is nearly proportional to the permeability μ . Since μ is strain dependent, V_r is a measure of the strain. This strain- V_r relationship is the basis of the coil-free device.

The theory is the following.⁴ We assume the domain structure

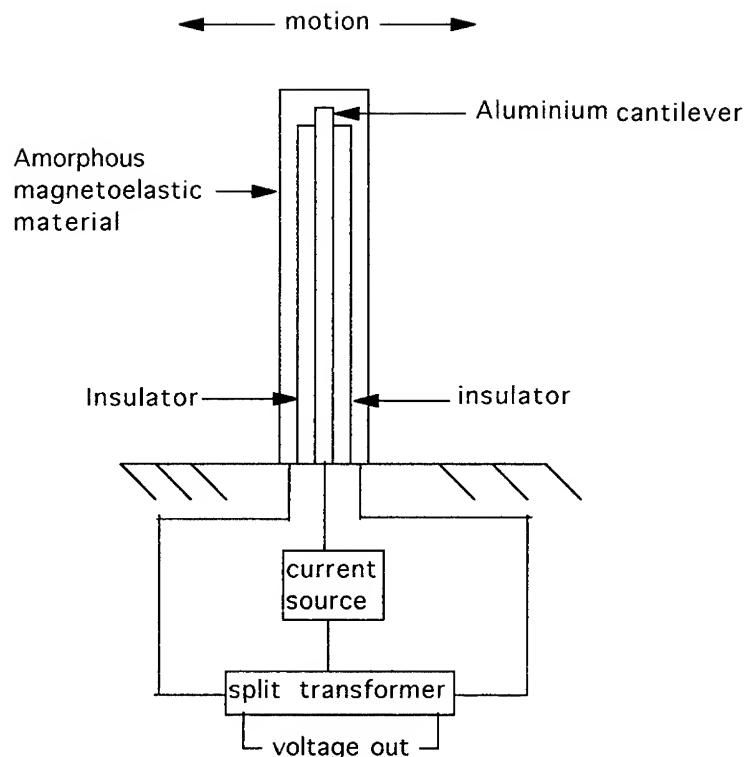


Fig. 6. Current excited single axis accelerometer or displacement sensor. The current flows up through the Aluminum (or other metal) and down through the active material. The frequency Ω is adjusted so that the magnitude of the dimensionless skin depth $d = (i\Omega\sigma\mu a/2)^{1/2}$ is about 1. In the drawing $2a$ is the thickness of the active material (the visible dimension above), σ the conductivity, and μ the strain-sensitive permeability. Values of μ are higher when the active material is in tension and lower when in compression. The design is complimentary so that there is no signal out when the cantilever structure is straight. When it bends to the left or right a signal out is realized. Layer thicknesses are not to scale.

is such that the magnetic moment vector is longitudinal, in the same direction as the current. This can be achieved in the fabrication process. Then we must solve Maxwell's equations in a conductor where the current density $\mathbf{j} = \sigma \mathbf{E}$, with \mathbf{E} the electric field vector and σ the conductivity. We assume the material has a large width W with respect to its thickness $2a$. Then, except near the edges, the only significant component of the magnetic field vector \mathbf{H} is H_t , the component of \mathbf{H} normal to current and the

thickness dimension, x . Then Maxwell's equations are $\partial^2 H_t / \partial x^2 = i\Omega\sigma\mu H_t$, with the solution $H_t = (I/2W) \sin(dx/a) / \sin d$. I is the total current. The dimensionless skin depth is $d = (i\Omega\sigma\mu a^2)^{1/2}$. Through μ it contains the strain dependence. Then the longitudinal electric field $j/\sigma = Id \cos(dx/a)/(2a\Omega\sigma \sin d)$. We then obtain the self-impedance:

$$Z = R_0 d \cot(d),$$

where R_0 is the dc resistance. Synchronous detection can be used so that only the imaginary part of Z , Z_r is measured. Then the figure-of-merit $FM = 1/Z_r \partial Z_r / \partial \epsilon$. If we choose Ω so that the magnitude of $d \approx 1$, expanding the $\cot(d)$ in a power series in d gives the same expression for FM as before. Thus in principle nothing has been lost by using this method of measurement. A hydrophone¹⁵ has been patented using ribbon material and this detection method. The proposed device is shown in Fig. 6. To fabricate the device an insulating layer is sputtered onto a cantilever. Then the amorphous ferromagnetic metal (AFM) is sputtered on the insulator. There must be several attempts here with different materials¹⁴ to achieve thermal expansion compatibility. The AFM has a rather low coefficient of expansion of about 6×10^{-6} per degree. The AFM must be in tension to achieve proper magnetic domain configuration. Magnetic domain observations will be extremely useful. Wide longitudinal in-plane domains with a regular shape are wanted. If there are deviations from this situation, the kind of deviation will indicate what must be done to achieve the desired domain structure. The proper domain structure is a necessary and almost sufficient characteristic.

SUMMARY

We have given a brief outline of amorphous magnetic materials. The subject is now mature. Applications will hopefully arrive more frequently. We can only wait and see.

REFERENCES

1. C. Modzelewski, H. T. Savage, L.T. Kabakoff and A. E. Clark, IEEE Trans. Magn. **MAG 17**, 2837(1981).
2. H. T. Savage, M. L. Spano, J. Appl. Phys. **53** (11), 8092(1982).
3. A. Hernando, M. Vasquez and J. M. Barandian, "Metallic Glasses in Sensing Applications," J. Phys. E **21**, 1129-1139 (1988).
4. H. T. Savage, "The ΔE effect in magnetoelastic materials Concise Encyclopedia of Magnetic and Superconducting Materials, Ed. Jan Evetts, Pergamon Press, 266(1992).

5. H. T. Savage and Charles Adler, Effects of magnetostriction in amorphous ferromagnets, *Material Science and Engineering*, **99**, 13-18 (1988).
6. M. Wun-Fogle, H. T. Savage, A. E. Clark, *Sensors and Actuators* **12**, 323-331 (1987).
7. Otto V. Nielsen, J. Gutierrez, B. Hernando and H. T. Savage, *IEEE Trans. Magnetics*, **26**, No. 1, 276(1990).
8. L. T. Kabacoff, H. T. Savage, M. Wun-Fogle and F. Randall Troetschel, "Thermal, Magnetic Magnetomechanical Properties of Amorphous Magnetron Sputtered Fe₇₈B₁₃Si₉", *IEEE Trans. Magnetics*, **MAG 22**, No. 5, 427(1986).
9. M. Wun-Fogle, H. T. Savage, L. T. Kabacoff, M. L. Spano, J. R. Cullen, G. A. Jones, and D. G. Lord, *IEEE Trans. Magn.* **25**, 3617 (1989).
10. R. Malmhall, K. Mohri, F. B. Humphrey, T. Manabe, H. Kawamura, J. Yamasaki, and I. Ogasawara, *IEEE Trans. Magn.* **MAG-23**, 3242(1987).
11. Dr. Manuel Vázquez, private communication.
12. M. Wun-Fogle, H. T. Savage, unpublished.
13. H. T. Savage, D-X Chen, C. Gómez-Polo, M. Vázquez and M. Wun-Fogle, *J. Phys D.:Appl. Phys.* **27**, 681(1994).
14. John L. Wallace, *J. Appl. Phys.*, **73** (10), 5360(1993).
15. H. T. Savage, U. S. Patent No. 4,497,046; Long Line Hydrophone.

MAGNETOMECHANICAL PROPERTIES OF CIRCUMFERENTIALLY- FIELD-ANNEALED METGLAS[®] 2605SC CYLINDERS

J. B. RESTORFF, M. WUN-FOGLE, A. E. CLARK, AND THU-VAN T. LUU
Naval Surface Warfare Center, 10901 New Hampshire Ave., Silver Spring, MD 20903

ABSTRACT

We have measured the magnetomechanical coupling coefficient of Metglas[®] 2605SC ($\text{Fe}_{81}\text{B}_{13.5}\text{Si}_{3.5}\text{C}_2$) ribbons that were annealed into 1.27 and 0.8 cm diameter cylinders. Lengths ranged from 0.6 to 5 cm. A novel furnace was constructed in which a cylindrical magnetic field was supplied by a current carrying copper rod. During the annealing, a 300 A current created a circumferential field of more than 6400 A/m. Annealing temperatures ranged from 380 to 420 °C. Large shifts in both the optimum bias field and the coupling coefficient as a function of length and diameter were found due to demagnetizing effects. Impedance vs. frequency measurements show large numbers of modes, some of which are field dependent. Effective coupling coefficients of the lowest order longitudinal mode were calculated from impedance measurements by using $k^2 = 1 - f_r^2 / f_a^2$, where f_r and f_a are the resonant and antiresonant frequencies respectively. Coupling coefficients for 5 cm long cylinders were as high as 0.58. When the demagnetizing factor is taken into account, we find material coupling coefficients as high as 0.89.

INTRODUCTION

Amorphous metallic ribbons were developed for use as low loss transformer cores in the electric power industry. In the late 1970's there were hints that ribbons annealed in a transverse magnetic field would have very large magnetomechanical coupling coefficients ($k > 0.85$)¹. The coupling coefficient k is a measure of the conversion efficiency between the mechanical and magnetic energies; perfect transduction would have $k = 1$. These high values of k make the ribbons good candidates for sensor applications. Then, in 1981, Modzelewski, et al.² produced ribbons with an astonishing coupling coefficient of 0.96 using a transverse magnetic field annealing process. Since that time, many sensors based on the ribbons have been proposed including strain gages³, force sensors⁴ and magnetometers⁵. A second effect of the coupling between the mechanical and magnetic properties is the ΔE effect, which is the change of Young's modulus with magnetic fields. At zero and high fields, the magnetic moments are locked; we call this the "hard" modulus. At intermediate fields, the material can change size by rotating the moments. In ribbon materials with the highest k 's, the material can be as much as ten times softer with the proper magnetic bias field.

Most of the devices use the ribbon in a flat form, but Bucholtz, et al.⁵ used the ribbon rolled into a cylindrical shape. In this paper, we will refer to this shape as a scroll because the inside and outside edges are not connected. The scroll shape has some advantages in that the magnetic circuit is complete around the circumference, eliminating demagnetizing effects in that direction. In this paper, we describe a systematic study of the magnetomechanical properties of circumferentially annealed amorphous ribbon scrolls of various diameters and lengths.

EXPERIMENT

Sample Preparation

Samples were cut from 5.1 cm wide, 15 μ thick ribbons of Metglas 2605SC ($\text{Fe}_{81}\text{B}_{13.5}\text{Si}_{3.5}\text{C}_2$). The ribbons were wrapped around either a 8 mm or 12 mm diameter mandrel. Because the as-cast ribbon is rather "springy" small pieces of high temperature tape were used to keep the ribbon in place. The length was chosen to wrap around the mandrel either once or twice, which we refer to as a one or two layer scroll. The ribbons were annealed in a furnace specially designed to develop a small circumferential magnetic easy direction, see Fig. 1. The furnace consists of an aluminum heater block surrounded by Nichrome heaters wound on mica insulators. The ribbon was placed inside the heater and a 6.3 mm diameter copper rod was placed through the center of the sample. The current through the rod was estimated to be 300 A from the field outside the supply lines. This gives a field of 8000 (100 Oe) and 12 000 A/m (150 Oe) for the 12 mm and 8 mm diameter samples respectively. These fields are sufficiently high to circumferentially align the magnetic moments at the annealing temperature.

The annealing process consisted of a 10 min. ramp to and a 5 to 15 min. hold at the annealing temperature, which was between 380 and 420 $^{\circ}\text{C}$. At the end of the anneal, the 300 A field current was applied to the rod and shortly thereafter air was forced through the furnace to achieve a rapid cooldown. The field current was removed when the sample cooled to below 200 $^{\circ}\text{C}$ (about 3 min).

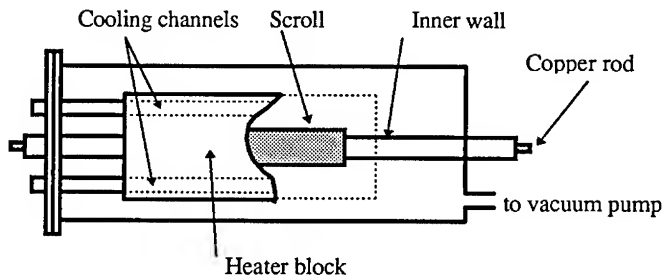


Figure 1. Furnace for annealing ribbon scrolls.

Measurement

Impedance versus frequency curves were measured in the apparatus shown schematically in Fig. 2 using an HP 3570A network analyzer over a frequency range of 10 - 250 kHz. Two identical coils were placed in the center of a long solenoid with two windings. The inner winding supplied the DC bias field, but had too much inductance to drive at high frequencies. A second coil with only a few turns supplied the AC drive. The sample was placed in one of the coils and the other was connected as a bucking coil. A typical data set is shown in Fig. 3. Notice the complicated features at about 125 kHz where the radial and length modes interact (see the discussion below). Effective coupling coefficients of the lowest order longitudinal mode were calculated from impedance measurements by using $k^2 = 1 - f_r^2 / f_a^2$, where f_r and f_a are the resonant and antiresonant frequencies respectively.

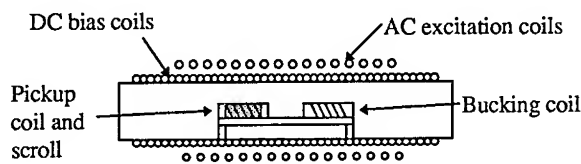


Fig. 2. Schematic of magnetomechanical coupling measurement.

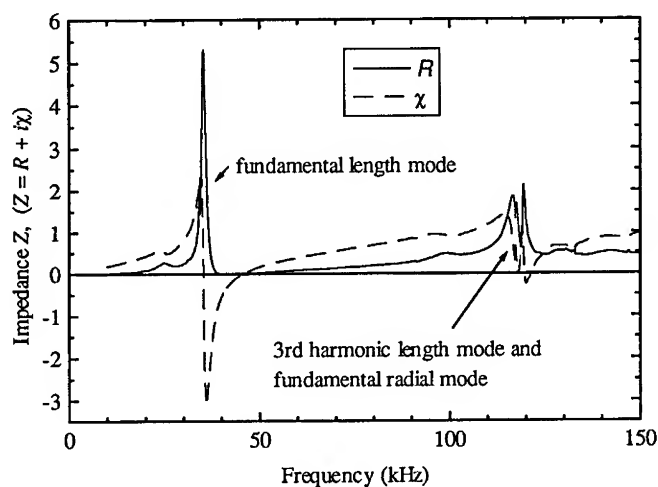


Fig. 3. A typical impedance data set. This set is from a 1.3 cm diameter x 5.1 cm long two layer scroll at maximum k , which for this scroll was 560 A/m.

RESULTS AND DISCUSSION

Modes

The fundamental modes for a hollow cylinder⁶ are a length mode (the whole cylinder becomes longer and shorter) and radial mode (the cylinder changes its diameter). These modes are coupled both through Poisson's ratio and magnetoelastic effects. The coupling is strongest when the length to diameter ratio is near 1.5. Using a value of 144 GPa for the elastic modulus⁷ and an estimated Poisson's ratio of 0.35, we calculate the frequency of the radial mode to be 180 and 119 kHz for the 8 and 12 mm diameter samples respectively. We also used the ANSYS finite element modeler to examine the modes of a thin cylinder. The results displayed the expected

fundamental modes as well as a host of other modes with an almost continuous distribution of frequencies.

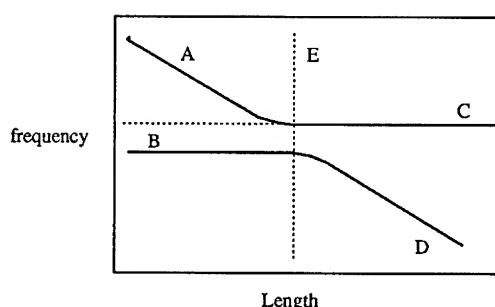


Fig. 4. Schematic of the fundamental radial and length modes.

Fig. 4 shows a frequency vs. length chart for fundamental modes of a cylinder. The sloped regions of lines A and D are the length mode, which depends mostly on the length. The horizontal regions of lines B and C are the radial mode, which is determined primarily by the diameter. Due to the coupling between the modes, the lines do not cross. The long-length radial mode (C) is at a higher frequency than the short-length mode; the radial oscillations occur too fast for the length mode to follow, hence the coupling between the modes due to the Poisson's ratio and magnetoelastic coupling is reduced. The line E is at the length to diameter ratio of 1.5 and represents the length at which the two uncoupled modes would have the same frequency.

Fig. 5 shows the experimental data for the scrolls taken at the field where the magnetomechanical coupling factor is the highest. The open symbols are assumed to be the radial modes; they occur at the expected frequencies and are sharper than the length modes. The slanted lines represent the fundamental and third harmonic frequencies of the length mode, calculated using the hard modulus. The data lie below these lines because the ΔE effect has softened the modulus. The two horizontal lines represent the radial modes of the large and small diameter scrolls, again using the hard modulus. On the right hand side of the figure, the small diameter radial modes lie directly on the line; on the left hand side the frequency drops as expected. It is difficult to say much about the radial modes of the large diameter cylinder because the high frequency portion overlaps the third harmonic modes.

Demagnetizing Effects

Demagnetizing effects are caused by unpaired magnetic poles at the ends of the sample and are a function of sample geometry. The effect of these poles is to create a field opposite to the applied field and results in a reduced field in the interior of the sample. The demagnetizing effect is largest when the sample is short and fat (field applied to the short dimension) and smallest when the sample is long and thin (field applied to long dimension). This in turn leads to coupling factors and optimum bias fields that depend on sample geometry. We distinguish between the system coupling factor k , which includes the geometry, and the material coupling factor k_{33} , which has been corrected for demagnetizing effects. The demagnetizing effects were estimated from

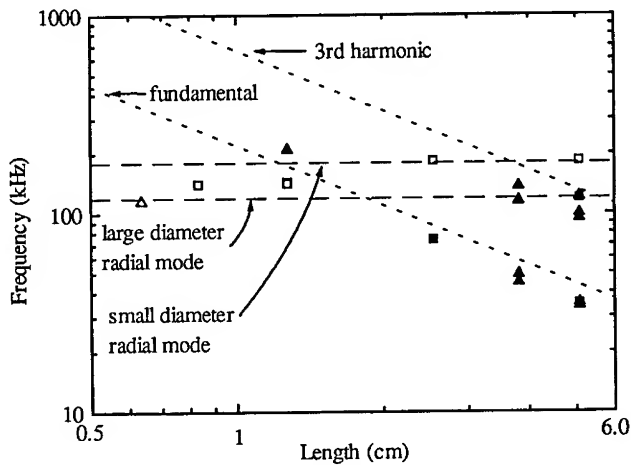


Fig. 5. Resonances observed in the circumferentially annealed scrolls. The squares mark small diameter scrolls and the triangles large diameter scrolls. The open symbols are what appear to be the radial modes and the closed symbols are length modes.

Joseph and Schlomann⁸ which calculated the demagnetizing factor of rectangular parallelepipeds. Since our cylinders complete the magnetic circuit around the circumference, we modify their approach by giving one of the dimensions infinite length. If the length of the cylinder and the applied magnetic field lie in the z direction, the demagnetizing factor N_{zz} is given by

$$N_{zz}(x, y) = \frac{2}{4\pi} \left[\cot^{-1}(f(y, z)) + \cot^{-1}(f(-y, z)) + \cot^{-1}(f(x, -z)) + \cot^{-1}(f(-x, -z)) \right]$$

where

$$f(y, z) = \frac{\lambda/2 - z}{t/2 - y}$$

λ is the length of the sample, t is the thickness and x and y are the positions in the material. The demagnetizing field is given by

$$H = N_{zz} \mu_0 M_s$$

where $\mu_0 M_s$ is the saturation magnetization, about 1.8 T in this material. Since the demagnetizing factor satisfies a sum rule, making the demagnetizing factor zero in one direction means that it must become larger in the other directions, thus the scrolls have a larger demagnetizing factor in

the length direction than a ribbon of the same length. Clark and Wun-Fogle⁹ give the material coupling factor in terms of the measured value of k as:

$$k_{33} = \left[\frac{k^2}{1 - N_{zz}\chi_e(1 - k^2)} \right]^{0.5} \text{ and } \chi_e = \frac{\chi}{1 + N_{zz}\chi}$$

where χ_e is the effective susceptibility and χ is the susceptibility, about 18 000 for the ribbon material. Table 1 shows a summary of the data.

Table 1. Summary of the experimental data for the circumferentially annealed scrolls.

	A	B	C	D	E	F	G	H
diameter (cm)	0.84	0.84	0.84	1.3	1.3	1.3	1.3	1.3
length (cm)	1.3	2.5	5.1	1.3	3.8	5.1	5.1	3.8
layers	2	2	2	1	1	1	2	1
N_{zz} ($\times 10^{-4}$)	20	7.6	3.8	7.6	2.5	1.9	3.8	2.5
H_{zz} (A/m)	2900	1100	540	1100	360	270	540	360
k	0.44	0.44	0.56	0.11	0.47	0.58	0.58	0.58
H_k (A/m)	2400	1100	720	1200	560	480	720	560
k_{33}	0.95	0.88	0.88	0.40	0.78	0.83	0.89	0.86

In conclusion, we have made the first systematic examination of the magnetomechanical properties of circumferentially field annealed scrolls. The annealing process produces scrolls with properties that make them useful for sensor applications.

REFERENCES

- ¹ M. Brouha and J. van der Borst, *J. Appl. Phys.* **50**, 7594 (1979) and M. A. Mitchell, J. R. Cullen, R. Abbundi, A. Clark and H. Savage, *J. Appl. Phys* **50**, 1627 (1979).
- ² C. Modzelewski, H. T. Savage, L. T. Kabacoff and A. E. Clark, *IEEE Trans. Magn.* **17**, 2837 (1981).
- ³ J. B. Restorff, M. Wun-Fogle, K. B. Hathaway and A. E. Clark, *J. Appl. Phys.* **69**, 4668 (1991).
- ⁴ E. Hristoforou and R. E. Reilly, *IEEE Trans. Magn.* **27** 5244 (1991).
- ⁵ F. Bucholtz, K. P. Koo, A. M. Yurek, J. M. McVicker and A. Dandridge, *J. Appl. Phys.* **61**, 3790 (1987).
- ⁶ Theodor F. Hueter and Richard H. Bolt, *Sonics*, (John Wiley & Sons, NewYork, 1955) pp.146 - 149.
- ⁷ Gordan Fish, Allied Corp., private communication; also agrees with values for ribbons measured here.
- ⁸ R. I. Joseph and E. Schlomann, *J. Appl. Phys.* **36**, 1579 (1965).
- ⁹ A. E. Clark and M. Wun-Fogle, *IEEE Trans. Magn.* **25**, 3611 (1989).

MATERIAL PROPERTIES AND RELATED CONSIDERATIONS FOR MAGNETOMECHANICAL SENSING DEVICES

IVAN J. GARSHELIS

Magnetoelastic Devices Inc., 17 Downing Three, Pittsfield, MA 01201

ABSTRACT

Suitability of specific materials for use in magnetomechanical sensors more often depends on combinations of properties than on an outstanding value of a single property. These combinations include ratios and products of properties from different physical families. While magnetic, magnetoelastic, electrical and strength properties often play key roles in determining the performance of the sensor, non-physical characteristics such as manufacturability, available forms, environmental compatibility, toxicity and costs strongly influence the device design and may well dominate the final choice of material. The development of materials specifically for use in this class of sensors is encouraged by their already broad and growing range of applicability.

INTRODUCTION

The mechanical forces exerted by and on the various members constituting a machine are often fundamental to the performance of its function. Immediate and accurate information concerning the most functionally important forces can be used to rationalize the control of the machine leading to its optimal performance and to also supervise other important aspects of operation such as safety and efficiency. These forces of interest are not limited to simple pushes and pulls but often appears as twisting or bending moments. They may also be distributed rather than localized, appearing e.g., as a pressure. Moreover, a force of interest need not be constant but may vary with time over a wide range of rates and over almost any conceivable interval.

Sometimes the important information is singular in nature, concerned only with identifying whether some action involving force is taking place, as for example that the driver of a motor vehicle is applying some force on the brake pedal. More often it is important to maintain a continuous flow of information concerning the magnitude of the force of interest (for example to improve the operation of an anti-skid braking system by considering the *amount* of force being applied to the brake pedal). In either case, processing, distribution and utilization of the information is made more convenient and immediate if it appears as an electrical signal. Devices that provide these electrical signals in response to mechanical force inputs fall into the general category of devices called *sensors*. Sensors that perform a *measuring* function by providing electrical signals having some feature that is proportional to a particular force quantity of interest are known as *transducers*. A sensor that provides an electrical signal that merely toggles between two values at a preset magnitude of the force of interest is known simply as a *switch*. While a variety of physical phenomena are readily utilizable in the construction of force sensors [1], attention here is to *magnetomechanical sensors*, i.e., devices based on the "inverse magnetostriction" manifestation of the magnetoelastic interaction [2] found in ferromagnetic materials. Magnetomechanical sensors are renowned primarily for their contactless mode of measurement, mechanical stiffness, robustness and high output signal levels [3]. They also provide remarkable versatility in application, compact form, comparative simplicity and economy. Recognition of these attributes was already encouraging sensor development almost

60 years ago [4]. Although the last decade has seen a significant inflation in the pace of development of new types of magnetomechanical sensors, as witnessed by the more than 100 relevant U. S. Patents and like number of articles in archival journals, commercial acceptance of the underlying technology is not a new phenomena. Consider for example that the classical torque and load measuring devices pictured in Fig. 1 have been continuously available since 1954 [5].

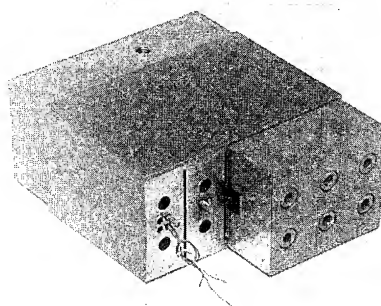
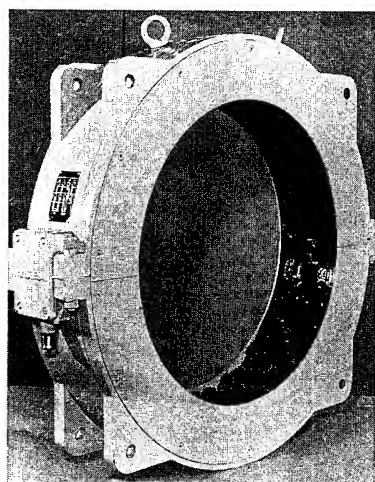


Fig. 1. The "Torductor" (left) for measuring torque on large shafts and the "Pressductor" (right) for measuring large compressive forces [5]. (Photos courtesy ABB Industrial Systems AB.)

The listings and associated references shown in Table I provide a sample indication of the persistent interest and wide range of application of this family of devices. The references reflect the especially high level of interest in transducers for both axial forces and torque.

TABLE I.

FORCE QUANTITY OF INTEREST	REFERENCES
Axial load - push, pull, weight	[4, 5, 6, 7, 8, 9, 10, 22, 25]
Bending moment	[6, 11]
Torque	[4, 5, 6, 12, 13, 14, 15, 16, 17, 23, 24]
Pressure	[18, 19, 20]
Acceleration, vibration	[21]

In this paper we examine how individual material properties, their combinations, and related considerations influence the configuration, performance and applicability of magnetomechanical sensing devices.

OPERATION OF MAGNETOMECHANICAL SENSORS

Two constructional features are essential to the operation of magnetomechanical sensors: a magnetoelastically active material (i.e., the sensing element) must be associated with the load

carrying member in such a manner as to be stressed in proportion to the force of interest and a suitable magnetic environment must be established to allow these stresses, via the magnetoelastic interaction, to modulate a *detectable* magnetic flux. In addition to these magnetic and mechanical features, a complete sensor also requires a means to accomplish the secondary step of converting the modulations of the detected flux into a correlated electrical signal.

There is no single manner for meeting the required "association" of the sensing element with the load carrying member. The load carrying member is quite often also used as the sensing element with or without compromising the choice of materials to serve both functions [5,7,8,9,10,11,12,14,18,19,20,23,25]. In torque transducers the sensing element is oftentimes a sleeve or ring [14,16,17] press fitted, soldered or otherwise attached to the shaft. Amorphous materials have been attached to the torqued shaft by cementing [18] or with shape memory alloy rings. Other methods of bonding including plasma (explosion) coating [24] have been suggested to assure the required transfer of stress from the loaded member to the sensing element.

Flux modulation results from the alteration, by the stress, of the effective magnetic anisotropy in the sensing element. (It is also possible to detect the stress induced variations in magnetic anisotropy by other means than flux detection, e.g., by sound velocity or resistivity changes, but these methods are not of interest here.) The modulated flux is made detectable by expanding at least some of the flux closure paths to include a large enough space *outside* the bounds of the sensing element to be intercepted by a practicable sensing means. As illustrated in Fig. 2, elimination of the complete internal compensation of the local magnetic moments that characterizes the unpolarized state establishes a bulk magnetic moment having flux closure paths that are now comparable in size to the sensing element itself. This polarization of the sensing element results from exposure to a magnetic field. With some sensing element materials and configurations adequate polarization exists only during application of the field while others remain permanently polarized after a single brief exposure to an adequately intense field. Since either situation provides a "suitable magnetic environment", their very distinction hints at the dependence of sensor operation on some specific properties of the material.

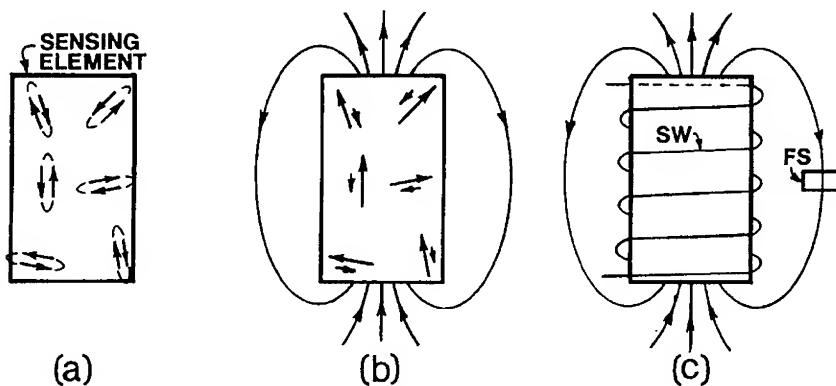


Fig. 2. The presence, small size and proximity of antiparallel domains in the unpolarized sensing element in (a) keeps flux closure within or close by the bounding surfaces of the element. The net magnetization characterizing the polarized state illustrated in (b) effectively expands many of the flux closure paths into the space outside the element. This flux can readily be detected by, e.g., its linkage with the turns of a solenoid (SW) or its density where it passes through a Hall effect device (FS) as indicated in (c).

MATERIAL PROPERTIES AFFECTING SENSOR OPERATION

It should be kept in mind that polarization serves only as a convenient means to make the effects of stress detectable since the altering effects of stress on the effective magnetic anisotropy take place whether or not the sensing element is polarized. Understanding that the detectable flux (ϕ) arises with the polarization it should also be clear that (for any one sensing element configuration and manner of mechanical loading) the rate of detectable flux (ϕ) change with stress (σ), i.e., $d\phi/d\sigma$ will vary with the intensity of the magnetization (M). Nevertheless, with M varying with field (H) in a generally non-linear manner that itself varies with the anisotropy (and other factors), it is not surprising that $d\phi/d\sigma$ has no simple dependency on either M or H , having instead a complex dependency on these and other factors including both intrinsic and structure dependent properties of the sensing element material. Clues to those factors affecting $d\phi/d\sigma$ that are important to the performance of a magnetomechanical sensor can be identified by carefully examining how stress affects the size and shape features of various types of M-H hysteresis loops. Major loops for two exemplary materials are shown in Fig. 3.

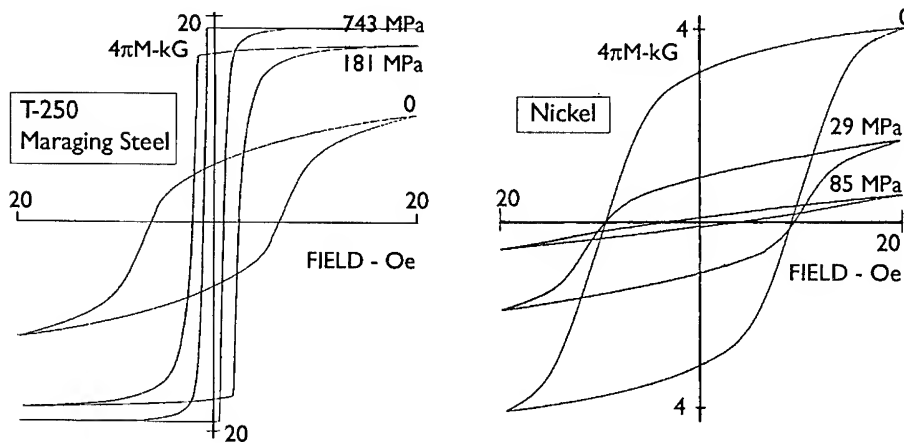


Fig. 3. (a) Quasi-static (DC) M vs H loops for an 18% Ni maraging steel [27] wire while under the tensile stresses indicated. (b) Similar loops for 99.9% nickel wire.

Immediately apparent upon examining these loops is that, although the loops for the unstressed wires of both materials are (except for the difference in vertical scales) reasonably similar in shape, the effects of tension on the M vs H characteristics of these two materials is profoundly different. This follows directly from the opposite signs of their respective saturation magnetostrictions (λ_s) since the major effect of stress anisotropy is to reorient the local moments from directions established by the quiescent anisotropy towards directions correlated with the stress. Thus since tension tends to elongate both specimens, both the elastic and the magnetoelastic strains will grow in the direction of this stress irrespective of the sign of λ_s . Since in maraging steels, $\lambda_s > 0$, any realignment of the magnetoelastic strain with the tension axis results in a similar realignment of the moments in the same direction. In nickel, $\lambda_s < 0$

hence any realignment of the magnetoelastic strain with the tension axis results in a correlated realignment of the moments at $\pi/2$ to the stress direction. Since the applied field was coaxial with the tension, the individual effects of field and stress on the bulk magnetization were complimentary in the maraging steel and contrary in the nickel wire. It should be obvious that under compressive stress these results will be interchanged between the two materials.

The effects of tension are seen in every feature of these loops. Tension makes the maraging steel loops taller and narrower. The more vertical portions become steeper and more uniformly vertical while the horizontal portions become both more, and more uniformly, horizontal. Curvature remains only in diminishing portions of the ascending limbs of the loops. On the other hand, the loops for the nickel specimen tend to be ever more compressed with increasing stress, tending towards closing into a single line only moderately inclined to the H axis. It takes little imagination to realize that, with either material, these effects of stress on M can be made to reflect a similar range of variation in ϕ and hence serve as the basis for operation of a magnetomechanical sensor. Closer examination of the loops shown in Fig. 3 with special consideration for the differences in specific features for these two materials will identify other properties besides λ_s that might affect $d\phi/d\sigma$. Consider the following:

1. The peak magnetization (at 20 Oe) in the unstressed maraging steel specimen is nearly 3 times that of the nickel specimen. This reflects the difference in saturation magnetizations, (M_s) between the two materials (approx. 19.5 kG for T-250 [27], 6.1 kG for nickel [28]).
2. The peak stress applied to each specimen was limited by the onset of yielding as indicated by failure to return to the original loop when the load was removed. The data indicates that even in the unaged condition maraging steel has a yield strength (σ_y) nearly 9 times that of nickel!
3. The near approach to perfect rectangularity of the loop for the maraging steel specimen at the highest loading indicates that the anisotropy has become effectively uniaxial in the field (and stress) direction. Thus the stress anisotropy component, i.e., $3\lambda_s\sigma_y/2$, must substantially exceed the quiescent anisotropy. Since the quiescent anisotropy can be no less than the magnetocrystalline anisotropy (K) (but may be larger due, e.g., to residual stresses) it is clear that in this material, $3\lambda_s\sigma_y/2 > K$.
4. Similarly, the approach of the loop for the nickel specimen to the single inclined line that is characteristic of a uniaxial anisotropy transverse to the field direction, indicates that in this material, the limiting stress anisotropy, $3\lambda_s\sigma_y/2$, is comparable to K.

Thus we see that $d\phi/d\sigma$ depends not only on M, H and λ_s , but also on M_s , K and σ_y .

In many materials, notably iron and steels of low alloy content, the effects of stress on M-H loop features is not so monotonic as in these exemplary materials. λ_s is rarely a single valued constant in crystalline materials and in many such materials its algebraic sign also varies with the direction of the moment relative to the crystal axes. Thus in many low alloy steels there is a "Villari" reversal [25] in $d\phi/d\sigma$ and hence in the visible effects of stress on M-H loop features. The limited utility of such materials for magnetomechanical sensor applications seems obvious and was in fact already recognized by Dahle [5].

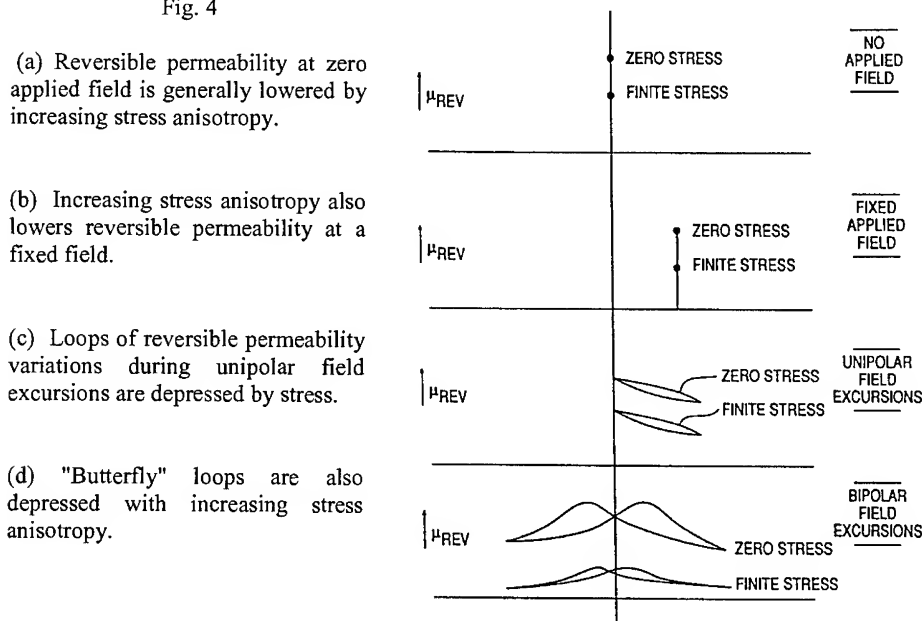
The loops in Fig. 3, in common with other major hysteresis loops, depict the combined effects of both reversible and irreversible magnetization altering processes. Further examination of these loops shows that stress not only alters the magnitude of the magnetization changes but also affects the distribution of processes by which these take place. In the maraging steel specimen for example, at a tensile stress of 743 MPa, magnetization changes are limited almost

exclusively to polarity reversal by irreversible processes, most probably by 180° domain wall motion. While increasing stress has increased the effective anisotropy, it has also narrowed the dispersion angle of its orientation, thereby reducing the range of fields required for reversal in the various domains. This reduction in dispersion also reduces the effective pinning energy of local variations in quiescent anisotropy and thus lowers the coercive force (H_c) [25]. In the nickel specimen, the reduction in dispersion angle leads towards a more uniformly transverse anisotropy thereby limiting magnetization changes to coherent rotation by the applied field, a process that is fully reversible. Since stress affects the dispersion of anisotropy, which in turn affects the size and shape of the hysteresis loops, it should be clear that the quiescent distribution of anisotropy orientations, including range and density of local variations, will also affect $d\phi/d\sigma$. Thus, in addition to intrinsic properties, all of the microstructural details of the sensing element material, including compositional variations, grain size and orientation, texture, defects, etc., will also affect the operation of the sensor through their effects on both $d\phi/d\sigma$ and σ_y .

Second order properties

Since stress alters both the slopes and intercepts of the lines comprising the loops, changes in specific features and combinations of features provide endless opportunities to sense the stress. The slopes represent magnetic susceptibility and the closely related quantity, permeability, (μ). In addition to the many permeabilities associated with regions on the major loops, reversible permeability (μ_r), a characteristic manifesting domain wall stiffness, may also be used to sense the stress. Examples of the effect of stress on μ_r under various conditions of applied field are illustrated in Fig. 4.

Fig. 4



One of the earliest attempts to utilize permeability variations for magnetomechanical measurement devices [5] recognized the value of an alternating (impulsive or pulsating) magnetization at a higher frequency than that associated with the application of the mechanical stress. Various workers have used excitation frequencies from those of the power line (50/60 Hz) to several tens or even hundreds of kHz. Eddy currents associated with such rapidly changing magnetization can distort the flux variation used to sense the force of interest. Thus the electrical conductivity of the sensing element material also becomes a factor affecting the sensor performance. In some specialized methods for sensing stress based on μ_r at high frequencies (magnetoabsorption [22]) permittivity also becomes a factor.

RELATED CONSIDERATIONS

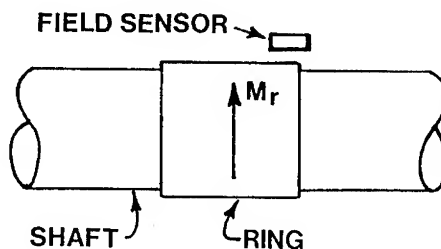
Sensor performance criteria

The function of a magnetomechanical sensor is to provide an electrical signal having a one to one correspondence with the force of interest. Depending on the application there are many factors that can be used to quantify how well the sensor performs this function. The most important of these are generally concerned with the concept of accuracy, i.e., how closely does the electrical signal represent the measured force quantity. Factors affecting accuracy include :

1. Repeatability - the closeness of agreement among repeated measurements of the output signal for the same value of the input force.
2. Hysteresis - the dependence of the output signal at a given value of the input force on the history of prior values of force.
3. Linearity - the closeness to which the electrical signal is a linear function of the force.
4. Stability - the non-variation over time of all other factors including zero force output signal and calibration.
5. Dynamic response - the immediacy with which the output signal follows the input force.

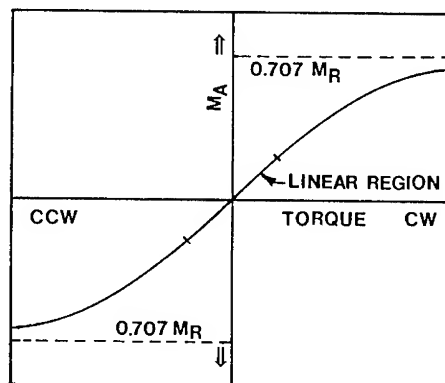
Sensor element properties have primary but not sole influence on the last four of these performance quantifying factors. Thus while hysteresis is a manifestation of irreversible magnetization processes, proper choice of the sensor element configuration can establish an operating mode in which the stress induced magnetization alteration is exclusively by coherent vector rotation. The torque transducer shown in Fig. 5 [14] provides an example of such a configuration. In this device a ring (typically of maraging steel), stretched to fit the underlying shaft, thereby placing it under a substantial circumferential tension is subsequently polarized in one circular direction. Since the positive principal stress associated with torsion lies along a 45° helix, the effect of torque on the shaft (coupled by friction to the tightly fitting ring) is to rotate the effective anisotropy towards this helix. The magnetization, already coherent under the action of the circumferential tension, and hence effectively a single domain, aligns with the reoriented anisotropy by pure rotation of the atomic moments. Other constructions while based on permeability variations, operate on similar principles [15]. More conventional magnetomechanical sensors operating on permeability variations swing the magnetization over a large enough excursion to minimize magnetomechanical hysteresis [3, 5, 17]. Still other methods are based on careful control of the composition and heat treatment of the sensor element material in addition to the proper choice of excitation parameters [23].

Fig. 5. Elements of a polarized ring torque transducer. The ring having a uniaxial anisotropy in the circumferential direction is polarized, i.e., has a remanent magnetization (M_r), in the circular sense indicated. The field sensor, e.g., a Hall element, senses the magnetic field arising from the axial component of M_r which develops when torque is applied to the shaft.



The desirability for linearity in the transfer function of a transducer is mostly a matter of convenience in further signal processing. Linearity in magnetomechanical sensors requires that either the sensitivity or the dynamic range of measurement be limited since all the effects of stress gradually approach saturated values. This circumstance is illustrated in Fig. 6 for the case of the polarized ring torque transducer shown in Fig. 5. Sensitivity (i.e., output signal per unit of applied force) is, for any one construction, proportional to $d\phi/d\sigma$ which in turn is proportional to the relative stress anisotropy, $3\lambda_s\sigma/K$. Thus to obtain a linear response over the largest possible range of applied force, wherein at the highest levels the working stress might well approach σ_y , it is necessary to keep λ_s/K small enough to stay within an adequately linear region. When using amorphous materials having very small values of K , it is desirable to also have a small value of λ_s . This requirement has been recognized [15] and it has also been applied to the development of new shaft materials for torque transducer applications [23]. Except for this limitation and the inherent limitation that hysteresis places on linearity, most non-linearities result primarily from the peculiarities of the flux change sensing means.

Fig. 6. The axial component of magnetization (M_A) varies linearly with the stress associated with the applied torque only over a limited torque range. At higher torques its slope diminishes continuously as it approaches its limiting value of $0.707M_R$ (the remanent magnetization) asymptotically.



Stability in performance depends on stability of the composition and microstructure of all materials used in the construction of the sensor. Relaxation of residual stresses, crystallization, phase changes, precipitation, corrosion, or any other physical, chemical or metallurgical processes that may be activated during the life of the sensor can clearly have adverse effects on sensor performance.

Dynamic response of magnetomechanical sensors is limited by both eddy currents and other lags associated with relaxation and creep phenomena (Snoek effect, Jordan lag, etc.). These effects rarely interfere with the adequate performance of the sensor. More important limitations on dynamic response come from the effective "sampling rate" of any associated magnetic excitation and the rate of transmittance of the stresses associated with the force of interest as determined by the velocity of sound in the intervening materials.

Non-repeatability in sensor performance is determined more by variations in dH/dt associated with the excitation circuits than by magnetic or magnetoelastic effects within the sensing element. If noise and ultimate resolution are included in repeatability measurements, then all irreversible magnetization processes, appearing for example as Barkhausen jumps, effectively limit the absolute repeatability and should therefore be avoided in critical applications.

Switch types of sensors are generally less demanding than transducers. In any event only stability and repeatability are of concern with such devices.

Operating Environment

Force sensing applications exist in machines and structures used in every industry. Due to this diversity in application it can be expected that some operating environments will be more rigorous than others. Some of the most important applications for magnetomechanical sensors are in environments that are particularly demanding, for example, those in which the sensor must be located in the engine compartment of a motor vehicle. Underhood operating temperatures range from a minimum of -40°C to at least $+140^{\circ}\text{C}$ (to 205°C near the exhaust manifold) [29]. Moreover, in these environments the sensor is likely to be exposed to water, oil and a great variety of chemical substances as well as the possibility of dust, sand and gravel bombardment [29]. While operating in these environments, the sensor may well be subjected to mechanical shock and vibration and possibly be subjected as well to substantial overloads. Many years of stable operation under these conditions is essential, especially if the safe operation of the vehicle depends on the accuracy of the sensor output signals. Hence the materials used for the sensor element as well as any bonding materials used to maintain the sensing element's required association with the load carrying member must have compositions, microstructures and dimensions that are unaffected by these environments. Since the operation of magnetomechanical sensors is fundamentally related to the detection of magnetic flux, the effects of ambient magnetic fields must also be considered. Shielding, sensing element location and orientation and other features of design must be included with material selection.

Examples of sensing element materials

Over the years a substantial variety of commercially available materials have been employed or at least recommended for use in magnetomechanical sensor applications. These have most often been chosen on the basis of availability in an appropriately useful form, shape and size or because of their ready manufacturability by conventional processes. For example, nodular iron is the material of choice for automotive engine crankshafts, and most steel compositions are available in a wide range of wrought forms. Examples of such materials are listed in Table II below. Also shown opposite each material is the range of forms in which they are commercially available. These materials generally fall into one or the other of two categories depending on whether they were chosen primarily to perform their mechanical function or their magnetoelastic function. Some materials chosen for their special suitability for one function are serendipitously found to also be ideal for the other, other materials simply sacrifice one function for the other.

TABLE II

MATERIALS	REFERENCE	AVAILABLE FORMS *
Nickel	[4]	B W S
Nodular Iron	[3, 16]	Cast
SAE 1018 Steel	[10]	B W S Sh
JIS S50 Steel	[11]	B W S Sh
Silicon Steel	[5, 17]	B S
JIS SCM415 Steel	[12]	B W
SAE 9310 Steel	[17]	B W
AISI 410 Steel	[19]	B W
18% Ni Maraging Steel	[6, 14]	B W S
Permalloy 50	[4]	B W S
Permendur	[14]	B W
Amorphous 2605SC	[8]	Ribbon
Amorphous $\text{Co}_{62}\text{Ni}_{15}\text{Si}_8\text{B}_{15}$	[9]	Ribbon
N-50 Ferrite	[18]	Molded

* B - Bar; W - Wire; S - Sheet or Strip; Sh - Shaped Bar

Toxicity

As seen in the foregoing there are a variety of materials from pure elements to complex alloys that may be used in the manufacture of magnetomechanical sensors. There are many opportunities for people to interact with these materials from the earliest stages of manufacture to the ultimate disposal of the sensor. Manufacturing may include processes wherein some of these materials may exist in the form of dust, fine powders or as gases in which forms they are easily inhaled, ingested or may lodge on a person's skin or clothing. These processes include machining (especially abrasive processes such as grinding), welding, plasma spraying and the early stages in powder metallurgy processing. As shown in Table III, some of the metals used in preparing magnetoelastically active materials, notably cobalt and even nickel, are considered hazardous enough in these forms to require special attention to safe practices.

Cost

The ultimate applicability of a sensor will be strongly influenced by economic considerations. To be selected for a particular application a magnetomechanical sensor will need to be cost competitive with similarly performing devices based on other sensing technologies. Thus the materials used in its construction and the processes used in its manufacture can not be chosen solely to maximize performance characteristics but must be concerned with a value parameter based on such ratios as cost per unit of performance. As seen in the last column of Table III the range of costs of materials having potential utility in magnetomechanical sensors spans three orders of magnitude. Prudent use of the most expensive materials can be made by limiting their content in alloys or by limiting the actual volume of the sensing element as with thin films. Any requirement for expensive processes to form such films must also be considered.

CONCLUSIONS

The well accepted utility of magnetomechanical sensing technology provides many opportunities for the use of magnetoelastically active materials. No single property of a material automatically recommends it for such use. Combinations of diverse properties including those

TABLE III

MATERIAL	EXPOSURE LIMIT - mg/m^3 [30]	PRICE - \$/kg [31]
Iron	10.0	0.18
Nickel	1.0	7.69
Cobalt	0.05	55.00
Chromium	1.0	0.88
Molybdenum	10.0	8.00
Titanium	15.0	7.72
Silicon	5.0	1.46
Aluminum	10.0	1.98
Terbium	10.0	1500.00
Dysprosium	10.0	350.00

not usually considered together have been shown to be better indicators of the utility of a material in these applications. Since the sensing element is usually only one part of the complete sensor, its compatibility with other materials, particularly in regard to thermal expansion coefficients must also be considered during the material selection phase of sensor design. The commercial viability of this class of sensors, together with the growing demand for sensors of all kinds is expected to encourage the development of economical materials specifically for this use..

REFERENCES

1. Sherif S. Gindy, *Experimental Techniques*, 28, (June 1985) ; 9 (July 1985).
2. William Fuller Brown, Jr., *Magnetoelastic Interactions*, (Springer-Verlag, NY, 1966).
3. William J. Fleming, SAE Paper No. 890482 (1989).
4. See for example: F. D. Smith and C. S. Wright, British Patent No. 442 441 (3 February 1936) and W. Janovsky, U. S. Pat. No. 2 053 560 (8 September 1936).
5. Orvar Dahle, IVA, 25, 221 (1954); U.S. Patent No. 2 912 642, 10 November 1959.
6. I. J. Garshelis, U. S. Patent No. 5 195 377 (23 March 1993).
7. D. Son and J. Sievert, *IEEE Trans. Magn.* **26** (5) 2017 (1990).
8. A. Hossain and M. H. Rashid, *IEEE Indus. Appl., Meeting Conference Record*, **2**, 1815 (1988).
9. T. Meydan and K. J. Overshott, *J. Appl. Phys.* **53** (11), 8383 (1982).
10. D. K. Kleinke and H. M. Uras, *Rev. Sci. Instrum.* **65** (5), 1699 (1994).
11. H. Yamada, S. Uchiyama, K. Takeuchi, H. Wakiwaka, S. Kishimoto and M. Ito, *IEEE Trans. Magn.* **MAG-23** (5), 2422 (1987).
12. I. Sasada, E. Nagano and K. Harada, *J. Appl. Phys.* **69** (8), 4919 (1991).
13. K. Blomkvist and J. Nordvall, U. S. Patent No. 4 506 554 (26 March 1985).
14. I. J. Garshelis, *IEEE Trans. Magn.* **28** (5), 2202 (1992); **29** (6), 3201 (1993); SAE Paper No. 920707 (1992).
15. T. Kobayashi, M. Sahashi, K. Inomata, U. S. Patent No. 4 762 008 (9 August 1988).
16. Y. Nonomura, J. Sugiyama, K. Tsukada, M. Takeuchi, K. Itoh and T. Konomi, SAE Paper No. 870472, (1987).
17. Francis E. Scoppe and Kenneth S. Collinge, AIAA-84 Paper No. 1280 (1984).
18. J. T. Russell and T. J. Davis, U. S. Patent No. 4 289 987 (15 September 1981).
19. K. Ara and M. J. Brakas, *IEEE Trans. Magn.* **MAG-11** (5), 1352 (1975).

20. H. Hase, R. Shoji and M. Wakamiya, SAE Paper No. 920700 (1992).
21. P. M. Anderson, III, D. Raskin, D. Reich, U. S. Patent No. 4 463 610 (7 August 1984); 4 479 389 (30 October 1984);
22. W. L. Rollwitz, J. P. Claasen, J. Arambula, U. S. Patent No. 3 612 986 (12 October 1971).
23. H. Aoki, S. Yahagi, T. Saito, U. S. Patent No. 5 107 711 (28 April 1992).
24. I. Sasada, S. Uramoto and K. Harada, IEEE Trans. Magn. **MAG-22** (5), 406 (1986).
25. I. J. Garshelis, J. Appl. Phys. **73** (10), 5629 (1993).
26. R. M. Bozorth, Ferromagnetism, (D. Van Nostrand, New Jersey, 1951), p. 602.
27. T-250 Grade, Teledyne-Vasco, Latrobe, PA; I. J. Garshelis, IEEE Trans. Magn. **26** (5) 1981 (1990).
28. R. M. Bozorth, *ibid.*, p. 270.
29. SAE J1211, Section 4, SAE Recommended Practice (1992)
30. 29CFR Part 1910 -1200, OSHA (1994).
31. U. S. Bureau of Mines (22 November 1994 - private communication).

MAGNETOSTRICTIVE METHODS OF DETECTING TORQUE FROM CASE-HARDENED STEEL SHAFTS

ICHIRO SASADA

Department of Electronics, Kyushu University 36, Fukuoka 812, Japan

ABSTRACT

This paper begins with a review of the current problems associated with the application of conventional magnetic-head-type shaft torque sensors. These sensors were first proposed in 1954. Newly developed low-profile magnetic heads for torque sensors which address the problems of the older type of sensors are then presented. The torque sensor which uses the low-profile pick-up heads is described in detail. Experimental results showing the basic performance of the torque sensor with carburized nickel chromium molybdenum steel shafts (SNCM 420 in JIS) are then described. In this combination of the heads and the shaft, the hysteresis of the input-output relationship is generally small and shows that the direction of traversal around the hysteresis loop changes as the amplitude of the excitation current changes. It is shown that an optimum operating condition exists for the torque sensor in which the hysteresis achieves a minimum value yet the sensitivity remains high. In a particular combination studied in this paper, the optimum excitation current was 0.3 A at the excitation frequency 60 kHz, where the total power loss at the pick-up heads was 0.37 W. Under this operating condition, the hysteresis was extremely small, and the linearity was better than 0.6%.

INTRODUCTION

The dynamic behavior and operating conditions of mechanical systems can be detected most accurately by extracting information pertaining to the forces applied to the moving components. Force sensors are therefore an essential component which allow a mechanical system to be controlled in a predetermined manner. The majority of mechanical systems involve rotation as a principal motion therefore the use of torque sensors is an important requirement if the system is to respond in an intelligent manner.

Dynamic operating conditions of the mechanical system can be obtained directly by means of a torque sensor. For example, the deterioration of mechanical components such as bearing fatigue can be sensed by the pattern of the torque sensor output waveform. Also, the smooth control of the end effector of robots is only possible if information related to the driving torque can be accessed in the proximity of the effector. Another example includes in-process monitoring of drilling torque to maintain precise machining quality of precision machining tools or to prevent the breakage of tools. In these cases, the waveforms of applied torque should be detected accurately.

The magnetostrictive effect is a useful method which can be exploited to detect the torque on rotating shafts[1-3]. In this paper, we focus our attention on magnetostrictive torque sensors which require magnetic head type pick-ups and which require no modification to the steel shafts [1][2]. Most steel shafts are case-hardened in order to strengthen their mechanical properties, therefore a technique which can be used to detect torque from these types of shafts is essential.

This paper begins by emphasizing the factors which contribute to a reduction in the accuracy of magnetostrictive torque sensors with magnetic head type pick-ups. Then the importance of the

low-profile, low-power pick-up head for building a multi-head structured torque sensor with improved accuracy is presented. In particular we present our approach using, as a pick-up head, a pair of figure-eight flat coils embedded in a ferrite disk. In this type of structure, the magnetic excitation field is effectively transferred to a case-hardened shaft. We conducted preliminary static characteristic studies on the torque sensors using a commonly available carburized nickel chromium molybdenum steel shaft. The studies show the existence of an optimum operating condition for the torque sensor in which the hysteresis achieves a minimum value yet the sensitivity remains high. Under optimum conditions, a highly linear input-output relationship with extremely small hysteresis is obtained.

TORQUE DETECTION FROM THE STEEL SHAFT

There are two basic methods to detect torque from a shaft; one method is based on measuring surface stress (or strain) and is shown in Fig. 1(a); the other method is based on the measurement of a torsion angle and is shown in Fig. 1(b). Steels exhibit the magnetostrictive effect and its inverse effect. The latter effect provides a convenient means of detecting stresses, and thus changes in the relative permeability. The shaft torque sensors which exploit this effect in steel were proposed four decades ago by R. A. Beth and W. W. Meeks [1] and O. Dahle [2]. These torque sensors require no modification to the steel shaft in order to establish the torque-to-voltage transformation, in which the magnetic head type pick-up used has the ability to detect differences between the permeability along the line of tension and along the line of compression. In contrast, torque sensors based on a torsion angle measurement are complex because they need a pair of identical disks mounted on the shaft to facilitate torsion angle measurement [4]. Due to its simple structure, the magnetostrictive method using magnetic head type pick-ups has the potential to yield compact, rigid and widely applicable torque sensors. However, the trade-off one must pay for simplicity is lower accuracy due to magnetic surface inhomogeneities on the steel shaft. For example, the offset (zero-level) may fluctuate and sensitivity may change as the shaft rotates [5]. In order to illustrate the zero-level fluctuation, the simple torque sensor, shown in Fig. 2 is used. The difference

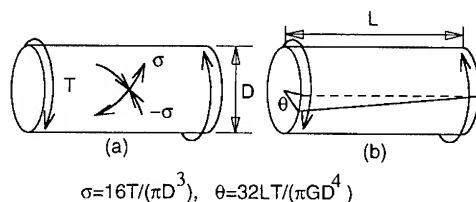


Fig. 1 Two basic methods to detect torque from a shaft.

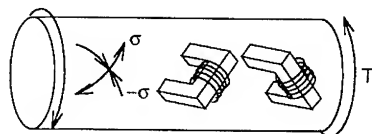


Fig. 2 Magnetostrictive torque sensor in the simplest form.

in inductances between the two magnetic heads, yield an output when connected into a bridge circuit [6]. Fig. 3 shows the measured waveform with an unheat-treated steel shaft of 12 mm in diameter, where waveform (a) shows the intrinsic zero-level fluctuation taken under balanced bridge conditions [6]. In this case, waveform (b) shows an example of zero-level fluctuation when the bridge circuit was made slightly unbalanced.

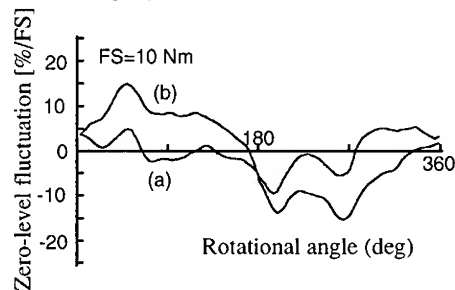


Fig. 3 An example of the zero-level fluctuations in the output of the magnetostrictive torque sensor shown in Fig. 2.

There are two methods to improve accuracy; coating the shaft with magnetostrictive material or taking the average of the signals from multiple heads situated around the shaft. The former method has been shown to be effective by an experiential study, in which a shaft was coated with a 300 μm thick layer of nickel using the plasma jet spraying technique [7]. The effectiveness of the latter method has been shown by O. Dahle [2]. To develop a widely applicable method for detecting torque, we have been pursuing the averaging technique with newly developed low-profile magnetic heads [8][9].

Fig. 4 shows the operating principle of the torque sensor using one of these [8], where a pair of figure-eight flat coils are placed close to the shaft surface. The inductances of these flat coils change with the applied torque because the mutual inductance between the two sub-loops in a coil is sensitive to the direction of the magnetic anisotropy induced by the applied torque. With an applied torque, the permeability in the direction of tension increases and in the direction of compression decreases, thus the self-inductance of coil (b) becomes larger than that of coil (a). Consequently, a difference in inductance occurs [8]. The coils can be stacked as shown in (c) because the inductances are mutually orthogonal. For a stacked arrangement, the total space

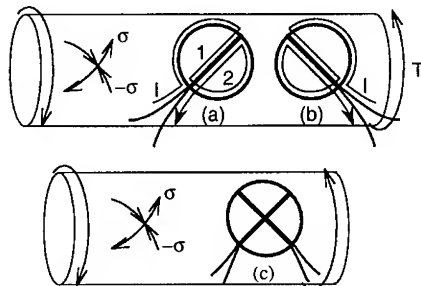


Fig. 4 Operating principle of the low-profile pick-up head, where change in self-inductance is a measure of the applied torque.

occupied by the pick-up coil is minimized and disturbances affecting commonly all the coils are canceled because of the subtracting nature of the bridge circuit. Since the height of the coil is low, it is easy to mount two or more coils close to the shaft and around the shaft's circumference. We can set up a full-inductance bridge circuit (see Fig. 14) using two stacked pick-up coils which are placed 180 degrees apart and around the shaft. Another type of low-profile pick-up coil is shown in Fig. 5, where the structure of the coil is the same but where the mutual inductance between the primary and the secondary coil is governed by the applied torque [9]. In this case, the applied torque can be detected using the setup shown in Fig. 6.

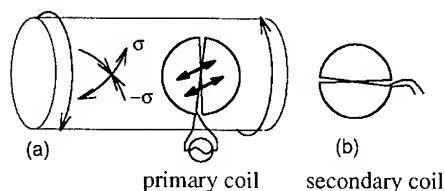


Fig. 5 Operating principle of the low-profile pick-up head, where mutual inductance between the primary and the secondary coil is a measure of the applied torque.

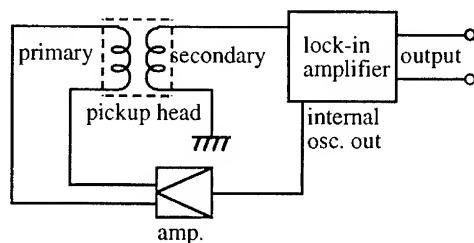


Fig. 6 Schematic diagram of the circuit used for the pick-up head shown in Fig. 5.

MAGNETIC PROPERTY OF THE STEEL SHAFT

The hysteresis loop and magnetostriction were measured for SNCM 420 steel of Japanese Industrial Standard (JIS) whose nominal compositions are as follows: Ni: 1.6-2.0%, Cr: 0.4-0.65%, Mo: 0.15-0.3% and the balance is iron. This steel is usually used to manufacture carburized shafts. The hysteresis loops were measured using ring samples. Ring samples of material in a as-received state were prepared by shaping a solid bar with a lathe to have an outer diameter of 25 mm, an inner diameter of 21 mm and a height of 2 mm. Ring samples of the carburized one were prepared by cutting out the inside of the carburized shaft with a lathe leaving only the case of the shaft and then sliced. Dimensions of them were as follows: the outer diameter was 24.2 mm, the inner one was 22 mm and the height was 3.4 mm. Circular pellets with a diameter of 25 mm and a height of 2 mm were used for the magnetostriction measurements. Half of the pellet samples were carburized after their fabrication. Fig. 7 shows the hardness profile of

the carburized shaft, from which the case-hardened-depth was determined to be 0.9 mm. The coercivity of the carburized steel becomes 3 times larger than that of unheat-treated steel as shown in Fig. 8. Fig. 9 shows the magnetostriction measured in the form of $(\lambda_{//} - \lambda_{\perp})$ using strain gauges glued to both surfaces of the pellet, where $\lambda_{//}$ is $\Delta l / l$ along the field direction and λ_{\perp} is that perpendicular to the direction. It was found that the value of magnetostriction changes only slightly after carburization, but that the magnetic field needed to establish the same level of magnetostriction becomes much larger after carburization.

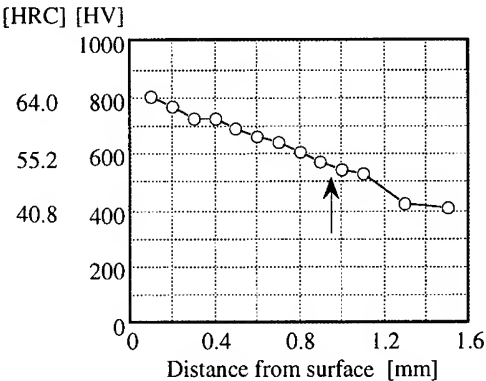


Fig. 7 Hardness profile of a SNCM 420 carburized shaft. An arrow shows the case-hardened-depth.

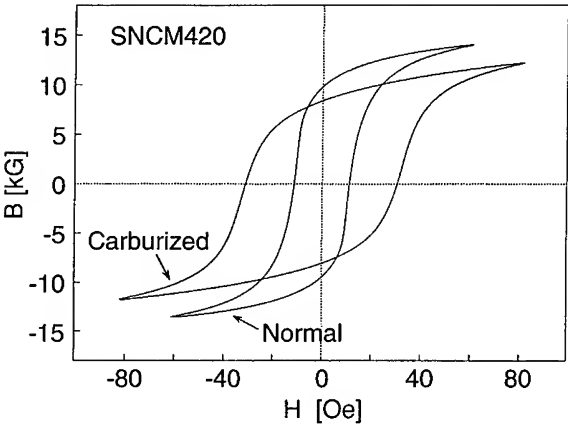


Fig. 8 Dc hysteresis loops before and after carburization for SNCM 420 shaft material.

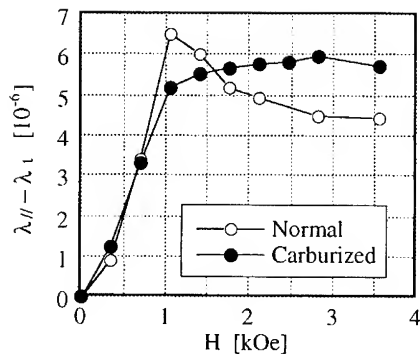


Fig. 9 Magnetostrictions before and after carburization for SNCM 420 shaft material.

BASIC CHARACTERISTICS OF THE TORQUE SENSOR

In order to increase the strength of the magnetic field which magnetizes the carburized shafts, we added a ferrite core to a pair of pick-up coils as shown in Fig. 10. The surface of the core was shaped to fit the surface of the 25 mm diameter shaft. The ferrite core was machined from a 12 mm thick MnZn ferrite substrate using an ultrasonic machining tool. Two coils were made by stacking two copper wires alternately into cross-shaped grooves. The number of turns of each figure-eight coil was 14, and the diameter of the core was 20 mm. The frequency characteristics of the head coupled to a SNCM 420 carburized shaft with a 1.3 mm air gap are shown in Table I. Two identical heads prepared in the fashion just described were then mounted to a SNCM 420 carburized shaft in a manner as shown in Fig. 11. Identical air gaps were introduced between the heads and the shaft. The flux distribution was calculated using a three dimensional FEM. The diameter of the shaft was assumed to be infinitely large so as to simplify the problem. The excitation frequency was 60 kHz. The magnitude of the flux density distribution at the surface of the shaft is shown in Fig. 12, where the coil pattern is projected on the surface of the shaft. The flux density pattern shows that the flux density is high along the cross branch of the coils and that the flux density is not symmetrical because the currents flowing at the outer circle of the core are additive

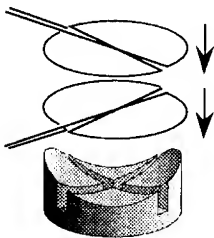


Fig. 10 Structure of figure-eight flat coils and the ferrite core to which coils are embedded.

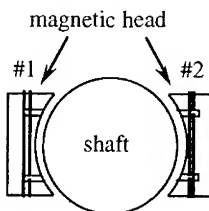


Fig. 11 Arrangement of the magnetic heads to the shaft.

Table I Frequency characteristics of the low-profile pick-up head.

Frequency [kHz]	L [μ H]	r [Ω]	Q
10	80.9	1.6	3.3
20	76.7	2.1	4.6
40	72.6	3.1	6.0
60	70.5	3.9	6.8
80	69.6	4.9	7.2

measuring current for a single figure-eight coil = 0.3A

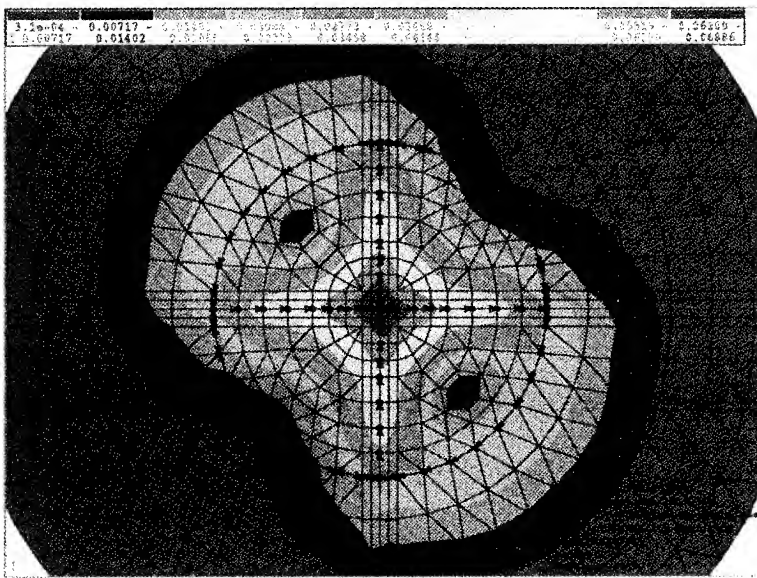


Fig. 12 Magnitude of the flux density distribution at the surface of the shaft, where the coil pattern is projected to the surface.

in the second and fourth quadrants but canceled in the first and third quadrants. Flux density along a direction perpendicular to the shaft surface is shown in Fig. 13 for two typical positions; at the maximum point at the center of the coils and at the minimum point in the second quadrant. Parameters used in the calculation were $\mu_r=2000$, $\sigma=0.1$ S/m for ferrite, $\mu_r=40$, $\sigma=2 \times 10^6$ S/m for carburized steel, and 4.2 ampere-turns for the excitation. This ampere turn corresponds to the total excitation current 0.3 A. Fig. 14 shows the schematic diagram of the experimental circuit, where a lock-in amplifier was used as a phase-sensitive-detector. In the following experimental results, the vertical scales are adjusted so that the gain of the detector is unity. Fig. 15 shows the dependence of the sensitivity on the phase of the detector under the condition that the range of the applied torque was ± 400 Nm and the excitation frequency was 60 kHz, in which the phase of the detector was defined taking the phase of the excitation current as a reference. The excitation current was taken to be a parameter in the figure. This excitation frequency was chosen because

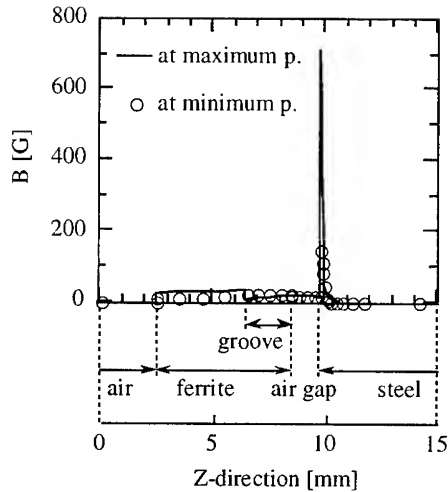


Fig. 13 Magnetic flux density along a direction perpendicular to the surface for two typical points; the maximum point (the center) and the minimum point in the second quadrant as shown in Fig. 12.

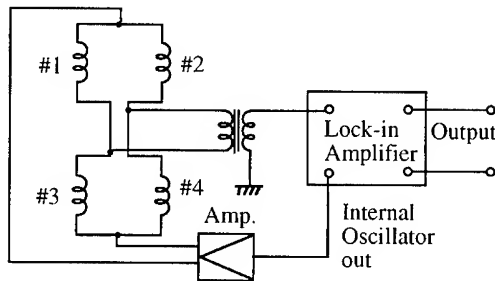


Fig. 14 Schematic diagram of the experimental circuit.

the sensitivity of the inductance of each pick-up coil increases with excitation frequency up to 40 kHz and reaches saturation above this frequency. The optimum phase for the highest sensitivity was 66 degrees. Hysteresis in the input-output relationship is also important for evaluating the accuracy and is shown in Fig. 16 for the same experimental condition. In this case, we plotted hysteresis as an absolute value along the vertical axis, that is, the difference between the branch corresponding to the increasing half cycle of the applied torque and the one corresponding to the decreasing half cycle rather than in a normalized form which is the absolute value divided by the maximum range of the output. Hysteresis in the normalized form can be acquired by combining the data from Figs. 15 and 16, and by recalling that the range of the applied torque was ± 400 Nm. Positive hysteresis corresponds to a counter clockwise loop and negative hysteresis to a clockwise loop. The direction of the loop is also changed by the phase of the detector but then the

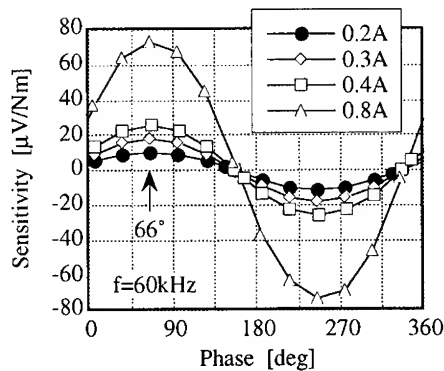


Fig. 15 Sensitivity vs. phase of the phase-sensitive-detector, taking the excitation current as a parameter.

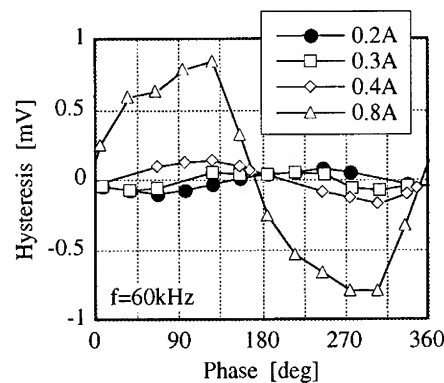


Fig. 16 Hysteresis vs. phase of the phase-sensitive-detector, taking the excitation current as a parameter.

sign of the sensitivity is changed also. In this case, loops are flipped with respect to the horizontal axis. An interesting thing to note is that the direction of the loop is influenced by the amplitude of the excitation current. Hysteresis measured using a SNCM 420 carburized shaft was generally small compared to other shafts such as a SCM 415 carburized shaft or a S45C induction heating case-hardened shaft. It is possible to reduce hysteresis further by optimizing the excitation condition and the phase of the detector. In the present case, the excitation current to the full-inductance bridge is 0.3 A and the excitation frequency is 60 kHz with a phase of 66 degrees. In this excitation condition, the power dissipated at the bridge circuit, namely at two pick-up heads, was 0.37 W. If one compares this power loss to that in our former design, where in order to enhance the excitation magnetic field amorphous yokes were used in place of the ferrite core of the present design [8], one will find that it becomes a magnitude smaller than the previous one. We have not established a model of hysteresis yet, but we have been studying various ways of identifying the model. We believe that radial profiles of stresses, hardness and texture induced in the shaft by the heat-treatment must be analyzed together to determine the behavior of hysteresis. Static

characteristics of the input-output relationship under this condition is shown in Fig. 17. Fig. 18 shows the sensitivity of the torque sensor as measured at various circumferential positions. The variation in signal between one position and another position is extremely small. Linearity of the torque sensor was also measured in the same way and was found to be less than 0.6% as shown in Fig. 19. Variations in the hysteresis of the torque sensor were also observed but were extremely small. The small dependence of hysteresis and linearity on the circumferential position of the shaft could result from the averaging effects observed using two pick-up heads and of the wide surface area of the core. We have not measured zero-level fluctuation yet, but we feel it should be much smaller than the waveform (a) in Fig. 3.

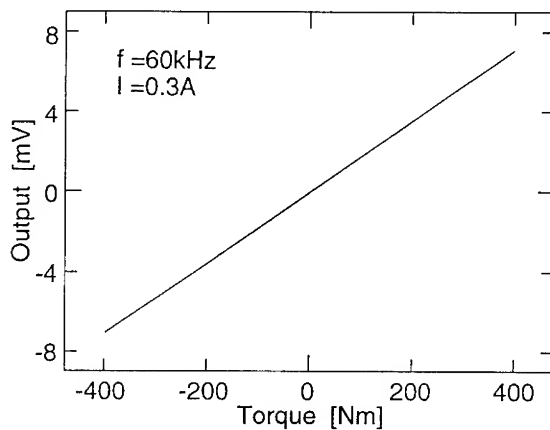


Fig. 17 Static characteristic of the input-output relationship under the optimum operating condition.

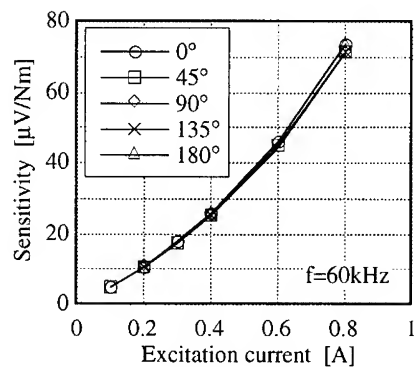


Fig. 18 Sensitivity vs. excitation current measured at the various circumferential points.

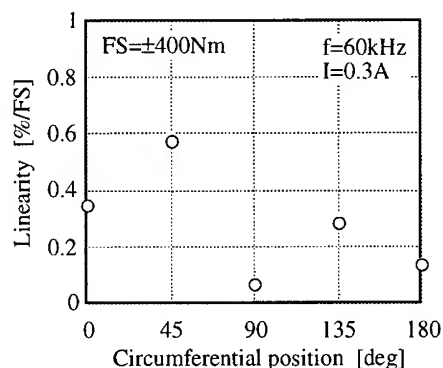


Fig. 19 Linearity of the torque sensor measured at the various circumferential points.

CONCLUSIONS

We demonstrated that the newly developed low-profile magnetic pick-up head substantially improves the performance of the magnetic head type shaft torque sensor which was first proposed four decades ago. We also presented the existence of the optimum excitation condition in the combination of the low-profile pick-up head and the SNCM 420 carburized shaft. We have not shown other cases with S45C induction heating case-hardened shafts or SCM 415 carburized shafts to avoid complexity, where the phase dependence of the sensitivity and that of the hysteresis behave in different fashions from those reported in this paper. For example, excellent linearity and small hysteresis was obtained with a S45C induction heating case-hardened shafts but at the cost of reduction in sensitivity by a factor of 2. In order to explain the underlying phenomena, we have to analyze physical structure of the case-hardened shaft, especially radial profiles of stresses, hardness and texture induced in the shaft by the heat-treatment together with the behavior of hysteresis.

In addition to the future direction mentioned above, it is practically important to recommend the guide lines of the heat-treatment condition adequate for some particular shaft material to assure the mechanical strength together with the accuracy of the torque sensor.

ACKNOWLEDGMENTS

The author would like to thank Mr. F. Koga for discussion and assistance with the experiments and also thank Mr. N. Suzuki for assistance with calculation.

References

- [1] R. A. Beth, W. W. Meeks, Rev. Sci. Instrum. Vol. 25, 603 (1954).
- [2] O. Dahle, ASEA Journal, Vol. 33, No. 3, 23 (1960).
- [3] I. Sasada, A. Hiroike, K. Harada, IEEE Trans Magn Vol. 20, No. 5, 951 (1984).

- [4] D. Ettleman, M.Hoberman, Machine Design, 1963, 134.
- [5] I. Sasada, T. Tanaka, M. Baba, K. Harada, IEEE Trans Magn, Vol. 24, No. 6, 2886 (1988).
- [6] I. Sasada, M. Baba, K. Harada, IEEE Trans. Magn, Vol. 25, No. 5, 3417 (1989).
- [7] I. Sasada, S. Uramoto, K. Harada, IEEE Trans. Magn, Vol. 22, No. 5, 406 (1986).
- [8] I. Sasada, F. Koga, K. Harada, IEEE Trans. Magn, Vol. 29, No. 6, 3231 (1993).
- [9] I. Sasada, F. Koga, J. Appl. Phys. Vol. 75, No. 10, 5916 (1994).

HIGH PRECISION ACTUATOR WITH $\text{Tb}_{0.27}\text{Dy}_{0.73}\text{Fe}_{1.95}$ SINGLE CRYSTAL*

QIANG LI, Y.L.CHANG, SHIXI OUYANG AND X.H.HUANG
Wuhan University of Technology, Advanced Materials Research Institute,
Wuhan, Hubei 430070, China.

ABSTRACT

It has been proved that the saturation magnetostrictive constant λ_s of $\text{Tb}_{0.27}\text{Dy}_{0.73}\text{Fe}_{1.95}$ single crystal is greater than the polycrystal and grains oriented crystal with the terfenol compositions, especially for its large linear magnetostrictive strain. $\text{Tb}_{0.27}\text{Dy}_{0.73}\text{Fe}_{1.95}$ single crystal also can produce large force and fast, precision motion at high efficiency and power levels. A proto-type micro positioning actuator with the single crystal was designed in our lab. The structure and performances are discussed in this paper.

INTRODUCTION

The advanced magnetostrictive material, known as Terfenol-D, exhibits about 10-50 times larger length change than conventional materials such as nickel and piezoelectric ceramics (PZT). With the huge saturation magnetostrictive strains and high energy density, Terfenol-D can produce large forces and give fast, precise motion at high efficiency and power levels. This device-quality magnetostrictive material has been widely used to design various actuators (such as linear motor, micro positioning actuator etc.) and can be manufactured from commercial available raw materials. M. Fahlander et al. introduced applications of Terfenol-D in the corresponding fields[1]. T.Akuta designed a new type of hybrid inch worm linear motor by using giant magnetostrictive materials and PZT together[2]. H.Eda et al. reported their proto-type ultra high precession micro positioning actuator with 10 nm resolution by using Feredyn Magmek 86 with water cooling system[3]. And R.D.Greenough et al. discussed the possibilities of actuation with Terfenol-D etc[4]. These developments of high precision micro positioning actuators have been recognized to be one of basic key technologies on electronics, information, communications, energies, aircraft, space and advanced materials processing etc.

For the high precision magnetostrictive actuator, giant magnetostrictive material often proves to be the critical point in its performance, because the high behavior magnetostrictive material can not only provide large magnetostrictive strains (λ_s , d_{33} and k_{33} etc.) and be driven at low applied field, but also make it possible to reduce the device size and simplify the design. The performance of $\text{Tb}_{0.27}\text{Dy}_{0.73}\text{Fe}_{1.95}$ single crystal, which has been prepared in our lab., has shown to be superior to commercially produced Terfenol-D, to a large extent, due to the elimination of a number of defects which may

*Supported by the State Key Lab. of Crystal Materials, Shandong University, China

exist in the Terfenol-D material. For instance, λ_s of single crystal could reach 2000 ppm and the linear magnetostriction is nearly about 1500 ppm at the field of 1 kOe. d_{33} for this single crystal approaches 4.8 ppm/Oe etc. These behaviors make the single crystal favorable for a variety applications, especially for the high precision micro positioning actuators.

DESIGN AND DISCUSSION

Material Properties

Terfenol-D is one of the best rare earth-transition inter-metallic compounds possessing large magnetostriction. It has been utilized as the drive material instead of PZT ceramics in designing and manufacturing of various actuators since the early eighties. With the grains oriented along the $\langle 112 \rangle$ direction, Terfenol-D usually can generate large magnetostrictive strains and response in a extremely short time. But defects (such as boundaries and second phases) existed in its microstructure heavily affected its magnetostrictive performance. It was suggested that to eliminate those defects will optimize the properties of Terfenol-D to a great extent. However to attain this goal is quiet difficult using the conventional Bridgman or float zone technique. Recently large boundary free $\text{Tb}_{0.27}\text{Dy}_{0.73}\text{Fe}_{1.95}$ single crystal has been prepared successfully by means of growth with a magnetic levitation technique in our lab. The performance of the single crystal have been improved, especially its performance at low applied field, by eliminating its structural defects. Table 1 is the comparison of main performances of $\text{Tb}_{0.27}\text{Dy}_{0.73}\text{Fe}_{1.95}$ single crystal and Terfenol-D

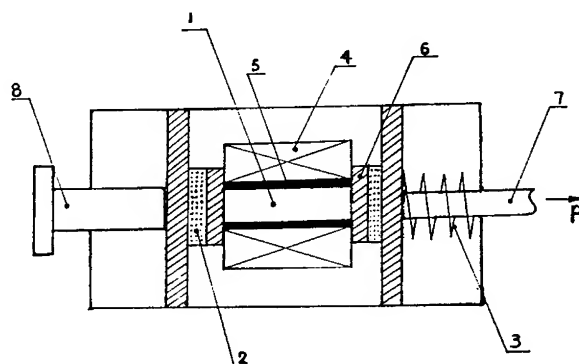
Table 1. comparison of the main performances

	$\lambda_s(\text{ppm})$	$\lambda^*_{1k}(\text{ppm})$	$d_{33}(\text{ppm./Oe})$	k_{33}
Terfenol-D	1500-2000	1000	1.0-2.0	0.65
$\text{Tb}_{0.27}\text{Dy}_{0.73}\text{Fe}_{1.95}$ single crystal	~2000	1500	4.8	0.94(k _{eff})

$$\lambda^*_{1k} = \lambda \text{ at } 1 \text{ kOe}$$

Bias Field and Exciting Coil

On the above researches, we have designed a high precision micro displacement actuator, with a simple structure and small size, by using the high quality $\text{Tb}_{0.27}\text{Dy}_{0.73}\text{Fe}_{1.95}$ single crystal. The actuator's primary parts consist of a $\text{Tb}_{0.27}\text{Dy}_{0.73}\text{Fe}_{1.95}$ single crystal rod, solenoid exciting coil, permanent magnets plus yokes and pre compressing spring etc.(see Figure 1). As the single crystal exhibits huge magnetostrictive and strains restricted hysteresis at low applied field, both the bias and exciting field could be decreased in our design. The magnetic density for bias field is approximately 200 Oe, and 300 Oe for max.



(1) single crystal, (2) Nd₂Fe₁₄B, (3) helical spring, (4) exciting coil
(5) isolate sheet, (6) yokes, (7) act bar, (8) fasten bolt

Figure 1 Designed structure of the actuator

value of the exciting field. A pair of permanent Nd₂Fe₁₄B magnets was used to provide the bias field with the well-distributed magnetic density through the half-ball shaped magnetic yokes. Copper wire ($\Phi 0.3\text{mm}$) was used to form a solenoid axial exciting coil. The number of turns varies from 900-2000 N/cm along the axial direction, in order to get an approximately homogeneous driving magnetic flux density in the center of coil. Figure 2

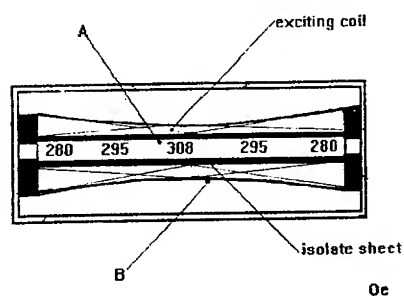


Figure 2. Distribution of applied field in the exciting coil

indicates the distribution of magnetic flux density in the center of exciting coil.

Pre compression and Temperature Stability

The size of the single crystal utilized is $\Phi 10 \times 50$ mm in the designed actuator. Helical spring pre compression technique was used directly to avail compressive force ($4 \text{ MPa}, \pm 0.3 \text{ MPa}$) to the rod in order to get a closely contact and rapid respond. Normally heat

produced by the DC current flowing the exciting coil would cause a thermal expansion, however lower power input ($V_{\text{max}}=1\text{ V}$, $I_{\text{max}}=1\text{ A}$) was usually provided to the actuator by the power supplied system. Figure 3 denotes the thermal expansion of $\text{Tb}_{0.27}\text{Dy}_{0.73}\text{Fe}_{1.95}$ single crystal at 18°C - 50°C . The linear expansion coefficient is about $1.86 \times 10^{-5}/^{\circ}\text{C}$. Therefore, stability of the working temperature is very important for the

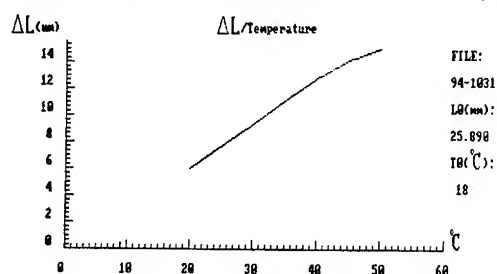


Figure 3. The thermal expansion coefficient

precision of the actuator. We have designed a thermal isolation protecting sheet (about 2 mm thick), composed of a polymeric compound and inorganic fibers, to minimize heat conduction from the exciting coil to the crystal rod. DC power was supplied (with 1V, 1W) to the solenoid exciting coil for about 50 min. in order to measure(see Figure 2)the temperature changes at A (surface of the crystal) and B (inner side of the coil). Figure 4

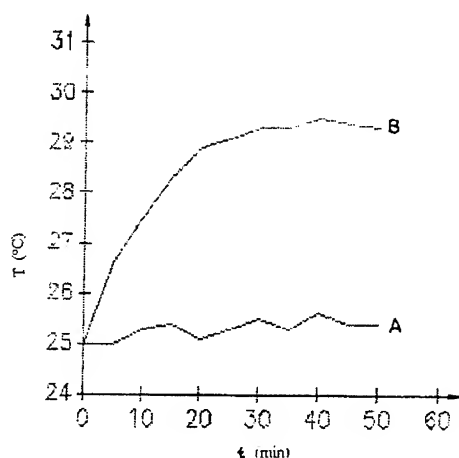


Figure 4. The time dependence of the temperature change

denotes the measure results at 25°C(room temp.). As shown in this Figure, the temperature for B is increasing from 25°C to 29.5°C when the power switch on, but the temperature for A is nearly no change (not more than 1°C) after the holding time. That is to say the influence of temperature changing of exciting coil, while is working, could be nearly ignored.

Test Results and Further Development

The overall size of Tb_{0.27}Dy_{0.73}Fe_{1.95} single crystal micro positioning proto-type actuator is $\Phi 40 \times 300$ mm. A specially designed constant voltage power source (for $V_{\max}=1$ V, $I_{\max}=1$ A, $I_{\min}=0.1$ mA) is used as the power supply assembly. The displacement characteristics for the proto-type actuator is plotted in Figure 5.

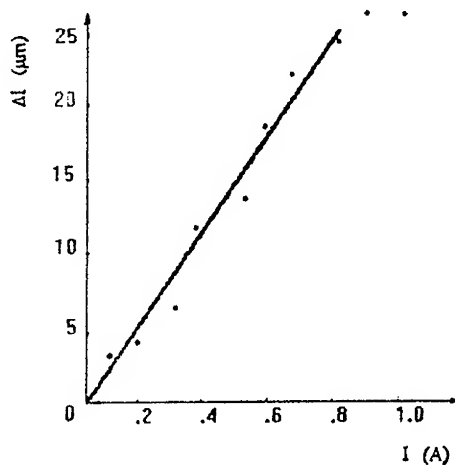


Figure 5. Act characteristics under 1 A DC current

The maximum displacement limit could reach 25 μm with the resolution of 1 μm . It has been suggested that this type of actuator, for its simple structure, small size and lower power consumed, can find various applications such as automatic control, laser focusing, micro stoning and robot system etc. in the near further. As the precision of the actuator assemblies is not as high as we designed, and the environmental temperature is in constant change, all these reasons prevent us from optimizing the precision of the micro positioning proto-type actuator. The further work will be focused on improving the manufacturing tolerances of actuator's assemblies (especially for its moving parts), and compensating the temperature influence on the single crystal rod timely by using a special designed computer. Then the precision of the micro positioning actuators can be expected to be increasing by 1-2 orders.

CONCLUSION

As the first design of a prototype magnetostrictive single crystal micro positioning actuator , we have developed a simple structure of small size and a reduced lower power consumption device. It has been demonstrated that to develop this kind of magnetostrictive actuator will improve the development of the applications of high precision micro positioning actuators in the corresponding fields.

REFERENCE

1. M.Fahlander and M.Richardson, in the 10th International Workshop on Rare-Earth Magnets and their Applications, (Kyoto, Japan, 1989), PP.289
2. T.Akuta, in the 10th International Workshop on Rare-Earth Magnets and Their Applications, (Kyoto, Japan, 1989), PP.359
3. H.Eda, T.Kobayashi and M.Sahashi, in the 10th International Workshop on Rare-Earth Magnets and Their Applications, (Kyoto, Japan, 1989),PP.31
- 4.Greenough, M.P.Schulze, A.G.J.Jenner and A.J.Wilkinson, IEEE Trans.Magn., 27, 5346, (1991)

Magnetostrictive Motor Development

JOSEPH P. TETER AND JOHN E. MIESNER
Code 684, Naval Surface Warfare Center
10901 New Hampshire Avenue
Silver Spring, MD 20903-5640

Abstract

This paper reviews the history and present state of magnetostrictive devices capable of controlled motion over large linear distances. Magnetostriction imparts the most force per unit weight of any technology however, the successful development of practical devices requires a multi-disciplinary effort involving materials science, magnetism, innovative mechanical design, electrical power engineering, and system control engineering. Advances to date have included demonstrations linear motors capable of 115 Newtons of force at 2.54 centimeters/second.

1-1 General Problem: A large class of active control problems exists such as ; deformable surface control, machine tool quieting and accurate positioning, vibration in heavy or bulky structures, etc. that need small, relatively light weight but, high force level devices that are not presently available. Currently used technology consists of hydraulics and shape memory alloys, both of which suffer from speed limitations and each have other problems. Two technologies that may overcome these limitations are the electrostriction/piezoelectric and magnetostriction/piezomagnetic phenomenon. In these technologies, mechanical force is developed from the interaction of electric and magnetic fields with the atomic states of the materials. Much work has already been done with electrostrictive materials whereas magnetostriction is only now experiencing an accelerated development pace due to improvements in the processing of the basic materials. In particular, the material commercially known as Terfenol-D is currently being investigated for a wide variety of high force level applications.

1-2 Magnetostrictives versus Electrostrictives: Each application or problem requiring the use of high force level material has to be examined to determine which technology (electrostrictive or magnetostrictive) represents the best solution. The current thinking is that electrostrictives, due to their non-metallic ceramic nature, are better at high frequencies while magnetostrictives, due to their larger elongation ability and high frequency eddy current losses, are better at low frequencies. However, three other properties strongly indicate that the best choice, within limits, is the use of the magnetostrictive material - Terfenol-D - up to a frequency of 20 kHz. The first property is the ability of Terfenol-D to maintain 80% of its maximum strain over a hundred degree Celsius temperature range. The limits of this temperature range can be adjusted by small changes in the material to cover cryogenic ranges and higher ranges to an upper limit of 350 Celsius. The second property of interest here is the fact that Terfenol-D has a energy density that is a factor of ten greater than electrostrictives. This means that a magnetostrictive device can be designed that would be one tenth the size of an equivalent power electrostrictive device. This concept was demonstrated through the construction and testing of two equivalent sonar projectors at high and low load levels, clearly showing a 10 dB improvement for the magnetostrictive material sonar.[1] The third property concerns the estimated cycle lifetime of the basic material. All of the ceramic based material have a finite lifetime due to the formation and subsequent catastrophic propagation of tree-like cracks in the material. Magnetostrictive materials, being formed through the use of metallic bonds, have no known limit of cycle lifetime.

1-3 Linear motor design guidelines: The central mechanical problem to be overcome is the elimination of all backlash in the device. For a linear motor, this will require more involved engineering than the rotary motor problem due to lack of circular symmetry. Other problems that may need additional attention are control algorithms, hysteresis variations, and device to device reproducibility. The necessary design parameters for magnetostrictive devices can be found in the listed references. The first is a new IEEE standard for nomenclature for the physical properties associated with

magnetostriction.[2] The following three show the relationships between relevant parameters needed for optimal matching of Terfenol-D to the mechanical and magnetic requirements in a device.[3,4,5]

The optimal design for an electrical power conversion system for magnetostrictive devices would both match the output/input impedance's and provide for an efficient coupling of the stored magnetic field energy to the electronic circuits. Magnetostrictive devices are energized by coils, thereby presenting the power supply circuits with an almost purely inductive load. Also, the large amount of energy stored in the magnetic field of the excitation coil(s) must be removed each half cycle. These two requirements can be met by several means, references [6,7] show two approaches. In the work by Schafer, a circuit was designed that can re-absorb the energy returning from the coils and then redirect it with opposite polarity back to the coil(s) on the next half cycle. In the work by Miesner, a capacitive component it added in order to create a purely resistive resonant circuit.

2-1 Magnetostrictive DC Inchworms: Due to the small stroke inherent in atomic force actuators, all linear motors (ceramic and magnetic) utilize some form of inchworm motion to effect gross movement. Examples range back to the 1930's for clamper/pusher linear motors based on the magnetostrictive element Nickel. In the modern era, with the discovery of high power and large elongation materials such as the electrostrictive ceramic PZT and magnetostrictive Terfenol-D, device construction has accelerated. For most of the designs, the mechanical structure can accept either material interchangeably.

An electrostrictive inchworm based on area contraction was developed by Burleigh in the mid 70's.[8] Then, in 1987, a magnetostrictive linear motor based on area contraction was constructed in Germany.[9] It should be noted that this unit and all others based on this design suffer from slow speed and excessive wear. An improvement can be realized by use of a magnetostriction enhancement inherent in float-zone growth Terfenol-D. This improvement makes use of a unique material orientation in the plane perpendicular to the rod long, or growth, axis.[10]

Conventional Clamper/Pusher inchworms are too numerous to mention all of the individuals, groups, and companies that have tried develop them. A generic schematic is presented in figure 1. One example working design can be seen in the work by R. Glob[11]. This example, along with all other work known to this author, uses a perpendicularly applied friction clamp to hold the device to the structure.

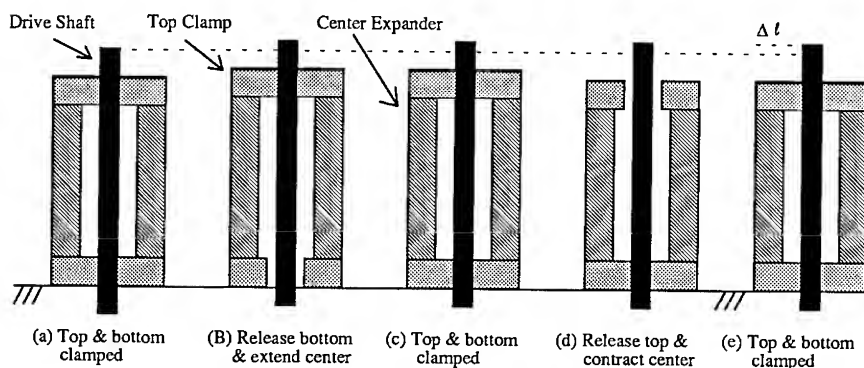


Figure 1. Generalized Inchworm Motor Operation

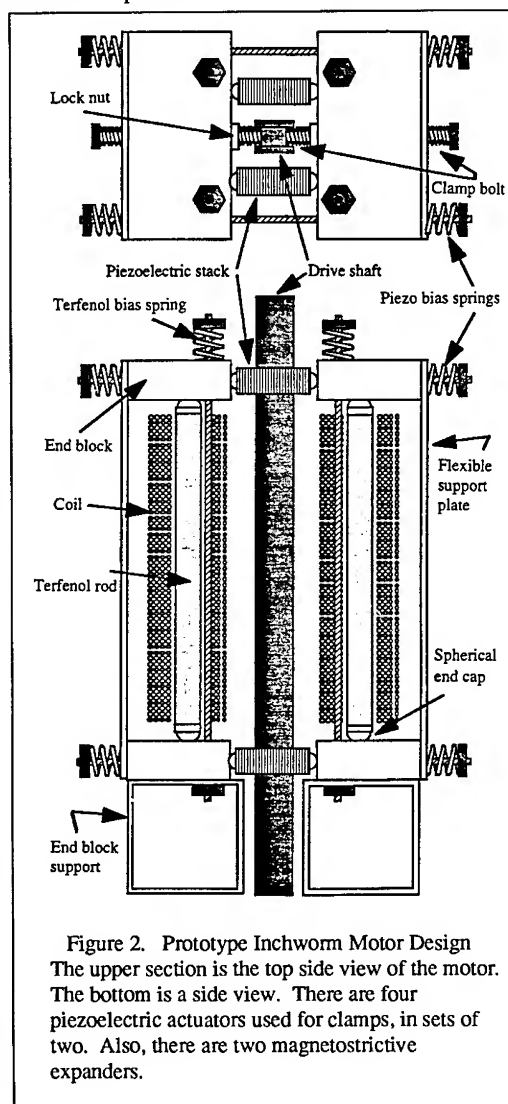
In (a) the system is at rest, both clamps being engaged. The sequence proceeds from (b) to (d), ending up at (e) in the new rest state. The shaft has now moved a distance Δl upward equal to the elongation that the center expander experienced. In this scenario, the bottom clamp is assumed fixed.

Other possible clamping mechanisms for inchworm travel are 1) concepts that rely on force and friction balancing between flexible structural components and, 2) the use of roller brakes or overrunning clutches instead of clamps.

2-2 Magnetostrictive / Electrostrictive Hybrids: Two conventional inchworm linear motors have been constructed that use magnetostrictive elements for the pushing section and electrostrictive elements for clamping sections.[7, 12] The first, built by Akuta, used a DC step actuation scheme to control the motion of the device. Performance of this unit was limited to smaller force levels and slower speeds than the second device built by Miesner. The difference is explained below.

Due to the fact that the inherent actuation principle of electrostrictives is capacitive and that the magnetostrictives are actuated by inductive coupling, when a combined electrostrictive/magnetostrictive device is actuated by a sinusoidal input energy the response of each section is 90 degrees out of phase with the other. This leads to a unique phenomenon - unidirectional relative motion. The work by Butler and Clark illustrates a schematic and performance of a successfully tested proof-of-principle hybrid device. [13] The front to back ratio of relative motion was 17 dB. It should also be noted that the output of such a unit could be significantly improved if the system is operated at mechanical/magnetic resonance.

This idea of using the actuating elements in an active resonant circuit was exploited in the linear motor built by Miesner, see Figure 2 for a schematic of the motor circuit. The performance of this proof-of-principle device was 115 Newtons of force at 2.54 centimeters/second. This motor operates at an electrical resonance, switching power internally between inductive and capacitive components. The normal electrical phase relationship between these components provides natural drive timing for the inchworm. The motor direction can be easily reversed by either changing the magnetic bias on the magnetostrictive Terfenol elements or by switching the piezoelectric element connections. This performance was attained though use of a new electrical power circuit designed and built for the motor. It is shown schematically in Figure 3. This power supply switches energy from a DC source. It supplies *exactly* the energy used by the motor in each inchworm cycle. It also tracks the motor circuit resonance and is not affected by frequency shifts.



3. Future Trends: For the near future, it is clear that hybrids will continue to be developed for both linear and rotary applications. Also, novel mechanical configurations such as discussed in 2-1 are being vigorously pursued. Much materials research remains to be done on exploring the

device potentials of the magnetostrictive phenomenon, such as materials for cryogenic temperature ranges and non-linear effects, to name just two.

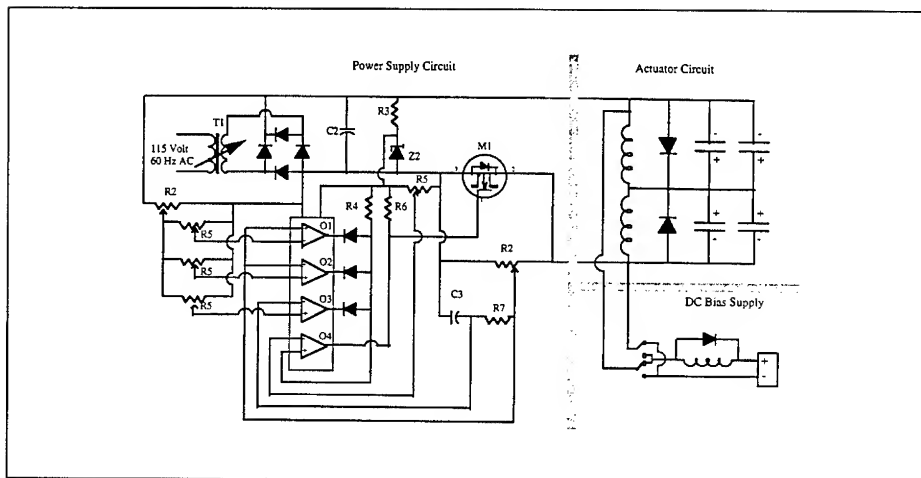


Figure 3. Power Supply Circuit.

The upper right of the schematic shows the four piezoelectric clamp elements and the two magnetostrictive expanders. The bottom right shows the magnetic bias circuit for the magnetostrictive expanders and the travel direction switch. The left side shows the comparators and power mosfet driver necessary in order to feed in incremental power to the resonant hybrid motor.

References:

1. M.B. Moffett, J.M. Powers and A.E. Clark, J. Acoust. Soc. Am. **90** (2), Pt. 1, pg. 1184, August (1991); M.B. Moffett and W.L. Clay, Jr., J. Acoust. Soc. Am. **93** (3), pg. 1653, March (1993).
2. IEEE Standard on Magnetostrictive Materials: Piezomagnetic Nomenclature, IEEE Std 319-1990 (Revision of IEEE Std 319-1971) February (1991).
3. A.E. Clark, J.P. Teter, M. Wun-Fogle, M. Moffett, and J. Lindberg, J. Appl. Phys., Vol. 67, 9 part 2A, pg. 5007, May (1990).
4. M.B. Moffett, A.E. Clark, M. Wun-Fogle, J.F. Lindberg, J.P. Teter, and E.A. McLaughlin, Journal of the Acoustical Society of America, **89** (3), pg. 1448, March (1991).
5. On Characterization, Modeling and Applications of Highly Magnetostrictive Materials, L. Kvarnsjo, Ph.D. thesis, TRITA-EEA-9301, ISSN 1100-1593, February, (1993).
6. Design Rules for Magnetostrictive Actuators, H. Janocha and J. Schafer, Conf. Proceedings Actuators '92, VDI/VDE Technologiezentrum, pg. 152, 24-26 June, (1992).
7. Piezoelectric/Magnetostrictive Resonant Inchworm Motor, J.E. Miesner and J.P. Teter, Submitted to the Smart Structures and Materials Conference, Orlando, FL, (1994); Piezoelectric/Magnetostrictive Resonant Inchworm Motor Development, J.E. Miesner doctoral thesis, George Washington University, Nov., (1994).
8. See for example; Piezoelectric Linear Motors, D. Ehrich, Burleigh Instruments, Burleigh Park, Fishers, NY., Published in Motion Mag., pg. 24, May/June (1986); Burleigh Instruments US Patent 3,902,084 (1975).
9. An Application of Terfenol in Linear Motors, L. Kiesewetter, Proceedings 2nd International Conference on Giant Magnetostrictive and Amorphous Alloys for Sensors and Applications, (1988).
10. J.P. Teter, M. Wun-Fogle, A.E. Clark, and K. Mahoney, J. Appl. Phys., Vol. 67, 9 part 2A, pg. 5004, May (1990).
11. A High Resolution Piezo Walk Drive, R. Glob, Conf. Proceedings Actuators '94, VDI/VDE Technologiezentrum Informationstechnik GmbH, pg. 190 (1994).
12. An Application of Giant Magnetostrictive Material to High Power Actuators, T. Akuta, Conf. Proceedings 10th International Workshop on Rare Earth Magnets and their Applications, pg. 359, 16-19 May, (1989).
13. J.L. Butler, S.C. Butler, and A.E. Clark, J. Acoust. Soc. Am., **88**(1), pg. 7, (1990).

A NEW SUPERFLUID LEAK TIGHT LOW TEMPERATURE VALVE USING A MAGNETOSTRICTIVE ACTUATOR

INSEOB HAHN*, M. BARMATZ*, AND A. CLARK**

*Jet Propulsion Laboratory, California Institute of Technology, 4800 Oak Grove Dr. Pasadena, CA 91109, **Clark Assoc., Adelphi, MD 20783

ABSTRACT

Low temperature valves play an important role in many research and development applications. Conventional low temperature valves primarily use actuation mechanisms depending on either gas or mechanical pressure. These actuation mechanisms usually require inconvenient operating procedures such as a gas handling system or manual operation. We developed a superfluid leak tight low temperature valve that can be activated by a magnetostrictive material. All that is required to activate this magnetostrictive valve is a magnetic field produced by a simple power supply and coil. This new valve consists of separate valve and actuator units. The valve unit is designed to be normally closed using a spring. The stem of the valve is made of a hard 440c stainless steel ball while the seat uses a softer 304 stainless steel.

INTRODUCTION

Low temperature valves are essential to isolate cryogenic fluid at low temperatures for various applications. There have been many efforts to develop better techniques to control the valve and the valve material at low temperatures. Recyclable, gas pressure operated, low temperature valves use Teflon/metal or German silver/hardened BeCu as a tip and seat [1] [2]. The former combination requires operating the valve only at low temperatures because of relatively large thermal contraction of the Teflon. The later combination is found to be leak tight at low temperature, however its life time is in question due to a relatively large difference in the hardness of the materials. Researchers have also used a diaphragm and a sharp knife edge metal surface for sealing. In this case a diaphragm is pushed against the seat by either gas pressure or mechanical actuator. This kind of valve usually has a short life time because its principle of the operation depends on the deformation of the material. Even more serious problems are associated with the actuation mechanisms of those conventional low temperature valves. Conventional techniques usually require a complicated gas handling system (pneumatic valve) or manual operation (mechanical valve) that are very difficult to control remotely. These actuation mechanisms also involve an additional heat leak to the low temperature environment. An intuitive solution to this problem is to use an electromagnetic force as an actuation mechanism. However, the force required to close the valve at low temperature is too large for the direct usage of the electromagnetic field. A new actuation mechanism that can be controlled remotely and introduces a minimal heat leak to the system is needed to overcome these difficulties.

When a magnetic material is exposed to a magnetic field, its physical dimensions change. This magnetostriction effect was first discovered in nickel in 1842 by Joule. Magnetostriction is a result of the rotation of magnetic moments that cause external strains in the substance. These strains result in expansion or contraction of the material in the direction of the magnetic field. The magnetostrictive effect is well described in ref [3]. Although magnetostriction occurs in most magnetic materials, the magnitude of the strain is extremely small ($\delta l/l < 10^{-5}$). This limits usage of this novel effect in any application requiring substantial displacements. Recently, a gigantic magnetostriction effect was discovered in an alloy of rare earth compounds

($\text{Tb}_x\text{Dy}_{1-x}$) [4]. The size of the strain can be as large as $8/1 \sim 10^{-2}$ at low temperatures. Our development of a new low temperature magnetostrictive actuator was motivated by the availability of these gigantic magnetostrictive materials.

PRELIMINARY TEST

Even though giant magnetostrictive materials have been known for a few years, almost no measurements have been performed on these materials at liquid helium low temperatures. We have carried out a simple experiment with a single crystal rod of $\text{Tb}_{0.76}\text{Dy}_{0.24}$ to study the size of the strain as a function of the magnetic field (see ref. [4]). This composition was chosen to have maximum strain at low temperatures. A schematic drawing of the test set up is shown in Fig. 1. A small superconducting solenoid wound with NbTi wire produced the required magnetic field. The induction/current ratio of the magnet was calculated to be 30mT/Amp at the center of the magnet.

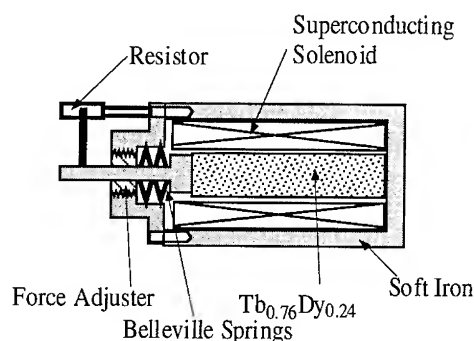


Figure 1. The schematic drawing of preliminary test apparatus.

An external assembly consisting of soft iron served as a flux path and a Bellville spring provided an initial stress of 8 MPa to the sample. A metal film resistor with a point contact on its surface was mounted to detect change in relative position between the sample and the housing. The most important result of this preliminary experiment was that the thermal contraction of the $\text{Tb}_{0.76}\text{Dy}_{0.24}$ sample relative to the soft iron closure was about a factor of two smaller than the positive strain due to the magnetostriction effect. This experimental observation simplified the design of the actuator for the low temperature valve.

VALVE CONSTRUCTION

The basic strategy in constructing this valve was modularization. The valve consisted of two main bodies that were completely separable. One modular component completely contained the valve mechanism while the other modular component contained the actuator. The schematic drawing of the valve is shown in Fig. 2. The valve was designed to be normally closed. This had several advantages over a normally opened valve. For many scientific applications the thermal heat leak to the system must be minimized. This valve provided near zero heat leak to the system since the superconducting solenoid dissipated zero heat. Also, a magnetic disturbance to other experimental apparatus near the valve due to the actuation will

only occur during sample loading time (valve open) when generally no experimental data is being taken. The force required to close the valve was determined experimentally during preliminary tests. Nevertheless, a force adjuster was built in for flexibility. We used about 150 lbs of force to close the valve at low temperatures. A stack of Belleville springs (BS 1-3.2-0.5) were used to obtain these high forces. Each of these springs provided 88 lbs of force under compression of 0.020 inch (50% of total travel length). The compression of the springs was made by rotating a 7/16"-28 brass screw. A stainless steel shim stock (302 stainless steel, 0.004" thickness) was used to seal the valve. This had advantages over a typical bellows sealed valve in terms of cleanliness and compactness. Solder joints were eliminated in the valve assembly by E-beam welding the diaphragm to the valve body. The actual seal was made between a stainless steel ball (440c stainless steel, 0.125" diameter) and 304 stainless steel body.

The novel feature of this valve is its actuation mechanism. A single crystal b-axis rod of $\text{Tb}_{0.76}\text{Dy}_{0.24}$ was grown at the (DoE) Ames Laboratory. It was initially compressed with about 8 MPa of pressure by a similar force adjuster as used in the valve body. The demagnetizing field was substantially reduced by a soft iron closure around the rod and the solenoid. The solenoid was constructed using superconducting NbTi wire. The induction/current ratio at the center of the magnet was roughly calculated to be 40mT/amp.

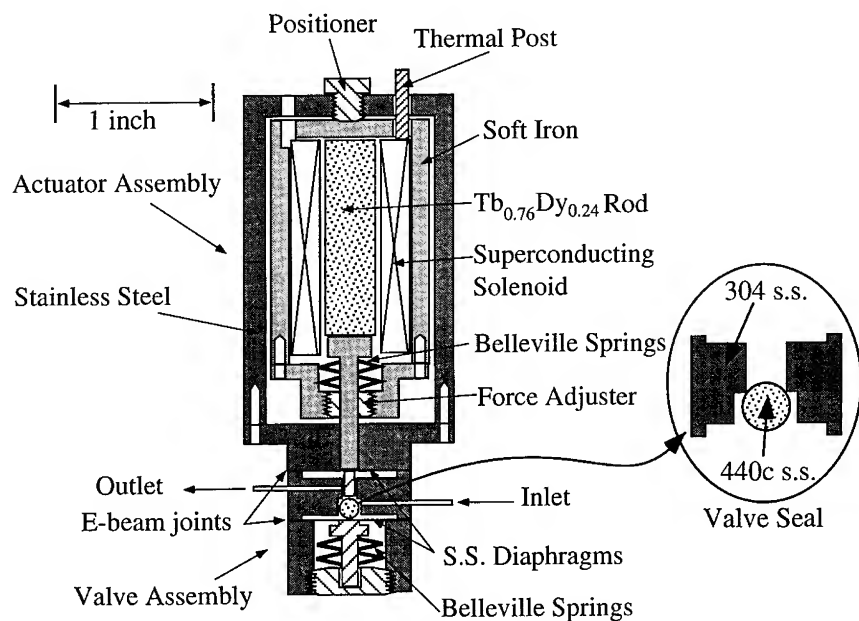


Figure 2 Schematic drawing of the valve assembly.

TEST AND RESULTS

The valve was initially shown to be leak tight (leak rate $< 10^{-10}$ atm cc/sec) at room temperature using less than 30 lbs of force. However, it required about 150 lbs of force to become leak tight in a 4.2 Kelvin liquid helium bath. The force required was obtained simply

by rotating a screw type force adjuster at room temperature that compressed the Belleville springs. The actuation test of the valve was also performed by supplying current to the solenoid. We used helium gas to pressurize one side of the valve while the other side was pumped out using a vacuum pump. The pressure on the pump side was monitored using a pressure gauge. Figure 3 shows the pumping side pressure normalized by the averaged pumping pressure of the fully opened valve as a function of the current through the coil. We opened and closed the valve more than 100 times without noticing any degradation in its performance.

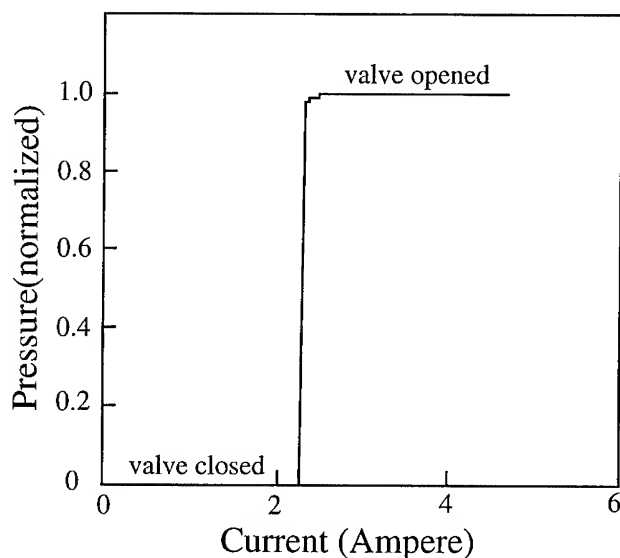


Figure 3. Pumping pressure vs. current through the solenoid. The pressure is normalized to the fully opened valve value.

A second experiment was carried out in a laboratory built cryostat. The cryostat had a helium evaporation cooler inside a vacuum can so that we could cool a ^4He sample down below its superfluid transition temperature. Since the superconducting magnet was operated in a vacuum can, thermal anchoring of the wires was crucial. The current leads of the magnet were thermally anchored to the cooling stages. Outside the vacuum can NbTi current lead wires were spot welded to copper clad NbTi wires by etching off copper. The copper clad wires extended up to the room temperature flange of the cryostat. A leak detector was connected to the outlet of the valve to determine whether the valve was superfluid leak tight. The helium fill line attached to the valve inlet was connected to the helium reservoir. A low temperature strain gauge connected to the reservoir monitored small pressure changes of the system after the valve was closed. We monitored the leak rate of the system while helium was condensed inside the reservoir. The observed leak rate was less than the maximum sensitivity of the leak detector ($\approx 10^{-10}$ atm cc/sec). The system was then slowly cooled below the superfluid transition temperature using the ^4He evaporation cooler. The leak rate of the valve remained constant at temperatures below 2.0 K.

In conclusion, we have developed a new liquid helium low temperature valve that can be activated by a magnetostrictive material driven by a lossless superconducting coil. We

demonstrated that this valve was leak tight at liquid helium temperatures both above and below the lambda point. We were also able to repeatedly actuate the valve at low temperatures by supplying current (~2.3 A) to the superconducting coil.

ACKNOWLEDGMENT

We would like to thank John Gatewood for his invaluable support in the design and fabrication of the valve components. This work was carried out by the Jet Propulsion Laboratory, California Institute of Technology under a contract with National Aeronautics and Space Administration.

REFERENCES

- (1) P.R. Roach, J.B. Ketterson, M. Kuchnir: Rev. Sci. Instrum. 43, 898 (1972).
- (2) T. Tsuda, and Y. Mori, Rev. Sci. Instrum. 62, 841 (1991).
- (3) B.D. Cullity, "Introduction to magnetic materials" (Addison-Wesley, 1972).
- (4) M.L. Spano, A.E. Clark, and M. Wun-Fogle, IEEE Trans. on Magnetics 25, 3794 (1988).

ULTRASONIC APPLICATIONS USING MAGNETOSTRICTIVE SMART MATERIALS

T. TOBY HANSEN AND SOLOMON R. GHORAYEB
ETREMA Products, Inc. 2500 North Loop Drive, Ames, Iowa 50010

ABSTRACT

Many of the innovations in ultrasonic technology make use of modern smart alloys and materials. As a result, the theory and application of ultrasonic energy have become extremely important in various disciplines such as ultrasonic surgery, cleaning and imaging. However, despite the fact that most of these ultrasonic devices are based on widely known materials, there remains a class of materials which have not been fully explored as potential active components in ultrasonic designs. In this paper, the giant magnetostrictive smart material, ETREMA TERFENOL-D®, is discussed to illustrate its potential for such applications. Frequency analysis, reliability and advantages of ultrasonic mechanisms using ETREMA TERFENOL-D® are also shown for a general broadband ultrasonic device. Frequencies between 1 kHz and 30 kHz were obtained for these applications.

INTRODUCTION

Recent developmental applications in the field of magnetostriction have covered areas ranging from the medical to the defense industry. A large volume of interest has focused on electroactive devices used for micropositioning, antivibration and antinoise. However, driven by technological and market forces, this interest has broadened to cover ultrasonic applications in both the medical and the nondestructive testing (NDT) arenas. As a result, new techniques are being implemented to refine, and thus outperform, the conventional electrostrictive technologies.

Magnetostriction, or the tendency of ferromagnetic materials to expand or contract in a magnetic field, is a well known phenomenon that has been exploited for many years for acoustic/sonic transducers. Magnetostrictive actuators using nickel and alloys of nickel, cobalt and iron were used extensively in the 1940's and 1950's, predominantly as ultrasonic vibration sources for acoustic cleaning, welding and machining. In the early 1970's a group of Navy scientists lead by A. E. Clark began experimenting with highly magnetostrictive rare earth metals [1]. In 1976, they discovered an alloy of Iron and Terbium which had high levels of magnetostriction. Furthermore, they determined that by adding Dysprosium to the mixture, they could vary the amount of magnetic hysteresis present in the material. The new material was called TERFENOL-D after its components Terbium (TER-), Iron (-FE-), Dysprosium (-D) and its place of discovery (Naval Ordnance Lab, -NOL).

Basic Actuator Configuration

An actuator is the general name for mechanisms that convert energy input to a displacement output. Magnetostrictive actuators convert electrical energy to mechanical

energy using the magnetic field induced by an electric current in a wound wire solenoid. The solenoid is usually wrapped around a rod or bar of the magnetostrictive material and displacement output is varied by controlling the current flow in the coil. The use of ETREMA TERFENOL-D® actuators offers several benefits and advantages over other motion technologies:

- (1) It is a solid state transducer whose motion is the result of the rotation of ferromagnetic domains. There are no moving parts subject to wear.
- (2) ETREMA TERFENOL-D® is a magnetostrictor, it does not depole (lose its electromechanical properties) due to high pressure or large reverse fields. In fact, the only way to deactivate it is to heat it beyond its Curie Temperature, 380 °C.
- (3) Actuators are mechanically simple. ETREMA TERFENOL-D® comes in rod form and does not require complex stacking arrangements.
- (4) No direct electrical terminations are required on the material. The only electrical terminations are the two leads to the solenoid and these do not move, so the terminations are not subject to continued fatigue loading and strain hardening.
- (5) Low input voltage is generally needed to develop current in low impedance coils. This offers advantages for applications where high voltage is undesirable such as with automobiles and medical devices.

There are two main types of ETREMA TERFENOL-D® actuators available: mono-directional (push only) and bi-directional (push-pull). A diagram of a basic mono-directional actuator is illustrated in Figure 1.

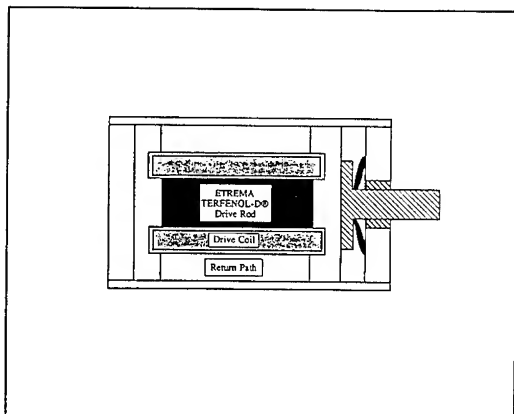


Figure 1. Basic mono-directional actuator configuration.

The basic components of the mono-directional actuator shown in Figure 1 are the ETREMA TERFENOL-D® rod, the field coil to activate the rod, the prestress housing to keep the rod in compression, and the push rod to couple the magnetostrictive motion to the device that needs to be controlled. The housing provides the prestress by the compression of belleville springs. The reason for this is twofold. First, the material can only support very little tensile or shear load but is quite strong in compression. Thus, to avoid the risk of tensile loading, a prestress housing is usually a must. Second, because of the nature of magnetoelastic coupling (the physical mechanism of

magnetostrictive transduction), the material achieves better performance when prestress is applied onto it. This occurs because the magnetic domain orientation can be manipulated by changing the state of stress in the material.

An interesting aspect of the ETREMA TERFENOL-D® magnetostrictive effect is that positive displacement results from the application of either positive or negative fields. For bi-directional operation, a permanent magnet is added in parallel with the field coil. The permanent magnet provides a bias field (this could also be obtained from a constant current) that the coil then adds to or subtracts from. The result is expansion or contraction relative to the initial biased length of the rod.

ETREMA TERFENOL-D® ULTRASONIC APPLICATION THEORY

For years, ETREMA TERFENOL-D® has been thought of as useable at only low frequencies (i.e. DC - 2 kHz). The main reason for this misconception is that the material was developed for sonar which implied a constraint on the material as being low frequency. Not to mention eddy currents were believed to be so large that high frequency operation was impractical. New investigations launched at ETREMA Products, Inc. have uncovered some important insights to the practicality of ETREMA TERFENOL-D® in the ultrasonic frequency range.

Lamination is a very well known means of reducing eddy currents in conducting media when time-varying magnetic flux is present in the material. The purpose of laminating such materials is to reduce the area and increase the length which magnetically induced current travels resulting in an increase in the overall resistance. This effectively reduces the amount of current created and hence decreases the amount of power that is lost within the material (i.e. power loss is equal to the square of the current). As a general rule of thumb, to keep power losses to a minimum, a laminate should be equal to twice the eddy current skin depth [2]. The frequency at which the size of the laminate equals twice that of the eddy current skin depth, is known as the critical frequency. ETREMA TERFENOL-D® is a hard and brittle material; it has certain lamination size limitations. One millimeter (0.04 inch) is the smallest laminate width that should be cut in the material. Using values of relative permeability of 5 and a resistivity of $60 \times 10^{-8} \Omega m$, the critical frequency is on the order of 120 kHz. This implies that the material can be operated from DC to 120 kHz with only minor losses caused from eddy currents. However, the coil windings that produce the magnetic flux to activate the magnetostriction effect induce eddy currents in each other which increase power losses. The net effect of eddy currents in both components places the practical operating frequency range of an ETREMA TERFENOL-D® driven device between DC-50 kHz without appreciable loss and the requirement of extravagant cooling measures.

ULTRASONIC APPLICATIONS

ETREMA Products, Inc. has been recently exploiting the potential of ETREMA TERFENOL-D® as applied to ultrasonic applications. ETREMA was approached by an ultrasonic surgery tool manufacturer to produce an ETREMA TERFENOL-D® device that would replace their existing piezoelectric (PZT®) ultrasonic motor. The advantages they were looking for to advance their technology were to: 1) Increase the power output by

producing more displacement at the surgical tip. 2) Reduce the size and hence weight of their existing device. 3) Have the ability to superimpose a 6000 V, 1 MHz signal to the transducer to cauterize "bleeders" introduced by the tip when it is applied to flesh.

A program was initiated and a device was built to accomplish the stated design goals. The resulting transducer has accomplished all of the goals. Figure 2 illustrates a comparison of the relative sizes of the original PZT® ultrasonic motor and the ETREMA ultrasonic motor. Each unit has basically the same design methodology. A quarter-wave active section is in intimate contact with a quarter-wave titanium section. This produces a half-wave resonating subassembly. Not shown in the Figure is an ultrasonic horn that is attached to the titanium side of each of the motors. Through geometry diameter ratios, the displacement from the ultrasonic motor titanium face is enhanced substantially to the tip of the horn (amplification of 15 to 30 X). The result is extreme acceleration at the tip that can pulverize tumorous flesh without harming healthy

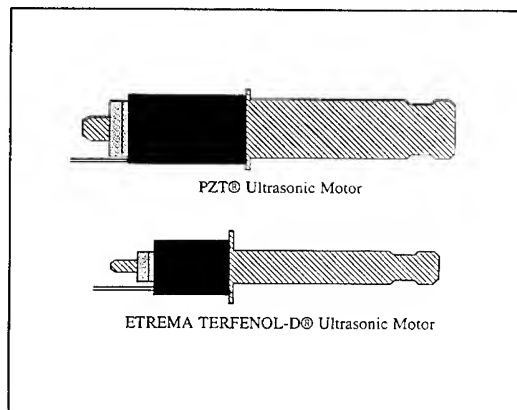


Figure 2. Ultrasonic motor comparison.

human tissue. Table 1 is a comparison of the two transducers in terms of active element mass, horn amplification, tip displacement and relative energy output based upon the displacement divided by horn amplification and active element mass (figure of merit). As can be seen, the ETREMA TERFENOL-D® ultrasonic motor produces significantly more displacement with much less amplification. The Relative Energy column shows that the ETREMA motor produces 4.8 times the displacement per gram than the PZT® motor.

Table 1. PZT® vs. ETREMA TERFENOL-D® Ultrasonic Motors

Motor	Element Mass (g)	Amplification (Q)	Displacement at Tip (Max. μm)	Rel. Energy ($\mu\text{m}^2/\text{g Q}$)
PZT®	18.9	25	240	0.51
ETREMA	7.5	19	348	2.44

Not shown is that the ETREMA motor is approximately half the weight of the PZT® motor. Among the obvious, quantitative advantages are two less noticeable advantages the ETREMA unit offers to this particular application. The unit has the potential for much longer service life than the PZT®. Since the material is always in compression, the stresses in the Titanium parts are below the endurance limit and there are no depoling mechanisms within the material, the ETREMA unit will be able to last longer than the service life of a PZT® unit of 170 hours (heavy tip loading). A second advantage is that it is an inductive device which will not be affected by the 1 MHz signal. This is in contrast to the PZT® device that is capacitive and cannot be easily isolated from the high frequency signal.

BROADBAND ULTRASONIC ACTUATOR

Transducer technology today uses two main materials for sonic and ultrasonic operation. Both of these, PZT® and Nickel, are high Q materials. This means that at specific, narrowband frequencies, levels of excitation are substantially enhanced by these materials due to the materials going into resonance. This characteristic of these materials has produced successful devices that are in use today such as ultrasonic welders, cleaners and imaging equipment. However, when these materials are operated off resonance, their output and efficiency, decreases markedly. This phenomenon also occurs if the boundary conditions of the device or load change since both are strong functions of the resonant frequency. Therefore, if a researcher is unaware of what specific frequency is needed to drive a process or knows that boundary conditions/load will be changing, then there is no alternative solution except doing exhaustive calculations or meticulous and time consuming trial and error experimentation. ETREMA TERFENOL-D® is a material that is a low Q material ($Q \leq 8$) that overcomes the narrowband limitations of PZT® and Nickel. It has the property of performing well over a significant range of frequencies even beyond first resonance.

ETREMA has designed and built a standard actuator that has the capability of producing high power excitation from 1 - 30 kHz. This unit is known as the Ultrasonic A actuator. This unit was built with a short, large diameter rod to increase the actuator's

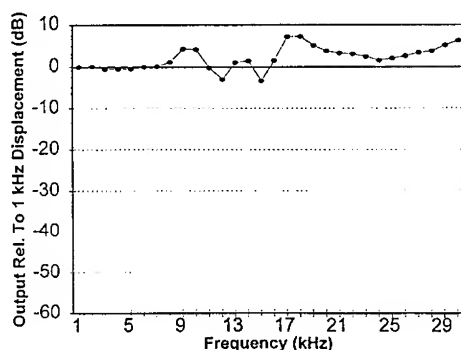


Figure 3. Ultrasonic A actuator output displacement vs. frequency.

fundamental frequency and produce high forces. Eddy current reduction has been one of the highlights of its design. Full operation of the unit requires a current input of ± 8 amps. Figures 3 and 4 depict the output from the device. In both Figures, the data was collected from a high acceleration accelerometer attached to the unit's push rod. Figure 3 is a plot of the output displacement per amp (normalized) relative to the displacement per amp at 1 kHz. As can be seen, this device has considerable potential for use as a broadband source. The deviation in the output does not vary by more than 7 dB for over a range of 1 kHz to 30 kHz. It should be noted that the data represented by Figure 3 is a comparison of output displacement per amp. Figure 4 illustrates the linear acceleration per amp of the device. With the acceleration increasing as f^2 , it can be readily seen that very large accelerations can be produced with the device (max. rated acceleration for the unit is 7500 g's). This very quality has attracted researchers to this device for studies ranging from liquefying metal to biological cell disruption.

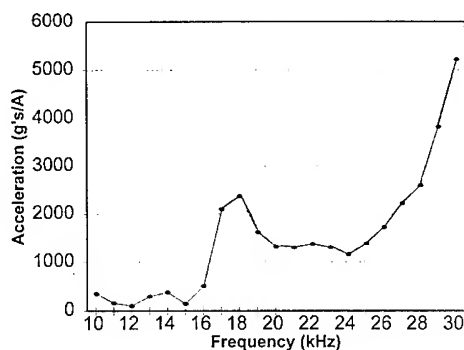


Figure 4. Ultrasonic A actuator acceleration vs. frequency.

CONCLUSIONS

In this paper, two applications of ETREMA TERFENOL-D® based actuators were discussed. The first was an ultrasonic surgical tool that was smaller, lighter weight and produced more output than an existing PZT® based ultrasonic surgical tool. It was also discussed that the ETREMA solution to the problem has a lot of potential to exceed the existing life time of the PZT® unit and offers the capability of cauterization during surgery. The other unit discussed, demonstrated the broadband nature of the low Q material of ETREMA TERFENOL-D® with its constant displacement output over 29 kHz and its capability of producing high accelerations.

REFERENCES

1. A.E. Clark, *Ferromagnetic Materials* **1**, 531-589 (1980).
2. L. Bergmann, *Ultrasonics and Its Applications in Science and Technology*, 1956.

DYNAMIC SHEAR CHARACTERIZATION IN A MAGNETOSTRICTIVE RARE EARTH - IRON ALLOY

PHILIPPE BOUCHILLOUX*, NICOLAS LHERMET AND FRANK CLAEYSSSEN
Cedrat Recherche, 10 Chemin du Pré Carré, ZIRST 4301, 38943 Meylan, France

*Now at Magsoft Corp., 1223 Peoples Ave., Troy, NY 12180

ABSTRACT

A previous study about the power limits of the magnetostrictive alloy called Terfenol-D, using a device biased by coils, showed the intrinsic superiority of this material compared to piezoelectric ceramics when used in high power sonar transducers. This fact was confirmed by another study where giant dynamic peak-to-peak deformations of 3500 ppm were measured with a transducer biased by permanent magnets.

Experience shows that the longitudinal functioning of magnetostrictive transducers is sometimes disrupted by interference caused by 'flexure' in the magnetostrictive rods. In fact, due to the shape of the rods, the flexure effects are strongly coupled to shear. Characterization of shear in Terfenol-D under conditions of magnetic bias and prestress is then necessary to control those effects. This was made possible by using a simple and original device that was designed totally with Computer Aided Design programs.

INTRODUCTION

A previous study about the power limits of the magnetostrictive [1] alloy called Terfenol-D [2] using a characterization device in which the magnetic bias was created by coils, showed the intrinsic superiority of this material compared to piezoelectric ceramics when used in high power sonar transducers [3,4]. Another study showed, with measured dynamic peak-to-peak deformations of 3500 ppm [5], that high power is obtainable even with a bias created by permanent magnets.

Experience shows that the functioning of transducers is sometimes disrupted by interference caused by flexure and shear of the magnetostrictive rods, which is also a cause of mechanical failure of the transducer. In earlier studies, it was established that the flexure modes are fully determined by the longitudinal characteristics of Terfenol-D, and that they are generated by non symmetrical magnetic excitation fields or mechanical structures. However, these results on flexure are not directly applicable to sonar transducers because in such devices the Terfenol-D rod length is rarely more than ten times its diameter, so that flexure effects are strongly coupled to shear. Thus, to calculate flexure/shear modes, both longitudinal and shear characteristics must be taken into account. As the longitudinal characteristics are well known [3,6], the purpose of the study was the characterization of shear in Terfenol-D.

The first step was to study, through calculations done with a Computer Aided Design program, how it is possible to make pure shear deformation modes appear in Terfenol-D with a simple device. This led to the design and construction of a Shear Characterization Device, called DCC. This device is a totally original concept, and it was designed to reproduce shear deformations in Terfenol-D identical to those found when it is used in sonar transducers; that is, with prestress and magnetic bias. The objective was to reproduce shear deformation modes as pure and as well coupled electrically as possible, in order to facilitate the shear deformation measurements and increase their accuracy. In the final stage of the study, the device was tested and operated.

SHEAR DEFORMATION IN TERFENOL-D

It is assumed that an electromechanically coupled pure shear deformation is produced under the conditions shown in fig. 1: a rod of Terfenol-D under a magnetic bias H_0 and a mechanical

prestress T_0 along axis 3 (the direction of easy magnetostrictive deformation) and excited by a magnetic field H_1 along axis 1 (the shear deformation is written as ΔU_1).

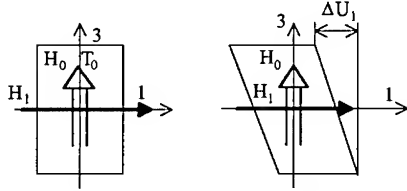


Fig. 1 : Schematic Representation of Shear Conditions and Deformation.

- Terfenol-D tensor [1,7] under pure shear conditions :

$$\begin{cases} S_5 = s_{44}^H T_5 + d_{15} H_1 \\ B_1 = d_{15} T_5 + \mu_{11}^T H_1 \end{cases} \quad (1)$$

where s_{44}^H is the shear elastic modulus at constant bias, μ_{11}^T is the transverse magnetic permeability at constant stress, and d_{15} is the shear magnetostriction coefficient. Thus :

$$\begin{cases} S_5 = s_{44}^H T_5 + d_{15} H_1 \\ B_1 = \frac{d_{15}}{s_{44}^H} S_5 + \mu_{11}^T \left(1 - \frac{d_{15}^2}{s_{44}^H \mu_{11}^T} \right) H_1 \end{cases} \quad (2)$$

Therefore, the shear magnetoelastic coupling coefficient is :

$$k_{15}^2 = \frac{d_{15}^2}{s_{44}^H \mu_{11}^T} \quad (3)$$

- Transverse Magnetic Permeability at Constant Strain μ_{11}^S : Terfenol-D is magnetically anisotropic. Its permeability along axes 1 and 2 is different from that along axis 3. Using the DCC, the transverse permeability at constant deformation can be found as :

$$\mu_{11}^S = \mu_{11}^T - \frac{d_{15}^2}{s_{44}^H} \quad (4)$$

This quantity is independent from the others and can be determined from the high-frequency measurement of the system inductance. This latter depends only on μ_{11}^S and on the system geometry. Using the Finite Element Program Flux3D [8], it is possible to determine the permeability by adjusting it until the computed inductance matches the measured one.

- Shear Elasticity at Constant Field s_{44}^H : this coefficient is responsible for the system shear resonance frequency at constant excitation field. This constant can also be determined by an adjustment method, using the Finite Element Program Atila [9], to match the theoretical mechanical resonance frequency to the measured one.

- Shear Magnetoelastic Coupling Coefficient k_{15} : this characterizes the ability of the material to convert a magnetic excitation energy into an elastic deformation energy. k_{15} depends on the three previous coefficients (equation 3) and partly controls the effective coupling coefficient k_{eff} :

$$k_{eff} = k_m \cdot k_e \cdot k_{15} \quad (5)$$

where k_m is the magnetic coupling coefficient and k_e is the elastic coupling coefficient, whose squares represent, respectively, the contribution of the magnetic and elastic energy in the smart

material to the magnetic and elastic energies of the entire system. k_{eff} is a function of the electric resonance f_r and antiresonance f_a frequencies, that are found by measuring the impedance.

$$k_{\text{eff}} = \sqrt{1 - \frac{f_a^2}{f_r^2}} \quad (6)$$

k_{15} is determined by equation (5), where k_m is calculated with Flux3D using μ_{11}^T , k_c is calculated with Atila and k_{eff} is found by equation (6) and by the measurements of f_r and f_a .

- *Shear Magnetostriction Constant* d_{15} : this constant links the magnetic excitation field H_1 to the shear deformation (equation 1) and controls the shear deformation amplitude for a given excitation field. It is determined by the three previous coefficients and by using equation (3).

DESIGN OF THE SHEAR CHARACTERIZATION DEVICE

Shear mode frequencies computed by the Atila program were compared to theoretical ones [10]. It was determined that the best shape to use for the Terfenol-D part to minimize flexure effects was a cube. The interference of flexure effects was thus minimized. Moreover, the cubic form decreases the resonance frequency, which is important for limiting the effect of eddy currents.

Using the Atila program it was possible to verify, by comparing the displacements in each direction, that the system possessed vibrating modes that were very close to pure shear modes.

The first system tested was a structure composed of a cubic bar of Terfenol-D and two counter-masses as shown in fig. 2. The counter-masses lower the system resonance frequency.

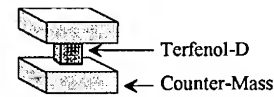


Fig. 2 : Diagram of Initial System.

A parametrized study showed that due to eddy currents in the Terfenol-D, the resonance frequency must be set below 1 kHz. The first system functioned at too high a frequency; lowering the frequency to an acceptable value would have required the use of unrealistically large masses.

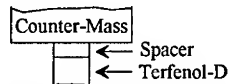


Fig. 3 : Placing of the spacers.

Nevertheless, this geometry allowed the study of details such as the spacers, shown in fig. 3. These are indispensable for the construction of the device (as explained later). The results obtained using Atila showed that the functioning of the structure was only slightly perturbed by those spacers, and that the locally induced concentrated stresses were acceptable. It also showed that the coupling coefficient decreases a little, as a result of the decrease in k_c caused by the added elasticity of the spacers.

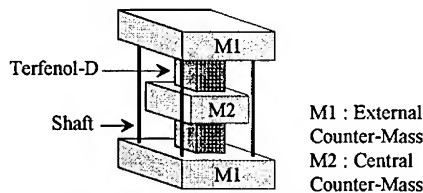


Fig. 4 : Diagram of Two-Cube System.

A new structure was created by adding a second cube of Terfenol-D and a central counter-mass (see fig. 4). Atila computations showed that a resonance frequency below 1 kHz was possible using Terfenol-D bars of small dimensions (10x10x10 mm).

Permanent magnets were used to simplify the construction of the device. Flux3D computations verified that the magnetic field H_0 was uniform and strong enough to bias the Terfenol-D (fig. 5).

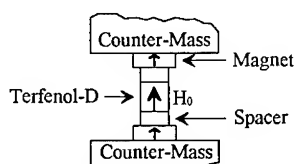


Fig. 5 : Magnet Placement and Magnetization Direction.

A study of the magnetic excitation field with the Flux2D program [8] showed that eddy currents in the Terfenol-D counteracted the excitation field almost completely for frequencies above 1 kHz, resulting in no net excitation. Actually, the difficulty was to create an excitation field that was both perpendicular to the bias, and strong and uniform enough (at least 1 kA/m) to insure a uniform deformation of the Terfenol-D. It was found that brass (non magnetic) was the most convenient material for the counter-masses and the spacers. Moreover, the high density of brass allowed heavy counter-masses of a reasonable size to be built.

To produce a uniform excitation field, the excitation coil needed to be placed as close as possible to the Terfenol-D. The solution was to wind a thin cable around the Terfenol-D cubes through notches made in the spacers, as shown in fig. 6.

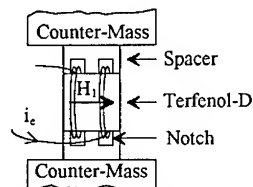


Fig. 6 : Placement of Excitation Coils.

All the previous conclusions were taken into account for the final design of the device, as shown in fig. 7. The DCC contains two 10 mm Terfenol-D cubes. The magnetic bias is created by permanent magnets having a 1.1 T remanent flux density. The excitation field is created by a wire passing through the two notches (with cross section of 2x2.5 mm and length of 10 mm) of each spacer. The counter-masses and spacers are made of brass. Their dimensions are 110x110x60 mm for each external counter-mass and 80x80x50 mm for the central one. The various parts of the device were kept in place with a stress placed on the four 6 mm diameter steel shafts. Centering of the elements was made easier by cutting slots in the counter-masses.

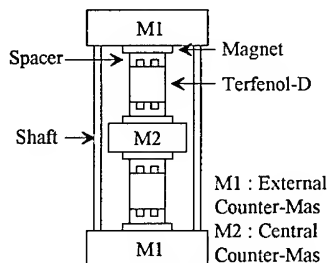


Fig. 7 : Diagram of Complete DCC Structure.

Some of the most important characteristics of this device, as calculated in the study, are shown in Table 1. The deformation given by Atila for one fourth of the structure (using symmetry planes) is shown in fig. 8; fig. 9 is a photograph of the DCC.

Electric Antiresonance Frequency	$f_e = 620 \text{ Hz}$
Effective Coupling Coefficient	$k_{\text{eff}} = 38 \%$
Magnetic Coupling Coefficient	$k_m = 60 \%$
Elastic Coupling Coefficient	$k_e = 70 \%$
Polarization Field	$H_0 = 90 \text{ kA/m}$
External Counter-Mass Weight	$M1 = 6.1 \text{ kg}$
Central Counter-Mass Weight	$M2 = 2.7 \text{ kg}$

Table 1 : Characteristics of DCC.

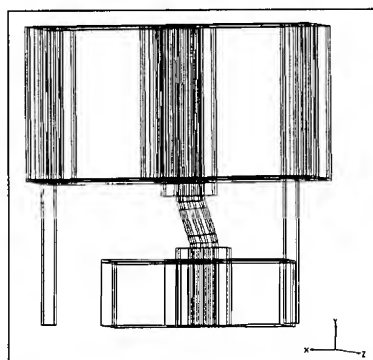


Fig. 8 : Atila Computation of DCC Deformation at Resonance.

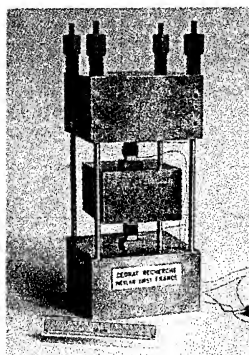


Fig. 9 : The Shear Characterization Device (DCC).

RESULTS OBTAINED

All tests were performed at Cedrat Recherche's laboratory. They consisted of making several measurements on the bench of fig. 10. A PC controlled the frequency and amplitude of the excitation current in the coils. It also processed data sampled by a digital oscilloscope.

The following variables were measured : electric impedance around resonance and antiresonance frequencies; central mass displacement around mechanical resonance f_m ; quasi-static inductance and displacement. Impedance and inductance were obtained from the excitation current I and voltage U . Displacements were obtained from the acceleration γ .

The DCC was tested for several values of prestress (30, 40, 50 MPa). In each case, useful results were obtained. An audible resonance was found around 600 Hz in the expected band of frequencies. The audibility at the low excitation level is a sign of weak absorption; this is confirmed by a spike in the measurements of mechanical displacement (fig. 11). The latter can be used to evaluate the mechanical quality factor Q_m of the device.

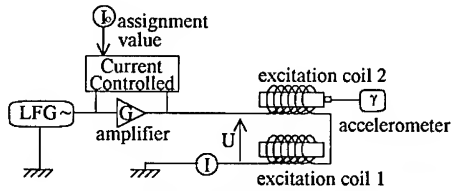


Fig. 10 : Diagram of Measurement Bench.

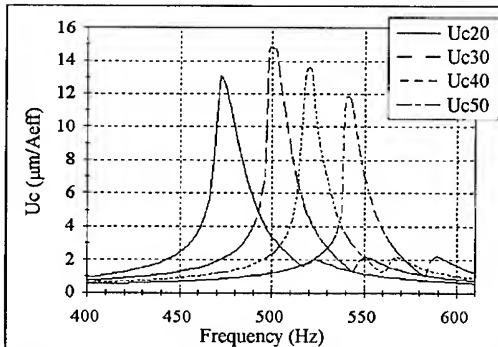


Fig. 11 : Central Mass Displacement Measured vs Frequency (Prestress $T_0 = 20, 30, 40$ & 50 MPa).

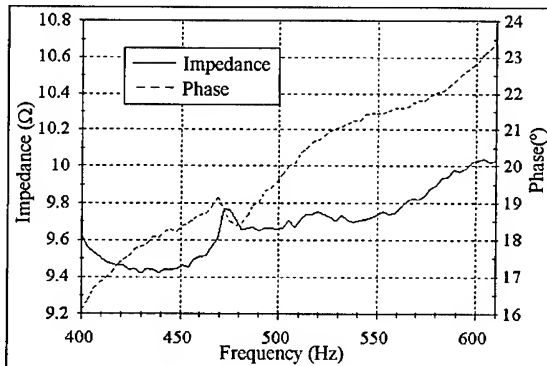


Fig. 12 : Magnitude of Measured Electric Impedance and its Phase vs Frequency (Prestress $T_0 = 20$ MPa).

The mechanical and electrical resonances demonstrate strong enough coupling to influence the impedance of the system (figures 12 and 13), proving that the coupling coefficient k_{15} has

significant values. This is essential because the calculation of the shear characterization parameters from the impedance values at resonance is valid only for an electrically coupled material.

The serial coil resistance lowers the measurement precision. The contribution of the resistance to the imaginary part of the impedance cannot be neglected. Consequently, to evaluate resonance and antiresonance frequencies and effective coupling coefficients correctly, it was necessary to use a modified impedance Z' , whose real part is defined as the real part of the measured impedance Z minus the serial resistance of coil R_0 . This new impedance presents more distinct variations, as shown in fig. 14.

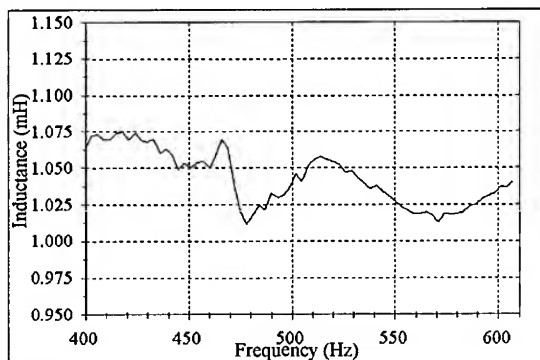


Fig. 13 : Measured Serial Inductance vs Frequency (Prestress $T_0 = 20$ MPa).

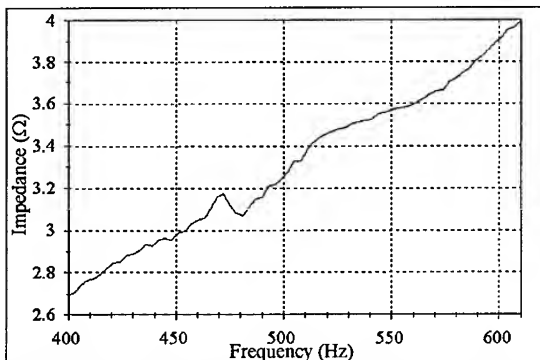


Fig. 14 : Magnitude of Corrected Impedance Z' vs Frequency (Prestress $T_0 = 20$ MPa).

T_0 (MPa)	f_a (Hz)	f_r (Hz)	k_{eff} (%)	f_m (Hz)	μ_{11}^T/μ_0	d_{15} (m/A)	s_{44}^H (m ² /N)	k_{15} (%)	Q_m
20	472	481	19	472	7.9	17.5×10^{-99}	3.15×10^{-10}	31	24
30	502	517	24	499	8.1	16.5×10^{-99}	2.40×10^{-10}	33	31
40	523	541	26	520	8.3	20.6×10^{-99}	1.90×10^{-10}	46	34
50	538	556	25	541	9.2	29.9×10^{-99}	1.55×10^{-10}	47	36

Table 2 : Values of Parameters Governing Shear for Several Values of Prestress.

A compilation of the results obtained for the parameters governing shear in Terfenol-D (biased and prestressed) can be found in Table 2. The value found for the shear piezomagnetic coupling

constant d_{15} is in rough agreement with the value H. T. Savage (22×10^{-9} m/A) obtained by measuring the torsion of a non prestressed Terfenol-D rod at resonance [11].

CONCLUSION

The study of unexpected behavior of Terfenol-D in magnetostrictive power transducers led to the study of flexure and shear effects, and involved the development of means of characterization.

Once the conditions of excitation of a coupled shear mode were highlighted in theory, the research led to the design, construction and testing of a Shear Characterization Device for Terfenol-D (called DCC).

The DCC is an original design based on calculations made with finite element programs. This device fulfills its purpose : it allows measurements that are necessary to characterize shear deformations in the smart material to be taken.

Tests of the DCC show that there is well-coupled shear in biased and prestressed Terfenol-D; that is, in usual sonar transducer operating conditions.

Finally, using the measurements from the DCC and an extraction method, the determination of the constants governing shear under conditions of magnetic bias and prestress is possible, providing a new set of characterization constants that will be very useful in any future studies involving Terfenol-D.

REFERENCES

- [1] DE LACHESSERIE E., Magnetostriction : Theory and Applications, Ed. CRC Press, USA, 1993, p. 410.
- [2] CLARK A. E., Magnetostrictive Rare Earth-Fe₂ Compounds, Ferromagnetic Materials, Ed. E.P. Wohl-Farth (US), Tome 1, 1980, pp. 531-588.
- [3] CLAEYSSSEN F., Giant Dynamic Magnetostrain in Rare Earth-Iron Magnetostrictive Materials, IEEE Trans. MAG. 27, No. 6, Nov. 1991, pp. 5343-5345.
- [4] CLAEYSSSEN F., Progress in Magnetostrictive Sonar Transducers, Proc. UDT93, Ed. Reed Exhib. (UK), 1993, pp. 246-250.
- [5] CLAEYSSSEN F., State of the Art in the Field of Magnetostrictive Actuators, Proc. ACTUATOR 94 conf., Ed. Axon, Bremen (G), 1994, pp. 203-208.
- [6] MOFFETT M.B., Characterization of Terfenol-D for Magnetostrictive Transducers, JASA, 89 (3), 1991, pp. 1448-1455.
- [7] CLAEYSSSEN F., Design and Building of Low-Frequency Sonar Transducers Based on Rare Earth-Iron Magnetostrictive Alloys. Doct. Thesis, INSA de Lyon (F), No. 89 ISAL 0065, Ed. Defence Research Inform. Cent. (HSMO, MoD, London) 1989, p. 414.
- [8] FLUX2D/3D, Finite Element Programs for 2D/3D Magnetic and Electric Field Analysis, LEG, Grenoble (F).
- [9] ATILA, 3D Finite Element Code For Piezoelectric and Magnetostrictive Transducers, ISEN, Lille (F).
- [10] BLEVINS, R. D. Formulas for Natural Frequency Mode Shape. PhD Thesis. Van Nostrand Reinhold Company. Litton Educational Publishing, Inc. 1979.
- [11] SAVAGE, H. T., ABBUNDI, R. Perpendicular Susceptibility, Magnetomechanical Coupling and Shear Modulus in Tb₂₇Dy₇₃Fe₂, IEEE Transactions on Magnetics, 1978, vol. Mag-14, no. 5, pp. 545-547.

A FACILITY FOR EVALUATION OF ACTUATORS BASED ON GIANT MAGNETOSTRICTIVE MATERIALS

H. TIBERG* AND G. ENGDALH**

*Dept. of Electric Power Engineering, Royal Institute of Technology, 100 44 Stockholm, Sweden

**Dept. of Power Engineering, ABB Corporate Research, 721 78 Västerås, Sweden

ABSTRACT

The recent development of actuators based on giant magnetostrictive materials in for instance hydroacoustic transducers has caused an increase in output forces from the drive elements used. The high stress levels make testing of the actuators with well defined mechanical loads difficult. The need for standards and improved evaluation methods has therefore become evident.

Based on experiences from earlier test facilities a new set-up has been designed with the intention to obtain

- higher resonance frequency
- facilitated assembly of test objects
- increased operating forces
- flexible choice of mechanical loads
- computer controlled measurement procedure
- controllable environmental conditions, for instance temperature.

In order to achieve the specifications, the test rig involves hydraulics for prestressing and clamping of the test object and the mechanical load. A method of mechanically disconnecting the prestress device from the fixture gives lower mass to stiffness ratio in the fixture and therefore a better high frequency performance.

The presented test rig is considered to have the prerequisites of serving as a platform for future evaluation and standardization of actuators.

BACKGROUND

In [1] is reported some deficiencies of an earlier test rig made for magnetostrictive rods with diameters of 6 mm. With the increased power levels that follow from rods with diameters up to 30 mm, these imperfections give strains in the fixture that exceed the magnetostrictive displacements in the test object. Therefore great efforts have been made on the design of a new stiffer construction that also facilitates mounting and allows higher prestressing.

BASIC DEMANDS

The test rig should provide an environment where actuators can be tested under well known mechanical and other conditions, e.g. temperature.

One demand of the evaluation facility is that a physical window with a fully controllable and continuously variable height is provided for the actuators with their mechanical loads. It should also be possible to clamp the actuator at an arbitrary stress level. During measurements this window should keep a fixed length. To prevent possible movements of the

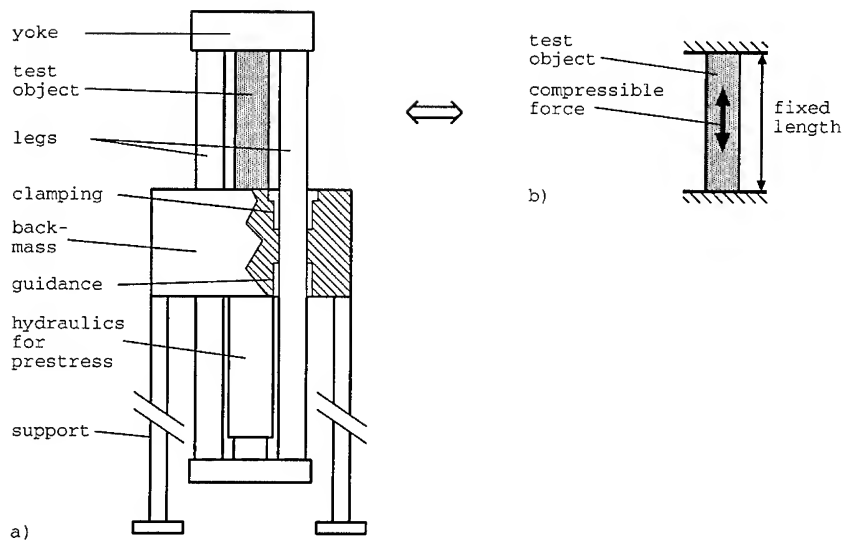


Figure 1: Schematic drawing of the test rig (a) and the desired mechanical equivalent (b).

actuator from influencing the loading conditions it should be fixed to a back mass.

The maximum width of the test object should be 200 mm and the height of the test window should be continuously adjustable from 500 mm down to 25 mm where it should be possible to apply a compressible force of up to 70 kN.

The total strain of the fixture when an actuator is stressed with 70 kN should be less than 5 % of the strain of the test object. To obtain this it is important to ensure that no part of the rig moves in resonance at the investigated frequencies. The specified resonance frequency is then chosen above 1 kHz.

The material choice must involve materials which give no magnetic interference with the test object.

The set-up must also be designed for easy exchange of actuators, loads and prestress levels.

PRINCIPAL DESIGN

Functional description

A schematic drawing of the fixture is shown in Fig. 1a. The yoke and the two legs form a fixture which clamps a test object to a back mass with an appropriate prestress. This clamping is for most loading conditions equivalent to an ideal clamping with a well defined length between the back mass and the yoke. The prestress is applied with a hydraulic cylinder. The clamping devices lock the legs of the fixture to the back mass. With the arrangement of a mechanical disconnection of the prestress device from the fixture the stiffness to mass ratio of the test-rig can be increased considerably, which is necessary in order to reach the resonance frequency specification.

Deviations in the performance from the ideal situation in Fig. 1b. are caused by strain and shear displacements in different parts of the fixture. Estimations of displacements in the yoke and legs and corresponding resonance frequencies has been done by the following approximations, where steel has been selected as fixture material due to its favourable stiffness to mass ratio.

Yoke

The bending and shear of the yoke will have its most negative influence on the measurements when short actuators are mounted in the rig. Therefore the yoke is designed for shear and bending of less than 5 μm .

The bending δ_b and the shear δ_{sh} at the middle of a horizontal bar of length L where a vertical force F is applied is

$$\delta_b = \frac{FL^3}{kEI}, \quad \delta_{sh} = \frac{FL}{2GA}, \quad (1)$$

where k is a constant depending on the support, E is the E-modulus, I is the surface moment of inertia, G is the shear modulus and A is the cross section area. In the actual geometry and loading condition it can be seen that the shear is much larger than the bending, with the assumption that the shear forces and the cross section is constant along the yoke.

A cross section area of $19 \cdot 10^{-3} \text{ m}^2$ will fulfil the specified displacements. This corresponds to a mass of 40 kg and a resonance frequency of approximately 3.5 kHz.

Legs

With the yoke that fulfils the specification above, the legs are mostly subjected to homogeneous tensile stresses. The design criterion is not the static strain but the resonance frequency of the legs plus yoke. It can be approximated by the resonance frequency of a mass and spring system as

$$f_r = \frac{1}{2\pi} \sqrt{\frac{K}{M}}, \quad K = \frac{AE}{l}, \quad (2)$$

where K is the stiffness of the legs, M consists of the yoke mass and one third of the legs mass, A is the cross section area of both the legs, E is the E-modulus of the legs and l the length of the legs.

By inserting different values of the area A , an appropriate diameter of the legs is chosen for the mass of the yoke chosen above. The chosen diameter of 100 mm gives a resonance frequency of 1.3 kHz which is acceptable. With a static compressible force between the yoke and the back mass the elongation of the legs is then 10 μm .

Clamping device

The movable fixture comprising yoke and legs can be in any position between 25 mm and 500 mm above the back mass. The test object including a passive or active mechanical load is at first inserted in the test window, where it can be prestressed by the hydraulic cylinder. At a chosen mechanical stress or strain level in the test object, the fixture is clamped to the back mass with self locking wedges which are operated by hydraulics. If the hydraulic force

of the cylinder is then released, the clamping device will take over the prestress force and therefore be subjected to a corresponding strain. This strain has been investigated with a finite element program and estimated to $0.5 \mu\text{m}$ at a force of 35 kN.

The effective mass of the fixture and the above compliance gives an resonance frequency of approximately 5 kHz.

TENTATIVE OPERATION PERFORMANCE

Initiation of measurement

When mounting a test object the hydraulic cylinder can be controlled either with respect to the position of the yoke or with respect to the prestress force or strain of the test object. The position of the yoke can be monitored with e.g. a differential transformer. The prestress force can be monitored by a force transducer placed within the test window and strain gauges can monitor the strain of the actuator and the load. An optional controller for the measurement initiations is preferably implemented digital in the monitoring and data acquisition system.

Mechanical load

A passive mechanical load can easily be made of springs, viscous dampers and masses. However, for the small displacements and high forces that are normally the output from magnetostrictive actuators it is very hard to make a pure resistive, compliant or mass load.

An alternative way of defining a load is to clamp the actuator against an identical actuator which works as an electronically controlled active load. It is then possible to control the resistance, spring and mass independently.

The next step is to build a special active controllable load with a higher mechanical performance than the test object e.g. based on magnetostrictive material. With this approach the loading conditions resistive, spring and mass load would be achieved with wide ranges.

Instrumentation

Two amplifiers excite the test objects. They can be put in either voltage or current amplifying mode. The movements and strains of the test objects are measured with piezo-electric accelerometers and strain gauges respectively. A force transducer measure the mechanical force in the transmission between the load and the actuator. The magnetic inductions and fields in the different parts of the actuator are measured with pick-up coils. A monitoring and data acquisition system controls the amplifiers and records all measurements.

Suggested measurements

There is a strong need for a standardization of the performance of actuators based on magnetostrictive materials. Due to the nonlinearity of the magneto-mechanical coupling in magnetostrictive materials and the resonance effects in the actuators this standardization can be done in numerous ways.

One way would be to load the actuator under small signal excitement with pure resistive loads in order to find the working area (bias current, prestress, input frequency, resistive load)

for which the actual actuator has its highest efficiency. At this driving condition efficiency, linearity, hysteresis, distortion, etc. should be measured for a number of increasing excitement levels.

Other interesting properties of an actuator are its maximum static displacements, frequency responses and phase shifts which however at high excitation levels are strongly non-linear with respect to the prestress, the load, the input amplitude and the magnetic bias level. A number of additional proposed standards for characterization of actuators then can be defined for different applications.

CONCLUSIONS

In conclusion, the proposed facility will offer an opportunity to evaluate actuators based on magnetostrictive materials and proposed standards for these in a well defined physical environment and under well known loading conditions. Experiments performed in the test rig can also point out the necessary performance of a cheaper and simpler test facility for standardization measurements on actuators.

REFERENCES

1. L. Kvarnsjö and G. Engdahl, IEEE Trans. Magn., **25**(5), 4195 (1989).

PART VII

Poster Session

LOW TEMPERATURE MAGNETIC BEHAVIOR OF Ni-Fe-Al-B SHAPE MEMORY ALLOYS: MAGNETIC SUSCEPTIBILITY AND MÖSSBAUER SPECTRA.

V. MARQUINA*, M. JIMÉNEZ*, M.L. MARQUINA*, R. RIDAURA*, S. ABURTO*,
R. GÓMEZ*, R. ESCUDERO**, F. MORALES** AND D. RÍOS-JARA**

*Facultad de Ciencias, Universidad Nacional Autónoma de México, 04510 México D.F., México

**Instituto de Investigaciones en Materiales, Universidad Nacional Autónoma de México, 04510
México D.F., México

ABSTRACT

Magnetic susceptibility measurements and Mössbauer spectra (MS) were performed on a series of $\text{Ni}_x\text{Fe}_y\text{Al}_2\text{B}$ shape memory ribbons obtained by a melt spinning technique. The MS at room temperature show quadrupole splittings of two iron sites. At low temperatures ($T < 120$ K) relaxed magnetic spectra begin to develop and, in one of the samples, a complete resolved magnetic spectrum at 13 K was observed. The overall magnetic susceptibility curves show non Curie-Weiss type behavior with peaks at around 60 K and 35 K. These curves also show magnetic hysteresis in the up-down temperature cycle used during the measurements. We relate our observations with a structural change occurring at temperatures between room temperature and 260 K, a second one around 200 K, and with the developing of spin-glass behavior at low temperatures, when the magnetic influences of Fe and Ni atoms almost compensate each other.

INTRODUCTION

In a recent paper¹, a high resolution electron microscopy study revealed the presence of FeAl, Fe_2Al , Al_5Fe_2 and FeNi phases in rapidly solidified Ni-Fe-Al-B shape memory alloys. It is well known that the addition of a small fraction of boron atoms improves the mechanical properties of the Ni-Fe-Al alloy², but the role that the iron atoms play in the shape memory effect (SME) is not clear. On the other hand, Al-Fe compounds and alloys are good examples of magnetically ordered systems at room temperature³. Thus the presence of these phases should be readily detected by Mössbauer spectroscopy. In order to get more insight of the possible influence of the Fe atoms in the properties of these alloys, systematic Mössbauer and magnetic susceptibility studies at different temperatures were performed.

EXPERIMENTAL

Rapidly solidified Ni-Fe-Al-B ribbon alloys were prepared by a melt spinning technique⁴; the nominal sample compositions are shown in Table I. Transmission Mössbauer spectra (MS) were obtained with a constant acceleration spectrometer using low velocity (≈ 2 mm/s) and high velocity (≈ 11 mm/s) scans. The ^{57}Co source was kept at room temperature whilst the samples were placed in a closed cycle helium refrigerator. The magnetic susceptibility curves were obtained with a squid susceptometer in the following way: First the samples were cooled down to 5 K, then a field of 100 G was applied and the susceptibility measurements were taken while

heating to room temperature. Next, the samples were cooled down to 5 K in the presence of the applied field.

Table I.
Alloy composition (in at%)

Alloy	Ni	Fe	Al	B
S1	61.66	13.70	24.47	0.17
S2	58.90	13.98	26.95	0.17
S3	56.90	13.98	28.95	0.17

RESULTS AND DISCUSSION

The room temperature MS of each one of the studied alloys show a quadrupole doublet with abnormal line widths (Fig. 1). The low temperature spectra showed relaxed magnetic sextets (Fig. 2a, b and c), more noticeable in the alloys with the higher Fe concentrations (S2 and S3). When magnetic relaxation was not present, the MS were fitted with two quadrupole doublets, using a constrained least squares fitting program in which the line widths were kept fixed to 0.3 mm/s. In samples S2 and S3 we only made fits down to 200 K, where the relaxed magnetic field starts to manifest itself. However, in the case of sample S1 the fitting process could be accomplished down to 13 K.

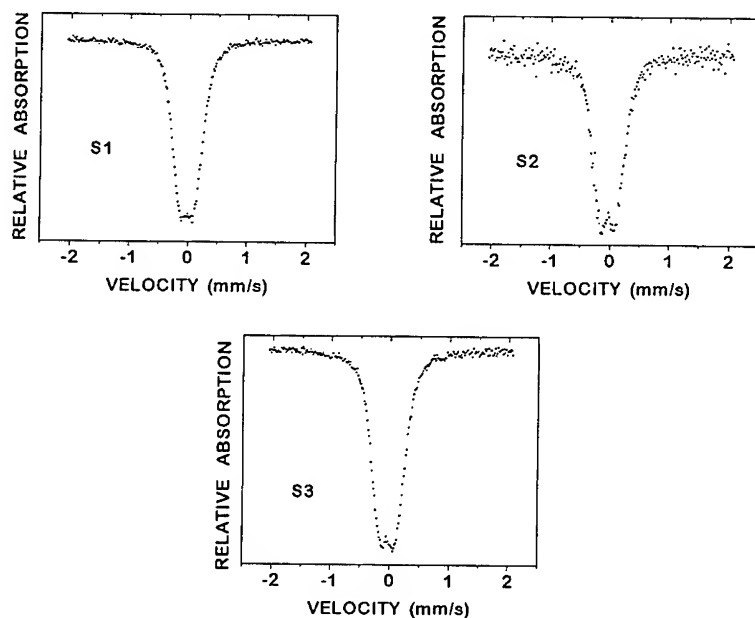


Figure 1. Room temperature Mössbauer spectra of the three samples.

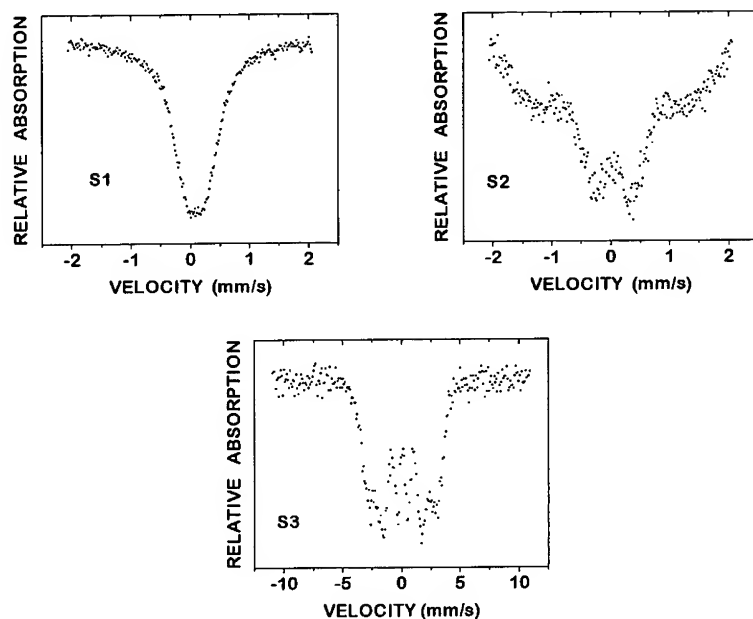


Figure 2. Mössbauer spectra of the three samples at 13 K.
a) and b) Samples S1 and S2 with low velocity scan (± 2.0 mm/s)
c) Sample S3 with high velocity scan (± 11.1 mm/s).

The common features observed in all samples (Fig. 3), are an initial increase of the isomer shift (δ) and of the quadrupole splitting (ΔQ) values between room temperature and 260 K. In the case of sample S1, δ is almost constant below this temperature, whereas ΔQ shows a steady increase as the temperature is lowered. We recall that, in the iron case, δ and ΔQ are given by

$$\delta = \frac{4\pi}{5} Z e^2 \left(\frac{\Delta R}{R} \right) \left[|\Psi(0)|_a^2 - |\Psi(0)|_s^2 \right] \quad (1)$$

and

$$\Delta Q = \frac{1}{2} e |Q V_{zz}| \left(1 + \frac{\eta^2}{3} \right)^{1/2} \quad (2)$$

where ΔR is the change of the nuclear radius R between the excited and the ground state, $\Psi(0)_{a,s}$ are the electronic wave functions at the absorber and source nuclei, respectively, Q is the quadrupole moment of the nucleus and

$$\eta = \frac{V_{xx} - V_{yy}}{V_{zz}} \quad (3)$$

is the asymmetry parameter, where V_{ii} are the components of the electric field gradient along each of its principal axes, defined in such a way as to have $0 \leq \eta \leq 1$.

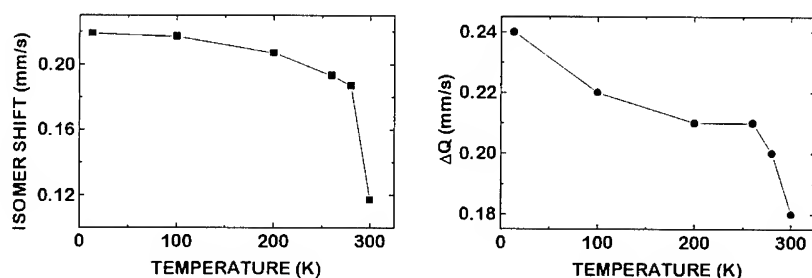


Figure 3. Isomer shift and quadrupole splitting as a function of temperature of sample S1

The combined room temperature values of δ and ΔQ , together with the temperature variation of the former, are indicative of a Fe(II) state. It is important to notice that the theoretical δ value is essentially temperature independent, in such a way that the observed increase between room temperature and 260 K, that implies a change in the electronic density $|\Psi(0)|_a^2$ at the nuclear site, can only be explained in terms of a structural change taking place in the system. On the other hand, ΔQ does not change from 260 to 200 K where it again shows a steady increase as the temperatures is lowered. This second change in ΔQ must be associated with electronic redistributions due to changes in thermal population of the different crystal field levels, thermal changes in the crystal structure or changes due to magnetic coupling of the system. Nevertheless, no indications of this changes have been observed in differential scanning calorimetry nor in electric resistance measurements. The absence of magnetic structure in the room temperature MS (Fig 1) indicates that the iron atoms are incorporated into the crystal structure and do not form appreciable amounts of the phases reported in reference 1.

On the other hand, the dc and ac susceptibility vs temperature curves (χ_{dc} and χ_{ac} respectively) show a very complicated behavior (Figs. 4 and 5), that differs from the Curie-Weiss law. There is an initial increase in a range of temperatures that corresponds to the one where the MS start to show magnetic effects. There is also a hysteresis in the warming and cooling measurement process. In all samples it is observed that there is a change in the slope of the $1/\chi$ around 200 K, which may be related with structural changes more clearly revealed by the MS. It is interesting to note that in all cases there is a linear portion whose extrapolation crosses the temperature axis at around 100 K, indicating a possible ferromagnetic character of these systems. However, in two of the samples the slope of the linear portion changes, as the temperature is lowered, from ferromagnetic to paramagnetic character (S1), whereas in sample S2 (the change is the other way around) it changes from paramagnetic to ferromagnetic. Preliminary ac -magnetic susceptibility measurements were performed on S1. The real part of the susceptibility is shown in Fig. 5a at different frequencies and a field of 5 gauss. Furthermore, in the expanded plot of χ_{ac} vs T, shown in Fig. 5b, one can notice that the peak of these curves shifts to lower temperatures when lower frequencies are used in the measurements, indicating a dependence of the freezing temperature T_f , which can be defined as the temperature at which the maximum in susceptibility occurs. Once again, this is what one would expect in a spin-glass system.

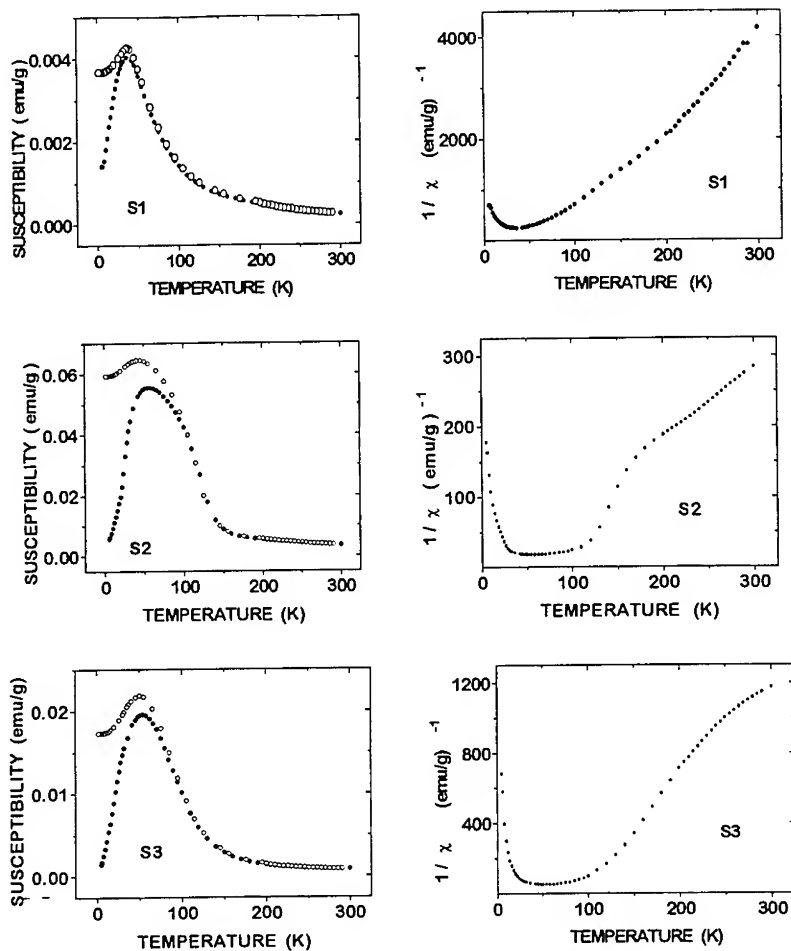
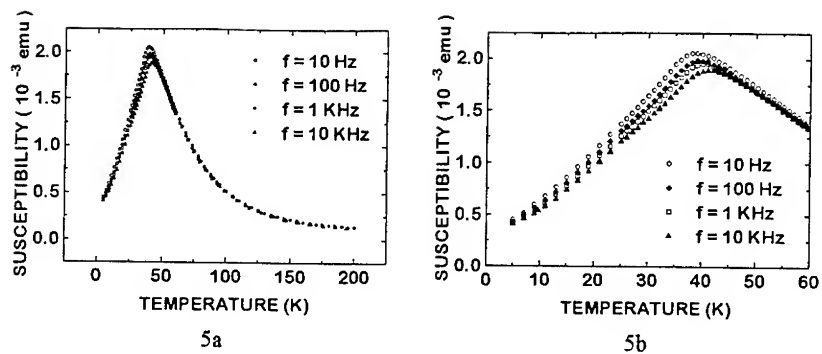


Figure 4. Magnetic susceptibility (dc) χ and $1/\chi$ vs T for the three samples.

CONCLUSIONS

We have used Mössbauer spectroscopy and dc and ac magnetic susceptibility to investigate some properties of a series of rapidly solidified AlNiFeB alloys. We find that the magnetic behavior of these systems is very sensitive to the alloys composition, varying from a completely resolve Mössbauer spectrum at 13 K, to one in which the local magnetic effects are hardly present at the same temperature. This fact, together with the observation of hysteresis in the dc -susceptibility at low temperatures and the peak-shift with frequency of the maximum of the real part of the ac -susceptibility, are clear indications of a spin-glass behavior.



Figures 5a and 5b. Magnetic susceptibility (ac) of S1 at four frequencies.

ACKNOWLEDGMENTS

The authors wish to thank R. Gómez Aíza, C. Munive and F. Silvar for their invaluable help. This work is supported by Consejo Nacional de Ciencia y Tecnología, México, project 1216-E9203, by Dirección General de Asuntos del Personal Académico, UNAM, México, projects 1N102693 and ES102993 and by Organization of American States.

REFERENCES

1. J.A. Juárez-Islas, R. Pérez and S.J. Savage, *Matt. Lett.* **14** (1992) 1.
2. S. Furukawa, a Inoue and T Matsumoto, *Matter. Sci. Eng.* **98** (1988) 515.
3. N.N. Greenwood and T.C. Gibb, *Mössbauer Spectroscopy*, (Chapmann and Hall Ltd, London, 1971) p 308.
4. Patrik Johansson, *Nickel-Iron Aluminium Shape Memory Alloys With Improved Properties by Rapid Solidification*, Examensarbete, Swedish Institute for Metals Research, 1988.
5. N.P. Raju, E. Gmelin and R.K. Kremer, *Phys. Rev. B* **46** (1992) 5405.

Compatibility of BaTiO₃ and SrTiO₃ with Shape Memory Alloy TiNi

Peter G. Mercado and A. Peter Jardine

Smart Materials Laboratory

Dept. of Materials Science & Eng., SUNY at Stony Brook, Stony Brook, NY 11794-2275

ABSTRACT

Thin film layers of shape memory alloys and ferroelectric ceramics can produce a family of 'smart' heterostructures capable of performing both sensing and actuating functions. The compatibility of sol-gel processed BaTiO₃ (BTO) and SrTiO₃ (STO) thin films with shape memory effect TiNi substrates were investigated. Important issues in the synthesis of these active structures are the ability to generate the appropriate crystalline phases of each material while producing defect-free homogeneous high quality films.

INTRODUCTION

A material system is considered 'smart' if it has the ability to perform both sensing, actuating and control functions. A family of smart materials can be fabricated by depositing piezoelectric ceramics onto shape memory alloys (SMA). These hybrid structures couple the broad mechanical stress-strain hysteresis properties of SMA with the mechanical-electrical relationship associated with piezoelectric materials.

Coupling SMA and ferroelectric ceramics produces a hybrid composite structure that can utilize the different active and adaptive properties of the individual bulk materials. Ferroelectric ceramics are very sensitive to applied stresses through the piezoelectric effect. Their response times are fast, but displacements are very small due to the small strain magnitude. SMA materials have large actuation displacements and are able to drive larger loads. However, cycling times are much slower since it is dependent upon the dissipation of latent heat of transformation.

An important issue is the ability to generate the appropriate phases of each material while minimizing unwanted mutual chemical interactions. The amorphous crystalline transformation for TiNi occurs at 490-520 °C and for temperatures above 540 °C, formation of Ti₃Ni₄, Ti₁₁Ni₁₄ and TiNi₃ precipitates are favored which can be detrimental to SME characteristics^[1,2,3]. In contrast, annealing temperatures to transform amorphous (sol-gel fabricated) ceramics to the ferroelectric perovskite phase range from 500 to 800 °C depending on the type of ferroelectric and at times the type of substrate^[4,5]. TiO₂/PZT have been previously deposited onto TiNi by the authors through the sol-gel process^[6]. The objective of this experiment is to investigate the compatibility of other perovskite type ferroelectrics with TiNi to improve the film quality of the ferroelectric layer. BaTiO₃ (BTO) and SrTiO₃ (STO) were chosen based upon their similar thermal expansion coefficient with TiNi, as illustrated in Figure 1.

EXPERIMENTAL PROCEDURE

Thin films of BTO or STO were coated onto SMA TiNi foils by sol-gel and spin coating techniques. The sols were synthesized using barium acetate, strontium acetate and titanium tetrabutylate alkoxides dissolved in acetic acid and anhydrous ethyl alcohol. The BTO sol was prepared by dissolving barium acetate in acetic acid and heated to 105 °C (while being mechanically stirred) to remove the water. Appropriate amounts of Ti-tetrabutylate were combined with ethyl alcohol and added to the barium precursor. Then 1.0 ml of water was added

to hydrolyze the solution. The STO sol was similarly prepared, by dissolving strontium acetate in acetic acid.

One centimeter square TiNi substrates were sheared from a 0.4 mm thick commercial sheet stock. The substrates were either etched in a mixture of $\text{HNO}_3\text{:H}_2\text{O:HF}$ or mechanically polished and cleaned in an ultrasonic bath of acetone, then methanol.

The BTO or STO sol was spun onto the TiNi substrates at 4000 rpm for 30 s and prebaked at 300 °C for 15 m to volatilize most of the organics. This procedure was repeated to produce thicker films. Several samples were prepared by varying the final annealing temperatures from 450 to 800 °C for a constant time of 30 m. The films were then characterized by x-ray diffraction (XRD) techniques to determine the minimum temperature needed to crystallize the ceramic to its ferroelectric phase. Other samples were prepared with varying film thickness, cooling rates and surface roughness to investigate their effects on the film quality.

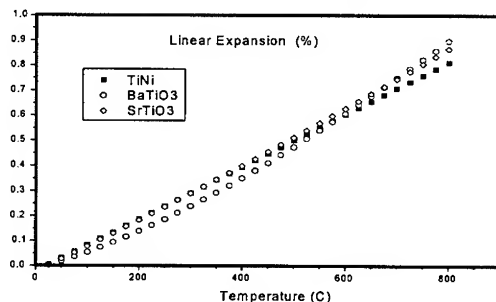


Figure 1: Comparison of linear thermal expansion coefficients for TiNi, STO and BTO

RESULTS AND DISCUSSION

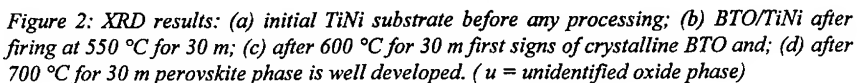
BaTiO₃ X-ray Diffraction Analysis

BTO was deposited onto TiNi substrates and annealed between 450 °C and 800 °C in increments of 50 °C. The BTO film final thickness was approximately 1 μm and room temperature XRD patterns were obtained. The diffraction patterns for the unprocessed substrate, BTO/TiNi annealed at 550°C, 600°C and 700°C are shown in Figure 2. The substrate was determined to be composed of the martensitic B19' phase of TiNi. Also present for the initial TiNi substrate diffraction pattern were 4 peaks that have not been conclusively identified (in the JCPDS database) at $2\theta = 20.70^\circ$, 23.54° , 24.87° , and 29.18° (for $\text{CuK}\alpha$ radiation). The peaks were present before the substrate undergone deposition, annealing or any other processing steps and seem to be some type of non-equilibrium oxide (Ti, Ni or TiNi) associated with the stock TiNi material. No further studies were attempted to find the exact cause, since the presence or lack of these peaks were not relevant to these synthesis studies

The peaks for the B19' phase of TiNi were distinctive until 650 °C. The B2 phase of TiNi appeared after annealing at a temperature of 450 °C with a major (100) peak at $2\theta=42.86^\circ$. B2 correlates to the high temperature austenite phase and its growth can be expected when B19' TiNi is annealed. The annealing process relieves stresses that are associated with the martensitic B19' phase which enables regions of the TiNi substrate to remain in the high symmetric B2 phase.

Peaks correlating to crystalline BTO appeared at a temperature of 600 °C. However, the peaks appeared to correspond to the cubic phase which does not have ferroelectric properties.

INTENSITY (cps)



The roughness of the substrate's surface was varied to investigate how it affects the quality of the ferroelectric film. One substrate was etched and another polished with 600 grit sandpaper. Five spin coat layers of BTO was deposited on each of the substrates and annealed at 600 °C for 30 m. The 1.0 μm thick BTO films were characterized by SEM and are presented in Figures 3a and 3b. The results showed that polishing reduced the amount of cracks present, however, the pinholes present in the films that seem to be produced by a blistering mechanism were not prevented or reduced.

289

The sample prepared with the polished superelastic TiNi was also viewed with secondary electrons, Figure 4. Unlike backscattered electrons (which are more sensitive to atomic number), secondary electrons are sensitive to surface morphology. The image viewed with secondary electrons have areas of lighter shade. Since these areas were not present in the backscattered image and no other elemental phases identified in the XRD study, these areas are believed to be sites of delamination. Closely comparing the backscattered and secondary images, some areas of delamination have slight cracks which were indicative of the formation of a blistered pinhole. The blistering effect implies that the substrate is in compression while the ceramic film is in tension. This could occur since the TiNi and ceramic film have significantly different cooling rates, so that the faster cooling TiNi is in compression with respect to the ceramic.

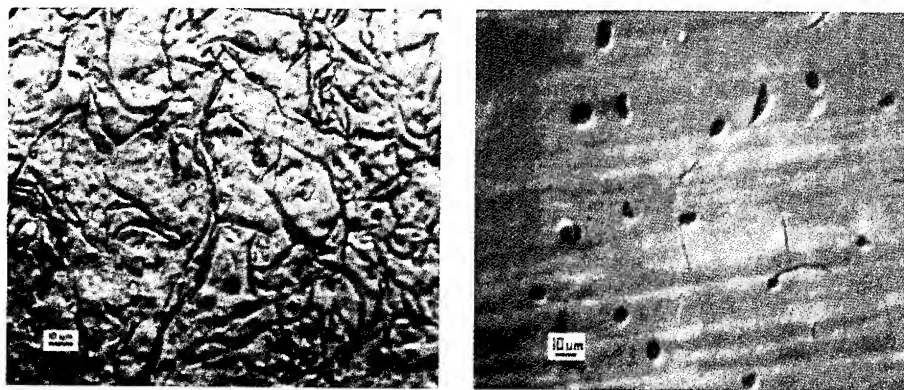


Figure 3: Backscattered SEM images of 1.0 μm layer of BTO on TiNi showing improved film quality when substrate was polished (mag = 500X). (a) etched and; (b) 600 grit polished substrate.

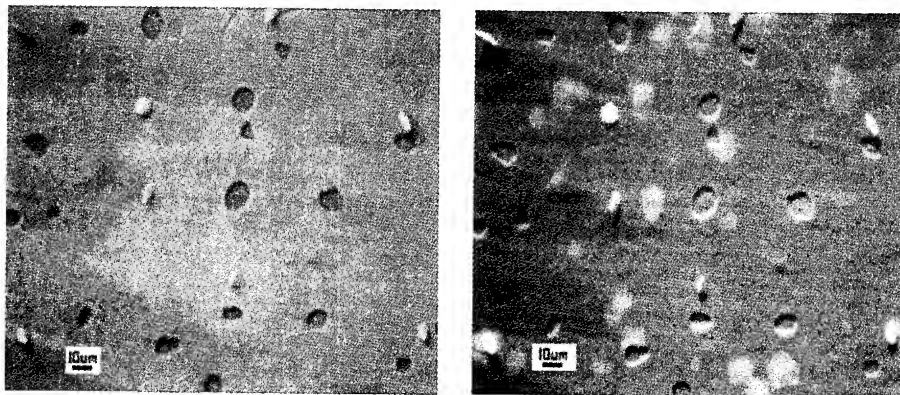


Figure 4: (a) Backscattered SEM image of 1.0 μm layer of BTO on 600 grit polished TiNi (mag = 500X); (b) Note presence of film blisters (lighter areas) only visible with secondary electron imaging.

Effects of Cooling Rate

All previous samples prepared were immediately removed from the furnace (at 600 °C) and allowed to quickly cool to room temperature (approximately 21 °C). A 1.0 µm BTO sample cooled slowly from 600 °C was prepared to determine if a slower cooling rate would yield a better quality BTO film. After the anneal, the furnace was turned off and the sample cooled to room temperature in approximately 6 h. Figures 5a and 5b shows the morphology of the quickly air cooled and slow furnace cooled samples. The slow cooled sample was substantially of better quality. There were no light areas or delamination sites observed, but pinholes were still present. The cracks on the slow cooled specimen were longer and tended to propagate randomly. The improved quality obtained by slow cooling supports the previous explanation of delamination. The metallic TiNi substrate dissipates heat faster than the ceramic film. After some time the intermetallic substrate is near its room temperature shape, but the ceramic film is still at a higher temperature. Even though the linear thermal expansion of BTO and TiNi are similar, if the two materials are at different temperatures then there will be a substantial strain mismatch. By slow cooling, the ceramic and the intermetallic substrate are approximately at the same temperature during the cooling process. This reduces the extraneous compressive force due to the strain mismatch.

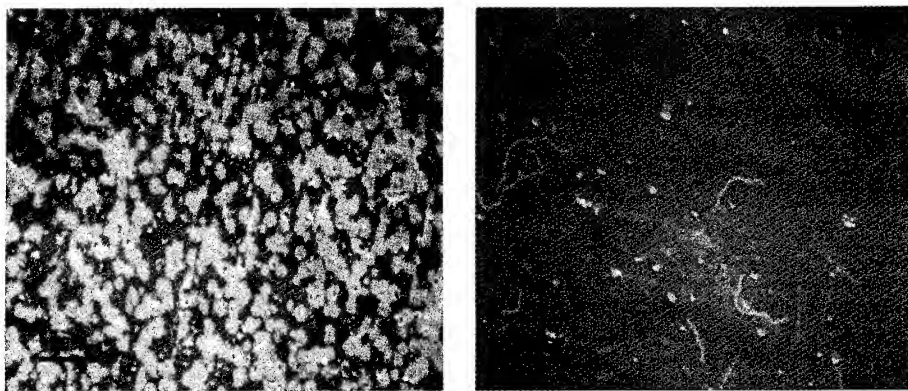


Figure 5: SEM image of 1.0 µm thick BTO on 600 grit polished TiNi (mag = 150X) for: (a) air cooled; (b) slow furnace cooled showing improved film quality without delaminations and fewer pinholes.

SrTiO₃/TiNi Heterostructures

Strontium titanate was also chosen for study based on its similar linear thermal expansion coefficient with TiNi. The substrates were first polished with 600 grit sandpaper, micro-polished with a 1 µm alumina/water solution, and cleaned in an ultrasonic bath of acetone. A sample with a total of 5 spin coats was deposited onto the substrate and another was prepared by dip coating. The samples were fired at a temperature of 700 °C for 30 m to crystallize the ceramic. The sample with the 3 dip coats had a final film thickness of 14 µm and 5 spin coats produced a 7 µm thick film. XRD results confirm the presence of the perovskite phase of STO.

An optical images of the STO film is provided in Figure 6. The sample prepared by spin coating exhibit defects. However, cross sectional SEM images reveal that the defects do not continue to the TiNi substrate and appear to be associated with grooving. The film prepared by

multiple dip coats had a very rough uneven surface full of grooves, and was not a high quality ferroelectric film.

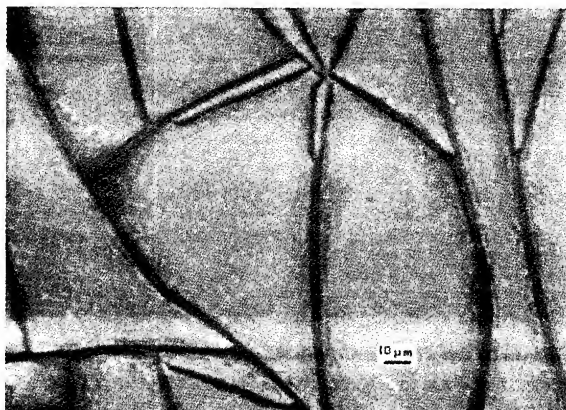


Figure 6: Optical image of 7.0 μm thick STO film on TiNi with grooving.

CONCLUSIONS

BaTiO₃ thin films were successfully crystallized onto SMA TiNi, although growth conditions for high quality films were not obtained. Polishing the substrate and a slow cooling rate were observed to significantly improve the BTO film quality, but the films still contained numerous pinhole defects which prevented any electrical characterization. The processing of sol-gel derived BTO was concluded to have poor compatibility with the TiNi substrate. No blistered pinholes or delaminations were observed in the STO films. However, the films had a rough morphology which contained many crack-like grooves.

ACKNOWLEDGMENTS

The authors are grateful for financial support for this project from the US Army under grant no. DAAH04-93-G-0213.

REFERENCES

- [1] J.D. Bush, A.D. Johnson et al, J. Appl. Phys. 68, p6224 (1990)
- [2] J.S. Madsen and A.P. Jardine, Scripta Met et Metall., 30, p.1189 (1994)
- [3] P.G. Mercado and A.P. Jardine, 'Thin Film Multilayers of TiNi/TiO₂/PZT: Material Fabrication', SPIE Proceedings: Smart Materials, Orlando Conference, v 2189, p26, (1994)
- [4] C.K. Kwok and S.B. Desu, 'Pyrochlore to perovskite phase transformation in sol/gel derived lead-zirconate-titanate thin films', Appl. Phys. Lett. 60 (12), p1430 (1992)
- [5] C. Zhixiong, Z.Fangqiao, L. Meidong, W.Guoan and P.Xiangsheng, 'Sol-Gel Derived BaTiO₃ Ceramics', Ferroelectrics, v 123, p66 (1991)
- [6] A.P. Jardine and J.S. Madsen, 'Fabrication of "smart" ferroelastic-ferroelectric heterostructures', Smart Materials, V.K. Varadan, v1916, p384-395, SPIE, Albuquerque (1993)

DEPOSITION PARAMETERS FOR SPUTTER-DEPOSITED THIN FILM TiNi

A. Peter Jardine, Dept. of Materials Science and Engineering
SUNY at Stony Brook, Stony Brook, NY 11794

Abstract

Sputter deposition of TiNi has been problematic due to the extreme reactivity of titanium. There are several advantages in depositing TiNi with other metals, such as Ti and Cu, as the Shape Memory Effect properties can be changed selectively, including coring of the thin film. Simultaneous co-deposition of cored material using sputter deposition becomes technically difficult as this implies that the sample to target distance increases. In this paper, we discuss a relationship developed so that a basic base vacuum pressure can be found with target-sample distance and correlated with the observed phases for both Ti and TiNi samples. Practical limitations imposed by the vacuum system on both devices and device quality are discussed.

Introduction

Thin film TiNi up to 20 μm thick have been developed using either DC or RF Magnetron sputtering^[1,2,3,4,5] and the related technique of ion-sputter deposition and IBED processing^[6] onto a variety of substrates such as: Si, GaAs, CdS, SiO₂ and NaCl. In all cases, base pressures for sputtering were in the range of 10^{-7} torr, with sputtering at higher base pressures of 10^{-6} torr generally not producing TiNi films. As thin films, there is a small thermal mass to heat and cool, resulting in fast cycling times. When grown on Si, a good heat conductor, good thermal coupling results which further decreases the cycling time^[7]. When deposited onto flat substrates, the material can be patterned using standard lithographic techniques.

Although still in its infancy, there are growing technical applications for thin film TiNi in Micro-Electro Mechanical Machines (MEMS) applications. Patents and commercial products for valves as well as in biomedical applications have also been developed^[8]. Of some interest is thus the manufacturability of these thin films and in particular the consistency of the TiNi's Shape Memory Effect properties over the substrate wafer.

There are several problems associated with DC sputter deposition. As seen in Figure 1, although the TiNi alloy is largely a stoichiometric intermetallic, there can exist small compositional deviations, with large changes in the resultant transformation temperatures^[9]. Thus, small changes in composition will result in large changes to the thermo-mechanical properties of the alloy. This can occur due to the extreme reactivity of the Ti atoms, which bond with reactive gas species to produce stable oxide and nitride species. (Typical argon sputtering pressures are of the order of 2 to 5×10^{-3} torr, which corresponds to a mean free path of any atom of 0.25 cm^[10].) As Ti and Ni migrate to the sample surface via collisions with the surrounding sputtering gas, any reactive impurities in the gas will result in stoichiometric shifts on the thin film.

Calculations were recently presented which relates the maximum base pressure of the sputtering system to sample-target distance [10], given that the film can tolerate a 1% Ni ($P=0.01$) or 0.1% Ni shift ($P=0.001$). Figure 2 shows the corresponding base pressure for a given probability of collision and total sputtering pressure of 2 mTorr. For a P_r value of 0.01, representing the lower limit, at a distance of 6.0 cm the base pressure was 5×10^{-7} torr. Using a more reasonable value of $P=0.001$, corresponding to a stoichiometric deviation of 0.1 at.%, a minimum pressure of 8×10^{-8} torr is required. These values are in agreement with the

observations of many workers that a pressure of 10^{-7} torr was needed to obtain stoichiometric TiNi. At larger distances of 15.2 cm (6 in), the requisite base pressure was approximately 2×10^{-8} torr for $P=0.01$ and 2×10^{-9} torr for $P=0.001$.

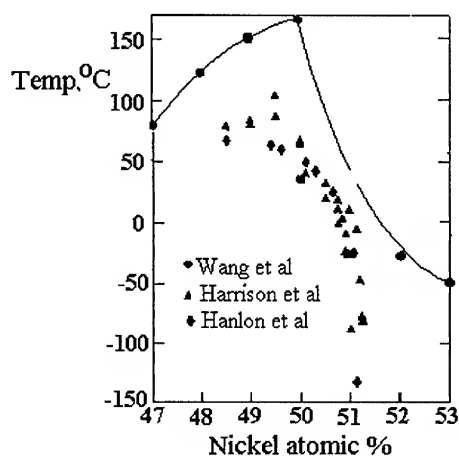


Figure 1: The variation of the TTR of TiNi with Changing Ti-Ni Stiochiometry. shown, changes in the Ti-Ni ratio can result in change of 100 °C in transformation temperatures. (From reference [9])

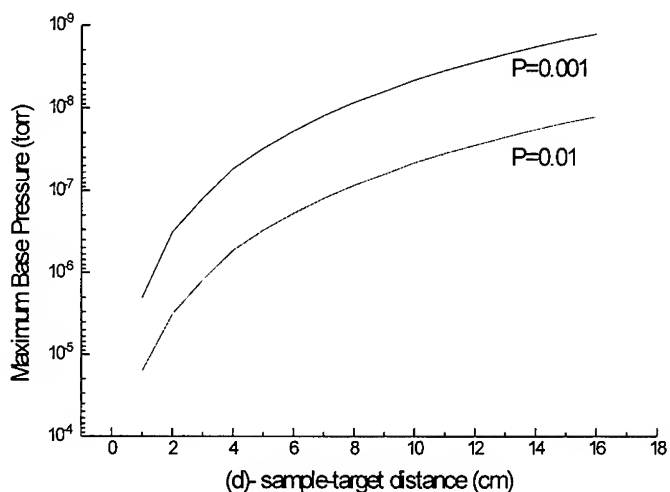


Figure 2: The variation of the maximum base pressure P_{cont} with sample-target distance. As seen, for most practical values of d , say at 6 cm, maximum base pressures range from 10^{-7} to 10^{-8} torr, with good stoichiometric uniformity over a substrate surface.

In this paper, an attempt to quantify the compositional differences imposed by the change in sample to target distance is discussed and related to X-ray Diffraction (XRD) observations of TiNi thin films deposited on quartz substrates.

Experimental Method

In order to control base pressure at high levels, a UHV deposition system was utilized. Samples were loaded onto an existing UHV compatible vacuum linear rod from a sample loading station. The sample and load-lock are pumped to 10^{-6} torr using a Leybold turbo molecular pump. In order to facilitate good removal of H_2O , this part of the system was illuminated with infrared irradiation to desorb water from the chamber walls without the danger of overheating and depoling the sample transfer rod magnets.

The vacuum was analyzed using a Dycor RGA so that the composition of the atmosphere before and after sample insertion and after the Ar gas was leaked in could be recorded. Titanium sublimation pumps (TSP) were used to scrub residual water vapor and oxygen prior to the insertion of Ar.

The sputtering methodology was as follows. Samples were introduced into the load-lock and pumped via the turbo-pump for 6 to 12 hrs prior to insertion into the deposition chamber. The load-lock was isolated by 1.5 in diameter gate valve and was opened to allow the sample to be inserted into the chamber. This method provided consistent base pressures, as measured by the RGA, prior to sputtering. Following a monitoring of the gas pressure, the ion-pump/TSP pumping well was then isolated and ultra-high purity Ar gas was leaked into the chamber. At a pressure of 10^{-4} torr, the content of the atmosphere was determined using the RGA and if acceptable, further Ar was leaked in to a final sputtering pressure of 2 to 4×10^{-3} torr. This pressure was monitored during deposition using a Leybold gauge. The sputtering pressures were too high for RGA operation, and therefore it was not possible to monitor gas atmospheres during deposition.

The sputtering yields are generally low for this system, and therefore sputtering times are relatively long to deposit several microns of material. In order to avoid contamination during deposition, the turbo pump system actively pumped on the Ar during deposition. After deposition, the Ar is pumped out of the system and the vacuum analyzed to determine the contaminant level.

The basic deposition geometry is shown in Figure 3. Two MDX-1K DC sputtering sources deposited material at a predetermined wattage and time onto quartz samples. The target to sample distance was controlled by positioning the sample via the linear feed-through. No in-situ annealing was available in the chamber, and therefore the films were amorphous after deposition.

To best characterize systematically the effect of sample to target distance, and to avoid systematic errors involved in contamination in communal vacuum tube furnaces and with atmospheric interactions, a vacuum furnace mounted onto a manipulator was installed inside the chamber. The sample heater consisted of two 500W halogen lamps surrounded by a 3 in diameter half cylinder of polished stainless steel, to both focus the radiation onto the sample and to impede heating of the chamber walls, which would result in an increase in base pressure. A type K thermocouple was aligned so that the bead was 0.5 inch out from the plane of the halogen lamps using ceramic thermocouple tubing. Samples were pressed onto the bead during annealing, thereby ensuring that all samples were aligned similarly in annealing and allowing measurement of the sample temperature. The heater was controlled by a variac and the temperature measured using a Keithly Model 52 thermocouple meter. Typical annealing times were for 0.5 hr at 520 °C to 540 °C.

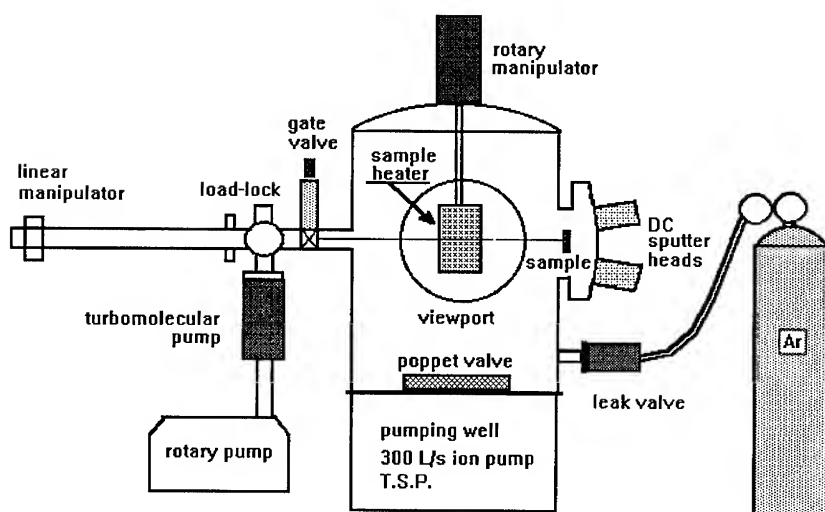


Figure 3: Schematic of the UHV sputtering apparatus. Not shown is the RGA which analyses the vacuum in the sputtering chamber. The sample was pulled along the plane of the deposition chamber using the linear feedthrough to vary the target to sample distance.

After deposition and annealing, the sample was retracted through the vacuum load-lock and isolated from the chamber. After shut down of the pumps, the sample was removed for characterization.

Results

Typical gas compositions for the sputtering chamber indicated the principal contaminants were N_2 and H_2O . Typical base pressures were of the order of 2×10^{-8} torr. When the load-lock was opened, there was little additional gas introduced. The introduction of Ar did not perceptibly raise the levels of reactive gas species. Finally after deposition, these levels were not demonstrably lower or higher.

To investigate the influence of the sample to target distance, TiNi was deposited from a TiNi target which was made by powder metallurgy techniques in the author's laboratory. XRD analysis of the target was a mixed B2 and B19' microstructure.

Deposition was at 100 W for 1 hr onto quartz substrates followed by a 30 min. anneal at 540 °C, as measured by the thermocouple. Figure 4 shows the extent of the influence of sample to target distance on the microstructure of TiNi with good base pressure. At the limit of stroke of the magnetic manipulator, corresponding to a minimum target-sample distance of 8.0 cm, the XRD of the sample shows two peaks, corresponding to the TiNi's B2 [100] peak at $2\theta = 43.352$ (2.12 \AA) and a peak at $2\theta = 43.352$ (2.09 \AA) possibly the B19 [020] peak (2.06 \AA) phases, which are similar in composition to the target material. Precise phase identification of the B19' phase is problematic, due to the lack of additional peaks. This is not uncommon in TiNi as the martensitic B19' phase are generally highly textured. The only other phase which might be

identified was Ti_4Ni_3 , which also has a principal peak at 2.09 \AA° , and its existence cannot be conclusively ruled out.

At a distance of 10 cm and greater, the profiles revealed only the B2[100] peak, however no nitrification or oxidation peaks observed. At a limiting distance of 25 cm, the XRD profile had additional peaks corresponding to the likely formation of oxides and nitrides on the surface. At large sample to target distances, the amount of material deposited onto the sample was small, thereby decreasing the number of peaks observed and making a meaningful phase identification difficult.

The results are in agreement with calculation at large distances, though at small distances of several mean free paths, the model breaks down. A sample to target distance of 10 to 15 cm, found in co-deposition or the sputtering of large area wafers, implies UHV conditions of 10^{-8} torr. Of interest is the change in XRD profile between 8 cm and 10 cm. The compositional changes in the Ti-Ni ratio required to produce these changes are slight, which using a minimum value of $P=0.001$ would suggest that a total pressure of reactive species of 1×10^{-8} torr. As base pressures before sputtering were measured 3×10^{-8} torr, and a significant amount of Ar is subsequently introduced, there may likely be larger compositional differences.

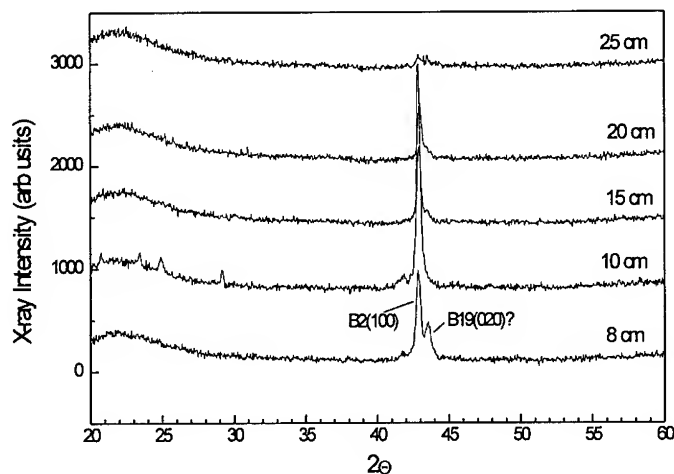


Figure 4: X-ray diffraction profiles taken for the TiNi samples with distance. At a sputter-target distance of 8 cm, peaks attributable to B2 and B19' phases were observed. At 10 cm to 20 cm, the B2 peak is observed, indicating low martensitic transformation temperatures. At 25 cm, B2 peak is difficult to identify and different peaks not associated with the transformation are observed

Conclusions

For successful deposition of TiNi, the reactivity of the TiNi determines the maximum base pressures to be used. The agreement of the model with the calculation indicates that at a distance of 10 cm (4 in), the maximum base pressures that can be tolerated are of the order of 10^{-9} torr.

Thus, UHV conditions are required for co-deposition of TiNi which then influences both the cost and throughput of fabrication of co-deposited TiNi devices.

The extreme composition dependence of the SME properties of TiNi suggests that sputtering distances and base pressures are important to ensure that the resultant transformations will be uniformly similar for TiNi devices made from a wafer, regardless of the position of the material on the substrate. These results therefore represent a first step in establishing the minimal base pressures required to preserve the phase of the material. In particular, correlation of both composition and transformation temperature with target-sample distance are required for a more accurate analysis and calibration of the model, which will be the subject of a forthcoming paper.

Acknowledgments

The author are grateful for financial support for this project from the US Army Research Office under grant no. DAAH04-93-G-0213. I would also express my appreciation to Mr. Rand Dannenberg for manufacture of the sample heater.

References

- [1] J.Busch, A.D.Johnson, C.H.Lee and D.A.Stevenson, 'Shape Memory Properties of Ni-Ti Sputter-deposited Film', *J.Appl.Phys.*, 68:6224-6228 (1990)
- [2] A.P.Jardine and L.D.Wasielesky, 'Development of Thin Film Shape Memory Effect Nickel Titanium as Micron Sized Shape Memory Effect Actuators', *Proc. M.R.S. Symp.*, 187:181-186 (1990).
- [3] K.Ikuta, H.Fujita, M.Ikeda and S.Yamashita, "Crystallographic Analysis of TiNi Shape Memory Alloy for Micro Actuator", *IEEE Micro Electro Mechanical Systems*, 90CH2832-4:38-39 (1990)
- [4] J.A.Walker, K.J.Gabriel and M.Mehregany, "Thin-film Processing of TiNi Shape Memory Alloy", *Sensors and Actuators A*21:243-246 (1990)
- [5] S.Miyazaki and A.Ishida, *Material Transactions, JIM*, 35, p.14-10 (1994)
- [6] B.Walles, L.Chang and D.S.Grummon, "Residual Stress, Adhesion and Crystallization of Ion-Sputtered and IBED processed NiTi Films", *Proc. MRS Symp.*246:349-354 (1991)
- [7] A.P.Jardine, "Cycling Times of Thin-Film NiTi of Si", *MRS Symp. Proc.*, "Shape Memory Materials and Phenomenon", 246:427-431 (1991)
- [8] A.D.Johnson, "Vacuum deposited TiNi Shape Memory film: Characterization and Applications in Microdevices", *J. Micromech. Microeng.*, 1:34-41 (1991)
- [9] K.N. Melton, "Ti-Ni Based Shape Memory Alloys", Engineering Aspects of Shape Memory Alloys, Butterworth-Heinemann Ltd, London, p21 (1990)
- [10] A.P.Jardine, submitted, *J.Vac.Sci.Tech. A* (1994)

DEFORMATION OF ADAPTIVE HETEROPHASE CRYSTAL

ALEXANDER L. ROYTBURD AND JULIA SLUTSKER

Department of Materials and Nuclear Engineering
University of Maryland, College Park MD 20742

ABSTRACT

A crystal which can be in two possible phase states is considered. During tensile extension the crystal is deformed elastically. After a certain amount of elastic strain a phase transformation begins. For each fixed level of strain an equilibrium mesostructure is established, which corresponds to a minimum in the free energy of the crystal. The equilibrium mesostructure consists of plane, parallel layers of a product phase separated by layers of an initial phase. The product phase itself consists of two or more different domains (twins) forming plane, parallel alternations. The volume fractions of the phases and of different twin components in the product phase are functions of strain and temperature. Above a critical temperature the product phase is a single domain (untwinned). The stress-strain curve which reflects the evolution of the equilibrium mesostructure is calculated. For deformation under a strain control the calculated equilibrium stress-strain curve has a section with negative slope that corresponds to a negative Young's modulus. If deformation proceeds under stress control, hysteretic stress-strain curves on loading and unloading will result from a section with negative slope.

INTRODUCTION

Reversible deformation as a result of solid-solid phase transformation is a subject of this paper. A product of phase transformation in solids is very often a polydomain mesostructure, i.e. an initial single crystal or a grain of an polycrystal is transformed into a conglomerate of domains of different phases or different oriented areas of one phase (twins). Due to their mechanical contact, domains interact elastically with each other and result in regular arrangements. The equilibrium mesostructure of the polydomain phase can be changed by changing the phase equilibrium through the shifting of external condition: temperature, mechanical stress. So the polydomain phases can adapt to external conditions and their structure and properties can be controlled by these conditions. Change of the mesostructure proceeds by the movement of interfaces and as a rule results in a macroscopic deformation. The response of this structure to mechanical stresses is the topic of this paper.

MODEL OF COHERENT TWO-PHASE SYSTEM

A crystal which can be in two possible phase states is considered. The relative stability of the phases is determined by the difference of their free energies $\Delta f = f_2 - f_1$, where f_1 and f_2 are free energies of undistorted initial and product phases, respectively. The phase transformation is accompanied by self-strain $\hat{\epsilon}$ which characterizes the lattice change at the transformation. The transformation with lowering of symmetry is considered: the symmetry of product phase 2 is lower than the symmetry of initial phase 1. Therefore the crystallographically different but physically identical variants, or domains, of a product phase can be formed.

In particular we consider the transformation of a cubic phase into a tetragonal one. In this case 3 different variants are formed with self- strains (Fig.1):

$$\hat{\epsilon}_1 = \epsilon_0 \begin{pmatrix} \chi & 0 & 0 \\ 0 & -1 & 0 \\ 0 & 0 & -1 \end{pmatrix}; \quad \hat{\epsilon}_2 = \epsilon_0 \begin{pmatrix} -1 & 0 & 0 \\ 0 & \chi & 0 \\ 0 & 0 & -1 \end{pmatrix}; \quad \hat{\epsilon}_3 = \epsilon_0 \begin{pmatrix} -1 & 0 & 0 \\ 0 & -1 & 0 \\ 0 & 0 & \chi \end{pmatrix} \quad (1)$$

For $\chi=2$ these self-strains describe the transformation of the BCC to the FCC lattice ("Bain-strain"). This case, which corresponds to some martensitic transformations in Cu-base shape memory alloys^{1,2}, is considered as an example.

As shown before³⁻⁴ the equilibrium mesostructure in general consists of plane parallel layers of a product phase separated by layers of an initial phase. The product phase itself consists of two or more different domains forming plane, parallel alternations (Fig.2). In the case of cubic-tetragonal transformation with $\chi>1$, under extension along [100] direction, the polydomain product consists of two domains, 1 and 2 (Fig.1) or 1 and 3, where 1 is always the largest fraction³. The average self-strain of the product phase is:

$$\hat{\varepsilon} = (1-\alpha)\hat{\varepsilon}_1 + \alpha\hat{\varepsilon}_2 = \begin{pmatrix} \varepsilon_1(\alpha) & 0 & 0 \\ 0 & \varepsilon_2(\alpha) & 0 \\ 0 & 0 & \varepsilon_3(\alpha) \end{pmatrix}; \quad \begin{aligned} \varepsilon_1 &= [\chi - \alpha(\chi+1)]\varepsilon_0 \\ \varepsilon_2 &= [-1 + \alpha(\chi+1)]\varepsilon_0 \\ \varepsilon_3 &= -\varepsilon_0 \end{aligned} \quad (2)$$

where α is the volume fraction of domain 2.

Under contraction along [100] the polydomain product consists of domain 2 and 3, then the average self-strain is

$$\hat{\varepsilon} = (1-\alpha')\hat{\varepsilon}_2 + \alpha'\hat{\varepsilon}_3 = \begin{pmatrix} \varepsilon_3(\alpha') & 0 & 0 \\ 0 & \varepsilon_1(\alpha') & 0 \\ 0 & 0 & \varepsilon_2(\alpha') \end{pmatrix} \quad (3)$$

where α' is the volume fraction of domain 3.

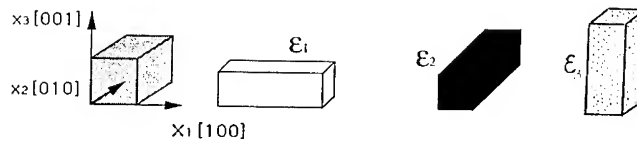


Fig.1 3 variants of the self-strain for a cubic tetragonal transformation.

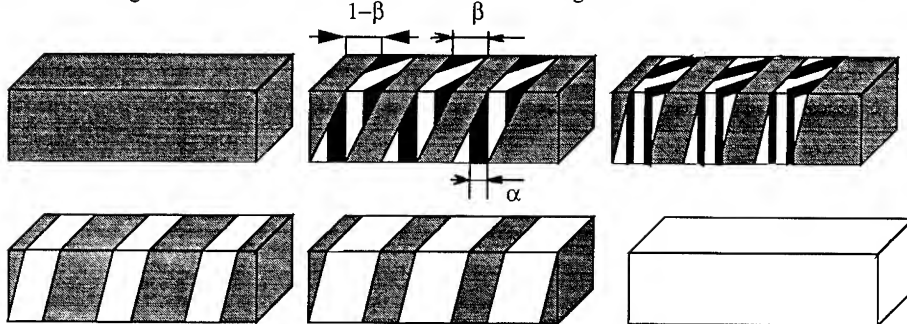


Fig.2 The evolution of the mesostructure under elongation.

The problem is to find the equilibrium mesostructure which corresponds to the minimum in free energy at a fixed temperature and a fixed external strain $\bar{\epsilon}$. It is assumed that there is no plastic deformation or fracture (i.e., the strains are compatible and the crystalline system is coherent). The difference of the elastic moduli of phases is neglected for simplicity.

EQUILIBRIUM MESOSTRUCTURE AND STRESS-STRAIN RELATION FOR THE DISPLACEMENT CONTROLLED DEFORMATION

For the two-phase crystal, containing a volume fraction β of the product phase, the average self-strain is $\hat{\epsilon} = \beta \hat{\epsilon}(\alpha)$. The free energy of the two-phase crystal per unit volume the product phase under the strain ϵ along [100] is:

$$\begin{aligned} F &= \Delta f \beta + (1/2) E (\bar{\epsilon} - \beta \epsilon_1(\alpha))^2 + e(n, \alpha, \beta) \quad \text{for elongation} \\ F &= \Delta f \beta + (1/2) E (\bar{\epsilon} - \beta \epsilon_3) \quad \text{for contraction} \end{aligned} \quad (4)$$

where $e(n, \alpha, \beta) = \beta(1-\beta)/2 E \epsilon^2 \chi(\alpha)$ is an energy of the internal stresses arising due to crystalline coherency. For simplicity it is assumed that the crystal is elastically isotropic.

For contraction $\epsilon_2(\alpha) = 0$ at $\alpha' = 1/\chi + 1$ and the coherent energy is absent. Thus the free energy of two-phase state is

$$\begin{aligned} f &= \phi \beta + [\epsilon - \beta(\chi - \alpha(\chi + 1))]^2 + \beta(1-\beta)[-1 + \alpha(\chi + 1)]^2 \quad \text{for elongation} \\ f &= \phi \beta + (\epsilon - \beta)^2 \quad \alpha' = 1/(\chi + 1) \quad \text{for contraction} \end{aligned} \quad (5)$$

where dimensionless parameters introduced are $f = F / (1/2 E \epsilon_0^2)$; $\epsilon = \bar{\epsilon} / \epsilon_0$; $\phi = \Delta f / (1/2 E \epsilon_0^2)$. ϕ is the dimensionless temperature with the phase equilibrium temperature T_0 as a reference temperature.

The equations of equilibrium:

$$\partial f / \partial \alpha = \partial f / \partial \beta = 0 \quad (6)$$

determine the equilibrium mesostructure, i.e. the equilibrium fractions of the product phase (β_0) and of domain 2 in it (α_0) as well as the orientation of the interfaces between the phases depending on α_0 and β_0 ³⁻⁴.

The strain dependencies of the equilibrium free energy, the stress $\sigma = \epsilon - \chi \beta$ (for elongation) $\sigma = \epsilon - \beta$ (for contraction) and the modulus as well as α_0 and β_0 for $\phi < 1$, $1 < \phi < 2\chi - 1$ and $\phi > 2\chi - 1$ are shown in Fig.3 and Fig.4.

If temperature $\phi < 1$ the transformation is started and completed with the formation of the polydomain product phase.

If $1 < \phi < 2\chi - 1$ the transformation starts with the formation of the polydomain phase which then degenerates to the single domain state. The single domain product phase spreads through the crystal and completes the transformation.

If $\phi > 2\chi - 1$ the transformation is started and completed with the formation of the single domain phase. The effective Young's modulus of the two-phase crystal is always negative under elongation and this fact corresponds to a convex free energy as a function of strain of the two-phase state.

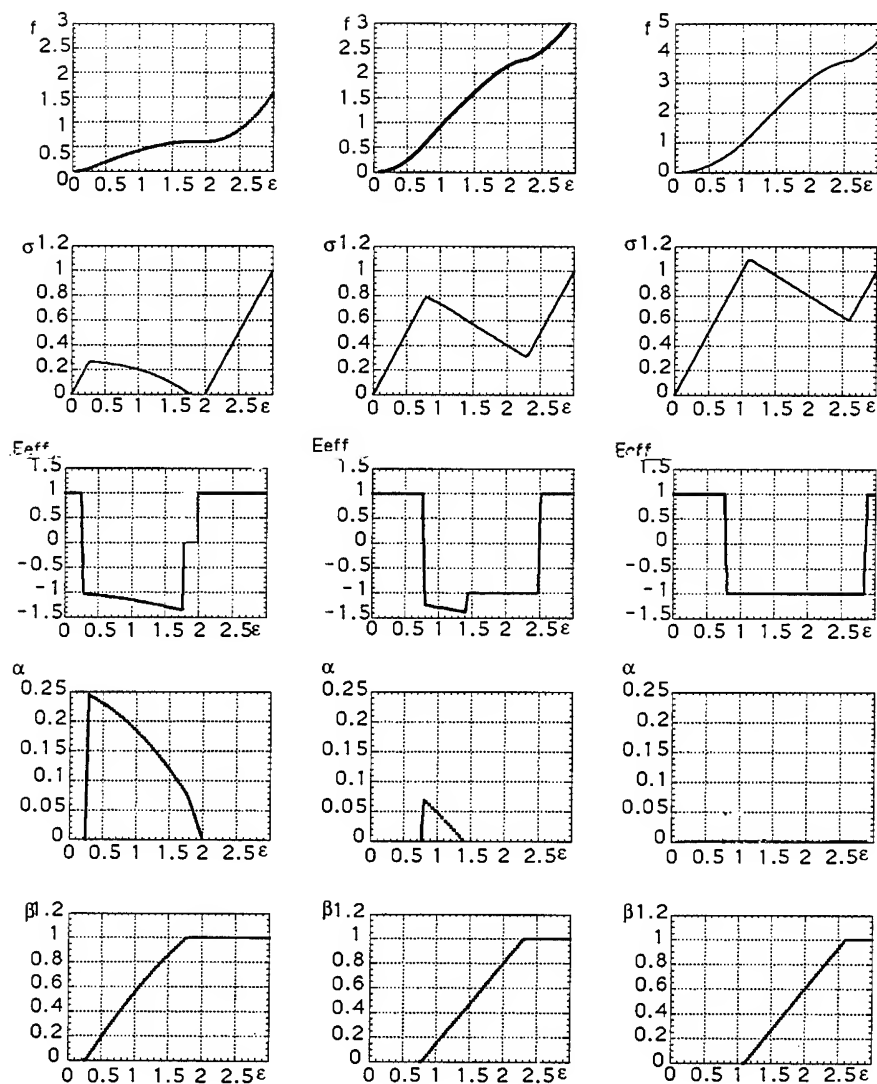


Fig.3 Strain dependence of the free energy (f), the stress ($\sigma = \partial f / \partial \epsilon$), the modulus ($E_{eff} = \partial^2 f / \partial \epsilon^2$) and mesostructures for $\chi=2$ and $\phi=0.6, 2.2, 3.4$.

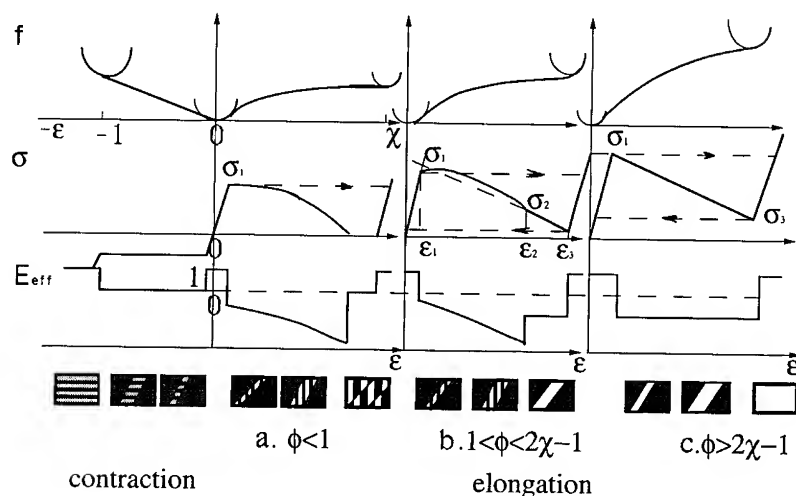


Fig.4 Strain dependencies of the free energy, the strain and the modulus at elongation and contraction. Hysteresis loops on σ - ϵ diagrams are shown by the arrows.

For contraction the transformation is started and completed with the formation of the polydomain product of the constant domain fractions at all temperatures. The effective Young's modulus of the two-phase crystal is zero, that corresponds to a linear dependence of the free energy on the phase fractions. The details of calculation will be presented in⁵.

THERMODYNAMIC HYSTERESIS OF LOAD CONTROLLED DEFORMATION

The deformation through coherent phase transformation considered above corresponds to the evolution of equilibrium heterophase mesostructure. The equilibrium is stable if the external strain is fixed. However, the equilibrium becomes unstable if the external stress is fixed instead of the strain. The equilibrium under stress is determined by the minimum in Gibbs free energy and the work of the external stress ($-\bar{\sigma} \hat{\epsilon}$) should be added to the external strain energy (the second term in Eq(4)). Then the equilibrium mesostructures correspond to saddle points of the Gibbs free energy and they are unstable with respect to changing β .

Thus, instead of a section of σ - ϵ curve with negative slope a hysteresis loop should be observed for transformation under stress (Fig.4). The horizontal branches of the loop correspond to unstable states of the heterophase system. Their positions correspond to the maximum stress σ_1 on loading and the minimum stress σ_3 on unloading. σ_1 is the yield stress of a more symmetrical phase when the first polydomain plates (if $\phi < 2\chi - 1$) or single domain plates ($\phi > 2\chi - 1$) are formed. The yield strength of the reverse transformation always corresponds to the formation of single domain plates. But if $\phi < 1$, there is a possibility of the formation of the high symmetry phase from the polydomain low symmetry one. In this case, the reverse stress can be zero. Fig.5

illustrates the temperature dependence of hysteresis of the stress induced transformation. The hysteresis is determined analytically as follows:

$$\begin{aligned} \sigma'_1 - \sigma_3 &= 1/\chi & \phi > 2\chi - 1 \\ \sigma_1 - \sigma_3 &= \sqrt{(\chi - 1)^2 + \phi} - (\chi - 1) - (\phi - 1)/2\chi & \phi < 2\chi - 1 \\ \sigma_1 - \sigma'_3 &= \sqrt{(\chi - 1)^2 + \phi} - (\chi - 1) & \phi < 1 \end{aligned} \quad (7)$$

The last expression describes the hysteresis with the reverse transformation of the polydomain tetragonal phase to the cubic one ($\sigma'_3=0$).

The thermodynamic hysteresis considered here gives only lowest value of the real hysteresis which can be considerably dependent on the kinetics of phase transformation.

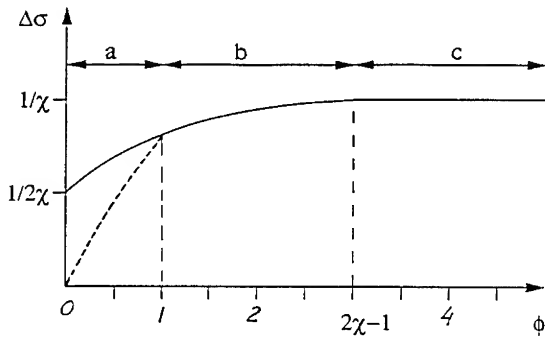


Fig.5 The temperature dependence of hysteresis of the stress induced transformation.

ACKNOWLEDGMENT

This work was supported by the Office of Naval Research, contract N00014-93-10506.

REFERENCES

- ¹Shape Memory Materials and Phenomena-Fundamental Aspects and Application Mat.Res.SocSymp.Proc. **246**, edited by C.T.Liu, H.Kunsmann, K.Otsuca and M.Wuttig (Pittsburgh: Material Research Society) (1992)
- ² Martensite Transformation Proceed. of International Conf. on Marten. Transformation (INCOMAT'93), edited by C.M.Wayman and J.Perkins (1993)
- ³A.L. Roitburd, *Solid State Physics* **33**, edited by Ehrenreich H., Seitz F. and Turnbull D. (New York: Academic Press), pp.317-390 (1978); *Soviet Physics-Izvestiya* **47**, 17 (1983)
- ⁴A.L.Roytburd, ref.1 pp.91-98; *Phase Transformations* **45**, 1-33 (1993)
- ⁵A.L.Roytburd and J.Slutsker *Scripta Met. and Mat.* **32**, #5 (1995); *J. Appl.Phys.*, submitted.

ELECTRO-MECHANICAL PROPERTIES OF PbZrO_3 - PbTiO_3 - $\text{Pb}(\text{Mn}_{1/3}\text{Sb}_{2/3})\text{O}_3$ CERAMICS UNDER VIBRATION-LEVEL CHANGE

SADAYUKI TAKAHASHI^{*,**}, YASUHIRO SASAKI^{*}, SELJI HIROSE^{**,***}
AND KENJI UCHINO^{**}

^{*}NEC Corporation, 4-1-1, Miyazaki, Miyamae-ku, Kawasaki-shi 216, Japan

^{**}The Pennsylvania State University, MRL, University Park, PA16802

^{***}Yamagata University, Jyonan, Yonezawa-shi, Yamagata 992, Japan

ABSTRACT

Electro-mechanical properties in the pseudo-ternary solid solution system of PbZrO_3 - PbTiO_3 - $\text{Pb}(\text{Mn}_{1/3}\text{Sb}_{2/3})\text{O}_3$ piezoelectric ceramics were studied by changing the vibration-level using a constant current / velocity driving method. The vibration velocity is proportional to the driving electric field under a relatively low field. The velocity, however, deviates from a linear relationship as electric field increases and converges on a certain value.

The increase of the vibration-level is accompanied by a large amount of heat generation as well, and this heat generation sets a practical upper limit of the vibration-level. The heat generation is caused by a dissipated-vibration-energy which is represented as a function of vibration velocity and the constants depending on the materials and transducers.

In these pseudo-ternary solid solution ceramics, the compositional ratio which shows excellent electro-mechanical properties under a relatively low vibration-level does not necessarily coincide with the compositional ratio which is excellent under a relatively high vibration-level.

INTRODUCTION

High-power piezoelectric ceramic devices, such as ultrasonic motors¹ and piezoelectric actuators,² have been watched with keen interest in recent years. A finite-level (large amplitude) piezoelectric vibration is necessary for these devices, and lead-zirconate-titanate (PZT) based ceramic materials are conventionally used as electro-mechanical transducers. It has been shown, however, that a great amount of heat generation as well as a marked change in electro-mechanical properties occurs in these materials under a finite-level vibration.³⁻⁷ A practical upper limit of an available vibration-level has been restricted by these phenomena.

We have been studying the vibration-level characteristics of electro-mechanical properties in PZT based piezoelectric ceramics, aiming to develop the high-power usage piezoelectric ceramic materials.⁸⁻¹³ Primarily a new method to evaluate the electro-mechanical properties continuously changing a vibration-level from low to high was established. Then the effects of compositional ratio of Zr / Ti and the effects of dopants on the vibration-level characteristics of electro-mechanical properties in PZT were studied. The empirical formulas which represented the relations of both Young's modulus versus vibration velocity and mechanical dissipation factor versus vibration velocity were found. It was also found that the heat generation was caused by dissipated-vibration-energy.

Some kind of pseudo-ternary solid solution ceramics consisting of a compound of $\text{Pb}(\text{M}, \text{M}')\text{O}_3$ (M, M' : metal ion) with PZT have been shown having high electro-mechanical coupling factor, high mechanical quality factor and high stability when they are driven under a relatively low vibration-level in comparison with the conventional binary solid solution PZT based ceramics. The ceramics with the composition of $x\text{PbZrO}_3$ - $y\text{PbTiO}_3$ - $z\text{Pb}(\text{Mn}_{1/3}\text{Sb}_{2/3})\text{O}_3$ (PZ-PT-PMS) have widely been used in a practical usage.¹⁴ These are regarded as one of the above pseudo-ternary solid solution ceramics in a sense, although the $\text{Pb}(\text{Mn}_{1/3}\text{Sb}_{2/3})\text{O}_3$ ceramics are not single phase perovskite. In this paper the effects of $\text{Pb}(\text{M}, \text{M}')\text{O}_3$ on the vibration-level characteristics of electro-mechanical properties in PZT are examined using the PZ-PT-PMS ceramics as a part of developing high power usage piezoelectric ceramic materials.

EXPERIMENTAL

Crystal structure and system of the pseudo-ternary solid solution PZ-PT-PMS ceramics are shown in Fig.1. The ceramics with a shaded compositional ratio were used as specimens here. These compositions are close to the morphotropic phase boundary (MPB) between the tetragonal ferroelectric phase (F_T) and the rhombohedral one (F_R). The ceramic specimens were prepared by the conventional powder metallurgy technology.

Electro-mechanical properties were measured on the fundamental length expansion vibration mode excited by a constant current / velocity driving method. Rectangular plate piezoelectric ceramic transducers with 43 mm long, 7 mm wide and 1 mm thick were used for all measurements.

The vibration-level was represented by the effective vibration velocity V_0 which was an universal parameter of the vibration-level. The V_0 value was determined by the following relation:

$$V_0 = \frac{1}{\sqrt{2}} \omega_0 \xi_m, \quad (1)$$

where ξ_m and ω_0 are a maximum vibration-amplitude and resonant angular frequency, respectively. The ξ_m was observed using an optical displacement sensor.

The temperature was measured by a thin thermocouple which was forced to contact the vibrational nodal line of the transducer. Initially, temperature increased with time and then gradually converged on its saturation value as heat generation and radiation approached their equilibrium state. This saturated temperature was defined as the transducer temperature here.

RESULTS AND DISCUSSIONS

Electro-Mechanical Properties under a Low Vibration-Level

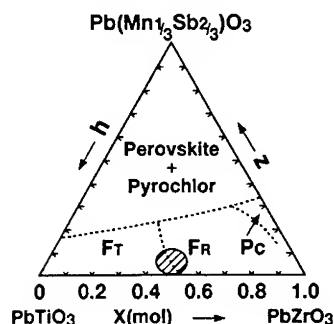


Fig.1 Crystal structure and symmetry of the pseudo-ternary solid solution PZ-PT-PMS ceramics.

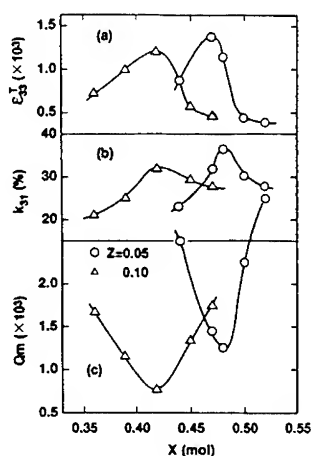


Fig.2 Dielectric constant ϵ_{33}^T (a), electro-mechanical coupling factor k_{31} (b) and mechanical quality factor Q_m (c) in PZ-PT-PMS ceramics under a low vibration-level.

Dielectric constant ϵ_{33}^T , electro-mechanical coupling factor k_{31} and mechanical quality factor Q_m under a relatively low vibration-level ($V_0 < 0.01$ m/s) are shown in Figs. 2(a),(b) and (c), respectively, where z is the fraction of $\text{Pb}(\text{Mn}_{1/3}\text{Sb}_{2/3})\text{O}_3$ content. The ϵ_{33}^T and k_{31} show maximum values close to the MPB, whereas the Q_m shows minimum. Each maximum or minimum value in the ceramics with the molar concentration of $z=0.05$ is larger than that in the ceramics with $z=0.10$.

Vibration-Level Dependence on the Driving Electric Field

The following relation is derived from the piezoelectric equations for the transducers vibrating in longitudinal expansion mode where both ends of the transducer are mechanically free:

$$-AtE_{do} + ZV_0 = 0, \quad (2)$$

where A , Z , E_{do} and t represent force factor, mechanical impedance at the transducer ends, effective driving electric field and the transducer thickness, respectively. Therefore V_0 is represented as a function of E_{do} as follows:

$$V_0 = \frac{At}{Z} E_{do} = \frac{4}{\pi} \sqrt{\frac{\epsilon_{33}^T}{\rho}} \frac{k_{31}}{Q_m^{-1}} E_{do}, \quad (3)$$

where ρ is density. Thus the V_0 should be proportional to E_{do} .

In Figs. 3 and 4, V_0 and mechanical dissipation factor Q_m^{-1} are shown as a function of E_{do} . It can be seen that the V_0 is actually proportional to E_{do} under a relatively low driving electric field. The V_0 , however, gradually deviates from the linear relationship as E_{do} increases and converges

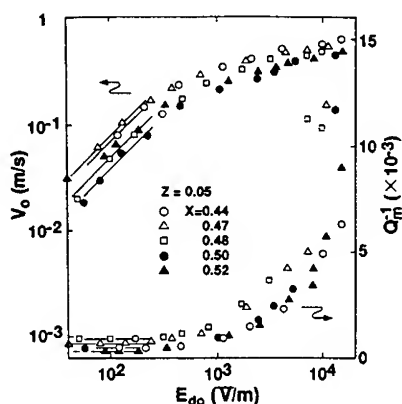


Fig.3 Effective vibration velocity V_0 and mechanical dissipation factor Q_m^{-1} in PZ-PT-PMS ceramics with $z=0.05$ as a function of effective driving electric field E_{do} .

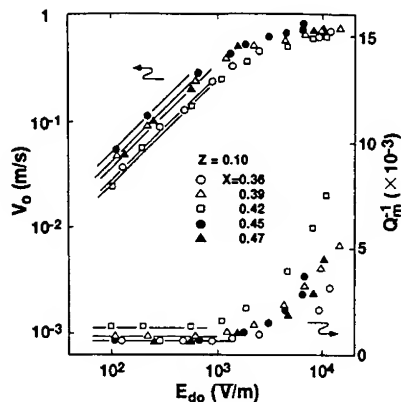


Fig.4 Effective vibration velocity V_0 and mechanical dissipation factor Q_m^{-1} in PZ-PT-PMS ceramics with $z=0.10$ as a function of effective driving electric field E_{do} .

on its saturation value after all. This phenomenon is considered to be caused by the increase of Q_m^{-1} with increasing E_{do} , since both the ϵ_{33}^T and k_{31} tend to increase with increasing E_{do} .¹¹ It is a fact that the Q_m^{-1} increases with increasing E_{do} in accordance with the V_o behavior.

Thus the available vibration-level does not necessarily increase with increasing driving electric field. The drastic increase of Q_m^{-1} which occurs when a driving electric field exceeds a certain value restricts a maximum of the available vibration-level magnitude.

Dissipated-Vibration-Energy Effect on Heat Generation.

In Figs. 5(a) and 6(a), the temperature rise of the transducers ΔT is represented as a function of V_o . The ΔT markedly increases when V_o exceeds a certain value depending on the ceramic compositions. This phenomenon essentially restricts a practically available magnitude of the vibration-level.

The dissipated-vibration-energy per one second $\omega_o W$ is represented by the following equation:

$$\omega_o W = U \omega_o Q_m^{-1} = \frac{1}{4} Y_o^E S_m^2 V \omega_o Q_m^{-1} = \frac{1}{2} M V_o^2 \omega_o Q_m^{-1} \quad (4)$$

$$U = \int u dV = \bar{u} V, \quad \bar{u} = \frac{K}{2} Y_o^E S_m^2, \quad (5)$$

$$Y_o^E = \frac{1}{\pi^2} l^2 \rho \omega_o^2, \quad S_m = \frac{\pi E_m}{l},$$

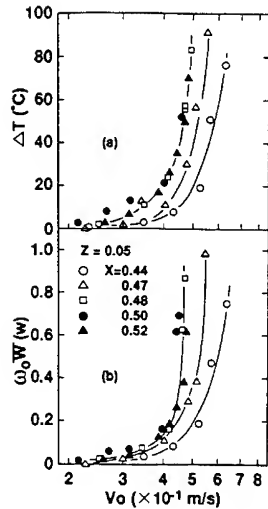


Fig.5 Temperature rise ΔT (a) and dissipated-vibration-energy per one second $\omega_o W$ (b) in PZ-PT-PMS ceramics with $z=0.05$ as a function of effective vibration velocity V_o .

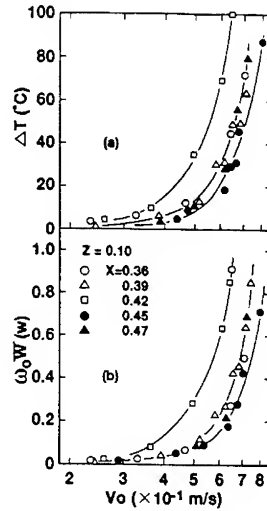


Fig.6 Temperature rise ΔT (a) and dissipated-vibration-energy per one second $\omega_o W$ (b) in PZ-PT-PMS ceramics with $z=0.10$ as a function of effective vibration velocity V_o .

where U , u , \bar{u} , Y_o^E and S_m are stored elastic energy, stored elastic energy density, average stored elastic energy density, Young's modulus and maximum strain, respectively. The κ is a constant depending on a shape and vibration mode of transducers, and here $\kappa = 1/2$.¹⁵ The M , V and l are mass, volume and length of the transducers, respectively.

Figures 5(b) and 6(b) show $\omega_o W$ value as a function of V_o . The behaviors are analogous to those of temperature rise (Figs. 5(a) and 6(a)). In Fig. 7 ΔT is plotted against $\omega_o W$ and a linear relationship can be approximated between them. Therefore, as was discussed previously, the dissipated-vibration-energy is regarded as the dominant cause of the heat generation.¹²

Practical Vibration-Levels in PZ-PT-PMS

As mentioned above, the heat generation phenomenon essentially restricts the upper limit of the vibration-level in the practical usage. If, for instance, $\Delta T < 40^\circ\text{C}$ in a certain actual usage, the maximum available V_o value in PZ-PT-PMS ceramics is represented in Fig. 8(a). In Fig. 8(b), V_o under a very low driving field ($E_{do} = 100\text{ V/m}$) is represented as well in comparison to (a). The results indicate that the available vibration-level of the ceramics with $z=0.05$ is higher than that of the ceramics with $z=0.10$ under a low driving field. It is seen, however, that the maximum of the practically available vibration-level is higher for the ceramics with $z=0.10$ than $z=0.05$. This fact suggests that the excellent piezoelectric materials under a low vibration-level are not necessarily excellent under a high vibration-level.

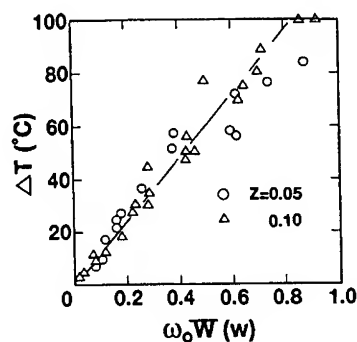


Fig.7 Relationship between temperature rise ΔT and dissipated-vibration-energy per one second $\omega_o W$.

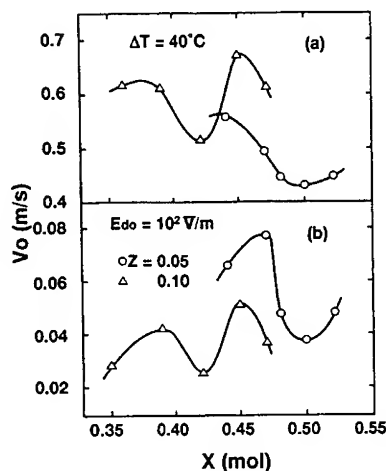


Fig.8 Maximum of the available effective vibration velocity when the temperature rise ΔT is below 40°C (a) and the effective vibration velocity under the relatively low driving electric field of 100 V/m (b).

CONCLUSION

Electro-mechanical properties in the pseudo-ternary solid solution system of $\text{PbZrO}_3\text{-PbTiO}_3\text{-Pb}(\text{Mn}_{1/3}\text{Sb}_{2/3})\text{O}_3$ (PZ-PT-PMS) ceramics were studied by changing the vibration-level using a constant current / velocity driving method as a part of developing high-power usage piezoelectric ceramics.

The vibration velocity linearly increases with a driving electric field under a relatively low level. However, the velocity gradually deviates from the linear relation as electric field increases and converges on its saturation value after all.

A high vibration-level generates a large amount of heat as well. This phenomenon sets a practical upper limit of the vibration-level. The heat generation is caused by a dissipated-vibration-energy which is represented as a function of vibration velocity and the constants depending both on the materials and transducers.

In PZ-PT-PMS ceramics, the compositional ratio which shows excellent electro-mechanical properties under a low vibration-level does not necessarily coincide with the compositional ratio which is excellent under a high vibration-level. The result suggests that there possibly exists excellent high power usage piezoelectric ceramics among the existing ceramics with multi-components, since the compositional ratio in the conventional multi-component piezoelectric ceramics has been determined to have excellent electro-mechanical properties just under a relatively low vibration-level.

REFERENCES

1. S. Ueha and Y. Tomikawa, *Ultrasonic Motors-Theory and Applications-* (Oxford, New York, 1993).
2. S. Takahashi, in *Ferroelectric Ceramics*, edited by N. Setter and E. L. Colla, (Birkhauser Verlag, Basel, 1993), p.249.
3. R. A. Gdula, *J. Am. Ceram. Soc.* **51**, 683(1968).
4. J. H. Belding and M. G. McLaren, *Ceram. Bull.* **49**, 1025 (1970).
5. H. J. Hageman, *J. Phys. C : Solid State Phys.* **11**, 3333 (1978).
6. K. Lubitz and W. Wersing, *Ferroelectrics*, **40**, 237, (1982).
7. K. Uchino, H. Negishi and T. Hirose, *Jpn. J. Appl. Phys.* **28**, Suppl.28-2, 47 (1989).
8. S. Takahashi and S. Hirose, *Jpn. J. Appl. Phys.* **31**, Pt.1, No. 9B, 3055 (1992).
9. S. Takahashi and S. Hirose, *Jpn. J. Appl. Phys.* **32**, Pt.1, No. 5B, 2422 (1993).
10. S. Hirose, Y. Yamayoshi, M. Taga and H. Shimizu, *Jpn. J. Appl. Phys.* **30**, Suppl.30-1, 117 (1991).
11. S. Takahashi, S. Hirose and K. Uchino, *J. Am. Ceram. Soc.* **77**, 2429 (1994).
12. S. Takahashi, S. Hirose, K. Uchino and K. Y. Oh, *Proceeding of the 9-th IEEE International Symposium on the Applications of Ferroelectrics*, (Penn. State, 1994). [to be published]
13. S. Hirose, S. Takahashi, M. Aoyagi and Y. Tomikawa, *Proceeding of the 9-th IEEE International Symposium on the Applications of Ferroelectrics*, (Penn. State, 1994). [to be published]
14. T. Ohno, N. Tsubouchi, M. Takahashi, Y. Matsuo and M. Akashi, *Technical Report of IEICE, Japan*, US71-37 (1972-02). [in Japanese]
15. K. Nagai and M. Konno, *Electromechanical Vibrations and Thier Application* (Corona-Sha, Tokyo, 1974), p. 41. [in Japanese]

CORRELATIONS BETWEEN THE BIPOLAR- AND UNIPOLAR-ELECTRIC FIELD INDUCED STRAIN IN $\text{Pb}(\text{Mg}_{1/3}\text{Nb}_{2/3})\text{O}_3$ - PbTiO_3 CERAMICS

JAE-HWAN PARK, BYUNG-KOOK KIM, and SOON JA PARK
Department of Inorganic Materials Engineering, Seoul National University, Seoul 151-742, Korea

ABSTRACT

Correlations between the strains induced by a unipolar-electric field and the strains induced by a bipolar-electric field were investigated for $\text{Pb}(\text{Mg}_{1/3}\text{Nb}_{2/3})\text{O}_3$ (PMN) and $0.9(\text{Pb}(\text{Mg}_{1/3}\text{Nb}_{2/3})\text{O}_3)$ - 0.1PbTiO_3 (0.9PMN-0.1PT) relaxor ferroelectric ceramics in the temperature range of $-50^\circ\text{C} \sim 150^\circ\text{C}$. The magnitudes of the unipolarly induced-strains are almost the same as the differences between the bipolarly induced-strains and the residual strains, which were attributed to the absence of change of spontaneous polarization direction when the unipolar-electric field is applied.

INTRODUCTION

Lately, special attention has been paid to $\text{Pb}(\text{Mg}_{1/3}\text{Nb}_{2/3})\text{O}_3$ (PMN)-based relaxor ferroelectric ceramics because of their high dielectric constants and high electrostrictive coefficients. [1-3] When they are applied to practical devices such as multilayer capacitors and/or electrostrictive actuators, characteristics of unipolarly induced-strains are of more practical importance than those of bipolarly induced-strains. Nevertheless, the characteristics of unipolarly induced-strains have been far less studied than those of bipolarly induced-strains. Furthermore most of the previous reports have devoted to the composition dependence of the electrostrictive characteristics at room temperature only, even though the temperature dependence is of great importance from the practical point of view. Systematic studies on the correlations between the bipolarly induced-strains and the unipolarly induced-strains in the wide temperature range are required for better understanding of the electrostrictive characteristics of PMN-based relaxor ferroelectric ceramics.

In the present paper, therefore, correlations between the strains induced by a unipolar-electric field and the strains induced by a

bipolar-electric field were investigated for $\text{Pb}(\text{Mg}_{1/3}\text{Nb}_{2/3})\text{O}_3$ (PMN) and $0.9\{\text{Pb}(\text{Mg}_{1/3}\text{Nb}_{2/3})\text{O}_3\} - 0.1\text{PbTiO}_3$ (0.9PMN-0.1PT) relaxor ferroelectric ceramics in the temperature range of $-50^\circ\text{C} \sim 150^\circ\text{C}$.

EXPERIMENTAL PROCEDURE

$\text{Pb}(\text{Mg}_{1/3}\text{Nb}_{2/3})\text{O}_3$ (PMN) and $0.9\{\text{Pb}(\text{Mg}_{1/3}\text{Nb}_{2/3})\text{O}_3\} - 0.1\text{PbTiO}_3$ (0.9PMN-0.1PT) powders were prepared via a columbite precursor method. After conventional solid state sintering, samples were prepared into disks of 1 mm thickness and 12 mm diameter. A strain gauge method was used to detect the changes of strains with an electric field. A strain gauge (B-FAE, Minebea, Japan) was attached on one side of the silver electrodes for the measurement of transverse strains and the gauge was connected to a Wheatstone bridge. The 0.05Hz electric field, which was generated by a digital-analog (DA) converter assisted by computer interfaces, was amplified by a high-voltage amplifier and applied to the sample continuously between -2 KV and $+2 \text{ KV/mm}$. The strain gauge was connected to a strain amplifier and outputs were recorded through computer interfaces. The strain measurements were performed in silicone oil in the temperature range of $-50^\circ\text{C} \sim 150^\circ\text{C}$.

RESULTS AND DISCUSSIONS

Figure 1 shows the temperature dependence of the dielectric constants in PMN and 0.9PMN-0.1PT at various frequencies. Both samples show typical relaxor type behaviors, and the magnitudes of diffuseness are similar to each other. Temperatures of maximum dielectric constant at 1 kHz (T_C) of PMN and 0.9PMN-0.1PT are *ca.* 0°C and 40°C , respectively. Dielectric constants at T_C are *ca.* 15000 and 17000 in PMN and 0.9PMN-0.1PT, respectively.

Figure 2 shows the plots of the strain versus the bipolar-electric field ($S-E_{bi}$ plot) and the plots of the strain versus the unipolar-electric field ($S-E_{uni}$ plot) in PMN and 0.9PMN-0.1PT at selected temperatures. The temperature dependence of the dielectric constants at 1 kHz is also shown. Above T_C , both samples show electrostrictive behaviors, that is, the strains are proportional to the squares of the electric field. However, as the temperature decreases below T_C , the $S-E_{bi}$ plots become butterfly-shaped: both the coercive fields and the residual strains increase. It implies that ferroelectricity increases as the temperature decreases below T_C .

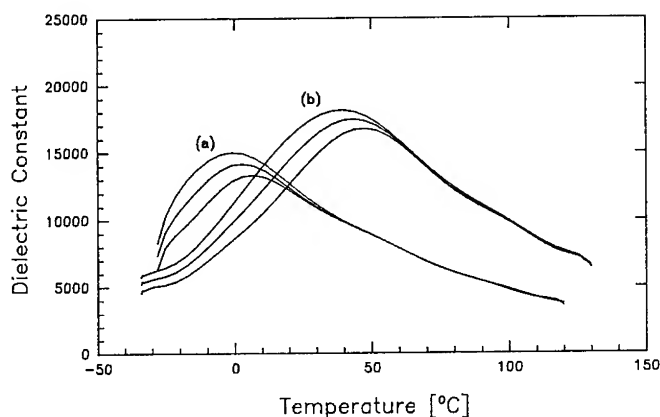
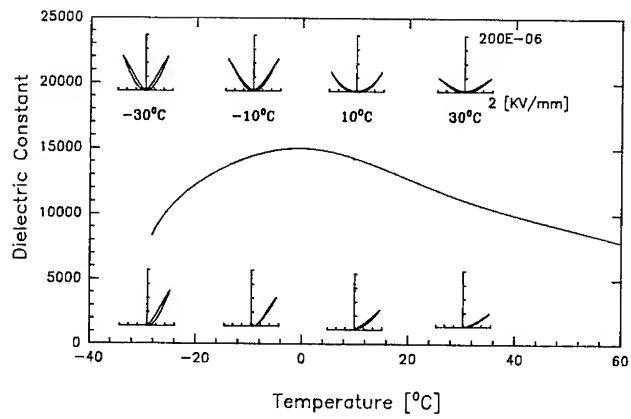


FIG.1. Temperature dependence of the dielectric constants in PMN (a) and 0.9PMN-0.1PT (b) at various frequencies.

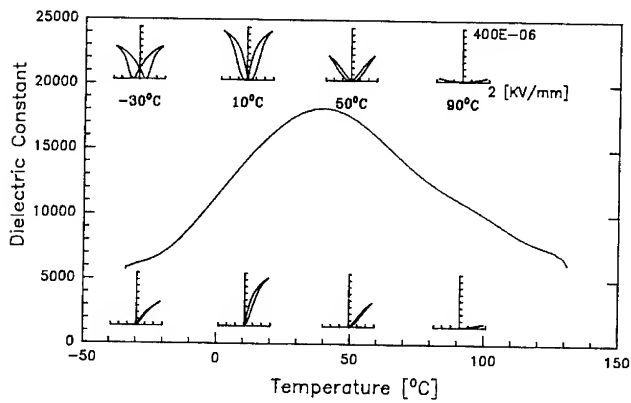
Figure 3 shows the temperature dependence of the magnitude of the strain induced by the bipolar- or the unipolar-electric field of 2 kV/mm in PMN and 0.9PMN-0.1PT. The induced strains of 0.9PMN-0.1PT reach maximum (*ca.* 400×10^{-6}) at *ca.* 10°C , which is lower than T_C by *ca.* 30°C . The induced strains of PMN increases as the temperature decreases below -30°C which is lower than T_C by 30°C , though the maximum was not confirmed due to the limitations of temperature control.

Above T_C where the paraelectric cubic phase dominates, both the unipolarly induced-strains and the bipolarly induced-strains decrease as the temperature increases and the magnitude of the unipolarly induced-strains equals that of the bipolarly induced-strains in PMN and 0.9PMN-0.1PT. However, the unipolarly induced-strains become smaller than the bipolarly induced-strains as the temperature decreases below T_C where the ferroelectric rhombohedral phase dominates, in PMN as well as in 0.9PMN-0.1PT.

For 0.9PMN-0.1PT, the residual strains and the differences between the bipolarly induced-strains and the unipolarly induced-strains are also shown in Fig.3. The unipolarly induced-strains are approximately equal to the differences between the bipolarly induced-strains and the residual strains, which results from the absence of the change of spontaneous polarization direction under the unipolar-electric field driving.

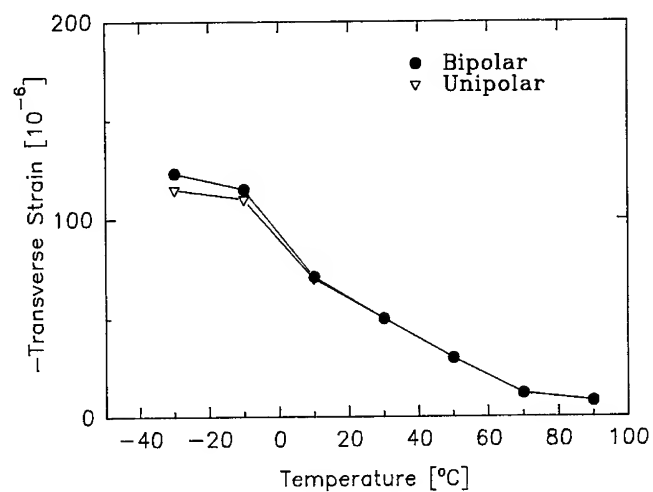


(a)

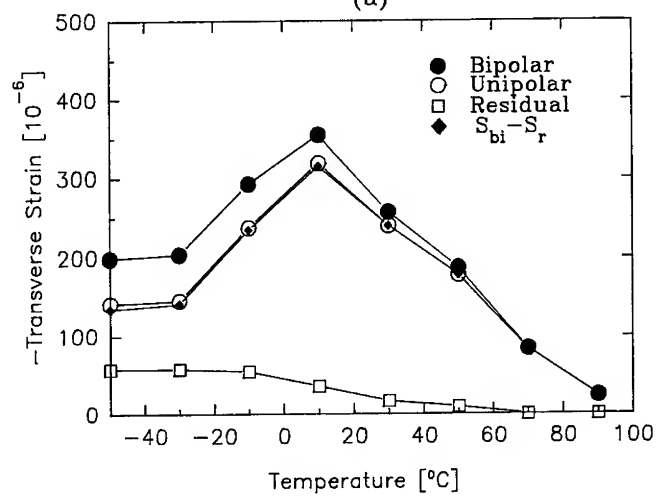


(b)

FIG.2. Plots of the strain *vs.* the bipolar-electric field and the strain *vs.* the unipolar-electric field in PMN (a) and in 0.9PMN-0.1PT (b) at various temperatures. Temperature dependence of the dielectric constants is also shown.



(a)



(b)

FIG.3. Temperature dependence of the magnitudes of bipolarly and unipolarly induced-strains in PMN (a) and in 0.9PMN-0.1PT (b). The electric field of 1.2 KV/mm was applied. For 0.9PMN-0.1PT, the residual strains and the differences between the bipolarly induced-strains and the unipolarly induced-strains are also shown.

SUMMARY

The strains induced by a bipolar-electric field and the strains induced by a unipolar-electric field were investigated in PMN and 0.9PMN-0.1PT in the temperature range of $-50^{\circ}\text{C} \sim 150^{\circ}\text{C}$. Above T_C , both samples show electrostrictive behaviors, that is, the strains are proportional to the squares of the electric field. However, as the temperature decreases below T_C , the $S-E_{bi}$ plots become butterfly-shaped which implies the increase of ferroelectricity.

Above T_C where the paraelectric cubic phase dominates, the unipolarly induced-strains equal the bipolarly induced-strains in PMN and 0.9PMN-0.1PT. However, the unipolarly induced-strains become smaller than the bipolarly induced-strains as the temperature decreases below T_C where the ferroelectric rhombohedral phase dominates, in PMN as well as in 0.9PMN-0.1PT. The magnitudes of the unipolarly induced-strains are almost the same as the differences between the bipolarly induced-strains and the residual strains, which were attributed to the absence of change of spontaneous polarization direction when the unipolar-electric field is applied.

REFERENCES

1. K. Uchino, *Ceram. Bull.*, **65**, 647 (1986)
2. R.E. Newnham and G.R. Ruschau, *J. Amer. Ceram. Soc.*, **74**, 4630 (1991)
3. K. Uchino, *Piezoelectric/Electrostrictive Actuators*, Morikita Press, Tokyo, (1986)

CARBON FIBER REINFORCED CONCRETE AS AN INTRINSICALLY SMART CONCRETE FOR DAMAGE ASSESSMENT DURING DYNAMIC LOADING

PU-WOEI CHEN AND D.D.L. CHUNG

Composite Materials Research Laboratory, State University of New York at Buffalo, Buffalo,
NY 14260-4400

ABSTRACT

Concrete containing short carbon fibers (0.2-0.5 vol.%) was found to be an intrinsically smart concrete that can sense elastic and inelastic deformation, and fracture. The signal provided is the change in electrical resistance, which is reversible for elastic deformation and irreversible for inelastic deformation and fracture. The presence of electrically conducting short fibers is necessary for the concrete to sense elastic or inelastic deformation, but the sensing of fracture does not require fibers. The fibers serve to bridge the cracks and provide a conduction path. The resistance increase is due to conducting fiber pull-out in the elastic regime, conducting fiber breakage in the inelastic regime, and crack propagation at fracture.

INTRODUCTION

Smart structures capable of damage assessment in real time are important due to the need to maintain the functions of critical civil infrastructure systems. The sensing provides an electrical, optical or acoustic response to damage in real time during dynamic loading. Requirements of the sensor include (1) low cost for both materials and implementation, (2) durability and reliability, (3) measurement repeatability and stability, (4) ability to provide quantitative signals with high sensitivity and resolution, (5) ability to provide spatial resolution, (6) fast response, (7) sensitivity to a wide dynamic range of strain, covering both the elastic and inelastic regimes of deformation, (8) not weakening the structure, (9) not requiring expensive peripheral equipment, and (10) applicability to both old and new structures.

No. 7 above refers to the ability to detect and distinguish between inelastic deformation (which corresponds to permanent damage) and elastic deformation. This ability is valuable for monitoring damage occurrence during dynamic loading, as it provides monitoring of the dynamic loading in its complete range, covering both the elastic and inelastic regimes. Thus, it allows determination of exactly in which part of which loading cycle damage occurs and does not require the load cycling to be periodic in time. No. 5 above refers to the ability to provide a measure of the degree and location of damage. This measure can be in terms of the inelastic strain, as strain in the inelastic regime is associated with damage. The greater is the inelastic strain, the greater is the damage. Due to the ability described in No. 7, the response due to the inelastic strain can be distinguished from that due to the elastic strain. Thus, the inelastic strain (or degree of damage) can be monitored in real time during dynamic loading.

In a new sensor technology [1], concrete itself is the sensor, which satisfies all of the requirements listed above. Moreover, the intrinsically smart concrete exhibits high flexural strength and toughness, and low drying shrinkage [2]. In this paper, the sensing ability and its origin are described in relation to the sensing of elastic deformation, inelastic deformation and fracture. In contrast to techniques such as acoustic emission, which cannot sense elastic deformation, this new sensor technology allows the sensing of elastic deformation, in addition to inelastic deformation and fracture. The signal provided is the change in the electrical resistance. Reversible strain is associated with reversible resistance change; irreversible strain is associated with irreversible resistance change; fracture is associated with irreversible and particularly large resistance change. The origin of the signal associated with fracture is crack propagation, which increases the resistance due to the high resistivity of the cracks. The origin of the signal associated with irreversible strain is conducting fiber breakage; the origin of the signal associated with reversible strain is conducting fiber pull-out. The detection of fracture does not require fibers in the concrete, whereas the detection of irreversible and reversible strains require the presence of short and electrically conducting fibers in the concrete.

EXPERIMENTAL

The fibers were unsized carbon fibers based on isotropic pitch and of diameter 10 μm , nominal length 5 mm and electrical resistivity $3 \times 10^{-3} \Omega \cdot \text{cm}$. Their amount was 0.5% by weight of cement. The aggregate was natural sand. The mortars studied were (i) plain mortar, (ii) mortar with latex, (iii) mortar with methylcellulose, and (iv) mortar with methylcellulose and silica fume. Latex, methylcellulose and silica fume were added to disperse the fibers, but they were used whether fibers were present or not in order to obtain the effect of the fibers alone.

The water reducing agent was TAMOLSN (Rohm and Haas), which contained 93-96% sodium salt of a condensed naphthalenesulfonic acid. The slump of carbon fiber reinforced cement tends to decrease with increasing carbon fiber content, so we used water reducing agent to maintain a flow of 150 ± 50 mm. The latex was styrene butadiene in the amount of 20% of the weight of the cement. The antifoam (Dow Corning 2410) used with the latex was in the amount of 0.5% by weight of latex. Methylcellulose in the amount of 0.4% of the cement weight was used; the defoamer (Colloids 1010) used with it was in the amount of 0.13 vol.%.

For the case of mortar containing latex, latex, antifoam and fibers first were mixed by hand for about 1 min. Then this mixture, cement, sand, water and water reducing agent were mixed in a Hobart mixer for 5 min. For the case of mortar containing methylcellulose, methylcellulose was dissolved in water. After that, the defoamer and then the fibers were added and stirred by hand for 2 min. Then this mixture, cement, sand, water and water reducing agent (and silica fume, if applicable) were mixed in the Hobart mixer for 5 min. For the case of concrete, only the formulation involving methylcellulose and silica fume [2] was used. After pouring the mix into oiled molds, a vibrator was used to decrease the amount of air bubbles. The specimens were demolded after 1 d and then cured in air (10% RH) for 7 d.

Table 1. Results of simultaneous compressive/tensile testing and electrical resistivity measurement along the stress axis. L = latex; M = methylcellulose; SF = silica fume; F = fibers.

Mortar	Vol. % fibers	Compressive			Tensile		
		Strength (MPa)	Ductility (%)	$\Delta R/R_o$ at fracture	Strength (MPa)	Ductility (%)	$\Delta R/R_o$ at fracture
Plain	0	35.6	0.16	69.5	0.88	0.004	0.88
L	0	38.6	0.24	30	3.03	0.0352	0.6
L	0.37	37.8	0.17	4.1	--	--	--
L	0.53	--	--	--	3.15	0.0413	0.053
M	0	34.5	0.17	3.4	1.37	0.0209	0.18
M	0.24	33.6	0.15	10.42	--	--	--
M	0.53	--	--	--	1.95	0.0192	0.034
M+SF	0	42.7	0.16	9.7	0.83	0.088	0.037
M+SF	0.24	41.0	0.19	21.14	--	--	--
M+SF	0.53	--	--	--	1.88	0.0173	0.051

Simultaneous to mechanical testing, resistance measurements were made at a DC current from 0.1 to 4 A. For each test, six specimens of each type were used. For compressive testing according to ASTM C109-80, mortar specimens were prepared by using a 2 x 2 x 2 in (5.1 x 5.1 x 5.1 cm) mold. For compressive testing according to ASTM C39-83b, concrete specimens were prepared using a 102 mm (4 in) diameter x 203 mm (8 in) length mold. Dog-bone shaped specimens were used for tensile testing. They were prepared by using molds of the same shape and size. The displacement rate was 1.27 mm/min. During compressive or tensile loading up to fracture, the strain was measured by the cross-head displacement in compressive testing or by a strain gage in tensile testing, while the fractional change in electrical resistance along the stress axis was measured using the four-probe method. The electrical contacts were made by silver paint. Although the spacing between the contacts increased upon tensile deformation and decreased upon compressive deformation, the increase was so small that the measured resistance remained essentially proportional to the resistivity. Testing was performed either in one cycle up to the breaking stress or in multiple cycles upon loading up to a fraction (1/3 under compression and ~ 1/2 under tension) of the breaking stress.

Table 1 summarizes the results of simultaneous compressive/tensile testing and resistivity measurement along the stress axis. The electrical probing gave the resistance R between the two voltage probes (a distance d apart) in the four-probe set-up. Table 1 gives the fractional change in R at fracture, i.e., $\Delta R/R_o$, where R_o is the original resistance. For compressive testing, d = 1 cm and 4 in for mortars and concretes respectively; for tensile testing d = 4 cm

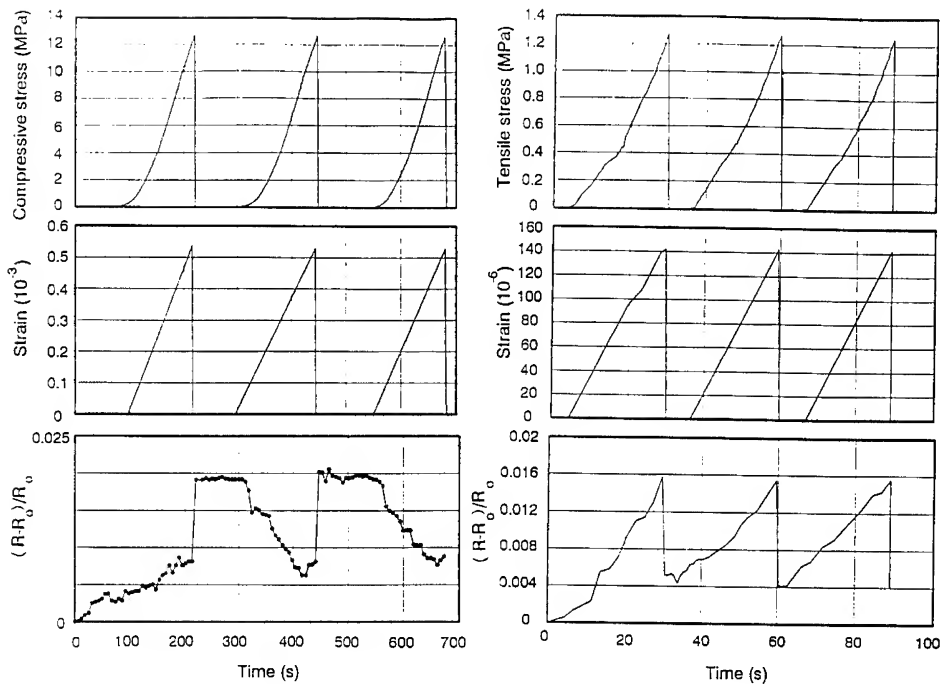


Fig. 1 Plots vs. time of $\Delta R/R_0$, compressive strain and compressive stress obtained during cyclic compressive testing for mortar containing latex and 0.37 vol.% fibers.

Fig. 2 Plots vs. time of $\Delta R/R_0$, tensile strain and tensile stress obtained during cyclic tensile testing for mortar containing latex and 0.53 vol.% fibers.

(for mortars only). In both compression and tension, $\Delta R/R_0$ is positive because flaws are generated. $\Delta R/R_0$ at fracture is larger under compression than tension. This is due to the higher ductility under compression. Without fibers, $\Delta R/R_0$ varies randomly with strain/stress up to fracture, at which $\Delta R/R_0$ abruptly increases. $\Delta R/R_0$ did not vary with the fiber content (if nonzero), though the original resistivity decreased much with increasing fiber content.

Under cyclic compressive/tensile loading, without fibers, no smart behavior was observed. With fibers, under cyclic compressive loading within the regime where the strain was essentially fully reversible (Fig. 1), the smart behavior was observed as (i) irreversibly increasing $\Delta R/R_0$ during the first loading, (ii) reversibly increasing $\Delta R/R_0$ during unloading in any cycle, and (iii) reversibly decreasing $\Delta R/R_0$ during the second and subsequent loadings. The irreversibly increasing $\Delta R/R_0$ during the first loading (which involved no irreversible strain) is attributed to the irreversible increase in the contact electrical resistivity at the fiber/matrix

interface due to the weakening of that interface. The reversibly increasing $\Delta R/R_o$ during unloading in any cycle is attributed to crack opening (i.e., increase in the length or height of a crack), which was hindered under compressive loading. The reversibly decreasing $\Delta R/R_o$ during the second and subsequent loadings is attributed to crack closure (i.e., decrease in the length or height of a crack) under compressive loading. The reversibility of the crack opening is attributed to the fiber bridging across the crack. Fiber pull-out requires a weak fiber/matrix interface; the interface weakening is associated with the irreversible increase in $\Delta R/R_o$ prior to fiber pull-out or crack opening. Under cyclic tensile loading within the regime where the strain was fully reversible (Fig. 2), the smart behavior was observed as (i) irreversibly increasing $\Delta R/R_o$ during the initial portion of the first loading, (ii) reversibly increasing $\Delta R/R_o$ during the latter portion of the first loading and during any subsequent loading, and (iii) reversibly decreasing $\Delta R/R_o$ during unloading in any cycle. The increase in $\Delta R/R_o$ during loading is attributed to crack opening, whereas the decrease in $\Delta R/R_o$ during unloading is attributed to crack closure. That the initial portion of the first loading exhibited irreversibly increasing $\Delta R/R_o$ whereas the latter portion was reversible is because the irreversible part is due to the fiber/matrix interface weakening, whereas the reversible part is due to crack opening. Though results were similar, $\Delta R/R_o$ was smaller for concretes than mortars.

The fractions $(\Delta R/R_o)_{\text{reversible}}/(\Delta R/R_o)_{\text{fracture}}$ and $(\Delta R/R_o)_{\text{irreversible}}/(\Delta R/R_o)_{\text{fracture}}$ vary with the stress amplitude in cyclic loading. In Table 2, the stress amplitude is expressed as the maximum stress divided by the fracture stress. The fractions listed are for compression of mortars containing latex and 0.37 vol.% fibers. The irreversible strain increases monotonically with the stress amplitude, but the reversible strain does not vary with the stress amplitude. Table 2 shows good correlation between the irreversible strain and the irreversible part of $\Delta R/R_o$.

Table 2. Effect of stress amplitude in cyclic compressive loading on the reversible and irreversible parts of $(\Delta R/R_o)/(\Delta R/R_o)_{\text{fracture}}$ and the reversible and irreversible parts of strain/strain_{fracture} for mortar containing latex and 0.37 vol.% carbon fibers.

Maximum stress Fracture stress	$(\Delta R/R_o)/(\Delta R/R_o)_{\text{fracture}}$		Strain/strain _{fracture}	
	Reversible	Irreversible	Reversible	Irreversible
0.75	0.039	0.244	0.29	0.44
0.65	0.037	0.102	0.29	0.33
0.50	0.032	0.115	0.38	0.12
0.40	0.0073	0.068	0.33	0.09
0.33	0.0034	0.0015	0.32	0.01
0.25	0.0025	0.0013	0.29	0.00
0.20	0.0027	0.0017	0.27	0.00

The effect of the fiber addition on the crack height was examined after compression to 70% of the fracture stress for (a) mortar containing latex but no fibers, and (b) mortar containing latex and 0.37 vol.% fibers. These mortars have similar compressive strength (Table 1). The crack height was 1 μm in (b) and 100 μm in (a), indicating that the fibers caused crack opening control, which in turn resulted in the smart behavior. Table 1 shows significant effects of the fiber addition on the tensile and flexural properties.

When the carbon fibers in the latex-containing mortar were replaced by stainless steel fibers (60 μm diameter, 5 mm length, $6 \times 10^{-5} \Omega \cdot \text{cm}$ electrical resistivity, 0.37 vol.%), an electrical response was observed under compression, though the plot of $\Delta R/R_0$ vs. strain was more noisy than in the carbon fiber case, probably because of the large diameter of the steel fibers. However, when the carbon fibers were replaced by polyethylene fibers (Spectra 900, 38 μm diameter, 5 mm length, 0.37 vol.%), no electrical response was observed. Thus, the conducting nature of the fibers is necessary for the electrical response to elastic or inelastic deformation.

CONCLUSION

Carbon fiber reinforced concrete was found to be an intrinsically smart concrete that can sense elastic and inelastic deformation and fracture. The signal provided is the change in electrical resistance, which is reversible for elastic deformation and irreversible for inelastic deformation and fracture. The presence of electrically conducting short fibers is necessary for the concrete to sense elastic or inelastic deformation, though the sensing of fracture does not require fibers. The fibers bridge the cracks and provide a conduction path. They do not need to touch one another. The electrical resistance increase is due to conducting fiber pull-out in the elastic regime, conducting fiber breakage in the inelastic regime, and crack propagation at fracture. The fractional change in resistance at fracture is higher under compression than tension, due to the higher ductility under compression.

REFERENCES

1. Pu-Woei Chen and D.D.L. Chung, *Smart Mater. Struct.* 2, 22-30 (1993).
2. Pu-Woei Chen and D.D.L. Chung, *Composites* 24, 33-52 (1993).

A MODIFIED TRANSMISSION LINE APPROACH TO THE ANALYSIS OF SUPERCONDUCTING MICROWAVE RESONATORS

EDWARD D. GOFF AND ROBERT J. WEBER

Microelectronics Research Center, Iowa State University, Ames, IA 50011

ABSTRACT

A technique for modeling a superconductor contacted piezoelectric microwave resonator is presented. A transmission line method of modeling the superconductor as a two fluid model is shown to agree with the London penetration depth, and is modeled to take into account the superconductor to normal transition. By including both the normal conductor effects along with the superconductor effects, crystal quality can be factored into this model using an analytical approximation. A two dimensional model for the superconductor, applying experimental results from $Y_1Ba_2Cu_3O_{7-x}$ for circuit elements, is analyzed. The superconducting layer is modeled as an electrical circuit in combination with an acoustical circuit to model its effect on a piezoelectric resonator. The acoustical equivalent of the superconductor including mass loading effects and terminations are taken into account in the Mason model acoustical equivalent circuit.

BACKGROUND AND OVERVIEW

The integration of piezoelectric and superconductive technologies will allow a greater range of possible microwave system applications to be fabricated on a smaller scale due to the increase in performance of the devices. The goal of this analysis is to model a hybrid superconductor piezoelectric resonator structure using transmission line theory. To accomplish this goal, an equivalent circuit must be set up which correctly approximates the entire structure. The structure to be simulated is a High-Temperature Superconductor / Aluminum Nitride / High-Temperature Superconductor resonator structure, hereafter abbreviated by HTSC - AlN - HTSC.

The calculation will be broken down into sections dealing with specific aspects of the analysis. The first section analyzed will be the equivalent inductance of the HTSC. The second section analyzed will be the terminating resistance at the free space boundary. The third section will be to add the Mason model to the circuit to model the piezoelectric resonator and the mass loading effects of the superconductor and the substrate. The results of this analysis are then presented. Figure 1 shows the electromagnetic model for the superconducting transmission line structure.

The results from this analysis agree well with predicted superconductor analysis, as well with superconducting theory. The penetration depth is found to be consistent with both measurements and this analysis.

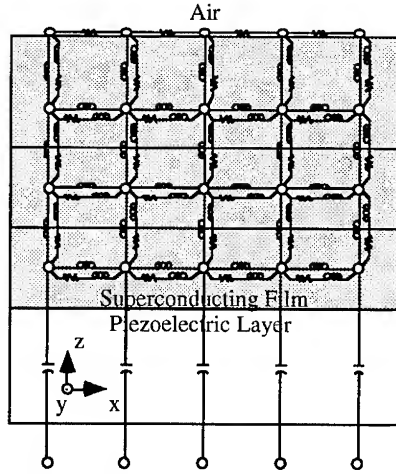


Figure 1: HTSC - AlN Resonator Equivalent Circuit Diagram

THEORY

Determining Equivalent Inductance For A Section Of Superconductor

The intent of the inductor analysis is to find an equivalent circuit element that may be used in the transmission line analysis. Using a section of material with dimensions of dx , dy , and dz , a current is introduced and assumed to flow in only the x - direction. There is assumed to be no magnetic field variation in the y - direction, or $\partial H_y / \partial y = 0$.

The magnetic energy stored in a section of material is given in equation 1 as

$$W_M = \frac{1}{2} \iiint_V \vec{B} \cdot \vec{H} \cdot dv = \frac{1}{2} \iiint_V \mu H^2 \cdot dv \quad (1)$$

Setting equation 1 equal to the energy stored in an inductor we obtain

$$LI^2 = \iiint_V \mu_o H^2 \cdot dv \quad (2)$$

where $\vec{B} = \mu \vec{H}$, $I = \iint_s \vec{J} \cdot d\vec{s}$, and $\mu = \mu_o = 4\pi \times 10^{-7}$ H/m in HTSC. Along with Ampere's Law in integral form, we now have two constitutive relations between the magnetic fields and the current passing through the sample. Analyzing the differential current traveling in the x -direction, and approximating the integrals as differentials while assuming that $\partial H_y / \partial y = 0$, Ampere's law can be approximated as

$$J_x(z) \approx -\frac{\partial H_y}{\partial z} \quad (3)$$

Substituting equation 3 into equation 2 we can now eliminate the current from the previous equations:

$$L \left(\iint_s -\frac{\partial H_y}{\partial z} \cdot dy \cdot dz \right)^2 = \iiint_v \mu_o H_y^2 \cdot dx \cdot dy \cdot dz. \quad (4)$$

Assuming a solution of the form $\vec{H} = \vec{H}_o e^{-\alpha z}$, we can solve equation 4 for the equivalent inductance in the circuit. Expanding the exponentials and simplifying, the resulting inductance is

$$L_x = \frac{\mu_o \Delta x}{\alpha^2 \Delta y \Delta z} \quad (5)$$

where L_x is the incremental inductance of a current flowing in the x - direction. A similar calculation was performed for L_z . These results are for a sample that is entirely superconducting. In this analysis, the case when the sample is not *entirely* superconducting will be investigated, since for most HTSC there remains a small finite resistance that will be accounted for in the transmission line analysis. The effective area of the superconductor will be treated as being decreased by a percentage equal to the ratio of superconducting to non-superconducting regions, i.e. equation 5 becomes

$$L_{x-sc} = \frac{\mu_o \Delta x}{\alpha^2 K \Delta y \Delta z} \quad (6)$$

where K is the ratio of superconducting to non-superconducting regions. Similarly, the non-superconducting region will have an inductive component and a resistive component to its impedance given by

$$L_{x-NSC} = \frac{\mu_o \Delta x}{\alpha^2 (1-K) \Delta y \Delta z}, \quad R_{x-NSC} = \frac{\rho \Delta x}{(1-K) \Delta y \Delta z} \quad (7)$$

where ρ is the resistivity of the superconductor just before the sample passes through the transition and becomes superconducting. [1]

Determining The Equivalent Resistance For The Air-Superconductor Interface

The equivalent resistance as shown in Figure 1 at the free space boundary of the sample simulates the power lost into the half space that may be used in the transmission line analysis. Assuming an area $\Delta x \Delta y$, we will consider the power in free space at the boundary. Starting with the Poynting vector in the z direction, $P_z = E_x \times H_y$, we then use plane wave relations to relate the electric and magnetic fields in free space, $H_y = E_x / \eta$, where $\eta = \sqrt{\mu_o / \epsilon_o} = 377 \Omega$. Applying these principles to the Poynting vector we obtain

$$P_z = E_x \times \frac{E_x}{\eta} = \frac{E_x^2}{\eta} \quad (8)$$

where the actual power in the z - direction can be found by multiplying by the area, $\Delta x \Delta y$. Equating this result with the standard power equation for a resistor, $P = V^2/R$ where V is found by using Maxwell's equation in integral form as the voltage drop across a distance Δx , or

$$V = -\int \vec{E} \cdot d\vec{l} = -E_x \Delta x \quad (9)$$

Equating the power of a resistor with the Poynting vector power, we obtain the equivalent resistance,

$$R = \frac{\eta \Delta x}{\Delta y} \quad (10)$$

Mason Model Calculation

In Figure 1 there is a capacitor across the AlN structure. This is only partially correct, since there are other effects due to the piezoelectric resonator structure such as mass loading. In a piezoelectric, the electric field interacts with the crystal structure of the lattice creating stress and strain across the lattice. The model chosen is the Mason model and is shown in Figure 2.[2] The electrical connections shown in Figure 2 will connect to every port in the x - direction of the simulated structure between both the top and bottom superconductor layer. The elements in the circuit shown in Figure 2 are calculated from the acoustical properties of the materials involved.

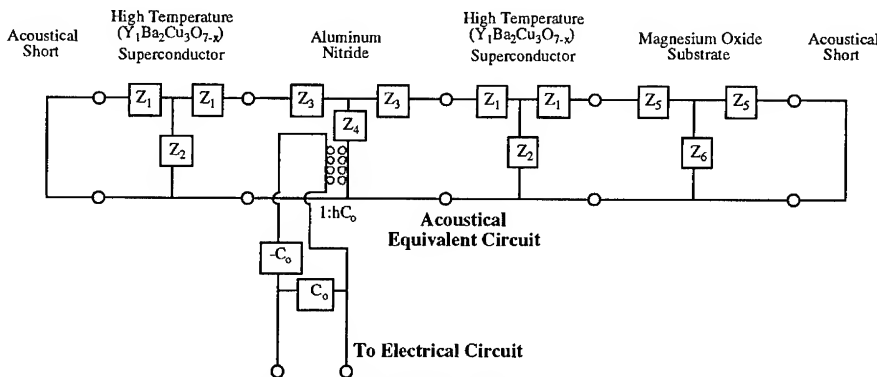


Figure 2: Mason Model Equivalent Circuit.

Note that both the piezoelectric and acoustic loading effects are taken into account in the Mason model, thus yielding a fairly accurate result. [2] The resulting electrical equivalent circuit for the Mason model is a reactance in parallel with a resistance. This circuit accurately models

the acoustic effects of the different layers, and introduces these effects correctly into the transmission line analysis.

To simulate this Mason model, a Libra^(tm) [3] circuit was designed that corresponds directly with Figure 2. Employing material constants for HTSC, AlN, and MgO, the circuit was simulated and the results were used to model the admittance at resonance. Since not all material constants are available for HTSC and to simplify the analysis of the structure, some approximations were made. The acoustical loss of the superconductor was assumed to be equivalent to that of Al and MgO was not included in the Libra simulation in order to an overmoded circuit response. The values for the real and imaginary admittance were found at the resonant frequency of 1 GHz and are equal to $Y_{\text{resonance}} = 707.88 + j64.60 \mu\text{S}$ for the area used. This is the acoustical equivalent to the HTSC - AlN - HTSC circuit for a $20 \mu\text{m} \times 20 \mu\text{m}$ square at the HTSC - AlN interface. This calculated result replaces the capacitor impedance of the AlN in Figure 1 and models the physical parameters of the piezoelectric.

RESULTS

FORTTRAN code was written taking all of these elements into account. The strategy used to solve this circuit was to input the admittance of each of the elements into the array, and then invert the array to obtain the impedances at each point in the matrix, $[Y]^{-1} = [Z]$. All the impedances are then referenced to the first upper HTSC node for a plane of reference. Assuming a 1A current passing into the sample, the potentials across the sample are equal to the impedance values of the Z matrix. Therefore, currents and the electric field potential may be found by

$$I = \frac{\Delta V}{Z} = \Delta V \cdot Y = (V_i - V_j) \cdot Y_{ij} \approx (Z_i - Z_j) \cdot Y_{ij} \quad (11)$$

$$E \approx \frac{\Delta V}{dx} \approx \frac{V_i - V_j}{dx} \approx \frac{Z_i - Z_j}{dx} \quad (12)$$

where i and j are adjacent node numbers in the calculation.

Values for the specific elements and some of the parameters for analyzing the circuit were found from the literature or were obtained from Libra. [4] The potential is shown in Figure 3 in the form of a contour plot, and the current is shown in Figure 4 in the form of a vector field plot. The conclusions that may be drawn from these plots are that the current in the superconductor remains near the lower edge of the sample near the AlN, and does not propagate above the superconducting penetration depth. As can be seen in the current density plot, there is very little current above the third tier of nodes, and in the potential plot, the values are even more remarkable. In the potential plot, the potential decreases rapidly both in the z - direction, as well as decreasing somewhat in the x - direction. These results verify the penetration depth in showing that the current does not flow in the upper regions of the superconductor.

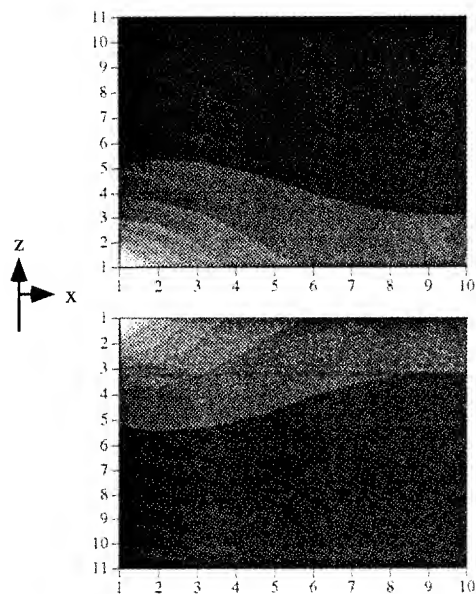


Figure 3: Potential of the HTSC Resonator Sample

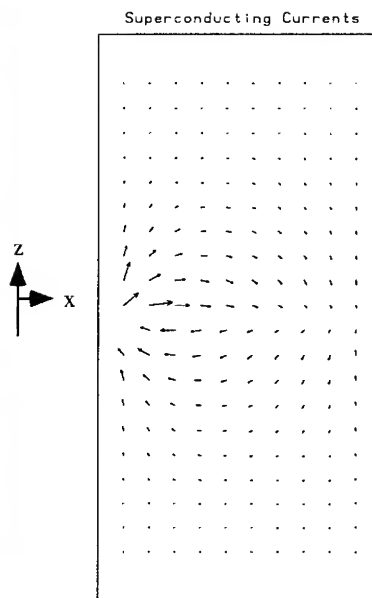


Figure 4: Current flow of the HTSC Resonator Sample

CONCLUSIONS

This theoretical presentation verifies that the penetration depth holds in microwave analysis of High Temperature Superconductors. The superconductor may be modeled using a transmission line model, while continuing to hold to the theoretical approximations. The Mason Model may be applied to High Temperature Superconductor contacted piezoelectrics to account for standard piezoelectric mass loading.

REFERENCES

1. D. W. Cooke, et al., J. Appl. Phys. **68** (5), 2514 (1990).
2. J. F. Rosenbaum, *Bulk Acoustic Wave Theory and Devices*, (Artech House, Boston, 1988), P. 167.
3. Libra (R) 4.0, (c) 1987-1992 EESOF Corporation.
4. H. Ledbetter and M. Lei., J. Mater. Res. **6** (11), 2253 (1991).

PRESSURE-SENSITIVE MICROVALVES MADE FROM POLYMER BRUSHES

E.M. SEVICK* and D.R.M. WILLIAMS**

* Department of Chemical Engineering, University of Colorado, Boulder, CO 80309-0424.

** Institute of Advanced Studies, Research School of Physical Sciences and Engineering, The Australian National University, Canberra, and Institute for Theoretical Physics, University of California at Santa Barbara, CA, 93106 and Department of Physics, University of Michigan, Ann Arbor MI 48109-1120.

ABSTRACT

We describe a novel microvalve, constructed from polymer chains end-grafted onto opposing surfaces of a narrow slit. The assembly of polymer chains acts as both sensor and valve for microflow control and bypasses the need to construct an external feedback mechanism. This microflow control results from densely grafted chains which repel one another and stretch away from the surface, forming a brush which acts as an elastic and impenetrable layer. The height of a sheared brush increases or decreases depending upon solvent quality, i.e the layer can show a negative Poisson's ratio. The discharge through the brush-lined conduit is a non-linear function of pressure enabling different modes of valve operation. For brushes which extend moderately into the inter-slit region the valve assembly maintains constant discharge over a wide range of pressure. For brushes which extend far into the inter-slit region the valve assembly cuts off flow above a critical pressure, limiting the maximum discharge.

1. INTRODUCTION

The physical properties of polymer brushes [1,2] are important in the modification of surfaces and the stabilization of colloidal properties. A polymer brush consists of a large number of polymers end-grafted onto a planar surface. The polymers are grafted so densely that they overlap strongly and are forced to stretch away from the surface, forming an elastic layer. Recent experiment and theory focus upon the response of such a brush to an applied tangential surface force. Klein *et al.* demonstrated that a pair of opposing brushes, slid past one another in the presence of a good solvent, experience a repulsive normal force [3-8]. This repulsion between sheared brush planes has been interpreted as a result of brush swelling under shear. In poor solvents, a sheared brush is predicted to shrink [9].

Here we study the response of two opposing brushes, in good solvent, to an applied pressure drop (Figure 1). The pressure differential results in laminar flow which imposes a shear stress on the brush, causing brush expansion. This brush swelling reduces the cross-sectional area and solvent flow, and thereby readjusts the prevailing shear stress. Both the tangential surface force and the brush swelling are determined self-consistently, resulting in a non-linear pressure-discharge relation.

It is convenient to describe this fundamental problem in terms of related applications. Experimental evidence for non-linear pressure-discharge relations exists in the ultracentrifugation literature, where membranes are "fouled" by adsorbed proteins [10-13]. There are several theories which explain the non-linear behaviour in terms of protein adsorption onto the exterior surface of the membrane and not within the internal pores. In contrast, the description presented here describes the non-linear pressure-discharge relation as a result of well-defined adsorption upon the internal pore surfaces. Rather than considering the disadvantageous process of pore fouling, we can consider the advantageous control of flow through these pores. The adsorbed polymer brush senses the shear force, responds by swelling, and thereby readjusts the shear, much like a series of sensors and valves used to control flow. Consequently, we can describe the system as a "brush-valve" whose pressure-sensitive response is the fundamental problem of interest [8].

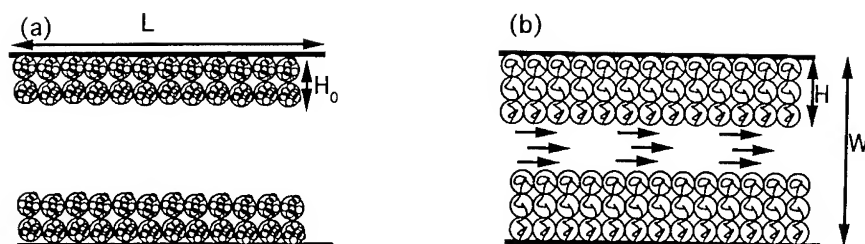


Figure 1:(a) The valve in the slit geometry. The polymer brushes, each of height H_0 , are grafted to the top and bottom of a slit of length L thickness W and width $Z \gg W$ normal to the page. (b) When a fluid flows through the slit the brushes swell (if the solvent is good) to a height $H > H_0$. The flow only penetrates the brushes weakly, so the hydrodynamic thickness of the slit becomes smaller under flow. The brush swelling produces a closing of the slit and a dramatic reduction in discharge.

The brush sense-and-respond function can be implemented as an unconventional microvalve. Microvalves have been successfully manufactured using “silicon” technology, i.e., by selectively etching a silicon wafer [14-17]. These silicon microvalves are essentially microscopic versions of macroscopic valves and have gaps of order $100\mu\text{m}$; i.e., about 10^4 times larger than the brush-valves discussed here. Polymer brushes are attractive alternative materials for two reasons. First, they are soft, i.e., their moduli [18] are small and they thus respond sensitively to pressure. Secondly, they can exhibit a negative Poisson’s ratio [19]; i.e., they expand under shear, providing the cut-off and constant discharge control described in this paper. The proposed brush-valves have five potential advantages over conventional valve technologies.

- (1) The polymer brush is both the sensor and the valve. The brush responds automatically to flow without any external feedback control.
- (2) The valve operates in very narrow tubes of the order of hundreds to thousands of Angstroms, where traditional valve technologies fail.
- (3) The valve is easily fabricated through self-assembly of end-functionalized polymers or block copolymers. Polymers can be adsorbed onto internal surfaces of porous media with pore sizes of order $100 - 4000\text{\AA}$ [20], or by microphase separation of a block copolymer matrix [21-24].
- (4) The valves should be less expensive to manufacture than silicon microvalves [14-17]. Moreover, the microvalves can be utilized in parallel, as for example, polymer brushes lining the pores of a micro-filtration membrane.
- (5) Through choice of polymer and solvent quality, the valve can be fabricated to either open at low pressure and close at high pressure or vice-versa.

These microvalves should have a number of practical applications, particularly in filtration systems, ink-jet printing, controlled drug release, and in systems of medical and biological importance. In particular the fact that the valve can limit the discharge to some maximum value, or can set the discharge to some steady value, might well prove useful in drug release systems. The reader should note that the brush-valve described in this paper is pressure sensitive and bi-directional, i.e., solvent can flow in either direction with equal ease.

Our description of brush-valves is limited to the case of good solvents where brush

swelling, rather than brush compression, occurs with shear. The reader should keep in mind that most of the numerical factors in the analysis are not accurate, but that our study should nevertheless provide a qualitative description of brush-valve operation.

2. BRUSH SWELLING AND VALVE OPERATION

In this section we discuss briefly the swelling under shear of a planar brush [25,5]. Each tethered chain in a brush can be pictured as a connected sequence of blobs [26]. The blobs are of radius $\xi = R_F^{5/2}/L^{3/2}$, where R_F is the Flory radius and L is the end-to-end distance of the chain. Within each blob the monomers are locally correlated as in a Flory excluded-volume chain. For distances larger than the blob size, the blobs act as hard spheres. The number of blobs per chain is given by $N_b = (L/R_F)^{5/2}$. The brush is an assembly of chains end-grafted onto the grafting plane with density $1/d^2$ where d is the distance between grafting points. The grafting density is assumed to be large, i.e. the chains overlap. Here we usually assume there are many blobs per chain, although experimentally N_b is often not much larger than unity.

When the brush assembly is sheared, the free chain-ends are displaced distance X in the x direction, the chain is tilted, and the end-to-end distance, L , is increased. The number of blobs per chain, N_b , increases with L , further enhancing the excluded volume interaction between blobs. As a consequence the brush will swell: the height of the brush changes from H_0 to H . This is the mechanism for brush swelling proposed by Barrat [5,25]. To analyze the expected degree of swelling and chain tilt with applied shear, the free energy of a chain in the brush assembly can be expressed [5,25,8] as

$$F(R_F/H_0)^{5/2}/kT = \frac{1}{2}(\Delta^2 + \epsilon^2)^{5/4} + \frac{5}{2}\Delta^{-1}(\Delta^2 + \epsilon^2)^{1/4} - f\epsilon. \quad (1)$$

The first term represents the stretching penalty of a Gaussian chain of blobs [27] that opposes brush swelling and shear, the second term is the excluded volume interactions amongst blobs that promote brush swelling, and the final term is the work performed by the shearing force $F_{||}$ which tilts the chains, displacing the free chain-end distance X in the x direction. Here $H_0 = (2/5)^{1/3}d^{-2/3}R_F^{5/3}$ is the unsheared brush height, and $\epsilon \equiv X/H_0$ and $\Delta \equiv H/H_0$ describe x -displacement and swelling under shear.

Minimizing the free energy under shear yields two equations, $\partial F/\partial \epsilon = 0$ and $\partial F/\partial \Delta = 0$, which can be combined to give an explicit relation between the dimensionless shearing force, f , and swelling, Δ [8]

$$f = \frac{5}{2}\Delta^{-3/2}(\Delta^3 - 1)^{1/2}(2 - \Delta^3)^{-3/4} \quad (2)$$

which has the form shown in figure (2). Here $f \equiv F\xi_0/kT$ where $\xi_0 = R_F^{5/2}/H_0^{3/2}$ is the unsheared blob size. Also of interest is the blob size dependence on swelling. This is [8]

$$\xi/\xi_0 = (H_0/L)^{3/2} = \Delta^{-3/2}(2 - \Delta^3)^{3/4}. \quad (3)$$

Having described the swelling of a single brush, we now go on to describe the valve operation for a double-brush system. For simplicity we study a channel formed from two parallel grafting planes of very large aspect ratio, i.e., the planar dimensions $L \times Z$ are large compared with the separation between planes, W . Flow is in the x -direction and is caused by a pressure difference between $x = 0$ and $x = L$ [28]. Consider the grafting planes lined with polymer brushes of height H (Figure (1)).

To a first approximation the fluid penetrates only weakly into the brushes and so can be described as laminar flow through a channel of effective height $W - 2H$. The dimensionless discharge, $q \equiv 6Q\eta\xi_0^3/(kTW^2Z)$ [28] is then

$$q = p(1 - \beta\Delta)^3, \quad (4)$$

where $p \equiv \frac{1}{2}WP'\xi_0^3/kT$ is a dimensionless pressure, $P' \equiv -(dP/dx)$, and $\beta \equiv 2H_0/W$ is

fraction of the gap taken up by the polymer brush in the absence of shear. Here η is the fluid viscosity and P is the pressure drop between $x = 0$ and $x = L$, and Q is the discharge. Equation (4) contains the pressure-discharge relation, but is not yet complete since the dependence of Δ on p is unknown. Our aim here is to find $\Delta(p)$.

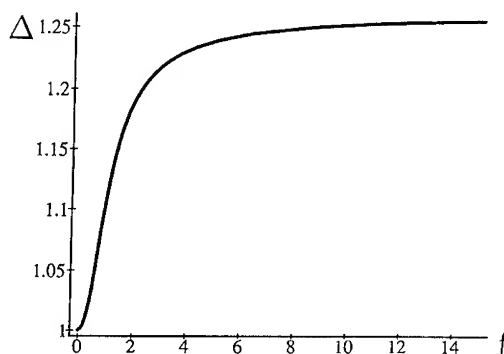


Figure 2: The dimensionless height of the brush Δ versus the dimensionless shear force per chain, f , according to the Barrat mechanism (equation (2)). Initially the height grows as the square of the force. At very large forces the height grows to a maximum of about 125% of the unsheared height.

The novel feature of this assembly is that H is a function of the pressure drop, P . This is particularly important since the discharge depends on the third power of $W - 2H$. Even a weak dependence of H on P provides a strong P dependence on the discharge, Q . Both theory [5,6] and experiment [3] indicate that H increases with increasing shear stress if the fluid is a *good* solvent for the grafted chains. As a result, the cross sectional area of the brush-lined slit diminishes with pressure. The discharge through the brush-lined channel is then a non-linear function of P . Equation (4) contains the pressure-discharge relation, but is not yet complete since the dependence of Δ on p is unknown.

The total shear force on the brush is [8]

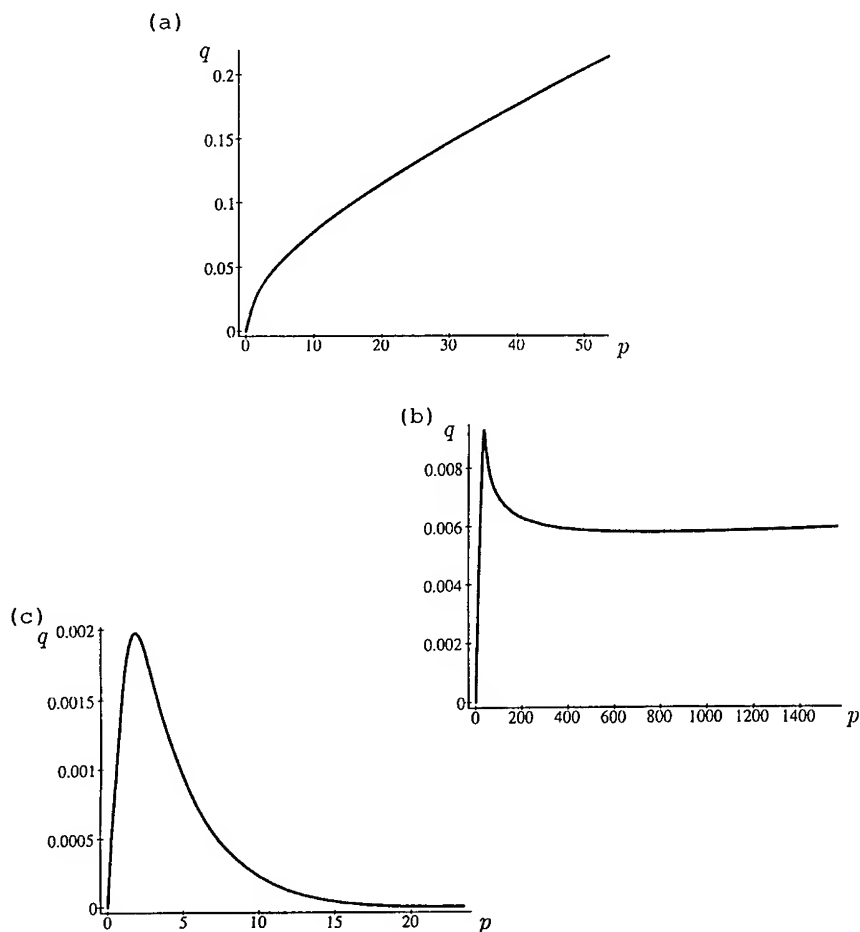


Figure 3: The dimensionless discharge q versus the dimensionless pressure p for various values of $\beta = 2H_0/W$, one for each regime. (a): $\beta = 0.7$. The gap is initially wide. At low pressures the height of the brush is not changed significantly by the flow. The discharge is thus proportional to the pressure. At high pressures the force on the brush is large and it expands to its maximum height of $2^{1/3}H_0$. However, there is still a large gap and the discharge is again proportional to the pressure. Intermediate to these two cases the brush expands. (b): $\beta = 0.79$. The gap is initially narrower than in (a). The discharge grows rapidly to a maximum, declines and then levels off to a constant value. It is constant over a wide range of pressures. Eventually the discharge increases again with pressure but this occurs off the graph. For this value of β the brush grows in height, but as in case (a) it never closes the channel completely. The slit acts as a "constant-discharge" valve. (c): $\beta = 0.85$. Initially there is a narrow gap. The brush thus expands to fill the gap and the flow is cutoff entirely at a critical pressure $p \approx 25$. The slit acts as a pressure sensitive valve - only letting flows through which have a small pressure gradient. In doing so it also limits the discharge to a maximum value.

$$F_{\parallel} = \xi^2 P' [\frac{1}{2}W - \xi] \approx (1/2)W P' \xi^2. \quad (5)$$

The blob size decreases with shear-induced swelling and extension and, from equation (5), the shearing force will also diminish with swelling. Using equation (3) and the dimensionless pressure $p \equiv \frac{1}{2}W P' \xi_0^3 / kT$, (5), can be written as

$$f = F_{\parallel} \xi_0 / kT = \frac{1}{2}W P' \xi_0 \xi^2 / (kT) = p(\xi / \xi_0)^2 p(\frac{2 - \Delta^3}{\Delta^2})^{3/2}. \quad (6)$$

A relation between the dimensionless pressure, p , and swelling, Δ , is constructed from the thermodynamic $f - \Delta$ relation given in equation (2) and the mechanical $f - \Delta$ relation of equation (6). It is

$$p = \frac{5}{2} \Delta^{3/2} (\Delta^3 - 1)^{1/2} (2 - \Delta^3)^{-9/4}. \quad (7)$$

This together with the relation (4)

$$q = p(1 - \beta \Delta)^3 \quad (8)$$

provides the implicit relation between pressure and discharge, for brush-valve of equilibrium brush height described by β . These two equations give the $q - p$ curve parametrically. To plot the $q(p)$ curve we merely fix β and vary Δ .

The $q(p)$ curves are plotted in Figure 3 for three characteristic regimes, depending upon the equilibrium height of the brush relative to the conduit spacing, i.e. β . For small brush heights, $\beta < \beta_1 \equiv 0.78$ [29], the dimensionless discharge increases monotonically with dimensionless pressure as would be expected in the absence of a brush. The flow differs from laminar flow in that there are two distinct regions of flow resistance: at small pressures the resistance is low, but increases at some crossover point, Figure 3a. Within a small window of moderate brush heights, $\beta_1 < \beta < \beta_c \equiv 2^{-1/3} = 0.79$, the discharge increases rapidly with initial pressure, attains a maximum followed by a plateau region that persists over a wide range of pressure with only mildly increasing q , Figure (3b). The plateau region corresponds a constant-flow valve where perturbations in pressure affect the discharge insignificantly. For larger brushes, $\beta > \beta_c$, the discharge increases with initial increase in pressure, reaches a maximum and falls to zero discharge. The cut-off pressure, i.e. the pressure at which the discharge zero, is found by setting $\Delta = \beta^{-1}$ in (8) and (7), giving

$$p_c = \frac{5}{2} \beta^{15/4} (1 - \beta^3)^{1/2} (2\beta^3 - 1)^{-9/4} \quad (9)$$

The ratio brush height to gap, β , is a design parameter which determines the cut-off pressure,

p_c , in the range $\beta > 0.80$, Figure (4).

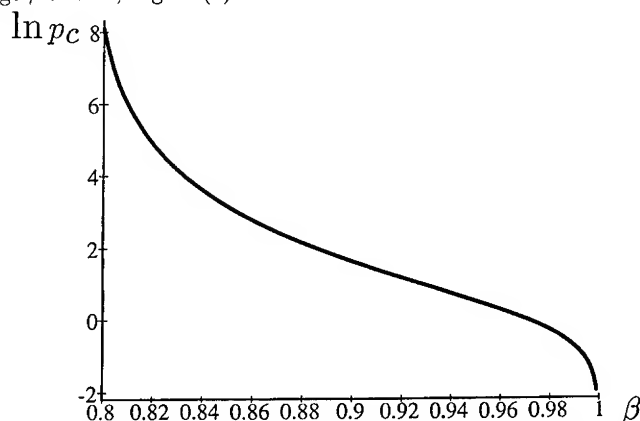


Figure 4: The natural log of the dimensionless cutoff pressure $\ln(p_c)$ versus the gap parameter, β , for a valve operating in mode 3. For small initial gaps $\beta \approx 1$ the cutoff pressure is very small, but for gaps approaching the critical value, $\beta_c = 2^{-1/3}$, the critical pressure can become very large.

The dimensionless pressure $p = \frac{1}{2}WP'\xi_0^3/kT$ is an important parameter in valve design. The term kT/ξ_0^3 is the osmotic pressure in the brush [26] and also the elastic modulus of the brush [18]. As the interesting valve behaviour occurs for values of p on the order of 1, (Figure 4), the operating range of P' must be roughly $kT/(W\xi_0^3)$. In other words, the valve effects occur when the applied force per unit area of the brush equals the osmotic pressure. Loosely grafted brushes are "soft", i.e., they have large blob sizes ξ_0 , small moduli, and are sensitive to small fluctuations in pressure. In contrast, more densely grafted brushes have smaller blob sizes ξ_0 , larger elastic moduli, and consequently do not respond as dramatically to pressure fluctuations. The appropriate pressure gradient $P' = kT/(W\xi_0^3)$ is clearly very sensitive to the blob size ξ_0 , and hence to the grafting density. To examine some numerical examples we take $W \sim \xi_0$, so $P' \approx kT/\xi_0^4$. For a weakly grafted brush $\xi_0 \approx 1000\text{\AA}$ and $P' \approx 4 \times 10^7 \text{Pa/m} \approx 10^2 \text{atm/m}$. For a membrane of thickness 1000\AA this corresponds to a pressure drop of 10^{-5}atm . However, for a more densely grafted brush with blob size $\xi_0 = 100\text{\AA}$ and again with $L = 1000\text{\AA}$ the pressure drop is much larger, 0.1atm .

3. VALVE MANUFACTURE AND DISCUSSION

There are several possible methods of fabricating the microvalves discussed above. In previous studies, polymer brushes have been constructed by adsorbing end-functionalized chains onto well defined surfaces. Klein adsorbed polystyrene with zwitterionic end-groups onto a pair of mica sheets separated 95-155 nm, in toluene, a good solvent [3]. For many practical applications the solvent will be water and hence water-soluble polymers must be used. Auroy et al. [20] adsorbed hydroxyl capped poly(dimethylsiloxane) onto a chromatographic silica support with well defined pores of diameter 4000\AA in a variety of solvents. Repeating Auroy's fabrication using a medium with uni-directional pores, i.e. a membrane, would result in a parallel array of microvalves. Such an array would facilitate measurement of microvalve function. Polymethylmethacrylate chains have also been end-grafted directly onto membrane pores [30], although no flow measurements for this system have yet been reported. From a practical point of view the reader might worry about chains being pulled off the surface by a flow. As discussed in [5] and [4] this appears to be unlikely for chains

which have zwitterionic stickers.

Besides end-functionalized polymers, diblock copolymers will assemble into a brush under appropriate solvent conditions. In a solvent poor for the shorter block, the shorter block will adsorb to a sorption plane and the longer block for which the solvent is good, will extend away from the plane forming a brush assembly. Webber *et al.* [31] have adsorbed diblock copolymers onto pores, but have used brush thicknesses which are much smaller than the pore radius. Finally, random copolymers having multiple functional or sorptive sites along the backbone may prove promising. Although the polymeric layer would be comprised of loops and trains rather than brush bristles, the excluded volume effect should still swell the layer under shear. The procedure runs the hazard of blocking the pore if a significant number of chains bridge opposing surfaces.

In this paper we have described the operation and fabrication of a pressure-sensitive switch or valve using polymer brushes. The microvalve control results from the swelling of polymer brush with shear. Our discussion was limited to the Barrat swelling mechanism and is approximate. However, the qualitative conclusions we draw should be general. For brushes which fill the gap or conduit moderately, the brush pair acts as a constant-discharge microvalve. For brushes which nearly fill the gap, i.e., > 80% of the distance between grafting planes, the brush pair behaves as a cut-off microvalve, limiting the maximum discharge. Loosely grafted or "soft" brushes respond more dramatically to pressure than densely grafted brushes, and are expected to provide the most sensitive valves. In the limit of very dilute grafted chains, below overlap, the flow distortion is described in a recent paper of Brochard-Wyart [32].

Jacob Klein is warmly thanked for his useful comments on the manuscript. EMS acknowledges financial support from Junior Faculty Development Award, administered by the Graduate School at University of Colorado at Boulder. D.R.M.W was funded by NSF PHY89-04035, DNR-91-17249, DMR-92-57544, by a QEII research fellowship, and by a PRF grant.

REFERENCES

- [1] A. Halperin, M. Tirrell and T.P. Lodge, *Adv. Polymer. Sci.* **100**, 100 (1992).
- [2] S.T. Milner, *Science* **905**, 251, (1991).
- [3] J. Klein, D. Perahia and S. Warburg, *Nature* **352**, 143 (1991).
- [4] J. Klein *Pure Appl. Chem* **64**, 1577 (1992).
- [5] J.-L. Barrat, *Macromolecules* **25**, 832-834 (1992).
- [6] V. Kumaran, *Macromolecules* **26**, 2464 (1993).
- [7] K. Sekimoto and L. Leibler, *Europhys. Lett.* **23**, 113 (1993). Note that this paper appears to contain an error which invalidates their central result: K. Sekimoto and Y. Rabin, *Europhys. Lett.* **27**, 445 (1994).
- [8] E.M. Seveck and D.R.M. Williams, *Macromolecules* **27**, 5285 (1994).
- [9] D.R.M. Williams, *Macromolecules* **26**, 5806 (1993).
- [10] J.A. Howell, V. Sanchez and R.W. Field, *Membranes in Biprocessing: Theory and Applications*; (Chapman and Hall Publishers, London, 1993).
- [11] M.S. Le and J.A. Howell *Chem. Eng. Res. Des.* **62**, 373 (1984).
- [12] J.A.G. Weldring and K. van't Riet, *J. Membrane Sci.* **38**, 127, (1988).
- [13] M.K. Ko and J.J. Pellegrino, *J. Membrane Sci.* **74**, 141 (1992).
- [14] D. Bosch, B. Heimhofer, G. Muck and H. Seidel, *Sensors and Actuators-A Physical* **37**, 684 (1993).
- [15] J. Tirén, L. Tenerz and B. Hök, *Sensors and Actuators* **18**, 389 (1989).
- [16] A. Emmer, M. Jansson, J. Roeraade, U. Lindberg and B. Hök, *J. Microcolumn Separations* **4**, 13 (1992).
- [17] M. Esashi, S. Shoji and A. Nakano, *Sensors and Actuators* **20**, 163 (1989).
- [18] (a) G.H. Fredrickson, A. Ajdari, L. Leibler and J.-P. Carton, *Macromolecules* **25**, 282 (1992). (b) D.R.M. Williams, *Macromolecules* **26**, 5096 (1993). (c) S.A. Safran and J. Klein, *J. Phys. Paris II* **3**, 794 (1993).

- [19] R.S. Lakes, *R.S. Advanced Materials* **5**, 293 (1993).
- [20] P. Auroy, L. Auvray, and L. Leger, *Macromolecules* **24**, 2523, (1991).
- [21] A. Halperin and E.B. Zhulina, *Europhys. Lett.* **16**, 337 (1991).
- [22] E.B. Zhulina and A. Halperin, *Macromolecules* **25**, 5730 (1992).
- [23] A. Halperin and E.B. Zhulina, *Prog. Colloid Polym. Sci.* **90**, 156, (1992).
- [24] A. Halperin and D.R.M. Williams, *Macromolecules* **26**, 6652 (1993).
- [25] Y. Rabin and S. Alexander, *Europhys. Lett.* **13**, 49 (1990).
- [26] P.G. de Gennes, *Scaling Concepts in Polymer Physics*; (Cornell Univeristy Press: Ithica, N.Y., 1979).
- [27] P.A. Pincus, *Macromolecules* **9**, 386 (1976).
- [28] L.D. Landau and E.M. Lifshitz, *E.M. Fluid Mechanics*, (Pergamon Publishers, Oxford, 1987).
- [29] β_1 is obtained as follows. In general the q versus p plot has a maxima and a minima. These are given by solutions of $0 = dq/dp$ which implies $0 = dq/d\Delta = (dp/d\Delta)(1 - \beta\Delta) - 3\beta p$. This equation only has two real roots for $\beta > \beta_1$. For $\beta < \beta_1$ there are no real roots and the $q(p)$ relation is monotonic.
- [30] H. Yamagishi, K. Saito, S. Furusaki, T. Sugo, F. Hosoi and J. Okamoto, *J. Membrane Sci.* **85**, 71 (1993).
- [31] R.M. Webber, J.L. Anderson, and S.J. Myung, *Macromolecules* **23**, 1026 (1990).
- [32] F. Brochard-Wyart, *Europhys. Lett.* **23**, 105 (1993).

LIGAND-RECEPTOR CONTACT INTERACTIONS USING SELF-ASSEMBLED BILAYER LIPID MEMBRANES

A. LEITMANNOVA OTTOVA AND H. TI TIEN

Membrane Biophysics Laboratory (Giltner Hall), Department of Physiology
Michigan State University, East Lansing, MI 48824 (USA)

ABSTRACT

Biological membranes play a crucial role in signal transduction and information processing as well as in energy conversion. This is owing to the fact that most physiological activities involve some kind of lipid bilayer-based receptor-ligand contact interactions. There are many outstanding examples such as ion sensing, antigen-antibody binding, and ligand/voltage-gated channels, to name a few. One approach to study these interactions *in vitro* is facilitated by employing artificial bilayer lipid membranes (BLMs). We have focused the efforts on ion and/or molecular selectivity and specificity using newly available self-assembled BLMs on solid support (i.e., s-BLMs), whose enhanced stability greatly aids in research areas of membrane biochemistry, biophysics and cell biology as well as in biosensor designs and molecular devices development. In this paper, our current work along with the experiments carried out in close collaboration with others on s-BLMs will be presented.

INTRODUCTION

The experimental bilayer lipid membrane (BLM) has been used as a model of biological membranes since its inception in 1960. In particular, the BLMs have been used to elucidate the molecular mechanisms of biomembrane function [1-3]. The BLM system, however, has one major drawback in that it is notoriously unstable, rarely lasting more than a few hours [3,4]. As a result, many attempts have been made to stabilize this extremely delicate lipid bilayer structure for fundamental studies and practical applications. In this connection, the first report was published in 1978 describing the formation of supported BLMs in the μM pores of polycarbonate filters with much improved stability to both chemical and mechanical disturbance [5,6]. For practical biosensors, a self-assembled bilayer lipid membrane (s-BLM) on a nascent metallic surface was later developed [4, see Ref. 7 for a review]. Other researchers have reported similar and/or related systems [8-11]. This new type of s-BLM-based probes is destined for micro-electronic fabrication. The present paper is mainly concerned with our recent experiments and the work on s-BLMs done in collaboration with others [12-25].

MATERIALS AND METHODS

Preparation and Characterization of Supported Bilayer Lipid Membranes (s-BLMs). Bilayer lipid membranes (or lipid bilayers) on solid support have been formed by a number of methods including the two-consecutive step technique as follows: Step (i) placing a Teflon-coated metal wire (e.g., Pt, stainless steel or Ag) to be cut in contact with a BLM-forming lipid solution and then cut it with a sharp knife and, Step (ii) immersing the lipid layer that has adsorbed onto the metal wire surface into an aqueous solution. For the best cutting of metal wires, a miniature guillotine has been used, where the sharp knife is moved vertically onto the wire placed on a flat surface and immersed in a lipid solution [see Ref. 12 for a summary of the s-BLM techniques]. Typically we used either a 1% glycerol dioleate in squalene or 1% phospholipid (lecithin) in n-

decane. Into these s-BLMs, three classes of compounds have been embedded as follows: (a) Electron acceptors, donors, and mediators including highly conjugated compounds such as meso-tetraphenylporphyrins (TPP), metallo-phthalocyanines (PLC), TCNQ (tetracyano-*p*-quinodimethane), TTF (tetrathiafulvalene), BEDT-TTF (*bis*-ethyldithio-tetrathiafulvalene), and tetraseleno-fulvalene), (b) Redox proteins and metalloproteins such as cytochrome *c*, and iron-sulfur proteins (ferredoxins and thioredoxins). Also included in this class are compounds partaking in ligand-receptor contact interactions; specifically, the ligand may be a substrate, an antigen, a hormone, ions, or an electron acceptor or a donor, and the corresponding receptor embedded in s-BLM may be an enzyme, an antibody, a protein complex, a carrier, a channel, or a redox species [1,3,4], and (c) Fine semiconductor particles (formed *in situ*) such as CdS, CdSe, and AgCl [7]. We have worked with some of these compounds in the past in conjunction with conventional BLMs. Hence, methodologies developed for *in situ* formation of semiconductor particles on conventional BLMs can be applied to s-BLM systems. Mention should be made that in s-BLMs, albeit attractive for certain purposes as described in this paper, the metallic substrate precludes ion translocation across the lipid bilayer. Therefore, the pursuit of a simple method for obtaining long-lived, planar BLMs separating two aqueous media has been an elusive one until now (H. Yuan, S. Hua and H. T. Tien, results of 1991-93, to be published). A brief description of forming a planar BLM on agar gel will be given below.

Techniques for agar gel supported BLMs. The formation procedure consists of three steps. In the first step, a chlorided Ag wire (Ag/AgCl) is inserted into a Teflon tubing which has been previously filled with a mixture of agar and KCl solution saturated with AgCl. The AgCl electrode and the filled Teflon tubing are glued together with wax at the point of insertion. In this way an Ag/AgCl-Teflon tubing salt bridge (sb) is constructed. In the second step, the tip of the other end of the Teflon salt bridge is cut *in situ* while immersed in a BLM-forming solution with a sharp knife, as done with the s-BLM technique. In the third and last step, the Ag/AgCl-Teflon salt bridge with the tip freshly coated with lipid solution is then immersed in 0.1 M KCl solution in the cell chamber. Alternatively, the second step described above may be carried out in air and then the freshly cut end of the salt bridge is immediately immersed in the lipid solution for a few minutes. In either case, the cell chamber filled with an appropriate aqueous solution (e.g., 0.1 M KCl) contains a Ag/AgCl reference electrode and a Ag/AgCl-Teflon salt bridge with a self-assembled BLM at its end. The lead wires of the two electrodes are connected to the measuring instrumentation [26]. In this connection, it should be noted that the salt bridge (sb) shown in Fig. 1 may be identified as items 1 and 2, thereby eliminating one of the chambers.

Electrical measurements. For studies on BLMs and experiments involving cyclic voltammetry, a Lucite block containing two adjacent 2 cm diameter chambers (8 ml), one of which holds a 10 ml Teflon cup, was used. The Teflon cup was referred to as the inside, and the other chamber as the outside. Earlier, the voltammograms of the BLM was obtained using an X-Y recorder fed by a picoammeter and the voltage generator (Princeton Applied Research, Universal Programmer Model 175). The voltage from the programmer was applied through the potentiometer to the calomel electrode (SCE) immersed in the inside solution. Another SCE immersed in the outside solution was connected to the picoammeter. The important feature of the setup was a very weak dependence of its input voltage on the current being measured. This means that the current was measured under "clamp voltage" with accuracy ± 1 mV. We have also used a three-electrode system for obtaining voltammograms in the following configuration: one calomel electrode (SCE) is placed in the Teflon cup and two other calomel electrodes are on the outside. An EC/225 Voltammetric Analyzer (IBM) in the cyclic voltammetry mode, in conjunction with an x-y

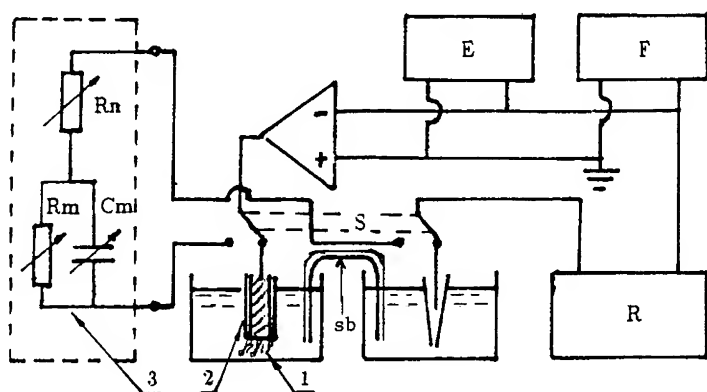


Fig. 1. A block diagram of the setup for cyclic voltammetry experiments of s-BLMs and sb-BLMs (from Ref. 20). 1 s-BLM. 2 Teflon-coated metallic wire. 3 BLM simulator. E electrometer. F Functional Generator. R x-y Recorder. S Switch.

recorder, was also used at times. With these setups, we were capable of studying the basic electrochemistry of membranes. For s-BLMs or sb-BLMs, the essential setups have been used. Additionally, a new setup of different design (Fig. 1) is used in order to measure the electrical parameters more accurately [20]. Briefly, an ideal BLM equivalent circuit is represented, as previously, in which a R_m is connected in parallel with a C_m . Since it is known that the current across R_m increases with the scan rate, the total current (I_t) is then given by

$$I_t = IR + I_c = V/R_m + C_m A \quad (1)$$

where A is the area of the BLM, $I_c = C_m dV/dt = C_m A$, and $I_m = V/R_m$. Thus, It is a straight line with slope = $1/R_m$ and intercept = $C_m A$. When the direction of the scan is suddenly reversed, the polarity of I_c drops down steeply. The voltammetric curve obtained by such a cycle is a parallelogram from which the R_m and C_m can be evaluated by the slope and intercept, respectively. However, the measured voltammetric curves of s-BLMs are not parallelograms. Instead, they are rising curves of certain regions. Since the performance of the instrument (Multi-function Analyzer (Model Ji-100, Sino Jinke Electronics Co., Ltd. Tianjin, PRC) has been found to be correct, the difference must be due to the assumed equivalent circuit, which needs some modification. The total impedance of the whole circuit except the R_m , C_m is the distributive capacitor (on the order of tenth of pF) of the circuit. Using this equivalent circuit, the voltammetric curve obtained from the s-BLM as well as sb-BLM experiment may be better evaluated, the details of which will be published elsewhere [20].

RESULTS AND DISCUSSION

Embedding of ferrocene on s-BLMs: an amperometric sensor of ferri-/ferro- cyanide ions. The redox reactions for a solid supported BLM containing vinyl-ferrocene as an electron mediator have been investigated using cyclic voltammetry. The results have shown that (i) ferrocene can be very easily embedded in the lipid bilayer on the surface of a metallic wire (s-BLM) system. This demonstrates that the s-BLM system offers a novel approach to the electrode modification by simple way of immobilization of compounds within BLM, and (ii) ferrocene in a bilayer lipid membrane increases about two orders of magnitude of the potassium ferri-/ferrocyanide ion sensitivity more than that of the platinum electrode [14]. Recently, substituted ferrocenes were incorporated into s-BLMs on Pt support and investigated using the cyclic voltammetry [25].

Hydrogen peroxide-sensitive s-BLMs. As described previously [1,3,7], the embedding of appropriate active molecules (modifiers) into the matrix of the lipid bilayer should be able to impart the functional characteristics of s-BLMs. We chose TCNQ (tetracyanoquinodimethane) and DP-TTF (dipyridyl-tetra- thiafulvalene) as modifiers because of their properties as typical electron acceptor and donor molecules, respectively. It was found that DP-TTF could improve not only the stability but also increased the range of s-BLM's sensitivity to hydrogen peroxide. In contrast, TCNQ-containing s-BLMs did not show much responses to H_2O_2 . This was not entirely unexpected since TCNQ should behave as an electron acceptor [16].

Modified s-BLMs as pH sensors. Of all the ions crucial to the functioning of cellular processes there is the hydrogen ion (H^+) which plays the leading role in enzyme catalysis and membrane transport. Thus, it is not surprising that, the measurement of pH is of the utmost importance. Currently, the pH glass electrode is routinely used in chemical and clinical laboratories. However, the large size and fragility of pH glass electrodes preclude their use in many situations such as *in vivo* cell studies and in monitoring membrane boundary potentials. For example, the hydrolysis of membrane lipids by phospholipid enzymes (lipases A and C) changes the boundary potential of BLM (or cell membrane) as a result of the local pH change. Additionally, it has been known for many years that BLMs formed from chloroplast extracts exhibited Nernstian behavior as a function of pH [1]. These observations suggest that s-BLMs can be used as a pH probe in membrane biophysical research and in biomedical fields where the conventional glass electrode presents many difficulties. To test our concept, we incorporated a number of quinonoid compounds (chloranils) into s-BLMs. We have found that, indeed, s-BLMs containing either TCOBQ (tetrachloro-o-benzoquinone) or TCPBQ (tetrachloro-p-benzoquinone) responded to pH changes with a nearly theoretical slope (55 ± 3 mV) [17,23]. This new pH-sensitive s-BLM offers prospects for ligand-selective probe development using microelectronics technologies.

Modified s-BLMs as ion sensors. S-BLMs containing six different kinds of crown ethers were synthesized and investigated using the cyclic voltammetry [21,22]. In particular, s-BLMs formed from a liquid crystalline *aza*-18-crown-6 ether and cholesterol-saturated n-heptane solution was found to be sensitive to K^+ in the concentration range of 10^{-4} to 10^{-1} M with theoretical Nernstian slope. The specificity for three alkali metal cations and NH_4^+ of five different kinds of bis-crown ethers in BLMs were investigated. The order of specificity for most of these bis-crown ethers was found to follow hydrated radii of cations, i. e., $NH_4^+ > K^+ > Na^+ > Li^+$ [22]. The results obtained with these s-BLMs compare favorably with conventional BLMs containing similar compounds such as valinomycin [7].

Modified s-BLMs as Molecular Sensors. Many authors have reported sensors for the detection of

the glucose using the glucose oxidase. Earlier, we have reported embedding glucose oxidase on a polypyrrole-lecithin BLM with good results. Interestingly, using s-BLMs containing redox compounds and electron mediators but without the enzyme, glucose was detected in a buffered solution. The results are very preliminary and further experiments are in progress. If highly conjugated compounds such as TCNQ is incorporated in the s-BLM forming solution, the resulting s-BLM was able to detect the presence of the ascorbic acid, which is consistent with the findings obtained with conventional BLMs [1,7].

Electrochemical Transduction of an Immunological Reaction via s-BLMs. As described earlier [4,7], s-BLMs can be employed to embed a host of compounds such as enzymes, antibodies, protein complexes (receptors, membrane fragments or whole cells), ionophores and redox species for the detection of their counterparts, respectively, such as substrates, antigens, hormones (or other ligands), ions, and electron donors or acceptors. In this connection, the first publication on direct electrical detection of Immunological reactions based on transient changes of electrical conductance in conventional BLMs was reported by del Castillo et al. Further studies of antigen-antibody reactions via BLMs have been carried out by others [15, for a review see 7]. In the present work we report a feasibility study of an antigen-antibody reaction using s-BLMs as biosensors with electrical detection. The antigen (HBs-Ag -- Hepatitis B surface antigen) was incorporated into a s-BLM, which then interacted with its corresponding antibody (HBs-Ab -- Monoclonal antibody) in the bathing solution. This Ag-Ab interaction resulted in some remarkable changes in the electrical parameters (conductance, potential and capacitance) of s-BLMs. The magnitude of these changes were directly related to the concentrations of the antibody in the bathing solution. The linear response was very good ranging from 1 to 50 ng/ml of antibody, demonstrating the potential use of such an Ag-Ab interaction via s-BLM as a transducing device [19].

S-BLMs on interdigitated electrodes by microelectronics techniques. The results of our recent research have confirmed a broad spectrum of possible areas of BLM applications [4,7]. All of these possibilities are based upon the fact that a lipid bilayer structure can be deposited on a solid substrate. This novel manner of lipid bilayer formation overcomes two basic obstacles in the way of the practical utilization of the BLM structure, namely: (i) its stability and (ii) its compatibility with a standard microelectronics technology. As has been repeatedly demonstrated by us and others, the solid supported BLM system (s-BLM) not only possesses the advantages of a conventional BLM structure but additionally gain the new important properties such as (a) long-term stability, (b) an anisotropic, highly ordered, yet very dynamic liquid-like structure, (c) two asymmetric interfaces, and (d) this type of probe is predestined for microelectronics fabrication. On this last mentioned property, we extended the experiment described above to the interdigitated structures (IDS). IDS are finger-like electrodes made by microelectronics technologies and used in micro-chip applications. By forming s-BLMs on IDS made of platinum with a window of 0.5 mm x 0.5 mm, we obtained the following interesting results. First, when an IDS coated with a BLM is formed from asolectin, it responded to pH changes with a 15 ± 2 mV/decade slope. The conductance of s-BLMs on IDS was about 50 times higher than the usual s-BLMs. Second, when an IDS coated BLM formed from asolectin plus TCOBQ (or TCPBQ), the pH response was linear with a 50 ± 1 mV slope. This very interesting finding suggests that (i) the lipid bilayer, the fundamental structure of all biomembranes, can be attached to an IDS with responses not unlike those found in the s-BLM, (ii) this type of structure (i.e., s-BLM on interdigitated electrodes) can be used to investigate ligand-receptor contact interactions, and (iii) s-BLMs on an IDS can be manufactured using microelectronics technologies which already exist without the explicit need of special modification. We consider this finding as a major 'breakthrough' in biosensor development

[17,18]. In this connection it should be mentioned that the experiment on the IDS-chip modified with a BLM is based on a common basic aspiration. That is to self-assemble a lipid bilayer containing membrane receptors so that a host of physiological activities, such as ion/molecular recognition can be investigated. At the molecular level, most of these activities may be termed collectively as receptor-ligand contact interactions [1,3]. The structures we have been reconstituting are inherently dynamic (see Concluding Remarks). Receptors and ligands in such close contact normally will vary as a function of time, frequently resulting in non-linear behavior. With the IDS-chip modified with BLMs, we now have at last a most unique system for an extensive experimentation which will be only limited by our imagination. Thus, insight gained from these studies will guide the preparation of functional BLMs on the IDS support. Our aim is to take advantage of microelectronics techniques and apply them to biochemical and neurosciences research.

CONCLUDING REMARKS

The development of BLMs and later s-BLMs and sb-BLMs have made it possible for the first time to study, directly, electrical properties and transport phenomena across a 5 nm ultrathin cell membrane element separating two aqueous solutions. As a result of these extensive studies, biomembranes have now been recognized as the basic structure of Nature's sensors and molecular devices. For example, the plasma membrane of cells provides sites for a host of ligand-receptor contact interactions such as the antigen-antibody formation. To impart relevant biofunctions in BLMs, a variety of compounds such as ionophores, enzymes, receptors, etc. have been incorporated. Some of these incorporated compounds cause the BLMs to exhibit non-linear phenomena. A modified or reconstituted BLM (or s-BLM, sb-BLM) is viewed as a dynamic system that changes both in response to environmental stimuli and as a function of time. This is best described by the *dynamic membrane hypothesis* as a basis of the biomembrane function. The self-assembled lipid bilayer, the crucial component of biomembranes, is in a liquid-crystalline and in a dynamic state. A functional cell membrane system based on self-assembled lipid bilayers, proteins, carbohydrates and their complexes should be considered in molecular and electronic terms; it is capable of supporting ion or/and electron transport and is the site of cellular activities in that it functions as a 'device' for either energy conversion or signal transduction [1,3,12]. Such a system, as we know it intuitively, must act as some sort of a transducer capable of gathering information, then processing it, and delivering a response based on this information. In the past, we are limited by our lack of sophistication in manipulating and monitoring such a system. Today, cell membranology is a matured field of research as a result of applications of many elegant techniques including membrane electrochemistry, patch-clamp techniques, spectroscopy, and membrane reconstitution. We now know a great deal about the structure of cell membranes, 'ion pumps', electroporation, and membrane channels. In membrane reconstitution experiments, the evidence is that intracellular signal transduction begins at membrane receptors. The work summarized here offers new and exciting opportunities for the preparation of a variety of supported lipid bilayer (BLM) probes with potential applications in membrane biophysics, biochemistry, physiology and biotechnology. For example, the membranes can function in such important processes as electron-transfer, signal transduction and cellular environmental sensing. These ideas will be pursued by us in the coming years.

ACKNOWLEDGMENTS

This work was supported in part by an USARO grant No. DAALO3-91-G-0062 and a grant from the USAID (HRN-5600-G-00-2024-00).

REFERENCES

- [1] H. T. Tien, "Membrane bioenergetics as viewed from reconstitution experiments," in *Redox Chemistry and Interfacial Behavior of Biological Molecules*, G. Dryhurst and K. Niki, eds., Plenum Publishing Corp., New York, NY, 1988. pp. 529-556.
- [2] H. T. Tien, in M. L. Mittal (ed), *Proc. Sixth International Symp. on Surfactants in Solution*, Vol. 8, Plenum, NY (1989). pp.133-178
- [3] H. T. Tien, "Electronic Processes and Redox Reactions in BLMs", in *Adv. Chem. Series*, 235 *Biomembrane Electrochemistry* (M. Blank, ed.) ACS, Washington, DC, 1994. Chapter 24
- [4] H. T. Tien, "Self-assembled lipid bilayers for biosensors and molecular electronic devices," *Advanced Materials*, **2**, 316-318, June 1990.
- [5] J. M. Mountz and H. T. Tien, "Photoeffects of pigmented BLMs in a microporous filter", *Photochem. Photobiol.*, **28**, 395-400 (1978).
- [6] M. Zviman and H. T. Tien, *Bioelectrochem. Bioenerg.*, in press (1994)
- [7] A. Ottova-Leitmannova and H. T. Tien, *Prog. Surface Science*, **41**(4) 337-445 (1992).
- [8] T. Hianik, J. Dlugopolsky and M. Gyepessova, *Bioelectrochem. Bioeng.*, **31**, 99 (1993).
- [9] W. Schulmann, S.-P. Heyn and H. E. Gaub, *Adv. Materials*, **3**, 388 (1991).
- [10] K. T. Kinnear and H. G. Monbouquette, *Langmuir*, **9**, 2255 (1993).
- [11] W. F. Ford and M. A. J. Rodgers, *J. Phys. Chem.* **98** (1994) 7415
- [12] A. Ottova-Leitmannova, T. Martynski, A. Wardak and H. T. Tien, Abstracts, USARO Workshop, Cashiers, April 26-29, 1992. (Edited, R.J. Campbell and S.R. Tove). p. 54; *ibid*, in *Molecular and Biomolecular Electronics* (R. R. Birge, ed.) *Adv. Chem. Series*, No, 240, ACS, Washington, DC. 1994. pp. 439-454.
- [13] K. O'Boyle, F. A. Siddiqi, and H. T. Tien, "Antigen-antibody-complement reaction studies on micro BLMs," *Immunol. Commun.*, **13**, 85 (1984).
- [14] H. T. Tien, Z. Salamon, W. Liu and A. Ottova, *Analyt. Lett.*, **26**, 819 (1993).
- [15] J. Kotowski, T. Janas, and H. T. Tien, "Immobilization of glucose oxidase on a polypyrrole-lecithin bilayer lipid membrane," *J. Electroanal. Chem.*, **253**, 277-282 (1988).
- [16] W. Liu, A. Ottova-Leitmannova and H. T. Tien, in "Polymer/Inorganic Interfaces", Vol. **304** (R. L. Opila, F. J. Boerio and A. W. Czanderna, eds) Materials Research Society, (1993).
- [17] W. Ziegler, D. Remis, A. Brunovska and H. T. Tien, in *Proc. 7th C-S Conference on Thin Films*, (V. Tvarozek and S. Nemeth, Eds.) pp. 304-311.
- [18] V. Tvarozek, H. T. Tien, I. Novotiny, T. Hianik, J. Dlugopolsky, W. Ziegler, A. L. Ottova, J. Jakabovic, V. Rehacek and M. Uhlar, *Sensors & Actuators: B. Chemical*, **19**, 597 (1994).
- [19] L. G. Wang, Y.-H. Li and H. T. Tien, *Bioelectrochem. Bioenerg.* in press (1994).
- [20] L. Gu, L. Wang, A. Ottova and H. T. Tien, *Bioelectrochem. Bioenerg.*, submitted (1994).
- [21] Y.-E. He, M.-G. Xie, S.-K. Liu, A. L. Ottova and H. T. Tien, *Anal. Lett.*, submitted (1994).
- [22] Z.-H. Tai, D. Wang, X.-Q. Sun, *Chem. J. Chinese Univ.*, **10**, 760 (1989).
- [23] A. Leitmannova-Ottova, W., Liu, T.-A. Zhou and H. T. Tien, in *Biomolecular Materials by Design*, M. Alper, H. Bayley, D. Kaplan and M. Navia, eds., *MRS Symp. Proc. Series*, Vol. 330, 1994.
- [24] A. Leitmannova-Ottova, D.-L. Guo and H. T. Tien, in *Proc. of the 1994 N.A. Conference on Smart Structures and Materials*, 13-18 Feb. 1994. Orlando, FL
- [25] Z.-H. Tai, T. Li and Z.-C. Yang, *Prog. Biochem. Biophys.*, **19**, 306, 391 (1992).
- [26] X. Lu, A. L. Ottova and H. T. Tien, *Bioelectrochem. Bioenerg.*, submitted (1994)

MAGNETIC AND MAGNETOELASTIC PROPERTIES OF HIGHLY MAGNETO- STRICTIVE AMORPHOUS FILMS WITH TbFe-FeB-TbFe SANDWICH STRUCTURE

T. Igari, S. Ishii, M. Inoue and T. Fujii

Dept. of Electrical and Electronic Engng., Toyohashi University of Technology
Tempaku, Toyohashi, Aichi 441, Japan

ABSTRACT

Amorphous $\text{Tb}_{40}\text{Fe}_{60}\text{-Fe}_{80}\text{B}_{20}\text{-Tb}_{40}\text{Fe}_{60}$ sandwich films were prepared by multitarget rf magnetron co-sputtering. Their magnetization and magnetostriction were studied to examine whether magnetic softening of the amorphous TbFe films could be achieved without losing their giant magnetostriction by introducing the simple sandwich structure. The results revealed that a considerably soft in-plane magnetization (coercive force $H_c \approx 6\text{Oe}$ and the squareness ratio $M_r/M_s \approx 0.8$) and a huge magnetostriction ($\lambda > 500\text{ppm}$) could be obtained in the sandwich films at room temperature, provided that the thickness of the FeB interlayer was within the range of 10% to 40% of the total film thickness ($1\mu\text{m}$).

INTRODUCTION

Cubic Laves phase TbFe_2 intermetallic compound is a very attractive material for magnetomechanical applications because of its ultra-high magnetostriction that exceeds $1700\text{ppm}^{1)}$ at room temperature. The huge saturation magnetostriction is, however, realized only when a considerably large magnetic field of more than 10kOe is applied due to the large magnetocrystalline anisotropy of the alloy.

Thus far, many efforts²⁻⁹⁾ have been made to reduce the magnetocrystalline anisotropy of the alloy and to increase its effective magnetomechanical coupling constant k_m^2 . Among them, the most successful anisotropy reduction was achieved in the pseudobinary alloy of $\text{Tb}_{0.27}\text{Dy}_{0.73}\text{Fe}_2$ (so-called Terfenol-D) having a k_m^2 of about 0.75. This k_m^2 value is still unsatisfactorily small especially when one applies the alloy to integrated magnetomechanical applications, such as micro-magnetic actuators and/or sensors.

Recently, we¹⁰⁾ have shown that the coercive force H_c of the amorphous TbFe film can be reduced greatly by inserting amorphous FeB layers between the TbFe films. The reduction of H_c occurs via ferromagnetic and magnetostatic interactions between magnetic layers which reduce the energy of magnetic domain walls. However, the magnetostrictive stress S which is proportional to the magnetostriction λ is also reduced in association with the increasing number of FeB interlayers. This was because all multilayer films investigated were subject to the oxide contamination at each interfaces.

In this work, we prepared the contamination free amorphous TbFe-FeB-TbFe sandwich films and studied their fundamental magnetic and magnetoelastic properties. The results suggest that, by controlling the thickness of the FeB interlayer, the simple sandwich film can possess both the ultra-high magnetostriction and considerably soft in-plane magnetization.

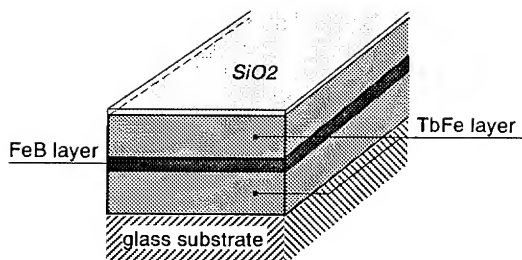


Fig.1 Sandwich structure of the sample.

EXPERIMENTAL

As illustrated in Fig. 1, the TbFe-FeB-TbFe sandwich films were fabricated onto soft glass substrates held at room temperature using the co-sputtering technique using a planar magnetron type rf-sputtering apparatus with three independent targets. Both sputtering targets for the TbFe and FeB films had composite designs: The TbFe target was an Fe plate, in which small Tb pellets of 0.25mm thick and 5mm in diameter were embedded uniformly. As for the FeB target, B chips with the average diameter of 3mm were uniformly placed on an Fe plate.

The TbFe film composition was controlled by changing the number of Tb pellets (from 0 to 50at.% Tb) and was measured by energy dispersive electron microanalysis (EPMA). The FeB film composition was controlled by changing the number of B chips (from 0 to 30at.% B) and was determined by inductively coupled plasma spectrochemical analysis (ICP). X-ray diffraction (XRD) was employed to determine the crystallographic structure of the films. Oxide contamination at each interface of the samples was studied from Auger electron spectroscopy (AES) depth profiles. Magnetic polarization and magnetostriction of the samples at room temperature were evaluated, respectively, using a vibrating-sample magnetometer (VSM) and a three-terminal capacitance bridge which detects the deflection of the free end of the cantilevered sample¹¹.

RESULTS AND DISCUSSION

Prior to the fabrication of the sandwich films, $\text{Tb}_x\text{Fe}_{100-x}$ ($0 < x < 50$) and $\text{Fe}_{100-x}\text{B}_x$ ($0 < x < 30$) monolayer films have been investigated so as to determine the respective film compositions which fulfill the following requirements: the TbFe film has an ultra-high magnetostriction with an in-plane magnetization, while the FeB film has a large magnetostriction and soft magnetism simultaneously. As described elsewhere^{10,12} in detail, these requirements are indeed satisfied in $\text{Tb}_{40}\text{Fe}_{60}$ and $\text{Fe}_{80}\text{B}_{20}$ amorphous films, respectively. In Fig. 2, polarization curves of the $\text{Tb}_{40}\text{Fe}_{60}$ film (a) and the $\text{Fe}_{80}\text{B}_{20}$ film (b) are shown against the magnetic field applied parallel ($//$) and perpendicular (\perp) to the film plane. It is seen that the magnetization of both films lies in the film plane when external field is absent (in-plane magnetization films). In-plane coercive force H_c are 1.6Oe (FeB film) and 100.5Oe (TbFe film). In Figs. 3 (a) and (b), magnetostriction of the TbFe film (a) and the FeB film (b) is shown against the magnetic field H applied parallel to the film plane. The magnetostriction λ at $H=10\text{kOe}$ is 660ppm for the TbFe film while 42ppm for the FeB film. We note that the magnetostriction of our amorphous TbFe film is the

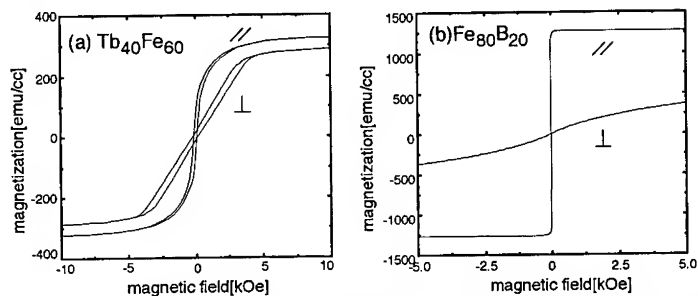


Fig.2 Magnetic polarizations vs. magnetic field for the $\text{Tb}_{40}\text{Fe}_{60}$ (a) and $\text{Fe}_{80}\text{B}_{20}$ (b) films.

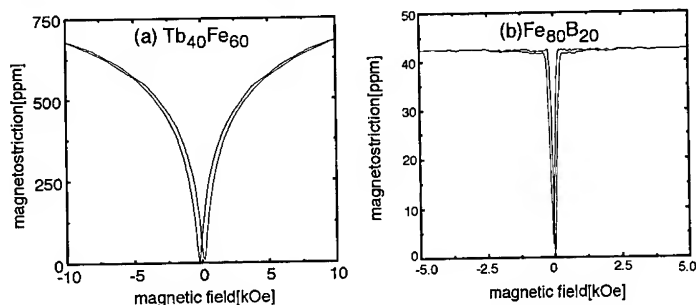


Fig.3 Magnetostriction vs. magnetic field for the $\text{Tb}_{40}\text{Fe}_{60}$ (a) and $\text{Fe}_{80}\text{B}_{20}$ (b) films.

largest among the values reported so far^{4,6,13}. Thus, we employed $\text{Tb}_{40}\text{Fe}_{60}$ and $\text{Fe}_{80}\text{B}_{20}$ compositions for the TbFe and FeB layers in the sandwich film, respectively.

The amorphous TbFe-FeB-TbFe sandwich films with the same total thickness of $d=2d_T+d_F=1\mu\text{m}$ were prepared, where the thicknesses of the top and bottom TbFe layers, d_T , were identical irrespective of the FeB interlayer thickness, d_F . We chose d_F as a parameter, because the degree of exchange and magnetostatic coupling between magnetic layers depends strongly on the respective film thickness¹⁴. As is discussed in ref.[10], an oxide layer is easily formed at the interface of TbFe and FeB layers mainly due to the selective oxidation of Tb, which results in the reduction of the magnetostrictive stresses of the samples. To avoid the

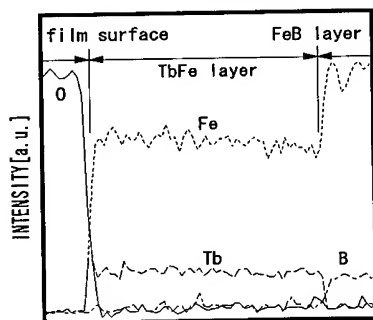


Fig.4 AES depth profile for the TbFe/FeB/TbFe film.

oxide contamination, we prepared the sandwich films in a cleaner atmosphere which prevented the invasion of oxygen during the film formation. Figure 4 is the AES depth profile showing the distribution of the elements at an interface of TbFe and FeB layers for the present film. It is obvious that the present multilayer film is almost free from oxide contaminations.

In Figs. 5 and 6, curves of the magnetic polarization and the magnetostriction of the samples are shown for three cases of $d_F=0.1\mu\text{m}$ ($d_T=0.45\mu\text{m}$), $0.3\mu\text{m}$ ($d_T=0.35\mu\text{m}$) and $0.6\mu\text{m}$ ($d_T=0.2\mu\text{m}$), where the meanings of the marks // and \perp are the same as those in Fig.2. These

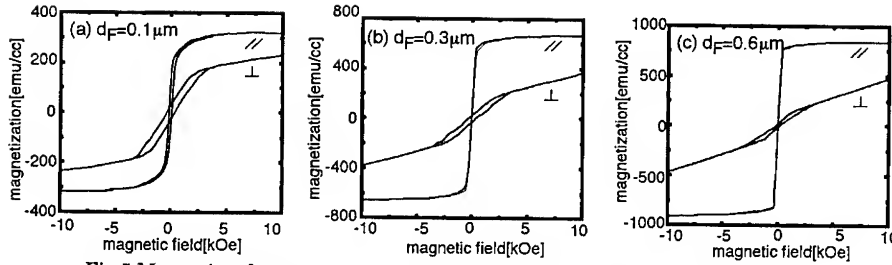


Fig.5 Magnetic polarizations vs. magnetic field for the sandwich films having $d_F=0.1\mu\text{m}$ (a), $0.3\mu\text{m}$ (b), and $0.6\mu\text{m}$ (c).

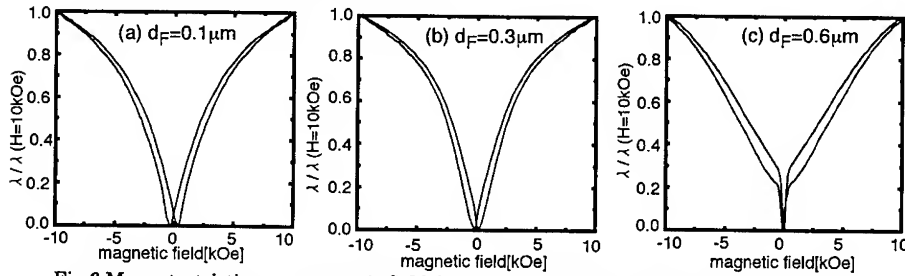


Fig.6 Magnetostriction vs. magnetic field for the sandwich films corresponding to Fig.5.

figures show that the saturation magnetization M_s increases with thickening the FeB interlayer. The in-plane magnetic softening also proceeds with increasing the FeB thickness. To make clear this situation, M_s and the in-plane squareness ratio M_r/M_s are plotted against the thickness of the FeB interlayer d_F in Fig.7: the saturation magnetization increases linearly with thickening the FeB interlayer, which suggests that (1) the contribution of mutual mixing of atoms through the interfaces is very small and (2) the thickness of each layer is well controlled. It is noteworthy that the squareness of the magnetic polarization is improved linearly by increasing the FeB interlayer thickness ($M_r/M_s=0.6$ when $d_F=0$, while $M_r/M_s=0.9$ when $d_F=0.6\mu\text{m}$).

In Fig.8, in-plane coercive force H_c of the samples is depicted against the FeB interlayer thickness d_F . As is seen in the figure, H_c of the sample drastically reduced down to 6Oe by inserting the FeB layer with $d_F>0.2\mu\text{m}$, the value of which is 5.8% of that of the TbFe monolayer film ($H_c=100.5\text{Oe}$). Therefore, the insertion of the FeB film markedly affects magnetic softening of the TbFe film. In Fig.8, we also plotted the values of magnetostrictive stress S defined by $S = \lambda E_f / (1 + \nu_f)$, where λ is the magnetostriction at 10kOe, and E_f and ν_f are the effective Young's modulus and the effective Poisson's ratio of the film, respectively. Here, we introduced S for evaluating the magnetoelastic properties of samples. This is because S can be measured directly by the cantilever technique and, moreover, S is a significant material parameter especially in integrated actuators which need high power and/or force. The figure shows that the magnetostrictive stress reduces slowly with increasing thickness of the FeB interlayer accompanying the magnetic softening. However, unless the thickness of the FeB interlayer is beyond 40% of the total thickness of the film, a considerably large magnetostrictive stress (magnetostriction) of more than 90% of that of the TbFe monolayer film is maintained. Therefore, it is concluded from Figs.7 and 8 that huge magnetostriction and soft magnetization can coexist in the sandwich films, provided that the thickness of the FeB

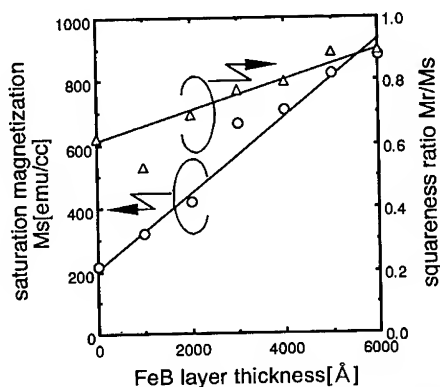


Fig.7 Saturation magnetization M_s and squareness ratio M_r/M_s vs. FeB interlayer thickness.

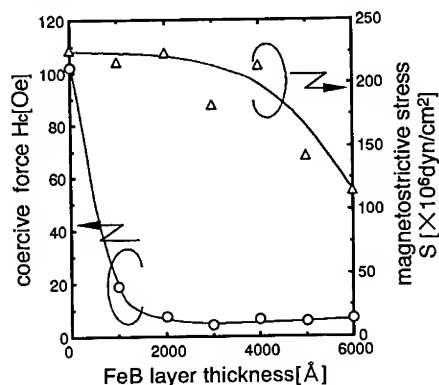


Fig.8 Coercive force H_c and magnetostrictive stress S vs. magnetic field.

interlayer is between 20% to 40% of the total thickness.

It is interesting that the magnetostriction of the sample with $d_F=0.6\mu\text{m}$ shows different field sensitivities at low and high magnetic fields (see Fig.6 (c)). This behavior is understood by assuming that the magnetostrictive expansion occurs independently in the TbFe and the FeB layers as the thickness of each layer becomes comparable. As a matter of fact, this situation was observed for all sandwich films whose d_F was larger than $0.4\mu\text{m}$. From the view point of integrated actuator applications, the magnetoelastic properties of such sandwich films are undesirable, because (1) the attainable magnetostrictive stress S is degraded as shown in Fig.8, and (2) the obtainable low field magnetostriction is limited to the magnetostriction of the FeB film itself.

On the contrary, for the sandwich films with $d_F<0.4\mu\text{m}$, the separation in magnetostriction-field characteristic disappears and their magnetostriction increases smoothly with the application of a magnetic field. However, the field sensitivity of magnetostriction is almost the same as that of the TbFe monolayer film (Fig.3

(a) although in-plane magnetic softening proceeds. Our recent study suggests that the field sensitivity of the magnetostriction of these sandwich films is governed primarily by the perpendicular components of the magnetization in TbFe films. Thus, to improve the field sensitivity of magnetostriction, it is presumably indispensable to eliminate the perpendicular magnetization in TbFe films by some means. Further discussion for this will appear elsewhere¹²⁾.

CONCLUSION

The present study reveals that the magnetic softening of amorphous $\text{Tb}_{40}\text{Fe}_{60}$ film with a huge magnetostriction is attainable by introducing a simple sandwich structure of TbFe-FeB-TbFe. Considerably soft in-plane magnetization (coercive force $\approx 6\text{Oe}$ and the squareness ratio ≈ 0.8) and huge magnetostriction (magnetostrictive stress $\approx 250 \times 10^6 \text{dyn/cm}^2$ comparable to that of the TbFe monolayer film) were obtained simultaneously when the thickness of the FeB

interlayer was 20% to 40% of that of the total film thickness.

However, no apparent improvement in the field sensitivity of magnetostriction was observed in these sandwich films despite their soft in-plane magnetization. This is presumably because that the field sensitivity of magnetostriction is determined by the local perpendicular component rather than the in-plane component of the magnetization in the TbFe film. Hence, to get films with large magnetostrictive sensitivity retaining soft magnetization, some measures for eliminating the perpendicular local magnetization of TbFe film will be necessary.

ACKNOWLEDGMENTS

The authors are greatly indebted to Prof. Dr. K. I. Arai and Drs. M. Yamaguchi and K. Ishiyama, all of Tohoku University, for their valuable discussions and encouragements throughout the study. The work was supported, in part, by the Grand-In-Aid for Encouragement of Young Scientists (A) from the Ministry of Education, Science and Culture of Japan (No.06750319, 1994) and also by the Sumitomo Foundation (No.94-100.5-284).

REFERENCES

1. A. E. Clark, H. Belson and R. E. Strakna: J. Appl. Phys., **44**, 2913 (1973).
2. A. E. Clark, J. P. Teter and M. Wun-Fogle: J. Appl. Phys., **53**, 2664 (1982).
3. A. E. Clark: AIP Conf. Proc., **18**, 1015 (1974).
4. D. W. Forester, C. Vittoria, J. Schelleng and P. Lubitz: J. Appl. Phys., **49**, 799 (1978).
5. N. S. Kazama and H. Fujimori: Proc. 4th Intern. Conf. on Rapidly Quenched Metals, 799 (1981).
6. Y. Hahashi, T. Honda, M. Yamaguchi and K. I. Arai: J. Magn. Soc. Jpn., **17**, 289 (1993), in Japanese.
7. H. Fukunaga and N. Akagi: Jpn. J. Appl. Phys., **28**, Suppl.28-1, 45 (1988).
8. T. Ooike, S. Ishio and T. Miyazaki: J. Magn. Soc. Jpn., **17**, 271 (1993), in Japanese.
9. Kikuchi, T. Tanaka, S. Sugimoto, M. Okada, M. Homma and K. I. Arai: J. Magn. Soc. Jpn., **17**, 267 (1993), in Japanese.
10. T. Igari, V. Kavalero, M. Inoue and T. Fujii: Proc. of the 1st Magneto-Electronics Intern. Symp., Nagano, Japan, 229 (1994).
11. K. Klokholm: IEEE Trans. Magn., **MAG-12**, 819 (1976).
12. T. Igari, S. Ishii, M. Inoue and T. Fujii: J. Magn. Magn. Mat., in preparation for publication.
13. E. Quandt: J. Appl. Phys., **75**, 5653 (1994).
14. e.g., T. Masuda, T. Tsunashima, T. Fujii and S. Uchiyama: Jpn. J. Appl. Phys., **11**, 1783 (1972).

MAGNETOSTRICTIVE DAMPING TO REDUCE NOISE AND VIBRATIONS

A. KARIMI, P. H. GIAUQUE, AND J. L. MARTIN

Institut de Génie Atomique, Ecole Polytechnique Fédérale de Lausanne CH-1015 Lausanne, (Switzerland)

ABSTRACT

The magnetomechanical damping capacity of cast and thermally sprayed Fe-Cr based alloys has been investigated using free and forced vibration techniques. The coatings were deposited using a vacuum plasma spraying method and the cast alloys were prepared in a high frequency furnace under an argon atmosphere. Three laboratory devices including a torsion pendulum, a resonant bar and a cantilever were used to cover a wide range of frequencies and amplitudes varying between $f = 1\text{ Hz}$ to 10 kHz , and $\epsilon = 10^{-6}$ to 10^{-3} . The damping capacity of the plasma sprayed coatings was found to be comparable to that of cast alloys. Appropriate heat treatments improved the damping capacity of both coatings and cast alloys by several times. The variation of the loss factor as function of the vibration amplitude showed a maximum, but versus frequency exhibited a slightly monotonous character. The magnetic domains were observed using the magneto-optical Kerr effect and their modification under heat treatments was associated with different values of the damping capacities.

INTRODUCTION

The magneto-elastic effects have been highlighted for many years to provide an important source of internal friction and thereby a high damping capacity in ferromagnetic materials [1-3]. The damping mechanisms were commonly associated with the stress-induced movements of domain walls [4, 5]. Under an external stress, the domain walls alter their positions and the spontaneous magnetization changes its direction resulting in irreversible modifications in the specimen dimensions. This remanent strain can only be reverted to zero by a compressive stress. As a consequence, the oscillatory motion of the domain walls can dissipate mechanical energy by a number of internal processes involving the contribution of macroeddy current, microeddy current and hysteretic effects [6-7]. It is believed that, in general, all three loss mechanisms can operate simultaneously, but their relative importance depends on the material properties such as the residual stress, and the experimental conditions including vibrational frequency and applied stress. Investigations were conducted under particular experimental conditions in order to separate each damping mechanism and to study their specific contribution to the whole magnetic damping of materials [8].

Among the magneto-mechanical damping materials, the high chromium ferritic steels have been particularly investigated because of their good mechanical properties, improved corrosion resistance and high damping capacity. Masumoto et al.[9] studied, for the purpose of vibration attenuation of machine parts, the internal friction of a number of Fe-Cr alloys at a low frequency of about 1.1 Hz using the inverted torsion pendulum. Accordingly, the variation of internal friction as a function of vibration amplitudes showed a maximum and annealing of specimens increased notably the damping capacity. Schneider et al.[10] using cantilever and resonant bar methods showed that the damping capacity was strongly dependent on the chemical composition and internal or residual stress, but independent of the test temperature. Heat treatments improved the damping capacity up to 8-10 times according to the alloy composition and vibration frequency. Amano et al.[11] observed that the damping capacity under both, bending and torsional oscillation, remains almost constant up to about 350°C , but increases with vibration amplitudes. Ferguson [12] characterized the damping behaviour of Fe-Cr-Al and Fe-Cr-Mo alloys for naval ship applications. In these alloys, the specific damping capacity measured using a resonant dwell technique was found to be more interesting at higher frequencies close to 2 kHz . The above results were obtained in bulk samples and cast alloys where the magneto-mechanical hysteresis damping is well established. The present work is

devoted to the behaviour of thick coatings of Fe-Cr-X alloys prepared by using a vacuum plasma spraying technique. The objective of this work is to characterize the crystalline and magnetic structures of such alloys in relation with their damping capacity. The attempts are focused, in particular, on the damping behaviour at higher frequencies and elevated amplitudes typical of urban transportation systems.

MATERIALS

The materials tested were basically coatings of Fe-16Cr and Fe-16Cr-2Al (wt.%) deposited onto ferritic stainless steel substrates using a vacuum plasma spraying (VPS) method. In order to provide a realistic comparison between the damping capacity of plasma sprayed coatings and bulk materials, cast alloys with the same chemical composition were also tested. As for coatings, a layer of 2 mm thickness of above alloys was coated on the plates of 130 x 100 x 20 (mm³) using a VPS method from Sulzer Metco AG. The coatings produced by such a way exhibit stratified microstructures where each layer corresponds to one passing of the plasma beam. To prepare the cast samples, raw materials of 99.9% purity were melted with deoxidized elements in an alumina crucible using a high frequency furnace with flowing argon. The ingots of 20 x 100 x 10 (mm³) dimension were obtained from which damping specimens were machined.

EXPERIMENTAL PROCEDURE

In order to measure the damping capacity of the samples over a wide spectrum of frequencies and amplitudes, three different laboratory devices based on free and forced vibration techniques were used. The torsion pendulum and the resonant bar were assigned to use the free vibration method, and measure the logarithmic decrement of successive amplitudes of the oscillatory system. Each of these devices is able to measure vibration in a particular range of experimental conditions [12]. In contrast, the cantilever uses forced vibrations to determine the loss factor of a beam specimen by measuring the response to excitation at modal frequencies. The beam specimen is excited by an electro-magnetic shaker using a sinusoidal signal which is first obtained by a signal generator and amplified by a power amplifier. This amplified signal is then used to drive a dynamic vibrometer to excite the samples. The system excitation inputs were measured by an accelerometer mounted just above the beam root. The outputs were recorded using a laser vibrometer adjusted at the specimen free tip. Both the input and output signals were compared by a two channel signal analyser to produce the transfer function frequency response from which the specific damping capacity of the beam material was calculated. The beam width and grip length were maintained fixed, but the vibrating length and thickness were left as variable, to obtain various resonance frequencies. By this technique, a wide range of frequencies (10 Hz to 10 kHz) and deformations ($\epsilon = 10^{-2}$ to 10^{-6}) can be tested. To observe magnetic domains which are considered to be at the origin of damping in Fe-Cr based alloys, an optical device was built based on the magneto-optical Kerr effect [13].

EXPERIMENTAL RESULTS

Comparison between cast and coated samples

The preliminary damping measurements were performed on both cast alloys and VPS coatings to provide a comparison between the two fabrication methods. As for VPS samples, the damping measurements were carried out exclusively on the coating material to avoid additional complications due to the substrate and the interface between substrate and coating. For this purpose, the substrates were removed first, and after machining or straightening of coatings, foils of 1 mm thickness were obtained from which test samples were cut. The results obtained using a torsion pendulum with the frequency $f=1$ Hz are shown in Fig. 1 for the cast samples and in Fig.2 for the coatings. Both samples have undergone several heat treatments as indicated on the diagrams. Here, the damping capacity Q^{-1} describes the logarithmic decay of free vibrations. According to these results the damping capacity of the as received specimens in both

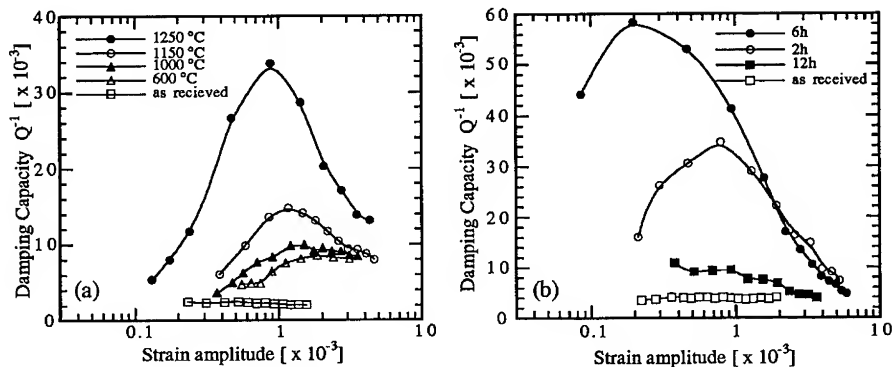


Fig. 1: Damping capacity versus strain amplitude in cast alloys. a) Fe-16Cr annealed 1 h at temperatures indicated, b) Fe-16Cr-2Al annealed at 1100°C with durations indicated on the diagram. $f = 1\text{Hz}$

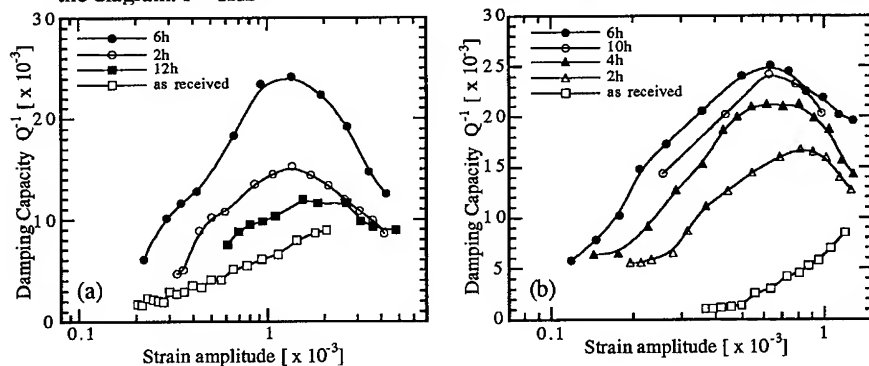


Fig. 2: Effect of annealing duration on the damping behaviour of VPS coatings. a) Fe16-Cr annealed at 1100°C, b) Fe-16Cr-2Al annealed at 950°C. $f = 1\text{Hz}$

Fe16-Cr and Fe-16Cr-2Al cast alloys are low and appear not to be significantly dependent on deformation. The heat treatments improve the damping capacity in general, but the effect of annealing is more pronounced for the particular amount of deformation including $\epsilon \approx 10^{-4}$ to 10^{-3} . The addition of 2%Al in iron-chromium alloys increased the damping capacity by a factor of about 2. The as-received coatings seem to be more sensitive to deformation than the as-received cast specimens and lead to a notable increase in the damping capacity with deformation (Fig. 2). Such a behaviour may be related to the particular microstructures formed during thermal spraying. Nevertheless, the effect of heat treatments on the damping capacity seems to be very similar to that observed in cast alloys. These results show that the ability of Fe-Cr based alloys to damp vibrations is not significantly altered by plasma spraying.

Effect of residual stress

The magneto mechanical damping results from the motion of magnetic domain walls which in its turn is restricted by the residual stresses of the samples. Heat treatments annihilate residual stress and provide higher damping capacities as illustrated in Fig.3 for coating Fe-16Cr-2Al. Accordingly, a higher annealing temperature and a longer annealing duration lead to an

enhanced damping capacity (Fig.3a). In general, the VPS coatings exhibit higher residual stress than cast alloys and therefore require more annealing to provide a damping capacity similar to cast samples. For example in Fe-16Cr-2Al, a heat treatment at 1250°C/8h produces almost the same damping capacity in the coating as 1100°C/6h in the cast alloy (see Fig.2 and 3). This behaviour was also observed under other vibration frequencies as depicted in Fig.3b.

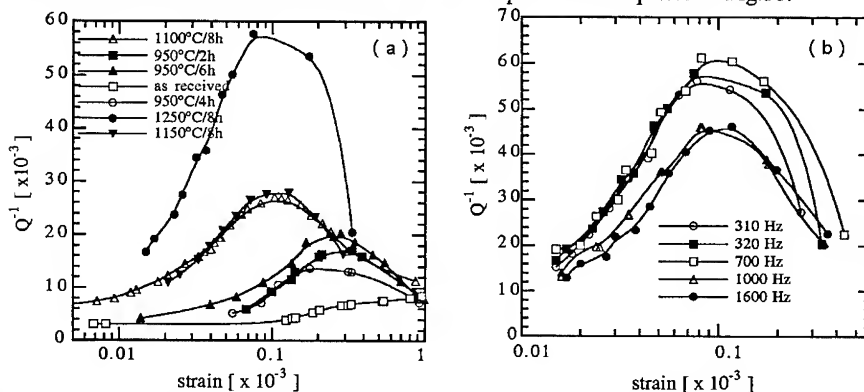


Fig. 3: Variation of the damping capacity in coating Fe-16Cr-2Al as measured using the cantilever method. a) $f = 400$ Hz, b) annealing at 1250°C/8h.

Effect of frequency

An example of variation of the damping capacity as a function of the vibration frequency is reported in Fig. 4. These values were obtained using the technique of cantilever beam modal analysis. The half power band width of the resonance peak corresponding to the natural frequency of mode I and II of resonance was used to determine the damping factor. As can be seen from these results, the damping capacity of Fe-16Cr-2Al coating remains almost constant when frequency increases from 10 Hz to 10 kHz. The magneto-mechanical damping is compared in general to the irreversible Barkhausen jumps of 90° domain walls [16]. Hence, the damping capacity is considered to be influenced by frequency only in the range close to the Barkhausen jumps frequency, i.e., in kHz and MHz ranges. For frequencies up to a few kHz, damping is expected to be independent of the vibration frequency.

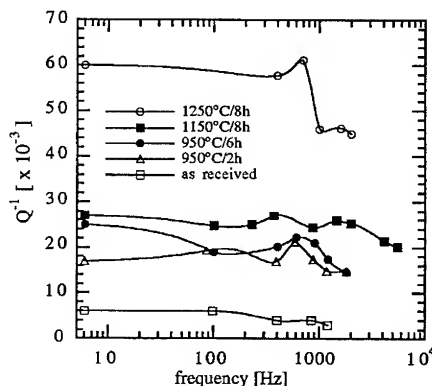


Fig.4: Variation of damping capacity versus frequency for coating Fe-16Cr-2Al.

Magnetic domains

The magnetic domains were observed using a particular optical device based on the magneto-optical Kerr effect which has been built for this study. This effect refers to the rotation of the direction of polarization of a linearly polarized light beam reflected from the surface of a magnetic material. Since the angle of rotation of the polarization axis depends on the direction of the magnetic moments, hence an image of domain structures at the surface can be formed. As

the angle of rotation is very small, about a few minutes of arc, and the contrast between the different domains is weak, high quality optical components and sample polishing are required.

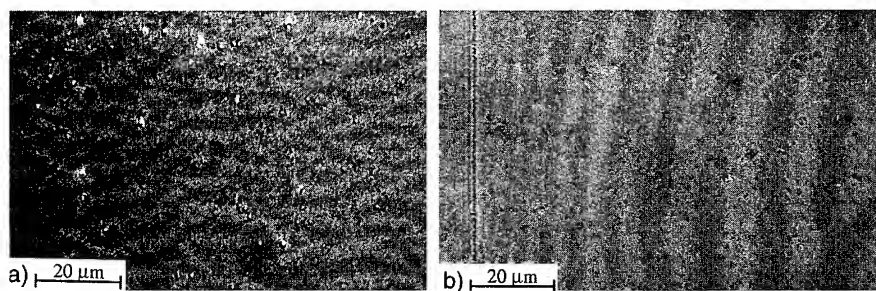


Fig. 5: Magnetic domain structures observed using the Kerr effect. a) as received Fe16Cr coating, b) same sample as a after annealing 1h at 1150°C.

Fig.5a corresponds to a domain structure in an as received cast Fe-Cr alloy. There are coarsely two different contrasts, a clear and a dark one, which form a layered structure of a width of 3 - 4 μm . Each contrast corresponds to a zone magnetized in a particular direction distributed uniformly inside the grains. After heat treatment for one hour at 1150°C and slow cooling, the domains exhibit the microstructure of Fig. 5. During annealing, domains were coarsened to a width of about 8-10 μm and were rearranged to be roughly parallel to one another. A particular remark concerning the example of Fig. 5b, is the variation of domain width near the grain boundary at the left of the picture. Domains near the grain boundary are narrow as compared to those inside the grains. Such a behaviour may be related to the higher internal stress at grain boundaries as compared to inside of the grains where annealing is not long enough to relax the stress. Longer annealing duration increases the domain size and favours the growth of crystallographic orientation domains. In spite of close similarities between the morphology of domains in coatings and cast specimens, their size appears to be smaller in the coating material. In addition transgranular domains occur frequently because of lower misorientations between grains in plasma sprayed coatings.

DISCUSSION

The potential damping mechanism in ferromagnetic materials is mainly associated with the magneto-mechanical hysteresis loss due to coupling between magnetism and elasticity effects [5]. Such an interaction was explained as follows: Upon application of an external stress, the initially randomly oriented domains align themselves in the direction of the resultant strain and produce an irreversible change in the dimension of the material. The total strain consists of a pure elastic strain and a strain due to domain wall displacements. The elastic strain is reversible and diminishes to zero by removing the stress. The magnetostrictive strain can be reverted to zero by a compressive stress. This causes a hysteresis loop on the stress-strain curve. The larger the area of the hysteresis loop, the greater the damping capacity of the material. In addition to the hysteresis damping some other mechanisms such as macroeddy and microeddy currents have also been suggested to contribute to magnetic damping. These mechanisms are believed to be more effective at high frequencies [4]. For the experimental conditions used in the present work, damping is essentially due to the hysteresis effect. The values of Q^{-1} versus the vibration amplitude which is expressed by strain in Fig.1-3, show a maximum for strains varying between $\epsilon = 10^{-4} - 10^{-3}$. Such a behaviour is well established in ferromagnetic materials and the works of Schneider et al.[10], Masumoto et al.[9] revealed the appearance of the peaks on the curves Q^{-1} versus ϵ in both cast and sintered Fe-Cr based alloys. This effect was then explained by analogy to induction curves (B vs H) and by using the Rayleigh law which predicts an energy

proportional to stress to the one third power, for lower amplitudes. On the contrary, at higher amplitudes, saturation occurs and damping decreases.

In general, heat treatments notably improve the damping capacity of Fe-Cr based alloys, but the mechanisms by which such improvements are brought about, are not yet clear. The general tendency to explain annealing effects is based on the reduction of the internal stress within the specimen which favors domain wall mobility [10]. Although such an explanation seems to be in agreement with the experimental observations, one should remember that the morphology of domains is also modified during heat treatments and their sizes increased as shown in Fig.5. Hence, the number of domains diminishes, leading probably to lower damping capacities. Statistically, damping may be assumed to be dependent on the product of domain number and mobility. This implies the existence of an optimal heat treatment to obtain a higher degree of damping for a given alloy. Such hypothesis seems to be verified in the case of the tested materials. Studying damping properties of Fe-Cr-Al alloys Amano et al. [11] observed also the presence of peaks on the variation of Q^{-1} versus the heat treatment temperatures.

The comparison of damping capacities measured using both free and forced vibration techniques show that the performance of coatings to dissipate mechanical energy is equivalent to that of cast alloys. From the point of view of application, these results are very important and allow one to consider coatings as candidate materials for high damping means. In particular, thermal spraying opens new applications where the use of cast alloys is difficult or inappropriate.

CONCLUSIONS

- The damping behaviour of Fe-Cr-X coatings produced using vacuum plasma spraying is similar to cast alloys of the same chemical compositions.
- The annealing of the samples improved the damping capacity, but the beneficial effect is more pronounced for particular deformation amplitudes.
- The variation of the damping capacity as a function of the vibration amplitude showed a maximum, while versus frequency exhibited slightly monotonous character.
- The damping capacity is related to morphology and mobility of magnetic domain walls.

ACKNOWLEDGEMENTS

The authors wish to thank A. Salito and G. Barbezat from Sulzer Metco in Wohlen for providing the VPS coatings and fruitful discussion of the results. The Swiss Priority Program on Materials (PPM) is acknowledged for financial support of the project.

REFERENCES

1. A.W. Cochardt; J. Appl. Mech. **20**, 196-200 (1953).
2. G.W. Smith and J.R. Birchak; J. Appl. Phys., **40**(13), 5174-5178 (1969).
3. J.T.A. Roberts and P. Barrand, Acta Met. **17**, 1685-1692 (1967).
4. J. Degauque and B. Astie; Phys. Stat. Sol. (a) **59**, 805-816 (1980).
5. J. Van Humbeeck; in Proc. Int. Symp. on Role of Interfaces on Material Damping, 13 - 17 Octobre 1985, Toronto, Ontario, Canada, ASM's Materials Week and TMS/AIME Fall Meeting, edited by B.B. Rath and M.S. Misra, American Society for Metals, 5-24 (1986).
6. B.S. Berry and W.C. Pritchett; J. Appl. Phys. **47**(7), 3295-3301 (1976).
7. V.F. Coronel and D.N. Bechers; J. Appl. Phys. **64**(4), 2006-2015 (1988).
8. H.V. Ganganna, N.F. Fiore and B.D. Cullity; J. Appl. Phys. **42**(13), 5792-5797 (1971).
9. H. Masumoto, S. Sawaya and M. Hinai; Trans JLM, **20**, 409-413 (1979).
10. W. Schneider, P. Schrey, G. Hausch and E. Török; Journal de Physique, C5, N° **10**(42), 635-639 (1981).
11. K. Amano, M. Sahashi, H. Tokoro and M. Nakagawa; Proc. 6th Int. Conf. on Internal Friction and Ultrasonic Attenuation in Solids, July 4 - 7, 1977, Tokyo, edited by R.R. Hasiguti and N. Mikoshika, University of Tokyo Press, 763-768 (1977).
12. D.B. Ferguson; Characterization of high damping Fe-Cr-Mo and Fe-Cr-Al alloys for naval ships applications, M.S. Thesis, Nval Postgraduate School, Monterey, California (1988).

MOLECULAR SIEVE COATED SAW DEVICE FOR THE DETECTION OF CARBON DIOXIDE IN THE PRESENCE OF WATER

JAMES T. SUN, CHRISTOPHER B. DARTT, MARK E. DAVIS
Chemical Engineering, California Institute of Technology, Pasadena, CA 91125

ABSTRACT

158 MHz SAW oscillators coated with organic polymers and zeolites were tested as sensors for monitoring the level of humidity and carbon dioxide in a flowing stream of nitrogen. All coatings exhibited responses to water vapor on the order of kilohertz frequency shifts, while the responses to carbon dioxide were significantly (generally one order of magnitude) smaller. The presence of CO₂ dramatically interfered with the detection of water with poly-(ethylenimine) (PEI) coatings. Poly-vinyl pyridine (PVP) coatings showed large responses to water without any interference from CO₂; CO₂ produced little response whether water was present or not. ZSM-5 coatings also showed no evidence of interference between water and CO₂; a detectable response for CO₂ is possible in humid nitrogen.

INTRODUCTION

The on-line measurement of carbon dioxide is an important problem in chemical sensing. For example, carbon dioxide is found in environments where there is biological activity. The concentration of CO₂ produced during respiration is known to indicate the level of physical stress and metabolic activity. In controlled environments such as space travel and underwater exploration it is crucial for health safety reasons that the breathing environment be monitored as closely as possible. Presently, commercial carbon dioxide sensors other than infrared (IR) and mass spectrometer (MS) based sensors are not able to cope with the interference of water. Because humidity levels from respiration can be quite high, difficulties in the precise monitoring of CO₂ are typically encountered.

Infrared and MS detectors are theoretically well-suited to solve the CO₂/H₂O problem, but in practice suffer from several disadvantages. They are large, complicated devices that require frequent tuning and maintenance. Additionally, their cost makes them prohibitive for many applications. The ideal sensor would have the following properties: small, lightweight, sensitive, selective, inexpensive, low-power consumption, simple, non-destructive, reproducible. The sensor chosen for this study is the surface acoustic wave (SAW) device. SAW devices belong to a class of chemical microsensors which owe their existence to the advent of microfabrication techniques used three decades earlier in the electronics industry. Not only have they become popular due to their small size and sensitivity, but other characteristics inherent to these microsensors such as their ruggedness and low power consumption offer important advantages over traditional sensors in various environmental monitoring and process control applications.

In the 1920s, Cady demonstrated that the converse piezoelectric effect could be exploited for the construction of very stable oscillator circuits.¹ By applying an alternating electric field across a piezoelectric substrate, an alternating strain induces the crystal to oscillate at a particular resonant frequency and generates acoustic standing waves. Changes in various properties of the crystal affected, for example, by its chemical or physical environment then act to perturb the acoustic waves such that a new resonant frequency is established. It is upon this transduction of mechanical vibrational energy to a detectable oscillating electrical signal that the SAW device relies in its detection of ambient chemical and physical conditions. In fact, because quartz crystals vibrate with minimal energy dissipation, they are nearly ideal oscillators and have been used widely in frequency control, filter circuits, and not surprisingly, chemical sensing.²⁻⁴

For chemical sensing, the perturbation of the acoustic waves usually results from the sorption of analyte. However, as quartz is fairly inert chemically, the SAW substrate itself is a nonselective sensor. Selectivity is imparted only by introducing a chemically sensitive layer to the

surface of the substrate, thus allowing a greater degree of interaction between the analyte and the acoustic wave. Because the SAW device ultimately relies upon the sensitivity of the surface waves to changes occurring in the thin surface film, this type of device has been used to determine such properties as polymer/vapor sorption thermodynamics and kinetics,⁵ adsorption/desorption isotherms,⁶ and pore size, surface area, and vapor diffusivity.^{7,8} One of the issues in chemical sensing with quartz-based SAW devices, then, is the development and design of coating materials that enables them to successfully probe the analyte of interest in a selective manner. The objective of our work is to develop a SAW coating material appropriate for detecting CO₂ in humid vapor streams. We report here our initial efforts on this topic.

EXPERIMENTAL

158 MHz dual SAW delay line oscillators, fabricated from aluminum interdigitated electrodes on polished ST-cut quartz substrates were purchased from Microsensor Systems, Inc. Poly-(ethylenimine) (PEI, average molecular weight 1,800) and linear poly-(4-vinylpyridine) (PVP, average molecular weight 50,000) polymers used as coating materials were obtained from Aldrich and Polysciences, respectively.

The synthesis of nanophase pure-silica ZSM-5 (pore aperture 5.3 x 5.6 Å) was based on the work of Zecchina *et al.*⁹ An aqueous solution of alkali-free tetrapropylammonium hydroxide (TPAOH, from Johnson Matthey) was added to tetraethylorthosilicate (TEOS, 98% purity from Aldrich) with stirring. This resulted in a two-phase solution that was gradually hydrolyzed upon further stirring. Finally, water was added so that the resulting clear single-phase solution had a molar composition of 1 TEOS : 0.56 TPAOH : 80 H₂O. This solution was charged into an autoclave and heated to 448 K and maintained for 120 hours at that temperature with stirring under autogenous pressure. After cooling to room temperature, the white precipitate was separated from the mother liquor by vacuum filtration, washed free of excess TPAOH with distilled water, and dried at 393 K overnight. The uncalcined sample was used as made. Calcination was achieved by further heating of the sample at 813 K for 2 hours in air. The X-ray powder diffraction pattern and TEM micrograph of the crystallites both confirmed the crystal structure to be that of ZSM-5 and established the crystal sizes to be fairly uniform on the order of 100 nm, respectively. Thermogravimetric analysis of this sample shows a 4.2 wt% weight loss due to water. A broad peak in the ²⁹Si MAS NMR spectrum indicates this zeolite sample has many framework defects. These defects (internal silanol groups) are the sites where this water adsorption occurs.

Coating Preparations

All surface films were prepared by spin casting a solution (for organic polymer films) or suspension (for inorganic crystalline films) of the material of interest onto a SAW device at approximately 3000 rpm with usually one drop from a transfer pipette. The coated SAW devices were then heated to 348 K in air for the films to cure and the volatile solvents to evaporate.

The organic solutions were prepared by simply dissolving the polymer in a volatile solvent—methanol for PEI and chloroform for PVP. In this study, 1.5 wt.% PEI and 2.8 wt.% PVP solutions were used. Preparations for the inorganic zeolite-silica suspensions were based on the technique used by Bein *et al.*,¹⁰ the principle being to embed the zeolite crystals in a polymerized TEOS matrix. This process is accomplished by suspending finely ground samples of zeolite crystals in solutions of TEOS and ethanol (with a small amount of acid and base).

Vapor Flow System

SAW devices were clamped into a stainless steel holder using small pressure clips. Lids attached to this holder were fitted with inlet and outlet tubes to provide a vapor flow path. Vapor stream flow rates were regulated using mass flow controllers. All plumbing was constructed of

either stainless steel or Teflon. Distances between parts of the apparatus were minimized, and nitrogen was used as the inert carrier gas.

RESULTS AND DISCUSSION

Organic Polymers

A typical SAW sensor response is illustrated in Figure 1. In this case, a poly(ethylenimine) (PEI) coated 158 MHz dual SAW device (average film thickness 272 Å) was exposed to pulses of water vapor (relative humidity ~95%) at room temperature. As the sensor is exposed to humidified pulses in the vapor stream, water is sorbed into the polymer coating layer, thereby increasing the mass loading on the SAW oscillator. The frequency of the sample SAW device (the device coated with the chemically selective film) is initially less than that of the reference uncoated SAW device due to application of the PEI coating. Vapor sorption then further decreases the oscillation frequency of the sample SAW device. As the reference SAW device is unchanged, however, this process increases the absolute difference frequency, Δf or $|f_{\text{reference SAW}} - f_{\text{coated SAW}}|$, which is the ordinate in this plot. Upon removal of the vapor, the frequency difference decreases and returns to the original baseline value. Such reversibility of response is essential for continuous monitoring applications. The repeatability of response is quite good.

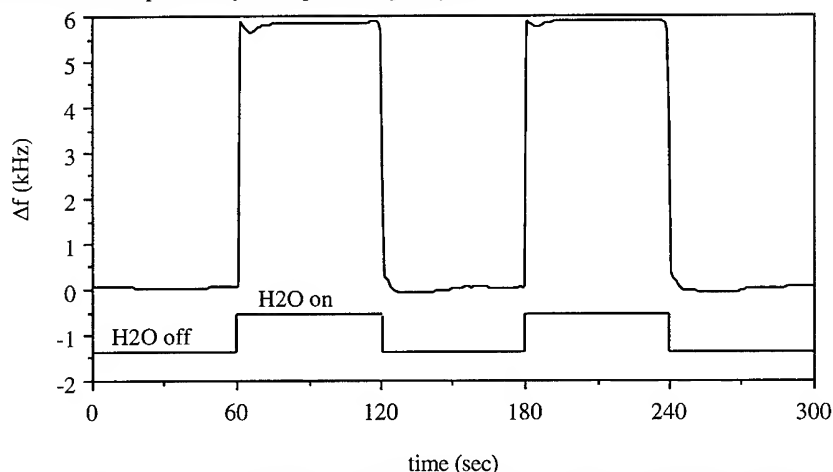


Figure 1. Typical response of a PEI coated SAW sensor to consecutive pulses of water vapor at room temperature

The frequency response to varying concentrations of water vapor was tested and it was found that the fit between the increase in difference frequency and relative humidity (RH) was non-linear. Small shifts in RH at higher RH would manifest larger changes in difference frequency than at lower RH. This may suggest that the sorption process is cooperative in nature; namely, the more molecules that are already sorbed, the further sorption is enhanced. On *a priori* grounds it would seem that the attraction of adsorbate molecules for each other exceeds their attraction for the adsorbent. In light of this, the fact that this vapor-coating system exhibits such behavior is not surprising as water is capable of forming hydrogen bonds.

Another important feature of SAW devices well illustrated by this example is the high level of detectability that can be achieved. Noise levels of uncoated devices do not usually exceed ± 16 Hz, and for PEI coated SAWs, no more than ± 25 Hz is achieved. These data give a signal to noise ratio on the order of 500 to 1. In theory a typical ST-cut quartz SAW vapor sensor operating at 158 MHz with an active surface area of 0.08 cm² will produce a frequency shift of about 400 Hz

per nanogram of mass loading. This would suggest that the detection limit for moisture attainable with a PEI coated SAW device would be on the order of 100 picograms.

The response of pulses of 2% dry CO_2 is on the order of 100 Hz (not shown) but tapers quickly to zero as the pulse continues. The initial response is most likely an artifact due to slight pressure fluctuations arising from the switching valve. PEI is therefore a poor sensor of CO_2 in dry environments.

Previous studies have demonstrated the sensitivity of PEI coatings to water vapor,⁸ but none have tested the possible interferences that the presence of other gases may have. Figure 2 shows the effect that CO_2 has on the detection of water vapor. A stream of humidified nitrogen (at approximately 65% relative humidity) is used to establish a baseline response in the SAW device. Upon introduction of 2% CO_2 at the same H_2O concentration (the amount of nitrogen being reduced to maintain a constant total flowrate), the SAW device responds quite rapidly in the initial phase, and then slows considerably after 20 to 30 seconds as it reaches the equilibrium value. A very striking feature of this response, however, is the fact that the frequency shift is negative, corresponding to a decrease in mass loading.

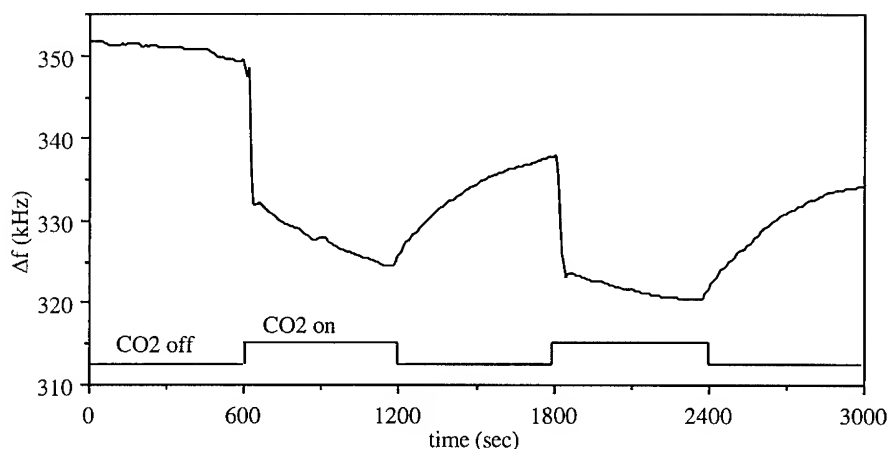


Figure 2. Response of PEI coated SAW to pulses of 2% CO_2 in humidified N_2 (65% RH)

Further experiments using a gravimetric adsorption technique confirmed the decrease in mass as CO_2 is introduced to a humidified nitrogen stream. A similarly coated SAW device was placed on Cahn balance fitted with gaslines to duplicate the same flow conditions as described above. Application of a greater amount the polymer was necessary to induce a response on the Cahn balance as its sensitivity was on the order of 0.1 μg . When CO_2 was introduced to a previously established humidified stream (the amount of nitrogen adjusted to keep a constant total flowrate), the mass did indeed decrease. Upon removal of CO_2 from the stream, however, the balance returned to its original equilibrium baseline value.

This phenomenon can be explained in terms of the possible absorptive nature of the vapor-coating interaction of water and PEI. It is known that most organic polymers are physically elastic, and this property allows the sorbing vapor molecules to diffuse below the surface into what are commonly referred to as "void spaces". For a given humidity level, equilibrium is established between the water molecules absorbed in these "void spaces" and ambient vapor molecules according to some effective partition coefficient. However, with the introduction of CO_2 (2% in this case) in the humidified stream, carbonic acid molecules could form either in the vapor phase or in the quasi-liquid phase within the "void spaces" after adsorbing and diffusing into the PEI film. The carbonic acid could significantly alter the pH of the absorbed "solution" in a manner that increases the polymer density and, hence, decreases the void volume. As the polymer responds in

this fashion, its capacity for absorption likewise decreases, and water, CO₂, and/or carbonic acid molecules are forced out of the surface film, thus resulting in the observed negative mass loading effect. A direct consequence of these changing polymer elastic properties can conceivably result in the observed hysteresis of the SAW frequency response after CO₂ has been switched off. While gravimetric analysis with the Cahn balance shows that mass loading returns to its original baseline rapidly, the SAW frequency exhibits a high degree of hysteresis, taking a significantly longer time to reverse only about half its initial change.

In light of the interference behavior between water and CO₂ which can possibly be attributed to the effects of carbonic acid, poly-4-vinylpyridine (PVP) was chosen to be tested with the water/CO₂ system. As pyridine has an sp²-hybridized nitrogen within an aromatic ring, PVP is likely to be much less basic than PEI which has aliphatic amine groups. The decrease in basicity should minimize the interactions (manifested as a negative Δf response and hysteresis) that were proposed to occur between PEI and carbonic acid.

Figure 3 shows the response of a PVP coated SAW device to pulses of varying humidity levels. It is evident that the response in the range of 10% to 25% relative humidity is fairly linear. However, humidity levels below about 8% induced a negative frequency shift. Since the analyte has not been changed, it is not likely that the same explanation used for PEI can be applied here. It remains unclear what factors other than the polymer elastic properties that may contribute to a negative frequency shift.

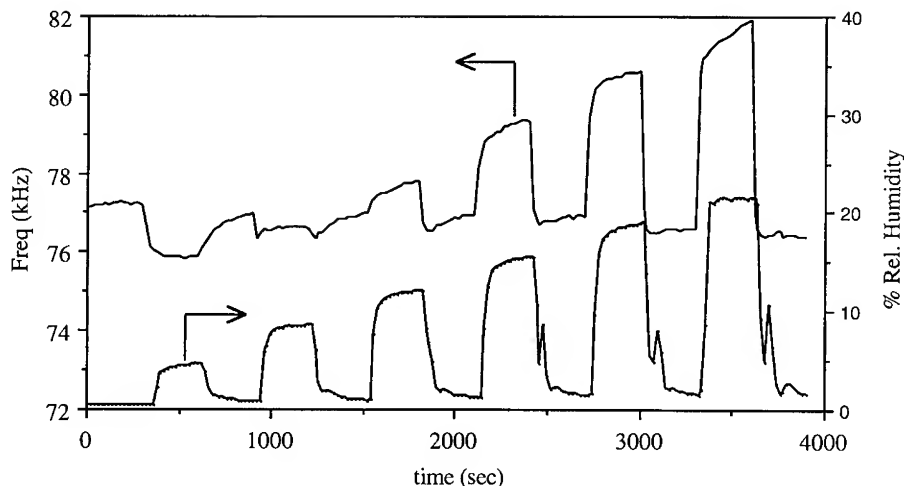


Figure 3. Adsorption of H₂O on PVP coated SAW

When challenged by dry CO₂, PVP showed almost no response, as frequency shifts consistently remained below 100 Hz for CO₂ levels of up to 6% by volume. Given the similar response of PEI to dry CO₂, this result was not unexpected. What was significantly different, however, was PVP's response to pulses of wet CO₂. Not only did PVP remain relatively insensitive to the presence of up to 20% CO₂ by volume, but its response to water was also unchanged. This absence of interference between CO₂ and water was indeed a remarkable departure from that observed with PEI, which all but precluded its use in continuous monitoring systems. PVP would then be a likely candidate for a SAW coating that can be used as a humidity sensor in environments where variable concentrations of CO₂ may be encountered provided the humidity levels were above ~10%.

Inorganic Coatings

Zeolites have long been known for their molecular sieving properties that are a consequence of crystalline pore structures with pore diameters in the range of molecular dimensions. It is the combination of mass sensitivity at the picogram level of SAW oscillators with molecular shape and size selectivity of zeolites that present a promising future for such microporous films in areas such as molecular recognition and interfacial chemistry. The microporous framework of zeolite films could endow the active region of the sensors with extensive surface area and volume for vapor sorption and provide for molecular exclusion and recognition sites. In addition to the molecular sieving abilities, zeolites can be tailored chemically to have specific types of adsorbate-adsorbent interactions. For example, the presence of cage cations such as sodium can participate in dipole-dipole or dipole-quadrupole interactions, while ion exchanging these cage cations with protons forming silanol groups in the porous network can enhance adsorption of hydrophilic species. Use of electronically neutral structure directing agents and careful choice of synthetic conditions can result in zeolites with minimal crystal defects, and these materials are extremely hydrophobic. Because zeolites are crystalline materials, zeolite films are less susceptible to significant elastic changes like these that have been observed with the organic polymer films. Additionally, zeolite films offer extremely high thermal stability (greater than 770 K) and chemical resistance.

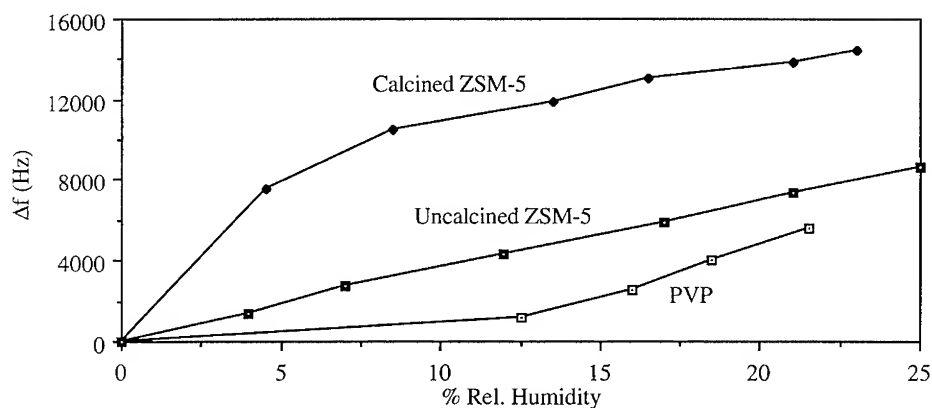


Figure 4. Water vapor adsorption isotherms

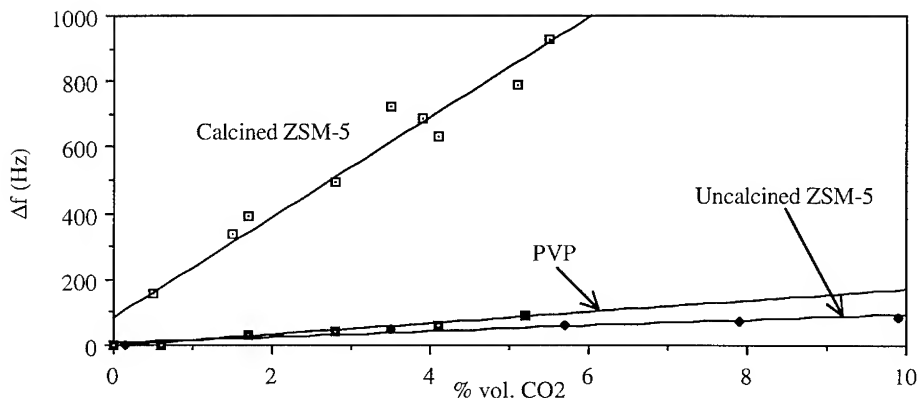


Figure 5. Carbon dioxide adsorption isotherms

In this study, a SAW device coated with nano-crystalline ZSM-5 embedded in polymerized silica was exposed to a variety of analytes in the vapor stream. Comparison of the water vapor adsorption isotherms obtained for calcined and uncalcined ZSM-5 coatings (see Figure 4) reveals that the two are qualitatively different. The uncalcined ZSM-5 crystals have essentially all of the porous network blocked with structure directing molecules used in the original synthesis. Thus, the observed response of the uncalcined ZSM-5 coated SAW device can only be attributed to adsorption occurring on the TEOS matrix and the crystal surface. This is manifested in the near linearity of the isotherm, as the amount of water adsorbed increases in proportion to the amount of water vapor present in the nitrogen stream. The adsorption isotherm of the calcined ZSM-5 coating, however, shows a region where a preponderance of water vapor adsorption occurs. This type I isotherm is typical of microporous materials.

The isotherm for the uncalcined ZSM-5 coating shown in Figure 4 reveals considerable adsorption of water vapor. Therefore, the amount of silanol groups on the crystal surface and in the silica matrix is likely to be quite substantial. The response of the uncalcined ZSM-5 coated SAW device dramatically decreased when the analyte was changed from water vapor to CO₂ (see Figure 5). The silica binder did not seem to have any significant affinity for CO₂.

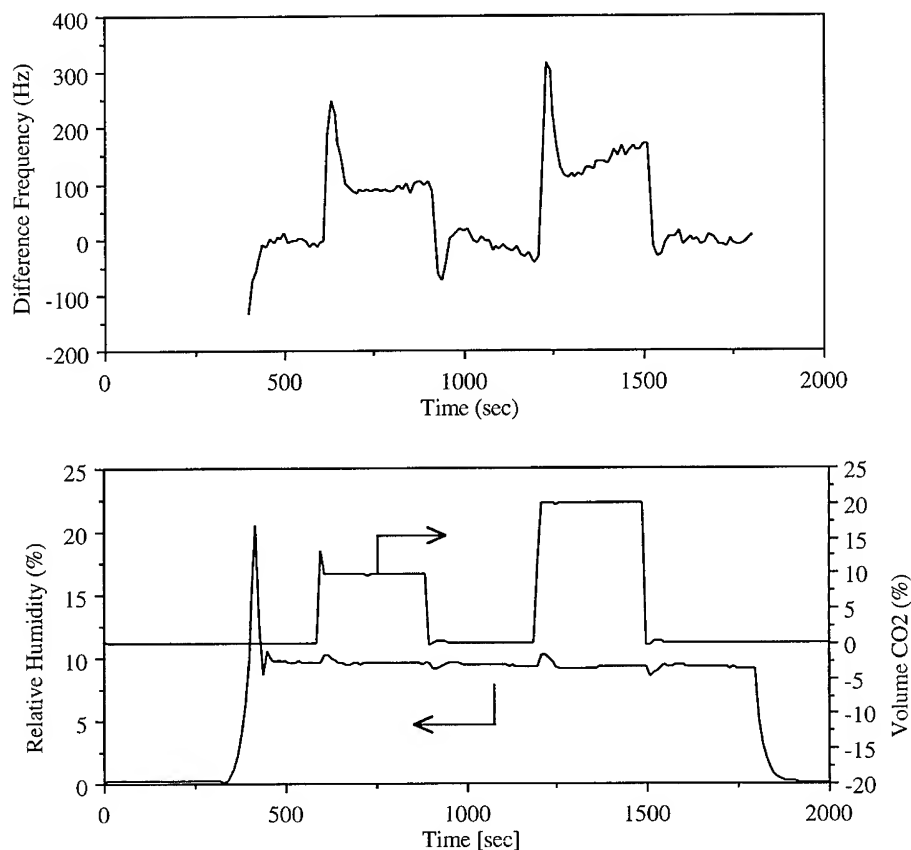


Figure 6. ZSM-5 coated SAW response to pulse of CO₂ in humidified N₂.

While both organic polymer films studied here exhibit effects that may be attributed to changes in elastic properties, no such phenomena are observed for the zeolite films. A very interesting consequence of this is the fact that little interference was found when both water vapor and CO₂ were present in the gas stream. The effects have been tested with both CO₂ pulses over a water baseline as well as water pulses over a CO₂ baseline. The former is illustrated in Figure 6. After the initial baseline with 10% relative humidity is established, pulses of CO₂ are introduced first at 600 seconds and again at 1200 seconds; the first pulse being about 10% volume and the second pulse about 20% volume CO₂. It is clear that the responses from each analyte species simply "superimpose" themselves, i.e., it is possible to see the CO₂ signals on top of the water signals and vice versa. This result would suggest that the ZSM-5 coating is a good candidate for sensing CO₂ in environments where the humidity is maintained at a constant level. Since the PVP film shows virtually no response to CO₂ in the presence of water vapor, an array of two SAW devices, one coated with PVP and another with pure-silica ZSM-5, could in principle provide a monitoring sensor for CO₂ in environments where the level of humidity is not constant.

ACKNOWLEDGMENTS

Financial support for this project was provided by an NSF Alan T. Waterman Award to MED. CBD is supported by a fellowship from Dr. Ralph Landau.

REFERENCES

1. M. D. Ward and D. A. Buttry, *Science* **249**, 1000-1007 (1990).
2. H. Bahadur and R. Parshad, in *Physical Acoustics*, edited by W. P. Mason and R. N. Thurston (Academic Press, New York, 1982), pp 37-171.
3. V. E. Bottom, *Introduction to Quartz Crystal Unit Design* (Van Nostrand Reinhold, New York, 1982).
4. G. Sauerbrey, *Z. Phys.* **155**, 206 (1959).
5. J. G. Brace, T. S. Sanfelippo, and S. G. Joshi, *Sens. Actuators* **14**, 47 (1988).
6. S. J. Martin, A. J. Ricco, D. S. Ginley, and T. E. Zipperian, *IEEE-Ultras* **34** (2), 143 (1987).
7. A. J. Ricco, G. C. Frye, and S. J. Martin, *Langmuir* **5**, 273-276 (1989).
8. H. Wohltjen, D. S. Ballantine, Jr., and N. L. Jarvis in *Chemical Sensors and Microinstrumentation*, edited by R. E. Dessy, W. R. Heineman, J. Janata, and W. R. Seitz (ACS Symposium Series **403**, American Chemical Society, Washington, DC, 1989) pp 157-175.
9. A. Zecchina, S. Bordiga, G. Spoto, L. Marchese, G. Petrini, G. Leofanti, and M. Padovan, *J. Phys. Chem.* **96**, 4985-4990 (1992).
10. T. Bein, K. Brown, G. C. Frye, and C. J. Brinker, *J. Am. Chem. Soc.* **111**, 7640-7641 (1989).

PART VIII

Thin Film Shape Memory Alloys

STRUCTURE AND THERMAL STABILITY IN TITANIUM-NICKEL THIN FILMS SPUTTERED AT ELEVATED-TEMPERATURE ON INORGANIC AND POLYMERIC SUBSTRATES

LI HOU, T. J. PENCE, AND DAVID S. GRUMMON
Department of Materials Science and Mechanics
Michigan State University, East Lansing, MI 48824

ABSTRACT

Deposition of crystalline titanium-nickel shape-memory alloys on polymeric substrates is complicated by the elevated temperatures that must be withstood either during deposition or during post-deposition crystallization anneals. In this paper we report results on thin films of titanium-nickel, with Ni-rich compositions, which were prepared by dc magnetron sputtering onto quartz substrates, and onto thin polyimide membranes, at various elevated substrate temperatures between 623K and 703K. All of the as-deposited films possessed ordered bcc microstructures and had nano-scale grain sizes. Films deposited at the higher end of the temperature range displayed familiar two-step transformation behavior in electrical resistivity experiments, with transformation temperatures that were stable with respect to annealing for 22-hrs at 700K. Classic shape-memory was observed for a bilayer consisting of an 7.6 μm thick Kapton[®] polyimide sheet onto which 3 μm of near-equiatomic TiNi had been sputtered at 703K. By applying a pattern-etch technique to the metallized polymer we were able to fabricate a prototype electrically-excitabile thin-film actuating element, potentially applicable to microelectromechanical and biomechanical systems.

INTRODUCTION

TiNi alloys that undergo thermoelastically-reversible displacive phase transformations can produce a large force-displacement product during the martensite-to-austenite transformation. The effect has been shown to be robust in sputtered thin films, offering the possibility for actuators having available work-energy densities greatly exceeding those available from electrostatic or piezoelectric actuator elements [1], albeit at reduced cycling rates. Although TiNi thin films have been integrated with silicon substrates in several devices [1-3], the versatility of this material in microelectromechanical settings would be improved if Ti-Ni thin films could also be applied to flexible polymeric substrates.

A prerequisite of the thermoelastic phase transformations underlying the shape-memory effect is an ordered crystalline parent structure. Ti-Ni films sputter-deposited at ambient temperature are amorphous and must be annealed to achieve crystallization, typically at temperatures exceeding 763K. At these temperatures, the outgassing rate of commercially available polyimide formulations is excessive, leading to compromised mechanical properties in the polymer, and contamination of thin film deposits. Although Walker *et al.* [4] demonstrated shape-changes during direct ohmic heating of a patterned TiNi thin film deposited on a silicon substrate having a polyimide interlayer, the crystallinity of the films in that interesting study remains uncertain, given the modest deposition and annealing (<623K) temperatures employed. Madsen *et al.* [5] reported that cold-working could reduce the crystallization temperature of free-standing thin films, but only to 673K. Ikuta [6] observed that deposition onto 673K glass substrates produced crystallinity, and Gisser, *et al.*, [7] found that Ti-Ni thin films deposited onto (100) silicon substrates at 733K were crystalline and had [110] texture. In the latter study it was demonstrated that deposition temperatures could be lowered to 623K, but only after nucleation of the crystalline phase at >733K.

This paper addresses the dependence of microstructure and transformation behavior on substrate temperature during deposition, and demonstrates the thermal stability of extremely fine-grained structures found to result from high-temperature deposition. We demonstrate the

feasibility of producing robust thermotractive thin film elements on conventional polymeric substrates. This offers the prospect for low-cost electrically-excitable thin-film actuators, integrated with flexible membranes, which may have wide-ranging applicability to microelectromechanical and miniaturized biomechanical systems.

EXPERIMENTAL METHODS

Ti-Ni thin films with thickness in a range of 3.1~9.2 μm were deposited onto both quartz plates and 7.6 μm thick DuPont Kapton[®]-NH polyimide films by a dc magnetron sputtering source fitted with a 50-cm binary alloy target. Two target compositions were used: Ti-50.96at%Ni and Ti-50.01at%Ni. Polyimide substrates were baked at temperatures exceeding 623K for 50 hours prior to deposition. During deposition, both quartz and polyimide substrates were heated to temperatures between 623 and 703K. After outgassing and with the substrate at temperature, the diffusion-pumped chamber maintained a base-pressure better than 4×10^{-5} Pa. High-purity argon at a working pressure of 0.73 Pa, a target-to-substrate distance of 58 mm, and cathode powers between 100 and 250 watts were used. Film growth rates ranged between 0.65~0.92 nm/sec.

After sputter deposition, free-standing Ti-Ni thin films for transmission electron microscopy and electrical resistivity measurements were obtained by peeling from the quartz substrates. Compositions of the films were determined by carefully calibrated energy-dispersive X-ray microanalysis, using ZAF corrections, in a Hitachi S-2500 machine with a silicon detector and a Link AN-1000 system. X-ray diffraction measurements to verify crystallinity were made on a Scintag XDS-2000 diffractometer using Cu-K α radiation. TEM specimens were thinned with a twin-jet electropolisher using 12% nitric acid and 88% methanol by volume at 223K. Using a masking technique, foils parallel to the plane of the deposit were obtained at three locations along the depth of the film: one at the film/substrate interface, one at the nominal midplane of the film, and one at the free-surface of the film, i.e., the last deposited. The specimens were examined in a Hitachi H-800 TEM at 200 kV with a single-tilt specimen stage.

Thin films on polyimide substrates were used in rudimentary shape-memory experiments in which the bilayer was manually deformed at liquid nitrogen temperature, and then allowed to convectively warm to ambient. TiNi-metallized polyimide sheets were also fabricated into a prototype electrically excitable thin-film microactuator by patterning and etching the serpentine configuration shown in Figure 1. These devices were deformed at LN₂ temperatures and transformed by application of a dc current at approximately 3 volts.

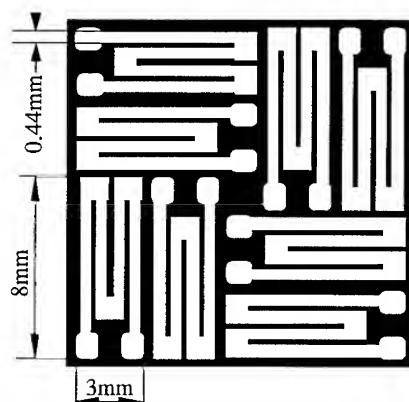


Figure 1. Pattern for electrically-excitable thermotractive TiNi/polyimide actuator elements.

RESULTS AND DISCUSSION

Sputtering conditions and resultant thin film compositions and transformation temperatures are given in Table 1. X-ray diffraction patterns from all of the films sputtered at temperatures at or above the minimum of 623K displayed a strong (110) peak from the B2

cubic austenite phase and were therefore nominally crystalline¹. Composition of the films was found to be a function of deposition temperature. In general, for both target compositions used, the nickel content of the films decreased monotonically with substrate temperature, in some cases giving resulting compositions which were leaner in Ni than the target. Films deposited onto both quartz and polyimide substrates at 700K (i.e., films #3 and #6) exhibited excellent ductility. Whether freed from quartz substrates, or adhered to polyimide, the films could be permanently deformed, at liquid nitrogen temperature, into a tight-radius hairpin configurations. Furthermore, this deformation was in each case fully recoverable upon heating to room temperature. On the other hand, deposition at 623K yielded films which were too brittle to suffer bending deformation without fracture. Films deposited onto polyimide substrates displayed slight extrinsic residual compressive stress due to the mismatch in the coefficient of thermal expansion between TiNi and polyimide, and assumed a 3 to 5mm radius of curvature at room temperature. Adhesion between TiNi and the polyimide substrates was excellent, and the films remained conformal even after bending to curvature radii on the order of 100 μ m.

Table I. Deposition Conditions and Thin Film Characteristics

ID	Substrate	Deposition Temperature (K)	Target Composition (a/oNi)	Cathode Power (watts)	Cathode Potential (volts)	Film Composition (a/oNi)	M _s (K)	M _f (K)	T _r (K)	A _s (K)	A _f (K)
#1	Quartz	623	50.96	100	537-492	53.1	(n/a)				
#2	Quartz	663	50.96	250	487-455	51.6	180	-	330	310	322
#3	Quartz	703	50.96	250	471-460	50.8	250	230	315	291	305
#4	Polyimide	678	50.01	150	607-558	53.9	(n/a)				
#5	Quartz	703	50.01	250	489-474	51.7	235	205	319	283	304
#6	Polyimide	698	50.96	250	644-619	50.8					
#7	Quartz	703 [†]	50.96	250	597-522	50.8	258	208	311	298	315

[†]This film received an additional 22hr post-deposition anneal at 700K

Figures 2(a,b) show electrical resistivity vs temperature behavior for as-deposited films #2, #3, and #5, together with film #7, which was similar in composition and deposition parameters to film #3, but which had been given a 22-hour isothermal anneal at 700K prior to the measurement. Film #2, deposited at 633K and having high nickel concentration, shows severely depressed M_s temperature and wide hysteresis. Films #3, #5 and #7 all display the classical B₂ \leftrightarrow incommensurate-phase \leftrightarrow R-phase \leftrightarrow martensite transformation sequence commonly observed in Ni-rich (>50.5at%Ni) bulk alloys aged at 673~773K after solution treatment [8,9]. Although film #5 has higher nickel content than film #2, M_s was much less depressed, indicating that the microstructure developed at the higher deposition temperature was closer to equilibrium, both in terms of returning the matrix composition toward stoichiometry, and lessening the precipitate coherency-strain effects on transformation temperature. Resistivity results for films #3 and #7 illustrate the thermal stability of the structures. Both were sputtered under similar conditions and have similar composition near stoichiometry, and show the higher of the recorded M_s temperatures. Film #7 was given a 22 hour anneal at 700K in the deposition chamber and showed only slight elevation of M_s relative to film #3, and displayed similar 2-step transformation behavior. It is concluded, in general, that hot-substrate deposition produces microstructures which, though extremely fine grained, are near-equilibrium and possess high thermal stability.

The microstructure of films deposited at 663K is typified by that shown for Film #2, in Figures 3(a-c), which represent, respectively, microstructures sampled at points near the original film/substrate interface, near the middle of the as-deposited film, and near the free

¹ As will be discussed below, a thin amorphous layer was found at the film/substrate interface in some cases.

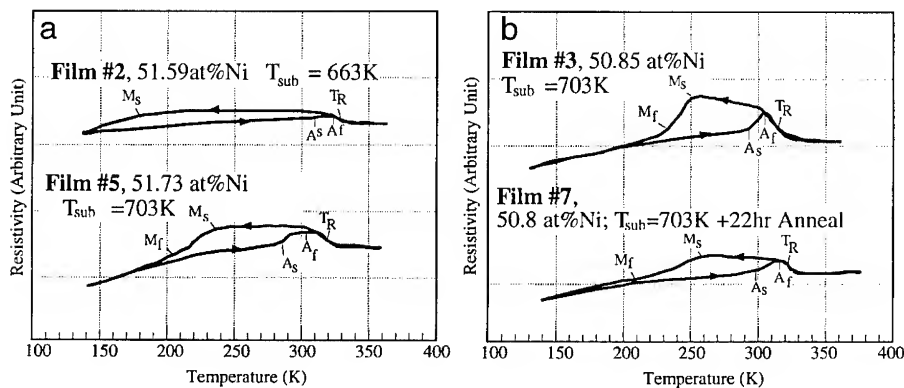


Figure 2. Electrical resistivity as a function of temperature for selected thin films.

(i.e., last-deposited) surface of the film. In Figure 3a, the first layer of the deposit is present as a gray area (marked with an arrow) surrounding the light-colored globular features, and is seen to be amorphous, producing a diffuse ring in the selected area diffraction pattern. The globular features are a cluster of small crystalline grains which have nucleated on the amorphous layer, indicating that the latter is less than a few hundred nanometers thick. The microstructure toward the center of film #2 (Fig. 3b) is fully crystalline, and shows evidence of the presence of small precipitates dispersed in a structure with extremely fine (<30nm) grains which were equiaxed in the plane of the foil. The structure is similar at the top surface of the film (Fig 3c), but with slightly coarser grain size. In each case, the extremely fine grain size is confirmed by the large number of sharp spots in the crystalline rings of the selected-area diffraction patterns. The crystalline ring patterns could be indexed to an ordered bcc cell with $a = 0.301$ nm. The absence of the (310) ring in the SADP indicates that the film had a sharp [110] fiber texture, similar to that reported in [7].

Figures 3(d-f) shows microstructures and diffraction patterns from film #3, deposited at 703K, in the interface/center/surface format used in Figure 3(a-c). The amorphous layer at the substrate interface, though thinner, is still evident in the diffraction pattern, and the grain size at the interface is approximately 10-20 nm. The thinner amorphous layer and exceptionally fine grain size, compared to film #2, reflect an enhanced crystallite nucleation rate at the higher deposition temperature. The midplane structure of film #3 contains small regions of self-accommodated R-phase that were apparently induced by the cold electropolishing solution, and, with $A_f \approx 305$ K, were stable at the temperature of observation. At the surface, the grain size has again coarsened to ~100 nm, and the high precipitate volume fraction observed in film #2 is absent, consistent with the lower nickel content of this film. Interestingly, the higher deposition temperature has greatly reduced the presence of [110] texture, as is apparent from the presence of the (310) diffraction ring. This observation is currently being studied in greater detail in tilting experiments and by X-ray pole-figure measurements.

Thin films deposited onto polyimide substrates exhibited robust shape-memory and were successfully patterned to produce a prototype electrically-excitabile thin film actuator element. Results of a rudimentary actuation experiment are shown in Figure 4. An 7.6-micron thick polyimide sheet with a 3-micron sputtered TiNi metallization, patterned as shown in Figure 1, was deformed into a ~100 μ m radius hairpin bend at LN₂ temperature as shown in

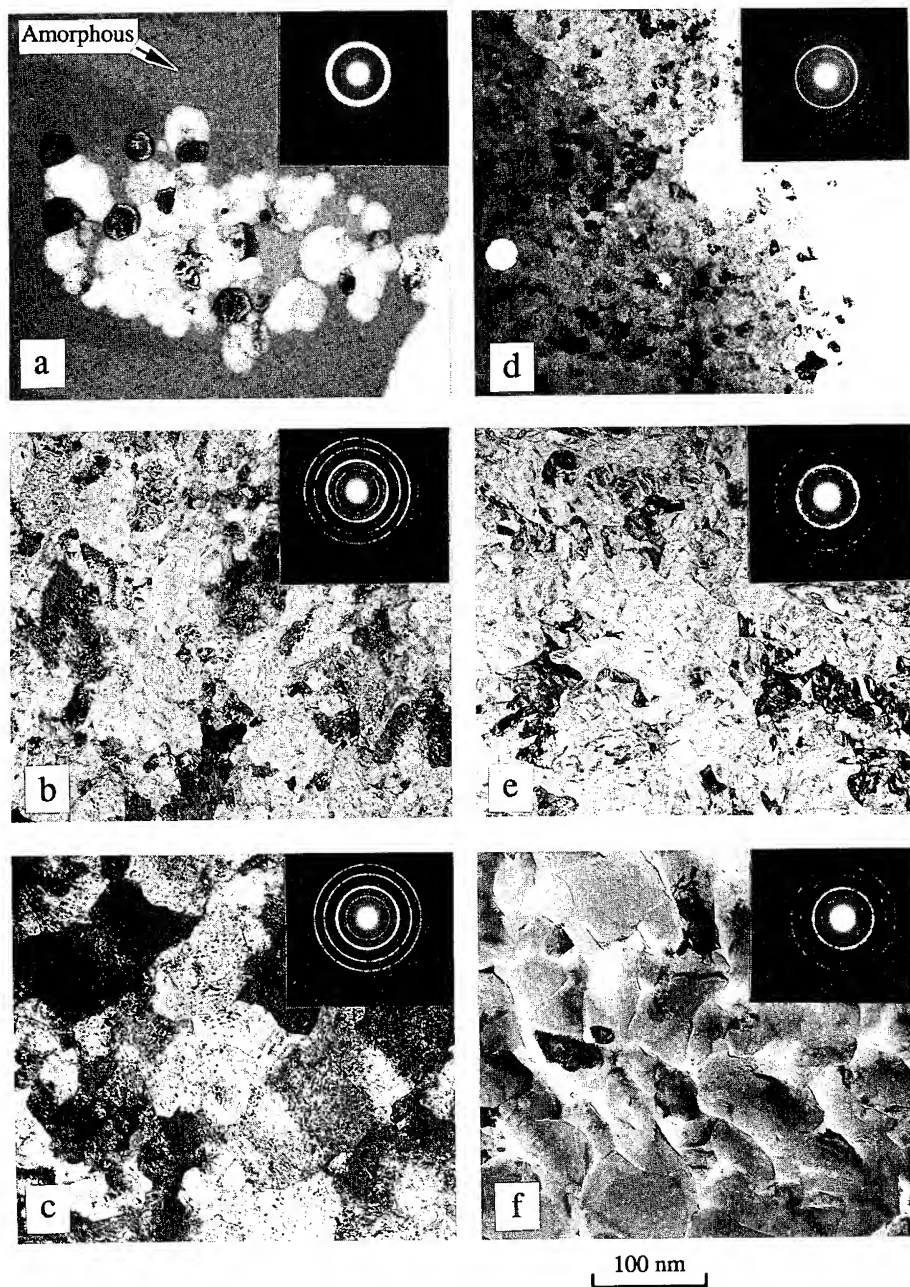


Figure 3. Microstructures and associated selected area electron diffraction patterns from films deposited at 663K and 703K: (a), (b), (c) are for film #2 deposited at 663K, taken from the film/substrate interface, the midplane, and the free surface, respectively. Images in (c), (d), and (f) are from the same locations in film #3, deposited at 703K.

Figure 4a. With the device still immersed in cold nitrogen gas, the application of approximately 3 volts dc at ~90 mA induced a rapid and complete recovery of the bending strain, leaving a flat sheet with no evident creasing or delamination, as shown in Figure 4b. The effect was repeatable for a number of cycles. The elastic biasing effect of the polymeric substrate was observed to induce a small reverse shape strain on cooling after removal of the current, indicating that the use of thicker substrates (whose net section modulus would be adjusted to roughly match that of the metallization) could give a convenient intrinsic biasing scheme for the realization of reversible actuators.

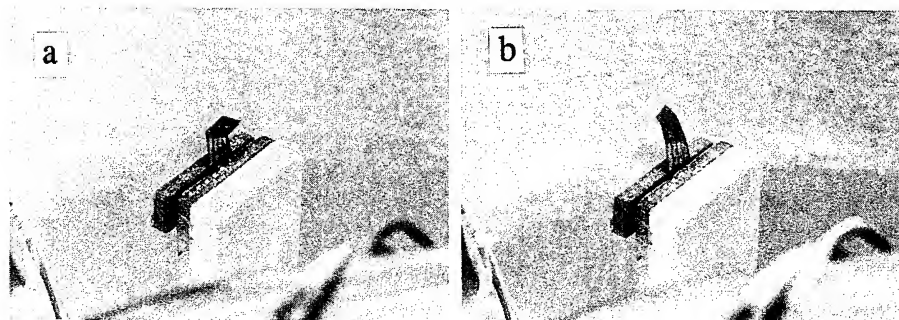


Figure 4. Prototype patterned TiNi/polyimide bilayer configured for electrical excitation of the austenite transformation. (a) bent to a hairpin at low temperature. (b) Shape recovered by application of 3 V at ~90 mA.

CONCLUSIONS

Elevated-temperature sputter deposition of titanium-nickel produces robust, ductile films capable of thermoelastic transformation behavior and shape-memory. Films deposited at temperatures above 700K are ductile and can be deformed to very tight bending radii. The grain size is extremely fine (<20-50nm), especially compared to the 1-3 μm grain size found in experiments employing cold-substrate deposition and post-deposition crystallization annealing [10]. These fine-grained microstructures are thermally stable at 700K with respect to shifts in transformation temperature.

It has been shown that sputter deposition of crystalline TiNi thin films onto polymeric substrates is practical, and results in robust, adherent metallizations that can be subsequently pattern-etched to produce electrically excitable thermottractive elements. Such devices may have wide-ranging utility as actuators in microelectromechanical systems and biomechanical devices.

ACKNOWLEDGMENTS

This work was funded by the National Science Foundation under grant #MSS9302270, by the Michigan State University Center for Fundamental Materials Research, and by the Ford Motor Company Scientific Research Laboratory.

REFERENCES

1. A. D. Johnson, J. D. Busch, C. A. Ray and C. Sloan, *Mat. Res. Soc. Symp. Proc.* **276**, 151 (1992).
2. C. A. Ray, C. L. Sloan, A. D. Johnson, J. D. Busch and B. R. Petty, *Mat. Res. Soc. Symp. Proc.* **276**, 161 (1992).
3. K. Kuribayashi, T. Taniguchi, M. Yositate and S. Ogawa, *Mat. Res. Soc. Symp. Proc.* **276**, 167 (1992).
4. J. A. Walker, K. J. Gabriel and M. Mehregany, *Sensors and Actuators*, **A21**, 243 (1990).
5. J. S. Madsen and A. P. Jardine, *Scripta Metall.*, **30**, 1189 (1994).
6. K. Ikuta, H. Fujita, M. Ikeda and S. Yamashita, *Proc. IEEE MEMS*, Napa Valley, CA, 38 (1990).
7. K.R.C. Gisser, J.D. Busch, A.D. Johnson and A.B. Ellis, *Appl. Phys. Lett.*, **61**, 1634 (1992).
8. M. Nishida and T. Honma, *Scripta Metall.*, **18**, 1293 (1984).
9. M. Nishida and T. Honma, *Scripta Metall.*, **18**, 1299 (1984).
10. A.D. Johnson, *J. Micromech. Microeng.* **1**, 34 (1991).

THERMO-MECHANICAL $\text{Ni}_{50}\text{Ti}_{50}$ /Si COMPOSITE THIN FILM SWITCH

T. KIM, QUANMIN SU AND MANFRED WUTTIG

Department of Materials and Nuclear Engineering, University of Maryland, College Park, MD 20742-2115, USA

ABSTRACT

The mechanical properties of $\text{Ni}_{50}\text{Ti}_{50}$ deposited on Si and 3C-SiC substrates were studied focussing on the interaction of the film and substrate. This interaction determines the transformation characteristics through interface accommodation and mechanical constraints exerted by the substrate stiffness. Substrate stiffness, controlled by the film/substrate thickness ratio, was found to have a substantial influence on the output energy of the film/substrate composite. A switch type composite based on this knowledge was fabricated and tested.

INTRODUCTION

The demand for mechanical actuators and sensors of micron dimensions has increased considerably in recent years. The new trend is to engineer materials into micron size dimensions and integrate material science and electronic engineering into one functional chip. Shape memory alloys (SMAs) possess the unique property of a large output strain. As a candidate material for micro-actuation SMAs attracted renewed interest in the last few years¹. However, SMAs suffer from a speed limit due to their slow cooling rate. If SMAs are made into thin films on a substrate with good thermal conductivity, such as Si, the frequency of operation can be increased to a few kilo Hertz². Although first successes of micron sized SMA actuators have been achieved^{3,4}, SMA film/substrate composites remain to be a challenging problem⁵. From an application point of view, the enhanced operation speed relies on the composite; from a material science point of view the SMA transformation under substrate constraints may involve new problems in contrast to bulk transformations.

An SMA film on a substrate is subjected to two types of constraints: 1. continuity at the interface and 2. substrate stiffness. The former is a structural constraint, systematically studied previously⁶, and the latter can be viewed as a mechanical constraint. This paper presents results aimed at making a thermal switch type SMA film/substrate composite as well as the consequence of mechanical constraints which affect the switching efficiency.

For cantilever film/substrate composite the SMA transformation exhibits itself as additional bending through transformation induced stress. The output of the composite is therefore a stress driven displacement. Another interesting configuration of the film/substrate composite is a membrane, as shown in Fig. 1. As transformation occurs, the large strain generated by the SMA is expected to tune the membrane resonance frequency through the change of the composite stress. Both configuration will be studied.

EXPERIMENT

Details of the film deposition process was reported in reference 5. The as deposited films are amorphous and were crystallized at 480 °C. All films were treated at 600 °C for grain growth which establishes well defined transformation properties. An epitaxial SiC membrane grown on Si was chosen for making the composite membrane. The superior mechanical properties of SiC, compared to Si, renders the membrane composite much more reliable. However, it also introduces substantial difficulties for film deposition since NiTi does not adhere well on as-grown SiC. Knowing that NiTi adheres properly to SiO₂, SiC was annealed in ambient at 950 °C to develop a SiO₂ layer⁷. NiTi film deposited on a thus treated SiC membrane does not visibly show adhesion problems.

For cantilever film/substrate composites the transformation induced stress is measured through the curvature of the cantilever as a function of temperature. The curvature induced deflection of the film/substrate composite can be converted into stress in the film using the Stonley equation⁸.

Stress in the membrane composite is measured by a dynamic method, i.e. via membrane vibration. The square of the membrane resonance frequency is directly proportional to the average stress of the composite membrane⁹.

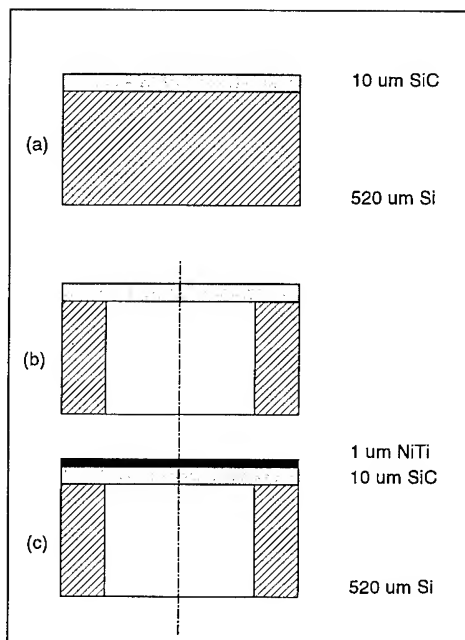


Fig. 1: Schematic of the membrane composite. a. As-grown SiC wafer; b. Stripping Si by masked wet etching; c. deposit Ni₅₀Ti₅₀ film.

RESULTS

Dynamic measurements and microstructure characterization which provide evidence of interface constraint in thin film martensitic transformation have been reported earlier¹⁰. Using the cantilever deflection method the output of the transformation strain manifests itself as an additional deflection. Quantitative studies found that this deflection is induced by the volume change during transformation. A typical measurement of stress in Ni₅₀Ti₅₀ film as a function of temperature is shown by the top curve in Fig. 2. The curve was measured as the temperature increased. As temperature increases the tension in the film decreases because the thermal expansivity of Ni₅₀Ti₅₀ is larger than that of Si. During transformation from the martensitic to the austenite phase the volume shrinks about 0.5%¹¹, fully accounting for the tension developed in the transformation step of the top curve in Fig. 2. As the temperature continues to increase the stress in the film decreases again due to thermal strains. The shape of the top curve is complicated because thermal and transformation induced stresses overlap. This complication not

only reduces the effective transformation energy output but also renders actuation temperature control more difficult. It is clear that the thermal stress of the composite must be compensated by depositing a suitable layer on the other side of the cantilever. In order to balance the thermal stresses throughout the temperature region, NiTi itself is the best choice. Based on the knowledge that amorphous NiTi does not show transformation, a layer of 0.5 μm NiTi is deposited on the other side of the composite cantilever at room temperature. Now the thermal stress in the tri-layer composite is reduced (center curve in Fig. 2). When the amorphous layer thickness is equal to the thickness of the crystalline layer, thermal stress is

compensated throughout the entire temperature region as can be seen from the bottom curve in Fig. 2. A well defined switch type NiTi/Si composite is thus developed. The composite has been preliminarily fatigue tested by cycling between low and high temperature up to 10^3 times at the end of which the output of the transformation, i.e. the step height in the bottom curve of Fig. 2, remains unchanged.

Another major concern for applications is the efficiency of transformation output as a function of the substrate stiffness. The effect of the substrate stiffness is schematically shown in Fig. 3. This figure shows the stress distribution in the film under the constraint of a stiff substrate. The length of the arrows is used to qualitatively show the magnitude of the stress. Except at the free edges the stress in the film is uniform and tensile in the case shown. If the substrate has finite stiffness it will bend under the surface traction of the film. The bending results in a redistribution of the stress accompanied by partial stress relief in the film, see Fig. 3b. A softer substrate permits more stress relief in the film thereby increasing the magnitude of substrate bending as shown in Fig. 3c. This problem has been systematically treated by Brenner & Senderoff¹². However, if one considers the bending resulting from this stress relief quantitatively, it is not very significant. In fact, the stress in thin films is determined by the shear at the interface located near the edge¹³. It is this localized interface shear stress which determines the stress in the film. In practice, this shear bonding may redistribute towards the interior of the

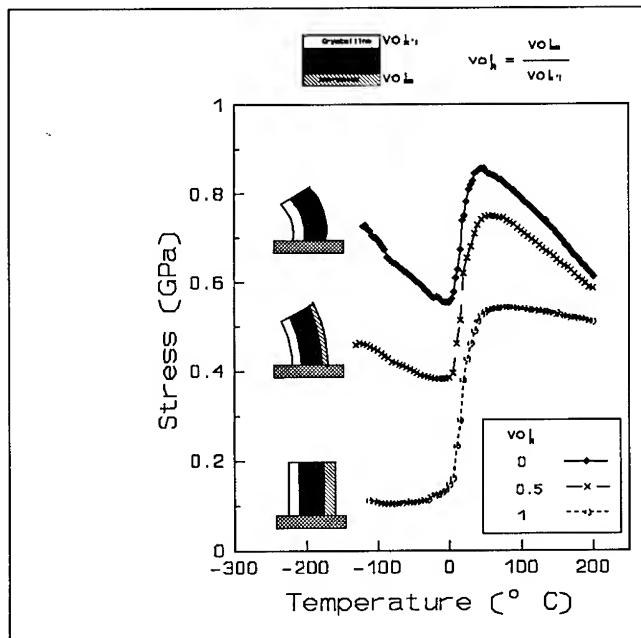


Fig. 2: Stress evolution of a switch type Ni₅₀Ti₅₀/Si cantilever. Top, 1 μm B19 NiTi on 90 μm Si; Center, 0.5 μm compensating amorphous NiTi; Bottom, 1 μm compensating amorphous NiTi.

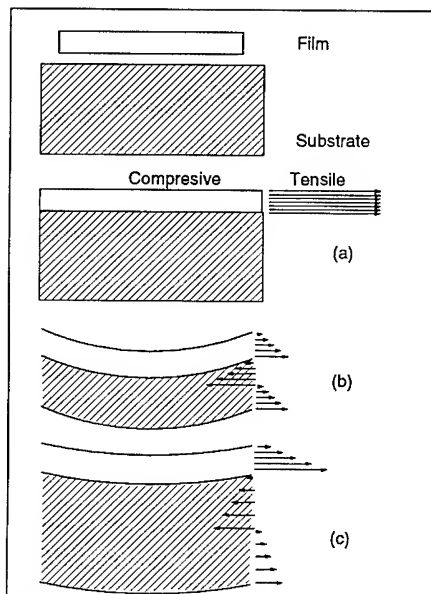


Fig. 3: Film stress relief due to substrate bending. The arrows represent the magnitude of the stresses. Film on a) a rigid, b) a semi-rigid and c) a soft substrate.

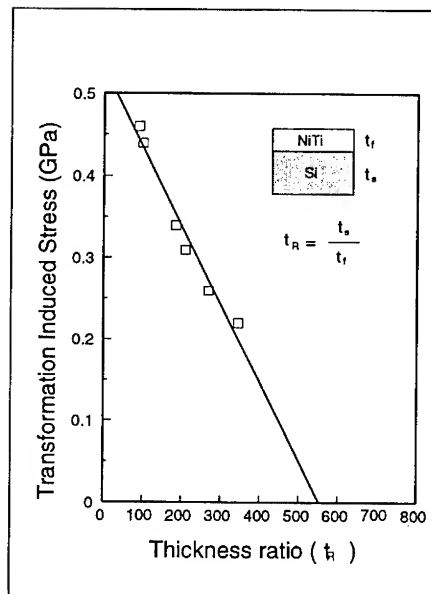


Fig. 4: The transformation induced stress output as a function of the film/substrate thickness ratio. The film thickness is $1\mu\text{m}$ in all cases.

film if the adhesion or microstructure are inhomogeneous. Interface shear stresses are known to be a difficult problem. It was studied by many investigators and yet no simple, universal solution has been given. A numerical solution shows that the shear stress maximum depends substantially on the thickness ratio¹⁴. It is concluded that the stress, which can be sustained by the present structurally inhomogeneous films, may depend predominantly on the relative stiffness of the substrate and film.

A martensitic transformation on a substrate with finite stiffness poses an even more complicated problem. The generation of stress in the film may now be determined by the distribution of variants in addition to the volume ratio of the transformed material. Both factors introduce heterogeneous structures which are substantially more complicated than those solved before. However, the effect of substrate stiffness is an inescapable problem since the final design of the SMA/Si composite actuator requires optimized output energy and speed. The substrate stiffness determines both.

The result of the transformation measured with different substrate stiffnesses is shown in Fig. 4. All films were deposited under the same conditions and heat treated together so that their microstructure is identical. The film thickness is $1\mu\text{m}$ for all specimens and the substrate thickness ranges from $90\mu\text{m}$ to $345\mu\text{m}$. The height of the step in the bottom curve of Fig. 2 is plotted for each specimen as the phase transformation stress on the ordinate. The result clearly shows that the relative substrate stiffness plays an important role in determining the efficiency

of the SMA film/substrate composite. The microscopic origin of this effect is still under investigation.

While the cantilever SMA film/substrate composite generates a deflection as the output parameter, the resonant frequency of a membrane composite is expected to be tuned by the transformation. Fig. 5 shows the results of 1 μm $\text{Ni}_{50}\text{Ti}_{50}$ on a 10 μm SiC membrane, as explained in Fig. 1. The sharp dip of the stress in the membrane occurs in the same temperature region as the transformation of a film of the same thickness on a

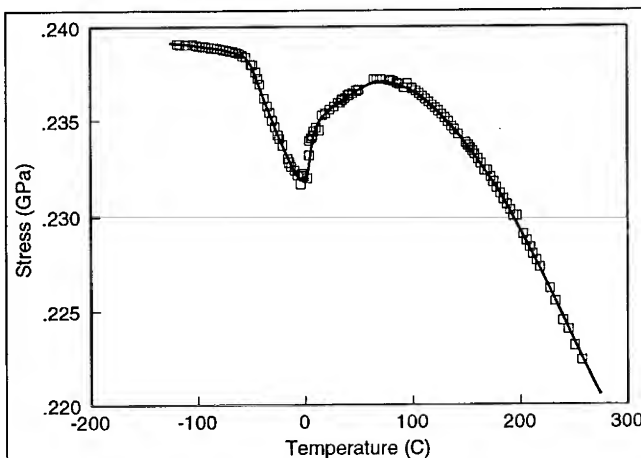


Fig. 5: Stress of the 1 μm B19 $\text{Ni}_{50}\text{Ti}_{50}$ /10 μm 3C SiC membrane as a function of the temperature. The radius of the membrane is 12.5 mm.

Si cantilever (Fig. 3) and is interpreted as being caused by the phase transformation in NiTi layer. However, the measured temperature dependence is complicated in two respects: a. much smaller variation of stress than expected is observed; b. no stepwise stress or resonant frequency change occurs. The former may be related to insufficient adhesion of the NiTi layer to the SiC membrane since the transformation strain can be fully effective only if the load transfer through the interface is purely elastic. Insufficient adhesion may relax the transformation strain by interfacial sliding and thus reduce the total output, resulting in a less than theoretical average stress of the membrane composite. The thermal stress in the membrane is much more difficult to eliminate in the case of the membrane because the simple compensation principle which is successful for cantilevers fails in stress controlled membranes.

CONCLUSION

A $\text{Ni}_{50}\text{Ti}_{50}$ (B19)/Si/SiO₂/ $\text{Ni}_{50}\text{Ti}_{50}$ (amorphous) composite thermo-mechanical switch exploiting the transformation volume change of crystalline $\text{Ni}_{50}\text{Ti}_{50}$ has been developed. The composite energy output depends on the film/substrate thickness ratio. A $\text{Ni}_{50}\text{Ti}_{50}$ /3C-SiC composite membrane exhibits transformation characteristics through a variation of its resonant frequency in the vicinity of the phase transformation of the SMA.

ACKNOWLEDGEMENTS

This study was supported by the Office of Naval Research, contract No. N00014-93-10506 and the National Science Foundation, Grant No. DMR-93-21185, it also benefitted from support

by the Army Research Office, contract No. DAAL03-92-G-0121.

REFERENCES

1. S. Miyazaki, Y. Sugaya, and K. Otsuka, *MRS Int'l Mtg. on Adv. Mats.*, vol. 9 p. 251 (1989)
J.D. Busch, A.D. Johnson, D.E. Hodgson, C.H. Lee and D.A. Stevenson, *Mat. Sci. Forum*, vol.56-58 p. 729 (1990)
2. A.P. Jardine, *MRS Symp. Proc.* vol. 246 p. 427 (1992)
3. A.D. Johnson, *J. Micromech. Microeng.*, vol.1, p. 39 (1991)
4. J.A. Walker and K.J. Gabriel, *Sensors and Actuators*, A21-A23 p. 243 (1990)
5. C. M. Su and M. Wuttig, in "*Damping in Multiphase Inorganic Materials*" edited by R. B. Baghat, ASM International Publication, 1993, p. 165
S. Z. Hua, C. M. Su and M. Wuttig, *MRS Proceeding on Thin Films-Stress and Mechanical Properties III*, Vol. 308, p. 525 (1993)
6. reference for - structural constraint, systematically studied previously
7. J. A. Dillon Jr. in *Silicon Carbide -A High Temperature Semiconductor*, Edited by J. R. O'Connor and J. Smiltens, Pergamon Press, 1960, p. 235.
8. G. G. Stoney, *Proc. Roy. Soc. London* A82, p. 172 (1909)
9. De Hartog, *Mechanical Vibrations*, McGraw-Hill, New York, 1947
10. Quanmin Su, S. Z. Hua and M. Wuttig, *Proceedings of the International Conference on Martensitic Transformations*, MRS-ICAM-93, Tokyo, 1993
11. reference for the volume shrinks about 0.5%
12. A. Brenner and S. Senderoff, NBS Report 1954 42, 1 (1949)
13. Mary F. Doerner and William D. Nix, *Critical Reviews in Solid State and Materials Sciences*, vol. 14, Issue 3, 1988, pp 225-268
14. Williams, J. *Thermal Stresses*, 8, 183 (1985)

SHAPE MEMORY BEHAVIOR OF Ti-Ni THIN FILMS ANNEALED AT VARIOUS TEMPERATURES

A. ISHIDA*, A. TAKEI*, M. SATO* AND S. MIYAZAKI**

*National Research Institute for Metals, 1-2-1, Sengen, Tsukuba-shi, Ibaraki 305, JAPAN

**Institute of Materials Science, Tsukuba University, Tennoudai, Tsukuba-shi, Ibaraki 305, JAPAN

ABSTRACT

Ti-Ni thin films with three different types of compositions, titanium-rich Ti-Ni, near equiatomic TiNi and nickel-rich Ti-Ni were prepared by sputtering. The sputter-deposited films were annealed at various temperatures between 773 and 973K in order to crystallize. After the heat treatment, the shape memory behavior was examined with a thermomechanical tester. The shape memory behavior of the near equiatomic composition films was not affected by the heat treatment. On the other hand, the shape memory behavior of the other composition films strongly depended on the annealing temperature. As the annealing temperature increases, the martensitic and reverse martensitic transformation temperatures of the nickel-rich films decreased and those of the titanium-rich films increased. These opposite behaviors of the transformation temperatures can be explained by the opposite dependence of the precipitation of the second phase on the annealing temperature. All the nickel-rich films exhibited good shape memory effect over a wide range of stress, while all the titanium-rich films exhibited a small plastic strain only in the stress range where the shape changes associated with both the R-phase and the martensitic transformations were observed.

INTRODUCTION

Micromachines such as manipulators and fluid microvalves are currently expected to be used in various fields such as medicine, biotechnology, micro optics and the semiconductor production. In order to work such a micromachine, an effective small actuator is necessary. Among the microactuators proposed at present, the actuator with shape memory thin films is considered to be an attractive candidate for a microactuator owing to their large deformation and strong recovery force. There have been several papers suggesting the potential of Ti-Ni thin films[1-4]. The present authors also showed in previous papers[5,6] that sputter deposited thin films of Ti-Ni exhibit almost perfect shape memory effect comparable to that in a bulk Ti-Ni. However, the shape memory behavior of Ti-Ni thin films is very sensitive to the heat treatment. In the present paper, we investigate the effect of the annealing temperature on the shape memory behavior of Ti-Ni thin films.

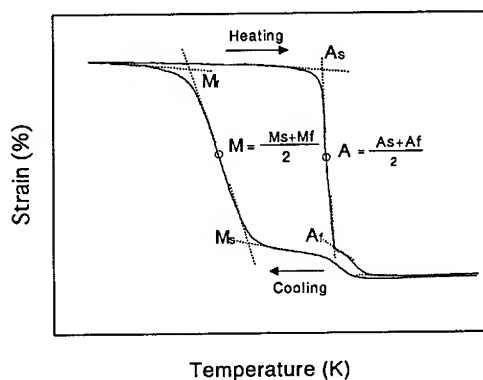


Fig. 1 Schematic strain vs. temperature curve obtained upon cooling and heating under a constant stress and definition of the transformation temperatures used in the present paper.

EXPERIMENTAL

Thin films of Ti-Ni with three different compositions were deposited on glass substrates by r. f. magnetron

sputtering. The sputtering conditions used in this study were as follows: substrate temperature, 523K; Ar gas pressure, 0.3Pa; r. f. power, 600W; substrate-to-target distance, 80mm; deposition time, 7.2ks. In order to obtain a variety of film compositions, several discs of pure titanium with a diameter of 10mm were placed on the 6 in. diameter target of Ti-50at.%Ni alloy. The thickness of the deposited films ranged from 6 to 9 μm . After the sputtering, they were removed from the glass substrates and then heat treated to produce crystallization of Ti-Ni. The heat treatments were carried out for 3.6ks at three different temperatures, 773K, 873K and 973K. Since transmission electron microscopy and X-ray diffractometry revealed that the three kinds of films exhibited a two-phase structure with a dispersion of fine Ti_2Ni precipitates in a TiNi matrix, a TiNi single-phase structure and a two-phase structure with a dispersion of fine Ti_3Ni_4 precipitates in a TiNi matrix, respectively, the film compositions were estimated to be Ti-rich Ti-Ni, near equiatomic TiNi and Ni-rich Ti-Ni. The shape memory behavior of the annealed films was measured with a small tensile tester equipped with an automatically controlled heater. The size of the sample used for this test was $1 \times 5 \text{ mm}^2$ and the thickness was in the range of 6 to 9 μm . This test involved loading the sample at a high temperature, cooling it down to 143K at a rate of -10 K min^{-1} and heating it back to the original temperature at a rate of 10 K min^{-1} . Figure 1 shows a schematic curve representing the typical behavior of the shape change in the films upon cooling and heating under a constant stress. The martensitic and reverse martensitic transformation temperatures were defined as the averages of their transformation start temperatures and their transformation finish temperatures which were determined by the tangential extrapolation method, as indicated in the figure.

RESULTS AND DISCUSSION

Shape memory effect of Ni-rich Ti-Ni

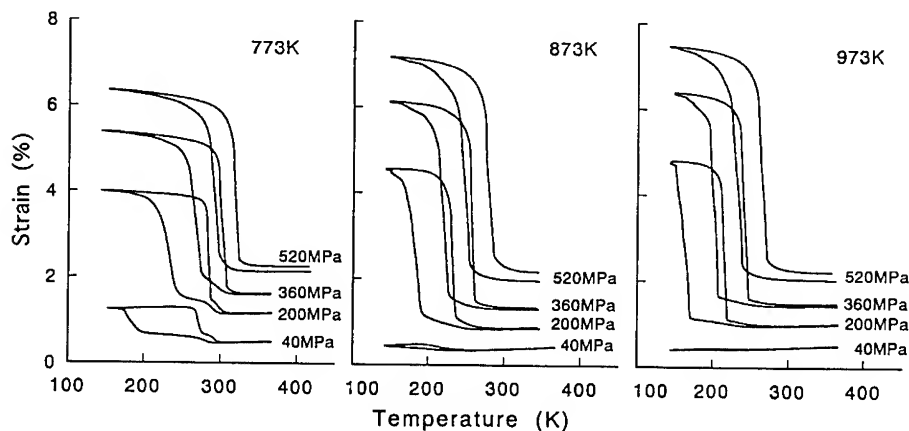


Fig.2 Strain vs. temperature curves at various constant stresses for nickel-rich Ti-Ni thin films annealed for 3.6ks at various temperatures.

Figure 2 shows the strain vs. temperature curves at various stresses for the nickel-rich Ti-Ni thin films annealed at various temperatures. For the film annealed at 773K, a two-stage shape change was observed upon cooling. The first stage of this shape change was attributed to the R-

phase transformation and the second stage to the martensitic transformation. On the other hand, for the films annealed at 873K and 973K, only one stage of a shape change was detected upon cooling, being attributed to the martensitic transformation. All the films showed very small plastic strains, indicating that they had good shape memory effect. The transformation strain of the films observed under an identical stress increased with increasing annealing temperature; e.g., under a stress of 360MPa, it was 3% for the annealing temperature of 773K, but amounted to 4.9% for the annealing temperature of 973K.

The transformation temperatures under a load of the films were determined from the curves in Figure 2 in the manner described earlier and are plotted as a function of the annealing temperature for each constant stress in Fig. 3. Both the martensitic and the reverse martensitic transformation temperatures decrease with increasing annealing temperature. This change in the transformation temperature seems to be related to the precipitation of Ti_3Ni_4 in these films. Such a precipitate was confirmed in the films annealed at 773K and 873K by the transmission electron microscopy and X-ray diffractometry studies, while, in the film annealed at 973K, such a precipitate could not be detected.

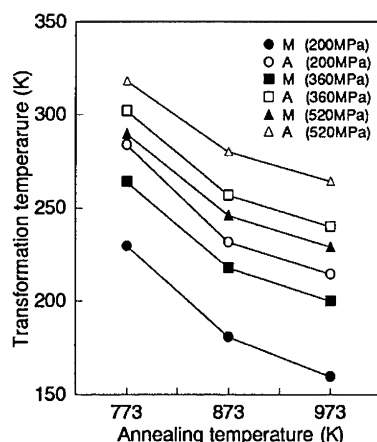


Fig.3 Annealing temperature dependence of the martensitic and reverse martensitic transformation temperatures (shown by M and A, respectively) under various stresses for nickel-rich Ti-Ni thin films annealed at various temperatures.

Shape memory effect of near equiatomic Ti-Ni

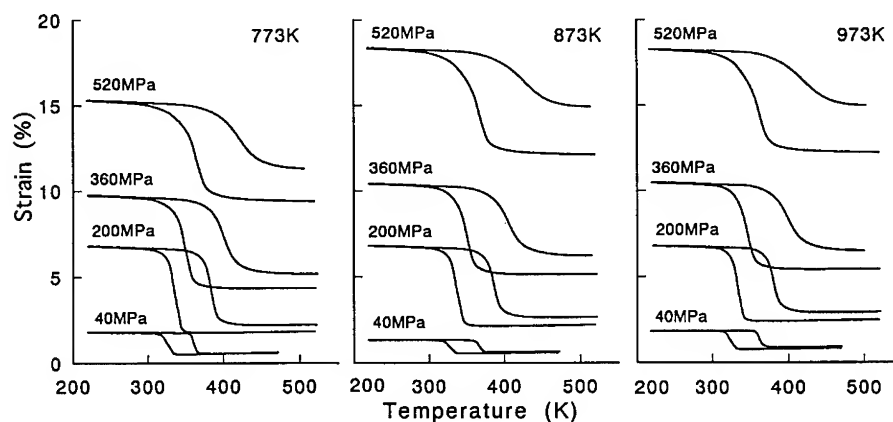


Fig. 4 Strain vs. temperature curves at various constant stresses for near equiatomic TiNi thin film annealed for 3.6ks at various temperatures.

Figure 4 shows the strain vs. temperature curves at various stresses for the equiatomic Ti-Ni thin films annealed at various temperatures. In this case, all the films exhibited a single-stage shape change relating to the martensitic transformation for all the annealing temperatures. As can be seen in the figure, the heat treatment seems to have no effect on the shape memory behavior. This seems to be reasonable since there were no second phase precipitates in these films. All the films showed a large plastic strain, reflecting the absence of the precipitation strengthening effect.

The transformation temperatures under a load obtained from the curves in Fig. 4 are plotted against the annealing temperature in Fig. 5. Both the martensitic and the reverse martensitic transformation temperatures are almost constant irrespective of the heat treatment. They are located at around 325K and 365K respectively under a stress of 40MPa; this

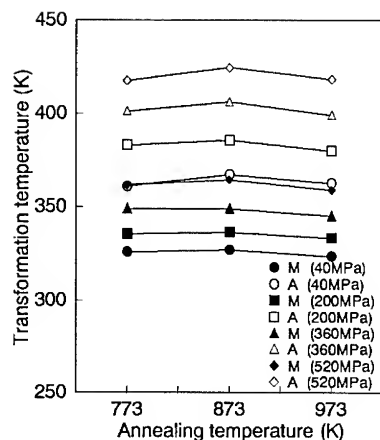


Fig. 5 Annealing temperature dependence of the martensitic and reverse martensitic transformation temperatures (shown by M and A, respectively) under various stresses for near equiatomic TiNi thin films annealed at various temperatures.

Shape memory effect of Ti-rich Ti-Ni

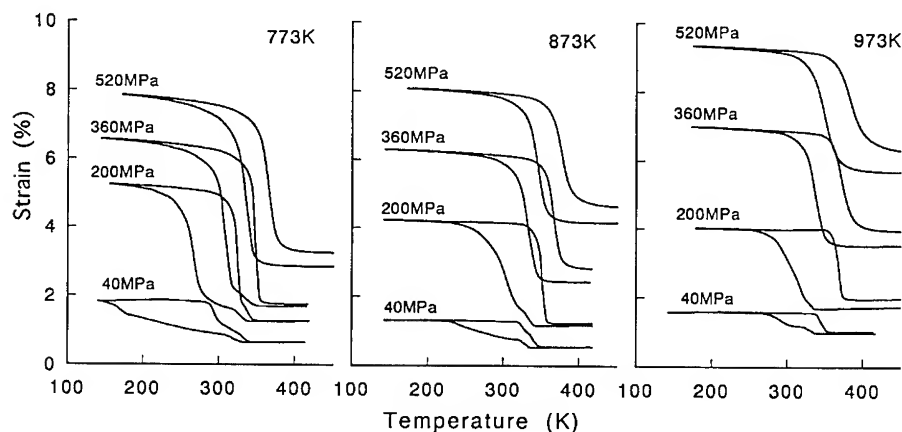


Fig. 6 Strain vs. temperature curves at various constant stresses for titanium-rich Ti-Ni thin films annealed for 3.6ks at various temperatures.

Figure 6 shows the strain vs. temperature curves at various stresses for the annealed thin films of titanium-rich composition. In the case of this composition, all the films exhibited a two-stage elongation under small stresses and then a single-stage elongation under high stresses. In the stress range where the two-stage shape change was observed upon cooling, the plastic strain

was very small, but it suddenly became large when the single-stage shape change appeared upon cooling. This suggests that the R-phase transformation is effective to reduce the introduction of dislocations associated with the martensitic transformation.

The transformation temperatures of the films obtained from Fig. 6 are plotted as a function of the annealing temperature for each constant stress in Fig. 7. In contrast to the Ni-rich films, both the martensitic and the reverse martensitic transformation temperatures increased with increasing annealing temperature. This change in the martensitic transformation temperature also seems to be related to the precipitation of the second phase Ti_2Ni , which was confirmed in all the annealed films by the transmission electron microscopy and X-ray diffractometry studies. The growth of the precipitates was prominent at a high temperature, contrary to the precipitates in the Ni-rich Ti-Ni thin films. This opposite dependence of the precipitation of the second phase on the annealing temperature seems to cause the opposite dependence of the transformation temperatures on the annealing temperature.

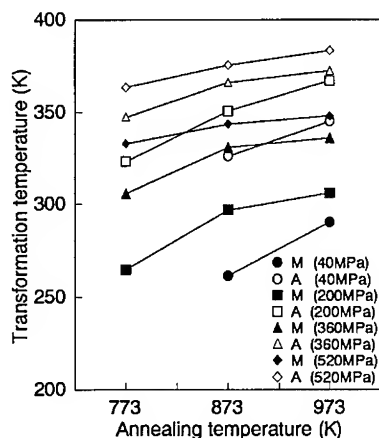


Fig. 7 Annealing temperature dependence of the martensitic and reverse martensitic transformation temperatures (shown by M and A, respectively) under various stresses for titanium-rich Ti-Ni thin films annealed at various temperatures.

CONCLUSION

The results of this study are summarized as follows:

- 1) For the near equiatomic Ti-Ni thin films, the heat treatment did not show any effect on their shape memory behavior. All the films exhibited a single-stage shape change. The plastic strains were large for all the films.
- 2) For the nickel-rich Ti-Ni thin films, the film annealed at 773K exhibited a two-stage shape change, while the films annealed at 873K and 973K exhibited a single-stage shape change. The plastic strains were very small for all the films. Both the martensitic and the reverse martensitic transformation temperatures decreased with increasing annealing temperature.
- 3) For the titanium-rich Ti-Ni thin films, all the films exhibited a two-stage shape change. The plastic strains were very small in the stress range where a two-stage shape change occurred, but it became large when a single-stage shape change appeared. Both the martensitic and the reverse martensitic transformation temperatures increased with increasing annealing temperature.

This work was supported by the research grant from the Shibata Foundation in the Surface Finishing Society of Japan.

REFERENCES

1. J. D. Busch, A. D. Johnson, D. E. Hodgson, C. H. Lee and D. A. Stevenson, Mater. Sci. Forum, **56-58**, 729(1990).
2. A. D. Johnson, J. Microemg. , **1**, 34(1991).
3. J. A. Walker, K. J. Gabriel and M. Mehregany, Sens. Actuators A, **21-23**, 243(1990).
4. A. P. Jardine, H. Zhang and L. D. Wasielesky, Mater. Res. Soc. Proc. **187**, Pittsburgh, PA, 1990, p.181.
5. A. Ishida, A. Takei and S. Miyazaki, Thin Solid Films, **228**, 210(1993).
6. S. Miyazaki and A. Ishida, Materials Transactions, JIM, **35**, 14(1994).

PART IX

Thin Films for Smart Systems

PIEZOELECTRIC FIBER COATINGS AND MICRO-TUBES

G.R. FOX,* D. DAMJANOVIC,* P.A. DANAI,* N. SETTER,* H.G. LIMBERGER,** and N.H. KY**

*Laboratoire de Céramique, EPFL, CH-1015 Lausanne, Switzerland

**Laboratoire d'Optique Appliquée, EPFL, CH-1015 Lausanne, Switzerland

ABSTRACT

Axially symmetric coatings of ZnO and PZT have been deposited onto fiber substrates by reactive dc magnetron sputtering. Multi-layer Cr/Au/ZnO/Cr/Au coating structures on optical fibers have been used to make integrated phase modulator devices. An analysis of the structural properties and piezoelectric response of the phase modulator devices will be presented. Micro-tubes of ZnO and Pt/ZnO/Pt multi-layers have been prepared by coating polyester fibers that act as a fugitive phase. After burning away the polyester fiber, up to 3 cm long micro-tubes with a 23 μm inside diameter and 3 to 9 μm wall thickness were obtained.

INTRODUCTION

Piezoelectric coatings on optical fibers are currently under study for the fabrication of integrated piezoelectric fiber optic phase modulator (PFOM) devices.^{1,2,3} A typical phase modulator structure consists of axially symmetric bottom electrode, piezoelectric, and top electrode layers, and the length of the top electrode defines the length of the modulator.^{4,5} When an electric field is applied across the piezoelectric layer, the inverse piezoelectric effect of the coating introduces a strain in the underlying fiber substrate. Due to the elasto-optic effect, a refractive index change occurs in the strained length of fiber. For a light signal passing through the optical fiber, the combination of path length change and refractive index change causes a phase shift that is dependent upon the electric field applied to the piezoelectric layer.^{2,6} This paper presents results on the fabrication and analysis of ZnO-based PFOM devices and shows initial results on multi-magnetron sputter deposition of PZT coatings on optical fibers.

The equipment developed for deposition of coatings on optical fibers has also been used for making ZnO micro-tubes. ZnO is sputter deposited onto polyester fibers and a subsequent annealing process burns away the polyester fiber fugitive phase.⁷ The technique could be used to make micro-tubes of a broad range of materials. This paper demonstrates the capability of making multi-layer micro-tube structures.

EXPERIMENTAL PROCEDURE

PFOM devices based on ZnO were prepared by using a combination of thermal evaporation and reactive dc magnetron sputtering techniques. Telecommunication optical fibers (125 μm diameter, 9 μm core diameter) were stripped and cleaned in dichloromethane and isopropanol in an ultrasonic bath. After chemical cleaning, the fibers were thermally treated at 400°C for 20 min to remove organic residues and enhance adhesion of the Cr/Au coating. The cleaned fibers were mounted in a fiber rotation sample holder that was mounted horizontally in an evaporation chamber where 13 nm thick Cr and 130 nm thick Au coatings were deposited at rates of 1 and 10 nm/min, respectively, using a fiber rotation speed of 2 rpm. Following the deposition of the Cr/Au bottom electrode layers, a 5 - 6 μm thick ZnO coating was deposited by sputtering from a 10 cm diameter Zn target using a mixed Ar and O₂ atmosphere with a total pressure (P) of 1.50 Pa, oxygen partial pressure (P_{O2}) of 0.70 Pa, and applied cathode power (PW) of 250 W. For sputter deposition, the fiber rotation holder was transferred to the sputtering chamber where it was mounted vertically in front of the target at a distance of 8.8 cm, and the fibers were rotated at

a rate of 5.6 rpm. Banded top electrode coatings, 2 and 6 mm in length, were deposited by evaporating 25 nm of Cr and 400 nm of Au on the ZnO surface. Shadow masks were used during each of the deposition processes to structure the coatings. The piezoelectric responses of the PFOM devices were determined by observing the resonances in the impedance spectrum with an impedance analyzer. Phase shift modulation with the PFOMs was measured at a wavelength of 1.56 μm using an all-fiber Mach-Zender interferometer.

The investigation of coatings for PFOM devices based on PZT was started by using multi-target dc magnetron sputtering. After chemical cleaning, fibers were sputter coated with 20 nm Ti by sputtering in an Ar atmosphere with $P = 0.50$ Pa, $PW = 200$ W, and a substrate to target distance (D) of 16 cm. Immediately following the Ti deposition, a 400 nm coating of Pt was deposited using $P = 1.00$ Pa, $PW = 200$ W, and $D = 15$ cm. Coatings of PZT up to 1 μm thick with a nominal composition of $\text{PbZr}_{0.52}\text{Ti}_{0.48}\text{O}_3$ were deposited onto the electroded fibers by reactive sputtering from targets of Pb, Ti, and Zr. The sputtering conditions were as follows: $P = 0.50$ Pa, $P_{\text{O}_2} = 0.35$ Pa, $PW_{\text{Pb}} = 30 - 40$ W, $PW_{\text{Zr}} = 250$ W, and $PW_{\text{Ti}} = 445$ W. During each of the coating processes, the fibers were rotated at 5.6 rpm and the deposition rates were monitored with a quartz crystal microbalance. To crystallize the PZT layer, the coated fibers were annealed at 650°C for 20 min using heating and cooling rates of 10°C/min.

Micro-tubes of Pt/ZnO/Pt multi-layers were fabricated by sputter depositing Pt and ZnO, as described above, onto 23 μm diameter polyester fibers. After coating the fibers, the samples were annealed between 450 and 550°C in air or flowing O_2 .

Microstructures of the optical fiber coatings and micro-tubes were observed by scanning electron microscopy. The crystal structures and textures of the fiber coatings and tubes were investigated with X-ray diffraction (XRD) by utilizing a Debye-Scherrer camera with a Cu radiation source and a densitometer to obtain intensity data from the exposed films.

RESULTS AND DISCUSSION

A fracture cross section of a ZnO-based PFOM is shown in FIG. 1. The axially symmetric ZnO coating consists of columnar grains that exhibit an [001] radial texture as determined by

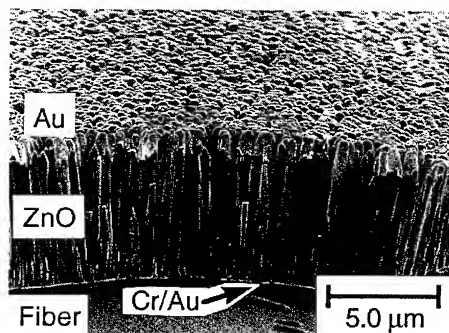


FIG. 1 Fracture cross-section SEM image of a Cr/Au/ZnO/Cr/Au PFOM.

X-ray diffraction. While the Cr/Au bottom electrode is quite smooth, the rough surface of the ZnO demands the use of Cr/Au coatings at least 300 nm thick for continuity of the top electrode. The top electrode coating forms caps on the ZnO grains. The piezoelectric response of the ZnO coating is demonstrated by the resonance at 22.3 MHz observed in the impedance spectrum (FIG. 2). This resonance corresponds to the radial mode resonance of the fiber, and, therefore, it occurs at the same position for elements with either 2 or 6 mm lengths. According to interferometric measurements, a maximum in the optical phase shift is observed at 17.7 MHz (FIG. 3) due to the radial mode resonance. The difference in the resonance frequency observed by impedance and optical phase shift measurements is believed to be due to differences between the sample holders

and the impedance of the driving circuitry used for the two types of measurements. A maximum normalized phase shift of 1.9×10^{-2} rad/V was observed for a 2 mm long PFOM driven in resonance.

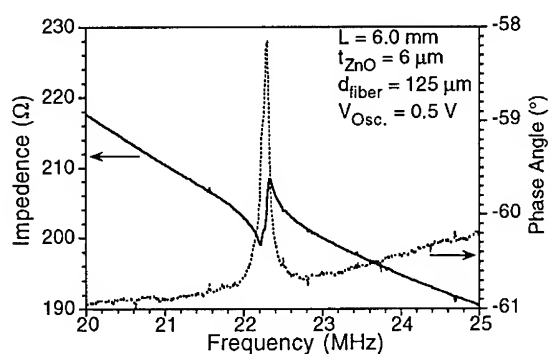


FIG. 2 Impedance spectrum showing the radial resonance of a ZnO PFOM.

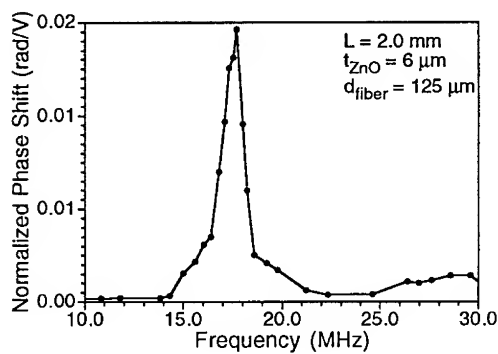


FIG. 3 Optical phase shift spectrum of a ZnO PFOM showing a maximum phase shift at the radial resonance frequency.

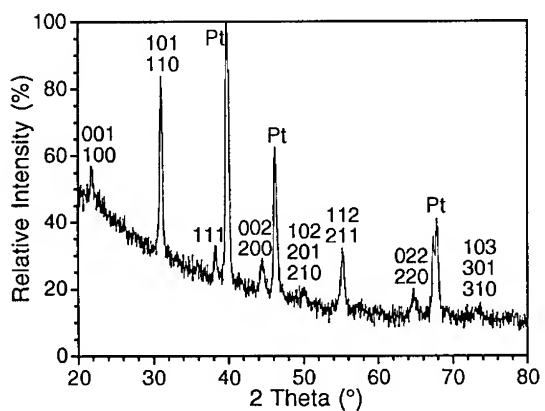


FIG. 4 XRD pattern of a multi-target sputter deposited PZT coating on a Ti/Pt coated optical fiber.

With the multi-target sputtering technique, axially symmetric coatings of Ti, Pt, and PZT were obtained. After annealing the coated fibers at 650°C for 20 min, the coating exhibited the perovskite phase and no second phases other than the Pt electrode were observed, as shown by the XRD pattern in FIG. 4.

A Pt/ZnO/Pt multilayer micro-tube resulting from the polyester fiber coating and burn-out process is shown in FIG. 5. Tubes exhibit smooth (on the order of 1 nm surface roughness) inside surfaces and an inside diameter of 23 μm . The inside Pt layer consists of a columnar microstructure with the length of the columns aligned along the radial direction (FIG. 6). The top

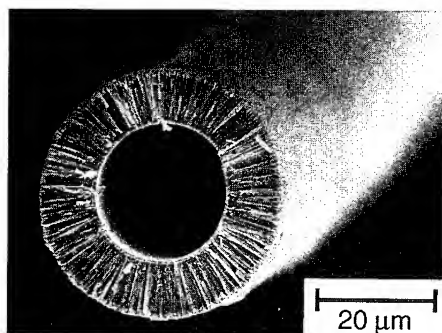


FIG. 5 Fracture cross-section SEM image of a Pt/ZnO/Pt micro-tube.

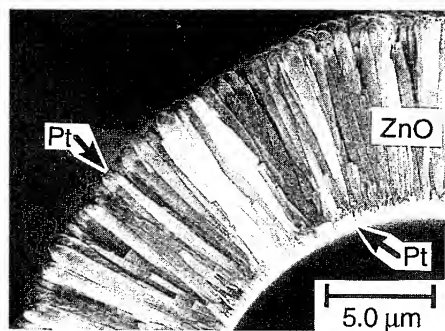


FIG. 6 SEM image showing the columnar structure of the ZnO and inside Pt layers.

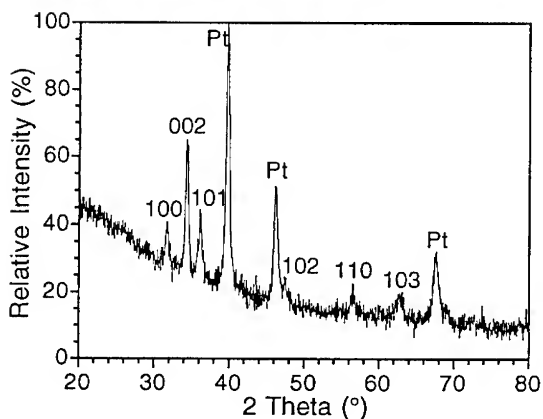


FIG. 7 XRD pattern of a Pt/ZnO/Pt micro-tube.

Pt layer is relatively rough and forms caps on the ZnO grains similar to the Au caps observed in the PFOM devices. Each of the radially oriented ZnO grains appears to nucleate from an underlying Pt column. X-ray diffraction (FIG. 7) confirms that the ZnO columnar grains have a [001] preferred orientation in the radial direction. The [001] radial texture causes the enhanced intensity of the 002 reflection in the XRD pattern, and the 002 ring normally observed on the Debye-Scherrer film reduces to an arc. With perfect radial orientation the 002 ring would become a spot, but an arc is observed due to deviation from perfect radial alignment. FIG. 8 shows the

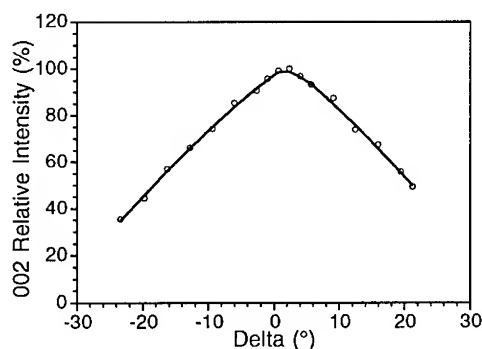


FIG. 8 Intensity vs. δ dependence for the 002 ZnO reflection.

variation in the intensity of the 002 arc vs. δ , the angular position with respect to the center of the Debye-Scherrer film. A correction of the intensities has been employed to compensate for the angular intensity variation introduced by the measurement method, and the background contributions have been substrated. For a polycrystalline material with random orientation the intensity will remain constant as a function of δ ; therefore, the variation in the intensity with δ provides a measure of the radial orientation quality with respect to the fiber axis. Both ZnO and Pt/ZnO/Pt micro-tubes with wall thicknesses between 3 and 9 μm and lengths up to 3 cm have been produced.

CONCLUSIONS

ZnO-based PFOM devices have been produced that can provide an optical phase shift of 1.9×10^{-2} rad/V (for a 2 mm long device) when driven at the radial resonance of the fiber structure. PZT fiber coatings exhibiting the perovskite phase have been deposited by reactive dc multi-magnetron sputtering. Deposition of coatings on polyester fibers and subsequent annealing have resulted in the formation of micro-tubes with an inside diameter of 23 μm .

ACKNOWLEDGMENTS

The authors would like to thank Roman Gubser at the Laboratorium für Kristallographie, Department für Erdwissenschaften, ETH Zurich for use of the densitometer for Debye-Scherrer film analysis. The authors are also grateful to Dr. Pedro Moeckli for the helpful discussion on X-ray analysis. This work was supported by the Optical Sciences, Applications, and Technology, Priority Program of the Board of the Swiss Federal Institute of Technology.

REFERENCES

1. J. Jarzynski, *J. Appl. Phys.*, **55**, 3243 (1984).
2. M. Imai, T. Yano, K. Motoi, and A. Odajima, *IEEE J. Quantum Electron.*, **28**, 1901 (1992).
3. D.S. Czaplak, J.F. Weller, L. Goldberg, F.S. Hickernell, H.D. Knuth, and S.R. Young, *Proc. IEEE Ultrasonics Symp.*, 491 (1987).
4. G.R. Fox, M. Kosec, P.A. Danai, and N. Setter, in *Electroceramics IV*, vol. 1, edited by R. Waser, S. Hoffman, D. Bonnenberg, and Ch. Hoffman (Proceedings of the 4th International Conference on Electroceramics and Applications, Aachen, Germany, 1994) pp. 253-258.
5. F. S. Hickernell, *Proc. IEEE Ultrasonics Symp.*, 417 (1988).
6. H.F. Taylor, *J. Lightwave Technol.*, **5**, 990 (1987).
7. G.R. Fox and P.A. Danai, *J. Mater. Res.*, **9** (11), (1994).

Pulsed Laser Deposition of ZnO Thin Films for Piezoelectric Applications

E.P. Donovan*, J.S. Horwitz*, C.A. Carosella*, R.C.Y. Auyeung**, D.B. Chrisey* And J.G. Smits ***

*Naval Research Laboratory, Code 6672, Surface Modification Branch, 4555 Overlook Ave SW, Washington, D.C. 20375-5345

** Sachs Freeman Associates, 1401 McCormick Dr., Landover, MD 20785

*** Boston University, Department of Electrical Engineering, 44 Cumming St., Boston MA 02215

Abstract

Transparent, insulating ZnO thin films have been deposited *in-situ* by pulsed laser deposition (PLD) from sintered targets. Films were deposited on substrates of fused quartz, <0001> Al₂O₃, polycrystalline and textured (111) Au, at several substrate deposition temperatures ($T_{\text{Substrate}} \leq 700^\circ\text{C}$) and background oxygen pressures ($P \leq 300\text{ mTorr}$). Film structure, morphology and electrical properties were characterized by X-ray diffraction, Rutherford backscattering spectrometry, optical properties were characterized by infrared transmission and reflection, and electrical resistivity was measured normal to the films. Films were crystalline, phase pure, and c-axis oriented. ZnO films deposited onto fused quartz and <0001> sapphire showed x-ray rocking curve full width at half maxima of 5° and 0.34° , respectively. The structure of ZnO films deposited on (111) textured Au was sensitive to the degree of texturing in the Au. The resistivity of PLD ZnO films was 61-63 k Ωcm which was a factor of three improvement over sputter deposited films. Deposition of Au by both PLD and IBAD showed a negative correlation between the crystalline texturing and film adherence.

Introduction

Bulk zinc oxide is a wide band-gap semiconductor (3.2 eV) with a hexagonal wurtzite structure with a ratio of c/a equal to 1.6¹. ZnO has several properties that make it useful for Micro-Electric Machine Systems (MEMS) applications. Zinc oxide exhibits the converse piezoelectric effect, so that an applied electric field produces an internal strain. The non-zero piezoelectric constants ($d_{ik} = \partial S_k / \partial E_i$) include $d_{13} = -4.7 \times 10^{-12}\text{ m/V}$. Therefore, an applied field across a c-axis oriented thin film causes an internal strain perpendicular to the c-axis. Sputtered zinc oxide has been used for MEMS "bimorphs"⁴. A bimorph is a cantilever of two layers (e.g., zinc oxide and silicon nitride), one of which is piezoelectric, plus electrodes on either side of the piezoelectric layer. An applied electric field causes displacements in the ZnO, some within the plane of the film, so the whole structure bends.

Sputtered ZnO is usually n-type², which may be due to excess zinc (oxygen deficiency). For example, in the bimorph work cited previously⁴, film resistivity was measured to be about 20000 Ωcm across the film. These sputtered ZnO thin films could not maintain a sufficiently high applied electric field. The result was Joule heating and unwanted bending due to thermal expansion differences. However, resistivities as high as $10^{10}\text{ }\Omega\text{cm}$ have been obtained for manganese doped ZnO sputtered films⁵.

Pulsed laser deposition (PLD) is a physical vapor deposition technique that has had great success in producing oxide structures of good crystal quality and high texturing⁶.

Excimer laser PLD of ZnO onto (100)Si has been found to produce highly textured films at room temperature⁷. Excimer laser PLD of ZnO onto silicon and glass substrates at temperatures greater than 300° C were c-axis oriented, and had resistivities in the range 0.1-0.01 Ωcm ^{8,9}. We investigated PLD of ZnO thin films, with the aim of producing films which are highly c-axis oriented and highly resistive, to maximize the piezoelectric response for applications to MEMS technology. As a test for the feasibility of fabricating the entire bimorph structure *in situ*, PLD of Au films was also investigated. ZnO thin film texturing on gold - including IBAD Au, IBAD Au/Cr, and sputtered Au/Cr - was also investigated.

Experimental

Reagent grade (99.9999% pure) zinc oxide powder was crushed with a mortar and pestle and pressed into a 0.75 inch diameter pellet at 22,000 PSI. The pellet was then sintered under flowing oxygen with the following temperature program: 5° C per minute to 850° C, 850° C for two hours, -1° C/min to room temperature.

Pulsed laser deposition was performed in a 50 l/s turbo-pumped, modified 4" conflat four way cross. The KrF excimer laser operated at a wavelength of 248 nm and delivered 300 mJ pulses at 10 Hz. A 50 cm focal length lens focussed the beam onto a rotating (~ 7 Hz) target at a 45° angle of incidence. The focal spot size of $\sim 0.14\text{ cm}^2$ resulted in an average fluence of about 1.8 J/cm² on the target. The substrate, 6 cm from the target, was attached with silver paint to a stainless steel block, which was heated by two quartz lamps. ZnO films were deposited onto insulating surfaces and Au. Insulators included fused silica, (100) MgO, and (0001) Al₂O₃.

Gold or Au/Cr metallization layers were deposited by PLD, by ion beam assisted deposition (IBAD)^{10,11}, and by sputtering⁴. IBAD of Au or Au/Cr films onto (100) Si substrates was performed in cryo-pumped chambers. The metal atoms were deposited by electron beam evaporation. During growth, the films were bombarded with ion beams of either pure argon or an argon/oxygen mixture, with energies ranging from 100 to 700 eV. The ion beams and vapor streams were each incident at an angle of 10° to the substrate surface normal.

Rutherford backscattering spectrometry (RBS¹²) was performed with 2 MeV ⁴He⁺⁺ ions with a detector angle of 165°. Spectra were analyzed by simulation with the commercial Genplot/RUMP program¹³ to obtain composition and areal density measurements. Repeated "Scotch Tape" adhesion tests were used to test metallization adhesion to the substrates. X-ray diffraction spectra (XRD) were obtained using a $\theta/2\theta$ geometry with a rotating anode source. X-ray diffraction rocking curves, scanning only θ , measured the full width at half maximum (FWHM, Γ) of XRD maxima. Electrical resistivity was measured normal to the film between the metallization and gold contacts on the surface. Infrared reflection and transmission spectroscopy was performed for optical characterization of the ZnO on insulator thin films.

Results : Metal Contact Layers

The structure and morphology of Au films deposited by several physical vapor deposition techniques were investigated before studying the growth of ZnO. These

P _{Argon} mTorr	T _{SUBSTRATE} °C	Pulses (~1 nm/100)	$\Gamma(\text{Au}, 111)$	I_{111}/I_{002}	Adhesion
0	100	40000	9°	>3000	Good
0	300	2000	6°+poly	11	Good
25	200	10000	8°		Poor
50	200	11000	3.6°	>10000	Poor
0, 50	24, 400	2000, 8000	4.8°	54	Good
0	76 to 210 @ 0.2/s	10000	8°		Good
Cr 0	100	4000	2.6°		Poor
Au 43	228	8000			

Table I: Pulsed Laser Deposition of Gold

techniques included PLD, IBAD, and sputtering. Typically, the deposited Au films were (111) textured with the degree of alignment dependent on the technique and the deposition conditions. The quality of the deposited film was determined from the $\Gamma(111)$ and the ratio of the intensities of the (111) and (002) reflections. The best aligned films had values of $\Gamma(111)$ from 2-3° with no measurable (002) intensity. Films were also tested for adhesion. In general, the more adherent films displayed the widest $\Gamma(\text{Au}, 111)$. In Table I are listed some typical PLD results. PLD gold films deposited in vacuum typically adhered well to the Si substrate, but were poly-crystalline ($\Gamma(\text{Au}, 111) = 7-10^\circ$). Different pressures of Argon (25-50 mTorr) were added to vary the kinetics of the arriving photo-ablated species onto the substrate. A narrower $\Gamma(\text{Au}, 111)$ of 3.6° was obtained with 50 mTorr Ar pressure and $T_{\text{substrate}} = 200^\circ \text{C}$; the film did not adhere. One film was deposited with a thin Au seed layer in vacuum (for good adhesion) followed by a thicker Au layer in 50 mTorr of Ar at $T_{\text{substrate}} = 400^\circ \text{C}$; it displayed good adhesion and a $\Gamma(\text{Au}, 111) > 4.8^\circ$. A film deposited with a thin Cr seed layer at 100°C followed by a thicker Au layer (43 mTorr Ar, 228°C) had a $\Gamma(\text{Au}, 111)$ of 2.6° but the film did not adhere. The surfaces of most metallizations were rough, as shown by the SEM micrograph (Figure 1A.)

Deposition of gold with IBAD and by evaporation, with and without a chromium layer, was also attempted, with results summarized in Table II. Again, there was a negative correlation between alignment and adhesion. We have been unable to duplicate published results on RF-sputtered ZnO on evaporated Au on Cr on fused quartz for Au quality and

Table II: IBAD Metallization Layers

Ion Species	Energy, eV	T _{SUBSTRATE}	$\Gamma(\text{Au}, 111)$	Adhesion
O	100	<100 °C	>10°	Good
Ar	100	<100 °C	>10°	Poor
Ar	700	<100 °C	6°	Poor
O+Ar(25 nm) then Ar	200	<100 °C	5°	Fair

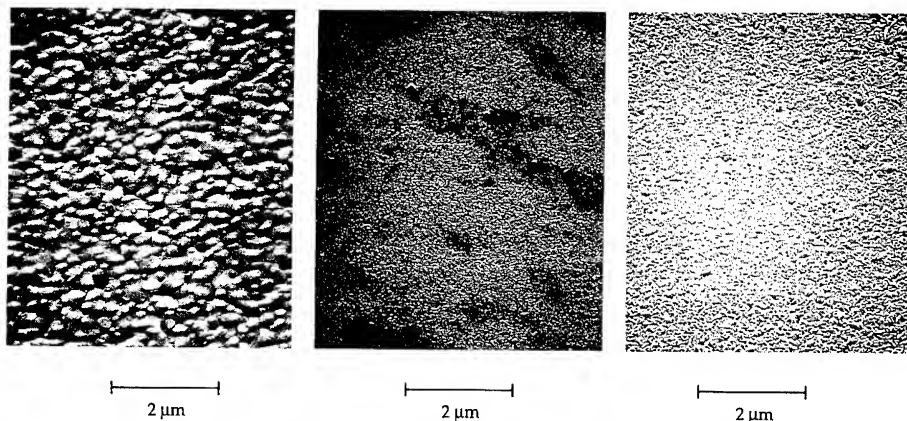


Figure 1: Scanning electron micrographs showing surface morphology for metallization layers. A) (left) PLD Au on Si. B) Sputter deposited Au/Cr on Si. C) PLD ZnO on sputtered Au/Cr on Si.

texturing¹⁴. One issue not faced with that work is that the PLD process takes place at high temperatures. Some films, that adhered well at room temperature, delaminated upon heating. Argon ion beam assisted deposition improved the crystal quality but not the adhesion. Oxygen ion beam assistance has previously been shown to improve Au adhesion on Si¹⁵. We obtained similar results, though again improved adhesion was accompanied by a wider rocking curve. Also, although adhesion with the oxygen beam was better than with no beam, it was inferior to the sputtered Au on Cr on Si metallization. For electrical characterization of ZnO, we used Si substrates that were sputter coated with Cr and Au layers as in prior work⁴. An SEM photomicrograph of the surface morphology of this metallization is shown in Figure 1B.

Results: PLD of ZnO

Before making the ZnO/Au/Cr/Si hetero-structures, PLD was used to deposit ZnO on several substrates. On $\langle 0001 \rangle$ Al_2O_3 , the rocking curve width $\Gamma(\text{ZnO}, 002)$ was 0.34° and the film was phase pure and exclusively c-axis oriented (Figure 2). Infrared reflection measurements for films deposited from 500°C to 700°C showed no sign of absorption over the 500-3000 nm range with index of refraction slightly less than 2. Phase pure ZnO was also obtained on fused silica substrates (Figure 2), though the rocking curve width was 5° . These films showed some absorption for wavelengths less than 600 nm. On $\langle 100 \rangle$ MgO, ZnO films showed a mixture of orientations, ($\Gamma(002)$

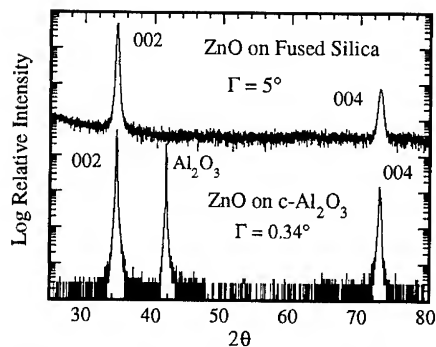


Figure 2: X-ray Diffraction Spectrum of Pulsed Laser Deposited ZnO on sapphire and (offset high) fused silica.

about 0.8° , $\Gamma(100)$ about 1.4° . ZnO on poly-crystalline Au was poly-crystalline.

ZnO films were deposited with PLD on the Au/Cr/Si hetero-structures. Typical deposition parameters were: ambient pressure = 300 mTorr O; $T_{\text{substrate}} = 400^\circ\text{C}$, 2500 laser pulses @ $1.8\text{J}/\text{cm}^2$ per pulse @ about .01 nm per pulse. Figure 1C is an SEM micrograph of a typical film showing the surface morphology. Figure 3 is an RBS spectrum, of a ZnO on oxygen+argon IBAD gold on Si. The solid line is a simulation of the data with stoichiometric ZnO of areal density 4.7×10^{18} atoms/ cm^2 , on 0.3×10^{18} atoms/ cm^2 Au on silicon. RBS alone cannot distinguish surface roughness from inter-diffusion, but the SEM micrographs clearly show roughness (Figure 1). To represent the surface roughness, the simulation of the interfaces proceeded in three steps, of total width 0.4×10^{18} and 0.15×10^{18} atoms/ cm^2 on the ZnO/Au and Au/Si interfaces, respectively.

The degree of texturing of the ZnO depended on the texturing of the nucleation surface. PLD of ZnO on poly-crystalline gold yielded poly-crystalline ZnO. The narrowest ZnO rocking curve came from the ZnO film grown on c-axis cut sapphire. Our data did not yield a conclusive relationship between the rocking curve widths of the ZnO and growth surface.

X-ray diffraction data from a PLD ZnO/sputtered Au/Sputtered Cr/Si structure is shown in Figure 4. Although $\Gamma(\text{ZnO}, 002)$ was 5.75° , the film was adherent. The underlying gold film is only somewhat textured. ZnO

films sputter deposited at the laboratory where the resistivity measurements were performed (B.U.) typically have a resistivity of $20000\ \Omega\text{cm}$. Resistivities measured perpendicular to films, as here, are often much lower than those measured in the plane of films. The resistivity of PLD ZnO films, measured in the same manner, were 61000 to $63000\ \Omega\text{cm}$, depending of the bias of the leads. This factor of three improvement means that PLD of ZnO has great promise as a deposition method for MEMS applications.

Summary

Pulsed laser deposition is a useful method for the growth of stoichiometric, phase-pure, high resistivity zinc oxide. The zinc oxide's crystal quality, surface roughness, and orientation depend on the substrate and deposition conditions. Improvements in the methods for the metallization layer are still needed. Neither pulsed laser deposition nor ion

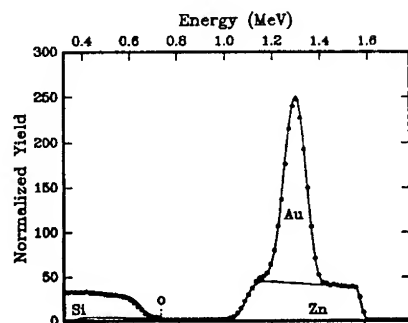


Figure 3: RBS Spectrum of Pulsed Laser Deposited ZnO on Sputtered Au/Cr on Si

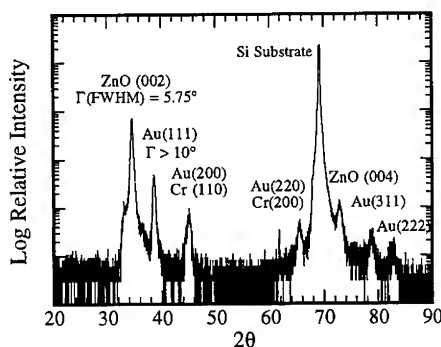


Figure 4: XRD of Pulsed Laser Deposited ZnO on Sputter Deposited Au/Cr on Si

beam assisted deposition have succeeded in producing a gold layer that is both highly oriented and adherent to (100) silicon at the ZnO deposition temperature. However, a factor of three improvement in resistivity of ZnO films has been obtained nonetheless.

In continuing this work, we plan to explore IBAD of silicon nitride as a possible improvement to the sputter deposited Si-N used previously in fabrication of MEMS bimorphs. If found suitable, and if a suitable electrode layer can be deposited on the silicon nitride, then prototype structures will be fabricated and tested. Gold adhesion on the IBAD silicon nitride may prove to be a concern. An alternative metallization would be fluorine doped ZnO¹⁶. We have recently mixed zinc oxide and zinc fluoride powders and sintered them to form PLD pellets. We can produce transparent (to visible light), conducting, fluorine-doped ZnO films. Their crystalline registry with a subsequent insulating ZnO layer would be excellent. Other possible oxide electrodes such as ruthenium oxide and La-Sr-Cu-O also may be explored.

References

- 1] R.J. Brook, R.W. Cahn and M.B. Bever, Concise Encyclopedia of Advanced Ceramic Materials, (1991) Pergamon Press, Oxford
- 2] A.R. Hutson, Phys. Rev. Lett. **4**, 505 (1960)
- 3] F. C. M. Van de Pol, Ceramic Bulletin **69** 1959-1965 (1990)
- 4] J.G. Smits and W.-S. Choi, Proc. 1994 IEEE International Control Symp. 139 (1994) IEEE cat. # 94CH3446-2
- 5] W Tjhen, T. Tamagawa, C.-P. Ya, C.-C. Hsueh, P. Schiller, and D.L. Polla IEEE #91CH2957-9
- 6] D.B. Chrisey and G.K. Hubler, Pulsed Laser Deposition of Thin Films (1994) John Wiley and Sons, Inc., New York
- 7] N.J. Ianno, L. McConville, N. Shaikh, S. Pittal and P.G. Snyder, Thin Solid Films **220** 92 (1992)
- 8] S. Amirhaghi, V. Craciun, F. Beech, M. Vickers, S. Tarling, P. Barnes and I.W. Boyd, Mat. Res. Soc. Symp. Proc. **285** 489 (1993)
- 9] V. Craciun, J. Elders, J.G.E. Gardeniers and I.W. Boyd, Appl. Phys. Lett. **65**, (1994)
- 10] F.A. Smidt Int. Mat. Rev. **35**, 61 (1990)
- 11] J.K. Hirvonen, Mat. Sci. Rep. **6**, 215 (1991)
- 12] W.-K. Chu, J.W. Mayer and M.-A. Nicolet, Backscattering Spectrometry, (1978) Academic Press, London
- 13] available from Computer Graphics Services, Ithaca, NY
- 14] K. Kushida and H. Takeuchi, J. Appl. Phys. **56** 1133 (1984)
- 15] P.J. Martin, W.G. Sainty, and R.P. Netterfield, Vacuum **35**, 621 (1985)
- 16] J. Hu and R.G. Gordon, Solar Cells **30**, 437 (1991)

AN EXPERIMENTAL EXAMINATION OF MEMS MICROACTUATOR MATERIAL ISSUES

T. G. COONEY*, D. E. GLUMAC**, W. P. ROBBINS**, AND L. F. FRANCIS*

*Department of Chemical Engineering and Materials Science

**Department of Electrical Engineering

University of Minnesota, Minneapolis, MN 55455-0132

ABSTRACT

Thermally induced interactions between materials in complex microactuator structures were investigated. The device structure contained a combination of a piezoelectric layer (lead zirconate titanate - PZT) an electrode with adhesion layer (Pt/Ti), buffer layer (SiO_2 or TiO_2), structural material (polysilicon and/or silicon nitride), and sacrificial oxide (SiO_2). The presence of a SiO_2 sacrificial layer did not affect either the bottom electrode or PZT layer. XRD results showed significant platinum and titanium silicide formation in the Pt/Ti electrode at 700 °C (PZT crystallization temperature) on both polysilicon and silicon nitride structural materials when no buffer layer was used. Auger analysis shows that the Ti adhesion layer oxidizes, that measured levels of silicon increase in the electrode zone, and that electrode elements diffuse into the structural material. Buffer layers of SiO_2 (0, 0.1, 0.73, 1.3, 1.5 μm) and amorphous TiO_2 (0.065 μm) were inserted between the electrode and the structural material. XRD and sheet resistance measurements demonstrated that SiO_2 thicknesses greater than 0.73 μm reduced pyrochlore formation in the PZT and reduced the degradation of the electrode. However, this thickness was incompatible with overall surface micromachining processes. The TiO_2 layer effectively prevented pyrochlore formation and electrode degradation, while being compatible with overall actuator processing.

INTRODUCTION

Materials characterization is an important component in the effort to develop surface-micromachined microactuators and PZT-based systems in general. A wealth of information has been presented detailing the effect of Si on Pt/Ti electrodes [1,2], the interaction of Ti with Si-based materials [3,4], and the effect of substrate and electrode materials on the microstructural development of PZT [5,6]. This information has been mainly oriented towards the characterization of material interactions and the development of ferroelectric random access memories (FRAM). Microactuator processing imposes limits on candidate structural materials, and the required response output of force or displacement limits the overall thicknesses.[7,8] The structural materials, silicon nitride (Si_3N_4) and polysilicon, are fairly common materials in IC fabrication [9], but have not been studied as substrates for the deposition of sol-gel derived PZT. In this paper, the effects of silicon nitride and polysilicon structural materials, sacrificial oxide wells, and barrier layers for silicon diffusion on PZT and electrode quality are examined.

EXPERIMENTAL PROCEDURE

The multilayer substrates fabricated in this study were designed to mimic materials interactions expected in microactuators, as shown in Figure 1. Multilayer substrates were prepared with a range of thermally grown oxide layers (0, 0.1, 0.73, 1.3, 1.5 μm). The structural layer was

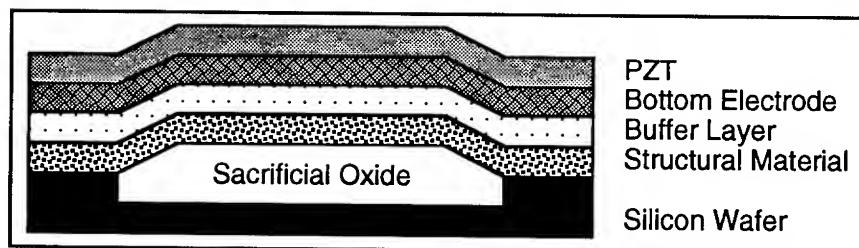


Fig. 1: Schematic cross section of a free-standing microactuator in an intermediate processing step. Further processing will pattern the PZT, deposit and pattern a top electrode, encapsulate the PZT, and free the device by removing the sacrificial oxide well. [8]

simulated by LPCVD deposited silicon nitride or polysilicon (1, 2 μm), or 0.2 μm polysilicon on silicon nitride (1, 2 μm). The thin layer of polysilicon on silicon nitride enhances adhesion. Thermal oxide was grown on silicon or polysilicon (0.1, 0.73, 1.3, 1.5 μm) for buffer layers. The TiO_2 buffer layer (0.065 μm) was deposited by sputtering titanium (Perkin-Elmer 2400 RF sputtering system) in an argon/oxygen (10 mtorr) atmosphere at 500 W. Electrode metallization was initiated with a 5 minute RF sputter etch at 300W, 10 millitorr of argon and 50 V substrate bias followed by the deposition of 300 \AA of titanium (30 min., 500 W, 10 millitorr of argon, 50 V substrate bias). Without breaking vacuum, 2000 \AA of platinum was then deposited (3.5 hours, 500 W, 10 millitorr of argon, 50 V substrate bias). PZT (0.34 μm) was deposited by spin coating an alkoxide solution based on 2-methoxyethanol. Deposition parameters and subsequent processing steps are described in detail elsewhere.[10]

All substrates were examined with and without the PZT layer. The thermal processing schedule was 2 min. at 200°C, 10 min. at 400 °C, and 15 min. at 700°C. X-ray diffraction (Seimans Diffractometer using $\text{Cu K}\alpha$) monitored phase development of intermetallics and crystallinity of the PZT ceramic. Auger analysis (Perkin Elmer 595 Auger) was used to determine elemental diffusion and depth profiling. Microstructural changes were examined on a Hitachi S-900 FESEM, while elemental analysis was performed on an EDS equipped Hitachi S-800. Electrode quality was evaluated using 4-point probe measurement (Veeco Co.).

RESULTS AND DISCUSSION

Figure 2 shows SEM micrographs of a $\text{Pt}(0.20 \mu\text{m})/\text{Ti}(0.03 \mu\text{m})/\text{Poly-Si}(1 \mu\text{m})/\text{Si}$ substrate with no heat treatment and heated at 700 °C for 15 minutes. The micrographs illustrate the difficulties encountered due to the high temperatures required for ceramic crystallization. Heating leads to grain growth and the formation of many large pores. EDS analysis indicated that the larger, raised surface grains contain titanium. Changing the polysilicon thickness and/or adding SiO_2 sacrificial layers does not alter the observed microstructural changes. SEM examination of silicon nitride substrates indicates that the same microstructural changes occur, but with a smaller grain size in both cases. Once again, structural material thickness and sacrificial oxide thickness do not affect the observed microstructural changes in the metallization. Substrates on which PZT had been crystallized were exposed by wet etching the ceramic.

XRD data for a heated $\text{PZT}(0.34 \mu\text{m})/\text{Pt}(0.20 \mu\text{m})/\text{Ti}(0.03 \mu\text{m})/\text{Poly-Si}(1 \mu\text{m})/\text{Si}$ sample is given in Figure 3. The data shows that platinum silicide (PtSi) develops at the PZT crystallization temperature when platinum is exposed to silicon. The diffraction pattern also shows that the PZT has crystallized into the nonferroelectric pyrochlore phase. Previous research has proven that silicon stabilizes the metastable pyrochlore phase over the perovskite phase.[11] SEM analysis of the PZT surface shows a dense microstructure comprised of 15 nm grains, the generally accepted morphology for surface pyrochlore grains.[12] XRD of a heat treated sample

without PZT shows that titanium silicide forms as well (Titanium silicide peaks are masked by the pyrochlore peaks.). The porosity formation observed in the metallization could enhance formation of silicides and the pyrochlore phase by allowing easier silicon diffusion. Changing the polysilicon thickness and/or adding SiO_2 sacrificial layers does not alter the heating induced-phase changes. XRD scans for substrates containing silicon nitride show the formation of platinum silicide (20% less than that formed on polysilicon by comparing average peak areas) and the formation of mixed perovskite and pyrochlore phases (35% perovskite by comparing perovskite (101) and pyrochlore (222) peak intensities).

Auger analysis of $\text{Pt}(0.20\text{ }\mu\text{m})/\text{Ti}(0.03\text{ }\mu\text{m})/\text{Poly-Silicon}(1\text{ }\mu\text{m})/\text{Si}$ substrate with no heat treatment and heated at $700\text{ }^\circ\text{C}$ for 15 minutes is given in Figure 4. Prior to heating, the platinum electrode, titanium bonding layer, and polysilicon structural material exist in fairly well defined zones. The oxygen level is negligible throughout. After heating, several trends are apparent. The thickness of the platinum region decreased, and the platinum level in the polysilicon increased. The titanium region became elongated, indicating that significant migration occurred both into the polysilicon and towards the surface. The oxygen level increase coincident to the titanium bonding layer indicates the possible formation of TiO_2 . The level of silicon in the electrode increased indicating a migration of the silicon from the structural layer. The Auger analysis is consistent with the microstructural and XRD investigations which showed microstructural changes along with the formation of intermetallic silicide compounds. Silicon nitride containing samples and PZT coated samples could not be analyzed due to sample charging during analysis.

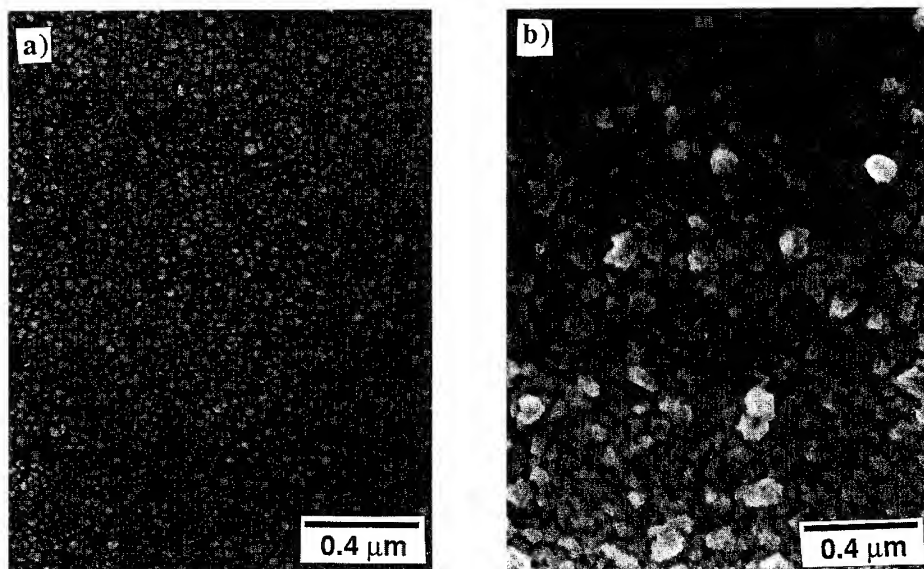


Fig. 2: FESEM micrographs of $\text{Pt}(0.20\text{ }\mu\text{m})/\text{Ti}(0.03\text{ }\mu\text{m})/\text{Poly-Si}(1\text{ }\mu\text{m})/\text{Si}$ substrates a.) no heat treatments, b.) heated at $700\text{ }^\circ\text{C}$ for 15 min.

The XRD patterns in Figure 3 illustrate the effect of SiO_2 buffer layers on electrode integrity and PZT phase formation after 15 minutes at 700 °C. Platinum silicide (PtSi) and pyrochlore PZT peaks are found for the sample with an electrode deposited directly on polysilicon. A 0.1 μm layer of SiO_2 eliminates platinum silicide peaks. Yet, a trace amount of pyrochlore is still observable. When 1.5 μm or 0.73 μm of SiO_2 was used, a perovskite pattern resulted. Unfortunately, SiO_2 is incompatible with current processing methods for microactuators. Thermal oxides of sufficient thickness can not be grown on either polysilicon or silicon nitride. The alternatives to thermal oxide, LTO-CVD (low temperature oxide) and PSG (phosphosilicate glass), are too porous to be effective barrier layers. Also, if an oxide of sufficient thickness could be grown, encapsulation methods could not protect the large expanse of exposed side surface during the sacrificial well etching. Figure 5 presents the XRD patterns for an amorphous TiO_2 buffer layer. The unheated sample shows a strong Pt (111) peak with a smaller Pt (200) peak. Heating at 700 °C for 15 minutes results in some platinum recrystallization, as evidenced by the sharpening of the (200) peak. PZT crystallizes into the perovskite phase when the TiO_2 buffer layer is present. The TiO_2 buffer layer resulted in perovskite PZT and silicide free electrodes on every sample tested. The TiO_2 buffer layer is compatible with current actuator processing methods. The relatively thin size of the layer does not contribute significantly to the overall bulk of the actuator beams.

The effect of heat-treatment on the sheet resistance of electrodes on different substrates is given in Table 1. Electrode degradation with heating results in a increase in the measured sheet resistance. The electrode directly deposited on silicon showed the worst increase at 67%. SiO_2 buffers decreased electrode degradation with an increase in buffer layer thickness. The 1.5 μm buffer layer yielded a measurable increase in sheet resistance of 5%. The sheet resistance increase in the silicon nitride and polysilicon samples was also high, at 30% and 46% respectively. In all cases, when the TiO_2 buffer layer was used, no measurable increase in sheet resistance with heating was observed.

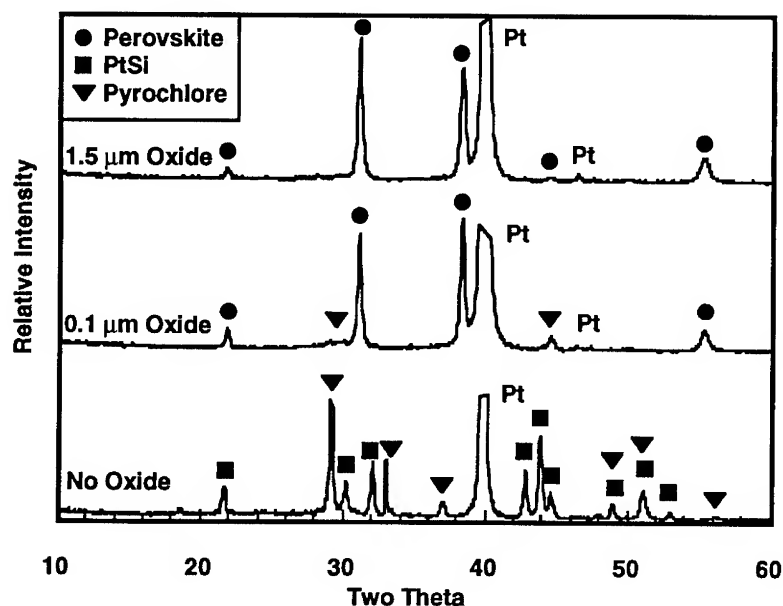


Fig.3: XRD patterns for PZT(0.34 μm)/Pt(0.20 μm)/Ti(0.03 μm)/ SiO_2 (various)/Poly-Si (1 μm)/Si samples showing the impact of SiO_2 buffer layers on PtSi and pyrochlore formation

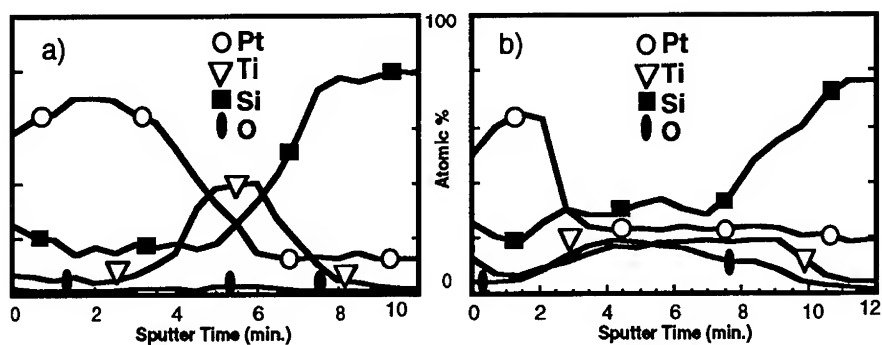


Fig. 4: Auger analysis of a Pt(0.20 μm)/Ti(0.03 μm)/Poly-Si (1 μm)/Si sample, a) no heat treatment b) after heating at 700 °C for 15 minutes.

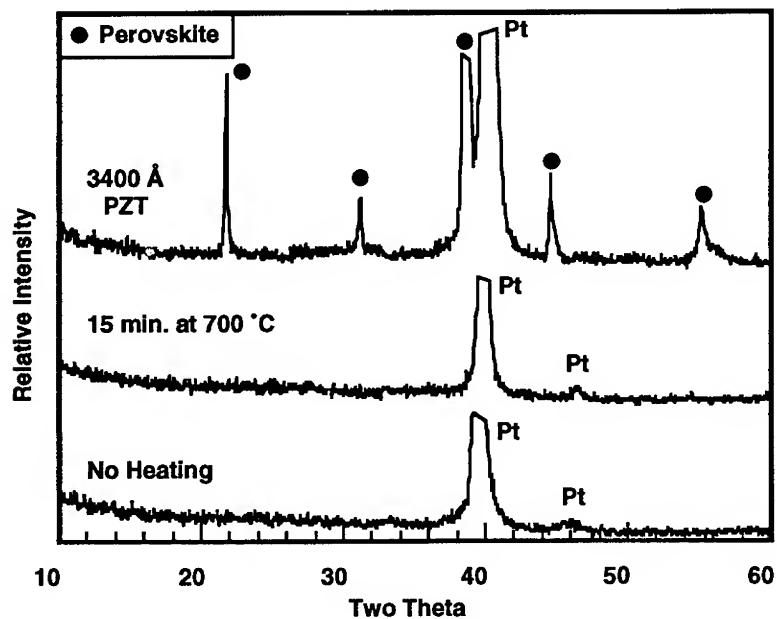


Fig. 5: XRD patterns for Pt(0.20 μm)/Ti(0.03 μm)/TiO₂ (0.065 μm)/Poly-Si (1 μm)/Si samples highlighting the effectiveness of the TiO₂ buffer layer at preventing silicide and pyrochlore formation.

Table 1 Comparison of heated and unheated electrodes in order to evaluate effectiveness of barrier

Substrate	% increase in Sheet Resistance after 15 minutes at 700 °C
Pt/Ti/Si	67%
Pt/Ti/0.10 μm SiO ₂ /Si	32%
Pt/Ti/0.73 μm SiO ₂ /Si	12%
Pt/Ti/1.50 μm SiO ₂ /Si	5%
Pt/Ti/Poly Si/Si	46%
Pt/Ti/Si ₃ N ₄ /Si	30%
Pt/Ti/TiO ₂ /Si	no change
Pt/Ti/TiO ₂ /Poly Si/Si	no change
Pt/Ti/TiO ₂ /Si ₃ N ₄ /Si	no change

ACKNOWLEDGMENTS

The authors wish to acknowledge the National Science Foundation (Grant EID 9212159), the University of Minnesota Surface Analysis Facility, the University of Minnesota Microscopy Center, and the University of Minnesota MLRE facility.

REFERENCES

1. K. Sreenivas, I. R. Reaney, T. Maeder, N. Setter, C. Jagadish, and R. G. Elliman, *J. Appl. Phys.* **75** (1), 232 (1994).
2. J. O. Olowolafe, R. E. Jones, A. C. Campbell, P. D. Maniar, R. I. Hegde, and C. J. Mogab, *Mat. Res. Soc. Proc.* **243**, 355, (1992).
3. A. E. Morgan, E. K. Broadbent, K. N. Ritz, D. K. Sadana, and B. J. Burrow, *J. Appl. Phys.* **64** (1), 344 (1988).
4. H. Bender, W. D. Chen, J. Portillo, L. Van Den Hove, and W. Vandervorst, *Applied Surface Science* **38**, 37 (1989).
5. S. A. Meyers, and E. R. Meyers, *Mat. Res. Soc. Proc.* **243**, 107 (1992).
6. C. J. Kim, D. S. Yoon, J. S. Lee, C. G. Choi, and K. No, *Jpn. J. Appl. Phys.* **33**, 2675 (1994).
7. D. E. Glumac, D. L. Polla, W. P. Robbins, *IEEE Transactions on Ultrasonics, Ferroelectrics and Frequency Control* **38** (5) (1991).
8. D. E. Glumac, T. G. Cooney, L. F. Francis, and W. P. Robbins, "Theoretical Predictions of Piezoelectric Microactuator Responses", this proceedings.
9. S. P. Murarka, M. C. Peckerr, *Electronic Materials: Science and Technology* (Academic Press, Inc., New York, 1989).
10. T. G. Cooney, E. A. Hachfeld, and L. F. Francis, *Ceramic Transactions* **43**, 197 (1994).
11. J. S. Wright, and L. F. Francis, *J. Mat. Res.* **8** (7), 1712 (1993).
12. C. C. Hsueh, and M. L. Mecartney, *J. Mat. Res.* **6** (10), 2208 (1991).

A THEORETICAL EXAMINATION OF MEMS MICROACTUATOR RESPONSES WITH AN EMPHASIS ON MATERIALS AND FABRICATION

D.E. Glumac, T.G. Cooney, L.F. Francis, and W.P. Robbins, University of Minnesota, Dept. of Electrical Engineering, Minneapolis, MN 55455

ABSTRACT

A free standing cantilever beam consisting of a support structural material (polysilicon/silicon nitride), a piezoelectric PZT ceramic layer, and metal electrode layers has been analyzed. Beam theory and finite element analysis were used to model the electric field induced deflections of this structure, and provided information as to how material choices influenced actuator function. Both support material and PZT thicknesses varied from 0-1.0 μm , and bulk piezoelectric coefficients and elastic moduli were assumed. The beam theory uses known (or assumed) material properties to predict actuator responses. Conversely, if device responses can be measured, material properties may be inferred from the theory. For a PZT thickness of 0.3 μm , a core layer thickness of 0.13 μm was found to maximize displacement. Also, the force output was found to be more dependent on the core thickness than that of the PZT. This information can then be used to predict the response of a more complex microactuator.

INTRODUCTION

Devices for microelectromechanical systems (MEMS) typically make use of a combination of materials including polycrystalline silicon, silicon nitride, and piezoelectric ceramics [1]. Improvement in the design and fabrication of such device structures will rely on the ability to model these materials and their combined response. A composite thin film piezoelectric cantilever beam (or unimorph), which could be integrated into MEMS, has been theoretically modeled to predict its displacement and force output characteristics (Figure 1). Actuation is provided when the piezoelectric material expands (or contracts) and the cantilever responds by bending to keep layer interfaces from slipping with respect to each other.

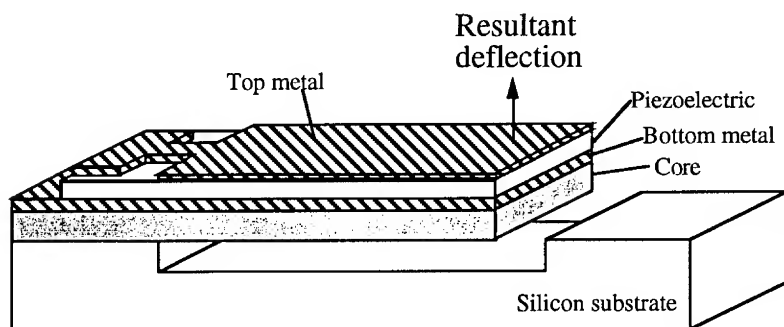


Figure 1 Surface micromachined cantilever structure.

The fabrication process for this structure is similar to a process that has been previously used to fabricate microsensors [2,3]. A trench is etched into the silicon substrate, and this trench is either oxidized or filled with a low temperature oxide layer to form an oxide well.

Building the sacrificial oxide into the substrate helps to preserve planarity for subsequently deposited layers. A 1 μm core material (low stress silicon nitride and undoped polysilicon), RF sputtered bottom platinum/titanium, sol-gel PZT, and RF sputtered top platinum/titanium layers are then successively deposited on the substrate. The polysilicon is used to promote the adhesion of the layers to follow, and the titanium aids in the adhesion of the platinum. Using standard photolithography techniques, the top metal, piezoelectric and bottom metal layers are patterned and ion milled. This structure is then encapsulated with RF sputtered chrome which is patterned and etched to expose the nitride/polysilicon core layer. The core layer is reactively ion etched thereby exposing the sacrificial oxide. The sacrificial oxide can be easily removed in a ten minute hydrofluoric acid vapor etch leaving a freestanding cantilever beam, and the chrome encapsulant is wet etched to complete the processing.

THEORY

Analytical

In modeling the cantilever structure in Figure 1, thicknesses assumed for the core, bottom metal, piezoelectric material, and top metal were 1.0, 0.2, 0.3, and 0.1 microns respectively. Several rigorous theories have been derived for piezoelectric devices [4,5]. A simple beam theory can be applied to the cantilever to determine how it will behave. This theory begins with redefining the thin film cantilever structure using the transformed sections method [6].

Figure 2a shows the actual cross-section of the cantilever structure. Each layer of the cantilever (core material, bottom electrode, piezoelectric material, and top electrode) should be properly accounted in terms of variations in thickness and Young's modulus. The transformed section method allows the width of the beam layers to be proportioned by the ratios of their Young's moduli, thereby defining the entire beam as having one Young's modulus. The moduli for the core, bottom metal, piezoelectric, and top metal are 16 , 15 , 7 , and $15 \times 10^{10} \text{ N/m}^2$, respectively [7]. The bottom metal transformed width is $15/16$ of the core width, the piezoelectric material width is $7/16$ of the core width, and the top metal width is $15/16$ of the core width as shown in the cross-section of Figure 2b. This transformed structure behaves as though it has a modulus of $16 \times 10^{10} \text{ N/m}^2$.

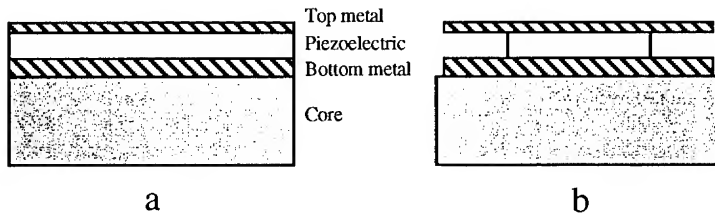


Figure 2 Cantilever cross-section before and after section transformation.

The neutral axis for the transformed cross-section is equal to the moments of the areas of the transformed layers divided by the total cross-section area [8]:

$$n = \frac{awt_t\left(\frac{t_t}{2}\right) + bwt_p\left(t_t + \frac{t_p}{2}\right) + awt_b\left(t_t + t_p + \frac{t_b}{2}\right) + wt_c\left(t_t + t_p + t_b + \frac{t_c}{2}\right)}{awt_t + bwt_p + awt_b + wt_c} \quad (1)$$

where a and b are the metal/core and piezoelectric/core moduli ratios; t_t , t_p , t_b , and t_c are the respective thicknesses of the top metal, piezoelectric material, bottom metal, and core; w is the core width; n is the distance of the transformed neutral axis measured with respect to the top of the top metal. Using the parallel-axis theorem [9], the area moment of inertia I_T is calculated for each layer as a moment of inertia plus a term relative to the transformed neutral axis:

$$I_T = \frac{awt_t^3}{12} + awt_t\left(n - \frac{t_t}{2}\right)^2 + \frac{bwt_p^3}{12} + bwt_p\left(t_t + \frac{t_p}{2} - n\right)^2 + \frac{awt_b^3}{12} + awt_b\left(t_t + t_p + \frac{t_b}{2} - n\right)^2 + \frac{wt_c^3}{12} + wt_c\left(t_t + t_p + t_b + \frac{t_c}{2} - n\right)^2 \quad (2)$$

In response to a voltage V (and hence an electric field) applied across the piezoelectric layer, the piezoelectric material will try to elongate or contract depending on the field polarity. The resultant stress T_p of this elongation (or contraction) is assumed to be at the centroid of the piezoelectric layer and will be equal to the piezoelectric force divided by the piezoelectric layer's cross-section:

$$T_p = \frac{d_{eff} E_p w t_p \frac{V}{t_p}}{w t_p} = d_{eff} E_p \frac{V}{t_p} \quad (3)$$

and

$$d_{eff} = (1-\nu)d_{33} + d_{13} \quad (4)$$

where d_{33} and d_{13} are the piezoelectric coefficients, E_p is the piezoelectric's Young's modulus, and ν is assumed to be 0.3. Because the piezoelectric layer is constrained in the cantilever, the effective piezoelectric constant must include d_{33} [10]. The centroid of the piezoelectric layer and the cantilever neutral axis are not the same, so a bending moment M_p will be generated. This moment is equal to the stress of equation 3 multiplied by the actual piezoelectric cross-section and the distance (moment arm) between the new neutral axis and the center of the piezoelectric:

$$M_p = T_p w t_p \left(n - \left(t_t + \frac{t_p}{2} \right) \right) \quad (5)$$

The displacement y for a cantilever that is bending due to a moment acting at its free end is:

$$y = \frac{M_p L^2}{2EI_T} \quad (6)$$

where L is the length of the cantilever, I_T is the transformed moment of inertia, and E is the elastic modulus of the core material layer since the other layers have been transformed with respect to it. Equations 1-5 can be substituted into cantilever equation 6 to yield the vertical displacement. Moment equation 5 can also be used to predict the output force, which is normal to the tip of the piezoelectric cantilever, as:

$$F = \frac{3M_p}{2L} \quad (7)$$

Finite Element Analysis

Finite element analysis was also employed to model this same cantilever structure using ANSYS® software. Since this software utilizes the complete piezoelectric constitutive equations, it makes a good comparison check for the analytical theory. The cantilever model consisted of 2,000 three-dimensional elements, 500 elements per each composite layer.

Theory Comparison

Values for d_{13} , d_{33} , and E_p of 274×10^{-12} meters/volt, 550×10^{-12} meters/volt, and 7×10^{10} newtons/meter² respectively were used in the analytical calculation since they are the values used by the piezoelectric finite element of ANSYS. Figures 4 and 5 are the graphical representations of data obtained from the analytical theory, and Figure 6 is a comparison between analytical theory and ANSYS. Mathcad® software was used to calculate the data. The cantilever structure studied has a length of 50 μm and a width of 10 μm ; and the top metal, piezoelectric, and bottom metal layers are 0.1, 0.3, and 0.2 μm thick respectively.

The graph in Figure 3 shows the cantilever's displacement and force output while varying the core layer thickness and keeping the metal and piezoelectric layer thicknesses constant. Only applied voltages of 1 and 3 volts are considered to keep the PZT strain within its elastic limit. The force output has a linear dependence with respect to core thickness, but the displacement curves are seen to exhibit a maximum for a core thickness of about 0.13 microns. Figure 4 shows the displacement and force output for a variation in piezoelectric layer thickness while keeping the metal and core layers at their original constant thicknesses. Again the force output has a linear dependence, but the displacement is without a preferred maximum over the range of PZT thicknesses studied.

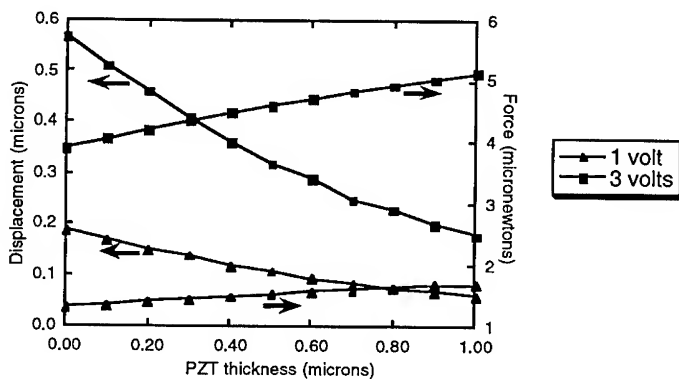


Figure 3 Displacement and force output versus the core material thickness.

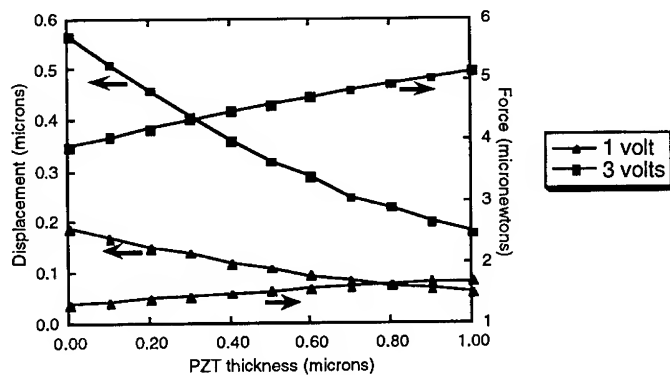


Figure 4 Displacement and force output versus the piezoelectric layer thickness.

Figure 5 shows a comparison between the analytically calculated displacement and the displacement calculated by ANSYS for 1 volt. The two sets of data agree reasonably well, and the differences are explained by the fact that the analytical calculation assumed that the beam width was much greater than the thickness.

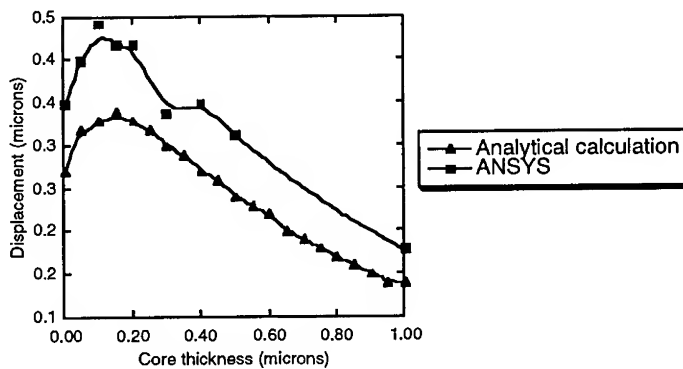


Figure 5 Comparison of analytical and finite element analysis data.

Intuitively, a decrease in core thickness will make the structure more compliant, and therefore more able to displace for a given piezoelectric stress. As the core thickness decreases, the moment arm also decreases; and when the core is $0.13 \mu\text{m}$ thick, the displacement falls off because the effect of the moment arm dominates that of the beam compliance. The force output is proportional to the elastic modulus of the beam, and naturally is expected to decrease as the core decreases.

There is no preferred maximum for displacement with a varying piezoelectric layer. Piezoelectric strain is proportional to applied electric field, and as the piezoelectric thickness decreases, strain (and hence displacement) increases. However, the piezoelectric layer thickness is limited by its breakdown field, for a given applied voltage, and values less than $0.1\text{ }\mu\text{m}$ possibly could be inadequate for voltages greater than 1 volt. Note that the force output varies less for the piezoelectric thickness variation than for the core layer thickness variation. The reason is that changing the core thickness moves the neutral axis more, relative to the resultant piezoelectric stress, than changing the piezoelectric thickness. The moment arm is more directly affected by changing the core, and the force is directly proportional to the moment.

CONCLUSION

Simple beam theory and finite element analysis have been used to study a piezoelectric cantilever beam structure which could be fabricated using silicon surface micromachining techniques. Specifically, variations in core and piezoelectric layer thicknesses were found to affect the displacement and force output of such a structure.

ACKNOWLEDGMENTS

We wish to thank the National Science Foundation, the Center for Interfacial Engineering (University of Minnesota), and the Microelectronics Laboratory for Research and Education (University of Minnesota). Thank you also to Mr. Arden Bedell for his assistance with the finite element analysis.

REFERENCES

1. W.P. Robbins, D.L. Polla, T. Tamagawa, D.E. Glumac, and W. Tjhen, J. Micromech. Microeng. **1**, 247-52 (1991).
2. D.E. Glumac, R.N. Rizq, W.P. Robbins, D.L. Polla, and J.C. Nelson in Electronic Packaging Materials Science VII, edited by P. Borgesen, K.F. Jensen, and R.A. Pollak (Mater. Res. Soc. Proc. **323**, Pittsburgh, PA, 1994) pp. 419-424.
3. P.J. Schiller, Monolithic Smart Sensor Systems Based on PZT Thin Films, Ph.D. Thesis, University of Minnesota (1994).
4. J.G. Smits, S.I. Dalke, and T.K. Cooney, Sensors and Actuators A **28**, 41-61 (1991).
5. Q. Meng, M. Mehregany, and K. Deng, J. Micromech. Microeng. **3**, 18-23 (1993).
6. S.P. Timoshenko and J.M. Gere, Mechanics of Materials (Van Nostrand Reinhold Co., New York, 1972).
7. J. Schwietz, MRS Bulletin **27**, 34-45 (1992).
8. Ibid 6.
9. Ibid 6.
10. Ibid 5.

ELECTRICAL CHARACTERISTICS OF BARIUM STRONTIUM TITANATE-OXIDE COMPOSITE FILMS

S. SENGUPTA*, L.C. SENGUPTA*, S. STOWELL*, D.P. VIJAY⁺ AND S.B. DESU⁺

*U.S. Army Research Laboratory, Materials Directorate, Watertown MA 02172-0001

⁺Dept. of Materials Science and Engineering, Virginia Tech, Blacksburg, VA 24061

ABSTRACT

In a previous work, composites of BSTO combined with other nonelectrically active oxide ceramics have been formulated and have demonstrated adjustable electronic properties which can be tailored for use in various electronic devices.¹ One application has been for use in phased array antennas and insertion has been accomplished into several working antenna systems.² To further accommodate the frequencies required by these phased array antennas, thin films of the composites have been fabricated using a Krypton Fluoride excimer laser as an ablation source. The electrical properties, including the dielectric constant and the tunability (change in the dielectric constant with applied voltage) have been measured. The results have been compared to those obtained for the bulk, ceramic composites and other BSTO/oxide composite thin film structures.³

INTRODUCTION

Phased array antennas are currently constructed using ferrite phase shifting elements. These antennas can steer transmitted or received signals either linearly or in two dimensions without mechanically oscillating the antenna. Due to the circuit requirements necessary to operate these present day antennas, however, these are costly, large and heavy. Therefore, the use of these antennas has been limited primarily to military applications which are strategically dependent on such capabilities. In order to make these devices available for many other commercial and military uses, the basic concept of the antenna must be improved. Towards this goal, a ceramic Barium Strontium Titanate, $\text{Ba}_{1-x}\text{Sr}_x\text{TiO}_3$, (BSTO), phase shifter using a planar microstrip construction has been demonstrated.¹ However, to meet the required performance specifications (e.g., maximum phase shifting ability), the BSTO electronic properties must be optimized. As part of this optimization process, various composites of BSTO and non-ferroelectric oxides have been formulated and proven successful.

However, in order to obtain higher operating frequencies (30 GHz and beyond) and to decrease the voltage requirements, thin film fabrication of the above candidate materials is necessary. This paper outlines the work on the characterization of the thin films of undoped and modified BSTO deposited by the pulsed laser deposition (PLD) method. The electronic properties of the films were measured using an HP 4194A impedance analyzer. The results of these measurements will be discussed.

EXPERIMENTAL

The metallized films used for the electrical measurements were: (1) Sapphire / RuO₂ / BSTO / Pt and (2) Sapphire / RuO₂ / BSTO with 1 wt.% oxide II / Pt. Prior to PLD, the sapphire substrates utilized underwent a cleaning cycle which included an ultrasonic cycle of TCE followed by two methanol ultrasonic cycles. The samples were then rinsed with methanol and air dried. The lattice parameters and dielectric constants of the sapphire substrates used in this experiment are 4.76 Å and 11 (at 300 K) respectively.

Prior to the thin film deposition, a ground plane electrode of Ruthenium oxide (RuO₂) was sputtered onto the substrates at a substrate temperature of 200 °C and a O₂/Ar ratio of 1:4 with a total pressure of 10 mT. The Ruthenium oxide films were 3000 Å thick. The resistivity of the as-deposited films were in the order of 160 μohms-cm. They were annealed at 600 °C for 30 minutes to lower the resistivity and were cooled by furnace quenching. The resistivity of the annealed films were measured to be 110 μohms-cm.

The targets chosen for this work were Ba_{0.6}Sr_{0.4}TiO₃ (BSTO) and BSTO with 1 wt.% of an additive oxide, referred to hereafter as oxide II. The PLD of the ferroelectric thin films was accomplished using a Questek 2000 krypton-fluoride excimer laser with a wavelength of 248 nm and a repetition rate of 10 Hz. The substrate was held parallel to the target and their separation distance was maintained at 55 mm. The average pulse energy was 300 mJ with a 20 ns pulse width. The oxygen partial pressure in the chamber was 100 mT and the substrate temperature was 500 °C, which was monitored by a thermocouple clamped between the heater and the substrate. The powder pressed ceramic targets were prepared according to a description published previously.² A Dektak-200 profilometer was used to measure the films thicknesses. It was measured to be 6000 Å for both the films. The compositions of the films were confirmed by Glancing Angle X-ray diffraction (GAXRD).

After the deposition of the thin films, the top Pt electrodes were deposited by electron beam evaporation. The thicknesses of the top electrodes were measured to be approximately 3000 Å using a Dektak-200 profilometer.

The dielectric constant (ϵ') and % tunability were determined for both thin film/substrate combinations. The % tunability of a material is determined using the following equation:

$$\% \text{ tunability} = \{ \epsilon'(0) - \epsilon'(V_{app}) \} / \{ \epsilon'(0) \} \quad (1)$$

The tunability measurements were taken with an applied electric field which ranged from 0 to +/- 3.3 V/micron (μm). The electronic properties were measured at two frequencies, 30 KHz and 0.5 MHz. Capacitance versus voltage (C-V) measurements for the films were taken using an HP4194 impedance / phase gain analyzer. The voltage, applied internally through the HP 4194A, was varied from -2.0 V to +2.0 V.

RESULTS AND DISCUSSION

Electronic Measurements

Fig. 1 shows the capacitance versus voltage characteristics at 30 KHz for the BSTO (undoped) film deposited on RuO₂/sapphire. The curve shows a symmetric capacitance-

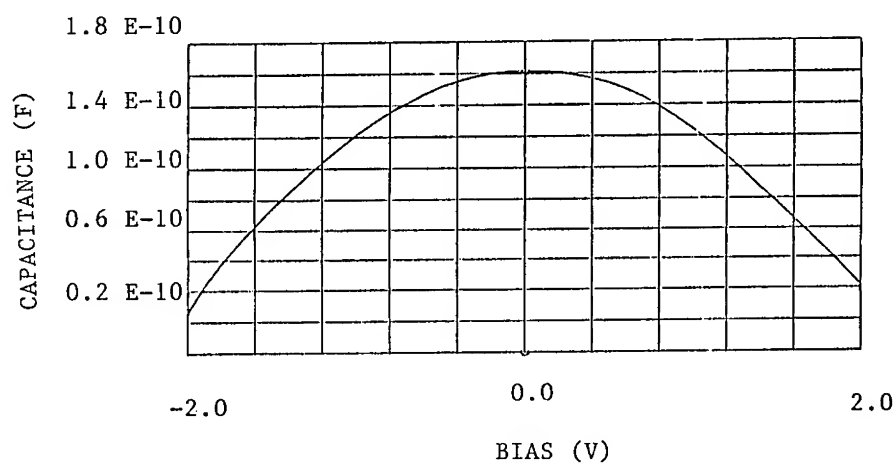


Figure 2. Capacitance versus voltage for BSTO /1 wt% Oxide II deposited on RuO₂ / Sapphire with Pt top electrode.

Table I

<u>Material</u>	<u>Applied Field (V/μm)</u>		<u>$\epsilon'(V=0)$</u>		<u>% Tunability</u>	
	<u>Film</u>	<u>Bulk</u>	<u>Film</u>	<u>Bulk</u>	<u>Film</u>	<u>Bulk</u>
BSTO	3.3	0.73	1380	3300	48	20
BSTO / OXIDE II	3.3	2.5	600	2700	34	46
BSTO / OXIDE III (Ref. 3)	2.0	2.3	398	1276	79	16

voltage relationship which is characteristic of *paraelectric* films. The dielectric constant at zero bias was calculated to be 1380 and the tunability is 48 % at a field of 3.3 V/ μ m. The bulk undoped material has a dielectric constant of 3300 and a tunability of 20 % at 0.73 V/ μ m.¹ It has been previously shown that the dielectric constant of ferroelectric films are inherently less than the bulk ceramic values due to oxygen defects at the electrode/ film interface.⁴ Also any porosity and/or leakage current in the films will tend to decrease the dielectric constants obtained.

The C-V curve at 30 KHz for the BSTO/ 1 wt.% oxide II film deposited on RuO₂/sapphire is shown in Fig. 2. The curve shows a typical paraelectric behavior (i.e., a symmetric capacitance) with positive and negative bias applied. The dielectric constant at zero voltage calculated from this curve is 600. The tunability obtained up to 3.3 V/ μ m was 34%. The value for the dielectric constant found in the bulk ceramic target of BSTO/ 1 wt.% oxide II was 2700 and a tunability of 46% at 2.5V/ μ m [1]. Table I summarizes the values of the dielectric constants and tunability of the various BSTO thin films measured at 30 KHz and their ceramic counterparts.

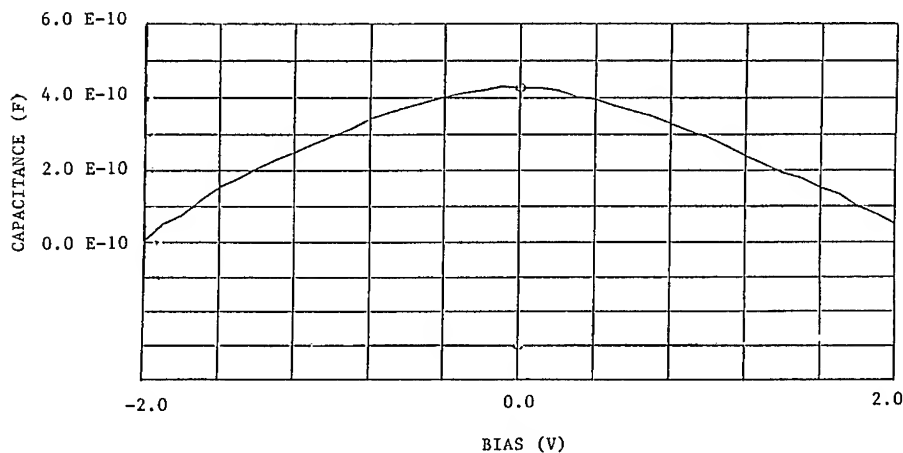


Figure 1. Capacitance versus voltage for BSTO (undoped) deposited on RuO₂ / Sapphire with Pt top electrode.

Similar measurements of the same thin films were also carried out at 0.5 MHz. For the undoped BSTO thin film, a dielectric constant of 940 and a tunability of 55% ($V_{\text{applied}} = 3.3$ V/ μ m) were obtained. For the BSTO/oxide II thin film, a dielectric constant of 310 and a tunability of 39 % ($V_{\text{applied}} = 2.0$ V/ μ m) were obtained.

CONCLUSION

Thin films of both undoped and oxide modified BSTO have been deposited by PLD onto RuO₂/Sapphire substrates. The electronic properties of the undoped and oxide modified BSTO thin films exhibited similar trends relative to the bulk materials as shown in Table I.

We have shown that the tailoring of the electronic properties of BSTO thin films in the low frequency region is possible through the incorporation of metal oxides. The lowering of the dielectric constants, alongwith a high tunability, plays an important role in the impedance matching of these films into the electronic circuits. Further investigation of such tailoring in the microwave region through the incorporation of such oxides is underway.

ACKNOWLEDGMENTS

The authors would like to thank Dr. Neville Sonnenburg of CPRL, M.I.T. for his help with GAXRD.

REFERENCES

1. L.C. Sengupta, S. Stowell, E. Ngo, M.E. O'Day and R. Lancto, *J. of Integrated Ferroelectrics*, (1994), in press.
2. R. Babbitt, T. Koscica, W. Drach, and D. Didomenico, *J. of Integrated Ferroelectrics*, (1994), in press.
3. S. Sengupta, L.C. Sengupta, S. Stowell, W.E. Kosik, E. Ngo, D.K. Vijay, and S.B. Desu, IEEE Transactions of the Proceedings of ISAF '94, Penn State, University Park, PA, (in press).
4. C.J. Brennan, *Integrated Ferroelectrics* 2, 73 (1992).

Smart Thin Film TiNi/PZT Heterostructures

Peter G. Mercado and A. Peter Jardine
Smart Materials Laboratory
Dept. of Materials Science and Eng., SUNY at Stony Brook, Stony Brook, NY 11794-2275

Abstract

Thin film layers of shape memory alloys and ferroelectric ceramics can produce a family of 'smart' heterostructures capable of performing both sensing and actuating functions. Important issues in the synthesis of these active structures are the ability to generate the appropriate crystalline phases of each material, while producing defect-free homogeneous high quality films. The compatibility of sol-gel processed $\text{Pb}(\text{Zr,Ti})\text{O}_3$ (PZT) thin films with thin film shape memory effect TiNi substrates were investigated. Thin film TiNi was deposited on quartz substrates by physical sputter deposition utilizing a TiNi target in a ultra-high vacuum chamber, and followed by in-situ vacuum annealing. PZT was deposited on TiNi by sol-gel and spin coating processes. The ferroelectric tetragonal phase of PZT was obtained by a 600 °C anneal for 5m in air. The heterostructures were nominally defect-free, unlike those obtained through deposition onto bulk TiNi substrates.

Introduction

A material system is considered 'smart' if it has the ability to perform both sensing and actuating functions with some inherent control between these functions. Smart materials are categorized as either passive or active. Passive smart materials respond to external stimuli without any assistance, whereas active smart materials employ a feedback loop to initiate an appropriate response. A family of smart materials can be fabricated by depositing ferroelectric ceramics onto shape memory alloys (SMA). These hybrid structures couple the broad mechanical stress-strain hysteresis properties of SMA with the mechanical-electrical relationship associated with piezoelectric materials. These hetero-structures may have effective applications for active suppression of large acoustic waves.

Many alloys exhibit the ability to be deformed at low temperatures and regain their original undeformed shape when heated to higher temperatures. This phenomenon is known as the shape memory effect (SME) and is associated with dramatic changes in temperature dependent mechanical properties. It is due to a first order martensitic phase transformation from a high symmetry and high temperature *austenitic* B2 phase to a low symmetry and low temperature *martensitic* B19' phase. At the low temperature phase, the SMA is easily twinned into many crystallographic twin variants. Crystallographic twins grow at the expense of others with an applied stress. Macroscopically, the martensitic material is easily deformed through the growth of these twins, which can accommodate seemingly plastic strains (up to 8% for TiNi) that are recoverable upon heating.

Unlike most materials which display first order phase transformations, martensitic transformations demonstrate a transformation temperature hysteresis with a start and finish temperature for each transformation. The austenitic to martensitic transformation starts at a temperature denoted as M_s and finishes at a temperature M_f . The reverse transformation to the austenitic phase starts at A_s and finishes at A_f . In TiNi, the austenitic phase is a B2 bcc phase and the martensitic phase is a B19' monoclinic face-centered tetragonal structure. The transformation temperatures are very sensitive to the chemical stoichiometry of the alloy.

Annealed TiNi can possess typical transformation temperatures of $A_f=100\text{ }^{\circ}\text{C}$, $M_f=30\text{ }^{\circ}\text{C}$, $A_s=60\text{ }^{\circ}\text{C}$ and $M_s=50\text{ }^{\circ}\text{C}$, although these have to be characterized for each alloy. Compositional deviations of 1% Ni rich TiNi will dramatically lower the transformation temperature A_f to $-100\text{ }^{\circ}\text{C}$ [1].

The piezoelectric effect is the linear interaction between the electrical and mechanical systems of a material. An applied mechanical stress on a crystal produces a proportional electrical field known as the direct piezoelectric effect, whereas an applied electrical field produces a strain on the crystal known as the converse effect. There are a large number of ferroelectric ceramics, but the most widely researched and utilized for thin film technology are the titanates and niobates with the perovskite structure (e.g., lead zirconate titanate, lead lanthanum zirconate titanate, and barium titanate (BaTiO_3)).

Coupling SMA and ferroelectric ceramics produces a hybrid composite structure that can utilize the different active and adaptive properties of the individual bulk materials. Ferroelectric ceramics are very sensitive to applied stresses through the piezoelectric effect. Their response times are fast, but displacements are very small (in the order of a few micrometers) due to the small strain magnitude. SMA materials have large actuation displacements and are able to drive larger loads. However, cycling times are much slower since it is dependent upon the dissipation of latent heat of transformation.

Smart active damping of mechanical vibrations is a possible application for these heterostructures. This requires the heterostructure to be able to sense the incoming stress wave and to actively respond. The logic of active damping by a ferroelastic-ferroelectric structure can be explained by considering an approaching stress wave shown in Figure 1. The stress wave propagates into the TiNi producing a martensitic-austenitic phase transformation in which some of the mechanical energy is converted to heat. This layer is designed to absorb most of the high energy waves. Acoustic waves that are not damped by the TiNi layer continue to propagate and strain the first ferroelectric layer (PZT). This strain produces a voltage through the direct piezoelectric effect which can be used to generate an out of phase stress wave by the second ferroelectric layer to attenuate any remaining stress waves. By varying the buffer layer (i.e., TiO_2) between the ferroelectric layers, it is possible to control the resistance and capacitance of the resulting circuit. To account for the possibility of the velocity of the stress wave to exceed the system's response time, a metallic mechanical impedance buffer (such as Al, Ti and TiNi) can be added to provide additional time for the counter-stress actuation to occur.

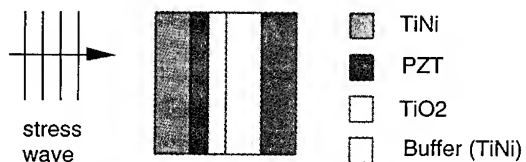


Figure 1: Schematic of a smart ferroelastic-ferroelectric active damping structure.

An important issue is the ability to generate the appropriate phases of each material while minimizing unwanted mutual chemical interactions. The amorphous crystalline transformation for TiNi occurs at $490\text{--}520\text{ }^{\circ}\text{C}$ [2,3] and for temperatures above $540\text{ }^{\circ}\text{C}$, formation of Ti_3Ni_4 and $\text{Ti}_{11}\text{Ni}_{14}$ precipitates are favored which can be detrimental to SME characteristics. Decomposition of the ferroelastic phase of TiNi into TiNi_3 has also been observed by the authors to begin at $450\text{ }^{\circ}\text{C}$ anneals with further decomposition at higher temperatures[4]. In contrast,

annealing temperatures to transform amorphous (sol-gel fabricated) ceramics to the ferroelectric perovskite phase range from 500 to 800 °C depending on the type of ferroelectric and at times the type of substrate^[5,6,7,8,9].

TiO₂/PZT have been previously deposited onto TiNi by the authors and others through the sol-gel process with a crystallization temperature of 600 °C ^[4,10,11]. The objective of this experiment is to investigate the compatibility of PZT ferroelectrics with sputter deposited TiNi to improve the heterostructures mechanical and ferroelectric properties.

Experimental Procedure

An Advanced Energy MDX-1K DC sputtering source deposited TiNi from a TiNi target at a power of 100 W for 1 h onto ambient temperature 25.4 mm (1") quartz substrates. The target to sample distance was controlled by positioning the sample via the linear feed-through, which varied from 8.5 to 26 cm. The TiNi deposition geometry and further details of the sputtering phenomena are discussed in an accompanying paper in this proceedings^[12].

The thin films were initially amorphous and were annealed after deposition using a sample heater consisting of two 500 W halogen lamps surrounded by a 76.2 mm (3") diameter half cylinder of polished stainless steel. Samples were annealed at 520 °C for 0.5 h. After deposition and annealing, the sample was retracted through the vacuum load-lock and isolated from the chamber. Following shut down of the pumps, the sample was removed for characterization.

The TiNi thin films did not receive additional treatment prior to PZT deposition. Thin films of PZT were coated onto SMA TiNi films by sol-gel and spin coating techniques. The complex sol was prepared using lead acetate, zirconium n-propoxide and titanium isopropoxide metal alkoxides dissolved in acetic acid and 1-propanol alcohol. The PZT sol was prepared by dissolving 8 gm of lead acetate in 4 ml of acetic acid and heated to 105 °C (while being mechanically stirred) until solid form. After evaporation of all liquid, 4 ml of acetic acid was re-added and stirred for 15 m. Appropriate amounts of Ti-isopropoxide was combined with Zr n-propoxide. The lead precursor was then added to the Zr/Ti precursor while being mechanically stirred. 40 ml of 1-propanol was added to the Pb/Zr/Ti precursor, followed by the addition of 1.0 ml of water to hydrolyze the solution. The general procedure is summarized in Figure 2. The PZT sol was filtered through a 0.22 µm filter before deposition onto substrates.

The PZT sol was spun onto the TiNi substrates at 4000 rpm for 30 s and prebaked at 300 °C for 15 m to remove most of the organics. This procedure was repeated (5 times) to produce thicker films. The PZT films were crystallized to their ferroelectric perovskite phase by annealing at 600 °C for 5 m. The samples were annealed on a ceramic block and allowed to air cool on the same ceramic block. This provided a slower cooling rate as compared to cooling the sample alone in ambient air. It is believed that by lowering the cooling rate, the TiNi intermetallic substrate and the PZT ceramic film composite will cool isotropically and inhibit large strain mismatch (which leads to cracking and delamination) due to linear thermal expansion behavior when rapidly air cooled. The films were characterized by x-ray diffraction (XRD) techniques, optical microscopy and a Radiant Technologies RT-66A ferroelectric test system was used to obtain ferroelectric properties.

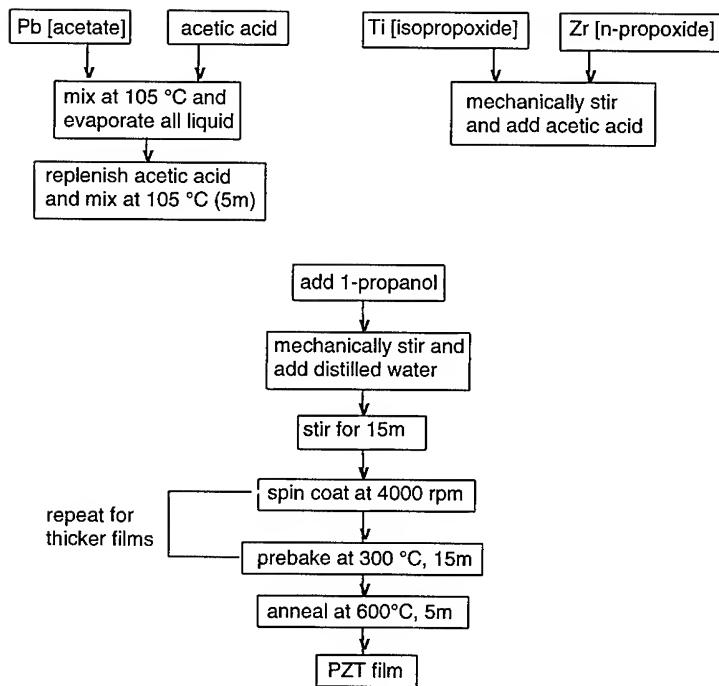


Figure 2: Sol-gel processing of PZT films on TiNi.

Results and Discussions

X-ray Diffraction Analysis

Room temperature XRD of the TiNi thin films prior to PZT deposition and synthesis procedures demonstrated that the microstructure of the TiNi was largely the high temperature B2 phase. The transformation temperatures were not completely determined for this material, but some preliminary evidence showed an $A_f = -10$ °C and $M_s = -40$ °C, thus characterizing the mechanical properties of the thin film as superelastic rather than as thermally activated shape memory effect.

The diffraction pattern for the TiNi/quartz substrate after in-situ annealing at 520 °C is shown in Figure 3a. The substrate was determined to be composed of superelastic austenite B2 phase of TiNi. Also present for the initial TiNi substrate diffraction pattern were 4 peaks that have not been conclusively identified at $2\theta = 20.70^\circ$, 23.54° , 24.87° , and 29.18° (for $\text{CuK}\alpha$ radiation). The peaks were present before the TiNi substrate undergone sol-gel deposition, annealing or any other processing steps. These peaks seem to be some type of non-equilibrium oxide (Ti, Ni or TiNi) associated with the stock TiNi material that were not identified from the analysis of the JCPDS database.

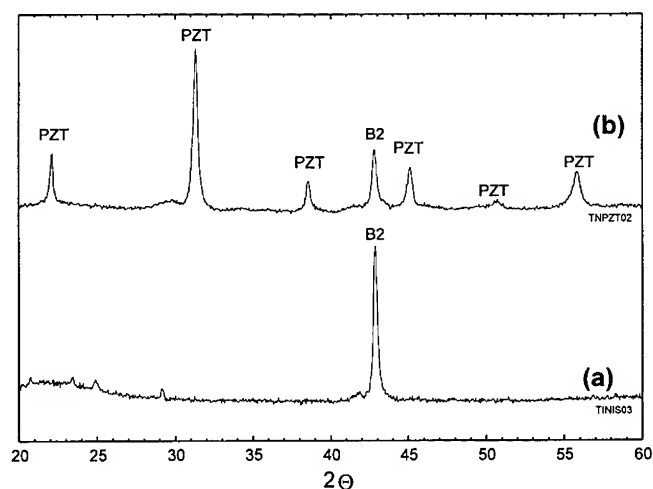


Figure 3: XRD results of PZT/TiNi heterostructures: (a) initial TiNi substrate before any processing; (b) after firing at 600 °C for 5 m, demonstrating the existence of both TiNi (B2) and PZT (perovskite) phases..

The PZT film final thickness was approximately 0.28 μm for a 5 spin coat layer at 4000 rpm. The thickness of the films were measured by a Rudolph Research AutoEl II-NIR-3 ellipsometer and using a typical refractive index of 2.4 for PZT^[13,14]. Room temperature XRD patterns were obtained for the PZT/TiNi and compared to the XRD of the starting substrate in Figure 3a and 3b. XRD analysis showed the presence of the tetragonal perovskite phase of PZT as well as the B2 phase of TiNi. No other peaks were observed, thus indicating minimal chemical interactions took place between the two thin films. Of particular interest is the lack of any peaks associated with TiNi-air interactions. The Ti-air interaction at 600 °C is dramatic and very brief exposures (5 s) to high temperature furnaces will generate large amounts of oxides. The lack of peaks associated with Ti-O system suggests that the amorphous sol-gel film strongly attracts oxygen to form the ferroelectric oxide (which deprives the TiNi substrate to oxygen exposure). Further, the densified ceramic may well act as a diffusion barrier to further oxygen attack of the underlying TiNi metal. This explanation is supported by experiments on PZT/Pt and PZT/Al systems by Barrow and et al^[15]. Their studies showed that crystallization of the amorphous ferroelectric film begins at the interface and nucleates towards the surface. They also observed reduced amounts of oxygen at the ferroelectric-metal interface which produces the cubic paraelectric PZT phase (near the interface).

Optical Microscopy

TiNi and PZT/TiNi film morphologies were characterized by optical microscopy. The sputtered TiNi films were atomically smooth, shown in Figure 4, with some semi-spherical features. The exact nature of these features are not currently known, but future experiments will be conducted to ascertain their cause.

The PZT film on the TiNi had a fine grain structure and exhibited no cracks over large areas. Optical micrographs at low and high magnification is illustrated in Figure 5. The lack of cracks is believed to be a result of the slowed cooling rate when the sample was left on the ceramic block to reach ambient temperature. Compared to samples prepared with commercially obtained bulk TiNi substrates, the sputtered TiNi films were atomically smooth. Experiments conducted by the authors showed that polished surfaces exhibited less cracking. Also, the sol was prepared differently from the past by diluting in a different alcohol and mixing order of precursors. This chemical modification of the sol may have reduced the evaporation rate of the gel, which has been known to greatly affect film quality during drying of sol-gel films.

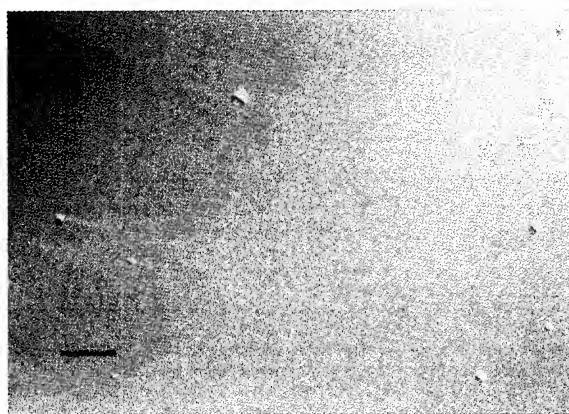


Figure 4: Optical micrographs of TiNi films on quartz substrate showing smooth surface at 1000X magnification (marker = 10 μ m).

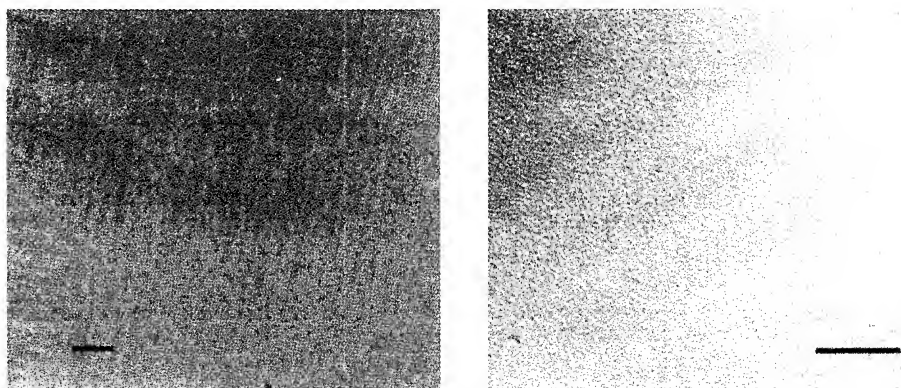


Figure 5: Optical micrographs of PZT films on TiNi/quartz substrates showing lack of cracks over large areas at: (a) 100X, marker = 100 μ m and; (b) 500X magnification, marker = 50 μ m.

Ferroelectric Characterization

Ferroelectrical properties of the spin coated PZT films were obtained using a RT-66A ferroelectric test system by Radiant Technologies. A 1.0 mm diameter electrode was deposited on top of the PZT film using silver paint and the TiNi substrate was utilized as the bottom electrode. The tests were conducted under room temperature conditions (21 °C) with an applied 10V. A remanent polarization value of $0.152 \mu\text{C}/\text{cm}^2$ and coercive field of -203 and 116 kV/cm were obtained for the $0.28 \mu\text{m}$ thick film. The capacitance and resistance were measured to be 0.52 nF and $6.2 \times 10^{11} \Omega\text{-cm}$ respectively. The hysteresis loop is illustrated in Figure 6. Typical P_r , P_s and E_c values for PZT are $23\text{-}30 \mu\text{C}/\text{cm}^2$, $45\text{-}50 \mu\text{C}/\text{cm}^2$ and $40\text{-}45 \text{ kV}/\text{cm}$ respectively.[16] The electrical values obtained for the PZT/TiNi are orders of magnitude different than typical values, but much better than values previously obtained by the authors for ferroelectric-ferroelastic systems[17]. It is believed that the low polarization and large coercive field values are due to problems associated with electrodes. The top electrode was painted onto the PZT substrate using a silver epoxy compound which was easily removed with pressure. The top electrode (Ag) differed from the bottom electrode material (TiNi) and therefore have different electron work functions. This could account for the difference between the $-E_c$ and $+E_c$ values. The large effects of electrode geometry, conductivity and material on the electrical values of the ferroelectric film have also been observed by others [18,19,20].

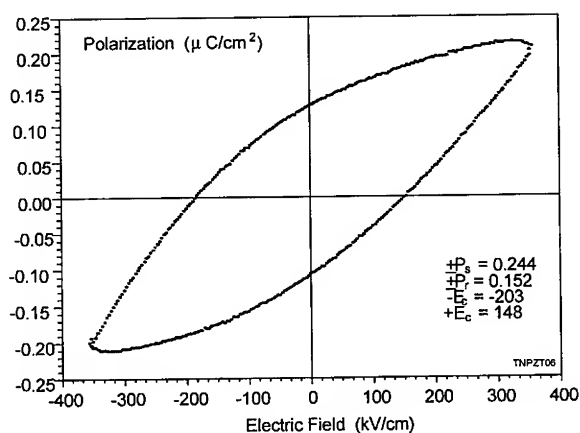


Figure 6: Ferroelectric hysteresis plot for $0.28 \mu\text{m}$ thick PZT film on TiNi at room temperature with a $P_r = 0.152 \mu\text{C}/\text{cm}^2$.

Conclusions

PZT thin films with a Zr/Ti of 53/47 were successfully crystallized onto thin film SMA TiNi. XRD patterns showed that the crystalline tetragonal phase associated with ferroelectricity was present after firing at a temperature of 600 °C for 5 m. XRD results also showed minimal chemical interaction with the B2 TiNi substrate and the perovskite PZT ceramic after annealing cycles. The PZT on TiNi had high mechanical qualities, showing lack of crack defects and strong adhesion with no signs of delamination. Ferroelectric properties were poor compared to literature values stemming from poor top electrode material and adhesion. However, polarization versus electric field plots reveal classical shape hysteresis loops, showing evidence of ferroelectricity.

Acknowledgments

The authors are grateful for financial support for this project from the US Army under grant no. DAAH04-93-G-0213.

References

1. K. Otsuka, K. Shimizu, 'Shape Memory Materials', Proc. MRS Intl. Meeting on Advanced9U Materials (1988)
2. J.D. Bush, A.D. Johnson et al, J. Appl. Phys., v68, p6224 (1990)
3. J.S. Madsen and A.P. Jardine, Scripta Met et Metall., v30, p1189 (1994)
4. P.G. Mercado and A.P. Jardine, 'Thin Film Multilayers of TiNi/TiO₂/PZT: Material Fabrication', SPIE Proc.: Smart Materials, Orlando Conference, v2189, p26 (1994)
5. G. Yi, Z. Wu, M. Sayer, 'Preparation of Pb(Zr,Ti)O₃ thin films by sol gel processing: electrical, optical, and electro-optic properties', J. Appl. Phys. 64 (5), p2717 (1988)
6. C.K. Kwok and S.B. Desu, 'Pyrochlore to perovskite phase transformation in sol/gel derived lead-zirconate-titanate thin films', Appl. Phys. Lett. 60 (12), p1430 (1992)
7. C. Zhixiong, Z.Fangqiao, L. Meidong, W.Guoan and P.Xiangsheng, 'Sol-Gel Derived BaTiO₃ Ceramics', Ferroelectrics, v 123, p66 (1991)
8. M.N. Kamalasanan, N.D. Kumar and S. Chandra, 'Dielectric and ferroelectric properties of BaTiO₃ thin films grown by the sol-gel process', J. Appl. Phys., v 74 (9), p5679 (1993)
9. Y. Suyama and M. Nagasawa, 'Synthesis of Single-Crystal Barium Titanium Isopropoxide Complex to Form Barium Titanate', J. Am. Ceram. Soc. v 77 (2), p603 (1994)
10. A.P. Jardine and J.S. Madsen, 'Fabrication of "smart" ferroelastic-ferroelectric heterstructures', Smart Materials, V.K. Varadan, v1916, p384, SPIE, Albuquerque (1993)
11. J. Chen, Q.C. Xu, M. Blaszkiewicz, R. Meyer, R.E. Newnham, 'Lead zirconate titanate thin films on nickel-titanium shape memory alloys: smarties', J. Am. Ceram. Soc., 75 (10), p2891 (1992)
12. A.P. Jardine, 'Vacuum Conditions for Sputtering Thin Film TiNi', this proceeding
13. C.H. Peng, J.F. Chang and S.B. Desu, 'Optical Properties of PZT, PLZT, and PNZT Thin Films', MRS Symp. Proc., Ferroelectric Thin Films II, v243, p21 (1992)

14. C.H. Peng and S.B. Desu, 'Low Temperature Metalorganic Chemical Vapor Deposition of Perovskite $\text{Pb}(\text{Zr}_x\text{Ti}_{1-x})\text{O}_3$ thin Films', Appl. Phys. Lett., v61(1), p16, (1992)
15. D. Barrow, C.V.R. Vasant Kumar, R. Pascual and M.Sayer, 'Crystallization of Sol Gel PZT on Aluminum and Platinum Metallization', MRS Symp. Proc., Ferroelectric Thin Films II, v243, p113 (1992)
16. S.J. Lockwood, R.W. Schwartz, B.A. Tuttle and E.V. Thomas, 'Solution Chemistry Optimization of Sol-Gel Processed PZT Thin Films', MRS Symp. Proc., Ferroelectric Thin Films III, v310, p275 (1993)
17. A.P. Jardine and P.G. Mercado, 'Thin Film Multilayers of $\text{TiNi/TiO}_2/\text{PZT}$: Mechanical and Electrical Characterization', SPIE Proc.: Smart Materials, Orlando Conference, v2189, p37 (1994)
18. S.P Faure, P.Gaucher and J.P Ganne, 'Influence of Geometrical Parameters on the Electrical Properties of Ferroelectric Thin Films', MRS Symp. Proc., Ferroelectric Thin Films II, v243, p129 (1992).
19. S.E. Bernacki, 'Polarization dependent Conductivity in Thin Film PZT Capacitors', MRS Symp. Proc., Ferroelectric Thin Films II, v243, p135 (1992).
20. D.J Eichorst and C.J., 'Effects of Pt Electrode Structures on Crystallinity and Electrical Properties of MOD-Prepared PZT Capacitors', MRS Symp. Proc., Ferroelectric Thin Films III, v310, p201 (1993).

PROPERTIES OF PIEZOELECTRIC PZT THIN FILMS FOR MICROACTUATOR APPLICATIONS

D. DAMJANOVIC, K. G. BROOKS, A. KHOLKIN, M. KOHLI, T. MAEDER, P. MURALT, and N. SETTER
Laboratory of Ceramics, Department of Materials, Swiss Federal Institute of Technology (EPFL), 1015 Lausanne, Switzerland

ABSTRACT

The piezoelectric properties of lead zirconate titanate (PZT) thin films deposited on thick silicon substrates and thin silicon membranes were investigated using optical interferometry. The effect of the geometrical constraints and clamping effects on the piezoelectric response is discussed. The study of the dielectric permittivity and the loss as a function of the amplitude of the alternating electric field reveals that extrinsic contributions to the dielectric permittivity become active at large fields. The DC electric field has the effect of freezing out the extrinsic contributions. The influence of the dielectric loss on the piezoelectric properties is discussed.

INTRODUCTION

The possibility of miniaturization and integration with silicon technology makes piezoelectric thin films interesting for various microactuator devices [1, 2, 3]. In recent years, there was a significant advance in the design and the processing of such devices, which has not been followed, however, by a similar progress in the understanding of the mechanisms which control and affect their piezoelectric response. Due to their essentially two dimensional geometry, thin films exhibit geometrical constraints which must be taken into account during characterization of their properties and interpretation of the data. Because of the small thickness of the films, the effects of the electrodes, the substrate and nonferroelectric layers on the properties cannot be neglected. Due to differences in the processing, the defect structure of the ferroelectric films is expected to be different than in ceramics of the same composition. Thus, the extrinsic contributions to the dielectric, elastic and piezoelectric properties, which are found to dominate the properties of ceramics, may be different in thin films.

In this work, we report and discuss properties of PZT films deposited on thick silicon substrates, and silicon membranes driven by thin PZT films. The films are used for micromotors [4] and various bimorph structures [5]. The piezoelectric properties of the films were investigated by optical interferometry. The effects of clamping of the films on the piezoelectric properties are discussed in detail. In the second part, we present and discuss dielectric permittivity and loss data, measured as a function of alternating (AC) electric field and electric field bias (DC), which demonstrate the presence of extrinsic contributions to the dielectric properties.

PREPARATION OF THIN FILM STRUCTURES

$\text{Pb}(\text{Zr}_{0.53}\text{Ti}_{0.47})\text{O}_3$ films on thick silicon substrates (abbreviated herein by FTSS) were prepared using a sol-gel method. The details of preparation are given in [6]. The thickness of the films was 0.3 to 1 μm with top electrodes 0.8 to 2.5 mm in diameter. The wafer was cut into smaller rectangular shaped pieces, with sides typically several millimeters long. Some of the investigated films were doped with Nb. The silicon membranes were micromachined (etched) from silicon wafers, after deposition of electrodes and sol-gel PZT films. The diameter of the

membranes was 4 mm, the thickness of the silicon was 10 to 30 μm , and the PZT film was 0.6 μm thick. The membranes were used to fabricate micromotors and full description of their preparation, and the configuration and performance of the micromotor can be found in Ref. [4], where results with sputtered PZT films are also presented.

CHARACTERIZATION OF THE PIEZOELECTRIC PROPERTIES OF FILMS USING OPTICAL INTERFEROMETRY

Determination of the piezoelectric coefficients of piezoelectric thin films is not a simple task because of the small thickness of the films and their strong clamping to the substrate. The expected displacements due to true piezoelectric effect, even for the electric fields comparable with coercive field, do not exceed 1 Å. Therefore, optical interferometry is often utilized to determine the longitudinal piezoelectric coefficient, d_{33} , by means of the inverse piezoelectric effect. Up to now, only few results concerning piezoelectric measurements of ferroelectric films have been reported [7-10].

In this investigation, a simple Michelson interferometer [11] was used to measure displacement of FTSS and membranes under external AC electric field. Details of the experimental setup and of the measurement method will be given elsewhere.

The main disadvantage of this experimental scheme is that the displacements of only one face of the sample can be monitored and therefore movement of the whole sample as a rigid body can not be excluded [11]. This problem may be overcome for the bulk samples by clamping the back side of the sample to a rigid holder, and by using samples in a cubic form to prevent the bending effects [12]. In the case of FTSS, the substrate and the film effectively form a bimorph structure resulting in large bending effects even if the frequency is much smaller than the resonance frequency of the flexural mode. Such a behaviour was observed earlier for transverse electrode PLZT films [13]. Under such circumstances, the measured response will not reflect the longitudinal piezoelectric coefficient d_{33} , but rather the transverse coefficient d_{31} which is effectively increased by the multiplication factor of the bimorph. This is illustrated in Fig. 1a and 1b where the displacement of the PZT film on free (unclamped)

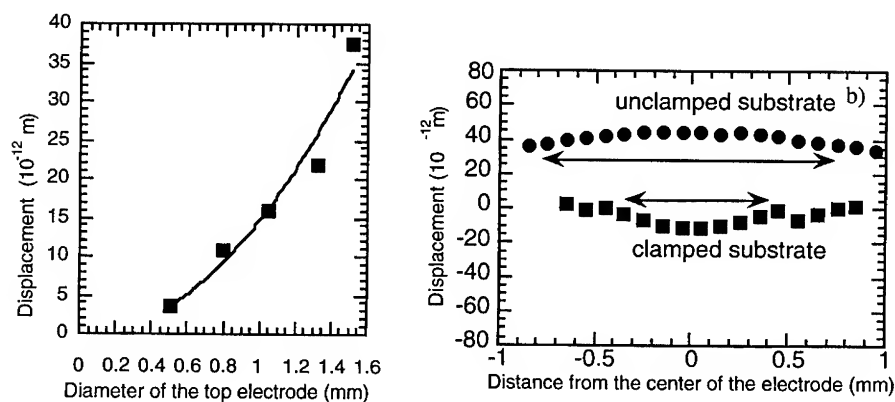


Fig 1. a) Displacement of the PZT film on unclamped substrate as a function of top electrode diameter. b) Displacement of the PZT film on unclamped and clamped substrate as a function of distance from the center of the top electrode. The arrows indicate electrode width. The frequency of the AC field was 1 kHz, with amplitude 0.1 V for the free and 0.2 V for the clamped substrate.

substrate is plotted as a function of the top electrode diameter and of the distance from the electrode center. The nearly quadratic dependence (Fig. 1a) and large values of the

displacements (Fig. 1b) even outside the area of the top electrode, clearly indicate that in this case we are dealing with the movement of the whole substrate. An improvement of the measuring method was achieved by fixing the substrate with rigid silver epoxy exactly under the top electrode. In this case the substrate is allowed to vibrate freely near the edges but is fixed near the point of the probing laser beam. In this way the bending effects were almost eliminated (Fig. 1b).

It should be noted that the direction of the polarization within the films was such to give displacement which was in antiphase with the driving AC voltage in the longitudinal (d_{33}) mode, and in phase for the bending mode which is dominated by the transverse d_{31} coefficient.

Elimination of the bending effects allowed a study of the low-signal piezoelectric response under DC electric field. The hysteresis loop of the piezoelectric coefficient for a Nb doped film is shown in Fig. 2, as an example. The observed butterfly-type loop is common for ferroelectrics

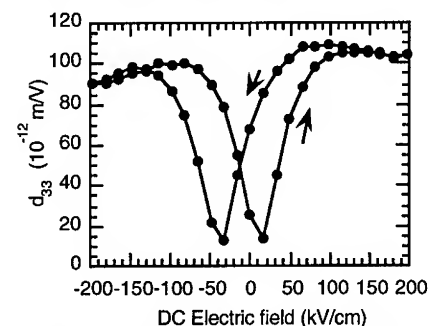


Fig. 2. Hysteresis loop of the piezoelectric coefficient for a 1%Nb-doped PZT film. Frequency of the AC field was 1 kHz.

with 90° domain wall movement. The loops for positive and negative fields are asymmetric, which is compatible with the measurements of the polarization hysteresis loops. The value of the piezoelectric coefficient at zero field ($d_{33}(0) \approx 70 \times 10^{-12} \text{ m/V}$) should be compared with the values for poled bulk ceramics of the same composition ($d_{33} = 200\text{--}300 \times 10^{-12} \text{ m/V}$). The large difference may arise from insufficient poling conditions (films are poled during the short-time hysteresis loop measurements, shown in Fig. 2) and from different micro-structure, domain wall structure and the nature and concentration of defects in ceramics and the films. Additional data which may offer support to these arguments will be given in the next section. Another reason for the difference certainly arises from the clamping

of the film to the substrate. Because of the clamping, the strains along the film surface are not allowed to fully develop and the measured piezoelectric coefficient is reduced, compared to the free material, according to relationship [10]:

$$d_{33}(\text{clamped}) = d_{33}(\text{free}) - 2d_{31}s_{13}/(s_{11} + s_{12}), \quad (1)$$

where s_{ij} are the elastic compliances at constant field. Using typical values of the elastic compliances for bulk PZT, and ratio $d_{33}/d_{31} = -2.3$ one obtains that d_{33} measured on clamped thin films may be as small as 50% of the value for the bulk [10, 14].

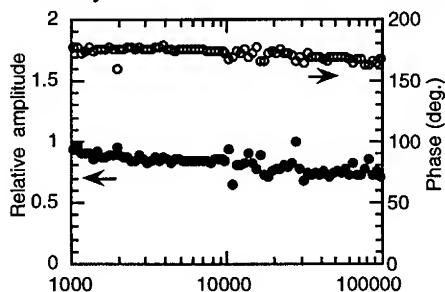


Fig. 3. Frequency dependence of the amplitude and the phase of apparent piezoelectric response of PZT film on clamped substrate.

The amplitude and phase of the interferometric signal are found to be frequency dependent (Fig. 3). The amplitude is slightly decreasing with frequency and is accompanied by a relatively large change of the phase (about 15° from 1 to 100 kHz). A similar behaviour was reported earlier [9] and was related to the influence of residual stresses and increase of the holding force near the film-substrate interface. An alternative explanation is that with increasing frequency the influence of bending vibrations becomes larger, resulting in a decrease of real (due to contributions of the opposite sign from bending, caused by d_{31}

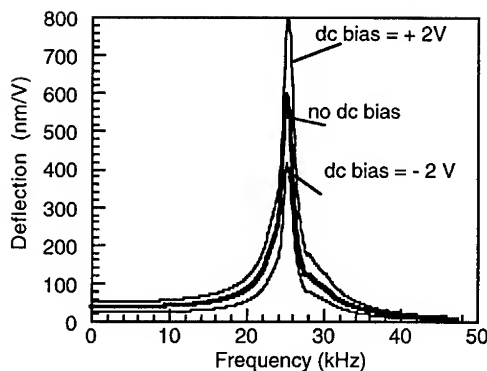


Fig. 4. Deflection of a silicon membrane covered with 0.6 μm thick PZT film.

mode) and increase of imaginary component of the apparent piezoelectric response (due to increase in phase angle as the resonance is approached). Other explanations for the frequency dependence of the apparent piezoelectric response, related to the properties of the material itself, must also be considered.

Fig. 4 shows deflection of a silicon membrane covered with sol-gel PZT film, as a function of frequency, near the fundamental mode. Measurements were made by the interferometer, probing the center of the membrane. The AC electric field was 50 mV. The effect of the DC electric field bias is also shown. Deflection is significantly larger for positive bias field. This is in accordance with asymmetry of the hysteresis in piezoelectric coefficient, which is similar to that shown in Fig. 2 for FTSS. Clearly, dependence of the

piezoelectric response on the magnitude of the applied electric field should be taken into account when designing devices based on the piezoelectric properties of ferroelectric thin films.

DIELECTRIC PERMITTIVITY AND LOSS OF PZT THIN FILMS AS A FUNCTION OF LOW SIGNAL AC ELECTRIC FIELD

Fig. 5 shows capacitance (C) of a 0.8 μm thick sol-gel PZT film as a function of AC electric field, with DC electric bias field taken as the parameter. Two regions in C vs. AC field are

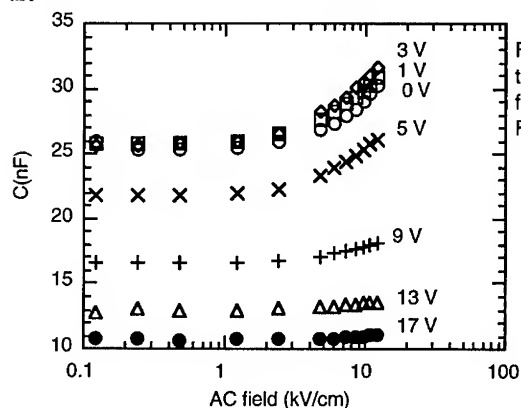


Fig. 5. Capacitance vs. amplitude of the AC electric field for a sol-gel PZT film deposited on thick silicone substrate. Frequency of AC field was 1 kHz. Diameter of the top electrode was 1.5 mm.

obvious: one, at low AC fields, where capacitance is almost constant with field, and the other, above approximately 1 kV/cm, where capacitance increases with the increasing AC field. An analogous behaviour was observed in loss vs. AC field. Similar dependence is reported in PZT ceramics and is interpreted in terms of domain wall motion which is frozen at low excitation fields, but becomes active at large amplitudes [15], where it contributes to the observed dielectric permittivity and loss. Important difference between ceramics and thin films is that the threshold field at which permittivity starts changing, is an order of magnitude higher in PZT

films (~ 1 kV/cm) than in ceramics (~ 0.1 kV/cm) [15]. Possible reasons for the higher threshold field in films are: (i) domains are less mobile in films due to the essentially two dimensional geometry of films (ii) domain walls are pinned by defects which are either not present in ceramics or possess higher activation energy in films than in ceramics, and (iii) the increase in apparent permittivity is not due to moving domain walls, but by some other type of defects or processes.

The difference between the threshold fields in the ceramics and in the films reflects similar difference in their coercive fields, which are roughly one order of magnitude higher than the threshold fields.

If domain wall vibrations are responsible for the observed behavior of the permittivity, it may be possible to use the same arguments to explain the comparatively low piezoelectric coefficients in thin films, discussed in the previous section. It has been shown that in piezoelectric ceramics, domain wall motion may be responsible for as much as 70% of the total observed piezoelectric effect [16]. If, as present data might suggest, mobility of domain walls in films is significantly smaller than in ceramics, one may expect to see lower piezoelectric coefficients in the films.

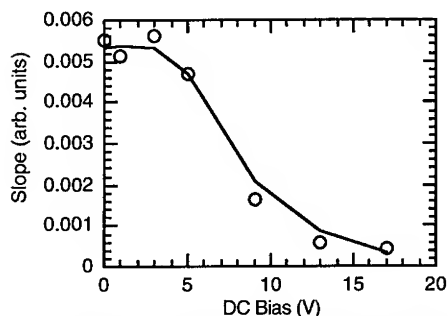


Fig. 6. Slope of capacitance vs. AC field (above 5 kV/cm AC field, Fig. 5) as a function of electric field bias.

Fig. 5 also shows that the slope of capacitance vs. AC field decreases with DC bias field, in the region above approximately 5 kV/cm, where domain walls (or other defects) are active. This effect of freezing of the domain walls by the DC bias, makes it more difficult for the weak AC field to move domain walls against the strong DC field. Fig. 6 plots slope of capacitance vs. AC field (from Fig. 5, slope above ~ 5 kV/cm AC field) vs. DC bias field. At low DC bias, the slope is constant, because the DC field is smaller than the amplitude of the AC field, and DC field cannot freeze the domain walls. The slope starts changing when DC and AC fields become comparable, and domain walls are becoming locked by the DC field.

Acknowledgments: This work was supported in part by the Swiss Federal Office for Science and Education and performed within the European research program on ferroelectric thin films (COST 514).

REFERENCES

- [1] G.-A. Racine, R. Luthier and N. F. de Rooij, Proc. IEEE-MEMS, Fort Lauderdale, USA, 1993, p. 128.
- [2] A. M. Flynn, L. S. Tavrow, S. F. Bart, R. A. Brooks, D. J. Ehrlich, K. R. Udayakumar and L. E. Cross, J. Micromech. Systems 1 (1), 44 (1992).
- [3] D. L. Polla, T. Tamagawa, C. Ye, P. Schiller, L. Pham, C.-Y. Tu, Proc. SPIE-Int. Soc. Opt. Eng. 1694, 173 (1992).
- [4] P. Muralt, M. Kohli, T. Maeder, A. Kholkin, K. G. Brooks, and N. Setter, submitted to Sensors and Actuators A.
- [5] K. G. Brooks, D. Damjanovic, N. Setter, Ph. Luginbuhl, G.A.-Racine, and N.F. de Rooij, Proc. 9th ISAF, The Pennsylvania State University, University Park, PA, Aug. 7-10, 1994 (to be published).

- [6] K. Brooks , D. Damjanovic, A. Kholkin, I. M. Reaney, N. Setter, Ph. Luginbuhl, G. A.-Racine, N. F. de Rooij, and A. Saaman, Proc. 6th ISIF, Monterey, CA, March 14-16, 1994 (to be published).
- [7] Z. Surowiak, D. Czekaj, A. M. Margolin, E. V. Sviridov, V. A. Aleshin, and V. P. Dudkevich, Thin Solid Films **214**, 78 (1992).
- [8] J. Chen, K. R. Udayakumar, K. G. Brooks, and L. E. Cross in Ferroelectric Thin Films II, ed. by A. I. Kingon, E. R. Myers and B. Tuttle (Mat. Res. Soc. Proc. **243**, Pittsburgh, PA, 1992) pp. 361-366.
- [9] J.-F. Li, D. D. Viehland, T. Tani, C. D. E. Lakeman, and D. A. Payne, J. Appl.Phys. **75**, 442 (1994).
- [10] K. Lefki and G. J. M. Dormans, J.Appl.Phys. **76**, 1764 (1994).
- [11] Q. M. Zhang, W. Y. Pan, and L. E. Cross, J. Appl. Phys. **63**, 2492 (1988).
- [12] J.-F Li, P. Moses, and D. Viehland, Ferroelectrics **153**, 365 (1994).
- [13] K. L. Lewis and K. F. Dexter in Ferroelectric Thin Films III, ed. by E. R. Mayers et al. (Mat. Res. Soc. Symp. **310**, Pittsburgh, PA) pp.99-105.
- [14] B. Jaffe, W. R. Cook, and H. Jaffe, Piezoelectric Ceramics (Academic Press, NY, 1971) p.146.
- [15] S. Li, W. Cao, and L.E. Cross, J. Appl. Phys. **69** (10), 7219 (1991).
- [16] E. I. Bondarenko, V. Yu. Topolov, and A. V. Turik, Ferroelectrics Lett. **13**, 13 (1991).

EFFECTS OF THE MULTILAYER STRUCTURE ON THE RESPONSIVITY OF PYROELECTRIC THIN FILM DETECTORS

ZHU JIANGUO, XIAO DINGQUAN, QIAN ZHENGHONG,
ZHANG WEN AND DU SIAOSONG

DEPARTMENT OF MATERIALS SCIENCE, SICHUAN UNIVERSITY,
CHENGDU 610064, CHINA

ABSTRACT

Pyroelectric thin film detectors have advantages of wavelength independent sensitivity, room temperature operation and direct incorporation with integrated circuit amplifiers. Pyroelectric thin films with good quality have been prepared by many advanced thin film technologies [1-2]. The responsivity of pyroelectric thin film detectors is dependent on the thermal properties of the substrate, on which pyroelectric thin film detectors are prepared. The heat conduction in the detectors was investigated using the one-dimensional heat flow equation and the expressions describing the detectors performance were derived for pyroelectric thin film detectors with multilayer structure. The numerical simulation showed that the pyroelectric thin film detectors need effective heat isolation. If the air gap could be the heat isolation layer, which is between the bottom electrode and substrate, the responsivity of detectors would be higher than that of detectors which have no heat isolation in certain modulation frequency range.

INTRODUCTION

Pyroelectric thin films have a set of unique properties that can be used as the pseudomonolithic pyroelectric thin film detector array/signal processor system, which has attracted attention for uncooled infrared focal plane imaging system. In the past years, pyroelectric detectors were made of thin crystals, which should be freely suspended in the air so that it can reduce the thermal heat loss to surrounding ambients and get the highest responsivity. But it is very difficult to construct a freely suspended structure for pyroelectric thin film detectors. A question that arises concerns the effects that the structure of detectors, thermal properties of substrate and electrode will have on the performance of the pyroelectric thin film detector array.

In this paper, we have extended the thermal analysis of the response of pyroelectric thin film detectors by using one-dimensional heat-flow equation. The effect of the detector structure, the thermal properties and thickness of substrate and the heat isolation layer between the bottom electrode and substrate on the responsivity of detectors are analyzed.

THEORETICAL ANALYSIS

The model of the multilayer-structure used in this paper is shown in Figure 1. We have assumed that the radiation energy, which is modulated sinusoidally by a mechanical chopper at an angular frequency ω , falls at the front electrode of detectors. A one-dimensional heat conduction equation, which assumes the lateral dimensions to be large when compared to the thickness of the total thickness of the detectors, is employed. Thus the lateral heat flow is neglected. The emissivity at the front electrode is assumed to be unity and at the back surface of the substrate to be zero.

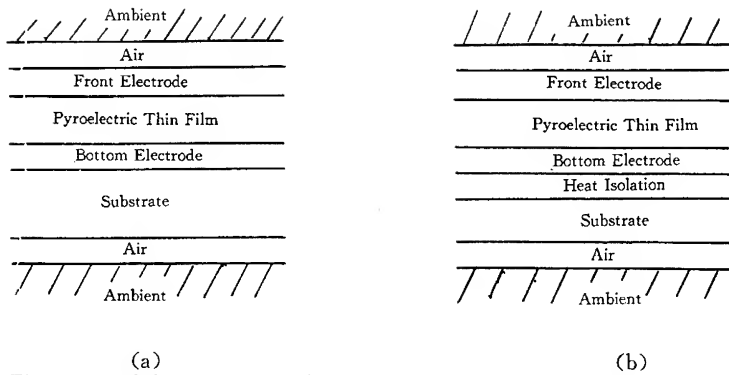


Figure 1 Multilayer structure of pyroelectric thin film detector used in the theoretical analysis.

(a) Model I, without heat isolated layer

(b) Model II, with heat isolated layer

For model I, the general solution to the heat conduction equation for each of the six individual layers as following[3-4]:

$$T(X_i) = A_i \cosh(U_i \cdot X_i) + B_i \sinh(U_i \cdot X_i)$$

The pyroelectric current per unit area which is the pyroelectric coefficient p multiplied by the time rate of change of the mean temperature of the pyroelectric thin film is given by following equation[5]:

$$I = \frac{p}{L} \times \frac{\partial}{\partial t} \left(\int_0^{L_p} T(X_p) dX_p \right) = \frac{p}{U_p \cdot L_p} \times \frac{\partial}{\partial t} [A_p \cdot \sinh(U_p \cdot L_p) + B_p \cdot \cosh(U_p \cdot L_p) - B_p]$$

The boundary conditions for the radiant heating of the detector in Model I and Model II are assumed that the temperatures and the heat flow are continuous at each interface.

The current responsivity R_i is defined as the pyroelectric current divided by the radiation power. We calculated, after some manipulation, the current responsivity is as following:

$$R_i = \left| \frac{p \cdot \exp(j\omega t) \cdot GX}{C_p \cdot D_p \cdot L_p \cdot GW} \right|$$

where :

$$\begin{aligned} GX &= K_p \cdot U_p \cdot GI \cdot \sinh(U_p \cdot L_p) + K_f \cdot U_f \cdot GH \cdot [\cosh(U_p \cdot L_p) - 1] \\ GW &= K_f \cdot U_f \cdot GU + K_a \cdot U_a \cdot GV \cdot \cosh(U_a \cdot L_a) + H_a \cdot GV \\ GI &= GV \cdot \cosh(U_f \cdot L_f) - GU \cdot \sinh(U_f \cdot L_f) \\ GH &= GV \cdot \sinh(U_f \cdot L_f) - GU \cdot \cosh(U_f \cdot L_f) \\ GU &= GT \cdot \cosh(U_f \cdot L_f) + GS \cdot \sinh(U_f \cdot L_f) \cdot [K_f \cdot U_f / (K_p \cdot U_p)] \\ GV &= GT \cdot \sinh(U_f \cdot L_f) + GS \cdot \cosh(U_f \cdot L_f) \cdot [K_f \cdot U_f / (K_p \cdot U_p)] \\ GT &= GR \cdot \cosh(U_p \cdot L_p) + GQ \cdot \sinh(U_p \cdot L_p) \cdot [K_p \cdot U_p / (K_b \cdot U_b)] \\ GS &= GR \cdot \sinh(U_p \cdot L_p) + GQ \cdot \cosh(U_p \cdot L_p) \cdot [K_p \cdot U_p / (K_b \cdot U_b)] \\ GR &= GN \cdot \cosh(U_b \cdot L_b) + GM \cdot \sinh(U_b \cdot L_b) \cdot [K_b \cdot U_b / (K_s \cdot U_s)] \\ GQ &= GN \cdot \sinh(U_b \cdot L_b) + GM \cdot \cosh(U_b \cdot L_b) \cdot [K_b \cdot U_b / (K_s \cdot U_s)] \end{aligned}$$

$$\begin{aligned} GN &= \text{ch}(U_s \cdot L_s) + K_s \cdot U_s \cdot GD \cdot \text{sh}(U_s \cdot L_s) \\ GM &= \text{sh}(U_s \cdot L_s) + K_s \cdot U_s \cdot GD \cdot \text{ch}(U_s \cdot L_s) \\ GD &= \text{th}(U_r \cdot L_r) / (K_r \cdot U_r) \end{aligned}$$

The symbols used in these relations are shown in Table I.

Table I	Principal	Symbols
L_i	Thickness of ith layer in a detector	
X_i	Depth in ith layer	
$a, f, p, b, h, s, r,$	Subscripts denoting upper air, front electrode, pyroelectric, bottom electrode, heat isolation, substrate and air under substrate layers, respectively.	
Φ	Amplitude of modulated power released in receiver, per unit area	
f	Modulation frequency	
ω	Angular frequency, $2\pi f$	
t	Time	
T_0	Thermodynamic temperature of environment	
$T(X_i)$	Temperature excess over T_0 , at depth X in ith layer	
α_i	Reciprocal of the thermal diffusion distance in ith layer.	
	$\alpha_i = \sqrt{\omega \cdot D_i \cdot C_i / 2K_i}$	
U_i	$(1+j)\alpha_i$, $j = \sqrt{-1}$	
K_i	Thermal conductivity of ith layer	
C_i	Specific heat of ith layer	
D_i	Density of ith layer	
H_a	Power radiated through the air layer from the front surface of the receiver, per unit area and per unit excess temperature	

According to Model II, some manipulation similar to Model I, and considering the effect of the heat isolation layer, we can calculate the relation of Ri for Model II as following:

$$Ri = \left| \frac{p \cdot \exp(j\omega t) \cdot FX}{C_p \cdot L_p \cdot D_p \cdot FW} \right|$$

where :

$$\begin{aligned} FX &= K_p \cdot U_p \cdot F1 \cdot \text{sh}(U_p \cdot L_p) + K_f \cdot U_f \cdot F2 \cdot [\text{ch}(U_p \cdot L_p) - 1] \\ FW &= K_f \cdot U_f \cdot FI + FG \cdot K_s \cdot U_s \cdot \text{cth}(U_s \cdot L_s) + FG \cdot H_a \\ F1 &= FG \cdot \text{ch}(U_f \cdot L_f) - FI \cdot \text{sh}(U_f \cdot L_f) \\ F2 &= FG \cdot \text{sh}(U_f \cdot L_f) - FI \cdot \text{ch}(U_f \cdot L_f) \\ FI &= K_p \cdot U_p \cdot FU \cdot \text{ch}(U_f \cdot L_f) + K_f \cdot U_f \cdot FV \cdot \text{sh}(U_f \cdot L_f) \\ FG &= K_p \cdot U_p \cdot FU \cdot \text{ch}(U_f \cdot L_f) + K_f \cdot U_f \cdot FV \cdot \text{ch}(U_f \cdot L_f) \\ FU &= K_b \cdot U_b \cdot FR \cdot \text{ch}(U_p \cdot L_p) + K_p \cdot U_p \cdot FQQ \cdot \text{sh}(U_p \cdot L_p) \\ FV &= K_b \cdot U_b \cdot FR \cdot \text{sh}(U_p \cdot L_p) + K_p \cdot U_p \cdot FQQ \cdot \text{ch}(U_p \cdot L_p) \\ FR &= K_h \cdot U_h \cdot FP \cdot \text{ch}(U_b \cdot L_b) + K_b \cdot U_b \cdot FQ \cdot \text{sh}(U_b \cdot L_b) \\ FQQ &= K_h \cdot U_h \cdot FP \cdot \text{sh}(U_b \cdot L_b) + K_b \cdot U_b \cdot FQ \cdot \text{ch}(U_b \cdot L_b) \\ FP &= K_s \cdot U_s \cdot FM \cdot \text{ch}(U_h \cdot L_h) + K_h \cdot U_h \cdot FN \cdot \text{sh}(U_h \cdot L_h) \\ FQ &= K_s \cdot U_s \cdot FM \cdot \text{sh}(U_h \cdot L_h) + K_h \cdot U_h \cdot FN \cdot \text{ch}(U_h \cdot L_h) \\ FM &= K_r \cdot U_r \cdot \text{ch}(U_s \cdot L_s) + K_s \cdot U_s \cdot \text{th}(U_r \cdot L_r) \cdot \text{sh}(U_s \cdot L_s) \\ FN &= K_r \cdot U_r \cdot \text{sh}(U_s \cdot L_s) + K_s \cdot U_s \cdot \text{th}(U_r \cdot L_r) \cdot \text{ch}(U_s \cdot L_s) \end{aligned}$$

The results of numerical simulation are shown in Figures 2 - 5 using the parameters given in Table II[5].

Table II Values of parameters used in the numerical simulation

Material	Specific Heat (J/g · K)	Density (g/cm ³)	Thermal Conductivity (W/cm · K)
PbTiO ₃	0.41	7.78	3.5×10^{-2}
Gold	0.13	0.345	1.0×10^{-3}
Silicon	0.70	2.328	1.45
Polymer	1.42	1.05	1.46×10^{-3}
SiO ₂	0.78	2.18	8×10^{-3}
Air	1.047	1.181×10^{-3}	2.6×10^{-4}
Al ₂ O ₃	0.75	3.98	4.18×10^{-1}

SIMULATION RESULTS AND DISCUSSION

Fig. 2 shows the current responsivity versus frequency with the thickness of silicon substrate as the parameter for Model I (a) and Model II (b). The thickness of PbTiO₃ thin film, the gold front and bottom electrodes are assumed to be 1 μ m, 0.1 μ m and 0.1 μ m, respectively. The pyroelectric coefficient of PbTiO₃ thin film is assumed to be 2.7×10^{-8} (C/cm² · K) and α is about 5.7×10^{-4} (W/cm² · K) at 293 K. The thickness of air layer is assumed 1mm.

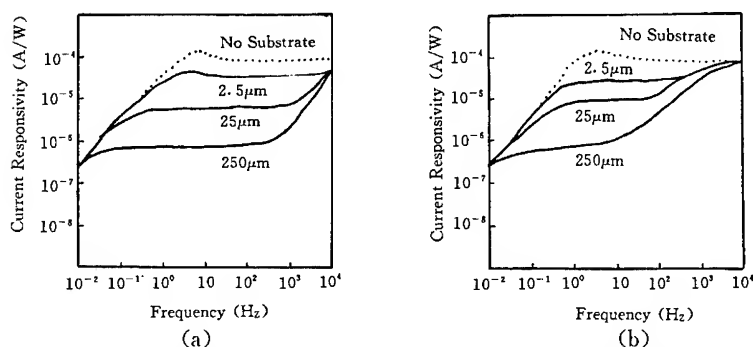


Fig. 2 Current responsivity versus frequency of 1 μ m PbTiO₃ thin film detector with silicon substrate thickness as parameter for Model I (a) and Model II (b).

From Figure 2, we can find that the current responsivity falls off with decreasing frequency. The lower the frequency, the lower the current responsivity. Physically, this is due to that the heat is able to conduct to the substrate and flows out to the air layer through substrate at lower frequency. We also found that the thinner the substrate, the higher the responsivity. Especially, the responsivity reaches a maximum when the substrate thickness becomes zero at 5-8 Hz in Fig. 2(a). Although this case can not to be for the thin film detector, we can also find the interesting fact that the current responsivity of detector with heat-isolation layer would be higher than that of detector without heat-isolation layer from Fig. 2(b). Using the microstructure technique, the heat-isolation layer would be made between the bottom electrode and substrate[7].

Fig. 3 illustrates the effect of different substrates, the thicknesses of which were 25 μ m, on the responsivity for Model I (a) and Model II (b) with 1 μ m air layer as heat isolation layer. We can find that the responsivity of Model II would be higher from 0.1 to 80 Hz range for polymer substrate and from 20 to 20000 Hz for Al₂O₃ substrate than those of Model I, respectively. From Fig. 3 (b), we also found that the responsivity of detector on silicon substrate is higher from 0.2 to 10 Hz than that of detector on Al₂O₃ substrate but is lower from 0.2 to

800 Hz than that of detector on polymer.

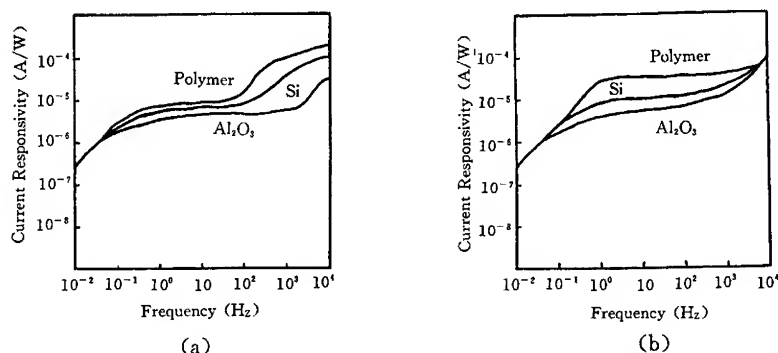


Fig. 3 Current responsivity versus frequency of $1 \mu\text{m}$ PbTiO_3 thin film detector with different substrate, which thicknesses were $25 \mu\text{m}$, for Model I (a) and Model II (b).

Fig. 4 shows the effect of different materials for heat isolation layer on the responsivity. We can find the very interesting fact that the responsivity of detector with $1 \mu\text{m}$ SiO_2 layer as heat isolation layer would be higher from 80 to 40000 Hz than that of detector with $1 \mu\text{m}$ air layer as heat isolation layer, both on $250 \mu\text{m}$ silicon substrate, the other parameters are also the same. But this advantage would diminish with a thinner substrate.

Fig. 5 shows the experimental and theoretical curves of current responsivity of $1 \mu\text{m}$ PbTiO_3 thin film on $250 \mu\text{m}$ on a silicon substrate without the isolation layer. It was found that both curves lie very close. However the experimental curve at and below 10 Hz was lower than the theoretical one. This is attributed to the thermal heat loss caused by the lateral heat conduction through the thin film and substrate. The lateral heat conduction, which was not considered in this one-dimensional analysis, would become significant particularly for small area arrays operating at very low frequencies. This study is now in progress.

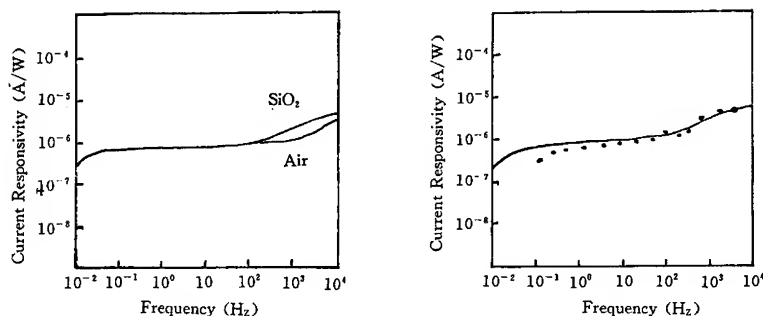


Fig. 4 Current responsivity versus frequency of $1 \mu\text{m}$ PbTiO_3 thin film with different materials as heat isolation layer.

Fig. 5 Current responsivity versus frequency of $1 \mu\text{m}$ PbTiO_3 thin film. Experimental curve: Theoretical curve: —

CONCLUSION

The effect of multilayer structure with and without a heat isolation layer on the current responsivity of pyroelectric detectors was discussed and the results of numerical calculation were given in this paper. The current responsivity decreases with decreasing frequency below certain frequency due to the flow of heat out of the substrate into air. The thinner the substrate, the higher the responsivity. The responsivity of detector with a heat isolation layer would be higher than that of detector without a heat isolation layer.

REFERENCES

1. G. H. Haerting, J. Vac. Sci. Technol. A **9**(3), 414 (1991)
2. S. L. Swartz and V. E. Wood, Condensed Matter News **1**(5), 4 (1992)
3. H. Blackburn and H. C. Wright, Infrared Physics, **10**, 191 (1970)
4. B. R. Holeman, Infrared Physics, **12**, 125 (1972)
5. S. Y. Wu, IEEE Transactions on Electron Devices, ED-27, No. 1, 88 (1980)
6. W. R. Blevin and Jon Geist, Applied Optics, **13**, 1171 (1974)
7. R. T. Howe, J. Vac. Sci. Technol. B, **6**(6), 1809 (1988)

PART X

Alloying Effects and Transformations in Shape Memory Materials

RECENT DEVELOPMENTS IN HIGH TEMPERATURE SHAPE MEMORY ALLOYS

JENO BEYER, JAN.H. MULDER

University of Twente, Department of Mechanical Engineering, Laboratory of Materials Science, P.O.Box 217, 7500 AE Enschede, The Netherlands.

ABSTRACT

The functional properties of Shape Memory Alloys (SMA's) are used successfully at present in a variety of industrial and medical applications. The use of these materials in smart structures is now emerging in the field of aeronautic/space technology. Many applications require higher operating temperatures than available to date, or higher cooling rates and/or a higher number of cycles. For this purpose the properties and fabricability of commercial alloys as Ni-Ti-(X), Cu-Al-Ni or Cu-Zn-Al are being adjusted and improved. Other feasible alloys are being developed. The research and development is directed towards the control of the stress, strain, temperature and time dependence of shape memory properties for a stable in-service behaviour. In this paper the various approaches taken up in recent years by academic and industrial laboratories for developing high temperature SMA's are reviewed.

INTRODUCTION

Shape memory materials have attracted considerable attention in recent years as functional materials with commercial applications in various engineering products. An extensive overview of the European activities has been given by Van Humbeeck recently [1]. Among the practical SMA's available today Ti-Ni alloys are being used most extensively because of the excellent mechanical properties, corrosion resistance and biocompatibility. The latter is important for biomedical applications, in particular for implants [2,3]. In recent years smart materials have been identified in the USA as an important emergent materials technology area for space and aerospace and a variety of other engineering fields [4,7]. SMA's belong to this group of materials because of their ability to perform both sensing and actuating functions. [6,7].

The operating temperatures of most SMA's are limited by their thermo-elastic martensite transformation temperatures (TT) to 400K. However, there is an increasing interest and need for high temperature SMA's in electronic engineering, aircraft and space industry, automobile industry, chemical industry, (oil and gas) exploration and geothermal industry. The major concerns in developing these new types of SMA's are high TT of the thermoelastic martensite transformation; because these alloys tend to operate at high temperatures, the stability of the alloy over a long period of time is equally important. In many applications the SMA will have to operate during many cycles either by repeated cooling and heating or loading and unloading. Therefore the stability of the shape memory behaviour has to be considered too [8]. Additionally the high temperature SMA's offer the possibility of shorter cooling times resulting in faster response, as compared to conventional SMA's. Cu-based alloys, among the best understood shape memory materials (with TT limited to 453K), are cost effective, but show a lack of stability at high temperatures, in cyclic applications and are prone to brittleness

due to intergranular fracture [9,10]. Considerable improvements have been obtained by alloying, grain refinement and thermo-mechanical treatment, resulting in the development of the Cu-Ni-Al-Ti-Mn alloys with TT up to 453K [9,11,12]. Their limitations however, concerning the requirements for high temperature applications, still exist. Therefore these alloys are not discussed here.

Binary alloys of Ti with the noble metals (Au,Pt,Pd) have high TT up to 1300K as shown by Donkersloot en van Vucht [13]. By alloying, the TT can be adjusted to the operating temperatures required. The fundamental understanding of the effect of alloying elements on the phase stability in these alloys has led to the development of Ti-Ni-X(Pt,Pd,Au), Ti-Ni-X(Zr,Hf) and Ni-Al-based alloys [10,14,15,16]. Recently the Ti-Ni-Zr and Ti-Ni-Hf alloys have been patented [17,18] and in the past two years more data became available. The martensite transformation in Ni-Al has been studied since the early 70's [19,20,21]. Further development as a SMA was retarded by the inherent lack of ductility of these alloys due to insufficient slip systems. Some success has been obtained recently by introducing a ductile second phase which toughens the Ni-Al-base alloys, by the addition of Fe and/or Mn [22,23]. The ductile phase, either γ or γ' , provides the room temperature ductility in these alloys. Another drawback was that the transformation behaviour of the binary Ni-Al alloys still was not well understood. Ageing effects in Ni-Al alloys are believed to limit the applicability of these SMA's to temperatures below about 523K [24].

In this paper the efforts which have been undertaken in recent years to overcome the limitations of the various alloys will be reviewed.

TI-NI-X ALLOYS (X=NOBLE METAL)

Martensite transformation and shape memory effect

To adjust the transformation temperatures to values higher than those available for binary Ti-Ni alloys, alloying is most frequently used. Donkersloot and van Vucht investigated the TT of the binary Ti-(Pd, Pt, Au) systems and determined their lattice parameters. Martensite TT's were recorded as high as 1323 K for the Ti-Pt system with a small (20K) hysteresis [13]. The mutual solubility of TiNi on one hand and TiAu, TiPd and TiPt on the other, initiated the research of the Ti-Ni-X(X=Au,Pd,Pt) systems. At present the Ti-Ni-Pd is most intensively studied although data for other systems also become available. The evolution of the transformation temperatures is qualitatively the same for all systems considered. Kachin et al [25,27] established the TT of the pseudo-binary alloy systems TiNi-TiX (X=Au, Pd, Pt). Small additions of third element X decrease the TT at first and then increase after $x > 10$ at.% up to the TT of the binary TiX alloy as shown in Figure 1. for the TiNi-TiPt system. The shape memory effect is primarily associated with the crystallography of the martensite transformation. The transformation alters, with increasing amount of third element X, from $B_2 \rightarrow B_{19}'$ (monoclinic), via $B_2 \rightarrow R \rightarrow B_{19}'$ and $B_2 \rightarrow B_{19}$ (orthorhombic) $\rightarrow B_{19}'$ to $B_2 \rightarrow B_{19}$. The corresponding change of lattice parameters is also given in Figure 1.

Kachin et al. [26,27] investigated the shape memory effect in the alloys and observed a maximum in the range of the $B_2 \rightarrow B_{19} \rightarrow B_{19}'$ transformation sequence. In this region one of the eigenvalues of the strain tensor is approaching unity, resulting in a coherent martensite/austenite interface without the need of a lattice invariant deformation. The macroscopic reversible deformation (lattice strain) is maximum (10-12%) with

the smallest hysteresis at this composition range. However the TT is low in this case and increasing concentrations of X lower the recoverable strain. A recoverable strain of 4% is obtained for an alloy with 37at.% Pd, attained by stress induced transformation (torsion, 200 MPa) and recovery by heating. Lindquist [28] investigated the shape recovery in Ti50Ni50-xPtx and Ti50Ni50-xPdx alloys. The recoverable strain varied with the amount of pre-deformation and composition. A maximum recovered strain of 2.5% after tensile loading up to 6% was reported for an alloy with 10at.% of Pd. Increase of x to 45 at.%Pd resulted in 100% recovery of only 1% strain.

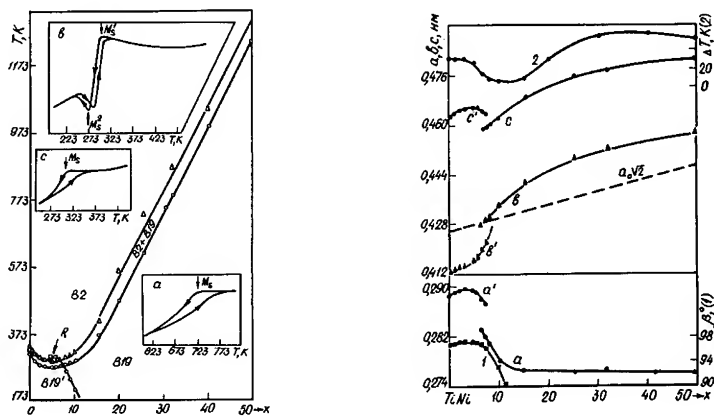


Figure 1 a) TT temperatures vs. composition x of Ti50Ni50-xPtx alloys and the temperature dependencies of resistivity for x=25at%(a), x=7.5at%(b), x=2at%(c).
b) Effect of composition on the lattice parameters. B19 (a, b, c) B19' (a', b', c', β) and hysteresis ΔT(2).

More detailed work is reported recently by Ueno et.al.[29]. Golberg et.al. [30] and Otsuka et.al.[31]. They carried out tensile tests at high temperatures on TiPd and Ti50Ni50-xPdx alloys. Ueno et.al. showed that the absence of shape recovery in a Ti50Pd50 alloy ($M_s=818K$), after deformation at high temperatures, was due to a low critical stress for slip at the test temperatures, although a strain recovery rate of 60% was obtained after deformation at room temperature. Furthermore, a Ti50Pd30Ni20 alloy was extensively characterised ($M_s=418K$). The alloy was plasma melted, hot rolled, cold rolled into 1mm thick sheet with final reductions of 16% and 24%. As is known from Ti-Ni alloys, thermomechanical treatments can improve the stability of the shape memory effect. These authors, therefore, investigated the influence of annealing temperature on shape recovery as well. Tensile tests at different temperatures showed a decreasing yield stress with increasing temperature up to M_s , above which the flow stress increased according to a Clausius-Clapeyron relationship. Recovery rates of 100% were found for

total strains up to 2% and the rates decreased with higher applied strains. A shape memory effect of 4% was obtained after 7% deformation at 443K. Unfortunately the permanent strain is also increased as the total strain exceeds 4%, which will have a negative effect on the cyclic behaviour of the material. The best shape memory characteristics for a Ti50Pd30Ni20 alloy were obtained by cold rolling and annealing at a temperature between the A_s temperature of the as rolled martensite phase and the recrystallization temperature (673-873K), as shown in Figure 2.

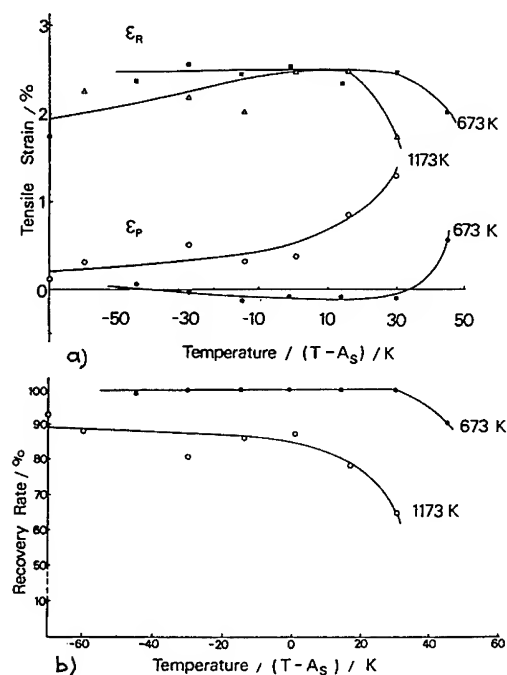


Figure 2 a) Permanent strain (ϵ_p) and recovered strain (ϵ_R) and
b) Recovery rate versus the value $(T-A_s)$ for solution treated Ti50Pd30-Ni20 alloy (1173K, 3.6Ks), T = tensile test temperature.[30]

The shape memory behaviour of the Ti50Ni50-xAux system has been investigated by Wu and Wayman [32,33,34]. A limited recoverable strain of 3% in bending tests in a 40at% Au alloy ($M_s=880K$) was observed. The samples broke after just a few cycles. For compositions with TT between 373-673K no SME was observed. Martensite stabilization was found in these alloys during ageing at 673K, resulting in an increase of A_p of 50K after 750 hrs.

An approach whereby the TT of the Ti50Pd50 are suppressed by the addition third elements as Fe, Cr, V, Mn and Co is followed by Enami et al [35]. Replacing Pd up to 10at% decreases the TT from 800K down to below RT. An accurate control of composition therefore seems to be important in these alloys. The shape memory effect has been

tested by hot compression tests. Up to 2% residual strain after unloading recovered almost completely. Over 2% residual strain could only be recovered partially, when the specimen was overheated more than 200K above Af. This was attributed to the relatively low critical stress for slip in these alloys. Some slip mechanism is associated with the reorientation of the martensite variants during deformation and this caused the retardation of the shape recovery during heating. These results are similar to the conclusions of Otsuka et al [29,31] for the Ti-Ni-Pd system. To increase the critical stress for slip three factors are mentioned:

- 1) solution hardening by the addition of third elements.
- 2) precipitation hardening by ageing treatment.
- 3) strengthening of the parent phase by thermomechanical treatment.

The latter two factors have already been shown to be effective in enhancing shape memory properties of Ti-Ni alloys [36]. An additional factor independent of the above mentioned is grain refinement, which can also be utilized for enhancing the critical stress for slip.

From the Ti-Ni-X(Pt, Pd, Au) systems, the addition on Pd is shown to be most promising; particularly in the composition range around Ti₅₀Ni₂₀Pd₃₀. Recoverable strains of 2% have been obtained. The alloys are stable against overheating. Improvement of the critical stress for slip needs more attention. If the processing can be optimized these alloys are very good candidates for high temperature shape memory application, despite the high price of Pd.

Limited amount of detailed information is available on the fabrication of high temperature SMA's. Processing of the alloy compositions under consideration in this section was not successful in the past. Eckelmeyer [37] reported that (Ni,Pd)-Ti alloys broke up during swaging. Cracking problems were described in alloys with about 25at.% Pd in the process of wire drawing. Tuominen and Biermann [38] used the addition of minor amounts of boron to Ti-Ni-Pd(20-35at.%) alloys in order to increase the tensile ductility and formability. They added up to 6000 atomic ppm B. The tensile fracture strain reached a maximum of 8% at a B-content of 2000 atomic ppm B. Wu [39] reported on the Rapid Solidification (R.S.) of Ti-Ni-Pd alloys that both the R.S. ribbons as well as the cast materials (with 18-22at.% Pd) were very brittle. The TT increased by R.S. The as cast material contained more second phases and showed a larger grain size. Most recently Otsuka et al [29,31] obtained good results by plasma melting and casting in a Cu-mould. After homogenization and hot rolling the plates could be cold rolled with reductions up to 25%, although no information was given concerning the hot ductility of the alloy. Second phase particles (Ti₂Ni and TiPd₂) have been reported in some cases [40]. Yi et al [41,42] produced Ti-Ni-Pd alloys by combustion synthesis (based on the large negative heat of formation of the reaction product TiPd). The ternary alloys were difficult to hot roll due to the low hot ductility of this system, as also noticed by Tuominen et al [38]. The alloy composition was difficult to control using this process.

From these data it seems that presently conventional casting and hot deformation is the best fabrication method. The problems encountered in these alloys seem to be similar to the processing problems met in the binary Ti-Ni system in the early 70's.

TI-NI-X ALLOYS (X= Zr,Hf)

As in the Ti-Ni-X(Pt, Pd, Au) the TT of Ti-Ni alloys can be raised by alloying with Zr or Hf. Replacing Ti by Zr or Hf up to 8 at% results in a decrease of Ms

followed by an increase up to 560K for 20at.% Zr. The Ni-Ti-Zr phase diagram on the Ni-poor side has been determined by Eremenko et.al.[43]. Mulder et.al.[44,45] determined the transformation temperatures of Ti-Ni-Zr alloys with 0-20at.% Zr. Above 10at.% Zr an increase of TT of 18K/at% Zr is observed. He noted that the Ni content should be controlled within a narrow range around 49.5at.%. The Ti-Ni-(Zr,Hf) alloys undergo a martensitic transformation from B2 - B19; the lattice parameters a, c and the monoclinic angle of the martensite continuously increase, whereas b slightly decreases with increasing Zr or Hf content [10,49]. However, Wu et al [46] noted that orthorhombic B19 martensite is present above 15at.% Hf. The present authors found, that in Ti-Ni-Zr alloys the lattice invariant shear is (001)M compound twinning. Xiaodong et al [60] reported (001)M type I twinning in Ti-Ni-Hf, but more information is needed on the crystallography of the martensite transformation in these alloys. A 50-60K hysteresis is observed in Ti-Ni-Zr alloys which is attributed to a positive volume change of about 1%.

Thermal cycling, as well as ageing in the austenitic condition at 623K of a Ti31.5Ni48.5Zr20 alloy resulted in a decrease of TT. No martensite stabilization was observed [44]. In order to make processing possible, the ductility of the alloys has to be improved. The oxygen pick-up during casting and heat treatments has to be avoided. It was shown that in a Ti35.5Ni49.5Zr15 alloy 2% shape recovery can be obtained by heating above Af stress inducing martensite at 463K and 500 MPa compressive stress and cooling to room temperature. A small two way effect is also recorded [45] as shown in Figure 3.

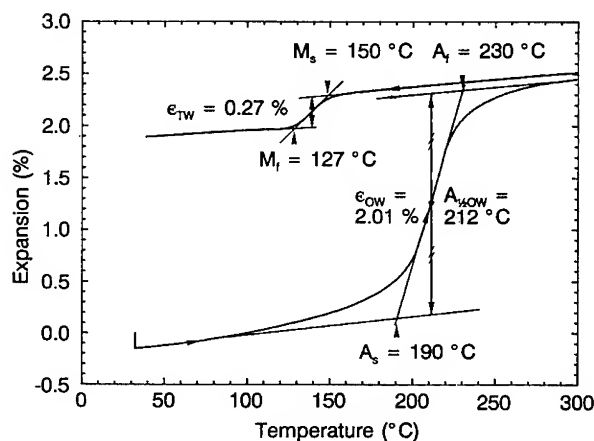


Figure 3: Shape recovery of Ni49.5TiZr15, 1153K/100 hr/WQ + 1153K/1 hr/HeQ, after stress inducing martensite by 500MPa compressive stress, resulting in 2.62% induced strain.

Ti-Ni-Hf alloys [18] could be hot rolled at 1173K with 10% reduction in area per pass. After cold rolling 25% and annealing at 848K/1h. Tensile stress-strain curves of martensite (at 348K) and austenite (at 480K) were measured. For the martensite a fracture strain at a tensile stress of 600MPa was found, whereas for austenite 6% strain at 980MPa was reported. Wu et al [46] characterized the SME by bending. A Ti33Ni47-Hf20 alloy with $A_s = 480\text{K}$ showed a 100% recovery rate up to 2.5% induced strain.

Deformation at 433K resulted in a considerable lower (50%) recovery rate. The amount of second phase increased with increasing Hf content, which was the primary reason for the deterioration of the SME and the ductility. Zhu et al [47] compared the high temperature stability of Ti-Ni-Pd and Ti-Ni-Hf alloys. They observed a higher stability of the TT after annealing at 773K at different times for the Ti-Ni-Pd alloys. The Ti-Ni-Hf alloys showed a decrease at short annealing times due to a precipitation reaction whereafter the TT stabilized. Tuominen [48] characterized the SME under tensile stress of a 0.55 mm thick Ti₄₁Ni₄₉Hf₁₀ alloy. Hot rolling at 1173K and 20% reduction resulted in edge cracking. Further hot rolling at 1023K and final cold rolling of 13% resulted in a 0.55mm sheet. The fraction of recovered strain upon heating to A_f was similar to that observed in Ti-Ni-Pd alloys [28]. A maximum of 2.1% under 276MPa stress however is less than half of the total strain observed in Ti-Ni-Cu alloys (5% at only 50MPa stress).

Russel and Sczerzenie [50] presented results on the workability of electron beam melted Ti-Ni-Hf alloys in comparison with that of Ti-Ni. Increasing Hf contents results in a strong limitation of the temperature range for deformation to 1073-1123K. They also made a comparison of the fabrication costs of various potential high temperature SMA's which is one of the important issues on the way to commercialization. The Ti-Ni-(Zr,Hf) alloys are therefore good candidates as shown in Figure 4, taken from this paper.

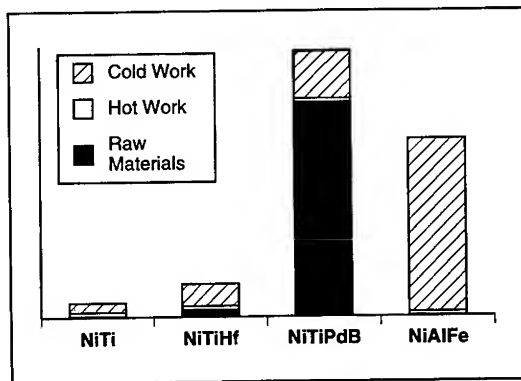


Figure 4 Cost estimates for producing cold drawn wires from TiNi, TiNiHf, TiNiPdB and NiAlFe shape memory alloys.

These results show a considerable advance in the development of both the Ni-Ti-Pd and Ti-Ni-(Zr,Hf) alloys for high temperature applications. However more detailed information is needed on the optimization of the fabrication process. Particularly the strong affinity of Ti, Zr and Hf for oxygen can result in deterioration of SME properties. In view of the improvements to be expected in fabrication of the alloys, by optimization of the thermo-mechanical processing, developments towards a useful alloy might be foreseen, particularly when the high temperature stability is under control. Complete recovery of 2% strain in cyclic applications seems to be feasible and is worth pursuing further. The shape strains are then close to those used for conventional Ti-Ni SMA's.

Ni-Al Alloys

The AlNi β phase alloys with excess Ni contents of 62-67at.% show a thermo-elastic martensite transformation from B2 to a L10 martensite (3R). The TT are strongly composition dependent. Ms temperatures up to 700K (66at.% Ni) have been reported [51]. It is now clear that several irreversible phase transformations can occur on heating the martensite. The 3R or 7M martensite can transform to Ni₅Al₃ instead of retransforming to B2 and that restricts the use of Ni-Al alloys to below the Ni₅Al₃ TT (523K) [10,52,59]. Extensive reviews of the different phase transitions which can occur in binary Ni-Al alloys have been given recently by George et al [53] and Khadkikar et al [54]. Additional to Ni₅Al₃, Ni₂Al, an omega-like phase and two types of martensite (bct and bco) have been reported. The omega-like phase is interpreted as a precursor for the Ni₅Al₃ and Ni₂Al phases.

The Ni₅Al₃ can easily form from the martensite before reversion to B2 and thereby destroying the reversibility of the martensite. The reversible martensitic transformation would be resumed by up-quenching to 573-673K just after quenching from homogenizing temperatures [52,55,56] of binary as well as ternary systems [59]. The precise transformation requirements for the Ni₅Al₃ to form are still not clear. It has been shown that the Ni₅Al₃ formation can also be suppressed by grain refinement using mechanical milling and sintering or HIP-ing technology. The fine grain size (< 5 micrometer) and the refinement of the martensite structure (high density of {111}-twins) are thought to be the cause of the change in kinetics of the Ni₅Al₃ phase formation. The presence of fine oxides after milling and sintering will also influence the phase transformation kinetics but also the deformability of the material. The microstructures obtained are shown in figure 5. [57,58].

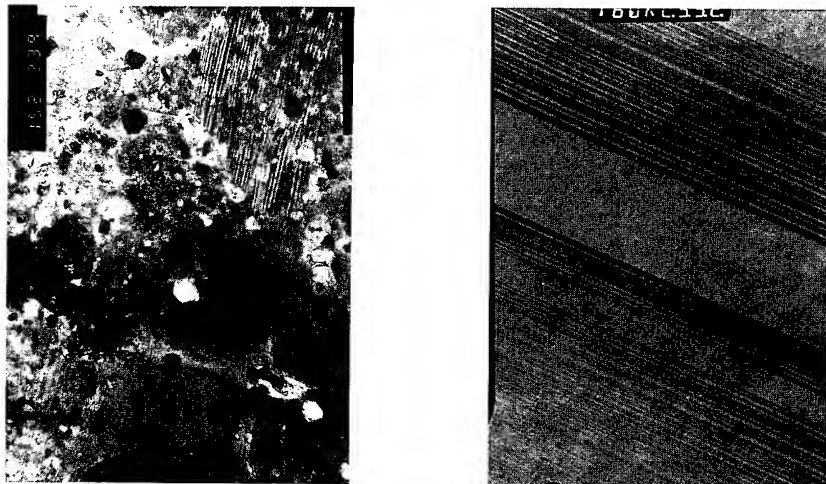


Figure 5 Micro structure of Ni₆₅Al, ball-milled and HIP-ed at 1473K

The inherent brittle behavior of NiAl can be improved by the addition of a third element. The addition of Fe and Mn to binary Ni-Al [23,22] results in a formation of a ductile fcc phase in an extremely brittle B2 matrix. The ternary phase equilibria [23], as

shown in Figure 6 for Fe and Mn additions, show how alloy developments are started. A Ni-19Al-12Mn-9Fe alloy was developed, having TT around 473K, independent of annealing temperature. Hot deformability was reported successful on rolling.

Cyclic experiments have been reported for the first time by Horton et al [22] in a Ni-25.5Al-16Fe-0.14B alloy where B was added to improve grain boundary cohesions. An optimum tensile recovery strain of 0.6% was observed after 1-2 % prestrain obtained by 115 MPa stress. Cycling 2000 times decreased the recovery to zero. Restraining restored the recovery partially. Longer annealing times at 773K resulted in loss of ductility and SME due to the formation of Ni₅Al₃. The transformation temperatures of Ni-Al-X alloys vary from 173-973K. Although not complete, these alloys have shown shape memory and seem very attractive as an alloy operating at high temperatures. Addition of Fe improves ductility, but lowers the TT, which can be compensated by lowering the Al content (by $A_{eq.} = Al + \frac{1}{2}Fe$) [53] or by the addition of Mn. The prospects for Ni-Al alloys for high temperature applications are not as good yet, as for the Ti-Ni-X based systems, although considerable progress has been made. The transformation kinetics must be clarified and the ductility needs improvement. Processing can then better be adopted to the material characteristics.

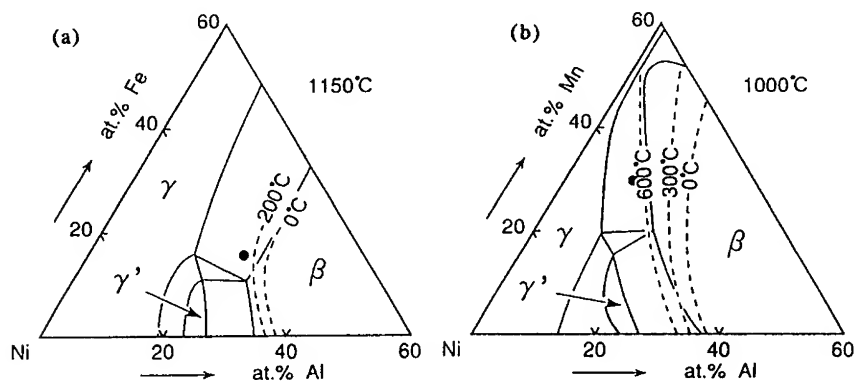


Figure 6 Phase equilibria and Ms temperatures of the β phase in a) Ni-Al-Fe and b) Ni-Al-Mn systems. Filled arcs indicate compositions of ternary specimens.

CONCLUDING REMARKS

The development of high temperature shape memory alloys showed considerable progress in recent years. The SME of Ti-Ni-Pd and of Ti-Ni-(Zr,Hf) alloys are in a range which are useful for practical applications. The mechanical stability of all alloys must be demonstrated through thermal cycling testing. Improvement of the phase stability of particularly Ni-Al alloys is crucial for their use as high temperature shape memory material. The processing needs optimization and the characterization and improvement

of the cyclic behaviour at those high temperatures need attentions in the near future.

Other type of alloys showing a thermoelastic transformation up to 473K as Ni-Mn or Mn-Cu alloys are not characterized well yet in order to be considered as feasible SMA's.

ACKNOWLEDGEMENTS

We wish to thank Joanna Wolska for providing us the transmission electron micrographs obtained as a part of her Ph.D. research work on NiAl.

REFERENCES

1. J. Van Humbeeck, in: Shape Memory Materials and Phenomena, ed. by C.T. Liu, H. Kunsmann, K. Otsuka, M. Wuttig (Mater. Res. Soc. Proc. **246**, Pittsburgh, PA, 1992), pp.377-387.
2. Y. Oshida, R. Sachadeva, S. Miyazaki and S. Fukuyo, Mat. Science Forum vol **56-58**, 705 (1990).
3. J. Beyer, M. Sanders and A.G. Veldhuizen, IUMRS-ICAM'93 (Tokyo, 1993, unpublished).
4. G.A. Rogers, Smart Materials, Structures and Mathematical issues. Technomic. publ. co. (1989).
5. R.E. Newham and G.R. Ruschau, J.Am.Ceram.Soc. **74**,466-480 (1991)
6. J. Beyer and M. Chandrasekaran, 75th AGARD Structures and Materials Panel Meeting Lindau, Germany, pp.13.1-13.7 (1992)
7. Conference on Structural Control, Los Angeles 1994.
8. M. Funakubo, Shape Memory Alloys, Gordon and Breach Science Publ, (1987)
9. S. Miyazaki and K. Otsuka, ISIJ International **29**,353 (1989)
10. J. Beyer and J.H. Mulder, IUMRS-ICAM'93 Tokyo 1993 Symp.Proc.(unpublished)
11. M.H. Wu, Engineering Aspects of Shape Memory Alloys, Rd. T.W. Duerig et al (Butterworth-Heinemann, 1990) pp.69-88.
12. I. Hurtado, J. v.Humbeeck and L. Deleay, J.d.Phys. C4 **247** (1991)
13. H.C. Donkersloot and J.H.N. Van Vucht, J.of Less Com. Met. **20**, 83 (1970)
14. D.B. Chernov.-Technical Physics **28**, 351, 1983.
15. S.A. Shabalovskaya, Solid State Communications **66**, 137 (1988)
16. V.I. Kolomytsev, SMM'94 Beijing, China 1994 Symp.Proc. p.136-143
17. Krupp, GmbH, Patent no. DE4006076 (1990)
18. Johnson Service Company, Patent no. US 5,114,504 (1992)
19. K. Au and C.M. Wayman, Scripta Met **6**, 1209 (1972)
20. F. Reynaud, J. Cryst. **9**, 263 (1976)
21. K. Enami and S. Nenno, Trans JIM **19**, 571 (1978)
22. J.A. Horton, C.T. Liu and E.P. George, Mat.Science Eng. (unpublished)
23. R. Kainuma, H. Nakano, K. Oikawa, K. Ishida and T. Nishizawa in Shape memory materials and Phenomena, ed. by C.T. Liu, H. Kunsmann, K. Otsuka M. Wuttig (Mater. Res. Soc. Proc. **246**, Pittsburgh, PA 1992), pp.403-409
24. J.H. Yang and C.M. Wayman, Mat. Sci. Eng. **A160**, 241 (1993).
25. V.N. Kachin, N.A. Matreeva, V.P. Silvokka and D.V. Chernov., Dokl. Acad. Nauk. SSSR **257**, 167 (1981)

26. V.N. Kachin, V.G. Rustin, V.P. Silvokka, V.V. Kodratyev, S.A. Muslov, V.P. Voronin, Yu.S. Zolothukhin and L.I. Yurchenko, *Phys. Met. Metall.* **67**, 125 (1989)
27. V.N. Kachin, *Revue Phys. Appl.* **24**, 733 (1989)
28. P.G. Lindquist and C.M. Wayman, *Eng. Aspects of Shape Memory Alloys*, ed. T.W. Duerig et al (Butterworth Heinemann 1990) pp.58-68
29. Y. Ueno, M. Piao, K. Oda and K. Otsuka, *Proc. 3rd. Japan Int. SAMPE* (1993) p. 1274-1279
30. D. Golberg, Y. Xu, Y. Murakami, S. Morito and K. Otsuka, *Scripta Metall et Mater* **30**, 1349 (1994)
31. K. Otsuka, K. Oda, Y. Ueno and M. Piao, *Scripta Metall et. Mater* **29**, 1355 (1993)
32. S.K. Wu and C.M. Wayman, *Shape memory materials*, ed. by M. Doyama, S. Somiya, R.P.H. Chang, (*Mater. Res. Soc. Proc.* **9**, Pittsburgh, P.A. 1988) pp. 141-145.
33. S.K. Wu and C.M. Wayman, *Scripta Met.* **21**, 83 (1987)
34. S.K. Wu and Y.C. Lo, *Mat. Science Forum* **56-58**, 619 (1990).
35. K. Enami, Y. Miyasaka and H. Takakura, *MRS Symp. Proc.* **9**, 135-140 (1989)
36. P.E. Thoma, A.M. Blok and M.Y. Kao, *Actuator'92 Proc.*, Bremen Germany, 1992, p.220-224
37. K.M. Eckelmeyer, *Scripta Met.* **10**, 667 (1976)
38. S.M. Tuominen and R.J. Biermann, *J. Metals* **40**, 32 (1988)
39. K.H. Wu, *MRS Symp. Proc.* vol. **246**, 361-366 (1992)
40. D.S. Qiang, Q.G. Ying, Y.H. Bo and T. ShiMing, in *Shape Memory Materials (SMM '94)* ed. by C. Youy and T. Mailing, *Int. Acad. Publ.* 1994, pp. 248-252.
41. H.C. Yi and J.J. Moore, *Mater. Sci. Forum* vol.**56-58**, 735 (1990)
42. H.C. Yi, J.J. Moore and A. Pebric, *Metall. Trans.* **A23**, 59 (1992)
43. V.N. Eremenko, E.L. Semenova and L.A. Tret'yachenko, *Poros Metall.* **8**, 49 (1991)
44. J.H. Mulder, J.H. Maas and J.Beyer, *Proc. ICOMAT'92*, ed. C.M. Wayman and J.Perkins, Monterey Inst. of Advanced Studies 1993 p.869-875
45. J.H. Mulder, J. Beyer, P. Donner and J. Peterseim, *SMST Conf. Pacific Grove*, 1994 (unpublished)
46. K.H. Wu, Z.Pu, H.K. Tseng and F.S. Biancaniello, *SMST Conf. Proc.*, *ibid*, (unpublished)
47. Y.R. Zhu, Z.J. Pu, C. Li and K.H. Wu, *Shape Memory Materials (SSM'94)* ed. C.Youyi and T. Hailing, *Int. Acad. Publ.* pp.263-268 (1994)
48. S.M. Tuominen, *SMST Conf. Pacific Grove*, 1994 (unpublished)
49. L.L. Meisner, V.N. Grishkov, in *Shape Memory Materials (SMM '94)* ed. by C. Youyi, T. Hailing, *Int. Acad. Publ.* 1994, pp. 263-268.
50. S.M. Russell and F. Scerzenie, *SMST Conf. Pacific Grove*, 1994 (unpublished)
51. J.L. Smialek and R.F. Hehemann, *Metall. Trans.* **4**, 1571 (1973)
52. J.H. Yang and C.M. Wayman, *Materials Letters* **16**, 254 (1993)
53. E.P. George, C.T. Liu, J.A. Horton, C.J. Sparks, M. Kao, H. Kunsmann and T. King, *Materials Characterization* **32**, 139 (1994)
54. P.S. Khadkikar, I.E. Locci, K. Vedula and G.M. Michal, *Metal Trans* **24A**, 83 (1993).
55. A. Elstrodt, M.Sc. Thesis University of Twente (1994)
56. J.H. Yang and C.M. Wayman, *Mat.Science Eng.* **A160**, 241 (1993)

57. J. Wolska, J.H. Maas, M. Chandrasekaran and J. Beyer, *Scripta Metall. et Mater.* **31**, 303 (1994)
58. J. Wolska and J.H. Maas, ISMANAM-94, Symposium Grenoble, 1994 (unpublished)
59. Y.D. Kim and C.M. Wayman, *Met. Trans.*, **23A** 2981 (1992).
60. H. Xiaodong, Z. Zhifang, L. Tongchun, L. Juntong, Y. Dazhi in *Shape memory Materials*, ed. by Chu Youyi and T. Mailing, Int. Acad. Publ. 1994, pp. 258-262.

ENGINEERING CONSIDERATIONS IN THE APPLICATION OF NiTiHf AND NiAl AS PRACTICAL HIGH-TEMPERATURE SHAPE MEMORY ALLOYS

SCOTT M. RUSSELL AND FRANK SCZERZENIE

Special Metals Corporation, 4317 Middle Settlement Road, New Hartford, NY 13413

ABSTRACT

NiTiHf and NiAl have shown the potential for development as high temperature shape memory alloys with transformation temperatures of 150°C or higher. However, various engineering considerations must be addressed before these systems can be used as practical high temperature shape memory alloys. These considerations include: fabricability, phase stability, mechanical stability, and cost. NiTiHf is attractive from a cost standpoint, although its fabricability must still be demonstrated on larger heats of material. The phase stability and mechanical stability of NiTiHf are unknown. NiAl requires great improvements in both fabricability and phase stability. The mechanical stability and costs for producing NiAl shape memory alloys are still unclear.

INTRODUCTION

Two frequently cited limitations to overcome if shape memory technology is to become a major factor in industrial product design are the alloys' maximum transformation temperatures and the maximum useful service temperatures. Many applications require a shape memory transformation temperature between 150 and 400°C with structural stability when heated for long periods up to 600°C. A number of alloy systems have exhibited transformation temperatures at or above 150°C, showing promise as high temperature shape memory alloys. These include alloys of the NiTiPd, NiTiPt, NiTiAu, NiTiHf, NiTiZr, CuAlNi, NiAl, and Fe-base systems. Unfortunately, only limited data exist for each of the above systems; the data which do exist are primarily phenomenological, addressing only transformation temperature characteristics and phase structures.

Of particular interest are the NiTiHf and NiAl systems due to their low cost and high transformation temperature potential. Many useful properties of the NiTiHf system are described by AbuJdom, et al in U.S. Patent No. 5,114,504¹. Transformation temperatures as high as 622°C (A_p) were recorded and a procedure for forming articles from the various alloys was also described. The main barrier to the application of NiTiHf as a commercial high temperature shape memory alloy appears to be a lack of engineering data rather than a prohibitive alloy deficiency.

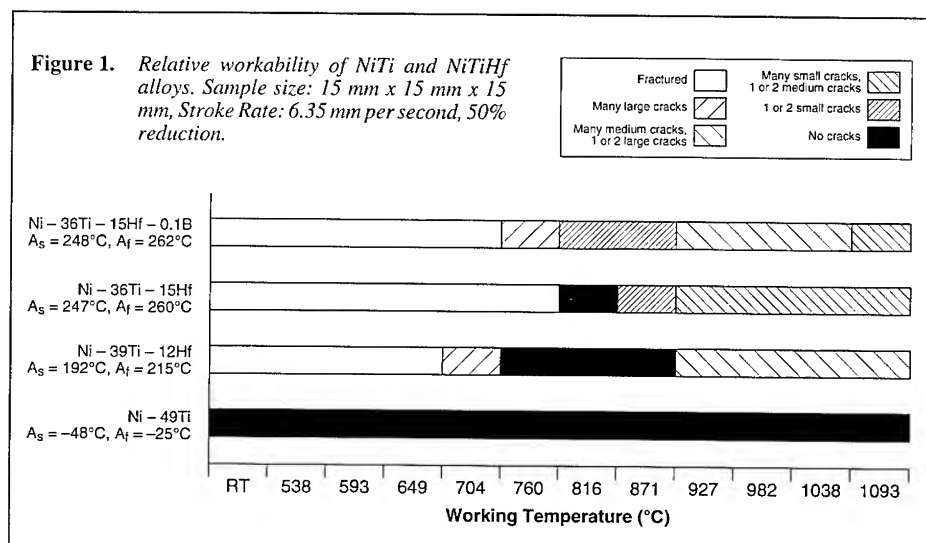
NiAl alloys have high thermal conductivity, good high temperature strength, and excellent oxidation and corrosion resistance. Further, the shape memory effect has been demonstrated at ambient temperature in binary NiAl alloys with nickel contents from 63–64%². Also, it has been determined that by increasing the nickel content sufficiently (to about 68%), transformation temperatures as high as 700°C have been reported^{3,4}. The main limitations to the application of NiAl as a high temperature shape memory alloy are its poor fabricability and insufficient phase stability.

In order to be applied as practical high temperature shape memory alloys, additional engineering data must be generated for both NiTiHf and NiAl, and alloy improvements must be made. Some of these important engineering considerations are: fabricability, phase stability, mechanical stability, and cost. Each of these issues will be addressed for the NiTiHf and NiAl systems with an emphasis on developing an alloy with a transformation temperature of 150°C or higher and mechanical stability and phase stability up to 600°C.

FABRICABILITY

Although the hot and cold workability of NiTiHf was demonstrated on a 20 gram ingot by AbuJdom, et al¹, it is necessary to determine whether or not these important laboratory results

can be scaled up to practical, industrial heat sizes. To determine the workability of larger ingots, a series of heats was produced of the following compositions: Ni – 49.12 % Ti, Ni – 39 % Ti – 12 % Hf, Ni – 36 % Ti – 15 % Hf, and Ni – 36 % Ti – 15 % Hf – 0.1 % B. Each alloy was produced in the form of a triple electron beam melted 900 gm drop cast ingot, approximately 100 mm x 25 mm x 40 mm. Differential Scanning Calorimetry (DSC) of a fully annealed sample from each casting was used to determine austenite start (A_s) temperatures of –48°C, 192°C, 247°C, and 248°C for the binary, 12 Hf, 15 Hf, and 15 Hf + B alloys, respectively. Samples approximately 15 mm x 15 mm x 15 mm were cut from the ingots and workability trials were conducted on each of the alloys from ambient temperature to 1093°C. A stroke rate of 6.35 mm per second was used and each sample was compressed to either failure, a maximum load of 22,680 kg, or a maximum of 50% reduction. The results are shown in Figure 1.



The results of the workability tests confirm that increasing Hf content has a negative effect on the workability. Further, B additions, which have been shown to improve the workability of NiTiPd alloys⁵, appear to have little (if any) effect on NiTiHf workability. These trials also confirmed the work of AbuJdom, et al¹, indicating that a suitable hot working temperature for these alloys is between 800 and 900°C. Based on these results, a 20 mm thick section from the bottom of the Ni – 36 % Ti – 15 % Hf ingot was canned in mild steel and hot rolled at 850°C to a final thickness of 2.7 mm with 1.3 mm reduction per pass and anneals between every pass (see Figure 2). Additional sections were taken from farther up on the same ingot and were rolled using the same parameters. Unfortunately, the additional sections fractured readily.

The cause of the poor fabricability of these sections is possibly related to both grain structure and intergranular precipitates. First, the section which was successfully rolled was taken from the bottom of the ingot (close to the chill) where the grains are expected to be finer. The other sections were taken from near the top of the ingot where the grains are coarser. Apparently a fine grain structure may be necessary for good fabricability. Second, metallography of the Ni – 36 % Ti – 15 % Hf casting revealed intergranular precipitates (see Figure 3). Scanning electron microscopy indicated that these precipitates are probably $(Ti+Hf)_2Ni$. In another study, Tuominen⁶ reported the presence of intergranular oxides of the form $(Ti+Hf)_xNi_2O_x$. However, no oxygen was detected in the intergranular precipitates in the current study. Future work to improve the fabricability of NiTiHf alloys will continue, focusing on optimizing the cast grain structure with larger, commercial grade ingots.

In the NiAl system, a considerable amount of work has been done in an attempt to improve the ductility and fabricability. Much of the work was aimed at developing an advanced structural material for gas turbine engines. Some improvements in the ductility of β phase NiAl have been realized from a wide variety of approaches: microalloying with Mo, Fe and Ga^{7,8}, macroalloying with Fe and Co^{4,9,10}, grain refinement¹¹, and precise control of binary alloy stoichiometry¹², among others. The highest tensile ductility which has been achieved in polycrystalline alloys is about 2.5%¹², while strains as high as 6% have been realized in $\langle 110 \rangle$ -oriented single crystals of NiAl with small additions of Fe⁸.



Figure 2. Hot rolled sections of NiTi-15Hf drop cast ingot rolled at 850°C with 1.3 mm reduction per pass. The bottom photo shows a roll-down of the bottom, finer grained portion of the casting, while the top photo is from near the top of the casting.

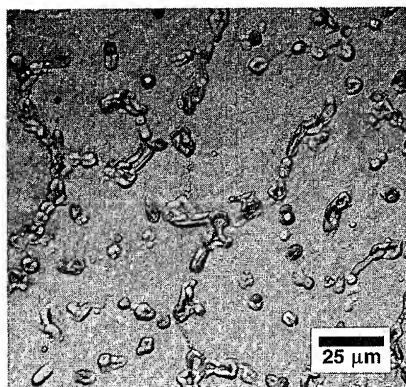


Figure 3. Microstructure of NiTi-15Hf drop cast ingot, showing grain boundary precipitates, which were determined to be of the form $(\text{Ti}+\text{Hf})_2\text{Ni}$.

However, additional ductility improvements still must be made. Further, the effect of these ductility improvements on the shape memory properties are as yet unknown and must be determined before NiAl alloys can be processed via conventional manufacturing methods for shape memory alloys.

PHASE STABILITY

As far as it is known to the authors, a review of the phase structures and their stabilities in NiTiHf has not yet been published. Binary NiTi begins to experience phase stability problems at 250–300°C¹³. It is unknown whether the same limitation applies to alloys of the NiTiHf system. Future work must be done to study the effects of long term high temperature exposure and thermal cycling on the transformation characteristics and shape memory properties of these alloys.

As previously mentioned, the shape memory effect has been observed in binary NiAl alloys with nickel contents from 63–68 at.-%^{2,3,4}. However, a careful study of the NiAl phase diagram reveals that the phase boundary between the NiAl and NiAl + Ni₃Al regions occurs at about 58 at.-% Ni (see Figure 4), i.e., all NiAl shape memory alloys are metastable. Further, an undesirable phase, Ni₅Al₃, can nucleate when NiAl alloys with 58–73 at.-% Ni are held for a length of time below 700°C¹⁵. Both of these issues cast doubt on the stability of NiAl shape memory alloys during

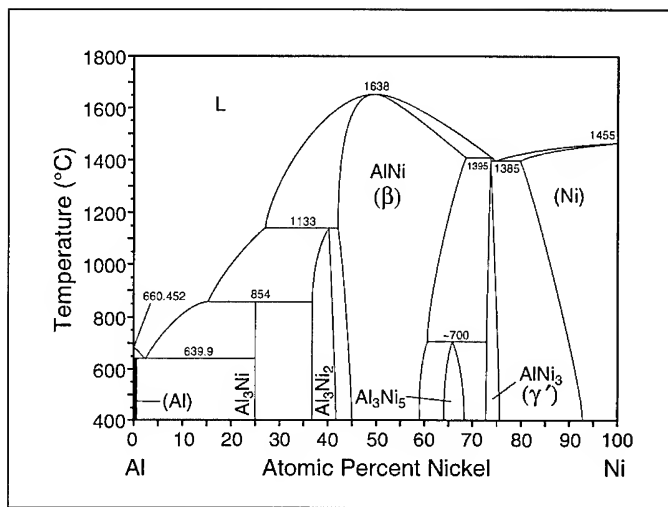


Figure 4. NiAl Phase Diagram after Nash, et al.¹⁴

rules, and solubility. Using these criteria, a number of alloys were selected with the goal of stabilizing the martensitic phase in NiAl. Additions of Sc, Ag, Mg, Cu, Zn, Ti, V, and Zr all were explored unsuccessfully¹⁶ in this program. It is possible that different alloying additions and/or approaches may prove more successful.

In spite of its apparent lack of high temperature phase stability, the excellent oxidation resistance of NiAl may make it a suitable candidate for a one-time use shape memory device, e.g., a connector, which, once assembled, no longer requires shape memory characteristics. An example of such an application may be a connector in the hot zone of a gas turbine engine which utilizes the shape memory effect for ease of assembly. While in service, the phase structure of the alloy can reach equilibrium without adversely affecting the integrity of the coupling. Therefore, while the martensitic phase stability of NiAl needs improvement, it does not altogether prevent the application of NiAl high temperature shape memory alloys.

MECHANICAL STABILITY

The mechanical stability is also an important consideration in the development of a practical high temperature shape memory alloy. Of particular interest are stress relaxation characteristics, i.e., the effects of long-term high temperature exposure on the recovery stress of the alloy. This is especially important for actuator design. For example, possible uses for a high temperature shape memory alloy include high power electrical circuit breakers and nuclear power plant safety devices. Although the total number of cycles required of such actuators may be small, the actuators may require the shape memory element to resist a bias force over a long period of time at a temperature just below its transformation temperature. In such a situation, if the stress relaxation characteristics of the alloy are poor, over time the stress exerted by the shape memory element against the bias force will decrease until the actuator is no longer effective. Similarly, for higher cycle devices, such as aircraft controls and vibration controls, the mechanical cyclic stability may be a limiting factor.

While both the cyclic stability and stress relaxation characteristics are unknown for both NiTiHf and NiAl shape memory alloys, creep strength can be used as an estimate of an alloy's potential stress relaxation limitations. A large amount of NiAl creep data has been generated in

processing as well as in service, especially as a high temperature shape memory alloy actuator.

To address these issues, a program was begun to find alloying additions which raise the transformation temperatures and therefore stabilize the martensitic phase at higher aluminum contents¹⁶. Lacking accurate ternary NiAl-X phase diagrams for guidance, the selection of potential alloying additions was based upon the well-known Pettifor structure maps¹⁷, the formation of B2 intermetallic compounds with Ni, Hume-Rothery

other studies^{4,6,18}. Typically the creep strength of NiAl alloys is considered to be good at 600°C. and above¹⁸. Additions of B, Hf, Ta, and Nb all have been shown to improve the creep strength of NiAl^{4,19}. However, the effects of these alloying additions on the shape memory characteristics are currently unknown. More data must be generated and alloy improvements may be required for alloys of both the NiTiHf and NiAl systems to be used for the sort of applications described above.

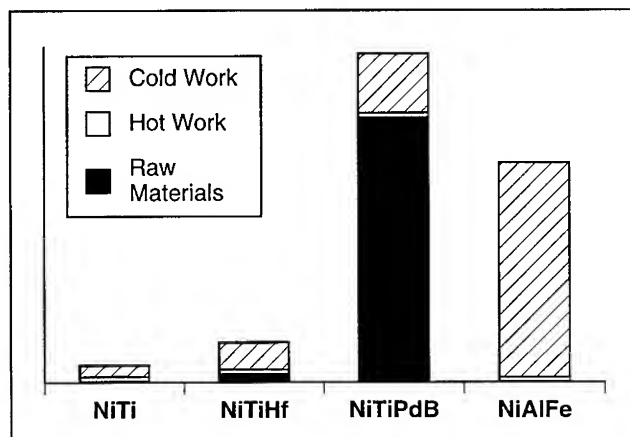


Figure 5. Cost estimates for producing cold drawn wires from NiTi, NiTiHf, NiTiPdBi, and NiAlFe shape memory alloys using conventional processing methods.

COST

One of the features of both NiTiHf and NiAl which makes them attractive as high temperature shape memory alloys is their relatively low cost. Contributing to the low cost potential of NiTiHf alloys is their moderate raw material cost, as well as the promise for both hot and cold workability. With NiAl, the raw material costs are low, but the processing costs are estimated to be very high due to its poor fabricability. A comparison of the estimated costs for producing cold drawn wires of NiTi, NiTiHf, NiTiPdBi, and NiAlFe are shown in Figure 5 and Table I. These rough estimates are based on a typical NiTi processing scheme from ingot to wire. Maximum cold work per pass limitations of 35%, 15%, 7%, and 2% were used for NiTi, NiTiHf, NiTiPdBi, and NiAlFe, respectively. These limitations are based on our own experience as well as empirical data from the literature^{1,5}. These cost estimates are thought to reflect minimum costs and assume that conventional processing methods can be applied. The actual costs may be even higher for NiTiHf, NiTiPdBi, and NiAlFe, especially if expensive alloying additions and/or special processing methods are required for acceptable fabricability. Of particular note is the NiTiHf system which, while more expensive than NiTi, does not appear to be prohibitively expensive, especially when compared with NiTiPdBi alloys.

Table I. Cost Comparison between NiTi, NiTiHf, NiTiPdBi, and NiAl

	NiTi	NiTiHf	NiTiPdBi	NiAlFe
Raw Materials:	1	6.0	190.0	0.5
Hot Rolled Bar:	1	2.2	44.5	0.9
Cold Drawn Wire:	1	2.3	18.7	12.5

CONCLUSIONS/FUTURE WORK

Both NiTiHf and NiAl alloys have shown potential for development as high temperature shape memory alloys. However, both systems still require further experimentation and development. In summary, the challenges that remain for these systems are:

- The fabricability of NiTiHf alloys must still be demonstrated on larger ingots. Preliminary results on small samples have shown promise for sufficient fabricability.
- The fabricability of NiAl is poor (<2.5% tensile ductility) and must be greatly improved.
- The phase stability of NiTiHf at higher temperatures is unknown and must be demonstrated.
- Improvements in the phase stability of NiAl are the key to its use as a high temperature shape memory alloy. The use of Pettifor Structure Maps as a guide for alloying additions to address this deficiency has proven to be unsuccessful.
- The mechanical stability of both NiTiHf and NiAl at higher temperatures must be demonstrated via cyclic testing and stress relaxation experiments.
- NiTiHf appears to have great potential to be a low cost, practical high temperature shape memory alloy.

REFERENCES

1. D. N. AbuJdom II, P. E. Thoma, M-Y Kao, and D. R. Angst, United States Patent Number 5,114,504 (1992).
2. K. Enami and S. Nenno, *Met. Trans.*, **2**, 1487 (1971).
3. J. L. Smialek and R. F. Heheman, *Met. Trans.*, **4**, 1571 (1973).
4. S. M. Russell, C. C. Law, M. J. Blackburn, P. C. Clapp, and D. M. Pease, "Lightweight Disk Alloy Development," Air Force Report WRDC-TR-90-4125 (1991).
5. S. M. Tuominen and J. Biermann, United States Patent Number 4,865,663 (1989).
6. S. M. Tuominen, in the Proceedings of the SMST Conference, Pacific Grove, CA, March 1994, to be published.
7. D. B. Miracle, *Acta Metall. Mater.*, **41**, 649 (1993).
8. R. Darolia, *J. Metals*, **43**, 44 (1991).
9. C. C. Law and M. J. Blackburn, "Rapidly Solidified Lightweight Durable Disk Material," Final Technical Air Force Report, F33615-84-C-5067 (1987).
10. S. Guha, I. Baker, P. R. Munroe, and J. R. Michael, *Mat. Sci. and Eng.*, **A152**, 258 (1992).
11. E. M. Schulson and D. R. Barker, *Scripta Met.*, **17**, 519 (1983).
12. K. Vedula, K. H. Hahn and B. Boulogne, *Mat. Res. Soc. Symp. Proc.*, **133**, 299 (1989).
13. M. H. Wu (private communication).
14. P. Nash, M. F. Singleton and J. L. Murray, in *Phase Diagrams of Binary Nickel Alloys*, edited by P. Nash, Vol. 1 (ASM International, Metals Park, Ohio, 1991).
15. P. S. Khadkikar, I. E. Locci, K. Vedula, and G. M. Michal, *Met. Trans. A*, **24A**, 83 (1993).
16. S. M. Russell, "The Effects of Alloying on the Phase Stability of NiAl," Masters Thesis, University of Connecticut, to be published.
17. D. G. Pettifor, *New Scientist*, 48 (May 29, 1986).
18. P. R. Strutt and B. H. Kear, *Mat. Res. Soc. Symp. Proc.*, **39**, 279 (1985).
19. K. Vedula, V. Pathare, I. Aslanidis, and R. H. Titran, *Mat. Res. Soc. Symp. Proc.*, **39**, 411 (1985).

ACKNOWLEDGMENTS

We wish to thank the following individuals and organizations for their invaluable assistance in this effort: Johnson Controls for providing a license to produce experimental quantities of NiTiHf alloys, Bruce Eckler for providing mechanical testing and DSC services, Prof. Phil Clapp and Dr. Chi Law for advice and direction for the NiAl development effort, Dick Wexler for NiAl alloy melting, and Lloyd Roberts, Bob Congdon, Pete Molesky and Dave Washburn for melting and hot working of NiTiHf alloys.

INFLUENCE OF Mn ADDITIONS ON THE THERMOELASTIC AND PSEUDOELASTIC BEHAVIOUR OF Cu-Al-Ni ALLOYS

M.A.MORRIS and T. LIPE

Institute of Structural Metallurgy, University of Neuchâtel,
Av. Bellevaux, 51, 2000 NE, Switzerland

ABSTRACT

The transformation properties of Cu-Al-Ni alloys modified by the additions of boron and manganese have been interpreted by studying the reversibility and stability of the martensitic transformation as a function of heat treatment and of manganese concentration between 2 and 4 wt%. The alloy containing 2% Mn exhibits a lack of thermoelasticity due to a decrease of the degree of B2 order and suppression of DO₃ order during quenching and the increase of both types of order during annealing. From the determination of the activation energies responsible for the martensitic and reverse transformations, we have deduced that, in both cases, the kinetics of the transformation are controlled by an atomic jump at the interface between the two phases.

INTRODUCTION

Cu-Al-Ni shape memory alloys have been shown to be potential candidates for obtaining transformation temperatures above 120°C, for a wide range of compositions, including additions of other elements [1-4]. On the other hand, compositional changes can modify not only the transformation temperatures but also the ductility [4, 5] and may even result in the loss of thermoelastic properties during thermal ageing [6,7].

For a thermoelastic transformation to occur, both the interface energy and the energy needed for plastic deformation must be so small that they can be neglected [8]. This is possible when during the transformation the structural and volume changes are small and when there is a good coherency between the two phases. Generally these conditions are satisfied if the alloy has perfectly ordered structures [9]. The stability of the thermoelastic transformation during thermal cycling is, then, closely related to the stability of the ordered structure.

The existing models concerning the martensitic transformation generally deal with the mechanism of nucleation of the martensitic phase. The classical theory of nucleation leads to very high values of the free energy of nucleation to be realistic and the assumption of pre-existing nuclei in the austenitic matrix has been considered in order to reduce the free energy of the transformation by reducing it to a growth process [10]. Other theories assume that the martensite forms from dissociated dislocations [11] within the parts of the material which are mechanically unstable or that dislocations help nucleation by relaxing the elastic strain associated with it [12].

The growth (or shrinkage during the reverse transformation) of the martensite is generally considered to take place rapidly, in the same way as shearing does, without the need of a substantial activating energy. However, this is the case of the transformation that proceeds at low temperatures and whose driving force is high. On the other hand, in many alloys the growth of the martensite takes place in two stages: during the first one, a spike-like growth of thin sheets occurs followed by a second stage which is their lateral thickening. These two stages have been observed by TEM during the martensitic transformation of CuZn [13] and CuZnAl [14] alloys. This means that at least two distinct mechanisms operate during growth.

The principles of the phenomenological theories, such as the invariant plane, the relief effect on a polished surface and the crystallographic transformation that are used to characterize a martensitic transformation, do not seem sufficient to distinguish transformations governed by diffusional or by shearing-like mechanisms [15]. If growth is only governed by a diffusional mechanism, then the transformation results in compositional or ordering changes. Many diffusional transformations like growth of needles or plates seem to satisfy the principles of the phenomenological theories of the martensite [16,17]. Although certain features of these transformations may be similar, the mechanisms occurring at atomic level are completely

different: the diffusional growth necessitates atomic diffusion and the shearing-like transformation is based on the cooperative movement of the atoms across the interface realized by the glide of dislocations. These mechanisms describe the two different transformations at high and at low temperatures that require a small and a large driving force respectively.

In the present study we have analysed the role that the transformation mechanisms may play in the lack of thermoelastic properties of one of our alloys with low manganese content as well as in the stability of the transformation in the case of the alloys rich in manganese. Different mechanisms regarding nucleation and growth (or shrinkage) of the martensite have been suggested with respect to the driving forces involved, the kind of interface and the change in the ordered state of the structure during thermal cycling.

EXPERIMENTAL

The alloys used for this study had nominal compositions Cu-12Al-4Ni-0.04B (wt%) with varying manganese concentrations, namely 2% (alloy M14), 3% (alloy M15), 4% (alloy M16). They were prepared by induction melting under helium atmosphere and subsequently heat treated at 820°C for 30 min prior to extrusion. After the extrusion the alloys were given a β -homogenisation heat treatment at 820 for 30 min followed by water quench. Subsequently, the materials were annealed at 300°C for periods of time ranging between 15 min. and 2h. The alloys were studied by thermal cycling between room temperature and 300°C using a Mettler TA 4000 differential scanning calorimeter (DSC) at a heating/cooling rate of 10°C/min. The samples used had a weight of about 60mg. Also thermal analyses were carried out at different heating/cooling rates, ranging between 5 to 25°C/min in order to determine the variation of the transformed fraction of the different phases. In those experiments, the same sample was used for each heating/cooling rate but the full thermal treatment was given in each case before carrying out the experiment in the calorimeter. Microstructural studies were performed by optical and transmission electron microscopy including in-situ heating experiments and also by x-ray diffraction. The mechanical properties of the alloys were evaluated by tensile testing. Details concerning the specimens and the tests conditions used have been described elsewhere [7]. The pseudoelastic effect has been studied by performing loading-unloading tests at temperatures above A_f for each alloy. Also, in-situ loading-unloading experiments have been performed using a tensile testing machine specially designed to work under the optical microscope [7].

RESULTS AND DISCUSSION

1. Thermoelasticity and related state of order of the structure.

The stability of the transformation degrades during thermal cycling of the quenched alloys and the best stability was obtained after annealing the alloys at 300°C for 30 min [7]. However, as shown in Figure 1, although the transformation temperatures of the annealed alloys with higher manganese content (M15 and M16) remained rather stable during thermal cycling, those of the M14 alloy containing 2% manganese were unstable during the first few cycles. Also in the latter case, the transformation enthalpy decreased rapidly from 9 to 5 J/g between the first and the fifth thermal heating cycles respectively. In contrast, the transformation enthalpies of the M15 and M16 alloys showed little variation during thermal cycling with values as high as 9-9.5 J/g, confirming that the complete transformation of these alloys was achieved.

Although in all cases the martensitic phase was analysed as the orthorhombic 18R structure [7], there were slight differences in terms of its state of order. An evaluation of the latter has been obtained by measuring, from the x-ray diffraction spectra, the difference in d-spacing (Δd) between pairs of planes (splitting) which would have identical peaks when the alloys have disordered structures but whose peaks would be split in the ordered state [18]. The higher the degree of order the larger Δd values will be obtained [18,19]. Figure 2 illustrates the variation of the measured Δd values as a function of annealing time and of the number of thermal cycles for all the alloys. Higher Δd values are obtained after annealing for 30 min. in all cases and also increasing manganese content leads to increasing Δd values (Fig. 2a). The latter remained rather constant during thermal cycling of the M15 and M16 alloys annealed at 300°C for 30 min. (see fig. 2b) but they decreased rapidly during the first few thermal cycles of the M14 alloy.

The decrease in the Δd values indicates a decrease in the distortion of the basal plane of the 18R structure and this can be interpreted as being due to a more disordered martensitic structure or to a higher degree of DO₃ order [19]. Also, an increase of the B2 or L2₁ order will lead to an increase of the distortion of the close packed planes and consequently of the Δd values. During

Fig. 1. Variation of the transformation temperatures during thermal cycling of the annealed alloys.

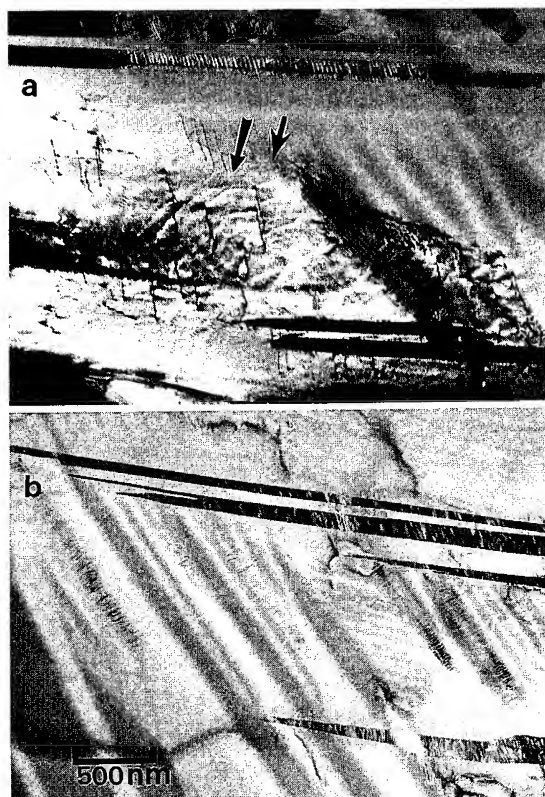
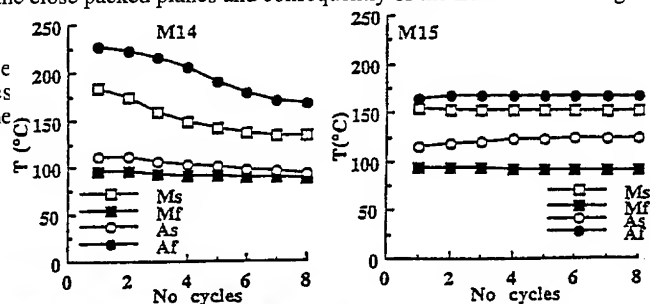


Fig. 3. Microstructure observed during reverse transformation by in situ heating experiments in the TEM: (a) dislocations produced by the accommodation of strain during the transformation of the M14 alloy, (b) Absence of dislocations in the austenitic phase of the transformed M15 alloy.

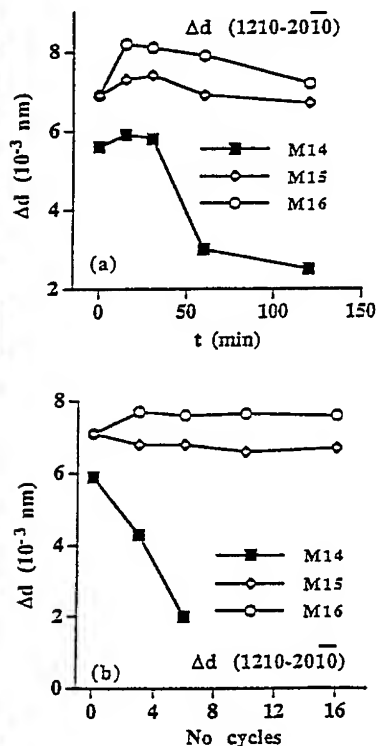


Fig. 2. Measured variation of splitting (Δd) between pairs of x-ray peaks (a) as a function of annealing time at 300°C and (b) as a function of thermal cycling between 20 and 300°C.

ageing at 300°C, ordering to the DO₃ structure (NNN order) can occur while at the same time the order parameter describing B2 ordering (NN order) can increase further. In the case of the M14 alloy with the lower manganese content, the quench produces a lower degree of B2 order and the suppression of DO₃ order [7]. However, DO₃ domains were present after annealing at 300°C and consequently a decrease in the Δd values was observed [7]. The thermoelastic transformation is closely related to the ordered structure of the lattice: for an ordered structure the transformation proceeds without inducing plastic deformation in the surrounding parent phase and this is thought to be the cause of the thermoelastic behaviour. In our alloys, in situ heating experiments carried out in TEM have shown that only the M14 alloy has dislocations in the austenitic phase during heating, as shown in figure 3a. In contrast we show in figure 3b an example where a typical dislocation-free structure is seen after transformation into the austenite phase of the M15 alloy. The dislocations seen gliding as the reverse transformation of the M14 alloy was taking place were produced to accommodate any misfit strain existing between the two phases due to the lack of a perfect coherency at their interface. The better transformation properties of the annealed alloys can be understood in terms of the ideal degree of order in the structure of the parent phase such that a one to one correspondence between atoms exists and coherent interfaces between the martensite and austenite phases are created.

2. Mechanical properties and pseudoelastic effect

All alloys have similar ductility at room temperature ($\approx 4.5\%$) while the alloy with the higher manganese content (M16) has better ductility at higher testing temperature (12% at 250°C) [7]. Examples of the stress-strain curves obtained from the loading-unloading cycling tests at $T_d \approx A_f + 50^\circ\text{C}$ are shown in figure 4 for the alloys M14 and M16. While the low manganese content alloy (M14) shows no pseudoelastic effect at all, the M15 and M16 alloys present a pseudoelastic effect of 3.5 and 4.5% strain respectively. The maximum recoverable strains are limited by these values irrespective of the total strain to which the specimens can be deformed. During in situ stress cycling experiments of the M15 and M16 alloys carried out under the optical microscope at temperatures above A_f we have observed the formation of stress induced martensite which disappeared on unloading [7]. Also, during these in-situ experiments, after several heating/cooling cycles of the M14 alloy, we noticed that the shrinkage of the martensitic laths did not occur on heating above A_f . This confirms that a decrease of the transformed fraction of the martensite occurs which explains the decrease of the transformation enthalpy values measured by DSC. We conclude that in the M14 alloy, the transformation strain is not accommodated elastically and it leads to the stabilisation of the martensite variants and to a non-recoverable strain, explaining the lack of pseudoelasticity of this alloy and the non-thermoelastic martensitic transformation.

3. Transformation mechanisms

In the case of the thermoelastic M15 and M16 alloys, richer in manganese, thermal cycling carried out at different heating/cooling rates has produced DSC curves which are not identical, as illustrated in figure 5 for the M15 alloy. The DSC curves shift towards higher temperatures when the heating rate increases during the reverse transformation, and towards the lower temperatures when the cooling rate decreases during the direct transformation. During these changes, it is not the start of the transformation that is altered (i.e. A_s and M_s) but rather the peak and tail of the curve. These observations show that only the kinetics of the process are changed. This confirms that the transformation is assisted by a thermally activated mechanism. The activation energies corresponding to the thermally activated mechanisms responsible for the reverse and direct transformation have been determined by two distinct methods [20]. The first one is the method of the fixed transformed fraction based on the relation: $\ln x = Q/RT + C_1$ where C_1 is a constant, R the gas constant and Q is the activation energy. The latter is determined using the measured times, t_x , and temperature T , at which a fixed fraction, x , has been transformed. The second one is the Kissinger method based on the relation: $\ln(\alpha/T_p^2) = Q/RT_p + C_2$ from which the activation energy is determined by measuring the temperature at the peak, T_p of the DSC curves obtained during thermal cycling at different heating/cooling rates, α . The results obtained from both methods are almost identical and the corresponding activation energies for the reverse

and the direct transformations are 70-75 kJmol⁻¹ and 150 kJmol⁻¹ respectively. Also from figure 6 we confirm that the activation energies obtained are independent of the transformed fraction and, therefore, that there is a unique mechanism controlling the transformation [21].

The general equation describing the evolution of a transformation [22] is $dx/dt=k(T)f(x)$, where x is the transformed fraction during the time t at absolute temperature T , k is the rate constant that fits the Arrhenius law $k(T)=k_0\exp(-Q/RT)$ and $f(x)$ is an empirical function that describes the transformation mechanism. The values $k_0f(x)$ have been deduced from this equation using the values of activation energy found experimentally. In this way we have obtained the experimental curves $\ln k_0f(x)$ versus $\ln(1-x)$ for both alloys and types of transformation [20]. These results have been compared to those obtained by studying the kinetics of the non-isothermal transformation of our alloys using the Johnson-Mehl-Avrami equation expressed as: $dx/dt=n K^{1/n} (1-x) [\ln(1-x)^{-1}]^{(n-1)/n}$. Here the value of the exponent " n " characterizes the rate of nucleation and the morphology of the growth [23].

By comparison between the experimental curves and the theoretical ones corresponding to the plot of $\ln f(x)$ versus $-\ln(1-x)$ for different values of " n ", it has been possible [20] to deduce the real exponent " n " of the Johnson-Mehl-Avrami equation which describes the transformation best. Thus, $n=2$ fits best the experimental curve corresponding to the reverse transformation. For the martensitic transformation a unique value of " n " has not been found. Two extreme values of this exponent, $n=3$ and $n=4$, have been determined such that the experimental curve lies within the area limited by the two corresponding theoretical curves [20].

The activation energy of about 70 kJmol⁻¹ necessary for the reverse transformation to occur indicates that the driving force is not so high that the transformation could take place spontaneously. The value of activation energy is practically half that for self-diffusion of copper alloys and is too small to explain a nucleation process of the austenitic phase within the martensite. Also the value of the Avrami exponent " $n=2$ " characterises a transformation without

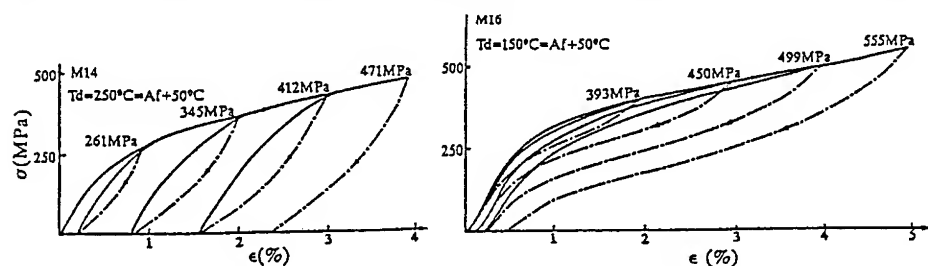


Fig. 4. Tensile curves obtained during stress cycling tests of the M14 and M16 alloys.

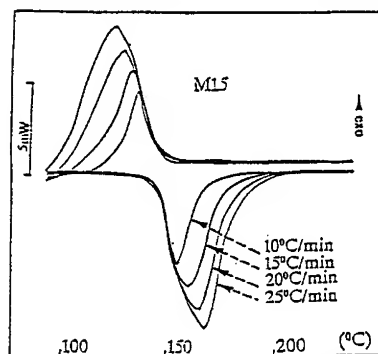


Fig. 5. Characteristic DSC curves obtained for different heating/cooling rates.

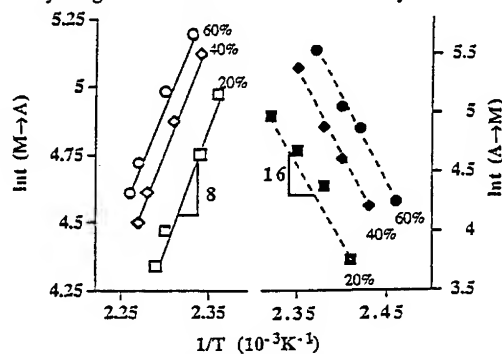


Fig. 6. Arrhenius plots of $\ln k$ versus $1/T$ for different transformed fraction of M15 alloy during direct transformation ($A \rightarrow M$) and reverse transformation ($M \rightarrow A$).

nucleation and whose growth (in this case the shrinkage of the martensite) is a two-dimensional one [23]. The thickness of the martensite laths is small compared with their length such that their morphology can be considered planar. Therefore, the shrinkage (or growth during the direct transformation) of the martensite laths is assisted by a thermally activated mechanism that takes place only at the interface between the two phases. The activation energy measured corresponds to that necessary for an atomic jump at the interface [24]. The process can be considered as a martensitic transformation whose rate is controlled by an atomic jump at the interface [20].

We have assumed that the shrinkage and the growth of the martensite are transformations with an identical energetic barrier and that the mechanisms for both shrinkage and growth are the same. The exponent "n" (≈ 3.5) is a parameter that depends on the nucleation rate and on the morphology of growth. The latter is the same during the reverse and the direct transformation but the nucleation is a process taking place only during the direct transformation. Then the difference in the activation energy between the reverse and the direct transformation (about 70 kJmol^{-1}) must be due to the nucleation process which is required for the direct transformation. The nucleation process cannot be described by the classical theory since the activation energy needed for it is more than twice that obtained experimentally. Since the activation energy necessary for the direct transformation is the same for different values of the transformed fraction, this implies that the mechanisms of nucleation and growth are the same. Therefore, the mechanism of the addition of one atom to the subcritical nucleus is the same as that during growth. Generally, it is accepted that for the direct transformation the nuclei of a critical size are stabilised after the quench and that the martensitic transformation is a growth process. However, we suggest that favourable predisposition of atomic arrangements exist that make easier the formation of critical sized nuclei such that the kinetics of nucleation are faster than predicted by the classical theory.

We conclude that the thermally activated mechanism assisting the transformation of the manganese rich alloys does not damage the ordered state of the martensitic structure and the transformation is a reversible thermoelastic one. Below a limiting value of manganese content (2%), the transformation strain is accommodated plastically and a lack of thermoelastic behaviour is observed.

REFERENCES

1. T.W. Duerig, J. Albrecht and G.M. Gessinger, *Journal of Metals*, 1, 14, (1982).
2. S. Eucken, E. Kobus and E. Hornbogen, *Z. Metallkunde*, 82, 640, (1991).
3. J. Van Humbeek, M. Chandrasekaran and L. Delaey, *ISIJ International*, 29, 388, (1989).
4. M.A. Morris, *Acta Metall. et Mat.*, 40, 1573, (1992).
5. S.W. Husain and P.C. Clapp, *Journal of Materials Science*, 22, 509, (1987).
6. P. Rodriguez and G. Guenin, *Materials Science and Engineering*, A129, 273, (1990).
7. M.A. Morris T. and Lipe, *Acta Metall. et Mat.*, 42, 1583, (1994).
8. L. Kaufman and M. Cohen, *Progress in Metal Physics*, 7, 165, (1977).
9. K. Otsuka and K. Shimizu, *Scripta Metall. et Mat.*, 11, 757, (1977).
10. M. Cohen, *Trans AIME*, 171, (1958).
11. Olson G.B. and Cohen M., *Metall. Trans.* 7A (1976) 1897.
12. K.E. Easterling and A.R. Thölen, *Acta Metall. et Mat.*, 24, 333, (1976).
13. R. Rapacioli and M. Ahlers M., *Scripta Metall.*, 7, 977, (1973).
14. M. Morin, PhD thesis, 1985, Université Claude-Bernard Lyon I.
15. H. Aaronson, *Metall. Trans.* 24 A, 241, (1993).
16. H. Aaronson, T. Furuhashi, J.M. Rigsbee, W. T. Reynolds and J.M. Howe, *Metall. Trans.*, 21A, 2369, (1990).
17. M.H. Wu, J. Perkins and C.M. Wayman, *Acta Metall.* 37, 1821, (1989).
18. Q. Xuan, J. Bohong and T. Y. Hsu, *Mater. Sci. Eng.*, 93, 205, (1987).
19. D.W. Roh, E.S. Lee and Y.G. Kim, *Metall. Trans.* 23A, 2753, (1992).
20. T. Lipe and M.A. Morris, *Acta Metall. Mat.*, in press (1994).
21. D. W. Henderson D.W., *Journal of non-crystalline solids*, 30, 301, (1979).
22. J. Burke, *The Kinetics of Phase Transformation in Metals*, 52, (1965).
23. J. W. Christian J.W., *The Theory of Transformation in Metals and Alloys*, 474, (1965).
24. Landolt-Börnstein, *Diffusion in Solid Metals and Alloys*, group III: Crystal and Solid State Physics, 483, (1990).

DEVELOPMENT OF NiAl(B2)-BASE SHAPE MEMORY ALLOYS

R. KAINUMA*, N. ONO** and K. ISHIDA*

*Department of Materials Science, and **Department of Machine Intelligence and Systems Engineering, Faculty of Engineering, Tohoku University, Sendai 980-77, Japan.

ABSTRACT

The basic concept underlying the alloy design and microstructural control method utilised in developing a new type of β (B2)+ γ (A1) two-phase ductile shape memory alloy in the Ni-Al base systems is briefly reviewed. The characteristic features of the shape memory effect (SME) in the Ni-Al-Fe and Ni-Al-Fe-Mn alloys are reported with particular reference to the transformation and deformation temperatures, the volume fractions of the γ phase, the morphology of the β + γ structure and the effect of cycling. Training by cycling treatment has a significant effect on the degree of shape recovery and pseudo-elasticity in the β + γ two-phase alloys. These duplex β + γ alloys also exhibit a combination of relatively high damping capacity and high yield strength. It is emphasized that these alloys could be expected to fill the need for a new group of shape memory alloys which operate at elevated temperatures over 100°C.

INTRODUCTION

The NiAl(β) phase alloy with the B2 structure containing 36 to 38at% Al is known to undergo a thermoelastic martensitic transformation from B2 to L10 (β') structure as shown in Figure 1 and also exhibit the Shape Memory (SM) effect [1]. One of the characteristic features of Ni-Al binary alloys is that the $\beta \rightarrow \beta'$ thermoelastic martensite transformation occurs over a wide range of temperatures between -200 and 900°C [2,3]. This means that the NiAl based alloy system can be expected to yield a group of SM alloys with high operating temperatures. However, the main drawback to the practical applications of NiAl base SM alloys has been their inherent brittleness at room temperature. Hence considerable efforts have been devoted towards the improvement in the ductility of β phase alloys as reviewed

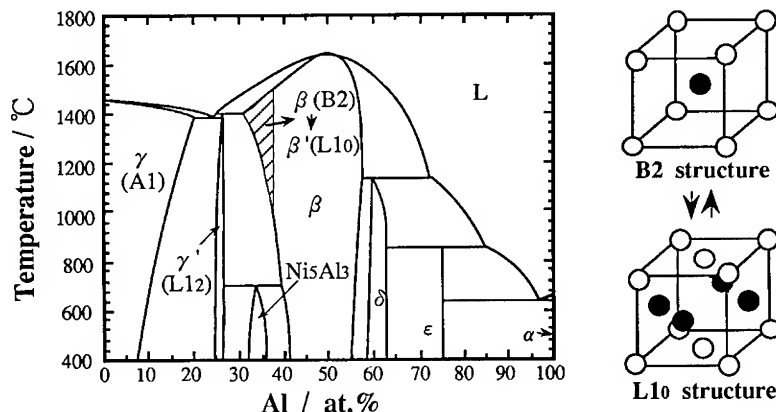


Fig.1 Phase diagram of the Ni-Al system.

by Liu et al [4]. However, only single β phase alloys of the Ni-Al-Fe system produced by melt-spinning techniques have been shown to have good ductility and also exhibit the SM effect[5-7]. No significant success in the attempts at improving the ductility of β phase by conventional methods in these systems has been reported so far.

The present authors have recently shown that the modification of the microstructure of the single β phase alloy by deliberately introducing the ductile disordered γ (Al) phase could result in a remarkable improvement in the hot-workability and room temperature ductility of these alloys [8-10]. Utilizing this technique of introducing a ductile phase into the brittle β matrix and using various combinations of thermal and mechanical treatments, a new type of ductile $\beta + \gamma$ two-phase SM alloys in the Ni-Al based alloy systems has been developed [11-13]. This paper describes the recent progress made in the developments pertaining to these $\beta + \gamma$ two-phase SM alloys.

ALLOY DESIGN

It has been clearly established [8,9], that the most promising method of improving the ductility of the β phase in these alloys is by the introduction of the ductile γ phase. Although the β/γ phase equilibrium is a metastable one in the Ni-Al binary system as shown in Figure 1, a stable β/γ equilibrium can be made to appear in appropriately chosen ternary systems. Figure 2 shows the four types of phase diagrams showing the relative dispositions of the phase fields in Ni-rich portions of Ni-Al-X ternary systems at elevated temperatures [14,15]. It can be seen that the β/γ equilibrium becomes stable by the addition of alloying elements such as Fe, Cr, Co, Cu and Mn. From these the Ni-Al-Fe, Ni-Al-Mn and a Ni-Al-Fe-Mn systems were chosen for selecting $\beta + \gamma$ two-phase SM alloys because in these systems the β phase could be formed over wide ranges of composition and temperature, and could be manipulated to great advantage in the control of the thermoelastic transformation temperature of the β phase. The phase equilibria and the iso- M_s temperature lines in the Ni-Al-Fe and Ni-Al-Mn systems are shown in Figure 3. It can be seen that these systems are appropriate choices for high temperature SM alloys operating above 100°C as will be discussed in a later section.

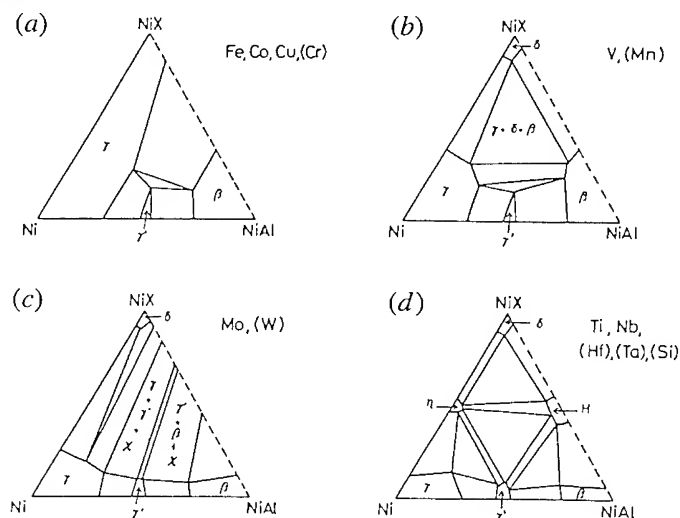


Fig.2 (a) through (d) schematical isothermal sections of phase equilibria in Ni-rich portions of the Ni-Al-X systems at elevated temperatures.

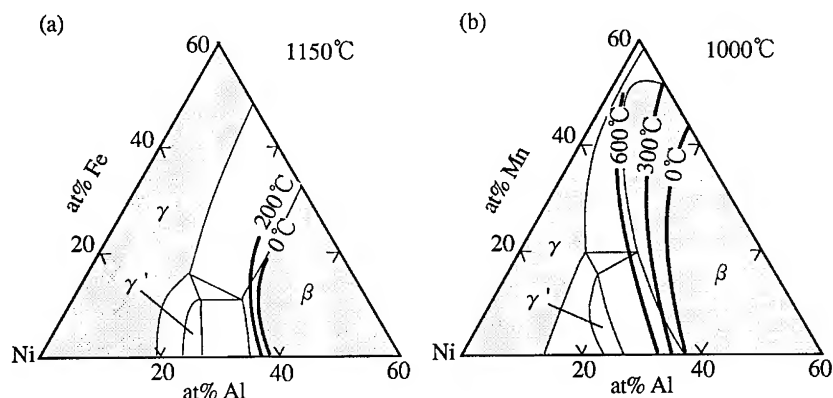


Fig.3 Isothermal sections of the (a) Ni-Al-Fe and (b) Ni-Al-Mn systems with iso- M_s composition lines.

HOT-WORKABILITY AND MICROSTRUCTURE

It has been shown that the hot-workability of β matrix alloys is strongly related to the phase diagram and also to the as-cast microstructure [8-10]. The following conditions should be satisfied for realising good hot-fabricability in the Ni-Al β base alloys.

- (i) Hot-working should be performed in the $\beta + \gamma$ two-phase region at elevated temperatures.
- (ii) The choice of alloy should be such that the $\beta + \gamma$ two-phase field is formed over a wide range of temperature, and the γ' (L12) or other intermetallic compounds are less stable in those temperature intervals.
- (iii) The microstructure before starting hot-working is such that the primary β phase boundary is decorated by the γ phase. The dendritic as-cast structure is to be avoided.

A typical example of the as-cast microstructure of $\beta + \gamma$ two-phase alloy in the Ni-Al-Fe and Ni-Al-Fe-Mn systems, with good hot-workability is shown in Figure 4. Figure 5 shows the microstructure of Ni-26at%Al-17at%Fe alloy annealed at 1155°C after hot-rolling. The microstructure consists of a mixture of about 90% by volume of β' and about 10% γ in the form of elongated fibres present mostly as an almost continuous decorating film on the grain boundaries of β' phase. This kind of microstructure is responsible for the observed significant improvement in room temperature ductility in these alloys.

TRANSFORMATION CHARACTERISTICS

The transformation temperatures of Ni-Al base alloys depend very steeply on alloy composition [16]. For example, the M_s temperature changes by about 30~35°C for every 0.1wt%Al change which makes it extremely difficult to control the transformation temperatures in single phase β alloys. In the case of $\beta + \gamma$ alloys, on the other hand, a better control of M_s temperature is more easily achieved by a proper choice of annealing temperature; this is made possible because the annealing temperature influences the M_s temperature through its effect on the composition of the β phase which is in equilibrium with the γ phase. Figure 6 shows the effect of annealing temperature on the martensitic transformation temperatures M_s (on cooling) and A_f (on heating) in the Ni-Al-Fe alloys as determined by Differential Scanning Calorimetry (DSC). The transformation temperatures increase with increase in annealing temperature because the equilibrium content of Al in the β phase decreases with increasing

Ni-25Al-15Fe

Ni-19Al-12Mn-9Fe

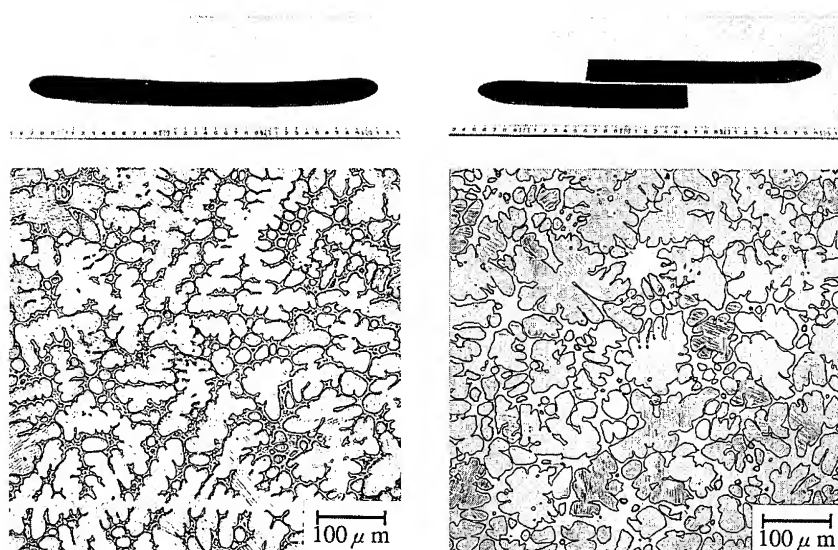


Fig. 4 Appearance of specimens after hot-rolling and their as-cast microstructures.

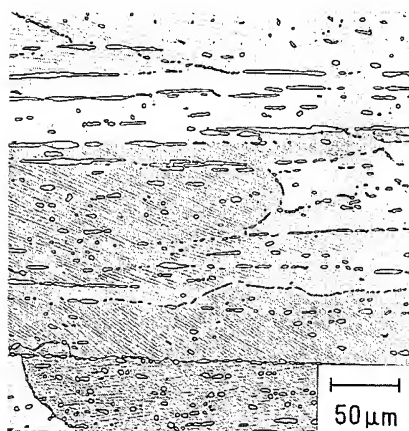


Fig. 5 Microstructure of Ni-26Al-17Fe alloy quenched from 1155°C.

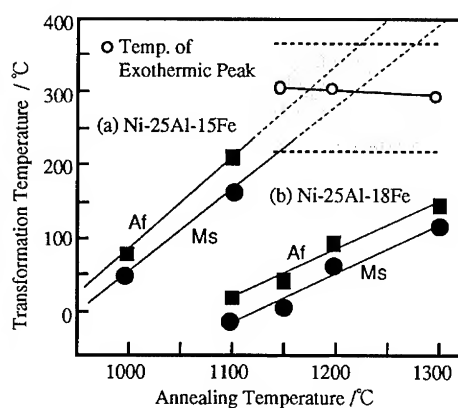


Fig. 6 Effect of annealing temperature on Ms and Af temperatures of (a) Ni-25Al-15Fe and (b) Ni-25Al-18Fe alloys.

temperature. In addition to the DSC endothermic and exothermic reaction peaks corresponding to the Af and Ms temperatures respectively, another exothermic peak is also observed upon heating the Ni-25at%Al-15at%Fe alloy after it had been annealed at temperatures above 1150 °C. Figure 7 is the DSC curve for a specimen of this alloy annealed at 1300°C and it shows

an exothermic peak appearing near 300°C. This reaction is to be attributed to the transformation of β' to Ni₅Al₃ (Pt₅Ga₃ type) phase, which is a stable phase between the γ' and β phases below 700°C in the Ni-Al binary as shown in Figure 1. According to Yang and Wayman[17], the $\beta \rightarrow \text{Ni}_5\text{Al}_3$ transformation occurs in NiAl base alloys with relatively higher Al temperatures, which is in good accordance with the results of Figure 6. Even though similar exothermic reactions are observed on heating the alloys of the Ni-Al-Mn and Ni-Al-Mn-Fe systems as shown in Figure 8, the phase change associated with them is somewhat different from that in the Ni-Al-Fe system. The details regarding this phase change will be reported in a separate paper[18].

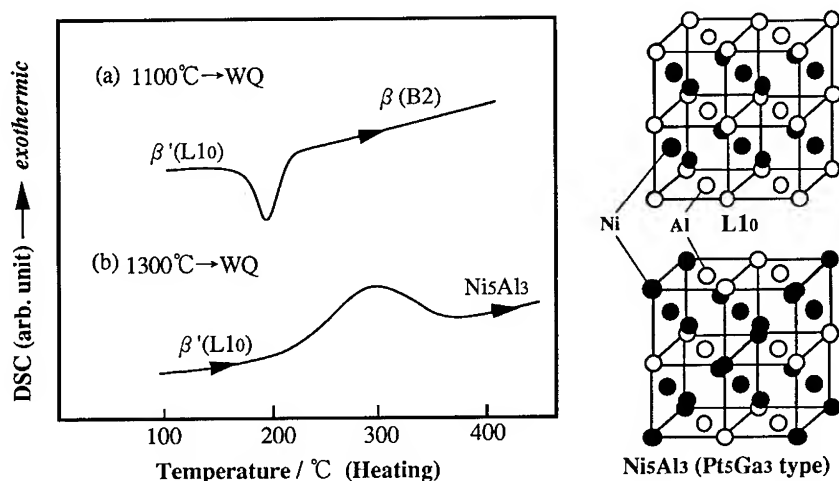


Fig. 7 DSC curves of Ni-25Al-15Fe specimens aged at 800°C for 24h after annealing at 1100°C and 1300°C.

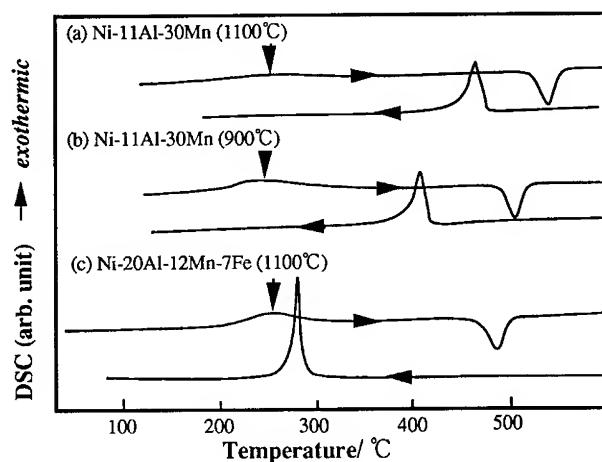


Fig.8 DSC curves from Ni-11Al-30Mn and Ni-20Al-12Mn-7Fe specimens annealed at 900°C and 1100°C.

It is also observed that the martensitic transformation temperatures of $\beta + \gamma$ two-phase alloys depend on the grain size. Figure 9 shows the variation of M_s and A_s with the grain size of β phase ($V_\beta = 90\%$) in the Ni-26at%Al-17at%Fe alloy [13], along with the data for the Cu-Zn-Al single phase [19]. It can be seen that there exists a Hall-Petch type relation between the transformation temperatures and the grain size in both the cases. This is because the presence of high elastic anisotropy in the β phase, which has been pointed out as the reason for this type of relationship between M_s and grain size in the Cu-Zn-Al single phase SM alloys [19], also holds good for the Ni-Al base alloys whose β phase also exhibits high elastic anisotropy of the order of $(A = 2C_{44}/(C_{11} - C_{12}) = 9)$ [20].

MECHANICAL PROPERTIES AND SHAPE RECOVERY

The $\beta + \gamma$ two-phase alloys produced by conventional casting, hot working and heat treatment exhibit good mechanical properties [8-10]. The typical stress-strain curves of the $\beta + \gamma$ SM alloys are shown in Figure 10. The tensile properties of the $\beta + \gamma$ SM alloys depend on the microstructure, volume fraction of the γ phase and the grain size [13]. Figure 11(a) and 11(b) show the microstructures of a Ni-25at%Al-18at%Fe alloy aged at 1150°C for 1h and 100h respectively, after a β phase homogenizing anneal at 1300°C for 15min. While short time ageing results in the precipitation of the γ phase both as a continuous film on the grain boundaries and as small precipitate particles in the β matrix, prolonged aging results in the formation of globular and massive γ phase precipitates at the grain boundary nodes and the grain interior as shown in Figure 11(b). The morphology of the $\beta + \gamma$ structure shown in Figure 11(a) is associated with better ductility and shape recovery than that of Figure 11(b). Figure 12(a) shows the effect of β volume fraction on the room temperature tensile properties of Ni-(14-26)at%Al-(29-17)at%Fe alloys after annealing at 1100°C. The elongation continuously decreases with increase in the volume fraction of the β phase, while the tensile strength reaches a maximum at about 35% β in the duplex $\beta + \gamma$ alloys and decreases slowly upto 60% and decreases sharply after the β percentage reaches 70%.

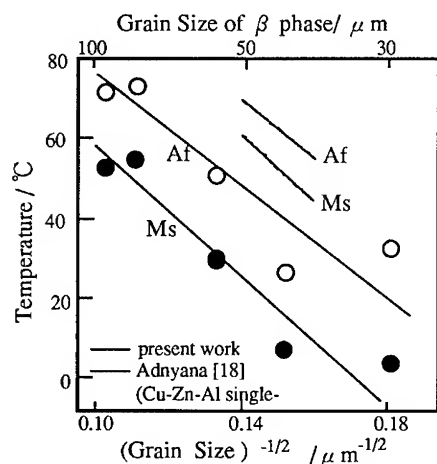


Fig. 9 Effect of grain size on the M_s and A_f temperatures of Ni-26Al-17Fe alloy.

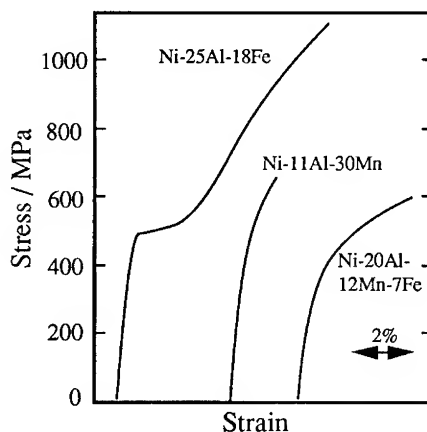


Fig.10 Engineering stress strain curves of $\beta + \gamma$ Ni-Al base alloys annealed at 1100°C.

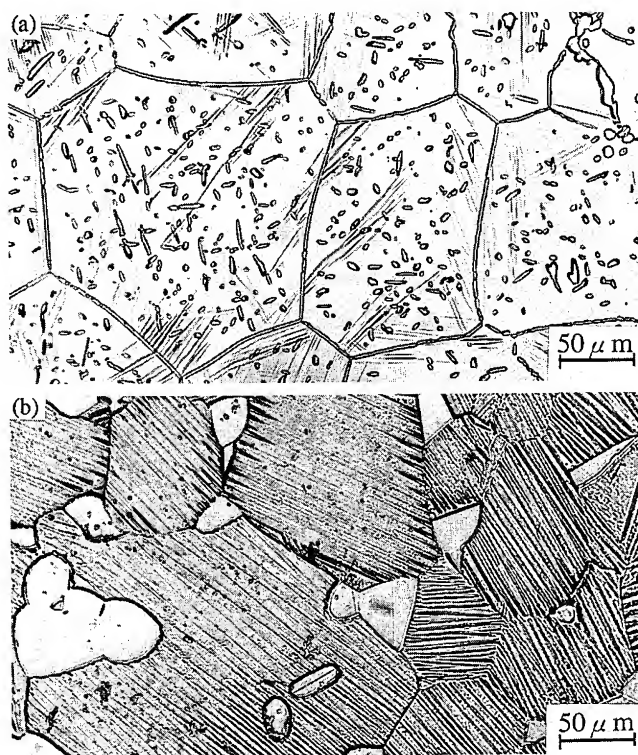


Fig.11 Microstructure of specimens cold-rolled (about 20%) and heat-treated: annealed at 1150°C (a) for 1h and (b) for 100h after homogenized at 1300°C for 15min.

Figure 12(b) shows the effect of β volume fraction on the shape recovery in the same series of Ni-Al-Fe alloys, whose M_s temperatures have been adjusted to be near about 6°C by controlling the annealing temperature[13]. The degree of shape recovery in these alloys was determined by winding straight strips of 0.15mm \times 4mm \times 40mm dimensions around a rod of 7.5mm radius, at M_s (6°C) and also below M_f (at -34°C) and measuring the changes in curvature after heating to 100°C above A_f temperature. It can be seen that, while the degree of shape recovery (SR) in specimens deformed at the M_s temperature is directly proportional to the volume of the β phase, it is much lower in alloys that were deformed at temperatures 40°C lower than the M_s temperature. This is most probably due to the difference in the deformation modes when the bending is conducted at M_s and well below M_s temperatures, as has been suggested in a previous paper[11]. When the specimen is deformed at M_s , the martensite transformation proceeds mainly in the stress induced transformation (SIT) mode. When it is deformed well below M_s in its martensitic state, the deformation stress would result in the rearrangement of martensite variants. The latter mode of deformation is likely to result in lower degree of shape recovery as compared to the former mode. However, it is to be noted that the specimen containing about 50% γ phase when deformed below M_f shows almost the same degree of recovery as the one deformed at M_s . This odd result may be due to a grain size effect[13].

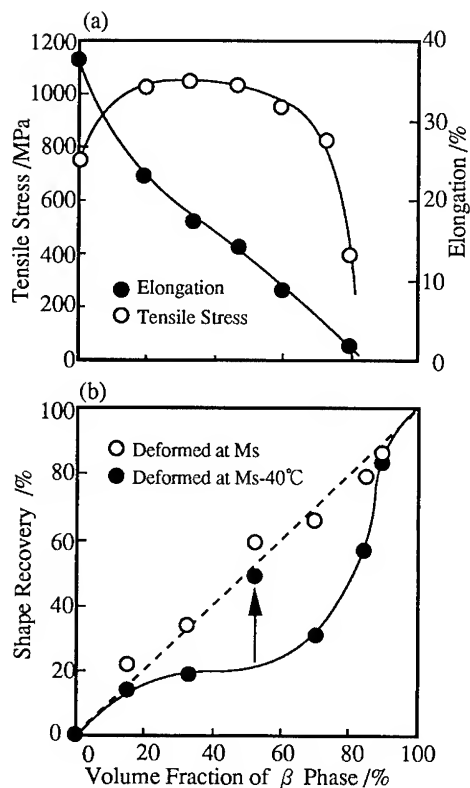


Fig. 12 Effect of β volume fraction on the tensile properties and on the shape recovery.

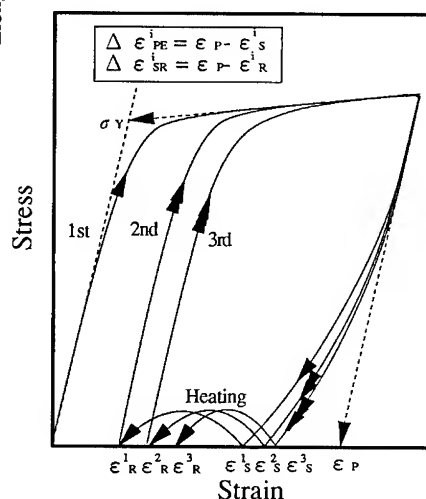


Fig.13 Schematic stress-strain curves demonstrating cycling effect where the pseudo-elastic strain ($\Delta \epsilon^i_{PE}$) and total shape recovery ($\Delta \epsilon^i_{SR}$) in the i -th cycle, and the yield stress (σ_y) are defined.

The effect of cycling on the shape recovery and pseudo-elastic property of these alloys has been investigated by tensile tests at various temperatures [21]. Figure 13 is a schematic illustration of the stress-strain curve wherein are defined the following shape-memory parameters: yield stress (σ_y), pseudo-elastic strain ($\Delta \epsilon^i_{PE}$) and the total shape recovery strain ($\Delta \epsilon^i_{SR}$) obtained by heating up to 120°C in the i -th cycle.

Figure 14(a) shows the effect of testing temperature on the yield stress of the Ni-26at%Al-16at%Fe alloy with 87% volume fraction of β phase whose transformation temperatures are $M_s=28^\circ\text{C}$, $M_f=6^\circ\text{C}$, $A_s=16^\circ\text{C}$ and $A_f=44^\circ\text{C}$. From the sharp change in the slope, $d\sigma_y/dT$, of the curve near M_s , it is evident that when the testing temperature is below the M_s temperature, the deformation proceeds mainly through the stress induced rearrangement of martensite variants, and when it is above M_s deformation proceeds in the stress induced martensitic transformation mode which is the dominant mode of transformation at temperatures ($T-M_s$) > 0 . Figure 14(b) shows the effect of testing temperature on pseudo-elastic (PE) recovery and the total shape recovery of the same specimen in the first cycle where strain of 1% ($\epsilon_p=0.01$) was applied. A shape recovery exceeding 90% is obtained at M_s temperature. Above and below M_s , the shape recovery is not high. The reason for the lower percentage of recovery below M_s would appear to be due to the presence of γ precipitates that could interfere with the rearrangement of martensitic variants and promote introduction and accumulation of

dislocation in the martensite. Above M_s , i.e. when $T - M_s > 0$ deformation is through the SIT mode. From Figure 14(a), it is clear that the higher stresses needed to induce the martensite transformation at these temperatures would also generate a lot more dislocations and as a consequence more irrecoverable plastic strain would accumulate leading to the decrease in the Shape Recovery (SR) levels. On the other hand, at M_s , where the SIT stress is the lowest, the irrecoverable plastic strain would be at its minimum and consequently shape recovery associated with deformation at M_s would be at its highest. Figure 15 shows the effect of cycling on the SR and PE properties. Shape memory training by cycling treatment at any temperature has a significant effect on increasing the levels of SR and PE. While almost complete SR recovery is realised within 5 cycles at temperatures above and below M_s , almost complete SR shape recovery and optimum PE recovery within 5 cycles are obtained when the training is done at temperature $T = M_s + 50^\circ\text{C}$.

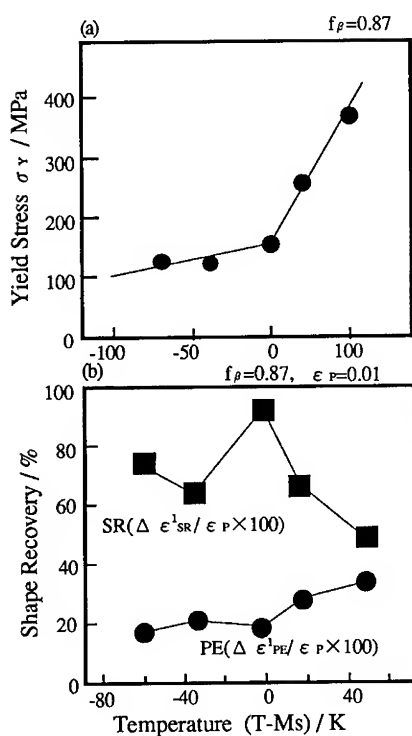


Fig.14 Effect of testing temperature on the yield stress and the shape recovery in the first cycle.

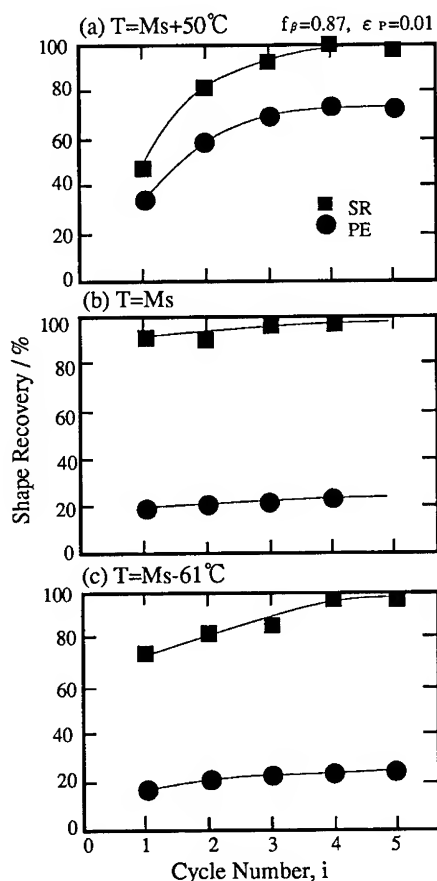


Fig. 15 Effect of cycling on pseudo-elasticity and total shape recovery.

DISTINGUISHING FEATURES

The $\beta + \gamma$ alloys of the Ni-Al base system are ductile SM alloys which not only exhibit the shape memory property, but also possess some unique extra features which are not to be found in other shape memory alloys. Although these alloys do not show a complete shape recovery in the first SM cycle due to the presence of the γ phase, the following characteristic features distinguish them from the other commercial Ni-Ti and Cu-base SM alloys.

(i) **Combined Magnetism and Shape Memory** : Since the γ phase is ferromagnetic, the $\beta + \gamma$ SM alloys have associated with it magnetic properties that can be varied by varying the volume fraction of the γ phase.

(ii) **High temperature SM capability**: As shown in Figure 3, the M_s temperatures of the two phase $\beta + \gamma$ alloys span a wide range depending on the composition. These SM alloys are therefore appropriate candidates for SM devices operating above 100°C . As an example, the variation of shape memory strain on heating a deformed specimen of the alloy Ni-20at%Al-12at%Mn-7at%Fe alloy with a 70% volume fraction β is shown in Figure 16. In this alloy the shape memory effect is observed in the region of 500°C . Figure 17 lists the different systems of SM alloys with their potential SM operating temperatures. Although high temperature Ti-Pd based SM alloys have been developed[22,23] they suffer from the limitations of high cost and poor fabricability. The Ni-Al base alloys on the other hand are less costly and more easily fabricated and are better suited for applications above 100°C .

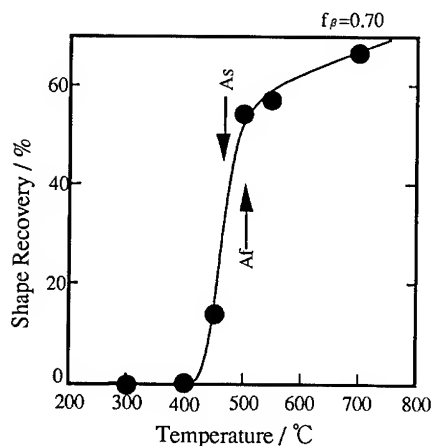


Fig.16 Effect of heating temperature on shape recovery of Ni-20Al-12Mn-7Fe alloy annealed at 1100°C .

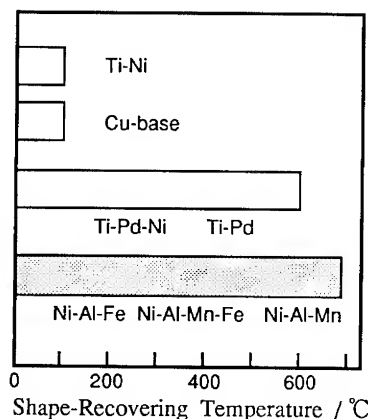


Fig. 17 Shape memory alloys for high temperature use.

(iii) **Damping capability**: Many SM alloys have the ability to act as damping materials. Damping capacity of a material arises from its ability to absorb mechanical energy through the stress-induced movement of magnetic domain boundaries, dislocations, twin boundaries, etc.[24, 25]. The movement of twin boundaries and interfaces between martensite variants or between martensite and parent phases accompanied by thermoelastic martensitic transformation is responsible for the high damping characteristics of these alloys. The damping characteristics of $\beta + \gamma$ Ni-Al-Fe alloys have been investigated by mechanical impedance tests [26]. Figure

18 shows the relation between the loss factor η , measured at room temperature, and the volume fraction of β phase in the Ni-(14-16)at%Al-(26-16)at%Fe alloys whose Ms temperatures are between about 70°C and 75°C. Loss factor η is a measure of damping obtained in the mechanical impedance test, and can be taken to be equal to the internal friction parameter, Q^{-1} , if the damping is low ($\eta \ll 1$) [25, 27]. From Figure 18 it is seen that the damping capacity is increased by increasing the volume fraction of the β phase as is to be expected. The other NiTi and Cu-based commercial SM alloys also exhibit high mechanical damping capacity [28,29], but their yield strengths are very low. Since a combination of high damping and high yield strength is required for most practical applications, SM alloys of the Ni-Al based ternary systems are the natural candidates, because the yield strength of these $\beta + \gamma$ two-phase alloys can be increased by proper control of the volume fraction of γ phase as shown in Figure 12. Figure 19 shows the η vs yield strength for several high damping alloys and it is self-evident that Ni-Al base alloys have the most attractive combination of yield strength and damping capacity.

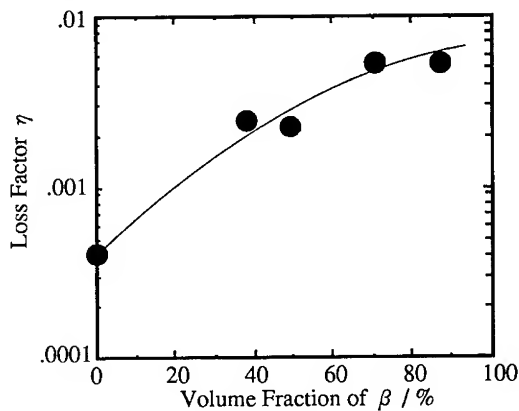


Fig. 18 Effect of β volume fraction on loss factor.

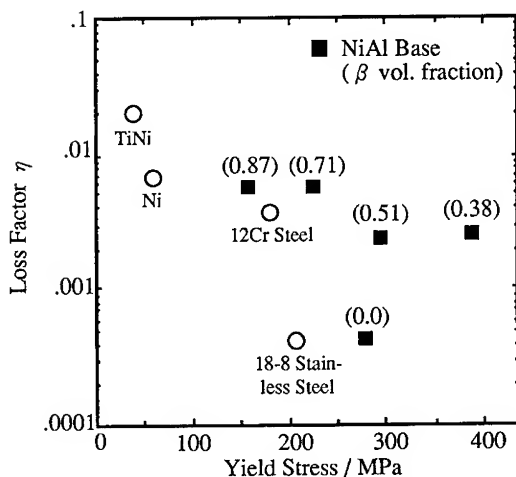


Fig. 19 Loss factor vs. yield stress of several damping alloys.

CONCLUDING REMARKS

Recent advances made in the development of $\beta + \gamma$ SM alloys in the Ni-Al base systems are presented. These $\beta + \gamma$ two phase alloys are amenable to microstructural control through alloy design and can be produced by conventional casting, rolling and heat treatment methods to yield ductile SM alloys with the desired transformation temperatures in the range 20 to 500°C. These $\beta + \gamma$ alloys are particularly suitable as low cost high temperature SM alloys with a good combination of strength, operating temperatures above 100°C that also possess a combination of high damping capacity and high yield strength.

ACKNOWLEDGEMENTS - The authors wish to thank Mr. A. Tsukahara, Mr. H. Nakano and Mr. K. Oikawa for their help in carrying out the work. This work was supported by the Grant-in-Aids for Scientific Research from the Ministry of Education, Science and Culture, Japan. The support from The Iron and Steel Institute of Japan and Kumagai Foundation for Science & Technology is also acknowledged.

REFERENCES

1. K.Enami and S.Nenno, Metall. Trans., **2**, 1487(1971).
2. J.L.Smialek and R.F.Hehemann, Metall.Trans., **4**, 1571(1973).
3. Y.D.Kim and C.M.Wayman, Scripta Met., **24**, 245(1990).
4. C.T.Liu, E.P.George and C.G.Mckamey, Proc. 3rd. Jpn. Int. SAMPE Symp., 1147(1993).
5. S.Furukawa, A.Inoue and T.Masumoto, Mater.Sci.Eng., **98**, 515(1988).
6. M.Wallin, P.Johansson and S.Savage, Mater. Sci. Eng., **A133**, 307(1991).
7. C.T.Liu, C.J.Sparks, J.A.Horton, E.P.George, Ming-Yang Kao and H.Kunsmann in Shape-Memory Materials and Phenomena - Fundamental Aspects and Applications, edited by C.T.Liu, H.Kunsmann, K.Otsuka and M.Wuttig (Mat. Res. Soc. Symp. Proc., **246**, Boston, MA, 1991) pp.169-176.
8. K.Ishida, R.Kainuma, N.Ueno and T.Nishizawa, Metall.Trans., **22A**, 441(1991).
9. R.Kainuma, S.Imano and K.Ishida, Proc. 3rd Jpn. Int. SAMPE Symp., 1410(1993).
10. K.Ishida, R.Kainuma and T.Nishizawa, Symp. Proc. on Mechanical Properties and Phase Transformations of Multi-phase Intermetallic Alloys, TMS, in press.
11. R.Kainuma, K.Ishida and T.Nishizawa, Metall. Trans.A, **23A**, 1147(1992).
12. R.Kainuma, H.Nakano, K.Oikawa, K.Ishida and T.Nishizawa in Shape-Memory Materials and Phenomena - Fundamental Aspects and Applications, edited by C.T.Liu, H.Kunsmann, K.Otsuka and M.Wuttig (Mat. Res. Soc. Symp. Proc., **246**, Boston, MA, 1991) pp.403-408.
13. R.Kainuma, K.Oikawa and K.Ishida, Proc. Int. Symp. Exh. on Shape Memory Materials, Beijing, The Non-ferrous Metals Society of China, 464(1994).
14. in Ternary Alloys, edited by G.Petzow and G.Effenberg (VCH, vol.3, 1990~vol.8, 1993).
15. C.C.Jia, K.Ishida and T.Nishizawa, Metall. & Mater. Trans.A, **25A**, 473(1994).
16. Y.K.Au and C.M.Wayman, Scripta Metall., **6**, 1209(1972).
17. J.H.Yang and C.M.Wayman, Mater. Sci. Eng., **A160**, 241(1993).
18. R.Kainuma, H.Nakano and K.Ishida, To be published.
19. D.N.Adnyana, Metallography, **18**, 187(1985).
20. K.Enami, J.Hasunuma, A.Nagasawa and S.Nenno, Scripta Metall., **10**, 879(1976).
21. N.Ono, A.Tsukahara, R.Kainuma and K.Ishida, To be published.
22. S.M.Tuominen and R.J.Biermann, J.Metals, **38 February**, 32(1988).
23. Y.Shugo, Mater. Sci. Forum, **56-58**, 631(1990).
24. I.G.Ritchie and Z-L. Pan, Metall. Trans., **22A**, 607(1991).
25. D.W.James, Mater. Sci. Eng., **4**, 1(1969).
26. Y.Tsugane, R.Kainuma and K.Ishida, Unpublished work.
27. H.Nagai, T.Shioa, M.Nishihara, Y.Tadokoro and Y.Togawa, Tetsu to Hagane, **72**, 95(1986).
28. R.R.Hashiguti and K.Iwasaki, J. Appl. Phys., **39**, 2182(1968).
29. K.Sugimoto, T.Mori, K.Otsuka and K.Shimizu, Scripta Metall., **8**, 1341(1974).

THE EFFECTS OF La ON RAPIDLY SOLIDIFIED Al - 66 at.% Ni

Baode Sun,* Yaohe Zhou,** Hui Lin,*** and Dongliang Lin*

*Department of Materials Science and Engineering, Shanghai Jiao Tong University, Shanghai 200030, P. R. China

**Department of Materials Science and Engineering, Northwestern Polytechnic University, Xi'an 710072, P. R. China

***Department of Materials Science and Engineering, University of Pennsylvania, Philadelphia, PA 19104, USA

ABSTRACT

This paper investigates the microstructure and ductility of Al - 66 at.% Ni by means of melt spinning technology combined with La microalloying. It shows that the Al - 66 at.% Ni without La exhibits coarse equiaxed martensite grains with Ni_3Al precipitating at the grain boundaries (GBs). An addition of 0.05 wt.% La suppresses the precipitation of Ni_3Al and a microstructure of complete martensite is obtained. When the amount of La is 0.2~0.8 wt.%, a "supersaturated" single phase of B2 structure NiAl results. The elongation of Al - 66 at.% Ni without La is only 0.8%. When 0.05, 0.2, and 0.8 (wt.%) La are added to the alloy, their elongations can be as high as 2.6, 3.0, and 3.2% respectively. This shows that the elongation increases with increasing La content. The microstructural morphology and the ductility enhancement mechanism are discussed.

INTRODUCTION

The Ni-Al phase diagram shows that single phase NiAl exists from the composition of Al - 45 at.% Ni to Al - 60 at.% Ni. The composition Al - 66 at.% Ni falls in the two-phase field. Recent research has focused on single phase NiAl, a potential high-temperature structural material which has many advantages over the Ni-based superalloys, but pays little attention to alloys in the two-phase field, which are potential high-temperature shape memory alloys. In fact, the alloys in the range Al - 60 at.% Ni ~ Al - 69 at.% Ni undergo thermoelastic martensitic transformations with M_s ranging from 100 K (Al - 60 at.% Ni) to 1200 K (Al - 69 at.% Ni) upon cooling rapidly from high temperature [1,2]. These alloys exhibit shape memory effects at various temperatures depending upon their compositions. But their widespread application has been hampered greatly by their room-temperature brittleness. In this paper we report the preliminary results on the improvement of ductility of Al - 66 at.% Ni by rapid solidification and microalloying with La.

EXPERIMENTAL PROCEDURE

Free jet melt spinning was used to produce the rapidly solidified Al - 66 at.% Ni ribbon. The melt stock was prepared from 99.99 wt.% Al and 99.999 wt.% Ni by induction melting in vacuum with an alumina crucible. A charge of approximately 10 g was placed into a dense alumina crucible in a melt spinning apparatus. The charge was heated to about 1870 K and ejected by pressurized argon onto an uncooled stainless steel wheel rotated at a surface speed of 20 m/s. Melt spinning was performed in a positive pressure argon atmosphere to suppress Al vaporization. The resulting ribbons were 0.035~0.040 mm thick and about 3 mm wide.

The composition of the rapidly solidified alloy was determined to be 66.4 at.% Ni. Scanning electron microscopy (SEM) and transmission electron microscopy (TEM) were used to examine the structure of the alloy and the elongations were measured on an Instron 1122 machine.

RESULTS

Morphology and Structure

As shown in Fig. 1, the microstructure of the Al - 66 at.% Ni alloy without La is coarse equiaxed martensite grains with the Ni_3Al precipitated at the GBs. An addition of 0.05 wt.% La

suppresses the precipitation of Ni_3Al at the GBs so that a microstructure of complete martensite is obtained, as shown in Fig. 2. When the amount of La is increased to 0.2~0.8 wt.%, we obtain columnar crystals, as shown in Fig. 3. Figure 4 is the selected area diffraction pattern of Al - 66 at.% Ni with 0.2 wt.% La, which shows the diffraction pattern of B2-structured NiAl with [111] direction. We can see from Fig. 4 that the La addition suppresses the martensite transformation and produces a "supersaturated" single phase of B2-structured NiAl.

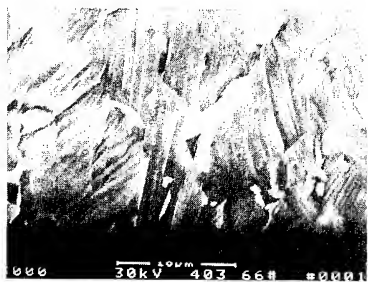


Fig. 1 Microstructure of alloy without La. Martensite + Ni_3Al .

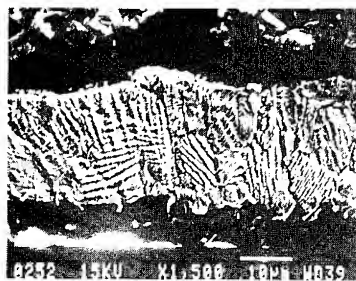


Fig. 2 Microstructure of alloy with 0.05% La. Fully martensitic.

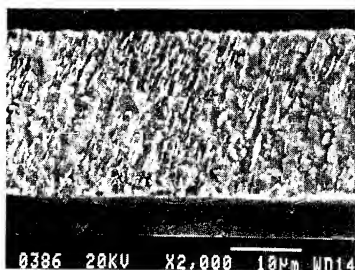


Fig. 3 Microstructure of alloy with 0.2% La. "Supersaturated" single phase NiAl.

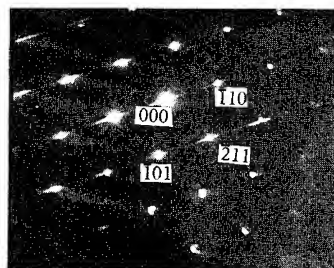


Fig. 4 Selected area diffraction pattern of alloy with 0.2% La. B2 NiAl [111].

Ductility

As shown in Fig. 5, the elongation of Al - 66 at.% Ni without La is only 0.8%. An addition of 0.05 wt.% La increases the elongation of the alloy to 2.6%. Further additions of La (0.2~0.8 wt.%) increase the elongations even more, to as high as 3.2%. This shows that the elongations of rapidly solidified Al - 66 at.% Ni increase with increasing La content.

DISCUSSION

The morphology of rapidly solidified alloys usually consists of columnar crystals growing from the wheel side to the free side. But here the Al - 66 at.% Ni alloy without La, or with 0.05 wt.% La, have completely equiaxed grains. We can explain it as follows:

When rapidly solidifying at a rate of $10^5\sim10^6$ K/s, Al - 66 at.% Ni first forms a few columnar crystals, in the expected manner, but the further cooling is so rapid that it makes the columnar crystals change from B2 to L1_0 martensite, that is to say, the B2 NiAl will undergo thermoelastic martensitic transformation ($\text{B2}\rightarrow\text{L1}_0$) when fast cooling from high temperature, so

the solid state transformation induces a stress from coherent strain (F1). On the other hand, during the melt-spinning process, there is a viscous shearing stress (F2) on the interface between liquid and solid (L/S). Therefore, as a result of the effects of F1 and F2, the growing columnar crystals will break up into fragments, which may get trapped in the liquid as heterogeneous nuclei and produce equiaxed grains. When the amount of La increases to 0.2~0.8 wt.%, as there is no martensitic transformation, instead of breaking into fragments, the columnar crystals will grow continuously, and fully columnar grains will develop. It can be concluded that crystal morphology is closely related to martensite transformation in rapidly solidified Al - 66 at.% Ni.

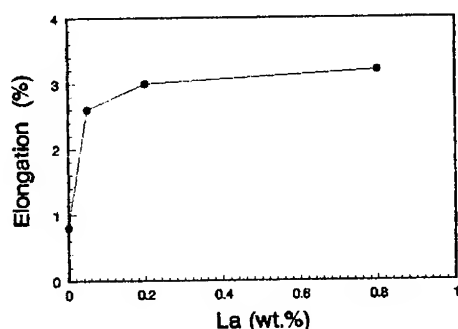


Fig. 5 The relationship between the elongation of Al - 66 at.% Ni and its La content.

After McLean and Northcott [3], the dispersing force of solute atom segregation at GBs is the lattice distortion energy difference between grains and the GBs, and the equilibrium segregation concentration C_{gb} of solute at the GBs is given by:

$$C_{gb} = (C_m A \exp(Q/RT)) / (1 + C_m \exp(Q/RT))$$

where C_m = solute atom solubility in grains, $C_m \ll 1$

A = vibrational entropy factor at the GBs

Q = lattice distortion energy difference of solute atoms in the grains and at the GBs

R = gas constant

T = absolute temperature.

From the above expression we can deduce that the more the difference between the solute atom radius and that of the solvent, the higher the value of Q , and thus greater the value of C_{gb} , indicating that the solute atoms will tend to distribute at the GBs. The La atom radius is 50 and 30% greater than that of Ni and Al, respectively, indicating that distortion energy of a La atom dissolved within the grains is much higher than when it is segregated at the GBs. The thermodynamics of segregation to the GBs are thus quite favorable in the case of La dissolved in NiAl. Therefore, when a small amount of La is added to the alloy, during the melt-spinning process, it concentrates at the growing L/S interface, restrains the expelling of the solute atom (here Ni), and prevents the formation of Ni concentration in front of the L/S interface, thereby suppressing the precipitation of Ni_3Al at the GBs and resulting in a completely martensitic microstructure.

During rapid solidification, since the L/S interface progresses very quickly "solute trapping" [4] might happen. When 0.2~0.8 wt.% La is added, some of the La segregates at the GBs, but part of it may be "trapped" in the grains as well. We did not find any La compounds in the grains, that is to say, La is probably present in the NiAl lattice in the form of interstitials or substitutionals. Because of its large atom size, it is unlikely that La is an interstitial; rather, it most probably substitutes for Ni and/or Al. Since the martensite transformation is a process of coordinated atom rearrangement, and La because of its large atom size as compared to Ni and Al is difficult to move in coordination with Ni and Al, it is reasonable to expect La to suppress the

martensite transformation. So, as more La is added, it not only suppresses the formation of Ni_3Al , but also the martensite transformation. As a result a "supersaturated" Ni-rich B2 NiAl (Al - 66 at.% Ni) can be obtained. In other words, La enlarges the NiAl solid solution zone.

Rapidly solidified Al - 66 at.% Ni has only 0.8% elongation since Ni_3Al at the GBs is brittle in nature, which lowers the ductility of the alloy. The addition of 0.05 wt.% La suppresses the Ni_3Al precipitation, eliminates the brittle Ni_3Al at the GBs, and thereby enhances elongation to 2.6%. Addition of 0.2~0.8 wt.% La makes the alloy "supersaturated" B2 single phase, and the elongation of the alloy can reach as high as 3.2%. The mechanism of ductility enhancement is not very clear. One possibility is that La removes the impurities from the GBs, thereby enhancing their cohesive strengths and ductilizing the alloy. But the more important reason may be that La keeps the alloy in the "supersaturated" B2 NiAl single phase, decreases the order, minimizes the covalent bonds [5,6] between Ni-Ni, Al-Al, and Ni-Al, and thus improves the ductility.

CONCLUSIONS

The conclusions of this study of rapidly solidified Al - 66 at.% Ni doped with different amounts of La are as follows:

1. The microstructure of the alloy without La is coarse equiaxed martensite grains with Ni_3Al precipitated at the GBs. An addition of 0.05 wt.% La suppresses the precipitation of Ni_3Al and produces a microstructure that is fully martensitic. The addition of 0.2~0.8 wt.% La can suppress the martensite transformation and obtain a "supersaturated" single-phase B2 NiAl.
2. The morphology of the alloy depends on the martensite transformation. When there is a martensite transformation, coarse equiaxed grains are obtained; otherwise columnar grains are obtained.
3. The elongation of the Al - 66 at.% Ni alloy without La is only 0.8%. With additions of 0.05, 0.2 and 0.8 wt.% La, the elongations increase to 2.6, 3.0 and 3.2%, respectively. The ductility of the alloy thus increases with increasing La content.
4. La could remove impurities at the GBs and enhance their cohesive strengths, thereby increasing the ductility of the alloy. In the alloy with 0.05 wt.% La, brittle Ni_3Al is removed from the GBs, which may be another reason for its ductility enhancement. In the alloys with 0.2~0.8 wt.% La, another important reason may be that La keeps the alloy in the single-phase B2 NiAl region, decreases the order, and minimizes the covalent bonds, thereby improving the ductility.

ACKNOWLEDGMENT

This work was supported by the National Natural Science Foundation of the P. R. China and Shanghai Scientific Committee Foundation.

REFERENCES

1. Y. K. Au and C. M. Wayman, *Scripta Metall.* **6**, 1209 (1972).
2. J. L. Smialek and R. F. Hehemann, *Metall. Trans.* **4**, 1571 (1973).
3. D. McLean and L. Northcott, *JISI* **158**, 169 (1948).
4. M. J. Aziz, *J. Appl. Phys.* **53**, 1158 (1982).
5. M. J. Cooper, *Philos. Mag.* **89**, 811 (1963).
6. A. G. Fox and M. A. Tabberner, *Acta Metall. Mater.* **39**, 669 (1991).

POROUS TiNi SYNTHESIS FROM ELEMENTAL POWDERS

Janet C. Hey and A. Peter Jardine,
Dept. of Materials Science & Engineering,
SUNY at Stony Brook, Stony Brook, NY 11794-2275

ABSTRACT

The shape memory alloy TiNi is produced by either Vacuum Induction Melting (VIM) or by Vacuum Arc Remelting (VAR) of pure metal ingots for actuator applications. Powder metallurgy techniques provide an alternative fabrication route for their use in passive damping applications where porosity and deviations in chemical homogeneity can be tolerated. In this study TiNi compacts were cold pressed from the blended elemental powders and sintered in vacuum for varying times at temperatures from 800°C to 1000°C. Two heating rates were used, 5 K/min. and 10 K/min. A TiNi microstructure could be produced after annealing at 1000°C for 6 h., although some TiNi₃ was still observed. Sintering above 900°C produced porous microstructures with green densities approaching 3.5 gm/cm³.

1. INTRODUCTION

There are many alloys exhibiting shape memory properties; however, TiNi possesses excellent mechanical properties and good corrosion resistance along with room temperature transformation temperatures, a large recovery force on heating and a long cyclic lifetime. Consequently, it has become the most commercially important of the shape memory alloys. Conventional synthesis of TiNi by either Vacuum Induction Melting or Vacuum Arc Remelting of the pure metals is costly but necessary if the material is used as a conventional actuator material. This is because the transformation temperature M_s is strongly dependent on chemical composition and multiple remelting is required to minimize the presence of impurities and to achieve homogeneity. The difficulties in working and mechanically machining TiNi also add to the high cost and limit the commercial availability of this material to wire and sheet stock. For passive damping and biomedical applications, powder metallurgy (PM) can provide near-net shape processing that minimizes the need for machining. As there are few commercial sources for TiNi powders, the purpose of this investigation was to characterize the microstructure of TiNi produced from Ni and Ti elemental powders by powder processing with subsequent heat treatment.

1.2 Powder Metallurgy

There are several synthesis issues that need to be considered. The first is the need to obtain a homogeneous TiNi alloys by interdiffusion while minimizing the formation of neighboring intermetallic phases, TiNi₃ and Ti₂Ni. The Gibbs free energies of the stable intermetallic phases, Ti₂Ni and TiNi₃, are lower than that for TiNi. Once formed, therefore, it is unlikely that these phases will entirely disappear. Many workers [1-5] obtained a mixture of the intermetallic phases TiNi, Ti₂Ni and TiNi₃ from the elemental powders via the PM route but the goal of homogeneous TiNi would seem to be difficult to achieve.

For porous TiNi, a major influence on the final sintered density is the initial green density which will increase with compaction pressure. In addition, a further factor was noted by Aksenov *et al* [1] and Igharo and Wood [3], in that while increasing the sintering temperature led to diffusional homogenization, it also led to a growth in diffusional porosity. This was due to Kirkendall void formation resulting from the difference in the diffusivity of the Ni and Ti elements (Ni diffuses faster than Ti)[7]. As a possible complication, high temperature sintering

of inhomogeneous material can lead to the melting of compositions of low melting point (m.p.) [3]. This liquid may be used to drive a densifying front through the entire sample as in the reactive sintering process[8]. However this phenomenon was not observed either by Igharo and Wood or by Morris and Morris who both associated liquid formation with the presence of large pores[3-4]. A plausible explanation has been suggested by Morris and Morris who point out that for liquid to form in this system it is necessary that solid state interdiffusion occurs to form the required low m.p. composition. As the liquid phase forms at certain locations, other regions of better or poorer interdiffusion will remain solid, thus creating a solid skeleton phase and inhibiting the free particle movement that is necessary for densification improvement. Instead, the liquid is drawn by surface tension forces to fill the nearby fine porosity leaving behind large pores.

Finally it must be remembered that when TiNi is formed from the elemental mixture, its temperature rises rapidly by the heat of formation. In addition, the formation reactions of Ti_2Ni and $TiNi_3$ from their elements are also exothermic. The temperature rise together with the formation of the eutectic liquid (24.5 at% Ni) may cause the deformation or the loss of the original compact shape and the formation of large pores. Kuroki *et al* [5] demonstrated that slowly heating from 550°C to 900°C at 2K/min. can control the compound-forming reaction and resulted in good preservation of the compact shape. The heating rate for the compact was changed from 10 K/min. only in the reaction temperature range thus saving time while preserving the shape and dimensions.

2. EXPERIMENTAL DETAILS

The nickel and titanium powders, 99.9% and 99.5% pure respectively, and both 44 μm , were combined in the ratio 50/50 atomic %. They were mixed by ball-milling in a ceramic chamber for four hours. The specimens were then compacted in a uniaxial die press under 27.5 MPa for 5 minutes. The compacted specimens were 29 mm in diameter and typically 3.5 mm thick. The compacts were heat treated in a 10^{-6} torr vacuum tube furnace for varying times at temperatures ranging from 800 to 1000°C. Two heating rates were used: a slow heating rate of 5 K/min and a faster heating rate of 10 K/min. The green and sintered densities were determined from weight and dimensional measurements. The surfaces of the specimens were ground and a Phillips PW 1729 diffractometer was used to determine the phases present. Some specimens were subsequently sectioned and the cross-sections examined in an ISI-SX-30 scanning electron microscope using backscattered electrons.

The alloy is an ordered intermetallic equiatomic compound. It has a high temperature austenitic, cubic B2 phase and a low temperature, martensitic B19' phase that is monoclinic. The TiNi (B19') and Ti_2Ni phases were identified on the basis of both Scanning Electron Microscopy (SEM) and X-ray Diffraction (XRD) analysis.

3. RESULTS

3.1 XRD Characterization

Shown in Figure 1 are XRD powder patterns for isochronal sintering for 12 h in vacuum at various temperatures. At 800°C, Ni, Ti, B2 (TiNi), Ti_2Ni and $TiNi_3$ peaks were present. No B19' (TiNi) peaks could be distinguished but it is possible that they were present yet masked by other peaks. As the temperature was raised above 800°C the elemental peaks decreased and the intermetallic peaks increased. At 900°C B19' peaks were seen, although the (111) peak at $2\theta=45^\circ$ was not observed until 1000°C. XRD patterns for isothermal sintering at 1000°C for various times were recorded, and after 1h Ni was observed along with $TiNi_3$ and both the TiNi phases, although the B19' (111) peak was not present. As sintering time increased the Ni and

TiNi₃ peaks decreased until at 12h only TiNi₃ was present with TiNi. The 1000°C-6h and 1000°C-12h samples both showed orientation effects. In some orientations the sample exhibited the B19' peak at $2\theta = 45^\circ$ and in others it did not.

Figure 2 shows the XRD patterns for the samples heated at 10 K/min. After 6 hours at 900°C, B19', B2, TiNi₃, Ni and Ti peaks were present. However the sample showed an orientation effect with the B19' (111) peak at $2\theta = 45^\circ$ present in some orientations and not in others. After 6 hours at 1000°C the elemental peaks were no longer observed, and the B19', B2 and TiNi₃ peaks remained. The B19' (111) peak was always present but the intensity variation of this peak with sample orientation was still seen.

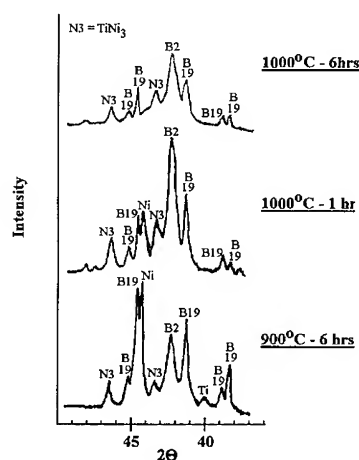
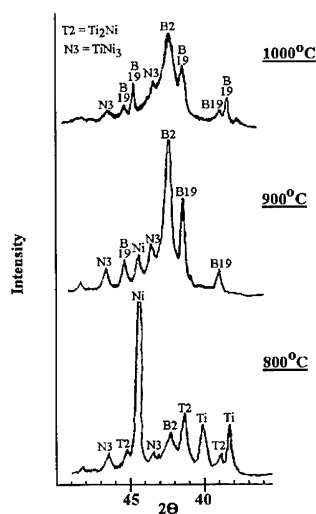


Figure 1: XRD profiles of TiNi powder samples, heated at 5 K/min after isochronal sintering for 12h in vacuum at the specified temperatures. Intermetallic phases are favored above $T_s > 900^\circ\text{C}$ and Single phase TiNi favored for $T_s > 1000^\circ\text{C}$.

Figure 2: XRD profiles of TiNi powder samples, heated at 10 K/min and sintered in vacuum for specified time and temperature. After 6 hours at 1000°C , the material is predominantly TiNi.

3.2 SEM analysis

Porosity was found to vary significantly with sintering temperature. SEM examinations of cross-sections taken at 800°C -12h (Figure 3) found the pores to be much smaller (typically $25\mu\text{m}$) and less interconnected than the 900°C or 1000°C samples. The microstructure was very smooth, i.e. contained no micro-voidage. The contrast in the backscattered mode indicates the different phases: TiNi, Ti₂Ni, TiNi₃, Ni and Ti, with the darkness of the phase corresponding to a larger Ti content. Porosity increased after sintering above 900°C . The 900°C -6h and 1000°C -1h microstructures were very open and contained large interconnected pores typically $80\mu\text{m}$ in diameter (Figures 4a and 4b). Much of the material contained voidage and appeared "sponge-like" in character. This phase had an average composition from EDAX of 49.8 at% Ti and was identified as TiNi. The sample also contained dense, "non-spongy" regions of TiNi along with

small areas of TiNi_3 and Ni particles. The microstructures of the 900°C-24h sample was slightly more connected and continuous than the 6h sample but still contained large pores $\sim 65\mu\text{m}$ in size (Figure 5). In both the 900°C-24h and the 1000°C-12h samples the sponge-like skeletal microstructure had been replaced by denser TiNi regions exhibiting fine voidage. Small regions of TiNi_3 remained but no Ni particles were observed.

SEM analysis of the 10 K/h samples showed that the 1000°C-1h microstructure was slightly more contiguous than the sample heated at the slower heating rate but still contained large pores approximately $50\mu\text{m}$ in diameter (Figure 4b). The sample had no sponge-like microstructure but much of the TiNi phase appeared dendritic in character. Energy Dispersive X-ray Analysis (EDAX) analysis revealed that the sample contained Ti_2Ni , seen in the SEM micrographs as a dark gray phase. This phase was not seen in the slow heating rate samples, nor was a Ti_2Ni peak seen in the XRD pattern although it is possible that it was masked by the larger B19' peaks. EDAX analysis confirmed the presence of TiNi, TiNi_3 and Ni.

4. DISCUSSION

4.1 Densities

The mean green densities were measured at 4.1 g/cm^3 , only about 65% of the theoretical density, 6.44 g/cm^3 . This is due to the comparatively low compaction pressure of 27.5 MPa. This low green density results in a low sintered density. The final sintered densities ranged from 3.5 to 3.8 g/cm^3 , or 54 to 60% of the theoretical density.

Slow heating rate (5K/min)

As the sintering temperature increased, the pore size was observed to increase. The pore size of the 800°C sample was much smaller than the 900°C/1000°C samples ($25\mu\text{m}$ as opposed to $75\mu\text{m}$). Igharo and Wood [3] noted a gradual fall in density with increasing sintering temperature which became dramatic as the temperature was raised to 1000°C. They attributed this to the formation of a transient liquid phase of a eutectic composition (24.5 at% Ni). Although this eutectic temperature is $>900^\circ\text{C}$ the formation of the intermetallic phases from their elemental components is an exothermic reaction and local temperatures could be higher than the furnace temperature. The increase in pore size seen at 900°C is therefore probably associated with the formation of a liquid phase. As proposed by Morris and Morris[4] this large-scale porosity is probably due to the liquid being drawn away by capillary action to fine voids, leaving behind large pores. At 800°C, however, it is probable that the formation reactions did not generate enough heat to melt the constituents and that little formation reaction was occurring due to poor solid state diffusion. SEM examination revealed that many of the samples sintered at 900°C and 1000°C contain a "spongy", skeletal structure with a composition that corresponds to TiNi. Closer examination of this phase showed voids separated by a skeletal network of TiNi. The most likely explanation for this voidage is that this is Kirkendall porosity due to the difference in Ni and Ti diffusivity. As the temperature and sintering time increased the spongy structure in these samples became a denser structure containing fine voids. This is in accordance with the above theory that, as sintering time and temperature increase, a liquid phase is formed that is drawn away by surface tension forces to the surfaces of fine voids. Thus the micro-voidage decreases.

From the SEM micrograph the 800°C-12h sample appeared inhomogeneous with Ti, Ni, Ti_2Ni , TiNi_3 and TiNi present. At 900°C and 1000°C, however, the samples appear well mixed with most of the material present as TiNi. After 24 h at 900°C or 6 h at 1000°C, few Ni particles remained and the sample was mainly TiNi with a few small areas of TiNi_3 . Since TiNi_3 has the smallest Gibbs free energy of all the stable intermetallic phases at 1000°C it is unlikely that this phase could be completely removed by solid-state diffusion.

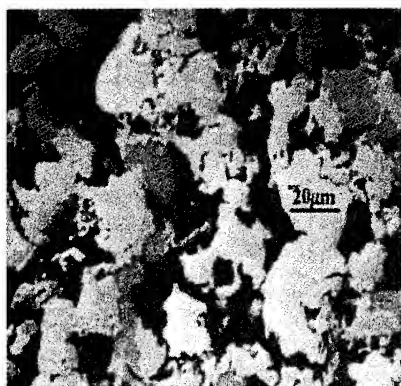


Figure 3: Backscattered SEM micrograph of the microstructure sintered at 800°C for 12 h. No interdiffusion was observed.

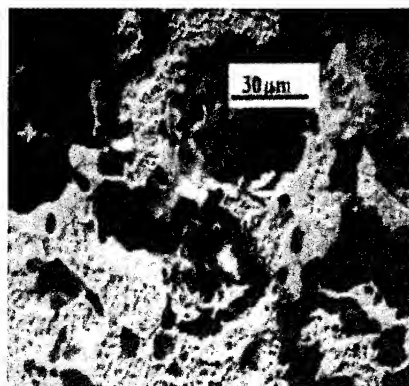


Figure 4(a): Backscattered SEM of the microstructure obtained on heating at 900°C for 6 h. The sample is porous and the sponge like character of the structure can clearly be seen.

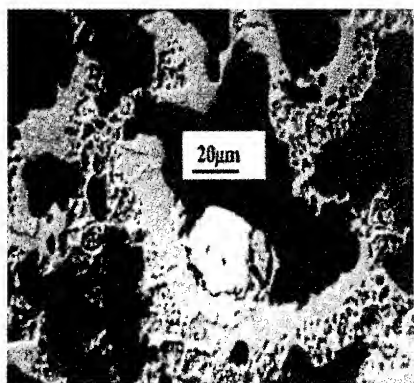


Figure 4(b). Backscattered SEM of the microstructure obtained on heating at 1000°C for 1 h. The sample is very porous with extensive microvoidage is associated with the TiNi phase

High heating rate (10K/min)

There is no evidence of the sponge-like TiNi phase that is present in the slower heating rate samples; however, the phase morphology was dendritic. It is likely that the higher heating rate resulted in greater heat being generated by the exothermic intermetallic formation reactions. More material would thus be melted than at the slower heating rate, leading to a more cast-like TiNi structure. SEM observations and EDAX analysis of the 1000°C-1h sample revealed the presence of Ti₂Ni along with TiNi, TiNi₃ and Ni. The equilibrium Ti-Ni phase does not predict

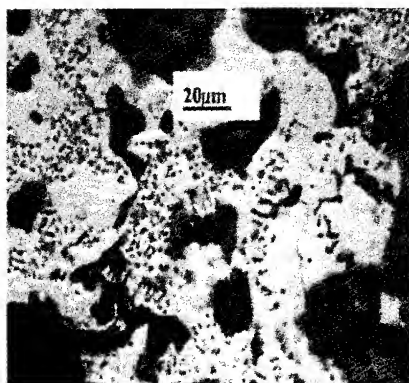


Figure 5. Backscattered SEM of the microstructure obtained on heating at 900°C for 24 h. Most of the material is TiNi but extensive microvoidage is still present.

that Ti_2Ni should exist at 1000°C . This phase was not seen in the slow heating rate samples however, and as the heating rate is raised the system will be increasingly non-equilibrium. However the sample appeared to be well mixed with the majority of the structure being TiNi and after holding for 6h at 1000°C XRD indicated that the Ni had vanished.

These results are in contrast to Zhang's study [6] who achieved mostly TiNi with a few small areas of TiNi_3 after sintering for 5h at 900°C . XRD indicates that the 900°C -6h sample in this study, (10 K/min heating rate), still contains Ni along with TiNi and TiNi_3 . However Zhang's study used initial heating rates of 20 K/min to 600°C and 10 K/min to 700°C and a final heating rate of 2 K/min to 900°C . It is evident from this study that heating rate greatly affects the types of phases formed and the resultant morphology.

5. CONCLUSIONS

At 900°C -24h and 1000°C -6h, heating at 5 K/min, the samples were mainly homogeneous TiNi with little Ni remaining and only small regions of TiNi_3 . The heating rate appears to have a significant effect on both the phases formed and on the resultant morphology. Increasing the heating rate appears to decrease the microvoidage present and at much greater rates might lead to densification through reaction sintering, however raising the heating rate also increases the likelihood of introducing non-equilibrium phases. A more complete discussion will be published in reference [9].

ACKNOWLEDGEMENTS

The authors are grateful for financial support for this project from the U.S. Army under grant no. DAAH04-93-G0213.

REFERENCES

1. G.I. Aksenov, I.A. Drozdov, A.M. Sorokin, D.B. Chernov and Y.A. Atyakshev, "Phase composition and properties of sintered specimens pressed from a nickel-titanium powder mixture", *Sov. Powd. Metall. Met. Ceram.*, Vol. 20, pp. 340-343, 1981
2. Y. Sekiguchi, K. Funami, H. Funakubo and Y. Suzuki, "Study on the hot pressed powder metallurgy of a TiNi shape memory alloy", *J. de Phys.*, C4, Vol 43, pp 279-284, 1982
3. M. Igharo and J.V. Wood, "Compaction and sintering phenomena in titanium-nickel shape memory alloys", *Powder Metall.*, Vol 28, No 3, pp 131-139, 1985
4. D.G. Morris and M.A. Morris, "NiTi intermetallic by mixing, milling and interdiffusing elemental components", *Mater. Sci. Eng. A*, Vol 110, pp 139-149, 1989
5. H. Kuroki, M. Nishio and C. Matsumoto, "Expansion and shrinkage of nickel/titanium mixed powder compacts during sintering", *MRS Int'l. Mtg. on Adv. Mats.*, eds. M. Doyami, S. Somya and R. Chang, Vol 9, pp 629-634, MRS, Pittsburgh, 1989
6. N. Zhang, P. Babayan Khosrovabadi, J.H. Lindenhovius and B.H. Kolster, "Assessment of the duration of time required for conventional Ti-Ni sintering", *J. de Phys. IV*, C4, Vol 1, pp 163-168, 1991
7. G. F. Bastin and G. D. Rieck, "Diffusion in the titanium-nickel system: II. Calculations of chemical and intrinsic diffusion coefficients", *Met. Trans.*, Vol 5, pp 1827-1831, 1974
8. D.M. Sims, A. Bose, R.M. German, "Reactive sintering of nickel aluminide", *Progress in Powder Metallurgy*, eds. C.L. Freeby and H. Hjort, Vol 43, pp 575-596, Metal Powder Industries Federation, Princeton, 1987
9. J.C. Hey and A.P. Jardine, "Shape memory TiNi synthesis from elemental powders", *Mater. Sci. Eng. A*, pp 291-300, 1994

EVOLUTION OF THE R-PHASE TRANSFORMATION TEMPERATURE OF $\text{Ti}_{50}\text{Ni}_{50-x}\text{Fe}_x$ SHAPE MEMORY ALLOYS WITH IRON CONCENTRATION.

R. GÓMEZ*, V. MARQUINA*, R. RIDAURA*, M.L. MARQUINA*, M. JIMÉNEZ*, S. ABURTO*, R. ESCUDERO**, F. MORALES**, D. RÍOS-JARA** AND A. CANALES**.

*Facultad de Ciencias, Universidad Nacional Autónoma de México, 04510 México D.F., México

**Instituto de Investigaciones en Materiales, Universidad Nacional Autónoma de México, 04510 México D.F., México

ABSTRACT

The evolution of the R-phase transformation temperature with iron concentration is studied by Mössbauer spectroscopy (MS), magnetic susceptibility and calorimetric measurements in a series of three $\text{Ti}_{50}\text{Ni}_{50-x}\text{Fe}_x$ samples, with $x = 1, 2$ and 3 . The changes in the Mössbauer spectra, from a single line at room temperature to a quadrupole doublet when the temperature is lowered below 280 K , are related to structural transformations occurring in the system. The temperature changes in the magnetic susceptibility are interpreted in terms of a gap opening characteristic of charge density waves (CDW) formation when the R-phase transformation takes place. The calorimetric measurements show specific heat fluctuations near room temperature in two of the samples ($x = 1$ and 3) whose peaks shift during the cooling and heating cycles.

INTRODUCTION.

The effect that the addition of iron has in the temperatures of the premartensitic (R-phase) and martensitic transformations (T_p and T_M , respectively) of the near-stoichiometric TiNi shape memory alloy, has been extensively studied by different methods¹ in the past years. Most of these studies, however, have been made with 3 at\% substitution of Ni by Fe. In this case, it was reported² that T_M depresses about 100 K more than T_p . However, the clearest indication that the martensitic transformation is actually taking place in this system is through the hysteresis shown by its magnetic susceptibility in the 4 to 200 K temperature interval³. If a smaller proportion of iron substitutes Ni, one would expect that the shift between these temperatures would be smaller. It seemed to us worthwhile to study the way that the observed temperature shift evolves with lower iron concentrations. In this paper we present results of Mössbauer spectroscopy, differential scanning calorimetry (DSC) and dc-magnetic susceptibility in three samples, labeled S1, S2 and S3, according to their iron content ($1, 2$ and 3 at\% , respectively).

EXPERIMENTAL

The TiNiFe alloys were prepared by melting the nominal quantities of Ti, Ni and Fe in an evacuated arc furnace. Homogenization was performed at 1000 °C in an evacuated fused quartz capsule. Calorimetric heating and cooling cycle measurements were performed with a commercial differential scanning calorimeter. The Mössbauer absorbers were obtained by cutting thin slices of the samples with a diamond saw and hand polished until $100\text{ }\mu\text{m}$ thickness was achieved. A heat treatment at 500 °C was done before placing the sample into a holder of a closed cycle helium refrigerator. The Mössbauer spectra were obtained in transmission geometry with a constant acceleration spectrometer, keeping the ^{57}Co source at room temperature. The magnetic susceptibility curves were obtained in a squid susceptometer. First the samples were cooled down to 5 K , then a field of 1000 G was applied and the susceptibility measurements were taken

while heating to room temperature. Later, the samples were cooled down to 2 K with the applied field on to get a complete cycle.

RESULTS AND DISCUSSION

Specific heat fluctuations are observed in samples S1 and S3. In sample S1, the fluctuation occurs around 245 K and the peak shifts about 2 K during the cooling and heating process. Similar results are obtained with S3, except that the fluctuation occurs around 280 K. No specific heat fluctuation was observed in sample S2.

The room temperature and 13 K Mössbauer spectra (MS) of the studied alloys are shown in Figs 1, 2 and 3. As can be seen in those figures the spectra evolve from what seems to be a single line to a quadrupole doublet. No magnetic splitting is observed at any temperature, indicating that the spectral features are due solely to electrostatic interactions. However, during the fitting process with a constrained least squares program it was realized that in samples S1 and S2, good fits could only be attained using two asymmetrical doublets, even at room temperature.

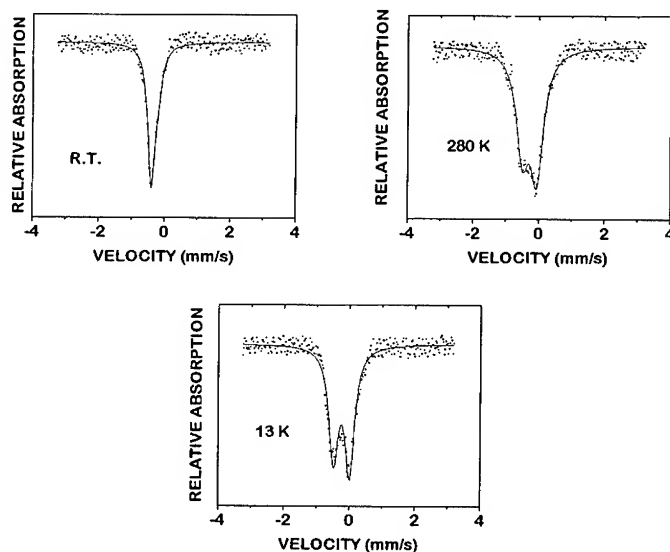


Figure 1. Mössbauer spectra of S1.

It is worthy to recall that electrostatic interactions manifest themselves in a MS through measurable quantities, known as isomer shift δ and quadrupole splitting ΔQ , which are related, respectively, with the electron density wave function at the nuclear site (s and $p_{1/2}$ wave functions) and with the symmetry of the electric field around the nucleus: the higher the symmetry, the lower ΔQ values. In the case of iron, the explicit expressions for these quantities are⁴:

$$\delta = \frac{4\pi}{5} Ze^2 \left(\frac{\Delta R}{R} \right) \left[|\Psi(0)|_a^2 - |\Psi(0)|_s^2 \right] \quad (1)$$

and

$$\Delta Q = \frac{1}{2} e |Q V_{zz}| \left(1 + \frac{\eta^2}{3} \right)^{1/2} \quad (2)$$

where ΔR is the change of the nuclear radius R between the excited and the ground state, $\Psi(0)_{a,s}$ are the electronic wave functions at the absorber and source nuclei, respectively, Q is the quadrupole moment of the nucleus and

$$\eta = \frac{V_{xx} - V_{yy}}{V_{zz}} \quad (3)$$

is the asymmetry parameter, where V_{ii} are the components of the electric field gradient along each of its principal axes, defined in such a way as to have $0 \leq \eta \leq 1$.

Normally, δ is an almost temperature independent parameter and if a sudden change occurs in its value, it is to be associated with a rearrangement of the electronic distribution within the system. On the other hand, the main reasons for changes in the ΔQ values are structural changes that affect the symmetry around the iron atoms.

It can be seen from Table I that both values change abruptly in the three samples, from room temperature to 280 K and then remain essentially constant down to 13 K, so a phase transformation has taken place near room temperature. In sample S3 the quadrupole splitting is due to the R-phase transformation, as it was previously reported³. The presence of a quadrupole doublet, with $\Delta Q_1 \approx 0.2$ mm/s, in the room temperature spectrum of sample S1, indicates that the premartensitic transformation has already taken place. Nevertheless, the magnitude of its quadrupole splitting changes, when lowering the temperature, to a value that is twice as much that of S3, so the transformation in each sample has to be of different nature. This has to be associated with the different shift in T_M and T_p expected with different Fe concentrations. Notwithstanding some evidence presented further down, we associate this change in ΔQ with the martensitic transformation; that is, due to the low iron concentration, there is only a minute shift in T_M . Actually, differential scanning calorimetry measurements show a specific heat fluctuation around 280 K in S1, in accordance with the Mössbauer results. However, in order to corroborate this assumption, calorimetric measurements to precisely determine the enthalpy change, δH , during this transformation are in process.

TABLE I

	RT	280 K	100 K	13 K
δ_1	-0.14	-0.16	----	-0.09
ΔQ_1	0.21	0.43	----	0.48
δ_2	-0.21	-0.08	-0.05	-0.08
ΔQ_2	0.16	0.25	0.23	0.24
δ'_2	not present	not present	0.39	0.38
δ_3	-0.18	-0.05*	-0.03	-0.03
ΔQ_3	0.0	0.23*	0.25	0.24

The units are mm/s. All the δ values are with respect to iron.

*In this only case, the temperature was 260 K

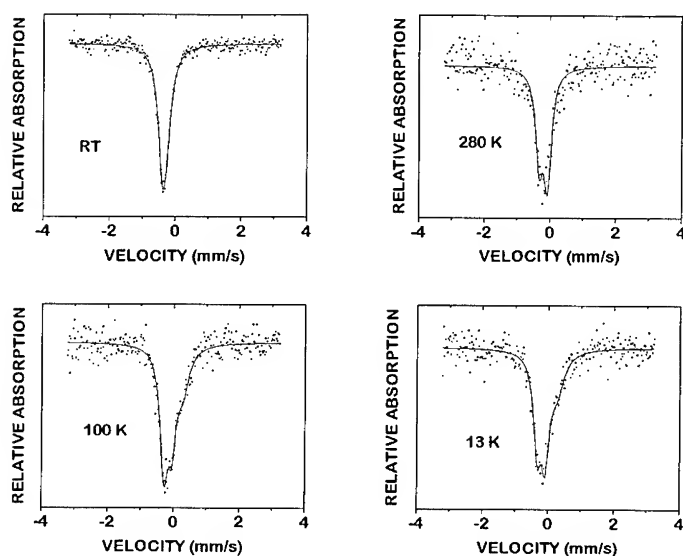


Figure 2. Mössbauer spectra of S2.

Instead of confirming this interpretation, the results obtained with the sample S2 make it more confusing. In this case, the quadrupole doublet is not so clearly resolved (see Fig. 2) and, besides, an additional single line with a comparatively large positive isomer shift value appears when the temperature is lowered. The Mössbauer parameters of this line have nothing to do with the value that can be associated with the CICs (B2) parent structure. On the other hand, DSC does not show any specific heat fluctuation at any temperature. This is not the first time that an anomalous behavior in the MS is seen in a 2 at% sample⁵. One possible explanation would be that, for unknown reasons, it is more difficult to have an homogeneous iron distribution when this percentage is used, favoring the formation of other stable phases (i.e.: $\text{TiNi}_{2-x}\text{Fe}_x$), in such a way that only a small fraction of the sample goes through the premartensitic transformation. However, this would not explain the appearance of the singlet at low temperatures. At present we do not have a convincing explanation for this feature.

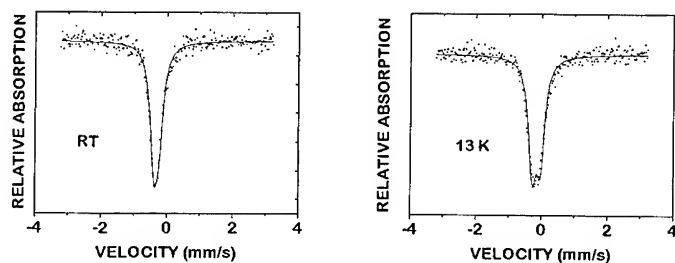


Figure 3. Mössbauer spectra of S3.

The dc-magnetic susceptibility curves, shown in Fig. 4, confirm the facts observed in our Mössbauer and DSC measurements. In sample S3 there is a clear hysteresis in the heating-cooling cycle between 4 K and 200 K, but S1 and S2 show no hysteresis at all. Several important differences exist between the susceptibilities of the three samples. Whereas in S2 and S3 the susceptibility χ shows a regular behavior near room temperature, in S1 the behavior is rather chaotic in the same temperature region. On the other hand, in S3 there is a sudden drop around 250 K and the sharp rise observed in S1 and S2 at low temperatures is absent. The chaotic behavior of χ could be due to an interplay between the effects associated with the martensitic phase and the R-phase. More measurements, at higher temperatures, are necessary in order to determine if the magnetization of the other two samples also show a sudden drop. In any case, the observed drop in S3 may be associated with an energy opening gap, that drastically diminishes the density of electronic states at the Fermi surface, with the concomitant drop in the Pauli susceptibility χ_P . On the other hand, the magnetic hysteresis observed in sample S3 can be associated with an irreversible transformation, most likely due to the martensitic phase transformation.

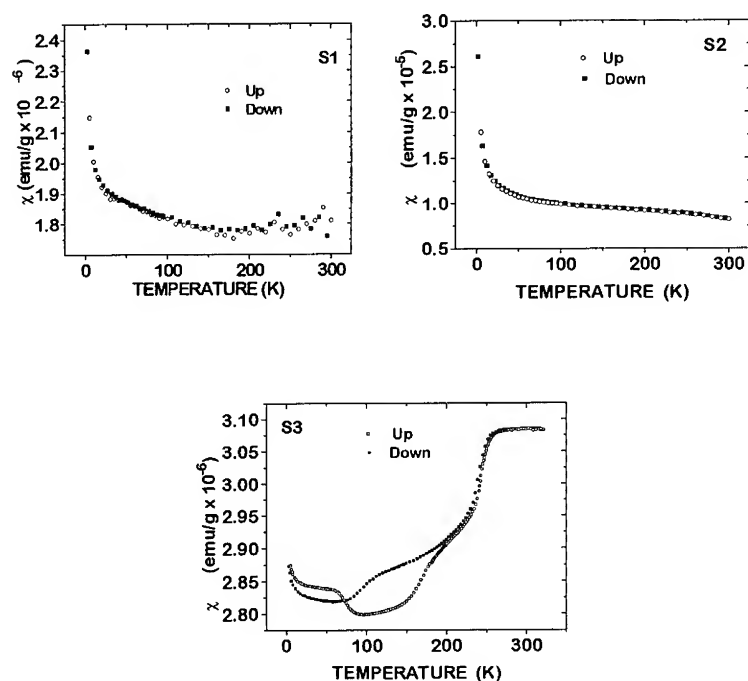


Figure 4. dc-magnetic susceptibility of the three samples.

CONCLUSIONS

Based in the evolution of the Mössbauer spectra of the $\text{Ti}_{50}\text{Ni}_{50-x}\text{Fe}_x$ system, with $x = 1$ and 3 , we have established that a phase transformation is taking place in these alloys near room temperature. However, the transformation is of different nature: in sample S3 the observed features are associated with a transition from the ClCs (B2) cubic phase to the R-phase, whereas in sample S1 the observed change is to be associated with the transition from the R-phase to the martensitic phase. The reason for the different behavior is related to the fact that, at low iron concentrations, the shift between T_p and T_M is very small.

On the other hand, the sharp drop of the dc-magnetic susceptibility of sample S3 near room temperature, clearly reveals the opening of a gap in the electronic density of the Fermi surface, characteristic of charge density wave formation, that we associate with the R-phase transformation, in accordance with our Mössbauer results. Even though the behavior of the dc-magnetic susceptibility differs from sample to sample, we believe that those differences are due to an interplay of effects caused by the R-phase and the martensitic phase. In order to clarify this situation, measurements of magnetic susceptibility at higher temperatures are necessary.

Finally, the anomalous behavior of the Mössbauer spectra of the sample with $x = 2$ does not allow us to arrive to any clear conclusion. We believe that, in this case, phases other than the $\text{Ti}_{50}\text{Ni}_{48}\text{Fe}_2$ phase are present in the alloy, that are responsible for these anomalies.

ACKNOWLEDGMENTS

The authors wish to thank R. Gómez Aíza, C. Munive and F. Silvar for their invaluable help. This work is supported by Consejo Nacional de Ciencia y Tecnología, México, project 1216-E9203, by Dirección General de Asuntos del Personal Académico, UNAM, México, projects IN102693 and ES102993 and by Organization of American States.

REFERENCES

1. M.B. Salamon, M.E. Meichle and C.M. Wayman, *Phys. Rev. B* **31**, 7306, (1985).
2. M. Matsumoto and T. Honma, *Trans. Jpn. Inst. Met. (Suppl.)* **17**, 199 (1976).
3. See, for example, M.L. Marquina et al., *Matter. Char.*, **32**, 189, (1994) and references there in.
4. N.N. Greenwood and T.C. Gibb. *Mössbauer Spectroscopy*. (Chapmann and Hall Ltd, London, 1971) p 308.
5. Y. Yoshida. Private communication. See also Y. Yoshida and F.E. Fujita. ICAME 93 book of abstracts, Vancouver, Can., (1993).

PART XI

Shape Memory Alloy Applications

PRESENT AND FUTURE APPLICATIONS OF SHAPE MEMORY AND SUPERELASTIC MATERIALS

T.W. DUERIG

Nitinol Devices and Components, Fremont, CA, 94539 USA

ABSTRACT

The utility of superelastic Ni-Ti alloys in the medical industry has been rather dramatically demonstrated in recent years. A great number of devices are now in production, and still others are staged to enter production during the next few years. This surge in interest from the medical community stems from an increased acceptance of Ni-Ti because of its biocompatibility, advances in micromachining techniques and trends towards less-invasive surgical techniques. In addition, there are a variety of new developmental concepts that will have a major influence on this and other markets during the next 5 years of commercialization. This review will highlight many of the properties of Ni-Ti by illustration in a variety of recent medical applications, and then discuss some of the newer developmental concepts. Medical applications that will be presented here include guidewires, laparoscopic surgical instruments, implants, stents, retrieval baskets, and bone anchors. Some of the new concepts and capabilities that are reviewed include microvalves made from thin films, high temperature alloys, fatigue resistant composites, and robotic actuators with tactile feedback.

INTRODUCTION

Thermoelastic materials are able to adjust their properties and shape according to changes in their environment: specifically, changes in applied stress and temperature. This capability to sense and react to change has often caused these materials to be dubbed a *smart material*. Ni-Ti, or Nitinol, alloys are the most important of the thermoelastic smart materials, able to change shape by strains greater than 8% and to adjust constraining forces by a factor of 5 times. The scientific foundations for these "smart" effects have been well-known for over 20 years. The ability to engineer successful devices using these effects, however, has been quite another story. The early product development history of Ni-Ti has been full of failures and disappointments. It seems that the materials were so smart, they out-smarted the designers. The infamous reference to shape memory as "*a solution looking for a problem*"¹ has finally been shaken. Though success has not come from the directions originally expected, few can doubt that the technology has now come of age. Success has largely come about by focusing on medical applications of Ni-Ti taking advantage of its superelastic properties.

Below, some of the more recent applications of Ni-Ti alloys are reviewed. Many older applications, such as pipe couplings, fasteners, and many actuator applications have been often reviewed elsewhere¹⁻⁵ and are not included in this review. Here we will concentrate first on the medical field that has recently had such a profound effect on the Ni-Ti engineering field. It will be evident to the reader that these devices are almost entirely superelastic in nature. After this, we will review some of the newer concepts and capabilities, and thus provide more of a look forward rather than over our shoulders.

MEDICAL DEVICES

As already stated, most successful medical devices take advantage of the superelastic properties of Ni-Ti. Some use shape memory for deployment, but in nearly all cases the choice of material is primarily dictated by the alloy's superelasticity attributes once at body temperature. Superelasticity refers to the ability of a material to reversibly transform from austenite to martensite when a stress is applied. The resulting stress-strain behavior is

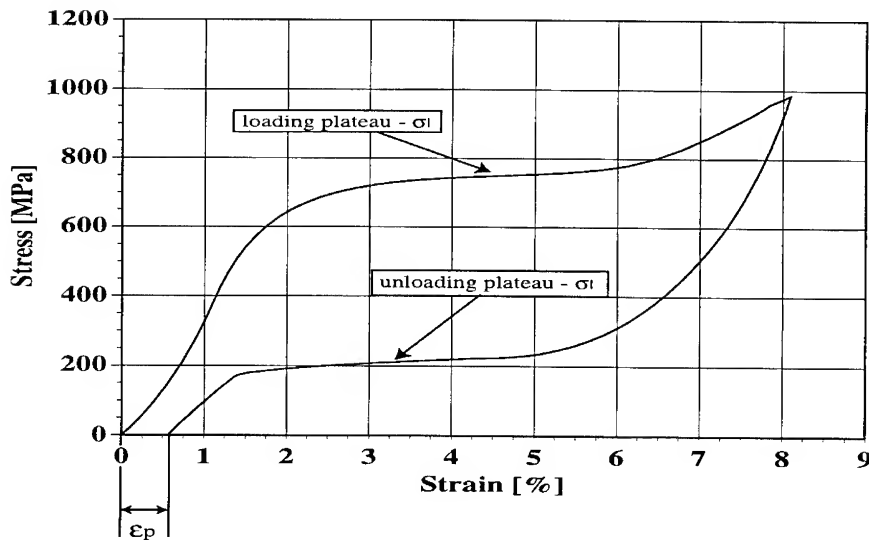


Figure 1: Superelasticity in a Ti-50.8 at. % Ni alloy pulled in tension. Shown are the design parameters: loading plateau- σ_l , unloading plateau- σ_u , permanent set- ϵ_p .

characterized by plateaus during both loading and unloading (Figure 1). In cases, the plateau may be somewhat ill-defined, but should in all cases exhibit at least an inflection point during unloading. As shown on Figure 1, the effect is parameterized by its loading stress, unloading stress, hysteresis (by implication), and permanent set. Strains of 10% can be nearly fully recovered, with the stress induced martensite responsible for approximately 8% and conventional elasticity for the balance. Superelastic properties can be observed at temperatures above A_r and below M_d . In fact full superelastic effects are found over an even narrower range—typically only 20-40°C in width. Further information concerning the origin and characteristics of the effect has been presented elsewhere^{6,7}.

At first it may not be clear why superelastic properties are an indication of a “smart” material, and in fact the term may be poorly applied—after all, any material dumbly obeys the laws of nature as programmed by its hopefully smart human designers. Still, two important features should be considered. First, the material reversibly alters its crystal structure and shape in order to relieve applied stresses. Secondly, and often neglected, is that the stress applied by a constrained superelastic device will rise and fall with temperature in a linear fashion, thus acting as a temperature sensor and actuator.

A superelastic spring does not follow Hook’s Law, but in fact delivers a constant stress when deformed between 1.5% and 7%. This can be very important in the field of medicine since one can engineer a device to deliver a certain, physiologically ideal stress and rely on the fact that the stress will be held constant. Prototypical of this type of application are orthodontic archwires, which also happen to be one of the first medical applications^{8,9}. Here the archwire is constrained while being installed into brackets mounted on the mal-aligned teeth. During treatment, the arch struggles to restore the teeth to their proper location, but always applies forces according to the unloading plateau of the arch’s stress-strain curve. This maintains a therapeutically ideal force while eliminating adjustments, causing the patient less discomfort and accelerating treatment. Superelastic archwires were researched in the mid-1970’s, and have been in widespread use since the early 1980’s. They are now an appliance used by virtually all orthodontists.

A second key property of Ni-Ti alloys is their biocompatibility. In 1975, Simon proposed

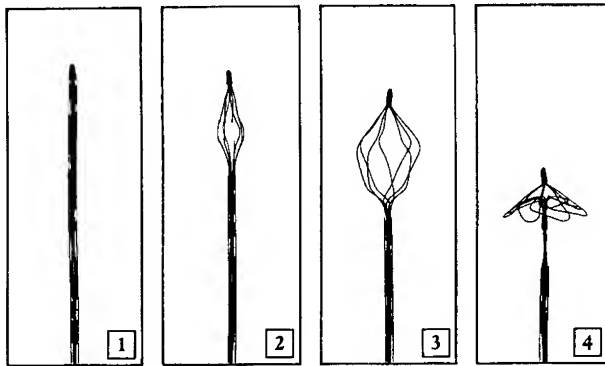


Figure 2: The Simon filter is inserted through a 2.3mm catheter (Frame 1), then thermally expands to form a filter used to prevent recurrent pulmonary embolism. Frame 6 (far right) shows the fully deployed filter from an end view.

using Ni-Ti for a *vena cava* filter (Figure 2), to break-up blood clots (thrombus) in the *vena cava*¹⁰ which can lead to life threatening pulmonary embolism. This application has now been approved by the FDA; very significant considering this is a permanent, critical, Class III implant. To date, nearly 10,000 installations have been completed. The filter is installed by sliding it forward through a 7 French (2.3 mm) ID catheter to the intended deployment location, then de-constraining it, allowing it to expand into place. This is an example of a device that utilizes both the shape memory and superelastic properties of the alloy. The A_f temperature is chosen so that the filter is martensitic at room temperature but superelastic once installed in the *vena cava*. Cool saline solution is flushed through the catheter during the installation procedure to keep the filter martensitic until release. This reduces the force of the filter against the catheter wall and reduces the force needed to slide the filter within the catheter. Once installed, its superelastic properties keep a constant stress against the vessel walls despite cyclical "breathing" of the vessel. During a two year clinical trial period involving 273 patients, there was a 91% success rate, which is considered excellent.

Still other applications take advantage only of the large springback strain afforded by superelastic Ni-Ti. One of the best examples of these is the bone anchor shown in Figure 3, used to re-attach torn ligaments to bone in the shoulders and knees¹¹. The device consists of a suture, a titanium tip, and superelastic Nitinol wires curved into a tight "C"-shape in its equilibrium state. The operative site is exposed, a small hole is drilled into the soft marrow of the bone, and the anchor is "injected" through the hole. The hard surface of the bone causes the anchor to temporarily straighten during passage, but it is again allowed to spring back to its equilibrium shape once entering the softer marrow of the bone. After springback, the anchor has locked itself underneath the hard bone surface much like a normal household moly bolt. The sutures are then used to tie the ligaments in place, and bone then grows over the operative site. The implant is again permanent. This product has dramatically shortened recovery periods with respect to traditional procedures involving large stainless steel screws.

The quickly growing field of laparoscopy involves performing operations through very small ports into the body called trocars and cannulae. Obviously the advantages are that the operation can be far less invasive than open procedures. The field requires, however, highly specialized and complex instruments in order to pass through a narrow cannula yet be able to perform tasks such as gripping, cutting, retracting, viewing, etc. The utility of superelasticity in the design of such instruments was recognized as early as 1981¹². In what seems to be the first such device, an endoscope was proposed that used a superelastic member to bend the tip of an optic fiber to right angles with respect to the cannula itself. Now, there are a great variety of instruments using superelasticity to articulate grasping ends¹³, to grasp sutures¹⁴, steer endoscopes¹², and to

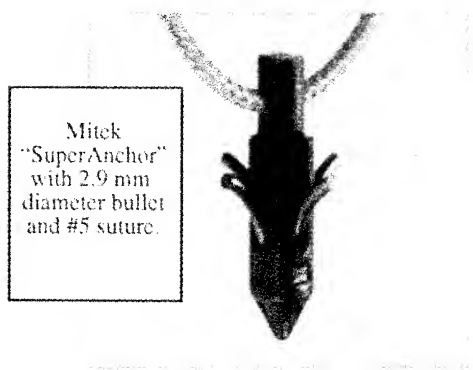


Figure 3: The bone anchor uses tightly curved superelastic Ni-Ti wires to lock itself beneath the hard mantle of the bond, anchoring a suture used to tie down torn ligaments.

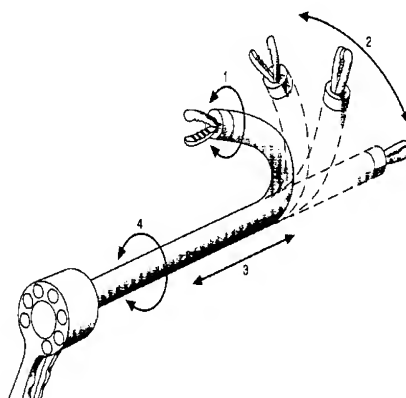


Figure 4: Surgical graspers use Ni-Ti tube and wires pre-shaped into a curved configuration to articulate away from the axis of the laparoscopic cannula.

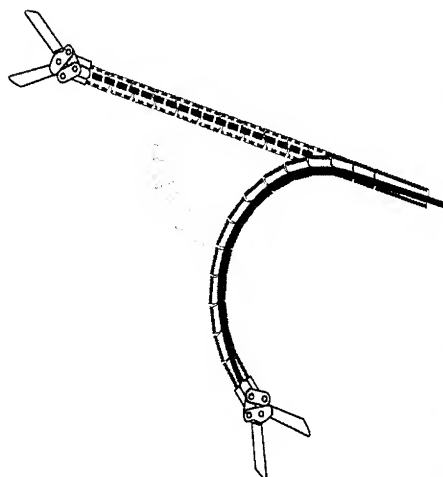


Figure 5: Retractor uses programmed stainless steel segments to accomplish articulation after passing through the cannula, but employs a stainless steel wire to maintain the normally-straight configuration of the instrument.

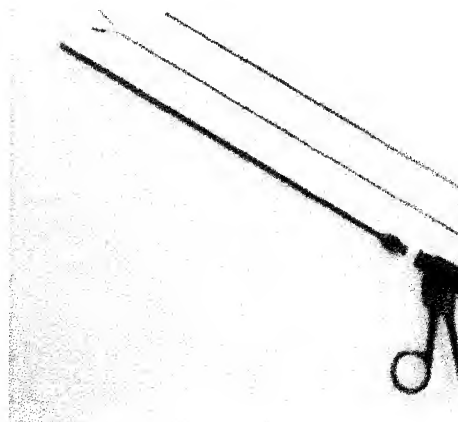


Figure 6: The great flexibility of Ni-Ti allows this grasper to open and close without employing hinges or other complex moving parts. The instrument can be easily dismantled and cleaned.

articulate staplers away from the cannula axis¹³. Figures 4 and 5 show typical examples of such articulated instruments. It is interesting to note that these two examples show similar functions achieved in opposite ways. The instrument in Figure 4 is articulated when the superelastic member is allowed to springback to its austenitic structure and shape. Figure 5

shows an instrument with a normally straight wire used to return the device to a straight configuration to allow insertion and withdrawal through the cannula—it is therefore articulated in its martensitic state.

Superelasticity also allows one to improve upon “hingeless” instruments, allowing convenient and thorough cleaning and paving the way for instrument re-use.¹⁵ Figure 6 shows such an example. Here a set of Ni-Ti graspers is closed by advancing a tube around the outside, thus constraining the normally-open jaws. Stainless steel instruments such as this have been on the market for many years, but Ni-Ti offers a substantially increased jaw opening. The instrument shown in Figure 6 can be very quickly disassembled into components each one of which has no moving parts or narrow nooks and crannies which would make the instrument difficult to clean. The graspers shown in Figure 6 also highlights another advantage of Ni-Ti. The grasping jaws in Figure 6 close with a fixed force. This force can be adjusted to prevent severe damage to tissue, and allowing a more “physiologically correct” squeeze. Though somewhat difficult to quantify, many surgeons have confirmed the value of this physiological feel.

Another feature of superelasticity is its extreme resistance to kinking.¹⁶ This has been the key attribute making Ni-Ti guidewires successful since the mid-1980's. Now, they would have to be considered the standard of the industry. Their advantage over conventional stainless steel is derived from the fact that they can be passed along very tortuous vessels without kinking, without undue frictional effects and damage to the vessel, and can thus be steered more easily by the surgeon. Several new angioplasty devices are now appearing which combine kink resistance with large elasticity. For example, wire baskets are being used to capture and retrieve kidney stones (Figure 7).

Still another use of Ni-Ti's kink resistance brings us back to surgical instruments. Kinking has long been the bane of traditional very long and small diameter instruments. Figure 8, however shows a small grasper with a diameter of only 1 mm. The entire instrument can be passed through tortuous passages without difficulty. This particular instrument uses a superelastic actuation wire within a superelastic tube. Of course the outer sleeve could be made from helical winding of stainless steel, much as a bicycle brake cable, but such an approach would lead to an instrument that is very difficult to clean and hermetically seal to a cannula.

Superelastic microtubing¹⁷⁻¹⁹ has just become available within the last 2 years, and is the recipient of great interest by the field of angioplasty. Until now, a guidewire has been used to lead the way for a subsequently inserted catheter. Now that superelastic tubing is available,

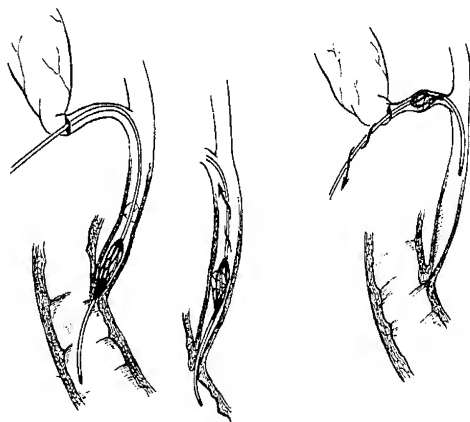


Figure 7: Ni-Ti superelastic wire is used to make a kink-resistant basket, passed through a 4 French catheter, then expanding to capture kidney stones.

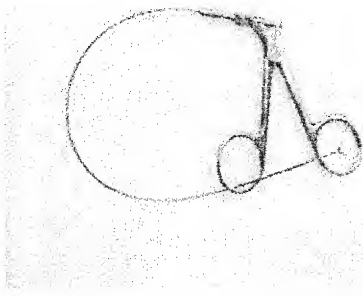


Figure 8: A superelastic wire inside a superelastic microtube is used to actuate a 1 mm diameter grasper. Normal materials could be used as well, but the instrument would be highly prone to kinking, which would disable its function.

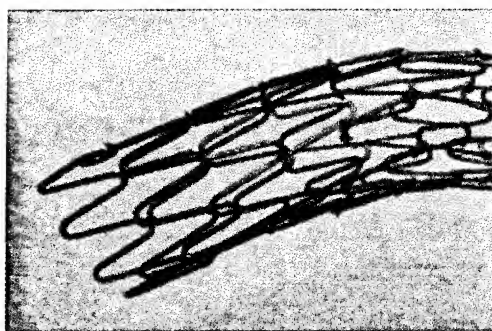


Figure 9: Stents of various configuration are used in a variety of procedures to open and maintain lumens. Some stents are made from wire (left), others are cut from sheet or tubing.

there is a great deal of activity focused on devising catheter products capable of being pushed directly into tortuous blood vessels. At the time of writing, no products are currently on the market using such concepts. Still confidence remains very high in the industry that this process simplification will take place.

Certainly one of the most interesting new applications of Ni-Ti is as stents. A stent can be defined as an object used to hold open a lumen. The lumen may be a blood vessel, a bile duct, the esophagus, etc. For example a cardiovascular stent can be used to maintain the lumen of a cardiac artery subsequent to angioplasty (reopening of stenosis). Two such devices are shown in Figure 9. Superelasticity in this case allows the stent to "breathe" with the artery, and apply a physiologically correct force against the vessel wall. It also allows a large stent to be delivered through a small catheter. Again deployment can take place via superelasticity or via the shape memory effect. Currently available stents have an A_f temperature between room temperature

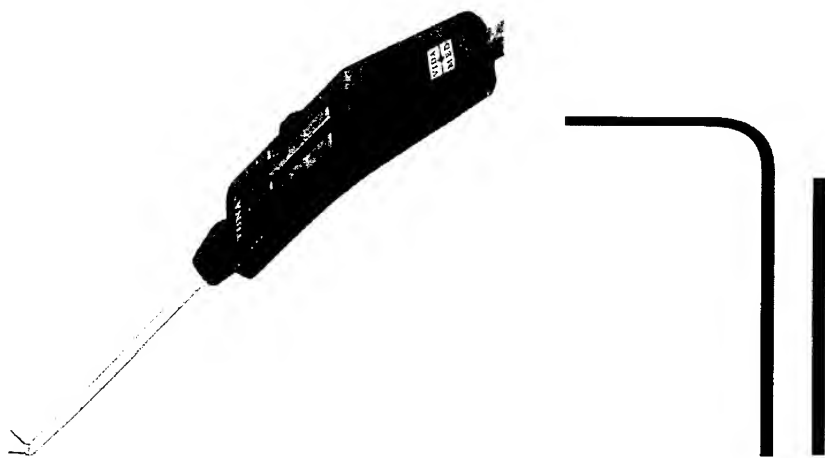


Figure 10: An instrument used to electrocauterize the prostate gland deploys two superelastic wires perpendicular to the axis of the instrument through tightly curved channels. The full instrument is shown on the left and a schematic representation of the bullet tip is shown on the right, with one wire deployed and the other withdrawn.

and body temperature and are expanded using body temperature. Af is generally controlled to provide a physiologically correct force against the lumen wall.

Another recent superelastic instrument is used for the transurethral ablation of prostatic tissue using two Ni-Ti wires to deliver high frequency radiation directly into the prostate (electrocautery). The advantage of Ni-Ti is that the wires can be deployed perpendicular to a small diameter cannula through which the instrument passes (Figure 10). Normal metals would exit the tip with a distinct curvature, and fail to penetrate the prostate tissue.

A variety of orthopaedic implants exist which take advantage of still another attribute of superelasticity: physiological, or mechanical compatibility with natural tissue. Considerable work has been done in Russia on bone implants for maxillofacial surgery, spinal, and orthopaedics²⁰. One key to successful bone implantation is to achieve a high degree of bony ingrowth. It has been found that this does not readily occur when rigid implants are used which do not flex and stress the healing interface to natural tissue. Ni-Ti has been found to form a tissue-implant interface with much greater elastic continuity than other metals. The result is that the interface is stressed during healing and superior bony in-growth is observed. Implants made from porous Ni-Ti have been found to further improve the mechanical compatibility of the interface. These implants are made by a combustion synthesis technique resulting in densities of approximately 50%. The porosity and high compliance appear to make this an ideal bone implant material.²¹

Any review would be remiss in leaving out superelastic eyeglass frames, which are not only a medical device, but without doubt the most commonly seen application for shape memory alloys. Advertised in the USA under the name Flexon[®] these frames have become the quality and performance standard of the industry in just 5 years. Well over one million superelastic frames have been sold in the USA alone. The frames are known for their near indestructibility, but are even more desirable because of their comfortable fit. Small fit problems with normal metal frames lead to discomfort, but with Ni-Ti, the forces are always in the comfortable range—even when the fit is poor, the pressure against the temple is consistent, firm and gentle. One should also note that Ni-Ti frames are welded, brazed, and plated—all operations once thought to be very difficult. In this sense too, eyeglass frames are truly a pioneering application.

Although the large majority of medical applications are superelastic in nature, there remain some classic shape memory applications. Perhaps the best known is the steerable catheter. Conventional catheters are inserted over a guidewire which is passively pushed through meandering vessels. Prototype devices exist, however, which allow active steering via a series of electrically activated shape memory actuators.²² Many versions of this device have been proposed and prototyped, but despite a flurry of very recent activity, there are no devices marketed today. A second new shape memory device is a removable cardiovascular stent (Figure 12). This device is expanded by traditional balloon catheterization, but unlike the superelastic stents, this device is fully martensitic during deployment and in use. Upon heating, the stent will shrink again, allowing easy removal.²³

THE FUTURE

Certainly one of the most interesting new technologies to interface with shape memory has been that of thin films. Films can be made by sputtering, laser ablation²⁵, or by vapor deposition using targets of pre-alloyed Ni-Ti²⁴. Such films are typically amorphous when deposited, but display bulk material shape memory properties after a short crystallization anneal²⁶. Films have been "micromachined" to form actuators²⁷ typically 10 microns in thickness and a millimeter on each side. The first application for such an application is in microvalves (Figure 11). To date, such valves have diameters in the 5-10 mm range. This is certainly small compared to competitive technologies, but by no means represents the limit of the technology. Valves in the sub-millimeter range are certainly possible. Such valves are being studied in the construction of small medical robots, able to travel through and inspect gastrointestinal systems and ultimately even smaller passages²⁸. Still another potential thin film application is for steerable catheters, using three or more thin film strips deposited along the length of microtubing. Actuation of

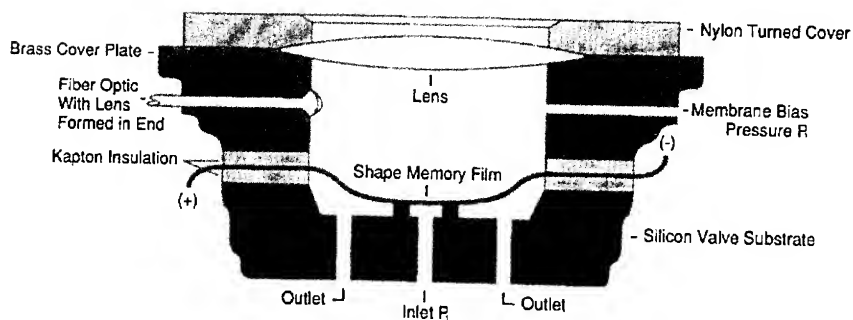


Figure 11: Thin films are used to construct microvalves used to control pneumatic devices on smaller scales than possible with other technologies. This particular device is shown in the closed state, and is actuated optically.

selected strips would cause the catheter to bend on command.

Rapidly solidification techniques have also been used to produce "thin" Ni-Ti strips. Though a great deal of experimental work has been done during the past 10 years, it is notable that at least one "commercial" application has now been developed. 30 micron thick strips of Ni-Ti-Cu have been incorporated into an optical switch with a response time of 8 milliseconds. It is far too early to know if the application will be commercially acceptable, but nevertheless it represents a breakthrough.²⁹

The resistance of Ni-Ti alloys exposed to strain controlled fatigue is known to be substantially greater than conventional alloys. This appears to be the case both in the superelastic temperature regime, and in the martensitic phase. This opens a rather large panorama of applications that really do not involve the shape memory effect *per se*. One example that is being seriously studied is again medical in nature: electrical leads for heart

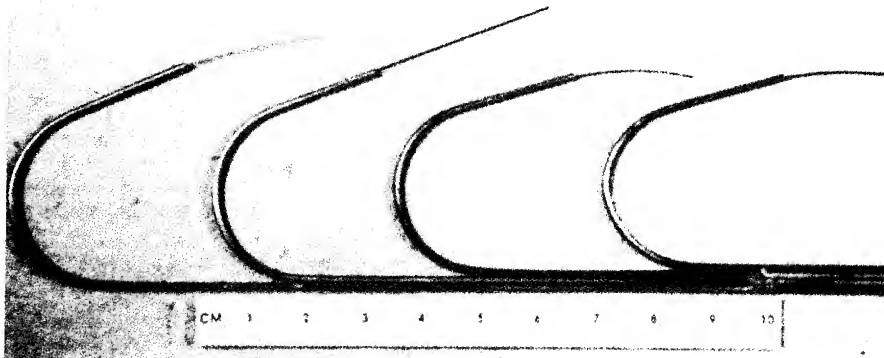


Figure 12: EDM electrodes made from various materials exiting a curved feed tube illustrate the advantages of Ni-Ti: from left to right are brass, Ni-Ti, copper and tungsten.

making it difficult to rely on an initial calibration for resistance and the volume fraction of martensite.

The maximum M_s temperature achieved in Ni-Ti binary alloys is 100°C. For many years, scientists have searched extensively for ways to increase this. Until just two years ago, the only alloys showing hope were extremely expensive: Ti-Pd-Ni and Ti-Pt-Ni alloys. Work on the Cu-Al-Ni and Ni-Al systems had been extensive, but both suffered from severe thermal stability and ductility problems. Recently, however, two new systems are showing a great deal of promise: Ni-Ti-Hf and Ni-Ti-Zr³³. It appears that transformation temperatures of over 300°C are possible³⁴. It is too early to know what the cost of the alloys will be, and if other properties will be as good as the binary alloys, but first indications are positive^{35,36}. There are some early indications that work production and recovery forces may be much lower than one would hope, but still, these alloys may well open up new vistas for application, particularly for automotive applications. Until now, automotive electrical actuators have been extremely interesting on the surface, but for the most part impossible due to the possibility of self-actuation on a hot day.³⁷ Similarly, circuit breakers using shape memory elements have been impossible because the low actuation temperature cause actuation at lower current levels on warm days. In both cases, it is felt that M_s temperatures of at least 160°C, and preferably 200°C are necessary.

SUMMARY

A sampling of recent and future shape memory applications and capabilities have been presented. Many others could have equally well been mentioned. Tennis racket strings have been tested in China and the USA claiming performance superior to existing string materials. Plugs have been strategically inserted in other metals to act as crack stoppers. A non-explosive release bolt has now been used to release a satellite in space. A variety of damping applications are being examined including such ambitious projects as railroad wheel tires and damping mechanisms for suspension bridges. Prototype piping in nuclear reactors has been wound with pre-stretched Ni-Ti wire, which has then been thermally recovered, leaving very high compressive stresses in the pipe. Brassiers and telephone antennae remain two of the highest volume applications worldwide. Medical applications are leading the way at the present time, but as manufacturing methods are perfected and costs reduced, we should expect to see more and more products in these other markets.

REFERENCES

1. L. McDonald Schetky, *Scientific American* 241, 74 (1979).
2. T.W. Duerig, *Mater. Sci. Forum* 56 (1990) 679.
3. K. Melton: *Shape Memory Materials '94* (Y. Chu and H. Tu, eds.) Inter. Academic Pub., (1994) 523.
4. *Engineering Aspects of Shape Memory*, (T.W. Duerig et al, eds.) Butterworth-Heinemann, Boston (1990).
5. Y. Suzuki: *Titanium and Zirconium* 30(4), (1982), 185.
6. T.W. Duerig and R. Zadno: *Eng. Aspects of Shape Memory Alloys* (T. Duerig, et al., eds) Butterworth-Heinemann, Boston (1990) 369.
7. S. Miyazaki and K. Otsuka: *Met. Trans. A* 17, (1986) 53.
8. K. Satanabe: *J. Dental Engineering* 23(6), (1982) 47.
9. R. Sachdeva and S. Miyazaki: *Eng. Aspects of Shape Memory Alloys* (T. Duerig, et al., eds) Butterworth-Heinemann, Boston (1990) 452.
10. M. Simon: *Blood Clot Filter*, US patent 4,425,908 (1984).
11. L.M. Wolford and D.A. Cottrell: "The Mitek Mini Anchor in Maxillofacial Surgery", to be published in *Proc. of Shape Memory and Superelastic Technologies (SMST)*, (A.R. Pelton, T.W. Duerig and D. Hodgson, eds.) (1995).
12. Endoscope, Japanese patent application 56-129791 (1981).
13. P.P. Poncet and R. Zadno: "Applications of Superelastic Ni-Ti in Laparoscopy", to be

- published in Proc. of Shape Memory and Superelastic Technologies (SMST), (A.R. Pelton, T.W. Duerig and D. Hodgson, eds.) (1995).
14. A. Melzer and D. Stöckel: "Performance Improvement of Surgical Instrumentation Through the Use of Ni-Ti Materials", to be published in Proc. of SMST, (A.R. Pelton, et al. eds.) (1995).
 15. A. Melzer, et al.: Endoscopic Surg. and Allied. Tech. 2(1) (1994) 77.
 16. J. Stice: Eng. Aspects of Shape Memory Alloys (T. Duerig, et al., eds) Butterworth Heinemann, Boston (1990) 483.
 17. A.R. Pelton, et al.: "Experimental and FEM Analysis of the Bending Behavior of Superelastic Tubing" to be published in Proc. of SMST, (A.R. Pelton, et al. eds.) (1995).
 18. J.L. Proft, et al.: "Superelastic and Shape Memory Ni-Ti Microtubing", to be published in Proc. of SMST, (A.R. Pelton, et al. eds.) (1995).
 19. H. Horikawa, et al.: "Superelastic Performance of Ni-Ti Thin Tubes" to be published in Proc. of SMST, (A.R. Pelton, et al. eds.) (1995).
 20. Y. Zhuk: Advanced Medical Applications of Shape Memory Alloy in Russia, Tetra Consult, Moscow (1994).
 21. S.A. Shabalovskaya, et al.: "Porous Ni-Ti: A New Material for Implants and Prostheses", to be published in Proc. of SMST, (A.R. Pelton, et al. eds.) (1995).
 22. P. Dario and M.C. Montesi: "Shape Memory Alloy Microactuators for Minimal Invasive Surgery", to be published in Proc. of SMST, (A.R. Pelton, et al. eds.) (1995).
 23. J.E. Bramfitt and R.L. Hess: "A Novel Heat Activated Recoverable Temporary Stent (HARTS System)", to be published in Proc. of SMST, (A.R. Pelton, et al. eds.) (1995).
 24. A. D. Johnson: J. Micromech. Microeng. 1 (1991) 34.
 25. K. Ikuta, et al.: "Laser Ablation of Ni-Ti Shape Memory Alloy Thin Film", to be published in Proc. of SMST, (A.R. Pelton, et al. eds.) (1995).
 26. S. Miyasaki, K. Nomura and He. Zhirong: "Shape Memory Effect and Superelasticity Developed in Sputter-Deposited Ni-Ti Thin Films", to be published in Proc. of SMST, (A.R. Pelton, et al. eds.) (1995).
 27. A.D. Johnson and J.D. Busch: to be published in Proc. of SMST, (A.R. Pelton, et al. eds.) (1995).
 28. C.A. Ray, et al.: Mat. Res. Soc. Symp. Proc. 276 (1992) 161.
 29. A.V. Shelyakov, et al.: "Optical Devices based on Shape Memory Effect for Signal Processing", to be published in Proc. of SMST, (A.R. Pelton, et al. eds.) (1995).
 30. J.S. DeFilippo and E.G. Adamski: "Electrical Discharge Machining Utilizing Smart Electrodes", to be published in Proc. of SMST, (A.R. Pelton, et al. eds.) (1995).
 31. M. Mertmann, E. Hornbogen and K. Escher: Shape Memory Materials '94 (Y. Chu and H. Tu, eds.) Inter. Academic Pub., (1994) 556.
 32. D. Honma, Y. Miwa, and N. Iguchi: Eng. 18 (1984) 274.
 33. J.H. Mulder et al.: "On the High Temperature Shape Memory Capabilities of Ni-(TiZr) and Ni-(TiHf) Alloys", to be published in Proc. of SMST, (A.R. Pelton, et al. eds.) (1995).
 34. Shape Memory Materials '94 (Y. Chu and H. Tu, eds.) Inter. Academic Pub., (1994) 253-266.
 35. S.M. Russel and F. Sczerzenie: "Engineering Considerations in the Application of Ni-Ti-Hf and NiAl as Practical High-Temperature Shape Memory Alloys", to be published in Proc. of SMST, (A.R. Pelton, et al. eds.) (1995).
 36. S.M. Tuominen: "High Transformation Temperature Ni-Ti-Hf Alloys", to be published in Proc. of SMST, (A.R. Pelton, et al. eds.) (1995).
 37. D. Stöckel: Metall. 46(7) (1992) 668.

THE INTERACTIVE RESPONSE OF SMA SPRINGS WHICH CONTROL THE POSITION OF DAMPERS IN PERSONAL ENVIRONMENTS™

Paul E. Thoma*, Yefim Ivshin*, and Kurt D. Schachner**

*Johnson Controls, Inc., Central Research, P. O. Box 591, Milwaukee, WI 53201-0591 USA

**Formerly with Johnson Controls, Inc., Milwaukee, WI 53201 USA

ABSTRACT

Personal Environments™ is a Johnson Controls, Inc. system for the control of indoor office environments. In this system, four SMA coiled extension springs interact to control the position of two dampers. Two opposing SMA springs connected to one damper control the percentage of primary conditioned air entering the system, and two opposing SMA springs connected to the second damper control the percentage of room air reentering the system.

The interactive operation of the SMA springs is discussed and a model is presented on the interactive response of the SMA springs. The SMA spring transformation temperatures, force - strain relationship, and the experimentally measured interactive response to temperature are presented and discussed.

INTRODUCTION

Personal Environments™ is a system (see Figure 1) to control indoor office environments that was developed by Johnson Controls, Inc. In this control system, an individual is able to control the temperature, light level, air flow, and degree of sound blocking in his or her workstation through a desktop controller. The heart of Personal Environments™ is the personal environment module (PEM). The PEM consists of two air mixing dampers, filters, fans, a white noise generator, speakers, and a direct digital controller (DDC). When an individual selects a temperature set point on the desktop controller, the set point signal is sent to the DDC, which signals an adjustment in the position of the dampers to obtain the proper mixture of conditioned air and recirculated air to achieve the desired temperature at the air outlet of the PEM. A sensor at the air outlet provides a feedback signal to the DDC to indicate when the mixed air temperature reaches the controller set point temperature. The position of the dampers is modulated until the temperature at the air outlet matches the set point temperature. Each damper is connected to two opposing SMA actuating springs. Damper position is controlled by the interactive response of the opposing springs. The interactive response is achieved by stress inducing the transformation to martensite in one SMA spring by the force generated by the second opposing SMA spring when it is electrically heated and transforms to austenite. SMA springs are used in Personal Environments™ to modulate the position of the dampers because of the small space they occupy and their quiet operation.

MATERIAL, DESIGN, AND PROPERTIES OF THE SMA ACTUATING SPRINGS

A near equiatomic NiTi SMA having an annealed austenite finish transformation temperature (A_f) of approximately 65°C (completely recrystallized state) is the material processed into the actuating springs. The SMA material is a cold worked circular cross-section wire having a diameter of 0.028 inch, which is formed into a normally closed extension spring having about 22 coils, a length of 0.63 inch, and an outer diameter of 0.23 inch. The closed springs are heat treated to obtain the transformation temperatures shown in Figure 2. A detailed explanation of the influence of cold work and heat treatment on NiTi SMA transformation temperatures is given in references 1 and 2.

To make connection to the damper assembly and the PEM housing, the SMA springs are terminated with high electrical conductance - low thermal conductance connectors of the type described in reference 3.

TA Instruments Differential Scanning Calorimetry (DSC) test equipment was used to obtain the curve and transformation temperatures shown in Figure 2. A DSC specimen having a weight of

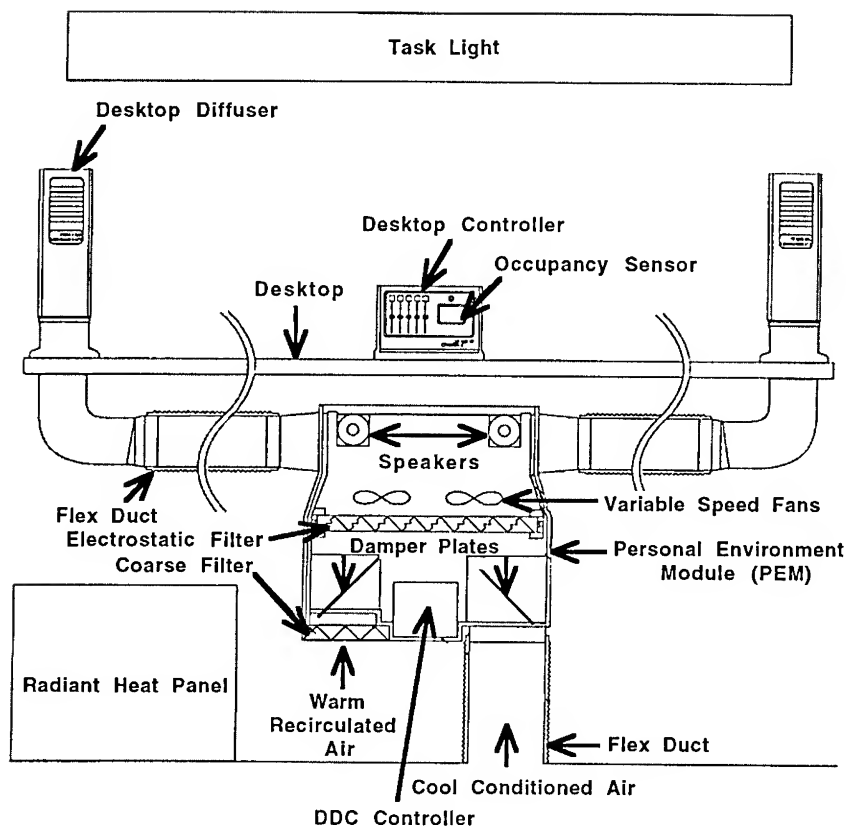


Figure 1. Schematic view of Personal Environments™.

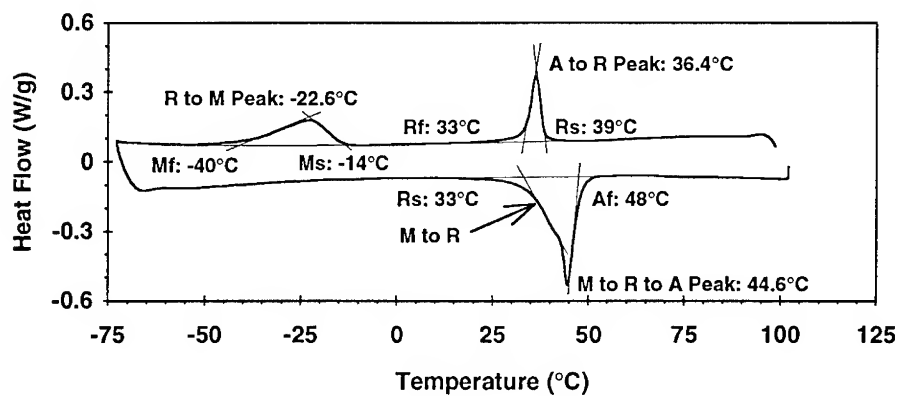


Figure 2. Austenite to martensite to austenite DSC curve.

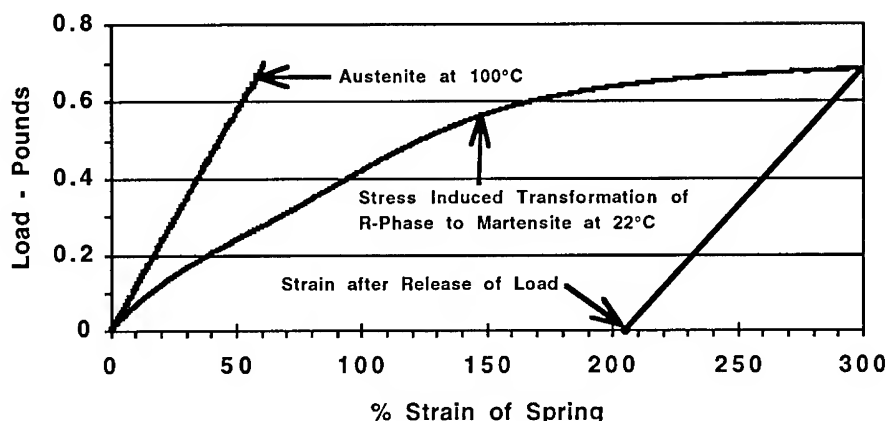


Figure 3. Force-strain curves of the SMA extension spring.

10.0 \pm 1 mg was prepared from a heat treated SMA spring using a low speed diamond blade saw.

Force-strain curves for the SMA spring are shown in Figure 3 at temperatures of 22°C and 100°C. In generating the stress induced martensite curve, the spring is in the R-phase before extension (spring is cooled from a temperature $>60^{\circ}\text{C}$ to 22°C) and transforms to martensite during spring extension. The force required to stress induce martensite and stretch the SMA spring 300% (the maximum spring extension during opening and closing of the damper) is about 0.7 pound (320 grams). The austenite force-strain curve is obtained by applying load to the spring at a temperature of 100°C and is completely within the elastic region when a maximum load of 0.7 pound is applied.

An Instron Model 1123 test system with a Series 2511-104 tension load cell and an Applied Test System Model 3710 environmental chamber were used to obtain the SMA spring's force-strain curves shown in Figure 3.

INTERACTIVE OPERATION OF SMA SPRINGS TO CONTROL DAMPER POSITION

The position of the PEM dampers is controlled by the interactive response of two opposing SMA springs which are connected to each damper assembly in the manner shown schematically in Figure 4. The damper assembly (shown in Figure 1) consists of a damper plate which is pivoted within the damper stack by pivot rods extending diametrically out from the damper plate. The pivot rods are positioned and pivoted at the base of diametrically opposite slots in the damper stack. A lever is connected to one of the pivot rods and has provisions to pivotally connect one end of the opposing SMA springs. The opposite end of the opposing SMA springs is pivotally connected to the damper housing. A fixed included angle of 45° is between the face of the damper plate and the lever arm. Schematics of the damper housing and assembly are shown in Figures 1 and 4 respectively.

When more recirculated air, conditioned air, or both are required, the damper in the respective air system is opened. This is accomplished in the following manner. If we assume that the opposing springs in a damper assembly are cooled to 22°C from a temperature $>A_f$ and stretched equally, each spring is partially transformed to martensite. If spring X in Figure 4 is electrically heated to a temperature $>A_f$, it contracts due to its transformation to austenite, and spring Y stretches due to additional stress induced transformation to martensite. The springs occupy the relative positions shown in Figure 4A. The damper plate is about 15° to the right of a vertical position and the lever approaches a mechanical stop. Spring X (austenite) at the elevated temperature occupies position C on the strain-temperature curve in Figure 5. Correspondingly, stretched spring Y (martensite) occupies position A on the curve. The moments of force produced

by springs **X** and **Y** are in balance, and the calculated forces exerted by springs **X** and **Y** under these conditions are approximately 0.23 pound and 0.75 pound respectively. As spring **X** cools to 22°C, it transforms from austenite to R-phase. In the process of transforming to R-phase, spring **X** stretches slightly due to a change in its force-strain relationship. When spring **X** is at 22°C, it occupies position **D** on the curve in Figure 5, and spring **Y**, which has remained at 22°C, occupies position **B** on the curve. The moments of force produced by springs **X** and **Y** are again in balance, and the calculated forces exerted by springs **X** and **Y** under these conditions are approximately 0.28 pound and 0.67 pound respectively. The damper plate moves to the vertical position as shown in Figure 4B, and the maximum amount of air flows through the damper.

The closing of the damper in the recirculated air and conditioned air systems is accomplished in the following manner. Spring **Y**, which is in a stress induced martensite state, is electrically heated to a temperature $>A_f$ and transforms to austenite. During this transformation, spring **Y** contracts and moves from position **B** to position **C** on the curve in Figure 5. Spring **X** stretches during its stress induced transformation from R-phase to martensite, and moves from position **D** to position **A** on the curve in Figure 5. The damper plate rotates to a position about 105° to the left of vertical and the lever approaches a mechanical stop (see Figure 4C). The moments of force produced by springs **X** and **Y** are in balance, and the calculated forces exerted by springs **X** and **Y** under these conditions are approximately 0.75 pound and 0.23 pound respectively. As spring **Y** cools to 22°C, it transforms from austenite to R-phase. During its transformation to R-phase, spring **Y** stretches slightly due to a change in its force-strain relationship, and moves from position **C** to position **D** on the curve in Figure 5. Spring **X**, which has remained at 22°C, moves from position **A** to position **B**. The moments of force produced by springs **X** and **Y** are again in balance, and the calculated forces exerted by springs **X** and **Y** under these conditions are about 0.67 pound and 0.28 pound respectively. The damper plate moves from the 105° position to a 90° left of vertical position, as shown in Figure 4D, and the least amount of air flows through the damper.

To position the damper plate at an intermediate position between vertical and horizontal, an extended SMA spring is partially transformed from martensite to austenite (R-phase) with pulse width modulated electrical heating of the spring. The opposing spring is partially extended by stress induced stretching of R-phase or transformation to martensite. The electrical heating control scheme permits heating of an SMA spring only after the other opposing SMA spring has cooled to the ambient temperature to prevent damage to the springs. With this control scheme and the use of pulse width modulated electrical heating of the SMA springs, the damper plates can be accurately positioned to obtain the desired amount of warm recirculated air and cool conditioned air.

MODEL OF THE INTERACTIVE OPERATION OF THE SMA SPRINGS

The position of the damper plates as a result of the interactive operation of opposing SMA springs is dependent on the force-extension relationship of the SMA springs (see Figure 3), and the geometry and dimensions of the actuating system's components. A schematic representation of the interactive operation of the opposing SMA springs is shown in Figures 4 and 6.

The position of the damper plate is determined by the requirement that the sum of the moments of force produced by the opposing springs is zero. The moments of force, M_x and M_y , produced by spring **X** and spring **Y** respectively can be expressed by the following equations:

$$M_x = F_x \cdot r \cdot \cos \gamma \quad (\text{spring X}) \quad (1)$$

$$M_y = F_y \cdot r \cdot \cos \delta \quad (\text{spring Y}), \quad (2)$$

where r is the distance between the pivot point of the lever and the spring attachment point on the lever; F_x and F_y are the forces produced by the respective springs and are dependent on spring phase or structure, extension, and temperature. The angles, γ and δ , are formed by a line through the longitudinal axis of the spring and the line perpendicular to the longitudinal axis of the lever (see Figure 6). Under equilibrium conditions, the sum of the moments of force produced by the opposing springs is zero. Then:

$$F_x \cdot r \cdot \cos \gamma = F_y \cdot r \cdot \cos \delta. \quad (3)$$

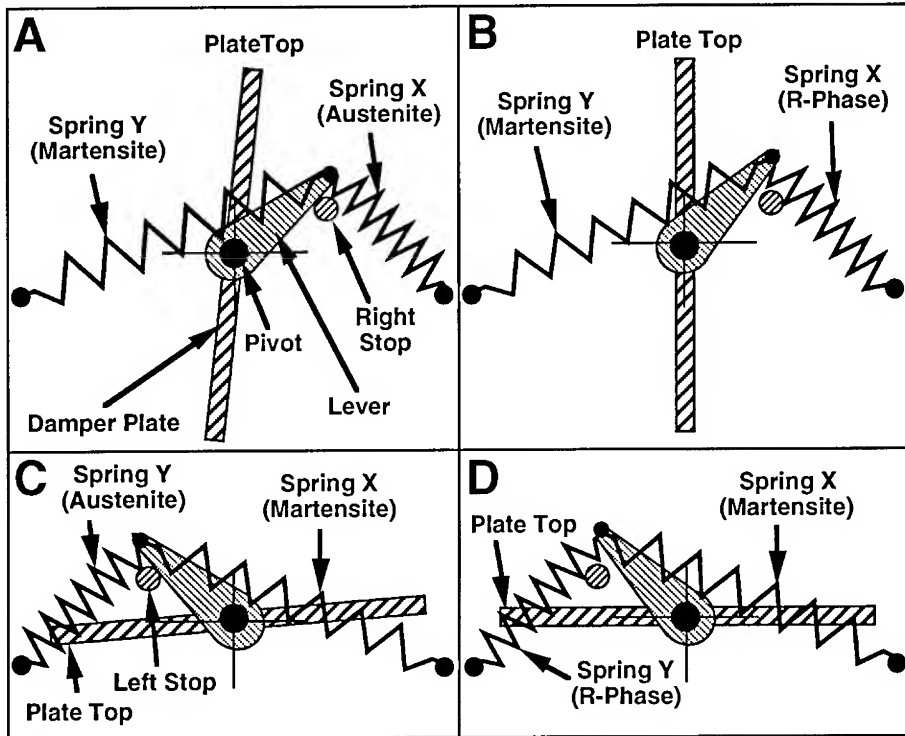


Figure 4. Interactive response of SMA springs and damper plate position.

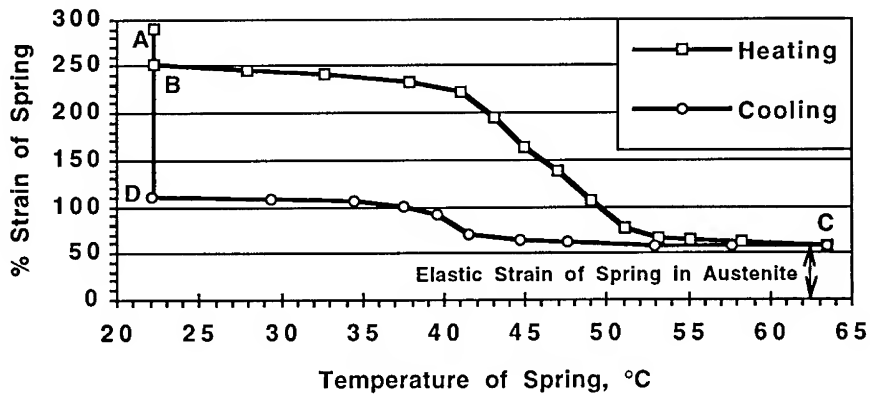


Figure 5. Strain of springs during opening and closing of the dampers.

SOME DURABILITY ISSUES ASSOCIATED WITH THE USE OF SHAPE-MEMORY ALLOY 'SMART' COMPOSITES

CLIFFORD M. FRIEND, NEIL B. MORGAN AND VIVIENNE D. WISE
Smart Materials Group, Cranfield University, Shrivenham Campus, Swindon, England

ABSTRACT

This paper presents the results from an experimental study on the durability of embedded Shape-Memory Alloy (SMA) hybrid composites. It shows that the cyclic actuation of such composites can be degraded due to the accumulation of internal damage within the host composite structure. This damage results from thermal effects within the host composite, and from mismatch in the strain capacities of the actuators and structural composite. The implications of this data for the design of embedded SMA actuator 'smart' composites is discussed.

INTRODUCTION

'Smart' structural materials are an emerging technology which will offer the possibility of engineering structures with enhanced functionality. Such structural materials will provide, for example, enhanced vibration control and real-time aeroelastic tailoring of structures, and real-time health-monitoring of safety critical systems. In most current 'smart' structural materials a mechatronic or 'Frankenstein' approach is adopted where separate sensors, signal processing and actuators are 'bolted together' to produce a 'smart' systems response. In the majority of these concepts the sensors and actuators are integrated within the host structural material since this is believed to produce a more highly integrated and advanced structural form. Many of the sensor and actuator materials are also familiar from more conventional sensing/actuation applications. The properties of some actuator materials employed in current 'smart' structural systems are shown in table I. This shows a wide range of response from high bandwidth low strain in piezoelectric materials to low bandwidth high strain capacity in Shape-Memory Alloy (SMA) actuators.

Table I - Typical Actuator Properties

	Piezoceramic (PZT)	Piezopolymer (PVDF)	Magnetostrict. (Terfermol-D)	SMA (NiTi)
Actuation Strain (μ strain)	1300	230 dc 690 ac	2000	80,000 20,000
Max Temp (°C)	360	80 - 120	380	~ 100
Bandwidth	high	high	moderate	low

In any application involving actuation it is important to consider the impedance mismatch between the actuator material and host structure¹. In the case of the materials in table I the most important properties are therefore their actuation strains. Typical host materials for 'smart' structures are advanced composites which have failure strains typically <1%. The actuation strains associated with piezoelectric and magnetostrictive actuators are therefore likely to be accommodated by the host structure. However, in the case of SMA actuators, the strain mismatch between actuator and host structure is substantial and likely to impact on the durability of such systems. SMA actuators are also usually driven by means of resistance heating which is likely to dissipate significant heat to the host composite. This latter feature is also likely to influence the durability of 'smart' structural materials based on SMAs.

The literature base on the integration of SMA actuators into composite structures is not extensive. However, their use has been investigated for vibration², acoustic radiation^{2,3}, damage⁴, buckling^{2,3} and shape² control. An interesting feature of this work has been a heavy bias towards modelling, with only limited attempts to experimentally verify the calculated results. Previously published work has also failed to produce a systematic database on the durability of SMA hybrid composites. The present work was undertaken to provide a preliminary appraisal of the durability issues associated with SMA 'smart' structural materials.

EXPERIMENTAL PROCEDURES

The samples employed in this programme were small glass-fibre reinforced epoxy cantilever beams (145 x 20mm) containing embedded Ni-Ti SMA actuators. Actuators were embedded since this is (i) a commonly proposed structural design, and (ii) this actuator arrangement is likely to reduce durability due to the mismatch in strain capacity between the actuator and host composite. Glass-reinforced epoxy was selected as the host material since (i) its lower elastic stiffness (cf CFRP) maximises measured shape changes, (ii) its poor electrical conductivity provides electrical insulation of the actuators, and (iii) its low thermal conductivity allows the effects of dissipated heat to be maximised.

The beams were constructed by hand lay-up and vacuum-bagging using Fibredux 913 unidirectional glass fibre pre-preg with a nominal cure temperature of 130 °C. The actuators were in the form of 300µm diameter wires with a transformation temperature (A_f) of 60°C. In the reported work the actuators were orientated parallel to the fibre direction. The beams were 6 ply in thickness with the actuators introduced between plies 2 and 3, ie off the neutral axes of the beams. Actuator volume fraction was varied systematically in the range 0 to 2.5 vol %. A strain of 6% was maintained on the actuators during composite cure which was carried out using a thermal cycle recommended by the pre-preg manufacturer. Prior to testing the actuators were restrained against the free ends of the beams since preliminary tests showed that in unconstrained hybrid beams actuation resulted in significant interfacial decohesion between the actuator and host composite which resulted in complete degradation of the actuation strains.

Since the actuators were off the beams' neutral axes bending was induced during actuation. Such deflections were used to characterise the mechanical responses of the hybrid beams. Laminate shape changes were activated electrically by means of resistance heating,

with the actuators connected in series to ensure that each volume element was subjected to the same heating current. During deflection testing the temperature of the actuators was increased over a period of approximately 2 seconds and was then allowed to stabilise for one minute prior to measurements being taken. Heating was therefore increased incrementally up to the maximum value for each cycle. The mechanical performances of the SMA hybrid beams were initially characterised by their deflection/ current responses. However, since the true drive variable for the actuators was temperature, experiments were also conducted to cross-correlate drive currents to actuator temperature rises. This was done by the use of fine thermocouples embedded within the host composites close to the actuators. Optical and electron metallography was also employed to investigate damage accumulation within the host composites during cyclic actuation of the laminates.

RESULTS AND DISCUSSION

Figure 1 shows the microstructure of a typical hybrid laminate with a large diameter SMA actuator embedded within the glass-fibres of the host composite.

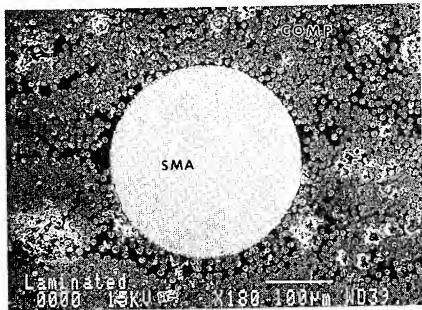


Figure 1 - Typical Hybrid Laminate

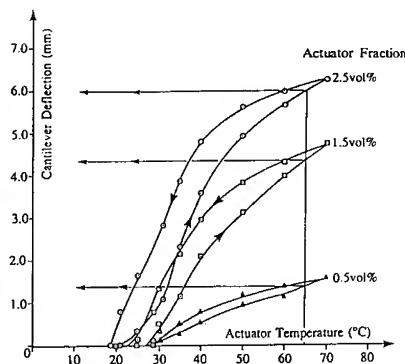


Figure 2 - Effect of Actuator Fraction on Deflection Output

Figure 2 shows the effect of actuator fraction on the deflection characteristics of the hybrid beams (actuator strain and beam stiffness being approximately constant). It can be clearly seen that as the volume fraction of actuator increased the maximum deflections of the cantilever beams also increased. Such observations are not unexpected and their origin has been discussed in an earlier paper⁷. Figure 2 also shows the hysteresis associated with the forward and reverse actuation pathways. This behaviour is a characteristic of the laminates due to the nature of the shape-memory effect in the actuators, and the variation in hysteresis with volume fraction has also been addressed in an earlier paper⁶.

The behaviour shown in figure 2 is the first cycle response of the beams. However, when considering the durability of these materials it is more important to consider the longer-term stability of such behaviour. Figure 3 shows data of this type for the 1 vol% material. The laminates employed for these measurements were cycled to a maximum actuator temperature of 150°C. The deflection data from these measurements differed slightly from that shown in figure 2. It is believed that this is due to laminate to laminate variations,

compounded with a small systematic error in the conversion of drive current to actuator temperature rise. However, this data does show that there was a systematic instability in response, with changes in deflection output over the first three actuation cycles. After these initial cycles a more stable behaviour developed.

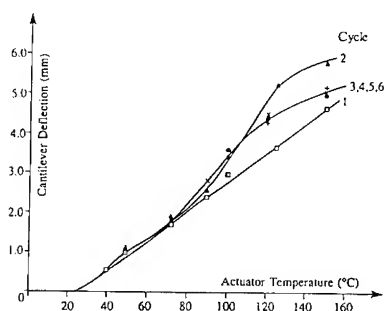


Figure 3 - Cyclic Data for 1 vol% Actuator



Figure 4 - Actuator/ Host Interfacial Failure

The origin of this instability was investigated in terms of damage accumulation within the cycled composites. Microscopy showed that during the first three actuation cycles damage was initiated within the beams. This internal damage consisted of interfacial breakdown between the actuators and host composite (figure 4). The actuator/composite interface gradually degraded with each actuation cycle until cycle 3 where gross delamination was present. This is interesting since figure 3 shows that this cycle coincided with the development of a reproducible deflection response. This suggests that during the first three cycles interfacial contact gradually decreased until the actuators were completely delaminated within the host composite and acted on the beams only through the mechanical constraints at the free ends. Following cycle 3 no further delamination was possible and there were then no further changes in the deflection responses of the beams.

It is clear from figures 3 and 4 that there are a number of durability issues associated with the use of embedded SMA actuators and that these appear to result from the interaction of two factors. The first is the mismatch in strain capacities of the actuators and host composite, and the second, the effect of heat dissipation on the properties of the host material.

Considering strain mismatch first, it is clear that when large actuation strains are employed it is relatively easy to exceed the interfacial shear strength of the actuator/host interface. This results in interfacial decohesion during the early actuation cycles, with the damage initiating at regions of high stress-intensity. Such regions have been investigated previously both experimentally⁷ and by FE analysis⁸ which have shown similar results to the current work, ie decohesion initiating at the actuator ends and propagating along the interfaces into the body of the hybrid composite. However, it is also clear that heat-dissipation contributes to this process since thermal effects both reduce the interfacial properties, and allow damage to develop elsewhere within the host composite material.

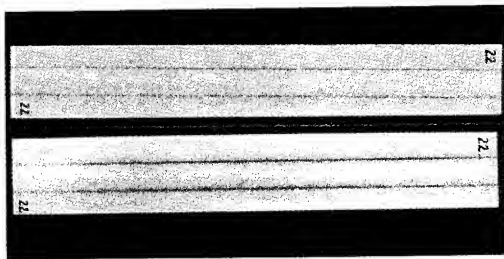


Figure 5 - 1.0 vol % hybrid actuator beam (a) before and (b) after 10 cycles to 150 °C

Figure 5 shows a typical hybrid beam before and after cycling. It is clear that following 10 actuation cycles there was significant damage to both the host composite and the actuator /host interface, with visible darkening of the composite material around the actuators. The origin of such damage was clearly associated with thermal effects and resulted from cycling the hybrid beams to 150°C which exceeded the nominal cure temperature of the resin system. It was also clear that in addition to the absolute temperature rise of the actuators, such thermal degradation also depended critically on the volume fraction of SMA due to coupling of the heat fluxes from multiple actuators. This effect is shown in figure 6 which presents thermocouple measurements on a laminate of the type shown in figure 5.

Figure 6 shows that due to the relatively low thermal conductivity of the host composite, the thermal fluxes from adjacent SMA actuators coupled, thus resulting in an extended volume of host composite which was subjected to temperatures close to those of the actuators. Heat dissipation therefore played a critical role in degrading both the host composite and interfacial properties, and when associated with a large mismatch in strain resulted in failure of the actuator/host interface.

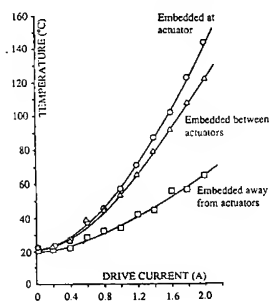


Figure 6 - Effect of Drive Current on Temperature Rise

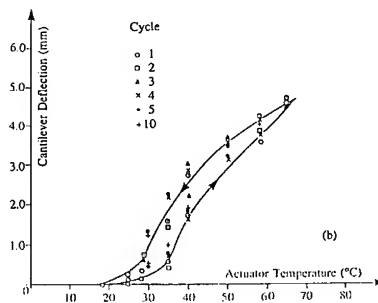


Figure 7 - Cyclic Data for a 1.5 vol % Hybrid Beam ($T_{max} = 65\text{ }^{\circ}\text{C}$)

These observations suggest that improved cycle to cycle reproducibility should be obtained if the maximum actuation temperature is reduced, since this should minimise both thermal effects within the host composite, and strain mismatch across the actuator/host interface (since cycling to lower temperatures results in a smaller shape-strain from the SMA actuator). This was confirmed by cycling beams to 65°C (figure 7). Under these conditions the deflection outputs were smaller than those obtained by cycling to higher temperatures, however, there was less thermal degradation of the host composite, and improved cyclic stability of the deflection output. The absolute value of deflection could also be maximised to some extent by selection of an appropriate actuator fraction as shown in figure 2.

CONCLUSIONS

The results presented in this paper begin to address some of the durability issues associated with the use of embedded SMA actuators within advanced composite materials. It has been shown that during cyclic actuation such hybrid composites can suffer from instabilities in deflection response due to accumulation of internal damage resulting from interfacial decohesion and thermal degradation. These effects can be minimised by careful selection of the maximum actuator temperature, and in such circumstances it is possible to achieve useable deflection outputs which are stable over many actuation cycles. In the wider context, this work suggests that the use of SMA actuators in an embedded form may not be the most appropriate way to exploit these materials due to their large strain capacity compared with advanced composites. This work also suggests that thermal dissipation effects are significant, and even if host degradation is minimised, there may be further problems, for example, due to the inadvertent operation of SMA actuators in push-pull designs resulting from dissipated heat within the structural composite.

ACKNOWLEDGEMENT

This work was partially supported by the Structural Materials Centre, Defence Research Agency.

REFERENCES

1. C. Rogers - Keynote Address presented at 2nd European Conf on Smart Struct and Mat, Glasgow, 1994 (unpublished)
2. C. Liang, J. Jia and C. Rogers, Proc 30th AIAA/ASME/ASCE/AHS/ASC Structures, Structural Dynamics and Materials Conf. (AIAA, 1989) pp 1504 - 1513
3. D. Thompson and O. Griffin, Proc Conf Recent Advances in Adaptive and Sensory Materials and their Applications (Technomic, 1992) pp 377 - 384
4. C. Rogers, C. Liang and S. Li, Proc AIAA 32nd Structures, Structural Dynamics and Materials, Baltimore, 1991
5. C. Friend and N. Morgan, Proc 2nd European Conf on Smart Struct & Mat (SPIE, Vol 2361, 1994) pp 94 - 97
6. C. Friend and N. Morgan, Proc Europ Symp on Martensitic Transf, Barcelona, 1994 (in print - Journal de Physique)
7. C. Doran, Proc 2nd European Conf on Smart Struct & Mat (SPIE, Vol 2361, 1994) pp 98 - 101
8. J. Bidaux, J. Manson and R. Gotthardt, Proc Europ Symp on Martensitic Transf, Barcelona, 1994 (in print - Journal de Physique)

INTELLIGENT MATERIAL DESIGN USING SHAPE MEMORY ALLOY

YASUBUMI FURUYA

Department of Materials Processing, Tohoku University, Sendai 980, Japan

ABSTRACT

Recently, shape memory alloy (SMA) is regarded as one promising material element natively with intelligent functions. I introduce the fundamental design concept and several trials for developing intelligent (smart) materials and structures by using shape memory alloy. Moreover, I introduce our recent works and point out the necessity for developing fundamental techniques to realize the intelligent materials using SMA.

INTRODUCTION

The newly created material design concept "intelligent material" is directed toward developing more higher functional materials which are able to manifest some active effects and maintain the most optimum conditions in response to the environmental changes (1). Generally, the basic concept of intelligent material is defined as the wise and multiple functional material which has a sensor, a processor and an actuator functions in the material or structure system itself by the reference of Wadas definition (2), as shown in Fig. 1.

From this viewpoint, the shape memory alloy (SMA) natively has the several functions such as a (1) thermo-sensor, (2) an actuator by recovery stress during thermoelastic phase transformation, and (3) memory and recovery function, so that, SMA can be treated as an "intelligent material element". Based on the above-mentioned native features of SMA, I explain the basic and important material properties of SMA in the approach to the intelligent material and then the fundamental design concept, and I introduce several trials for developing intelligent (smart) composite materials and structures by using shape memory alloy. Experimentally, I introduce our recent trials for developing shape memory composites, i.e. metal matrix, polymer or concrete matrix composites for the machinery, structural and building material. Finally, I point out the necessity for developing fundamental techniques to realize the SMA intelligent materials, i.e. an artificial control of the thermoelastic transformation behaviors of SMA by metallurgical treatment as well as an advanced material processing using electromagnetic effects etc..

FUNDAMENTAL DESIGN CONCEPT

(1) Intelligent material property natively with SMA

Material functional properties of SMA depending on the increasing temperature are summarized in Fig. 2 (3). It should be noticed as a unique property that SMA shows more higher stiffness (2-3 times) and large recovery stress at the higher temperature region due to inversely thermoelastic phase transformation in opposition to becoming weak in the general metals. SMA also has high damping and high wear resistance as one of the machinery materials. In consequence, from the view point of the factors for intelligent materials, SMA natively has the intelligent functions i.e., (1) sensor (thermal, stress), (2) actuator (shape memory deformation), (3) active responsibility from (1)+(2), (4) memory and shape recovery (namely, processor function), and its material properties can be controlled by the environmental stimulus of temperature and force by the thermoelastic or the stress-induced martensitic transformation.

(2) Intelligent material design by combining the control shape memory phase transformation with evaluation of SMA.

One of the design concept for intelligent material element using SMA is shown in Fig. 3. If the basic SMA material element shows the non-linear (ON-OFF digital) type strain vs. temperature hysteresis (i.e. type 1) reported in melt-spun Ti50Ni40Cu10 alloy ribbon in our previous paper (4), very clear acoustic emission (AE) pulses are apt to outbreak by the simultaneous domain movements at the phase transformation. So that, it seems suitable to create a multi-layer intelligent SMA film by utilizing the pulses as a logical signals from SMA, and this former type SMA film seems to be suitable for micro-devices (i.e. macro machine) actuator. On the other hand, linear analog type SMA has been recently developed by the authors (4) by control the phase transformation in Ti50Ni48Co2 alloy wire. This latter linear type (i.e. type 2) of SMA seems suitable for smart composite material design because the active feedback control of linear type SMA becomes considerably easy in comparison with the former large hysteresis type. So that, the latter linear type SMA seems to be suitable for self-strengthening at higher temperature region, suppression of thermal expansion and active damping control smoothly. Based on these features of each type of SMA 1, 2, it will become possible to materialize the more intelligent

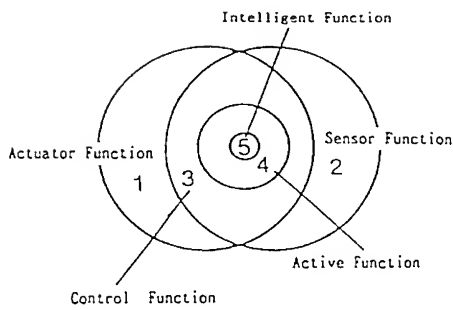


Fig.1 Material functions necessary for intelligent structural material.

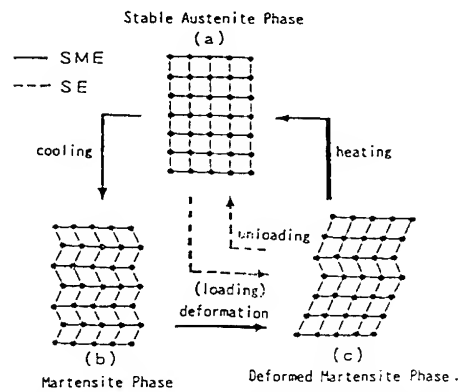


Fig.2(a) Crystal lattice deformation mechanism in shape memory effect (SME) and superelasticity (SE).

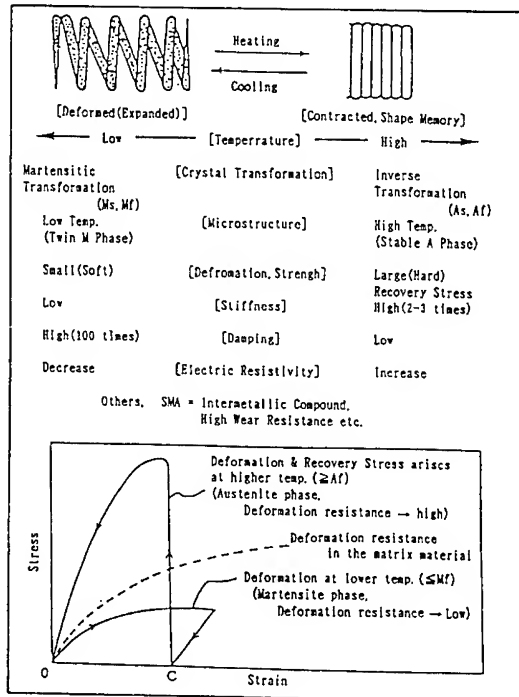


Fig.2(b) Material properties of shape memory alloy (SMA) depending on the increasing temperature.

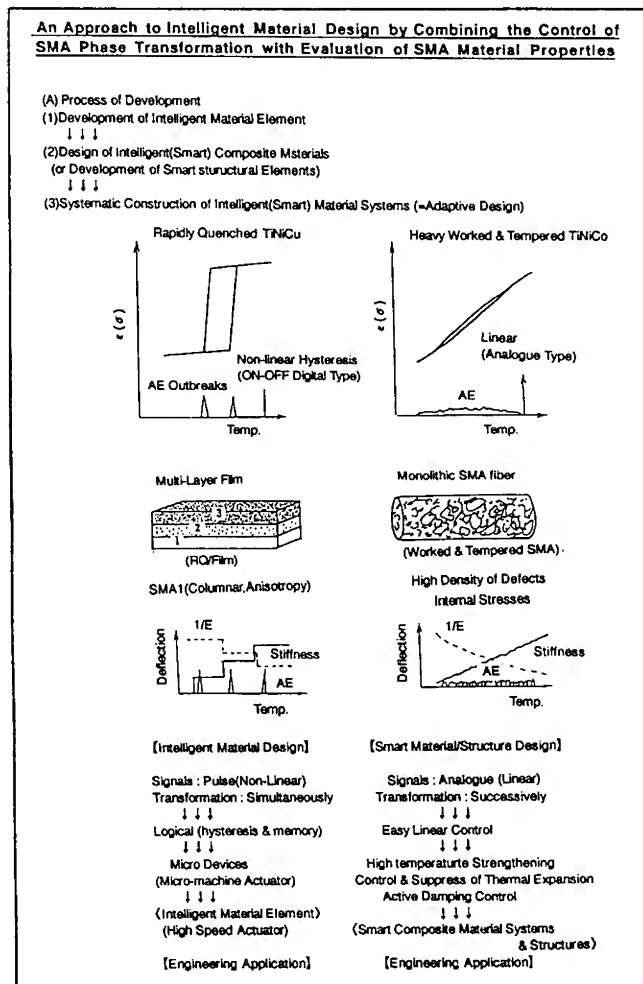


Fig.3 An approach to intelligent material design by combining the control of SMA phase transformation with evaluation of SMA material properties.

materials and structures having more concrete processor function in itself in the form of engineering devices or bulk composite material systems in two each different engineering application field.

(3) Active control of intelligent materials/structures by utilizing SMA.

In engineering application of SMA intelligent materials/structures, we use SMA fiber as an artificial sensor (i.e. a nervous system) as well as actuator (i.e. artificial muscle system), so that, Intelligent SMA materials/structures is generally suitable to become some composite structures containing SMA fiber in its surface or the inner part. An active and feedback material property control flow (i.e. self-monitoring → self-adjustment & self-strengthening function) creation able in the intelligent shape memory

composites(SMC) is shown in Fig.4. When the thermoelastic phase transformation(i.e.shape memory effect) or stress induced phase transformation (i.e.super-elasticity) of SMA occurs by the environmental parameter change of temperature or stress, the physical properties,i.e. electric resistivity(ρ), ultrasonic velocity change (V_t), internal friction (damping, $\tan \delta$), acoustic emission(AE) outbreaks etc. occur as shown in Fig.4. When some information concerning these physical properties can be detected nondestructively by the sensor set on the SMA composite, thermal(strain) energy is applied to SMA fibers by direct current method,and shape memory shrinkage or stiffness changes occur by SMA phase transformation. By this flow chart, several intelligent functions such as self-strengthening, stiffness changes,self-shape recovery and active damping control etc. can be actualized actively from the SMA to intelligent (smart) composite and structures.

RESULTS AND DISCUSSION

1. DEVELOPMENT AND EVALUATION OF SMA INTELLIGENT COMPOSITE

MATERIALS / STRUCTURES

(1) Shape memory composite(SMC)

On the basis of the intelligent material properties of SMA shown in Fig.2 and active control of SMA composites shown in Fig.3,4, I introduce our trials for materializing the intelligent metal matrix composite and a structural building material containing SMA in itself. Shape memory TiNi fiber reinforced Al matrix composite has been designed and developed by squeeze casting method[6] by the authors. The design concept and material processing of shape memory metal matrix composite is shown in Fig.5. A typical cross-sectional view of the composite is shown in Fig.6. Pre-strained tensile TiNi/Al composite specimens whose TiNi fibers are martensitic phase below M_f ($\approx 293K$) are heated to 363K just above the austenite finish temperature($A_f=336K$) and then, tensile test are conducted. The stress vs strain curves of unreinforced Al, 9% volume Ti50Ni50 fiber/1100 pure Al composite with pre-strain $\epsilon=0$ or 4% are show in Fig.6. A comparison with and without pre-strain of 4% clearly indicates the improvement of strength by shape memory contraction effect of fibers with pre-strain $\epsilon=4\%$. Damping property(i.e. internal friction $\tan \delta$) with increasing temperature in TiNi/Al composite is discussed in comparison with unreinforced 1100 Al and SUS304 stainless steel. At both side of transformation finishing temperatures, M_f , A_f , damping has been improved due to the some effects relating to stiffness and damping changes by thermal transformation of embedded SMA fibers. Moreover, this composite will also be expected to show high wear resistance by SMA fillers above A_f (336K) temperature. By these characteristic features of SMA TiNi/Al composite, this composite will be able to be applicable to the machinery materials for very high speed transportation vehicles in aerospace or railway as well as the engine components material.

Same approach has been applied by the authors to a building wall material as similar as the pre-stressed concrete[7]. Some improvements of the fracture toughness and damping are confirmed by the building wall material model(SMA TiNi+plaster composite) designed for improving shape memory strengthening as well as damping because it contains two different properties of shape memory contracted TiNi fibers($>A_f$) and TiNi high damping particles($<M_f$).

(2) Intelligent composite system materials

Intelligent(smart) SMA TiNi fiber/polymer matrix composite plate for active control of acoustic vibration damping and resonance points was studied by C.Rogers in 1989 [8] by utilizing the stiffness change caused by the transformation of embedded SMA fibers by direct current heating method. However, heat response of SMA generally is too slow in cool process for active control of SMA fibers. To this problem, I have recently proposed a design for intelligent wave frequency damping tunable panel containing SMA fillers which cause stress-induced transformation rapidly by depending on the external force from actuator as shown in Fig.7[9].

Active damage control is one of the most important subjects in the material/structure strength. Fig.8 shows schematically the intelligent material system for active control of fatigue crack propagation from notch-root and fatigue life by the contractions of SMA lines type actuator at the notch-root. Experimentally, the enhancing crack-closure phenomena and stress intensity factor K-value have been studied in the pre-cracked TiNi fiber/epoxy resin matrix specimen by using photoelastic fringe pattern. By a photoelastic fringe pattern analysis as shown in Fig 9, K value has been decreased as much as about 50% depending on the pre-strain value and direct current heating degrees [9].

(3) Intelligent material systems and structures

As one more macroscopic approach than SMA composite material, intelligent material systems and structures using SMA has been proposed on the basis of the feedback control flow shown in Fig.4 for active control of strength and vibration damping of a high building,dam, bridge and aerospace structures etc. [3,4]. This type of SMA intelligent(smart) concrete material systems and structures will be expected for elongation of the machinery life, prevention of the sudden failure and maintaining the safety of the structures such as aerospace and atomic power generation system etc.

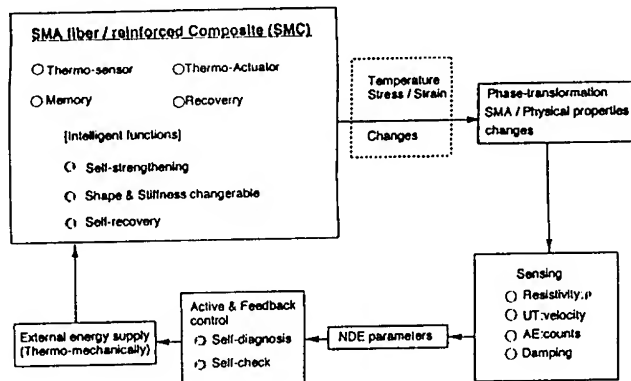


Fig.4 Active and feedback control flow for the intelligent shape memory composite(SMC).

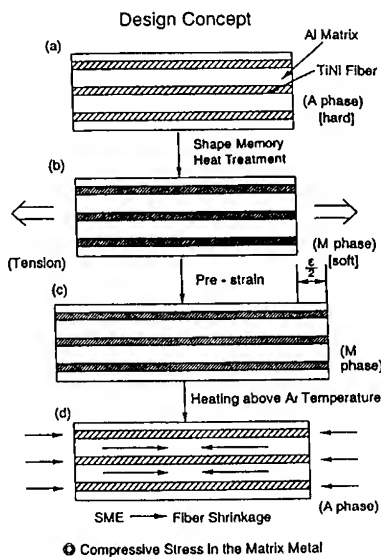


Fig.5 Design concept and material processing of shape memory fiber/metal matrix composite.

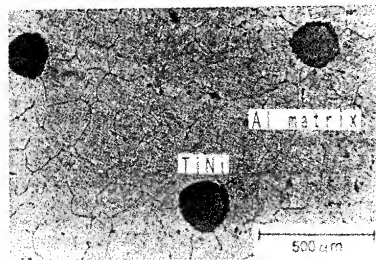


Fig.6(a) A optical microstructure of cross section of TiNi/Al composite.

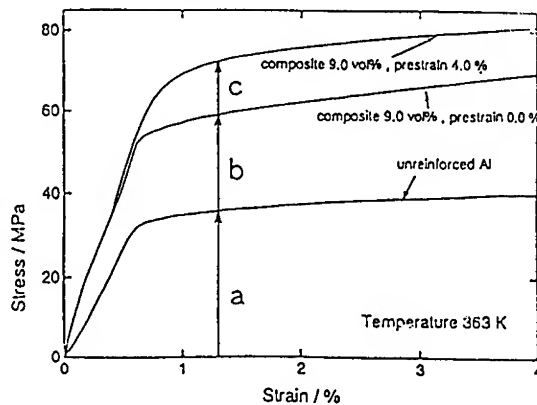


Fig.6(b) Stress vs strain curves of shape memory fiber reinforced TiNi/Al matrix composite(temp>A1). (a:matrix strength,b:fiber reinforced strength, c:shape memory and deformation strengthening)

Absorption-Waves Frequency Variable Panel (Rapid Response is Possible)

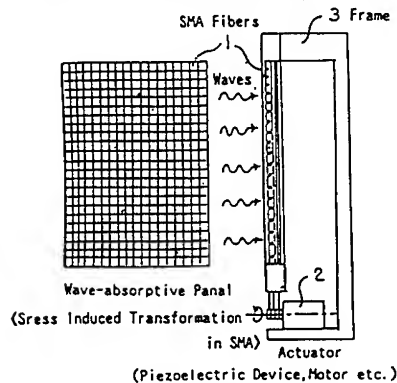


Fig.7 The design for intelligent, wave frequency and damping tunable panel containing SMA fillers which are stress-induced transformed rapidly by external force from the actuator.

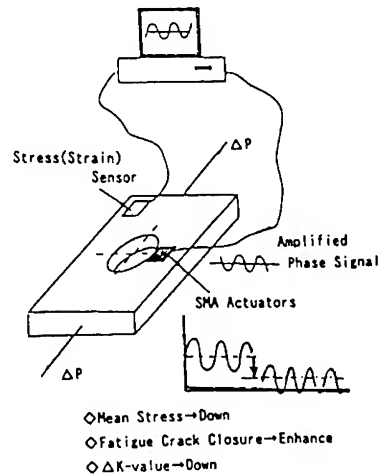


Fig.8 Active fatigue damage control of fatigue crack propagation at the notch-root.

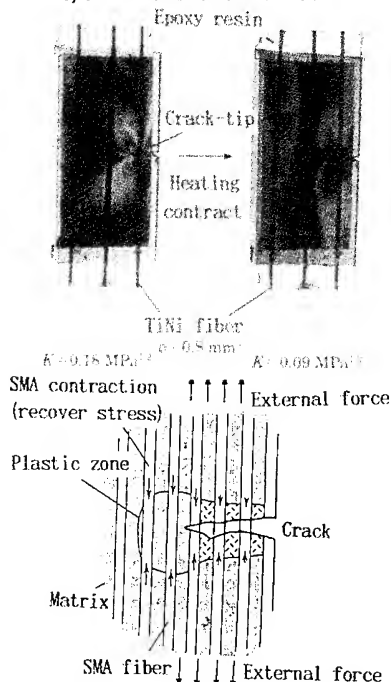


Fig.9 Decrease of stress concentration at the crack-tip caused by rapid contraction of SMA TiNi fibers by electrical heating.

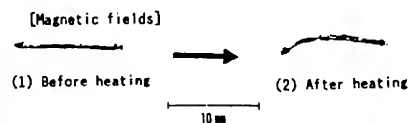


Fig.10(a) Self-heating and self-deformation of intelligent ferrite-coated TiNi pin in the high frequency magnetic field.

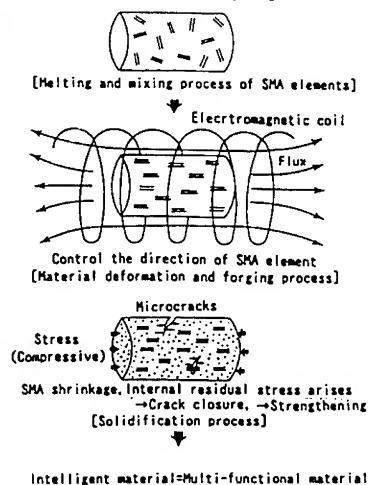


Fig.10(b) Fabrication process of shape memory composite using electromagnetic force. ("Intelligent material processing")

2. NECESSITY FOR DEVELOPING FUNDAMENTAL TECHNIQUES TO REALIZE SMA INTELLIGENT MATERIALS

(1) Material problems for using SMA

The merits of SMA actuator are summarized as follows. (1) large shape memory deformation (stroke), (2) high power/weight ratio, (3) simple and small size, (4) noiseless and clean etc. However, for more extension of practical use, next main technical problems remain to be solved. (1) more high thermo-mechanical energy convertibility, (2) stable response and high resistance to thermal fatigue, (3) rapid actuation in cooling process etc. Especially, the achievement of SMA rapid response is very important problem and several countermeasures have been proposed to promote the thermal diffusion by adopting SMA fiber or thin plates having high surface/mass ratio etc.

(2) High performance in rapidly solidified SMA material element

As one of the countermeasures of above-mentioned SMA technical problems, recently, rapidly solidified melt-spun TiNiCu ribbon samples have been produced (4). The ribbon sample has 30 μ m thickness and fine columnar microstructures having strong crystal anisotropy. This Ti50Ni40Cu10(at%) ribbon shows the high performance material properties, i.e. sharp digital (ON-OFF) type transformation strain vs temperature relationship as shown in Fig.3, high thermal energy convertibility $\eta \geq 3$ times, narrow transformation temperature range $\Delta T \leq 10$ K, high thermal fatigue resistance (=maximum 10 times) and corrosion resistance (=100 to 10000 times) etc. These high performance material properties are caused from simultaneous transformation in the microstructures having strong crystal anisotropy of fine columnar crystals and it seems to be suitable for fillers of SMA composites.

(3) Linear type SMA

Special type SMA having linear hysteresis of transformation strain vs temperature has been expected because linear type SMA is necessary to make analog type thermal sensor/actuator whose control become considerably easy than hysteresis type SMA. It is also suitable for bio-material softly fitting to the human body etc.. Tempering at low temperature about 625K in Ti50Ni48Co2(at%) alloy, almost linear recovery strain(stress) vs temperature relationship from 240K to 373K has been achieved by the authors(9). It may be caused from successive phase transformations by internal stresses around the heavily developed defects and precipitates which are introduced by heavily working and a following tempering.

(4) Intelligent material processing using electromagnetics

The author previously developed the intelligent ferrite-coated SMA TiNi pins for local hyperthermia system using high frequency magnetic field for the cure of cancer in the deep part of human body (10). This type of ferrite-coated SMA element has several intelligent functions such as self-heating and self-deformation by combination of eddy current joule heat and shape memory effect of ferrite-coated TiNi pin. Utilizing this type of intelligent characteristics of SMA pins (or fibers) as a filler embedded in the SMA composites, the direction of fillers can be controlled by external electromagnetic force, and then SMA self-contraction for self-strengthening also can be achieved in the material fabrication process as schematically shown in Fig.10(7,10).

SUMMARY

Shape memory alloy (SMA) natively has the several functions such as (1) thermo-sensor, (2) an actuator by recovery stress during thermoelastic phase transformation, and (3) memory and recovery function, so that, SMA can be treated as an "intelligent material element". I explain the basic and important material properties of SMA in the approach to the intelligent material and then the fundamental design concept and several trials for developing intelligent (smart) composite materials and structures by using SMA. Experimentally, I introduce our recent trials for developing shape memory composites, i.e. metal matrix, polymer or concrete matrix composites for the machinery, structural and building material. Finally, I point out the necessity for developing fundamental techniques to realize the SMA intelligent materials, i.e. an artificial control of the thermoelastic transformation behaviors of SMA by metallurgical treatment as well as an advanced material processing using electromagnetic effects etc..

REFERENCES

1. T. Takagi, Intelligent Materials, in Japanese, 1-1, (1991).
2. B. K. Wada, J. L. Fanson, E. F. Crawley, J. Intell. Mater. System Struct. 1-2, 157 (1990)
3. Y. Furuya, Intelligent Materials, in Japanese, 3-3, 22 (1993)
4. Y. Furuya, M. Matsumoto, T. Matsumoto, MRS Proc. 246, 335 (1992)
5. Y. Furuya, H. M. Kimura, T. Matsumoto, M. Aiba, JIM Spring Meeting Proc. No. 224, 135 (1994)
6. Y. Furuya, A. Sasaki, M. Taya, Mater. Trans. JIM, 34-3, 224 (1993)
7. Y. Furuya, Science of Machine, in Japanese, 44-9, 87 (1992), 44-10, 80 (1992)
8. W. S. Anders, C. A. Rogers, Proc. 1st US/Japan Joint Conf. on Adaptive Struct. 1-2, 157 (1990)
9. A. Shimamoto, Y. Furuya, M. Taya, Proc. Japanese Mechanical Engineer, 940-6, 660 (1994)
10. Y. Furuya, KAST-REPORT (Kanagawa Academy, in Japan), 5-3, 6 (1993)

SMART DAMPING TREATMENT FOR FLEXIBLE STRUCTURE

Q. CHEN AND C. LEVY

Florida International University, Mechanical Engineering Department, Miami, FL 33199

ABSTRACT

The mathematical model of a flexible cantilever beam with a constrained viscoelastic layer and shape memory alloy layer called smart damping treatment (SDT) is presented. It is shown that a change of the elastic modulus of the shape memory alloy layer will affect the system loss factor and resonance frequency. The recovery stress of the SMA layer leads to an inhomogeneity in the governing differential equation. The recovery stress also functions as an excitation to the system. The effects of the different parameters found in the analysis are discussed in the paper.

INTRODUCTION

Unconstrained and constrained viscoelastic layer damping treatments were first analyzed and developed in the late 1950's. Kerwin¹ presented the first analysis of the problem followed by Ditaranto², Rao³, Mead⁴ and Mead and Markus⁵. The response of a damped sandwich beam to random excitation was discussed by Xi et al.⁶ Chen and Xi⁷ obtained the improved differential equations for the damped sandwich-type beam. That analysis was continued by Levy and Chen⁸ who investigated the double sandwich type cantilever beam, which may be used as a model for robot arms and space structures. Also, the effects of a concentrated mass attached at the free end of such a structure was studied by Chen and Levy⁹.

In recent years, improvements in materials and manufacturing processes, and more specifically, advances in data acquisition and computer technologies, have made it possible to apply sophisticated active control techniques to vibrating structures¹⁰. Buehler and Wiley¹¹ presented the first analysis of Shape Memory Alloys (SMA). Composites with SMA have shown the ability to change material properties, induce large internal forces in the materials, modify the stress and strain state of the structure and alter the configuration¹². These characteristics are very useful for vibration control. The application of SMA composites for vibration and structural acoustic control was presented¹³⁻¹⁵. It was shown that for an SMA hybrid beam with a nitinol volume of 15%, the first natural frequency of the SMA hybrid beam increased from 21 Hz at room temperature to 62 Hz

when the actuators were heated to 300°F (149°C)¹⁵. For uncompensated vibration modes, there is a need to improve the robustness of the system to model uncertainties.

In this paper, the mathematical model of a flexible cantilever beam with a constrained viscoelastic layer and shape memory alloy layer is presented. It is shown that change of the elastic modulus of the shape memory alloy layer will affect the system loss factor and resonance frequency. Also, the recovery stress of the SMA layer functions like an excitation, thus changing the right side of the governing equation, i.e., adjusting the excitation. The effects of different parameters found in the analysis are discussed in the paper.

FORMULATIONS OF THE PROBLEM

The cantilever beam with SMA and viscoelastic treatments is shown in Figure 1. The following assumptions are made in the analysis: (1) the beam deflection is small and uniform across any section; (2) the primary beam and the constraining layer are assumed to be isotropic; (3) the longitudinal and rotatory inertia effects of the beam are neglected; (4) the damping layers carry shear, but no direct stress, and are assumed to be linear viscoelastic; (5) no slip occurs at the interface between the layers; and (6) the shape memory alloy layer is very thin. With these assumptions, the governing differential equations of motion and the corresponding boundary conditions are found to be¹⁶:

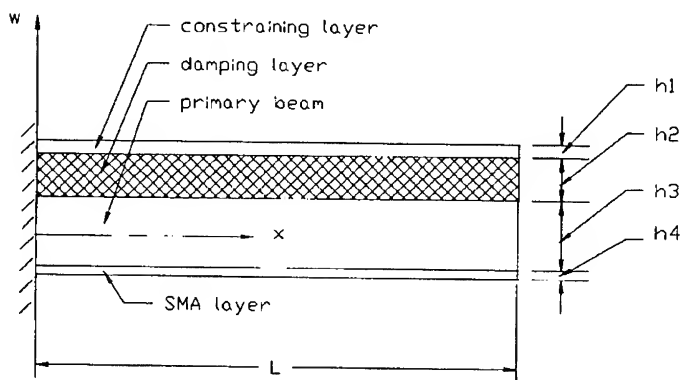


Figure 1 Cantilever beam with a constrained damping treatment and shape memory alloy.

$$\begin{aligned}
& \frac{D_t E_1 h_1 h_2 C_3}{G} \frac{\partial^6 w}{\partial x^6} - \left(D_t C_1 + E_1 h_1 d^2 C_2 C_3 - \frac{1}{2} E_a^* C_1 h_2 h_4 d \right) \frac{\partial^4 w}{\partial x^4} \\
& \quad - \frac{m}{b} \left(\frac{E_1 h_1 h_2 C_3}{G} \frac{\partial^4 w}{\partial x^2 \partial t^2} - C_1 \frac{\partial^2 w}{\partial t^2} \right) \\
& = - C_1 q(x, t) + \frac{E_1 h_1 h_2 C_3}{G} \frac{\partial^2 q}{\partial x^2} + (E_1 h_1 + 2 E_3 h_3) h_4 d \frac{\partial^2 \sigma_r^*}{\partial x^2} . \quad (1)
\end{aligned}$$

At $x = 0$ (the cantilever end):

$$w = 0 \quad (2)$$

$$\frac{\partial w}{\partial x} = 0 . \quad (3)$$

$$S = D_t \frac{\partial^3 w}{\partial x^3} . \quad (4)$$

At $x = L$ (the free end):

$$\begin{aligned}
& \frac{\partial^4 w}{\partial x^4} - \left(C_2 + \frac{C_1 C_4}{E_1 h_1 d C_5} \right) \frac{G d^2}{D_t h_2} \frac{\partial^2 w}{\partial x^2} + \frac{m}{D_t} \frac{\partial^2 w}{\partial t^2} \\
& - \frac{G d h_4}{D_t E_1 h_1 h_2} \left(\frac{d C_1}{C_5} - 1 \right) \sigma_r^* = 0 , \quad (5)
\end{aligned}$$

$$\begin{aligned}
& \frac{\partial^5 w}{\partial x^5} - \left(C^2 + \frac{C_1 C_4}{E_1 h_1 d C_5} \right) \frac{G d^2}{D_t h_2} \frac{\partial^3 w}{\partial x^3} + \frac{m}{D_t} \frac{\partial^3 w}{\partial x \partial t^2} \\
& - \frac{G d h_4}{D_t E_1 h_1 h_2} \left(\frac{d C_1}{C_5} - 1 \right) \frac{\partial \sigma_r^*}{\partial x} = 0 , \quad (6)
\end{aligned}$$

$$\frac{\partial^4 w}{\partial x^4} - \frac{G d^2 C_2}{h_2 D_t} \frac{\partial^2 w}{\partial x^2} + \frac{p}{D_t} + \frac{h_4}{D_t} \sigma_r^* = 0 . \quad (7)$$

where

$$\begin{aligned}
C_1 &= E_1 h_1 + E_3 h_3 + E_a^* h_4 \\
C_2 &= 1 - \frac{h_3 + h_4}{2d} \frac{E_a^* h_4}{E_1 h_1} \\
C_3 &= E_3 h_3 + E_a^* h_4 \\
C_4 &= D_t + \frac{1}{2} E_a^* (h_3 + h_4) d_1 h_4 \\
C_5 &= E_3 h_3 d + E_a^* d_1 h_4
\end{aligned}$$

b is the width of the beam; E_a^* , the Young's modulus of SMA; E_i , Young's modulus of the i th layer ($i=1,2,3$); $G=G_r(1+j\eta_c)$. G_r , the real shear modulus of the damping layer; $j=\sqrt{-1}$, thickness of the i th layer; L , the length of the beam; m , the mass per unit length of the beam; q , the applied transverse loading; w , transverse displacement; $d = h_2 + (h_1 + h_3)/2$; $D_t = (E_1 h_1^3 + E_3 h_3^3)/12$; and η_c , the loss factor of the damping material.

In order to discuss the effect of E_a^* on the resonant frequency and loss factor of the beam, we seek the homogeneous form of equation (1). We assume a solution in the form:

$$w = B e^{j\Omega t} e^{kx}, \quad (8)$$

where Ω and k are the unknown complex natural frequency and characteristic values.

Substituting equation (8) into (1) and also consider the boundary conditions, we obtain two non linear complex equations

$$\begin{aligned}
&\frac{C_3 D_t E_1 h_1 h_2}{G} k^6 - \left(D_t C_1 + E_1 h_1 d^2 C_2 C_3 - \frac{1}{2} E_a^* C_1 h_2 h_4 d \right) k^4 \\
&- m \Omega^2 \left(\frac{E_1 h_1 h_2 C_3}{G} k^2 - C_1 \right) = 0.
\end{aligned} \quad (9)$$

$$\det(\Omega, k) = 0. \quad (10)$$

NUMERICAL RESULTS

$b=0.05$ m, $L=0.5$ m, $h_1=0.02$ m, $h_2=h_3=h_1$, $E_1=20.6 \times 10^{10}$ N/m², $E_3=E_1$, $G_r / E_1=0.005$, $\rho_1=\rho_3=7850.0$ Kg/m³, $\rho_4=5632.0$ kg/m³, $\rho_c=3140.0$ Kg/m³.

Effect of the SMA Young's Modulus

The effect of the SMA layer's Young's modulus on the system frequency factor is shown in Figure 2. The frequency factor in the figure is the ratio of the real resonant frequency of the constrained SMA beam to the natural frequency of the original uncovered beam. For a very thin SMA layer, ($h_4/h_1 = 0.005$), the change of E_a^* will have negligible effect on the frequency factor. For $h_4/h_1 > 0.05$, the change of E_a^* will change the frequency factor. Since the natural frequency of a Euler beam is directly related to the flexural rigidity of the beam [16], an increase in rigidity implies an increase in the natural frequency. An increase of E_a^* will increase the flexural rigidity of the beam, and thus, the frequency factor. Hence, we can adjust the resonance frequency by changing the value of E_a^* , e.g., by changing the temperature of the SMA layer.

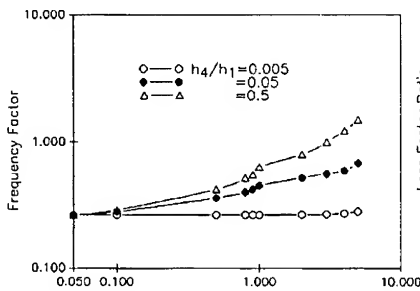


Figure 2 Frequency factor vs. E_a^*/E_1 .

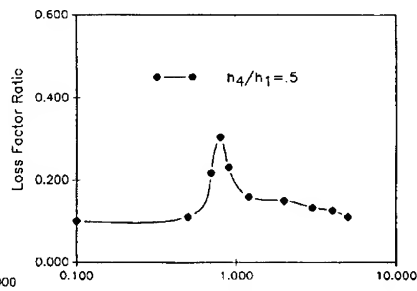


Figure 3 Loss factor ratio vs. E_a^*/E_1 .

Figure 3 shows the effects of the SMA layer's Young's modulus on the system loss factor. It may be seen that there exists an extreme value of the ratio, E_a^*/E_1 . At this value, the system loss factor is maximized. For the given data, the maximum system loss factor occurs near $E_a^*/E_1 = 0.9$.

CONCLUSIONS

The effects of different parameters found in the analysis lead to the following conclusions: 1) an increase of E_a^* will increase the frequency factor. Though h_4 is unchangeable after design, we can avoid resonance by actively adjusting the value of E_a^* ;

and 2) there exist optimal values of E_a^*/E_1 , which maximize the system loss factor. Thus, we can properly design the system (passively through the viscoelastic layer), or properly adjust the system (actively through the SMA layer) to damp the vibration of a given structure.

REFERENCES

1. E.M. Kerwin, *Journal of the Acoustical Society of America*, **31**, 952 (1959).
2. R.A. Ditaranto, *Journal of Applied Mechanics*, **87**, 881 (1965).
3. D.K. Rao, *Journal of Mechanical Engineering Science*, **20** (5), 271 (1978).
4. D.J. Mead, *Journal of Sound and Vibrations*, **83** (3), 3623 (1982).
5. D.J. Mead and S. Markus, *Journal of Sound and Vibration*, **10** (2), 163 (1969).
6. D. Xi, Q. Chen, and G. Cai, *Journal of Vibration, Acoustics, Stress and Reliability in Design*, **108**, 65 (1986).
7. Q. Chen and D. Xi, *Journal of Zhejiang University*, **21** (3), 32 (1987).
8. C. Levy and Q. Chen, accepted for publication by *Journal of Sound and Vibrations* (in press).
9. Q. Chen and C. Levy, *Int. J. Solids Structures*, **31**, (17), 2377 (1994).
10. W.J. Buehler and R.C. Wiley, U.S. Patent No. 3174851.
11. C.A. Rogers, C. Liang, and D.K. Barker, *Smart Material, Structures and Mathematical Issues*, Technomic, Lancaster, PA., 1989, 39.
12. C.A. Rogers, *Journal of the Acoustical Society of America*, **88** (6), 2803 (1990).
13. W.R. Saunders, H.H. Robertshaw, and C.A. Rogers, *Proceedings of the 31st Structures, Structural Dynamics and Materials Conference*, AIAA 90-1090 (1990).
14. C.A. Rogers, C. Liang, and C.R. Fuller, *Journal of the Acoustical Society of America*, **89** (1), 210 (1991).
15. W. Weaver, Jr., S.P. Timoshenko, and D.H. Young, *Vibration Problems in Engineering* (John Wiley & Sons, Inc., 1990).
16. Q. Chen and C. Levy, to be submitted to the *Journal of Dynamic Systems, Measurement, and Control*.

PART XII

Chemical Sensors

CHEMICAL MICROSENSORS FOR SATELLITE APPLICATIONS

B. H. Weiller, J. D. Barrie, K. A. Aitchison and P. D. Chaffee
The Aerospace Corporation, Mechanics and Materials Technology Center,
PO Box 92957/M5-753, Los Angeles, CA 90009-2957

ABSTRACT

We have been investigating several chemical microsensor technologies for the detection of chemicals found in propellant and rocket exhaust plumes and as contaminants for satellite components. In this work we have developed a catalytic metal sensor for the detection of H_2 contamination in electronic device packages. The sensor is based on the resistance of a thin film Pd/Ni alloy. Data have been obtained on its response at room temperature to various levels of H_2 as well as the effects of H_2O and O_2 on its performance. Hydrogen levels to 10.5 ppm have been detected and the responsivity is about twice that of similar sensors. The sensor is insensitive to H_2O but its response to H_2 is strongly inhibited by O_2 .

INTRODUCTION

The detection of chemical species has become increasingly important to the successful production, launch and operation of satellites. Many of the chemicals used or produced by launch vehicles are either highly toxic such as hydrazine (N_2H_4), nitrogen dioxide (NO_2), and hydrogen chloride (HCl) or explosive such as hydrogen (H_2) and are controlled by environmental regulations. Tracking plumes of these chemicals is expensive and labor intensive when standard analytical instrumentation is deployed in the field. Other needs for trace detection are in the areas of contamination of spacecraft optical and electronic components and the detection of propellant leaks in-flight. All of these applications would benefit greatly from inexpensive chemically specific sensors that could provide remote quantitative data on trace chemical concentrations. Not only would the ability to meet launch schedules be greatly improved but spacecraft functionality and lifetimes could be enhanced.

Chemical microsensors offer many benefits for these applications. These lightweight, miniature devices can be integrated with microprocessors and wireless communication to form intelligent sensors for autonomous health and safety monitoring of equipment and personnel. They consist of a transducer with a coating that selectively alters the transducer signal in response to the chemical of interest.¹ Chemically selective coatings are critical elements in all chemical microsensors and continuing research in this area is required to develop sensors for specific applications.

Examples of sensor technologies that have been useful to detect relevant species are chemiresistors, surface acoustic wave devices (SAW) and catalytic metal devices. Chemiresistors use microelectrodes to detect a change in resistance of a thin film of an organic semiconductor, such as a phthalocyanine² or a conducting polymer,³ and have been used to detect hydrazines and NO_2 . SAW devices are ultra-sensitive mass sensors that can be coated with materials like amines to adsorb molecules of interest (i.e. HCl).⁴ Perhaps one of the most well-developed chemical sensor technologies is the use of catalytic metals in MOS devices to detect H_2 .⁵ When Pd is used as the gate metal in these devices, H_2 is selectively dissociated to form the hydride. This reversibly changes the electrical characteristics of the device and creates a very sensitive detector for H_2 . More recently thin film, Pd-based chemiresistors were demonstrated to be effective sensors for H_2 .⁶ In this case the resistivity of the resulting hydride is greater than the initial metal film and can be used to monitor a wide range of H_2 concentrations. Here we have explored the suitability of this simple technology for the detection of H_2 contamination in microelectronic device packages.

A serious problem in the reliability of certain high speed GaAs devices is contamination by H_2 gas.^{7,8} In hermetically sealed device packages, large partial pressures of hydrogen have been found and apparently evolve from the metallic materials used in the packaging. Hydrogen has been suggested as the cause for the premature failure of these devices. One possible mechanism for this failure is that the Pt used in the metallization is catalytically active for the dissociation of H_2 to form a hydride which alters the device's performance.⁷ Another possibility is the formation of a

hydride or reduction of an oxide in other circuit components such as resistors.⁸ To confirm that H₂ is indeed responsible, we have developed and tested a Pd chemiresistor for *in-situ* detection of H₂ in these device packages. Furthermore, such sensors could be incorporated into the packages to serve as simple passive monitors for H₂ levels to verify their health prior to launch.

EXPERIMENTAL

Figure 1 shows a photograph of the sensor developed. It consists of thin films of Pd/Ni alloy deposited using RF planar magnetron sputtering from separate Pd and Ni targets. The deposition rate was 10 Å/min. and the film thickness was 500 Å as determined by quartz crystal monitors and confirmed by stylus profilometry. Film composition was measured by energy dispersive x-ray spectroscopy (EDX) of witness samples and determined to be 10.1 ± 0.5 % Ni. The pattern of stripes for resistance and dots for capacitance measurements was obtained by photolithography and liftoff. Gold contact pads (2000 Å thick) for wire bonding were sputtered onto the Pd/Ni using a separate mask. The substrate was a 2" diameter Si(100) wafer with 250 Å of thermal oxide. Testing of sensor response was performed using two separate apparatus, a flow cell for testing atmospheric pressure gas mixtures (obtained using flow meters and dynamic mixing) and a static cell for exposure to sub-atmospheric pressures of pure gases. Both cells are standard NW-40 crosses and both apparatus use a multimeter (HP 3478A) interfaced to a Macintosh computer with LabView software for data acquisition and automated testing. Two resistors on separate devices were tested, resistor A is 0.15 x 4 mm and resistor B is 0.15 x 2 mm.

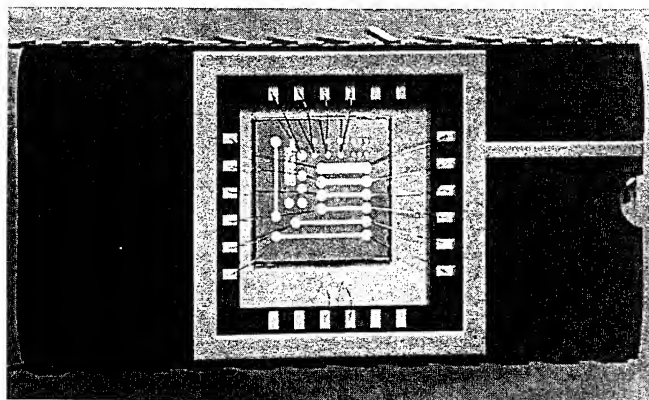


Figure 1. Photograph of the Pd chemiresistor developed for hydrogen detection.

RESULTS AND DISCUSSION

Figure 2 shows the response of resistor A to pressures of pure H₂ over the range from 1.1 to 82.9 torr. The data was taken in the static cell and similar data have been obtained at pressures as high as 1000 torr. When the percent change in resistance as a function of H₂ pressure is plotted, all of the points lie on a smooth curve showing that there is no hysteresis in the sensor response to varying levels of H₂. As shown in the figure, the response times to these concentrations of H₂ are quite fast, less than one minute. The temperature is ambient and at higher temperatures it should be possible to achieve faster response times.

Figure 3 shows the response of resistor B to varying levels of H₂ in the flow cell. Six hour time periods were used and the sequence of gas mixtures consisted of the following: 0, 1.00×10^3 , 0, 1.00×10^4 , 0, and 3.00×10^4 ppm H₂ in N₂ respectively. Note that the response to an increase

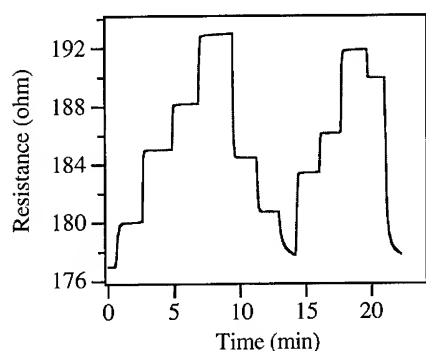


Figure 2. Response of the sensor to various pressures of pure hydrogen in the static cell. The pressures are as follows: 0.0, 1.1, 17.7, 38.9, 82.9, 13.8, 1.9, 0.0, 8.5, 23.5, 70.6 and 51.6 torr respectively.

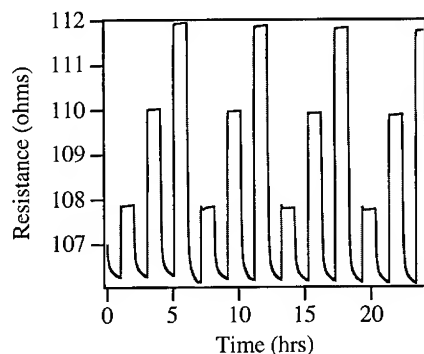


Figure 3. Response of the sensor to hydrogen in the flow cell. The sequence of gases is 0, 1.0×10^3 , 0, 1.0×10^4 , 0 and 3.0×10^4 ppm H_2 in argon buffer gas at a total pressure equal to ambient.

in H_2 at these levels is fast (less than 2-3 min.), but that the response to the purge is much slower. This may be due to the flow characteristics of the cell that lead to long purge times. Similar data was obtained over the range from 150 to 1000 ppm in a separate run. When this data is plotted as % change in resistance vs. H_2 together with the data from Figure 2, the points at 1000 ppm overlap showing good repeatability from different devices.

The ultimate sensitivity of the sensor will determine its effectiveness in monitoring H_2 contamination. Figure 4 shows the long term response of resistor B to cycling between high purity argon and a mixture of 10.5 ppm hydrogen in nitrogen in the flow cell. Drift in the baseline was observed (corrected in the figure) and is probably the result of the gradual purging of the experimental apparatus and temperature drifts. Given the relatively high signal-to-noise ratio of the data, once temperature compensation is incorporated into the device it should be possible to detect H_2 pressures down to 1 ppm. This would give a single sensor with a potential dynamic range of six orders of magnitude.

Figure 5 shows a plot of all data obtained from the different sensor elements, devices, apparatus and laboratories plotted on the same graph. Significantly all of the data lie on a smooth curve indicating that the sensor response is insensitive to variations in environment and data acquisition. Therefore the calibration for H_2 response should be robust and independent of experimental conditions. The form of the data in Figure 5 is similar to that obtained by Hughes and Schubert at Sandia for a similar device. As discussed elsewhere,⁹ the expected functional form for this data is $\Delta R/R \sim (pH_2)^{0.5}$. Hughes and Schubert found their data at room temperature fit the form $\Delta R/R = \alpha(pH_2)^\beta$, where $\alpha = 0.71, 0.29$ and $\beta = 0.39, 0.34$ for 8 and 15 % Ni-Pd respectively. Their data shows that the sensitivity for H_2 is greater for the sensor with less Ni. When our data is fit similarly, we find $\alpha = 1.7$ and $\beta = 0.37$ as shown by the solid line in Figure 5. Also shown is the fit to the Sandia data at 8% Ni. Surprisingly, our sensor with greater Ni concentration (10 %) is more than twice as sensitive as the Sandia sensor. We are currently studying our films to determine the source of this increased sensitivity. One possibility is that the different deposition techniques used (e-beam evaporation vs. magnetron sputtering) could result in a contamination or different morphology in the films.

A concern in the development of chemical sensors is the selectivity for the molecule of interest. The number of potential interferences is limited for the application of interest, especially if the devices are sealed in a controlled inert atmosphere. Water is a particular concern since as much as 5000 ppm are often observed in such packages. Therefore we examined the response of the sensors to this level of H_2O as shown in Figure 6. The response to 4.1 torr of pure H_2O (5395

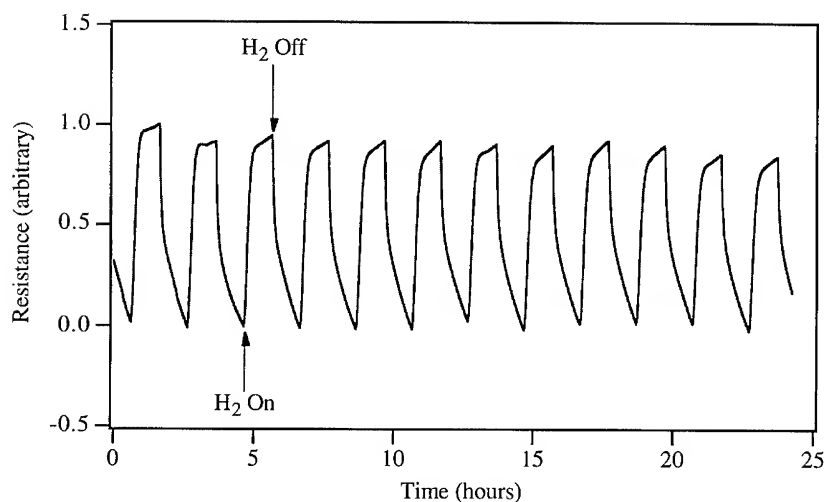


Figure 4. Response of the sensor to 10.5 ppm H_2 in the flow cell.

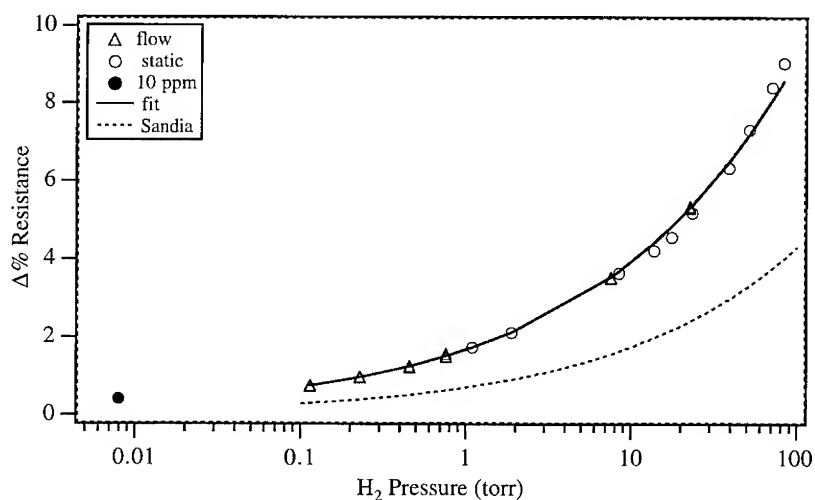


Figure 5. Combined response curve for data obtained in static and flow cells and for different sensor elements, devices, and background temperatures. The observation of a smooth response to all implies a robust calibration. Also shown is the response curve for a similar sensor developed at Sandia.

ppm, vapor pressure at 0 °C) is less than the observed response to 10 ppm H_2 . Alternatively stated, the sensor is more than 500 times more sensitive to H_2 than H_2O . A related concern is the potential inhibitory effect of H_2O on the H_2 response. As Figure 7 shows, the presence of this level of H_2O does not inhibit the response to H_2 .

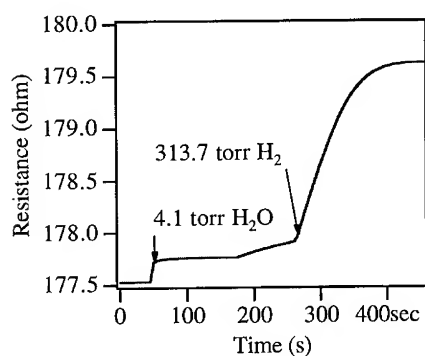


Figure 6. Response of the sensor to 4.1 torr H_2O . The response to 5400 ppm H_2O is less than the observed response to 10 ppm H_2 .

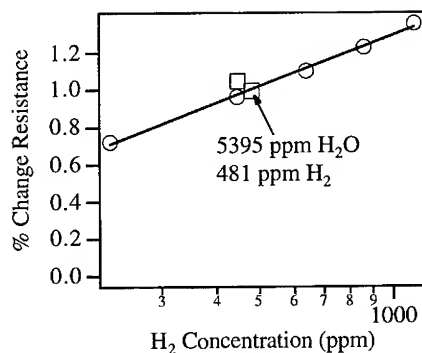


Figure 7. The response of the sensor to H_2 in the presence of H_2O , from Figure 6. No inhibition by H_2O is observed.

Others have noted that the response of Pd-based chemical sensors to H_2 is strongly affected by the presence of O_2 .⁵ It is believed that with O_2 , H_2O is formed catalytically thereby reducing the hydride concentration and the effective response to H_2 . Although there should be little O_2 present in the hermetically sealed packages, we have examined the effect of O_2 on the sensor response to a fixed level of H_2 (1000 ppm). Figure 8 shows the response at 0, 4 and 8 % O_2 and that significant inhibition is observed as expected. When the data are plotted in terms of the normalized $\Delta R/R$ vs. O_2 fraction, we see that 1 % O_2 gives a 10 % reduction in response while 8 % O_2 gives a 50 % reduction. Therefore in order to determine the H_2 concentration reliably, the O_2 concentration must be accurately known in the atmosphere to be tested. A simple solution to this issue would be to seal the device in a well-controlled, oxygen-free atmosphere. Alternatively, it may be possible to use a separate O_2 sensor or pattern recognition techniques to deconvolute the H_2 and O_2 concentrations.¹⁰

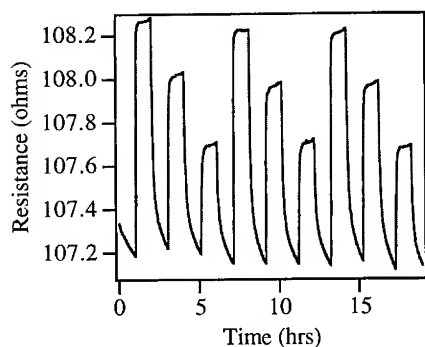


Figure 8. Effect of O_2 on sensor response. The H_2 concentration was held constant at 1000 ppm and various levels of O_2 were added: 0, 4 and 8 %.

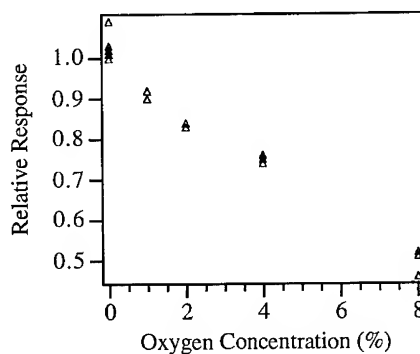


Figure 9. Inhibition of H_2 response by O_2 . Plotted as normalized % change in resistance.

CONCLUSIONS

Chemical microsensors have great potential to aid the launch, production and operation of satellites through the detection of chemicals ranging from propellants, exhaust species and contaminants. In this work we have developed a chemical sensor for the detection of H₂ contaminants in GaAs device packages. The sensitivity to H₂ at room temperature is at least 10 ppm and appears sufficient to detect concentrations of interest. The sensor is insensitive to H₂O but its H₂ response is strongly inhibited by O₂. Therefore oxygen must either be excluded from the packages during sealing or independently determined. If not then a separate *in-situ* oxygen sensor could be used or pattern recognition techniques could be developed to determine both the H₂ and O₂ concentrations. We are currently working on improving this sensor as well as detecting other chemicals with this and related technologies.

ACKNOWLEDGMENTS

The authors acknowledge the financial support of the Aerospace Sponsored Research Program. The authors also acknowledge helpful discussions with J. Hurrell at Aerospace and R. Hughes at Sandia National Laboratories.

REFERENCES

- 1) R. C. Hughes, A. J. Ricco, M. A. Butler, and S. J. Martin, *Science*, **254** 74 (1991).
- 2) J. W. Grate, S. Rose-Pehrsson, W. R. Barger, *Langmuir*, **4**, 1293-1301 (1988); A. W. Snow, W. R. Barger, M. Klusty, H. Wohltjen and N. L. Jarvis, *Langmuir*, **2**, 513-519 (1986).
- 3) M.R. Zakin, L. S. Bernstein and R. A. Moody, JANNAF Safety and Environmental Protection Sub-Committee Meeting, 1990, p. 121 -128, CPIA Publication #543.
- 4) W. D. Bowers, R. L. Chuan, and T. M. Duong, *Rev. Sci. Instrum.* **62**, 1624- 1629 (1991)
- 5) I. Lundstrom and C. Svensson, in "Solid State Chemical Sensors," J. Janata and R. J. Huber, eds, Academic Press, Orlando, FL, 1985.
- 6) R. C. Hughes and W. K. Schubert, *J. Appl. Phys.* **71** 542 (1992).
- 7) W. O. Camp, R. Lasater, V. Genova, and R. Hume, *IEEE GaAs IC Symposium* p. 203 (1989).
- 8) P. Schuesslar and D. Feliciano-Welp, *Hybrid Circuit Technology*, **8**, 19 - 26 (1991).
- 9) W. Auer and H. J. Grabke, *Ber. Bunsenges. Phys. Chem.* **78**, 58 (1974).
- 10) R. C. Hughes, D. J. Moreno, M. W. Jenkins, and J. L. Rodriguez, Solid-State Sensors and Actuators Workshop, 13- 16 June 1994, Hilton Head SC; report #SAND-94-0047C.

PART XIII

Late Papers Accepted

THERMAL AND X-RAY DIFFRACTION STUDIES OF DOPED AND UNDOPED SINGLE CRYSTAL AND POLYCRYSTALLINE BaTiO₃

L.G. CARREIRO*, J.V. MARZIK* and K.K. DEB**

*US Army Research Laboratory, Materials Directorate, Watertown, MA 02172

**US Army Research Laboratory, Infrared/Optics Technology Office, Fort Belvoir, VA 22060

ABSTRACT

Calorimetric changes in a series of pure and doped single crystal and polycrystalline BaTiO₃ were studied using differential scanning calorimetry over the temperature range of -110°C to 200°C. The dopants, oxides of niobium and iron were varied from 0.5 to 8 mole percent, and strontium was varied from 5 to 35 mole percent. Endotherms were observed corresponding to three crystallographic transitions. The highest observed thermal transition corresponds to a tetragonal to cubic crystallographic transition and is also associated with the Curie temperature in these materials. Two additional endothermic transitions were also observed, an intermediate-temperature orthorhombic to tetragonal transition, and a low-temperature rhombohedral to orthorhombic transition. The three dopants decreased the crystallographic transition temperatures and Curie temperature as the dopant concentration was increased. X-ray diffraction was used to identify phases present and to determine the extent of solid solution. It is expected that these materials will display improved infrared detection as well as opto-electronic properties.

INTRODUCTION

A ferroelectric is normally a spontaneously polarized material with its polarization reversible under an external electric field. Barium titanate is a perovskite ferroelectric with three possible orientations for the polar axis [1]. The large electro-optic effect displayed by single crystals of BaTiO₃ enables it to be used in photonic switching devices [2]. The storage of holograms using the photo refractive effect of undoped, and niobium- and iron-doped BaTiO₃ crystals has also been demonstrated [2-3]. Resolutions as high as 0.25 μm have been reported. The holograms of BaTiO₃ were comparable with those obtained for commonly used iron doped LiNbO₃ or (K,Ta) NbO₃ crystals [4]. The hologram characteristics were found to vary greatly with crystal quality and dopants. Barium strontium titanate is another interesting ferroelectric material for uncooled IR detectors [5]. This material typically operates near the phase transition temperature, with dc bias applied [6]. Therefore, it would be interesting to make a careful study of the variations of the Curie temperature (T_c) in BaTiO₃ single crystals with effects of doping with foreign ions. Although the effect of doping on the crystallographic transition temperatures of BaTiO₃ has been studied [7], little work has been reported for single crystal materials. For opto-electronic applications, single crystal materials are highly desirable. In this paper we report the effect of doping with Nb, Sr and Fe on the three crystallographic transitions of BaTiO₃ using differential calorimetric techniques and x-ray diffraction.

EXPERIMENTAL

Solid State Synthesis of Ceramic Powders

BaTiO₃ was prepared by treating a stoichiometric mixture of BaCO₃ and TiO₂ with concentrated nitric acid. The acid was added dropwise until a paste formed, and then the mixture

was fumed by gentle heating in a drying oven at 150°C for approximately 12 hours. The sample was allowed to cool, then ground in an agate mortar, transferred to an alumina crucible and heated in air at 600°C for 12 hours. The resulting product was allowed to cool, ground then reheated at 1200°C for a total of 72 hours. During the final heating period the sample was cooled and reground three times.

$\text{BaTi}_{1-x}\text{M}_x\text{O}_3$ ($\text{M} = \text{Nb}, \text{Fe}$) and $\text{Ba}_{1-x}\text{Sr}_x\text{TiO}_3$ were prepared according to the procedure described for barium titanate. Nb_2O_5 , Fe_2O_3 and SrCO_3 were used as dopants in these syntheses.

X-ray Analysis

Powder diffraction patterns of the products were obtained with a Philips diffractometer using a monochromated high intensity $\text{CuK}\alpha$ radiation ($\lambda = 1.5405 \text{ \AA}$). Patterns were taken from $12^\circ < 2\theta < 70^\circ$ and cell parameters were determined by a least squares refinement of the reflections.

Differential Scanning Calorimetry (DSC)

Transition temperatures associated with the three phase transitions were measured on a Perkin-Elmer DSC-4 TADS system following the procedure described in reference [6]. The temperature was controlled by a Perkin Elmer CCA7 cooling accessory.

RESULTS AND DISCUSSION

Niobium and Iron Doped Barium Titanate

DSC curves for single crystal and polycrystalline $\text{BaTi}_{1-x}\text{Nb}_x\text{O}_3$ are shown in Figures 1 and 2 respectively. The high temperature peak in each of the DSC curves is associated with a tetragonal to cubic (T-C) crystallographic transition. The lower temperature peaks are associated with an orthorhombic to tetragonal (O-T) transition. For pure barium titanate, the transition temperatures for the single crystal samples agreed very well with those observed in the polycrystalline sample, although peak broadening was observed in polycrystalline BaTiO_3 . In both the single crystal and polycrystalline samples the transition temperatures decreased with increasing amounts of Nb dopant (Figure 3). In the 3 mole% niobium doped polycrystalline material the O-T transition was not observed, and in the 5% and 8% niobium doped polycrystalline materials, no thermal transitions were observed, which may be attributed to a disorder effect. Cell parameters for the niobium-doped system are plotted in Figure 4. At dopant levels <3% the materials were slightly tetragonal. At dopant levels of 5% and 8% the x-ray diffraction patterns were indexed on the basis of a cubic cell.

Under the synthetic conditions investigated here, iron doping levels greater than 0.5% resulted in the crystallization of a second phase identified as the hexagonal polymorph of BaFeO_3 , and no thermal transitions were observed. However at the 0.5% iron dopant level, the material was single phase according to x-ray diffraction, and the T-C transition temperature was significantly shifted from 122°C to 95°C (see Figure 4).

Barium Strontium Titanate

DSC curves for the system $\text{Ba}_{1-x}\text{Sr}_x\text{TiO}_3$ are shown in Figure 5. For this system the thermal study was extended to lower temperatures so that in addition to observing the thermal transitions due to the T-C and O-T crystallographic transformations, a third thermal transition was observed at lower temperatures which is associated with a rhombohedral to orthorhombic (R-O) crystallographic transition. A plot of transition temperature vs strontium doping level is shown

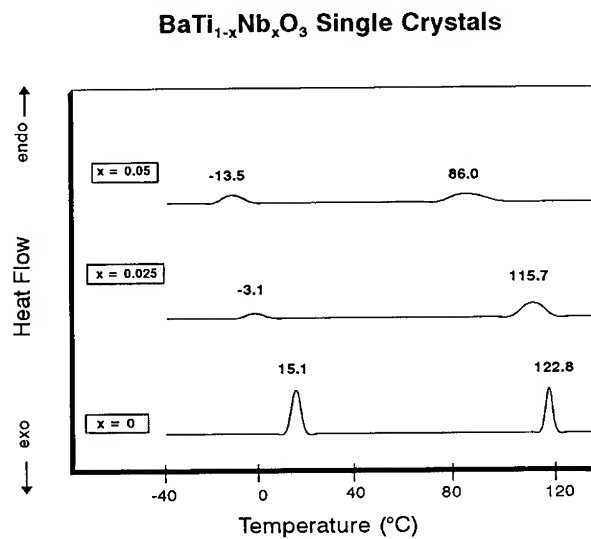


Figure 1. Differential scanning calorimetry (DSC) curves showing endotherms corresponding to crystallographic transitions in niobium-doped barium titanate single crystals

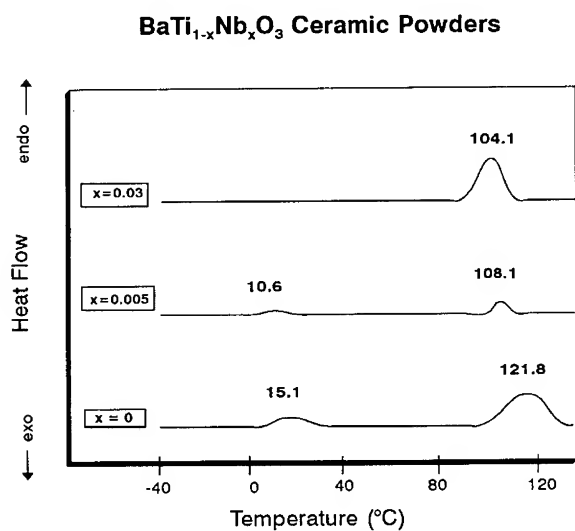


Figure 2. Differential scanning calorimetry (DSC) curves showing endotherms corresponding to crystallographic transitions in niobium-doped barium titanate powders

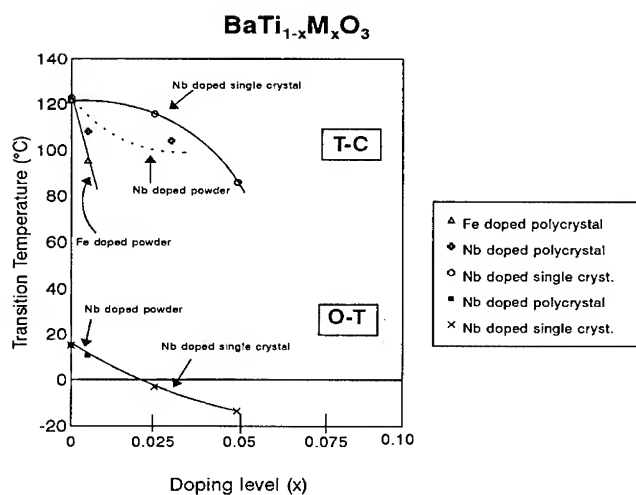


Figure 3. Crystallographic transition temperatures as a function of doping level in the system Ba_{1-x}M_xO₃. The upper family of curves corresponds to a tetragonal to cubic (T-C) transition. The lower curve corresponds to an orthorhombic to tetragonal (O-T) transition.

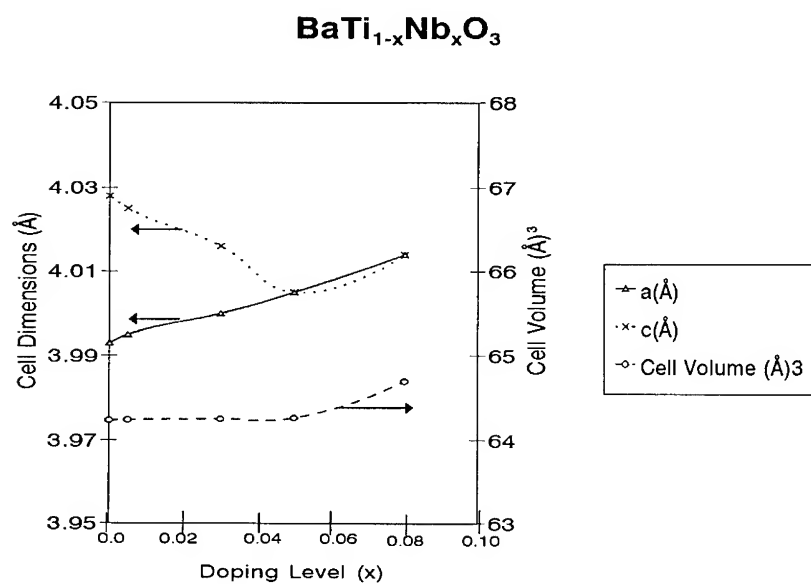


Figure 4. Cell parameters for the BaTi_{1-x}Nb_xO₃ system

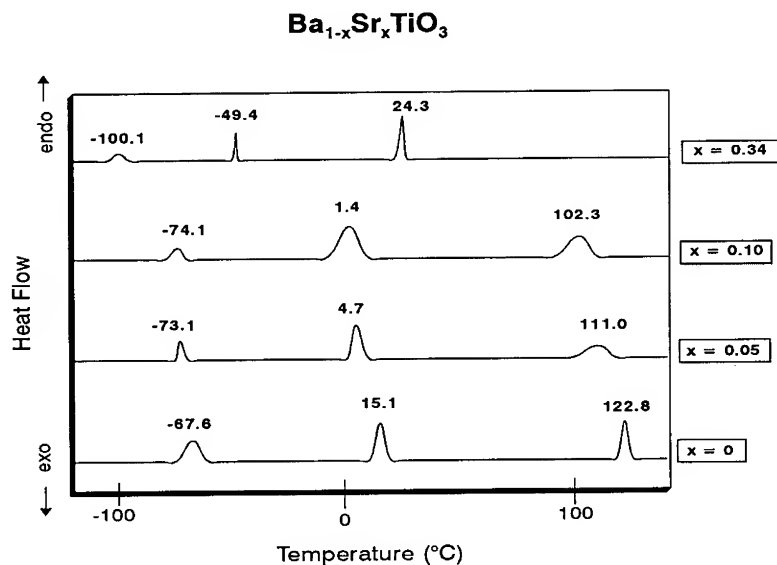


Figure 5. Differential scanning calorimetry (DSC) curves showing endotherms corresponding to crystallographic transitions in the barium strontium titanate system (Ba_{1-x}Sr_xTiO₃)

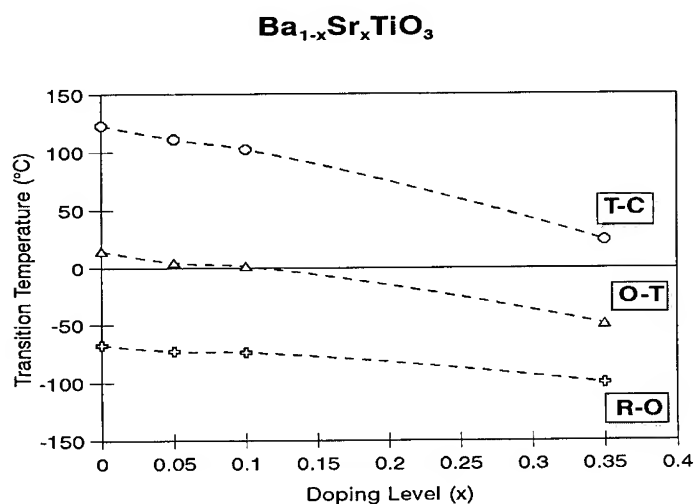


Figure 6. Crystallographic transition temperatures as a function of strontium doping level (x) in the system Ba_{1-x}Sr_xTiO₃. The upper curve corresponds to a tetragonal to cubic (T-C) transition; the middle curve corresponds to an orthorhombic to tetragonal (O-T) transition; the lower curve corresponds to a rhombohedral to orthorhombic (R-O) transition.

for the T-C, O-T and R-O transitions in Figure 6. Note that the T-C transition (and thus the Curie temperature) is approaching room temperature at the 35% doping level. The O-T and R-O transitions were also significantly shifted to negative values relative to undoped barium titanate. The observed shift of T_C to about 23°C with a strontium addition of 34 mol% is in good agreement with the data reported much earlier by Rushman and Strivens [8]. The present result also agrees with the T_C value recently determined from the variations of the pyroelectric coefficient and dielectric constant as functions of temperature [5,9]. However, we observe some discrepancies between our results and the data reported by Herbert [7]. For example, the author reported a T_C of about 0°C at a Sr concentration of 20 mol% in BaTiO₃ which represents a much faster shift of T_C than what was observed in our study.

CONCLUSION

A series of pure and doped single crystal and polycrystalline barium titanates were characterized using differential scanning calorimetry and x-ray diffraction. Small amounts of niobium and iron were substituted on the perovskite B site, while strontium was substituted on the A site. Three thermal transitions were observed in pure barium titanate corresponding to three crystallographic transitions. In all the compounds studied in this work, doping resulted in a controlled negative shift in the thermal transitions, thus enabling tailoring of these materials for infrared and opto-electronic applications.

REFERENCES

1. M.E. Lines and A.M. Glass, Principals and Applications of Ferroelectrics (Clarendon Press, Oxford, 1977), p. 244.
2. J.C. Burfoot and G.W. Taylor, Polar Dielectrics and their Applications (University of California Press, Berkeley and Los Angeles, 1979), p. 312.
3. R.E. Aldrich, F.J. Kroland and N.A. Simmons, IEEE Trans. Electron Devices, ED-20, 1015 (1973).
4. G. Monteme, M. Ingold, H. Looser and P. Gunter, Ferroelectrics, **92**, 281 (1984).
5. D.E. Witter, H.R. Beratan, B.M. Kulwicki and Ahmed Amin, Texas Instrument Technical Journal, **11**, 19 (1994).
6. A. Patel, D.A. Tossell, N.M. Shorrocks, R.W. Whatmore and R. Watton, Mater. Res. Soc. Proc., **310**, 53 (1993).
7. J.M. Herbert, Ceramic Dielectrics and Capacitors, (Gordon and Breach Science Publishers, New York, 1985), p. 151.
8. D.F. Rushman and M.A. Strivens, Trans. Faraday Soc. **42A**, 231 (1946).
9. K.K. Deb, M.D. Hill and J.F. Kelly, J. Mater. Res. **7**, 3296 (1992).

SHAPE MEMORY PROPERTIES OF AN IRON MODIFIED NICKEL ALUMINIDE ALLOY

J. A. Horton, C. T. Liu, and E. P. George
Metals and Ceramics Division, Oak Ridge National Laboratory
P.O. Box 2008, Oak Ridge, TN 37830-6115

ABSTRACT

The ordered intermetallic NiAl with aluminum levels near 36% undergoes a B2 to martensite transformation. Shape memory alloys based on NiAl+Fe have the potential for transition temperatures of greater than 150°C. While binary alloys appear inherently brittle, alloying with iron and boron results in two phase alloys with L1₂ and B2 phases and with about 7% room temperature tensile ductility. These alloys show a two-way shape memory effect over a range of transition temperatures with austenite peak temperature, A_p, between 100 to 200°C based on composition. Unfortunately, the B2 phase and its low temperature body centered tetragonal martensitic form are not stable and both can transform to Ni₃Al₃ with a loss in ductility. These alloys with a constant tensile load show a two way shape recovery of up to 0.6% during temperature cycling between 100 and 200°C. A thorough survey of the shape memory properties of one such alloy with a composition of Ni-25.5 Al-16 Fe-0.12 B (at.%) as a function of prior cold work, tensile loading and other training steps is presented. Nanoindentation was used to independently measure the mechanical properties of the two phases.

INTRODUCTION

Nickel-rich NiAl has been shown to have a thermoelastic martensitic transformation from the L1₀ to the B2 structure.¹ Only a small bending shape memory effect was found in the binary alloy due to its limited ductility.^{1,2} Iron additions result in improved ductility.^{3,4} Rapid solidification produces a ductile alloy with a quenched-in martensitic structure that showed some shape memory effect (SME).^{5,8} Later work found that with appropriate heat treatments and quenching procedures, cast material could be produced with room temperature ductility and SME.^{9,10}

Alloying NiAl with Fe and B results in a fabricable alloy with a room temperature ductility in excess of 7%.¹⁰ In the binary alloy, phase separation occurs during slow cooling, producing B2 and a metastable L1₀ phase. The L1₀ phase can transform to Ni₃Al₃ upon annealing below 700°C. Quenching suppresses the phase separation and results in a fully martensitic L1₀ structure. In the NiAl alloys with iron additions, annealing temperatures and quenching technique were optimized to produce a two-phase alloy consisting of approximately 5% L1₂ phase and the remainder an L1₀ martensite.¹⁰ Yang and Wayman¹¹ found that in specimens of Ni-25 Al-15Fe (at. %) annealed at 400°C, Ni₃Al₃ formation occurred more rapidly (one day) when the alloy was in the martensitic state than when it was in the austenitic state (one year).

EXPERIMENTAL PROCEDURE

Baseline properties were measured on a reference alloy, SMA-23, with a composition of Ni-25.5 Al-16 Fe-0.14 B (at. %). Previous reports concerned the microstructure and crystallography of the phase transitions,¹² alloying effects and processing conditions to produce a ductile alloy,¹⁰ and Al/Fe ratios vs. transformation temperatures.¹³

The alloy was arc melted as ≈400 g buttons in an argon atmosphere and drop cast into rectangular copper chill molds. The ingots were clad in stainless steel and hot rolled at 1000-1200°C at 15-20% reduction in thickness per pass to a final thickness of 1.3-1.9 mm. The sheets were annealed in flowing argon at 1300°C for one half hour and then oil quenched to room temperature. Sheet tensile specimens were electrodischarge machined.

The microstructures were examined by light microscopy, x-ray diffraction (XRD), and

transmission electron microscopy (TEM). XRD was carried out with Cu K α X-rays and a graphite diffracted-beam monochromator. TEM was carried out with a Philips CM30 operated at 300 kV with a GATAN heating stage. Heating to 200°C typically required only a few minutes to reach a point where the transformation was complete. Ductility measurements were made in a screw-driven Instron testing machine at a strain rate of $3.3 \times 10^{-3} \text{ s}^{-1}$.

Shape memory recoverable strain measurements were made with a constant tensile load in a modified creep frame using an LVDT for length measurement. A current of up to 12 amps was passed through the predeformed sheet tensile specimens for heating. Typical dimensions for the specimens were $3.17 \times 0.7 \times 25 \text{ mm}$. A chromel-alumel thermocouple spot welded to the center of the gage length was used with a standard temperature controller. Cycle times of 40 s were typically used to cycle from 100 to 200 and back to 100°C. The main disadvantage of this arrangement was the grip end cooling effects; when the center of the specimen was at 200°C, at some point near the grip ends the temperature was such that some transformation would still be in progress. While this effect widens the apparent transformation temperature range (hysteresis), the setup does mimic many potential applications for shape memory alloys where self heating is typically used.

Aging embrittlement was studied by aging x-ray specimens and narrow bend strips in air at 100 or 200°C. Ductility measurements, XRD and TEM were also done on specimens after up to two thousand constant load temperature cycles. Hardness and modulus data were determined using standard nanoindentation techniques.¹⁴

RESULTS AND DISCUSSION

An optical micrograph of the as quenched microstructure of the reference alloy SMA-23 is shown in Fig. 1. The alloy was annealed at 1300°C for 30 min. followed by an oil quench. TEM examination showed that the matrix was fully martensitic and the second phase had the L1₂ structure. Compositional analysis, Table I, by wavelength dispersive spectroscopy showed that the majority of the iron additions did remain in the matrix martensitic phase. Generally, as the level of iron was increased, the ductility of the alloy increased. The L1₂ phase did contain a larger percentage of iron, however, the amount of second phase was small enough so the iron level in the martensite was close to the nominal composition. The fracture mode generally changed from transgranular cleavage in the binary alloy to mixed intergranular fracture with higher iron levels. The iron additions appear to improve the cleavage strength. All of the alloys in Table I contained the same 300 wppm level of boron. The boron was added to improve the grain-boundary cohesion.

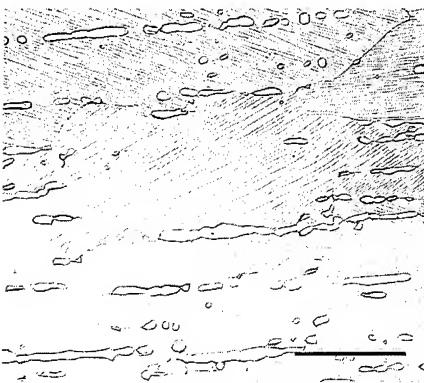


Fig. 1 Optical micrograph of Ni-25.5 Al-16 Fe-300 wppm B (SMA-23) after anneal for 0.5 hr at 1300°C and oil quenched. Scale marker is 50 μm .

The resistivity of Ni-40 Al is approximately 40 $\mu\Omega\text{-cm}$.¹⁵ This allowed direct joule heating of the specimens. Many shape memory actuators use direct resistance heating to control the shape memory element.

A typical shape memory effect measurement is shown in Fig. 2. A sheet tensile specimen was prestrained 2.1% at room temperature. A tensile load of 40 MPa was applied, a current was passed through the specimen to vary the temperature from 100 to 200°C at approximately 40 s per cycle and elongation was measured. The prestrain obviously elongated the specimen in the martensitic form. Upon heating the specimen changes to B2 and decreases in length. Note that the decrease in length due to the shape memory effect has to overcome thermal expansion of approximately 0.15%. In this example, the first cycle shows a larger one way effect as compared to the subsequent two way cycles. The austenite start temperature was 130°C, the austenite

Table I Compositions and Ductility as a Function of Iron Level*

		Ni	Al	Fe	ductility	fracture
SMA-11	nominal	63.7	28.3	8		
	martensite	63	29	8	brittle	mostly TG
	L1 ₂	69	23	8		
SMA-15	nominal	59	27	14		
	martensite	59	27	14	slight ductility	mostly IG
SMA-23	nominal	58.5	25.5	16		
	martensite	58	26	16	7%	
	L1 ₂	60	16	24		
SMA-17	nominal	56.1	23.9	20		
	martensite	57	24	19	12%	mixed
	L1 ₂	58	13	29		

*Compositions in at.%, determined by WDS, TG- transgranular, IG- intergranular

finish around 180°C and the martensite finish was around 110°C, all in close agreement to DSC results.¹³

The magnitude of the shape memory effect was measured as a function of prestrain, load and number of cycles. Fig. 3 shows an example of the shape memory recoverable strain as a function of the amount of prestrain. SMA-59 is a modified version of SMA-23. The optimum strain level was found to be between 1 and 2%. A prestrain of 5% would prevent a shape memory recovery. There is a steady decay or "loss of memory" as the specimens are cycled.

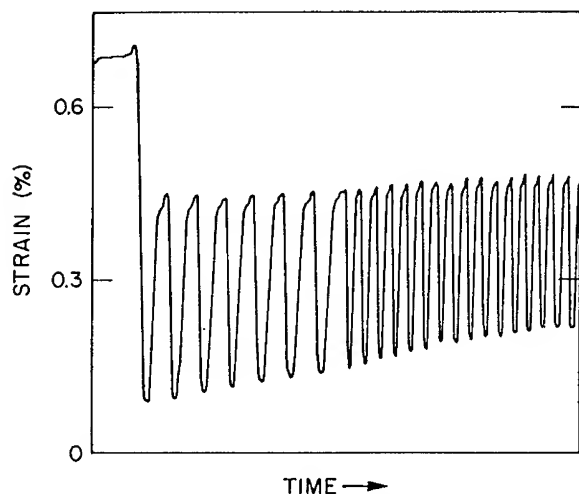


Fig. 2 Two way shape memory recovery in SMA-23 with a tensile load of 40 Mpa, prestrain of 2.1%, 100 to 200°C, resistively self heated, ≈40 s per cycle.

Fig. 4 shows shape memory recoverable strain as a function of load. The amount of shape memory recovery was relatively independent of load. This does show that the SMA-23 alloys could do work in a shape memory setting. Restraining, Fig. 5, results in some but not complete recovery of the shape memory effect. When a restrained specimen is cycled, a steady decay again continues. The example in Fig. 5 was strained 0.8% initially and then was deliberately restrained 0.45% at the 1000 cycle mark.

An in situ heating cycle was done in a TEM on a specimen that had had 2100 temperature cycles under load. At room temperature the specimen was fully martensitic and at 200°C the martensitic

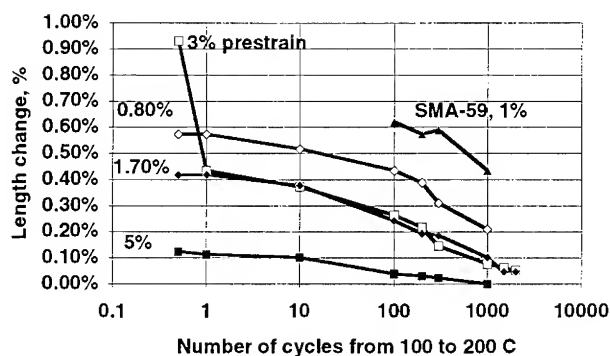


Fig. 3 Plot of amount of shape memory tensile recovery under load as a function of prestrain and number of cycles from 100 to 200°C.

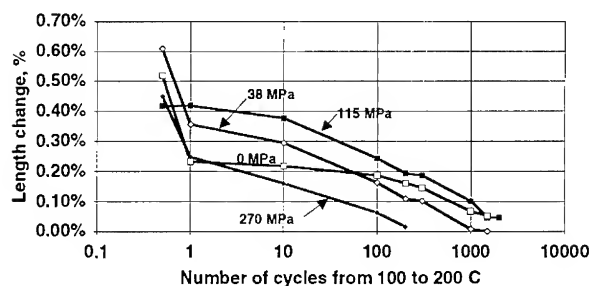


Fig. 4 Plot of amount of shape memory tensile recovery as a function of load and number of cycles from 100 to 200°C.

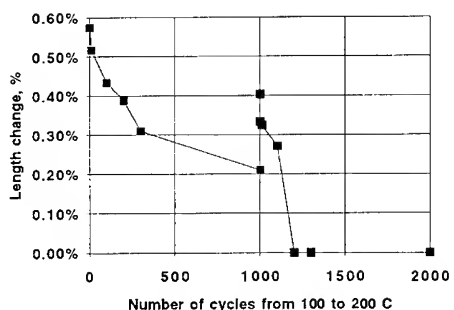


Fig. 5 Plot of amount of shape memory tensile recovery with a constant 60 lb load for a specimen that was prestrained 0.8% initially and then was restrained at 1000 cycles an additional 0.45%.

platelets did not completely disappear. Such cycling on a new specimen results in a complete martensite to B2 transformation in a matter of approximately 1 min. These results have been previously described.¹⁶ Figure 6 shows a TEM micrograph made at 240°C in a B2 region with a tweed appearance. During the heating cycle, the martensitic platelets mostly disappeared and this tweed structure was left. The tweed structure is presumably a precursor to formation of the Ni_5Al_3 phase.

Specimens were annealed in air at temperatures from 300 to 500°C and then strained to failure at room temperature. After 1 hour at 500°C or 10 hr at 400°C, the ductility dropped to about 1%, see Fig. 7. This corresponded with direct identification by x ray diffraction of the Ni_5Al_3 phase. Cycling under load was found to speed up the formation of Ni_5Al_3 as compared to the static anneals. One specimen was cycled 2100 times from 100 to 200°C in approximately 24 hrs under load and then strained to failure. The total strain to failure was 2.2% which includes the prestrain before the shape memory cycling, and some accumulated strain during the cycling under load. Static anneals showed a slight loss in bend ductility after 10 d at 100 or 200°C.

Load-unload, vs strain curves showed no hint of pseudoelasticity when tested at several temperatures relative to the martensitic transformation. Nanoindentation was done at room temperature on a metallographically polished specimen of SMA-23.

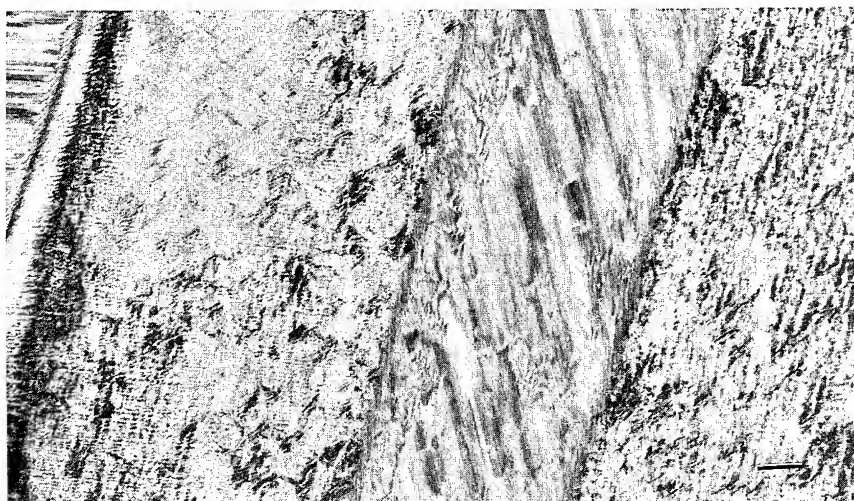


Fig. 6 TEM micrograph at 240°C of a specimen of SMA-23 after 2100 cycles. Upon heating in the TEM, the martensitic plates mostly disappeared. However, in some of these regions without martensite a tweed structure remained that is probably a precursor to Ni_3Al_3 formation. Scale marker is 100 nm.

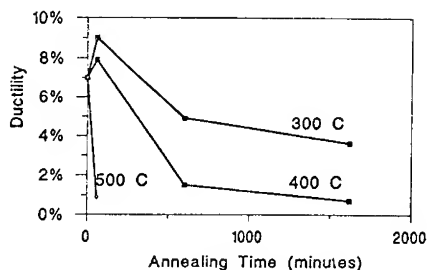


Fig. 7 Tensile ductility versus time and temperature for static anneals in air.

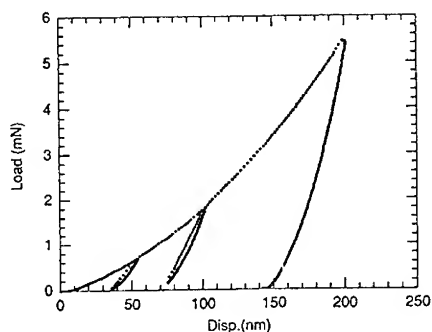


Fig. 8. Load displacement curve made by nanoindentation from the martensitic region. Similar curves for the L1_2 phase did not show the loops at the unload-reload points but instead traced out the same curve.

Table II shows the hardness and modulus data for the martensite and for the L1_2 phase. As expected the L1_2 phase is harder and stiffer. The load displacement curves from the nanoindentation showed an extra loop at each unload-load segment. This extra loop, see Fig. 8, was present in the martensite but not present in the L1_2 phase. The presence of the extra energy absorbed as represented by this loop is consistent with some pseudoelasticity in the martensitic phase. The lack of evidence of pseudoelasticity in the bulk alloy is also complicated by the hardening effects of the boron additions plus the two phase nature of the alloy.

Table II. Hardness and Modulus as determined by Nanoindentation¹⁷

	Hardness	Modulus
Martensitic Phase	5.7 GPa	155 GPa
L1 ₂ Phase	6.4 GPa	205 GPa

CONCLUSIONS

Iron and boron additions to Ni-36 Al results in a two phase alloy with an increase in ductility from near zero to approximately 7% room temperature ductility. Boron presumably increases the grain boundary strength while the iron additions improves the cleavage strength. The shape memory potential in the major martensitic phase could then be characterized and typically resulted in a two way shape recovery of 0.6% when the temperature is cycled from about 100°C to 200°C. Nanoindentation on the two phases showed a higher hardness and higher modulus in the L1₂ phase compared to the martensite. Cycling under a constant tensile load resulted in a steady decay of shape memory effect. Between one and two thousand cycles, the SME usually decayed to near zero, just offsetting thermal expansion. Alloy modifications have the potential for delaying this decay. However, the premature formation of Ni₃Al₃ and the resulting loss of ductility does limit the potential of the alloy for shape memory applications.

ACKNOWLEDGEMENTS

The authors would like to thank E. H. Lee, C. A. Carmichael, D. H. Pierce, J. L. Wright, for technical assistance and I. Vergara for the nanoindentation. Research sponsored by the Division of Materials Sciences, US Department of Energy, U. S. Department of Energy, under contract DE-AC05-84OR21400 with Martin Marietta Energy Systems, Inc.

REFERENCES

1. K. Enami and S. Nenno, *Metall. Trans.* **2**, 1487 (1971).
2. Y. K. Au and C. M. Wayman, *Scripta Metall.* **6** 1209 (1972).
3. J. A. Horton, C. T. Liu, and M. L. Santella, *Met. Trans. A*, **18A**, 1265 (1987).
4. S. Guha, P. R. Munroe, and I. Baker, *Proc. of MRS*, Vol. **133**, 633 (1989).
5. S. Furukawa, A. Inoue, and T. Masumoto, *Mats. Sci. and Engr.* **98**, 515 (1988).
6. M. Wallin, P. Johansson, and S. Savage, *Mat. Sci. Engr. A*, **133**, 307 (1991).
7. C.T. Liu, C.J. Sparks, J. A. Horton, E. P. George, and C. A. Carmichael, *Proc. of MRS*. Vol. **213**, 169 (1992).
8. D. S. Easton, C. T. Liu, J. A. Horton, E. P. George, and J. J. Campbell, *Proc of IUMRS* **8/93**.
9. K. Ishida, R. Kainuma, N. Ueno, and T. Nishizawa, *Metall. Trans. A*, **22A**, 441 (1991).
10. E. P. George, C. T. Liu, C. J. Sparks, M. Kao, J.A. Horton, H. Kunsmann, and T. King, *Proc. of MRS*. Vol. **246**, 121 (1992).
11. J. H. Yang and C. M. Wayman, *Intermetallics* **1**, 111 (1994).
12. J. A. Horton, E. P. George, C. J. Sparks, M. Y. Kao, O. B. Cavin, and P. Thoma, *Proc. of MRS*. Vol. **246** 61 (1992).
13. E. P. George, C. T. Liu, J. A. Horton, C. J. Sparks, M. Kao, H. Kunsmann, and T. King, *Mats. Char.* **32** 139 (1994).
14. W.C. Oliver and G.M. Pharr, *J of Mats. Res.*, **7**, (6), 1564 (1992).
15. H. Jacobi and H. -J. Engell, *Acta Metall.* **19**, 701 (1971).
16. J. A. Horton, C.T. Liu, and E. P. George, *Mats. Sci and Eng.* (in press)
17. I. Vergara, unpublished results.

Author Index

- Aburto, S., 281, 489
 Aitchison, K.A., 535
 Aoyagi, Manabu, 15
 Auyeung, R.C.Y., 395

 Barmatz, M., 253
 Barrie, J.D., 535
 Barrow, D.A., 103
 Bennett, J.W., 91
 Beyer, Jeno, 443
 Bouchilloux, Philippe, 265
 Braski, D.N., 139
 Brooks, K.G., 429

 Canales, A., 489
 Carosella, C.A., 395
 Carreiro, L.G., 543
 Chadi, J.D., 91
 Chaffee, P.D., 535
 Chang, Ching-Chao, 97
 Chang, Y.L., 183, 243
 Chen, Pu-Woei, 317
 Chen, Q., 527
 Chrisey, D.B., 395
 Chung, D.D.L., 317
 Claeysen, Frank, 265
 Clark, A., 253
 Clark, A.E., 213
 Clark, Arthur E., 171
 Claus, Richard O., 121
 Cooney, T.G., 401, 407
 Cross, L. Eric, 157

 Dai, Xunhu, 3
 Damjanovic, D., 389, 429
 Danai, P.A., 389
 Dartt, Christopher B., 359
 Davis, Mark E., 359
 De Graef, M., 189
 Deb, K.K., 127, 543
 Desu, S.B., 413
 Devlin, G.E., 91
 Dingquan, Xiao, 435
 Dogan, A., 33
 Donovan, E.P., 395
 Dooley, Jennifer, 189
 Du, H., 9, 77
 Duerig, T.W., 497

 Engdahl, 273
 Escudero, R., 281, 489

 Fanson, James L., 109
 Fernandez, J.F., 33
 Fielding, J.T., 33
 Forst, Donald, 3
 Fox, G.R., 389
 Francis, L.F., 401, 407
 Friend, Clifford M., 513

 Fujii, T., 347
 Furuya, Yasubumi, 519

 Gallois, B., 9, 77
 Garshelis, Ivan J., 219
 George, E.P., 549
 Ghorayeb, Solomon R., 259
 Giauque, P.H., 353
 Glumac, D.E., 401, 407
 Glumac, T.G., 401
 Goff, Edward D., 323
 Gómez, R., 281, 489
 Gong, Xiao-Yan, 83
 Grummon, David S., 369

 Hahn, Inseob, 253
 Hansen, T. Toby, 259
 Hey, Janet C., 483
 Hirose, Seiji, 15, 305
 Horton, J.A., 549
 Horwitz, J.S., 395
 Hou, Li, 369
 Huang, X.H., 243

 Igari, T., 347
 Inoue, M., 347
 Ishida, A., 381
 Ishida, K., 467
 Ishii, S., 347
 Ivshin, Yefim, 507

 Jan, Lijun, 77
 Jardine, A. Peter, 287, 293, 419, 483
 Jianguo, Zhu, 435
 Jiménez, M., 281, 489

 Kainuma, R., 467
 Kang, S.B., 77
 Karimi, A., 353
 Kholkin, A., 429
 Kim, Byung-Kook, 311
 Kim, T., 375
 Kohli, M., 429
 Kulesha, G.A., 9
 Ky, N.H., 389

 Lancto, R., 45
 Levy, C., 527
 Lhermet, Nicolas, 265
 Li, Jie-Fang, 3
 Li, Qiang, 183, 243
 Limberger, H.G., 389
 Lin, Dongliang, 479
 Lin, Hui, 479
 Linke, R.A., 91
 Lipe, T., 461
 Liu, C.T., 549
 Lonberg, Franklin, 97
 Lu, Guo-Quan, 145

- Luu, Thu-Van T., 213
- MacDonald, R.L., 91
 Maeder, T., 429
 Markowski, K.A., 33
 Marquina, M.L., 281, 489
 Marquina, V., 281, 489
 Martin, J.L., 353
 Marzik, J.V., 543
 Matsui, Yoshikazu, 53
 May, Russell G., 121
 Mercado, Peter G., 287, 419
 Meyer, Robert B., 97
 Miesner, John E., 249
 Miyazaki, S., 381
 Mizuta, M., 91
 Morales, F., 281, 489
 Morgan, Neil B., 513
 Morris, M.A., 461
 Mulder, Jan H., 443
 Mural, P., 429
- Nakamura, Kiyoshi, 21
 Newnham, R.E., 33
 Ngo, E., 45
- O'Day, M.E., 45
 Ono, N., 467
 Osborne, N.R., 139
 Ottova, A. Leitmannova, 339
 Ouyang, Shixi, 183, 243
- Park, Jae-Hwan, 311
 Park, Soon Ja, 311
 Pence, T.J., 369
 Petroff, T.E., 103
- Restorff, J.B., 213
 Ridaura, R., 281, 489
 Ríos-Jara, D., 281, 489
 Robbins, W.P., 401, 407
 Roytburd, Alexander L., 151, 299
 Russell, Scott M., 455
- Sasada, Ichiro, 231
 Sasaki, Yasuhiro, 305
 Sato, M., 381
 Savage, H.T., 201
 Sayer, M., 103
 Schachner, Kurt D., 507
 Schinazi, Robert G., 145
 Schindler, Paul M., 121
- Setter, N., 389, 429
 Sevvick, E.M., 329
 Sczerzenie, Frank, 455
 Sengupta, L.C., 45, 413
 Sengupta, S., 413
 Shaw, John K., 121
 Shiokawa, Showko, 53
 Siao Song, Du, 435
 Slutsker, Julia, 299
 Smits, J.G., 395
 Spaepen, Frans, 145
 Stowell, S., 45, 413
 Su, Quanmin, 195, 375
 Sun, Baode, 479
 Sun, James T., 359
- Takahashi, Sadayuki, 15, 305
 Takei, A., 381
 Teter, Joseph P., 249
 Thakoor, A.P., 157
 Thakoor, Sarita, 157
 Thio, Tineke, 91
 Thoma, Paul E., 507
 Tibergh, H., 273
 Tien, H. Ti, 339
 Tomikawa, Yoshiro, 15
- Uchino, Kenji, 15, 305
- Viehland, Dwight, 3
 Vijay, D.P., 413
- Wallis, J., 33
 Weber, Robert J., 323
 Weiller, B.H., 535
 Wen, Zhang, 435
 Williams, D.R.M., 329
 Wise, Vivienne D., 513
 Wun-Fogle, Marilyn, 201, 213
 Wuttig, Manfred, 195, 375
- Yamada, Ken, 21
 Yang, Z., 77
 Yoshida, T., 65
 Yu, Yongsik, 151
 Yuan, R.Z., 183
- Zheng, Y., 195
 Zhenghong, Qian, 435
 Zhou, Yaohe, 479
 Zhuang, Zhiqiang, 9, 77
 Zurbuchen, J.M., 139

Subject Index

- accelerometer, 201
- activation energies, 461
- active control, 519
 - mirror, 109
- actuators, 273, 375
 - ceramic, electrostrictive, 83
 - cyclic, 497, 513
 - design, 513, 519
 - electrostrictive, 77, 109
 - embedded, 513
 - high precision, 243
 - magnetostrictive, 171, 195
 - piezoelectric, 21, 33
- amorphous films, 347
 - magnetoelastic alloys, 201
 - metallic ribbons, 213
- angular velocity sensor, 65
- antiferroelectric, 3
- antiresonance, 15
- Auger analysis, 401
- B2 order, 461
- back-propagation network, 121
- barium strontium titanate, 45, 413
- BaTiO₃, modified, 127
- biocompatibility, 497
- biomechanical, 369
- biosensor, 339
- bipolar, 311
- buffer layer, 401
- calcium doping, 9
- capacitors, 45
- carbon
 - dioxide, 359
 - fibers, 317
- chemical microsensors, 535
- chemiresistor, 535
- circumferentially field annealed, 213
- composites, 45, 375, 413, 513
- concrete, 317
- constrained viscoelastic layer, 527
- control, 507
- Cu-Al-Ni, 461
- damage assessment, 317
- damping, 195, 353, 467, 527
- data storage, high-density, 91
- deformation, 151
- detectors, 435
- devices, 91, 103
 - contamination, 535
- dielectric loss, 127, 429
 - permittivity, 429
- domains, 189, 299
 - ferroelectric, 9
 - inversion, 21
- ductility improvement, 467, 479
- durability, 513
- DX centers, 91
- dye-dispersed, 97
- electrical properties, 395, 413
- electro-mechanical, 305
- electrode degradation, 401
- electrostrictive, 249
- equivalent circuit, 65
- erasable submicron devices, 91
- extension springs, 507
- Fe₈₀B₂₀, 347
- feedback, negative, 97
- ferroelectric, 3, 9, 151, 157, 419
 - inversion, 21
- ferromagnetic, 151, 353
- fiber coatings, 389
- fiber-reinforced composite, 519
- finite element analysis, 83, 407
- flexible cantilever beam, 527
- fluid pump, 53
- force sensors, 231
- GaAs device contaminations, 535
- green density, 483
- heat treatment, 381
- helix pitch, 97
- heterostructures, 419
- high-power characteristics, 15
- Hubble telescope, 109
- hydrogen sensor, 535
- hysteresis, 231, 353
- intelligent material, 519
- interactive operation, 507
- interdigital electrodes, 65
- ion beam assisted deposition, 395
- ionic structure, 139
- Kerr effect, 353
- La doping, 479
- Laves phase, 183
- layer composite, 151
- lead
 - magnesium niobate, 77
 - titanate, 3, 9
 - zirconate titanate, 77, 419, 429
- linear motors, 249
- lipid bilayer, 339
- liquid crystal, cholesteric, 97
- LiTaO₃, 21
- Lorentz TEM, 189
- low-temperature valve, 253

- magnetic domains, 353
 - field sensors, 201
 - softening, 347
 - susceptibility, 281, 489
- magnetics, 249
- magnetoelastic, 219
- magnetomechanical, 213
- magnetostriction, 171, 249, 259, 265, 347
- magnetostrictive devices, 249
 - actuators, 171, 195
 - effect, 231, 243
 - materials, 183, 273
 - valve, 253
- magnetron sputtering, 201
- martensite, 381, 479
- mechanical
 - properties, 151, 375
 - stability, 455
- medical applications, 497
- melt spinning, 281, 479
- membranes, 339, 429
- memory capacitors, 157
- metallic patterns, 91
- micro-
 - electric machine systems (MEMS), 395, 407
 - micro-tubes, 389
- microactuator, 401
- microflow, 317
- micromotors, 429
- micropositioning, 243
- microstructural control, 467
- microvalve, 329
- microwave resonator, 323
- modelling, 323
 - mathematical, 527
- modulus, elastic, 527
- molecular devices, 339
- Mössbauer spectroscopy, 281, 489
- neural network, 121
- Ni-Al-Fe, 467
- Ni-Al-Mn, 467
- Ni-Fe-Al-B, 281
- Ni-X(Pt,Pd,Au), 443
- NiAl, 443, 455, 467, 479
- nickel-iron-manganite, 139
- NiTi, 109, 311, 369, 375, 381, 419, 483
- NiTiHf, 455
- Nitinol, 497
- noise, 353
- optical
 - diffraction, 91
 - interferometry, 429
- oxide composites, 413
- palladium, 535
- persistent photoconductivity, 91
- personal environments, 507
- phase
 - stability, 455, 461
 - transformations, 299, 489
- phased array antennas, 45, 413
- photoresponse, noninvasive, 157
- physical properties, 151
- piezocomposites, 33
- piezoelectric, 103, 323, 389, 395, 429
 - actuators, 21, 33
 - anisotropy, 9
 - ceramic cylinder, 65
 - ceramics, 305, 407
 - materials, 15
 - sensors, 35
- planetary camera, 109
- plasma spraying, 353
- Poisson's ratio, 329
- polarization, reversal, 21
- polyimide, 369
- polymer brushes, 329
- polymeric substrates, 369, 381
- polysilicon, 407
- porous microstructures, 483
- powder metallurgy, 483
- pseudoelasticity, 467
 - applications, 497
- pulsed laser deposition, 395
- pyroelectric, 435
 - coefficient, 127
- PZT, 389, 401, 407
- R-phase, 381, 489
- rapid solidification, 201
- rare earths, 171
- reflector, 97
- residual strains, 311
- resonance, 353
 - frequency, 527
- resonant bar, 353
- responsivity, 435
- reversibility, 461
- sandwich films, 347
- satellites, 535
- SAW, 53, 359
- sensor, hydrogen, 535
 - strain, 121
 - micro, 535
 - torque, 231
- sensors, 359
 - magnetomechanical, 219
 - piezoelectric, 33
- shape memory
 - alloys, 281, 287, 369, 375, 419, 443, 455, 467, 483, 489, 497, 507, 513, 519, 527
 - applications, 497
 - cost, 455
 - fabricability, 443, 455
 - high-temperature, 443, 455, 467
 - behavior, 381
 - composites, 513
 - properties, 443
 - springs, 507
- shear characterization, 265
- signal transduction, 339
- silicon nitride, 401, 407

single crystal, 183, 243
 smart composites, 513, 519
 sol gel, 103, 419
 sputter deposition, 293
 sputtering, 389, 369, 381
 stents, 497
 strain hysteresis, 77
 electric-field-induced, 3, 311
 mismatch, 513
 sensors, 121
 streaming force, 53
 stress-strain curve, 299
 stresses, 83
 superconductor, 323
 superfluid, 253
 switching behavior, 77
 system loss factor, 527

 tactile feedback, 497
 $\text{Tb}_{0.27}\text{Dy}_{0.73}\text{Fe}_{1.95}$, 243
 $\text{Tb}_{40}\text{Fe}_{60}$, 347
 $\text{Tb}_x\text{Dy}_{1-x}\text{Fe}_{1.95}$, 183
 terfenol, 189, 195, 265
 thermal aging, 139
 thermistor, 139
 thermocouples, refractory, 145
 thermoelastic martensite, 443
 thermoelectric, 145
 thick PZT film, 103

 $\text{Ti}_{50}\text{Ni}_{50-x}\text{Fe}_x$, 489
 thin film, 195, 287, 369, 375, 413, 419, 435
 $\text{Ti-Ni-X}(\text{Zr}, \text{Hf})$, 443
 torque sensors, 231
 torsion pendulum, 353
 transduction, 171
 transformation, 461
 transmission line, 323

 ultrasonic, 259
 unipolar, 311

 varistors, 45
 vibration, 195, 353
 control, 171
 level change, 305
 water drop, 53
 vibratory gyroscope, 65

 water vapor, 359
 wide field camera, 109

 x-ray photoelectron spectroscopy (XPS), 139

 Young's modulus, 299

 zeolites, 359
 ZnO, 389, 395